THE NATURE AND ORIGIN OF THE ~1880 MA CIRCUM-SUPERIOR LARGE IGNEOUS PROVINCE

Matthew John Minifie

Submitted in partial fulfilment of the requirements for the degree of Ph.D.

December 2010

ProQuest LLC
789 East Eisenhower Parkway
P.O. Box 1346
Ann Arbor, MI 48106-1346

DECLARATION

This work has not previously been accepted in substance for any degree and is not concurrently submitted in candidature for any degree.

Signed ..... (candidate)
Date ....1/12/10....

STATEMENT 1

This thesis is being submitted in partial fulfilment of the requirements for the degree of PhD.

Signed ..... (candidate)
Date ....1/12/10....

STATEMENT 2

This thesis is the result of my own independent work/investigation, except where otherwise stated.

Other sources are acknowledged by explicit references.

Signed ..... (candidate)
Date ....1/12/10....

STATEMENT 3

I hereby give consent for my thesis, if accepted, to be available for photocopying and for inter-library loan, and for the title and summary to be made available to outside organisations.

Signed ..... (candidate)
Date ....1/12/10....

STATEMENT 4

I hereby give consent for my thesis, if accepted, to be available for photocopying and for inter-library loans **after expiry of a bar on access previously approved by the Graduate Development Committee**.

Signed ..... (candidate)
Date ....1/12/10....

ABSTRACT

The Circum-Superior Large Igneous Province (LIP) consists predominantly of ultramafic-mafic lavas and sills with minor felsic components distributed as various segments along the margins of the Superior Province craton. Ultramafic-mafic dykes and carbonatite complexes of the LIP also intrude the more central parts of the craton. Most of this magmatism occurred at ~1880 Ma. Previously a wide variety of geodynamic settings have been proposed for the different segments of the Circum-Superior LIP with the upper mantle as the source of magmatism.

New major and trace element and Sr-Nd-Pb-Hf-Os isotopic data reveal that the segments of the Circum-Superior LIP can be treated as a single entity formed in the same tectonomagmatic environment. In contrast to most previous studies, the Circum-Superior LIP is interpreted to have formed from a single mantle plume and this is consistent with the high MgO and Ni contents of magmas, oceanic-plateau-like incompatible trace element profiles, ocean-island-like positive Nb-Ta anomalies, Icelandic plume-like Nb/Y and Zr/Y ratios, oceanic-plateau-like Zr/Nb and Nb/Th ratios and Nd-Hf isotopic compositions which differ from that of the estimated depleted upper mantle at ~1880 Ma. Further support for a mantle plume origin comes from calculated high degrees of partial melting, high mantle potential temperatures and the presence of a radiating dyke swarm. The location of most of the magmatic rocks along the Superior Province margins probably represents the deflection of plume material by the thick cratonic keel towards regions of thinner lithosphere at the craton margins.

There is no obvious geochemical distinction between segments of the Circum-Superior LIP which host ore deposits and those which do not. The geochemistry of the Circum-Superior LIP differs markedly from that of other ~1880 Ma igneous provinces on other cratons which questions the validity of the formation of a very large LIP and the occurrence of a superplume event at ~1880 Ma.

ACKNOWLEDGEMENTS

I would like to first say a big thank you to my supervisors, Andrew Kerr, Julian Pearce and Richard Ernst, for all their help and advice over the last four years. In particular, Andrew has been very kind and helpful to me over the last few years and has always made time for my silly questions, not just throughout my PhD but also during my undergraduate days at Cardiff. I thank Richard for his efforts in helping me obtain samples for this project as well as for providing me with accommodation and showing me the sights during my stay in Ottawa. I'd also like to thank Alan Hastie who has always made time available to help me despite not being one of my official supervisors and being under no obligation to do so. Claude Herzberg has also been a big help with his guidance on the PRIMELT2 software and other petrological matters.

I owe a large debt of gratitude to Bob Baragar, Guy Desharnais, Don Francis, Henry Halls, Larry Hulbert, Steve Kissin, Andre Lalonde, Jim Mungall, Steve Sheppard, Rajesh Srivastava and Vince Vertolli for allowing me to use some of their samples in this study. I am very grateful to Andrey Bekker, Gerry Benger, Ken Buchan, Bill Cannon, Tim Corkery, Peter Dahl, Norman Halden, Richard Herd, Garth Jackson, Dan Layton-Matthews, Mike Lesher, Richard Ojakangas and Sally Pehrsson who were very helpful to me in my attempt to obtain samples for this study. I also thank Steve Kissin, Jenny Moss and Ben Rabb who were kind enough to assist me in the field.

Iain McDonald and Ley Woolley were extremely efficient at running hundreds of sample solutions on the mass spectrometers at Cardiff and very kind to teach me the methods for sample preparation in the geochemistry laboratory. I thank Iain McDonald, Tony Oldroyd, Tom Gregory, Iain Neill and Heather Birch for being my 'HF-buddies' in the many attempts it took to get the HF-HNO_3 acid digestion method to work. Pete Fisher was of invaluable assistance during my time on the SEM. Lawrence Badham and Peter Greatbatch were also kind enough to produce hundreds of polished thin sections.

I am indebted to Ian Millar who allowed me to prepare samples for Sr-Nd-Pb-Hf isotopic analysis at NIGL. Without Ian I would not have been able to do this and I thank him for his supervision and for running the samples on the various mass spectrometers at NIGL. Dennis and Kath Oakley were kind enough to accommodate and entertain me during my stay in Keyworth. I also owe a large thank you to Ian Parkinson and Marc Davies who supervised me in the laboratory at the Open University whilst I prepared samples for Os isotopic analysis and who also allowed me to run some of the samples on the expensive mass spectrometer there. Pierre Bonnand very kindly provided me with free accommodation for my visit to Milton Keynes.

My officemates Chris Brough, Kerry Howard, Caroline Johnson and Iain Neill deserve a big thank you for putting up with me for the last few years and for entertaining non-work-related discussions. I also thank Tracy Aze, Heather Birch, Jake Ciborowski, Laura Cotton, Andy Gray, Tom Gregory, James Griffiths, Alan Hastie, Falko Mathes, Elaine Mawbey, Paola Moffa Sanchez, Jenny Moss, Ben Rabb, Ben Saunders, Luca Traverso, Peter Webb and Martin Wolstencroft for their moral support mainly in the form of coffee drinking and football playing/watching. A big thank you also to my family for their moral and financial support over the last few years.

I acknowledge the funding for this project from NERC (studentship number NER/S/A/2006/14009) and a small contribution from BHP Billiton. Small additional travel grants from the Geochemical Society, the Mineralogical Society of Great Britain and Ireland and the Volcanic and Magmatic Studies Group to attend conferences are greatly appreciated.

CONTENTS

LIST OF FIGURES

LIST OF TABLES

1. INTRODUCTION

1.1. Project rationale

Large igneous provinces (LIPs) have erupted throughout Earth's history (Ernst & Buchan, 2001a; see also the Large Igneous Provinces Commission website http://www.largeigneousprovinces.org) and consist of large volumes (>0.1 × 10^6 km^3) of predominantly mafic magmatism, most of which is emplaced over a relatively short time period (~1-5 m.y.) via mechanisms that are distinct from normal sea floor spreading and subduction-related processes (Coffin & Eldholm, 1991, 1992, 1993a, 1993b, 1994; Bryan & Ernst, 2008; Heaman, 2008). Although most LIPs are comprised of mafic igneous rocks, some LIPs also contain significant ultramafic and felsic components (Bryan & Ernst, 2008). Ernst et al. (2004) have proposed a global campaign to study LIPs with a particular focus on the geochronology, palaeomagnetism and geochemistry of LIPs in order to fully characterise and better understand their origin as well as using LIPs as tools for palaeocontinental reconstructions.

The Circum-Superior LIP is a less-well known LIP of Palaeoproterozoic age located in and around the Superior Province craton of the Canadian Shield. The Circum-Superior LIP has no known Phanerozoic analogue as the igneous rocks which constitute this province occur in segments which are widely distributed around the margins of the Superior craton as well as within the interior of the craton (Chapter 2 describes the geology of the Circum-Superior LIP in more detail) and it is only recently that these igneous rocks have been classified as a LIP (Ernst, 2004; Ernst & Buchan, 2004; Bryan & Ernst, 2008). Prior to this study, only a few segments of this LIP have been studied geochemically and there are very little data in the literature obtained using modern analytical techniques. The tectonomagmatic environment of formation of the igneous rocks of the Circum-Superior LIP is far from clear with previous models suggesting a range of settings such as mid-ocean ridge spreading, back-arc basin rifting, foredeep basin flexing, arc volcanism and mantle plume volcanic activity. Until recently, previous interpretations of the nature and origin of the various segments of igneous rocks have not considered the Circum-Superior LIP as a single entity. The most recent studies tentatively link the various segments of the

Circum-Superior LIP as a single province and suggest an upper mantle origin for these rocks (French et al., 2008; Heaman et al., 2009). This study represents the first attempt at characterising the geochemistry and isotopic composition of all the segments of the Circum-Superior LIP and assessing whether their mode of formation and petrogenesis is consistent with derivation from a mantle plume.

A clearer understanding of the petrogenesis of the Circum-Superior LIP is important because large Ni, Cu and platinum group element (PGE) deposits are found within certain areas of this LIP but are absent in others. This provides a good opportunity to assess the effects of mantle sources and magmatic processes in the generation of Ni-Cu-PGE ore deposits. The Circum-Superior LIP is also interesting as it temporally correlates with a period of enhanced crustal growth (Condie, 2000) and a major environmental crisis represented by enhanced black shale deposition, a high chemical index of alteration for shales, an increased amount of preserved intracratonic, passive margin and platform sediments, a low in the $^{87}Sr/^{86}Sr$ isotopic ratio of seawater, and a peak in the carbon isotopic composition of carbonates (Condie et al., 2000).

The magmatism of the Circum-Superior LIP is also coeval with magmatism of possible LIP-affinity from a number of different Archaean cratons worldwide (French et al., 2008). The correlation of coeval magmatic units from different continents is becoming more common in reconstructing the positions of the cratons in the Precambrian (Bleeker, 2003; Bleeker & Ernst, 2006). Further geochronological, palaeomagnetic and geochemical studies are needed on the Circum-Superior and its coeval LIPs in order to help assess the validity of worldwide reconstructions of the cratons during the Palaeoproterozoic.

1.2. Aims of the project

This study is the first to examine the geochemistry of the Circum-Superior LIP as a single entity using elemental data generated in the same laboratory at Cardiff University and isotopic data generated at the NERC Isotope Geosciences Laboratories and the Open University. The principal aims of the project are to:

- Produce an up-to-date and cohesive whole-rock geochemical and isotopic database for the igneous rocks of the Circum-Superior LIP.
- Investigate the nature and origin of the igneous rocks of the Circum-Superior LIP by deducing the geodynamic setting(s) in which the rocks were emplaced and examining the mantle source region(s) from which the rocks were derived.
- Test whether the Circum-Superior LIP was produced by partial melting of a single mantle plume impinging beneath the Superior Province.
- Determine which magmatic processes can explain the differences in the geochemistry between the various segments of the Circum-Superior LIP.
- Assess whether it is possible to observe in the geochemical signature of the volcanic rocks a fingerprint which can highlight if an area is fertile or barren in terms of the presence or absence of Ni-Cu-PGE sulphide deposits.

Another aim of this study was to age date a few select samples using the accurate and precise U-Pb dating method to further constrain the duration of the Circum-Superior magmatism and to test if certain undated igneous units are actually part of the Circum-Superior LIP as they are considered to be on the basis of other geological criteria. However, the NERC Isotope Geosciences Facilities Steering Committee denied permission for any U-Pb age dating of Circum-Superior igneous rocks. Some samples have been sent to the Jack Satterly Geochronology Laboratory at the University of Toronto but unfortunately as yet none of the samples have been processed and so no results are available.

The geochemical and isotopic results from this study may have wider implications than just the nature of the source region(s) and geodynamic setting(s) of the Circum-Superior LIP. The geochemistry of the volcanic rocks will provide an opportunity to evaluate the temperature of the mantle from which the magmas were extracted, thus allowing for an assessment of the secular cooling of the Earth's ambient upper mantle or a comparison of the temperatures of Proterozoic mantle plumes with those in the Archaean or the more recent geological record.

There is also a close similarity between what occurred on Earth at the time of formation of the Circum-Superior LIP and during the mid-Cretaceous (~120-90 Ma).

In the mid-Cretaceous the eruption of a number of plume-derived oceanic plateaux in many distant locations around the world coincided with a major environmental crisis (e.g. Larson, 1991a, 1991b; Kerr, 1998, 2003). Many authors have suggested the large amount of volcanism in the mid-Cretaceous represents a superplume event (e.g. Larson, 1991a, 1991b; Condie, 2001, 2004; Abbott & Isley, 2002). A number of superplume events are postulated to have occurred throughout Earth's history (e.g. Condie, 2004) and the Circum-Superior LIP could have formed during one of these events in which a number of mantle plumes bombard the base of the lithosphere within a relatively short time period.

1.3. Thesis structure

This thesis is split into six chapters. After this short introductory chapter into the rationale and aims of the project, Chapter 2 describes the geology of the Circum-Superior LIP and previous work and interpretations on the origin of this LIP as well as providing some information on coeval magmatic provinces from other Archaean cratons and the evidence for an environmental crisis and superplume event. Chapter 3 gives information on how and where samples were collected and summarises the key petrographic features of the Circum-Superior igneous rocks. The whole-rock geochemical results for all of the various segments of the Circum-Superior LIP are described in Chapter 4 as well as the radiogenic isotope compositions of analysed samples. Chapter 5 is a discussion of the geochemical and isotopic results and focuses on geochemical modelling to account for any differences in the geochemistry of the various magmatic segments of the Circum-Superior LIP through a variety of igneous processes. Chapter 5 also discusses the nature and temperature of the mantle source region, the mechanisms for the generation of magmatism at craton margins, and the potential for geochemically discriminating between ore-bearing and ore-barren magmatic provinces. The potential occurrence of a superplume event and the relative positions of continental fragments at ~1880 Ma are also assessed in Chapter 5. A short concluding summary of the thesis is provided in Chapter 6. Additional sample information, analytical methodologies, data tables and information on the accuracy and precision of data are provided in the appendices of this thesis.

2. GEOLOGICAL OVERVIEW

2.1. The Superior Province

Archaean cratons are large complex areas of continental crust that have remained stable for long periods of time. The Canadian Shield consists of an amalgamation of Archaean cratons and Proterozoic orogens (Hoffman, 1988) (Fig. 2.1). The largest craton in the Canadian Shield, covering an area of ~1.5-2.4 × 10^6 km^2 (Goodwin, 1991; Kerrich et al., 1999), is the Superior Province, which is also the largest of the ~35 cratons known worldwide (Bleeker, 2003).

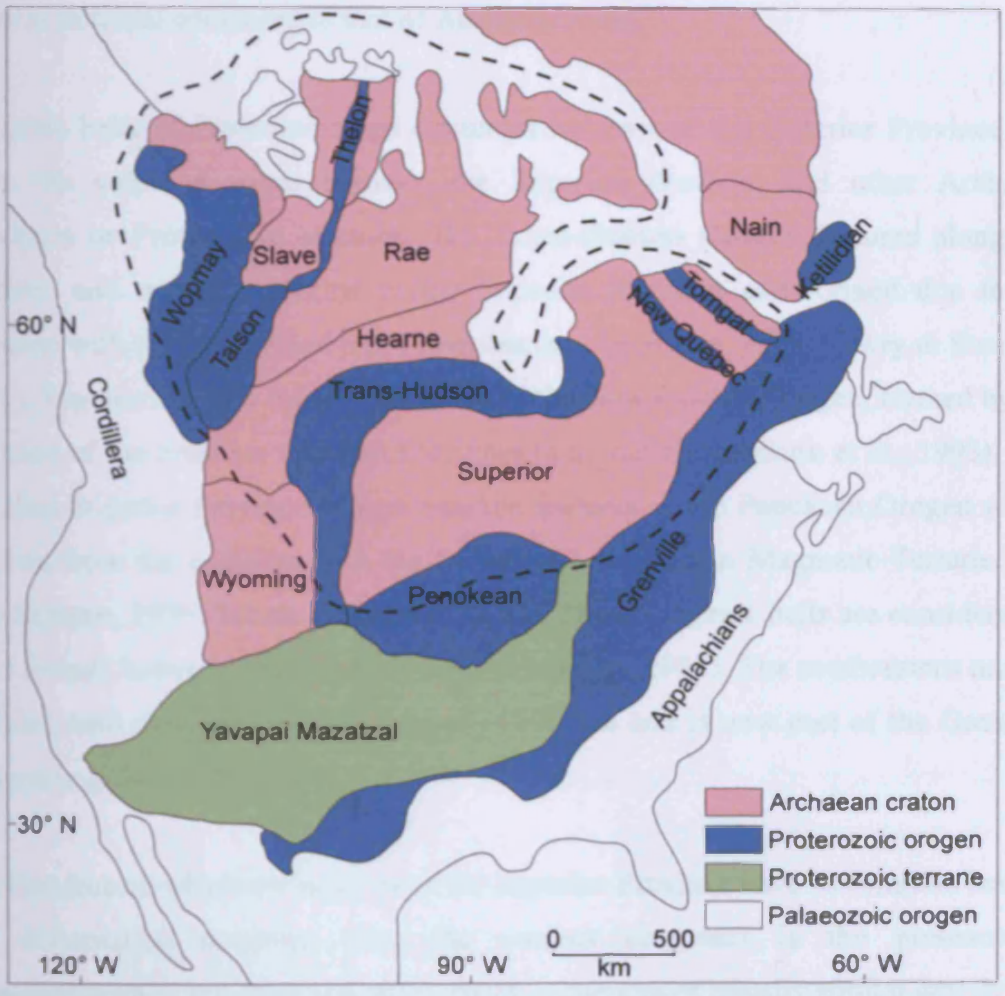

Fig. 2.1. Schematic map highlighting the major tectonic elements of Laurentia, an ancient landmass constituting much of the United States, Canada and Greenland. The Canadian Shield forms the core of Laurentia and its extent is marked by the dashed line. Map adapted from Hoffman (1988).

Comprehensive reviews of the geology of the Superior Province are given by Card (1990) and Stott (1997) and form the major source of the brief summary given here. Card & Ciesielski (1986) divided the Superior Province into a number of volcano-plutonic, metasedimentary, plutonic, and high grade gneiss subprovinces (see Fig. 1 in Card, 1990) based on age, lithological, structural, metamorphic, geophysical, and metallogenic characteristics. The central portion of the Superior Province is largely composed of alternating volcano-plutonic and metasedimentary subprovinces which are surrounded to the north and south by high grade gneiss subprovinces. The rocks of the Superior Province are predominantly Archaean in age, mostly in the range of ~3.1 to 2.7 Ga. The volume of Proterozoic volcanic rocks, mafic dyke swarms and alkalic rock-carbonatite complexes, and Proterozoic and Phanerozoic sedimentary cover is minimal compared to that of Archaean rocks.

Orogenic belts of Proterozoic age circumscribe most of the Superior Province and mark the collision zones between the Superior Province and other Archaean provinces or Proterozoic terranes. The Trans-Hudson Orogen features along the northern and western margins of the Superior Province and formed due to the collision with the Hearne and Rae Provinces (e.g. Hoffman, 1988; Lewry & Stauffer, 1990). The northeastern margin is the site of the New Quebec Orogen, formed by the collision of the Superior and Rae Provinces (e.g. van Kranendonk et al., 1993). The southern Superior Province margin exhibits features of the Penokean Orogen which resulted from the collision with the Proterozoic Wisconsin Magmatic Terrane (e.g. Van Schmus, 1976; Schulz & Cannon, 2007). These orogenic belts are considered to have formed between 1900 and 1800 Ma (Hoffman, 1988). The southeastern margin collided with the Grenville Province at ~1100 Ma and is now part of the Grenville Orogen (e.g. Davidson, 2008).

Another feature which the margins of the Superior Province have in common besides the deformation resulting from the various orogenies is the presence of Palaeoproterozoic volcanic and sedimentary sequences of broadly similar gravity and magnetic properties, stratigraphy and lithologies (e.g. Dimroth et al., 1970; Gibb & Walcott, 1971; Baragar & Scoates, 1981). Baragar & Scoates (1981) linked together into a single entity nine segments distributed around the Superior Province margin and coined the term 'Circum-Superior Belt'.

2.2. Circum-Superior Belt

The Circum-Superior Belt of Baragar & Scoates (1981) consists of nine discrete segments of Palaeoproterozoic volcanic and sedimentary sequences unevenly distributed around the Superior Province margin (Fig. 2.2). These segments are the Cape Smith Belt, eastern Hudson Bay area, Sutton Inlier, Fox River Belt, Thompson Nickel Belt (and Molson dykes), Lake Superior area, Mistassini-Otish Group, Southern Labrador Trough, and Labrador Trough. Hudson Bay waters, Phanerozoic sediment and Grenvillian deformation obscure any possible proof that the Circum-Superior Belt may be totally continuous.

Prior to Baragar & Scoates (1981), correlations between different parts of the belt had been made. Dimroth et al. (1970) suggested a link between the segments found around the Ungava Peninsula and to the south of the Labrador Trough and formulated the term 'Circum-Ungava Geosyncline'. Bell (1971) proposed a link between the Thompson Nickel Belt and Fox River Belt and speculated that these belts may correlate with the 'Circum-Ungava Geosyncline'. Gibb & Walcott (1971) also suggested a relationship between the Thompson, Fox River and Circum-Ungava belts on the basis of gravity anomalies. The presence of large iron formations in the Lake Superior area and Labrador Trough led Goldich (1973) to postulate a link between these two regions. The term 'Circum-Superior Suture' was also introduced by Thomas & Gibb (1977) to describe the boundaries of the Superior Province which had collided with the Rae and Hearne Provinces.

Not all the segments which constitute the Circum-Superior Belt contain magmatic rocks. However, in those segments that contain magmatic rocks, recent advances in U-Pb zircon/baddeleyite geochronology have shown that there is a marked synchronicity between the magmatic rocks, with ages ranging from 1885 to 1864 Ma (Ernst & Buchan, 2004 and references therein). This synchronicity, combined with the widespread extent of magmatism along the cratonic margins and its predominant mafic-ultramafic composition, has led Ernst (2004) to classify the 1885-1864 Ma Circum-Superior Belt magmatic rocks as a large igneous province (LIP) (Coffin & Eldholm, 1994; Bryan & Ernst, 2008) termed the Circum-Superior LIP (Fig. 2.2).

Fig. 2.2. Map of the Superior Province showing the location of the various segments of the Circum-Superior Belt and the Circum-Superior LIP. Adapted from Baragar & Scoates (1981). The Rae and Hearne Provinces are assigned the same shade of grey as these two provinces are often combined in the literature to constitute the Churchill Province.

2.3. Circum-Superior LIP

Recent U-Pb dating (see Table 2.1) has led to the recognition of coeval magmatism surrounding the Superior Province margins and also to the presence of ~1880 Ma magmatism in the interior of the craton, prompting Ernst & Bell (2010) to rename the 1885-1864 Ma Superior Province igneous rocks as the Pan-Superior LIP. However, as the magmatism of the cratonic interior is largely in the form of dykes, which converge back to a focal point located near to the craton margin, and a small number of carbonatite complexes which are of limited areal extent, the name Circum-Superior LIP is retained by the current study.

Fig. 2.2 shows the location of the various portions of the Circum-Superior LIP. It is an unusual LIP as there is currently no known Phanerozoic analogue with large amounts of magmatism dispersed over such a large area (composite strike length ~3000 km) around the margins of a continental block. A review of the geology of the various segments of magmatism belonging to the Circum-Superior LIP is given below. Table 2.1 also summarises the various age determinations made on rocks from the different magmatic segments.

2.4. Cape Smith Belt

2.4.1. Geology of the Cape Smith Belt

The mapping of Bergeron (1957, 1959) identified that the Cape Smith Belt extends ~375 km from west to east across nearly the entire Ungava Peninsula of northern Quebec (Fig. 2.3) and consists of volcano-sedimentary and plutonic suites structurally emplaced onto the Archaean basement of the Superior Province. The belt can be divided into two domains separated by the Bergeron Fault (Bergeron 1957, 1959; Picard et al., 1990). The parautochthonous southern domain is composed of the Povungnituk and Chukotat Groups while the Spartan, Parent and Watts Groups make up the allochthonous northern domain (Fig. 2.4).

In the northern domain, the Watts Group is an assemblage of sheeted dykes, layered intrusions and extrusive basalts which has been identified as an ophiolite complex

(Scott et al., 1989, 1992; St-Onge & Lucas, 1990). This ophiolite is known as the Purtuniq ophiolite and has a U-Pb age of 1998 ± 2 Ma (Parrish, 1989). The Watts Group structurally overlies turbiditic greywackes interbedded with pelites and fine-grained quartzites belonging to the Spartan Group (St-Onge et al., 1988, 1989; St-Onge & Lucas, 1990). The Parent Group is possibly the lateral equivalent to the Spartan Group and consists of siltstones, sandstones and greywackes which are intercalated with arc-like calc-alkaline lavas and pyroclastic rocks (Picard et al., 1990). U-Pb age dating of dioritic intrusions and rhyolite lavas places an age range of Parent Group magmatism of 1874 +4/-3 Ma to 1860 ± 2 Ma (Machado et al., 1993). The Spartan, Parent and Watts Groups are interpreted to be fragments of an island arc and its underlying oceanic lithosphere which were amalgamated with the southern domain of the Cape Smith Belt during the collision of the Superior Province with the Rae Province to the north (Lucas & St-Onge, 1992; St-Onge & Lucas, 1992; Randall, 2005) at ~1840 Ma (Machado, 1990). The Parent Group magmatism is not considered part of the Circum-Superior LIP due to its subduction-related origin to the north of the Superior Province margin.

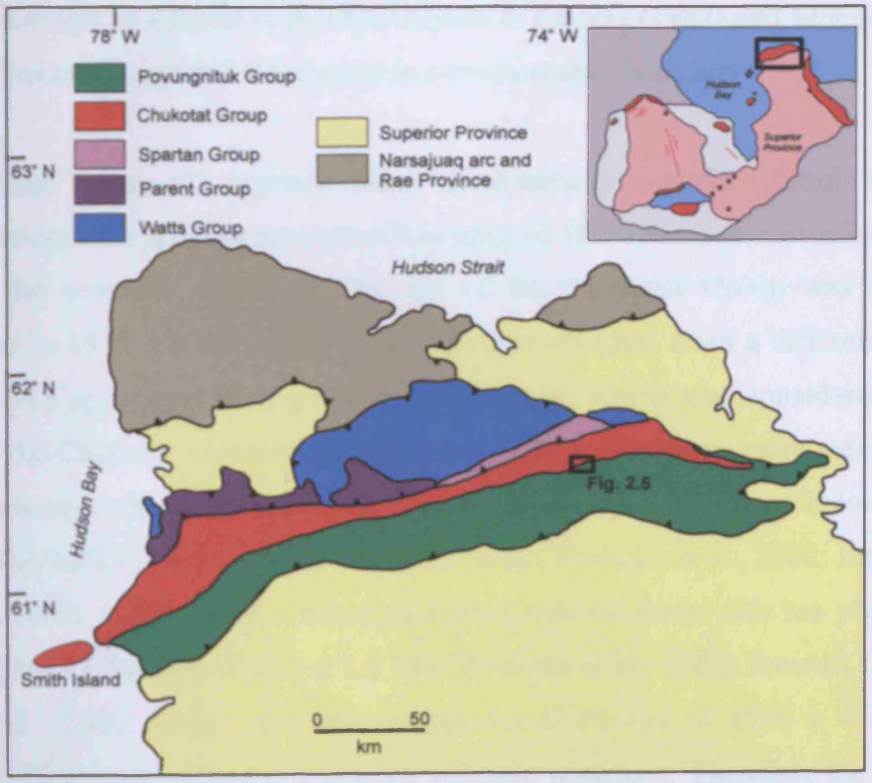

Fig. 2.3. Generalised geological map of northern Ungava Peninsula. Adapted from St-Onge & Lucas (1994).

The Povungnituk Group of the southern domain can be subdivided into four formations (Mungall, 2007) (Fig. 2.4). The basal formation, known as the Dumas Formation, unconformably overlies the Archaean Superior Province basement and comprises ferruginous sandstones, arenites, pelites, iron formations and carbonate sediments intercalated with minor gabbroic sills, one of which has yielded a U-Pb zircon age of 2038 ± 3 Ma (Machado et al., 1993). The Beauparlant Formation overlies the Dumas Formation and is predominantly composed of extrusive basaltic volcanic rocks with minor intercalated graphic pelites and carbonates. A dioritic dyke intruding the Beauparlant Formation has been U-Pb dated at 1991 ± 2 Ma (Machado et al., 1993). The Beauparlant Formation basalts are overlain by nephelinites, basanites, phonolites, rhyolites and pyroclastic rocks belonging to the Cecilia Formation. Parrish (1989) obtained a U-Pb age of 1958.6 +3.1/-2.7 Ma for a rhyolite from the Cecilia Formation. The uppermost unit of the Povungnituk Group is the Nuvilik Formation which contains laminated semi-pelites and minor amounts of carbonates, conglomeratic quartzites and graphitic argillites. The Chukotat Group lies above the Nuvilik Formation but the nature of the contact is unclear. St-Onge et al. (1992) and Baragar (2008) interpreted the contact between the Povungnituk and Chukotat Groups as a thrust fault whilst Hynes & Francis (1982) and Mungall (2007) disputed this and suggested the contact is a conformable boundary.

The Chukotat Group is comprised mainly of ultramafic to mafic volcanic rocks and intrusive rocks with a minor amount of fine grained siliciclastic sediment intercalated amongst the volcanic sequence. The age of the Chukotat Group was originally thought to be 1918 ± 9 Ma based on a U-Pb date obtained from a differentiated sill intruding the upper part of the Povungnituk Group which was considered to be a feeder to the Chukotat volcanic rocks (Parrish, 1989). However, more recent studies have questioned whether this sill is part of the feeder system of the Chukotat Group and also the validity of the geochronological data (Wodicka et al., 2002; Ernst, 2004; Mungall, 2007). U-Pb dating of other gabbroic Chukotat feeder sills has yielded ages of 1887 +39/-11 Ma and 1882.7 ± 1.3 Ma (Wodicka et al., 2002; Randall, 2005). St-Onge et al. (1992, 2000) have also reported a U-Pb age of 1870 ± 4 Ma for a gabbroic sill intrusive into the Chukotat volcanic sequence. Therefore the Chukotat Group appears to represent an igneous episode which occurred ~1885-1870 Ma and is considered in this study as part of the Circum-Superior LIP.

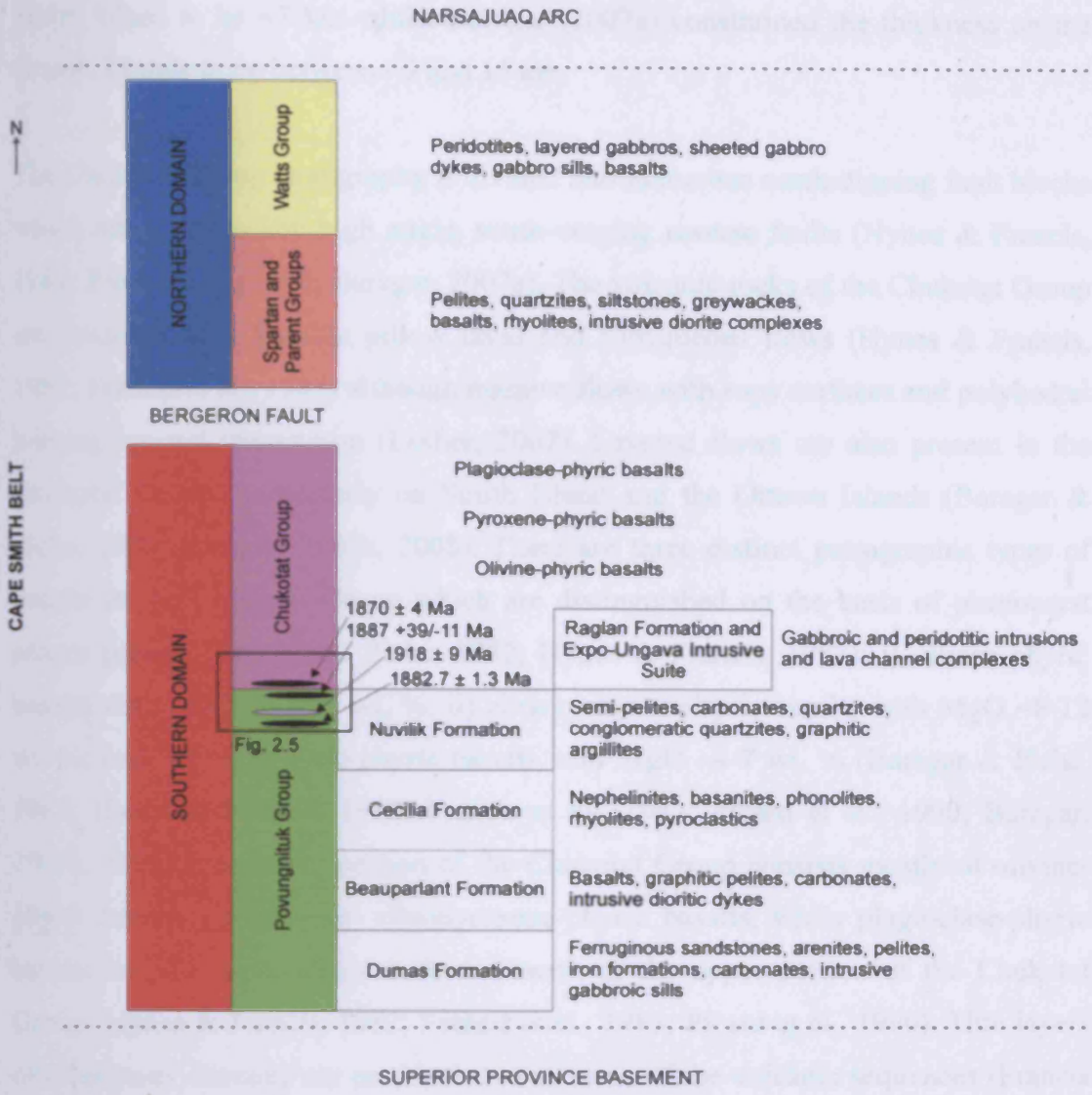

Fig. 2.4. Generalised tectonostratigraphic column of the Cape Smith Belt. Adapted from Lesher (2007). The black sills represent those which are part of the Raglan Formation and Expo-Ungava Intrusive Suite while the grey sill is of questionable age and origin.

2.4.2. The Chukotat Group

The thickness of the Chukotat Group does not appear to be uniform across its entire length. Studies in the central and eastern portions of the Cape Smith Belt have suggested a thickness of ~4-5 km (Hynes & Francis, 1982; Randall, 2005; Mungall, 2007). However, mapping in the western Cape Smith Belt, in particular on Smith Island and the Ottawa Islands, has led to larger estimates of the thickness of the group. Baragar (2008) interpreted the exposed thickness of the Chukotat Group on

Smith Island to be ~7 km whilst Baragar (2007a) constrained the thickness on the Ottawa Islands to be between ~9 and 15 km.

The Chukotat Group stratigraphy is divided into numerous north-dipping fault blocks which are separated by high angle, south-verging reverse faults (Hynes & Francis, 1982; Picard et al., 1990; Baragar, 2007a). The volcanic rocks of the Chukotat Group are predominantly basaltic pillow lavas and subaqueous flows (Hynes & Francis, 1982; Francis et al., 1983) although massive flows with ropy surfaces and polyhedral jointing are not uncommon (Lesher, 2007). Layered flows are also present in the Chukotat Group, particularly on Smith Island and the Ottawa Islands (Baragar & Piche, 1982; Baragar, 2007a, 2008). There are three distinct petrographic types of basalts in the Chukotat Group which are distinguished on the basis of phenocryst phases present (Baragar & Piche, 1982; Hynes & Francis, 1982): i) olivine-phyric basalts with MgO ~12-19 wt. %; ii) clinopyroxene-phyric basalts with MgO ~8-12 wt. %; and iii) plagioclase-phyric basalts with MgO ~4-7 wt. % (Baragar & Piche, 1982; Hynes & Francis, 1982; Francis et al., 1983; Picard et al., 1990; Baragar, 2007a, 2008). The lower portion of the Chukotat Group consists mostly of olivine-phyric basalts grading into clinopyroxene-phyric basalts, while plagioclase-phyric basalts become more common further north in the upper portion of the Chukotat Group (Hynes & Francis, 1982; Francis et al., 1983; Picard et al., 1990). Thin layers of often rusty siltstone are present between some of the volcanic sequences (Francis et al., 1983).

2.4.3. The Raglan Formation

Numerous ultramafic-mafic bodies are present in the upper Povungnituk Group and lower Chukotat Group (Fig. 2.5). In the east-central part of the Cape Smith Belt these ultramafic-mafic bodies appear to define a discontinuous but stratigraphically distinct, regionally mappable unit over ~85 km in length which Giovenazzo et al. (1989) named as the Raglan Horizon and Lesher et al. (1999) renamed the Raglan Formation. The Raglan Formation contains numerous Ni-Cu-PGE deposits and showings including those in the areas known as Cross Lake (e.g. Thibert, 1999), East Lake (e.g. Stewart, 2002), Zone 2-3 (e.g. Mallinson 1999a, 1999b), Katinniq (e.g. Barnes et al., 1982), Zone 5-8 (e.g. Mallinson, 1999c), Zone 13-14 (e.g. Vicker &

Federowich, 1999), West Boundary (e.g. Charland, 1999), Boundary (e.g. Stilson et al., 1999) and Donaldson (e.g. Lesher & Vicker, 1999) (Fig. 2.5). The Ni-Cu-PGE mineralisation in the Raglan Formation tends to form lenses of massive, net-textured and disseminated sulphides at or near the bases of the ultramafic-mafic bodies and lenses of patchy to uniformly distributed sulphides within the ultramafic-mafic bodies (Lesher, 2007 and references therein). Sulphide mineralisation is mostly in the form of pyrrhotite, pentlandite and chalcopyrite but may also contain magnetite, pyrite, ferrochromite and trace amounts of sphalerite, arsenopyrite and platinum group minerals. Lesher (2007) noted that at the end of 2005, total production in the Raglan area was 6.89 Mt at 3.11% Ni and 0.9% Cu, mineral reserves were 14.85 Mt at 2.8% Ni and 0.77% Cu (measured) and 7.7 Mt at 3.0% Ni and 0.8% Cu (inferred).

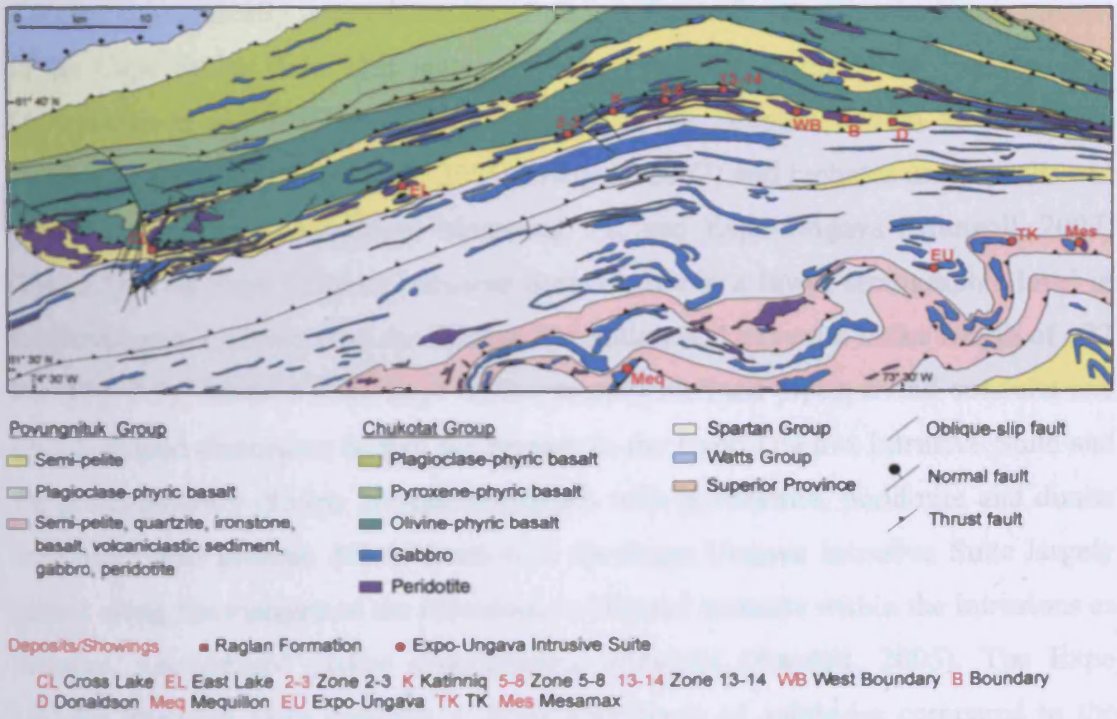

Fig. 2.5. Geological map of the Raglan area showing localities of some of the major ore deposits within the Raglan Formation and the Expo-Ungava Intrusive Suite. Adapted from St-Onge & Lucas (1993) and Lesher (2007).

The volcanological settings and modes of emplacement of the mineralised Raglan ultramafic-mafic bodies are not universally agreed upon. Interpretations include feeder sills to the Chukotat volcanic rocks, lava ponds and deeply erosive lava

conduits (Barnes et al., 1982; Hynes & Francis, 1982; Bedard et al., 1984; Giovenazzo et al., 1989; Barnes & Barnes, 1990; Gillies, 1993). Lesher (2007) has divided the Raglan bodies into two different facies assemblages: i) a conduit facies assemblage with very thick but laterally restricted units composed mainly of massive olivine mesocumulate (peridotite) and ii) a channelised sheet facies assemblage with laterally restricted units of olivine orthocumulate (olivine-pyroxenite) and gabbros. The former facies assemblage is termed the Katinniq Member whereas the latter assemblage is known as the Cross Lake Member. The age of the Raglan Formation ranges between 1887 +39/-11 Ma and 1870 ± 4 Ma as determined by U-Pb dating (St-Onge et al., 1992, 2000; Wodicka et al., 2002).

2.4.4. The Expo-Ungava Intrusive Suite

Another economically important suite of ultramafic-mafic intrusive bodies is present in the Cape Smith Belt. This suite has been identified in the Delta Horizon (e.g. Giovenazzo et al., 1989) and more recently it has become known as the Expo-Ungava Intrusive Suite (Randall, 2005; Mungall, 2007) and includes ore deposits and showings known as Mequillon, Mesamax, TK and Expo-Ungava (Mungall, 2007) (Fig. 2.5). The Expo Ungava Intrusive Suite occurs at a lower stratigraphic level in the Povungnituk Group than the Raglan Formation and covers a strike length of ~32 km (Fig. 2.5). Stacked sills, large dykes, steeply inclined pipes, ovoid conduits and trough-shaped discordant bodies are present in the Expo Ungava Intrusive Suite and are predominantly olivine melagabbronorites with pyroxenite, peridotite and dunite lithologies also present. Mineralisation in the Expo Ungava Intrusive Suite largely occurs along the margins of the intrusions or internal contacts within the intrusions as massive, net-textured and/or disseminated sulphides (Randall, 2005). The Expo Ungava Intrusive Suite contains a lower abundance of sulphides compared to the Raglan Formation which St-Onge & Lucas (1994) ascribed to the fact that the Raglan bodies were emplaced into a different facies of the Povungnituk Group containing more sulphidic and graphitic pelitic rocks than the facies which the Expo Ungava Intrusive Suite intruded through. The age of the Expo Ungava Intrusive Suite has been determined by U-Pb zircon dating of a melagabbro from the Expo-Ungava deposit which yielded an age of 1882.7 ± 1.3 Ma (Randall, 2005).

2.4.5. Geodynamic setting

The current consensus on the origin of the Chukotat Group is that the olivine-, clinopyroxene-, and plagioclase-phyric basalts represent oceanic crust. Baragar & Scoates (1981) invoked a model of in-situ rifting of the Superior Province margin, producing oceanic crust for a short time period before the total spreading movement was assumed by an opening rift near the southern margin of the Superior Province. Francis et al. (1983) concluded that the Chukotat Group in the central Cape Smith Belt displayed trace element patterns similar to that of normal mid-ocean ridge basalt (N-MORB) (i.e. depletion of the more incompatible elements). Other studies in different parts of the Cape Smith Belt have shown that the Chukotat Group displays varying trace element patterns (Baragar & Scoates, 1987; Picard et al., 1990; Hegner & Bevier, 1991; Baragar, 2007a). Picard et al. (1990) explained this variation by the transition from actual continental rifting to actual sea floor spreading. However, Baragar (2007a) has questioned the validity of an N-MORB source for the Chukotat volcanic rocks. Arndt et al. (1987) argued for an N-MORB source for the Chukotat volcanism on the basis of Nd isotopic ratios although Hegner & Bevier (1991) suggested the involvement of a mantle plume from similar Nd isotopic ratios as obtained by Arndt et al. (1987). St-Onge et al. (2000) postulated that the impingement of a mantle plume beneath the Ungava Peninsula led to the eruption of the Chukotat basalts and rifting of the peninsula with the breakaway of the Meta Incognita microcontinent now preserved in southwest Baffin Island. Dunphy et al. (1995) have also highlighted the possibility of a mantle plume playing a role in the evolution of the Cape Smith Belt although these authors concluded that the Chukotat Group originated from an N-MORB source.

2.5. Eastern Hudson Bay islands

The Belcher Islands lie ~150 km west of the western coast of the Ungava Peninsula (Fig. 2.2). The geology of these islands is dominated by numerous sedimentary units and two volcanic formations (Fig. 2.6). The Sleeper Islands consist of two major and many smaller islands which lie ~100 km north of the Belcher Islands (Fig. 2.2). Unlike the Belcher Islands, the geology of the Sleeper Islands is dominated by one volcanic formation and associated sills (Fig. 2.8).

2.5.1. The Belcher Islands

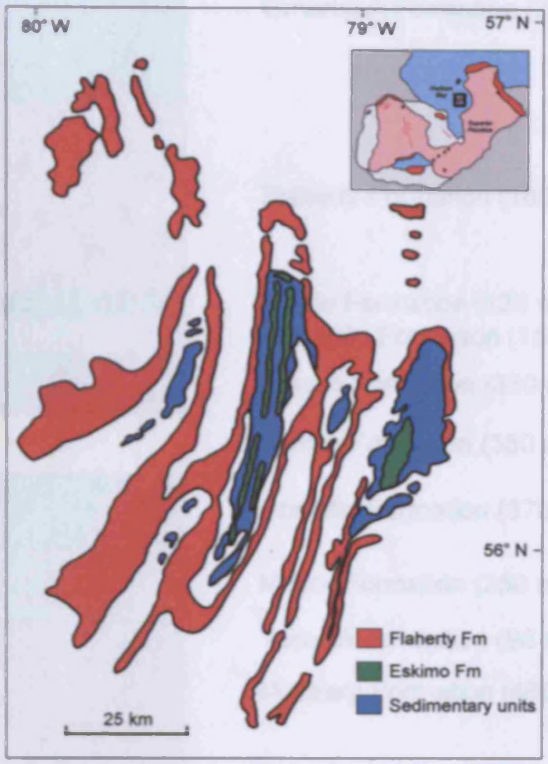

Fig. 2.6. Generalised geological map of the Belcher Islands in Hudson Bay. Adapted from Legault et al. (1994).

Jackson (1960) conducted the first detailed geological mapping of the Belcher Islands and divided the stratigraphy into sixteen formations. Ricketts & Donaldson (1981) redefined the stratigraphy and outlined fourteen formations (Fig. 2.7). The entire thickness of the Belcher Islands succession varies from west to east. The succession is ~9 km thick on the westernmost island and only ~2 km on the easternmost island (Mukhopadhyay & Gibb, 1981). No basement rocks are exposed but gravity profiles collected by Mukhopadhyay & Gibb (1981) show that the Belcher Islands succession sits on Superior Province crust. The lowermost formation, according to Ricketts & Donaldson (1981), is the Kasegalik Formation which consists of a maximum of 1200 m thick evaporitic and stromatolitic dolostones. The Kasegalik Formation is overlain by the Eskimo Formation, a unit of columnar-jointed flood basalts which attain a maximum thickness of 900 m. Overlying the Eskimo Formation are ~2000 m of carbonate and siliciclastic rocks which are divided

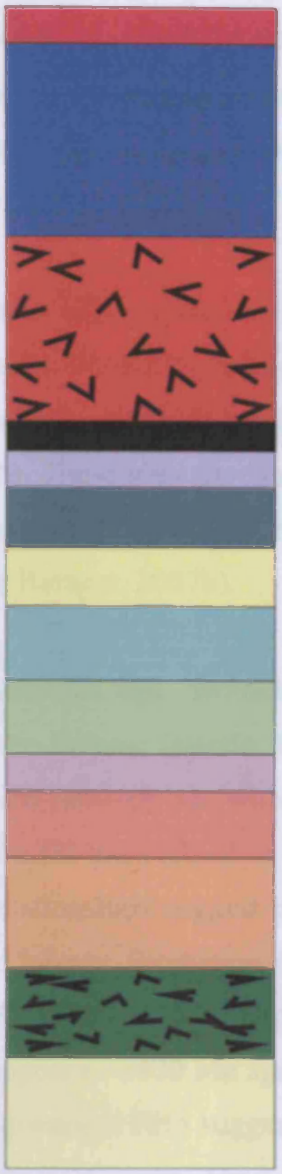

Fig. 2.7. Stratigraphic column of the formations exposed on the Belcher Islands. The numbers in brackets represent the maximum thickness of each formation. Adapted from Dimroth et al. (1970), Ricketts & Donaldson (1981) and Legault (1994).

into the Fairweather, McLeary, Tukarak, Mavor, Costello and Laddie Formations. The next three overlying formations consist of pelagic and carbonate sediments (the Rowatt Formation), quartz arenites (the Mukpollo Formation), and a jasper-bearing banded iron formation, ferruginous argillites and laminated micrites (the Kipalu Formation). The Kipalu Formation underlies the pillowed and massive basalt lava flows of the Flaherty Formation. The Flaherty Formation also contains pyroclastic flows and volcaniclastic sediments (Ricketts et al., 1982). The Flaherty Formation is

thought to have a maximum thickness of 1600 m (Ricketts et al., 1982) and could once have covered an area of 15,500 km^2 (Legault, 1994; Legault et al., 1994). The Flaherty Formation is overlain by argillites, shales and greywackes of the Omarolluk Formation. The topmost formation in the Belcher Islands succession is the Loaf Formation which mainly consists of arkosic red beds.

Doleritic-gabbroic sills, known as the Haig sills and ranging up to 300 m in thickness, intrude the Eskimo Formation and overlying sediments up to the base of the Flaherty Formation (Jackson, 1960; Dimroth et al., 1970; Baragar & Lamontagne, 1980; Baragar, 2007b). These sills are considered to have fed the Flaherty Formation lavas and are not thought to be related to the Eskimo Formation (Dimroth et al., 1970; Cadieux, 1980; Baragar, 2007b).

No reliable absolute age determinations have been obtained for the Flaherty Formation on the Belcher Islands. The only age comes from Todt et al. (1984) who obtained a Pb-Pb isochron age with a large error of 1960 ± 80 Ma. However, U-Pb dating of a Haig sill has yielded an age of 1870 ± 1 Ma (M. Hamilton, pers. comm. 2008). Field relationships suggest that the Haig sills are the intrusive equivalent to the extrusive Flaherty Formation (Jackson, 1960; Baragar & Lamontagne, 1980; Cadieux, 1980; Ricketts & Donaldson, 1981; Baragar, 2007b). Palaeomagnetic studies also support a ~1870 Ma age for the Flaherty Formation. Schmidt (1980) and Schwarz & Fujiwara (1981) suggested a time-stratigraphy correlative link between the Flaherty volcanic rocks, Haig sills and the dolerite-gabbro sills of the Sutton Inlier because of the similarity of the preliminary pole positions for all three of the igneous suites. As the Haig sills and Sutton Inlier sills are now accurately dated at 1870 Ma, it seems probable that the Flaherty Formation is also ~1870 Ma in age. The Eskimo Formation currently remains undated. It underlies the Flaherty Formation and so is older. Given the thickness of sedimentary rocks separating the two volcanic formations, the Eskimo Formation is likely to be significantly older than the Flaherty Formation and so is not considered part of the Circum-Superior LIP. There are currently no known Ni-Cu-PGE sulphide deposits associated with the Flaherty Formation or Haig sills on the Belcher Islands.

2.5.2. The Sleeper Islands

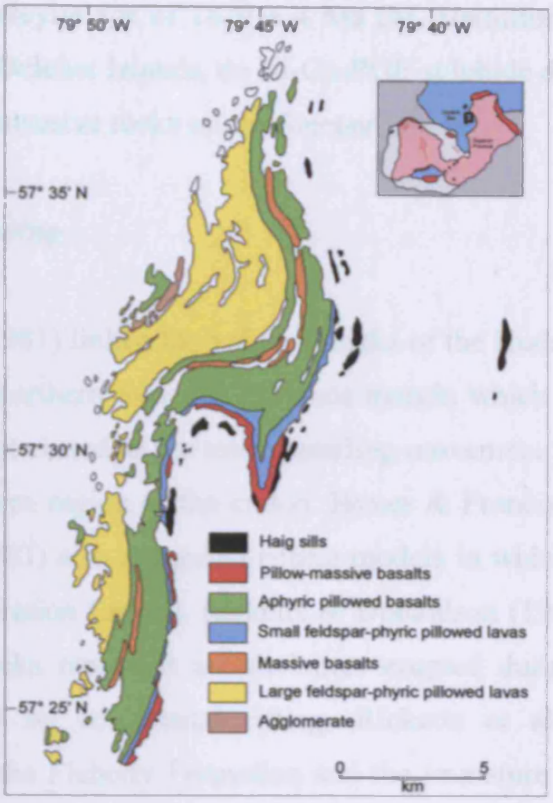

Fig. 2.8. Geological map of the Sleeper Islands in Hudson Bay. Adapted from Baragar & Lamontagne (1980).

The geology of the Sleeper Islands is dominated by the Flaherty Formation and has been divided into six lithologies by Baragar & Lamontagne (1980) (Fig. 2.8). The lowermost unit consists of thin basalt flows which are pillowed at the base, massive in the centre, and capped by a thin hyaloclastite top. The lowest unit is overlain by aphyric, dark grey basalts which are commonly pillowed and capped by massive tops. Feldspar-phyric pillowed lavas comprise the next unit and are overlain by a unit of massive basalt flows. Another unit of feldspar-phyric pillowed lavas overlie the massive basalts and are themselves overlain by agglomerate lenses with irregular lava masses set in a matrix of lapilli tuff.

The Haig sills are also present on the Sleeper Islands (Baragar & Lamontagne, 1980; Cadieux, 1980; Baragar, 2007b). There is at least one gabbroic sill, with a plagioclase glomerophyric base and overlying normal mass of gabbro (Cadieux,

1980), which outcrops along the eastern coast of the two major islands and on the many small islands off the eastern coast of the major islands (Fig. 2.8). This Haig sill yielded a U-Pb baddeleyite age of 1870 ± 4 Ma (M. Hamilton, pers. comm. 2008). As is the case on the Belcher Islands, no Ni-Cu-PGE sulphide deposits are associated with the volcanic or intrusive rocks on the Sleeper Islands.

2.5.3. Geodynamic setting

Baragar & Scoates (1981) linked the volcanic rocks of the Hudson Bay islands to the in-situ rifting of the northern Superior Province margin which did not fully develop into an oceanic rift but closed as the total spreading movement was assumed by a rift opening in the southern region of the craton. Hynes & Francis (1982), Doig (1983) and Francis et al. (1983) also suggested rifting models in which an oceanic basin of limited width and duration formed. Ricketts & Donaldson (1981) proposed that the Flaherty volcanic rocks represent arc tholeiites erupted during the closure of an ocean basin formed by continental rifting. Ricketts et al. (1982) also noted similarities between the Flaherty Formation and the immature Tonga-Kermadec arc but concluded on the basis of the styles of volcaniclastic rocks and facies associated with the Flaherty volcanism that the Flaherty Formation was probably erupted through ensialic crust but in a submarine environment. Gibb (1983) and Chandler (1984) have also argued for a mid-oceanic or island arc setting for the Flaherty Formation. Arndt et al. (1987) postulated that the eruption of the Flaherty Formation represented the transition between continent and ocean environments as rifting of a continental margin continued. All the above models essentially promote an upper mantle source for the Flaherty Formation volcanic rocks.

Alternative models to rifting for the geodynamic setting for the ~1870 Ma volcanism in the eastern Hudson Bay area include a foredeep basin setting (Hoffman, 1987) and the melting of a mantle plume (St-Onge et al., 2000). The plume model of St-Onge et al. (2000) attempted to explain all the ~1.88-1.87 Ga magmatism located around the Ungava Peninsula.

2.6. Sutton Inlier

Very little has been published on the rocks of the Sutton Inlier. The Sutton Inlier occurs in an area near Sutton Lake in the Hudson Bay Lowlands where Archaean and Proterozoic rocks are exposed through the Palaeozoic cover (Bostock, 1971) (Fig. 2.2). Carbonates, greywackes, siltstones, iron formation and intrusive mafic sills form the Proterozoic succession which unconformably overlies Archaean basement gneisses (Baragar & Scoates, 1981).

Palaeomagnetic work by Schwarz & Fujiwara (1981), Schwarz et al. (1982) and Schwarz & Freda (1983) suggested that the Sutton Inlier sills are coeval with the Flaherty Formation volcanic rocks and Haig sills of the Belcher and Sleeper Islands (section 2.5). The Sutton Inlier sills have been dated (U-Pb baddeleyite method) at 1870 ± 2 Ma (M. Hamilton, pers. comm. 2008). U-Pb age determinations of ~1870 Ma from the Haig sills in the Hudson Bay islands therefore support the age correlations made by palaeomagnetic methods.

No Ni-Cu-PGE sulphide mineralisation has been reported from the Sutton Inlier sills.

2.7. Fort Albany dykes

Hamilton & Stott (2008) have obtained a U-Pb baddeleyite age of 1870.7 ± 1.1 Ma from a dolerite dyke underneath Palaeozoic cover near Puskwuche Point on the west coast of James Bay (Fig. 2.9). Aeromagnetic data show this dyke to trend northwesterly and be colinear with another northwest trending dyke ~150 km northwest of Puskwuche Point. Together these dykes have been referred to as the Fort Albany dykes (Hamilton & Stott, 2008). There is no known Ni-Cu-PGE mineralisation associated with the Fort Albany dykes.

Hamilton & Stott (2008) suggested that given the trend of the Fort Albany dykes they may form part of a radiating dyke swarm along with the Molson (see section 2.11) and Pickle Crow (see section 2.12) dykes converging back to a mantle plume centre just to the north of the Thompson Salient.

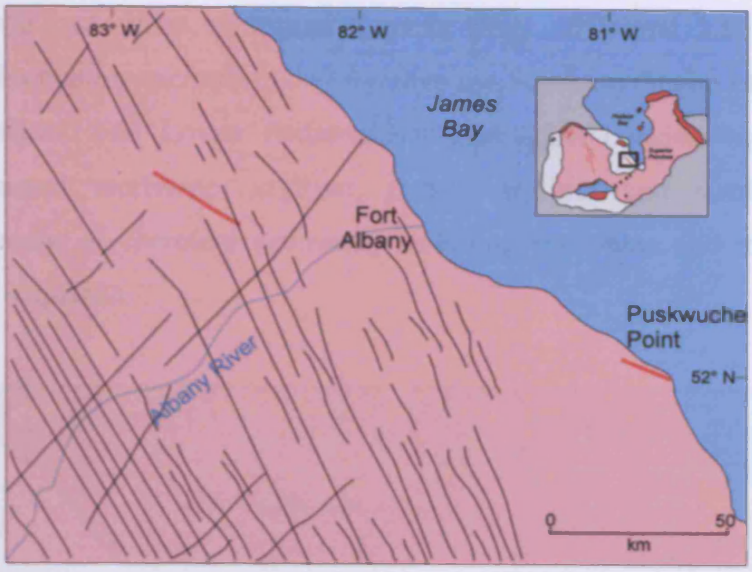

Fig. 2.9. Location map of the Fort Albany dykes on the western side of James Bay. The Fort Albany dykes are shown in red. Black lines represent other dykes of various ages. Adapted from Hamilton & Stott (2008).

2.8. Fox River Belt

2.8.1. Geology of the Fox River Belt

The Fox River Belt is an east-striking, north-dipping and north-facing monoclinal supracrustal sequence of rocks that borders the Superior Province in northern Manitoba (Fig. 2.10). The Fox River Belt is ~300 km long, 10-30 km wide and ~15 km thick and comprises siliciclastic and chemical sediments enclosing thick sequences of mafic volcanic rocks and intruded at different levels by ultramafic-mafic intrusions (Scoates, 1981). Outcrop is extremely poor in the Fox River Belt and most previous work in the region focussed on drill core data and geophysical surveys. Merritt (1925) was the first to recognise the presence of ultramafic rocks in the area whilst the presence of both volcanic and sedimentary rocks was not noted until Springer (1946) traversed several rivers in the area. Quinn (1955a, 1955b) described layering in the Fox River Belt ultramafic rocks. However, the most detailed reports on the geology of the area are by Scoates (1981, 1990) and are the source of the geological information below unless otherwise stated.

The Fox River Belt stratigraphy is divided into three sedimentary and two volcanic formations with two suites of intrusive rocks (Figs. 2.10 and 2.11). The Lower Sedimentary Formation unconformably overlies the Southern Gneiss of the Archaean Superior Province. The Lower Sedimentary Formation consists mostly of fine-grained laminated mudstone, argillite, pyritic argillite and siltstone with an increasing amount of chemical sediment, including carbonate and iron formation, upward in the sequence.

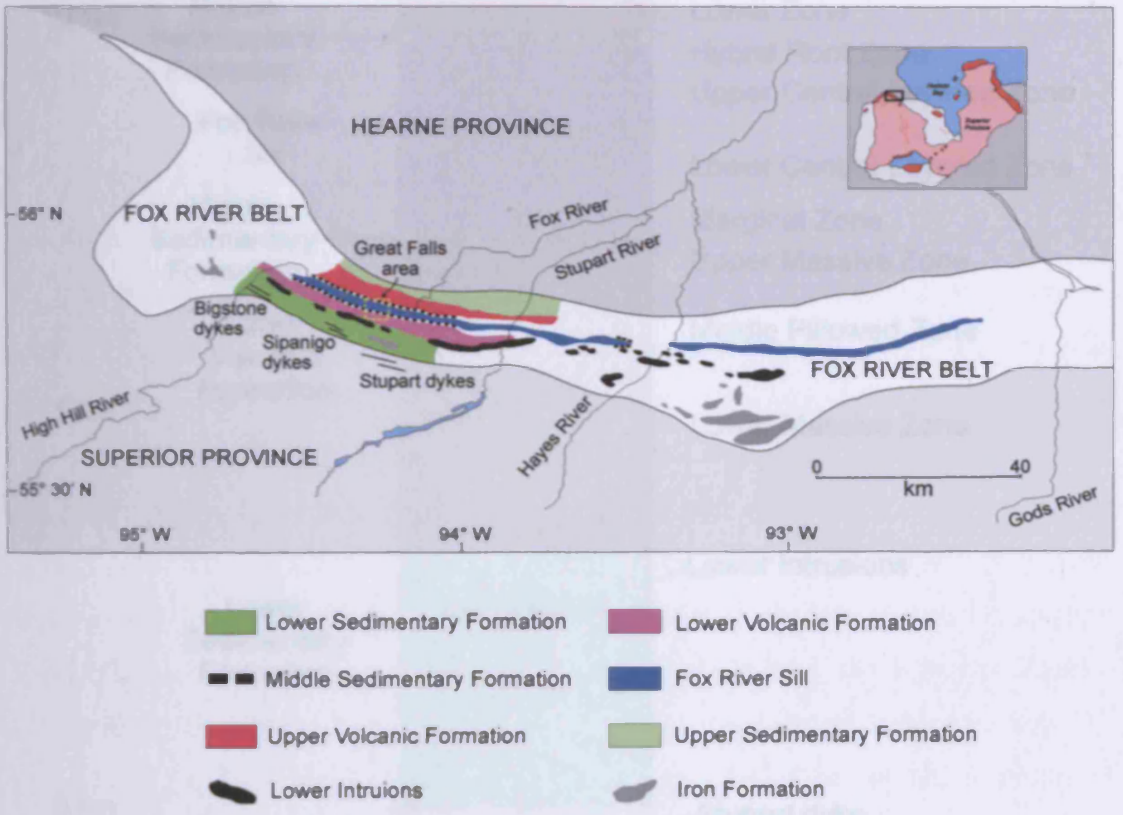

Fig. 2.10. Map of the general geology of the outcropping sections of the Fox River Belt. Adapted from Scoates (1981).

A number of east-striking gabbroic dykes have recently been recognised in the Fox River Belt region (Peck et al., 2000; Desharnais, 2005). The Bigstone gabbro refers to a number of gabbronorite bodies that intrude the Lower Sedimentary Formation up to ~1 km above the contact between the Southern Gneiss and the Fox River Belt (Peck et al., 2000). More east-striking gabbroic dykes have also been recognised intruding the Southern Gneiss to ~2 km south of the southern boundary of the Fox River Belt. These dykes have been referred to as the Stupart dykes (Peck et al., 2000).

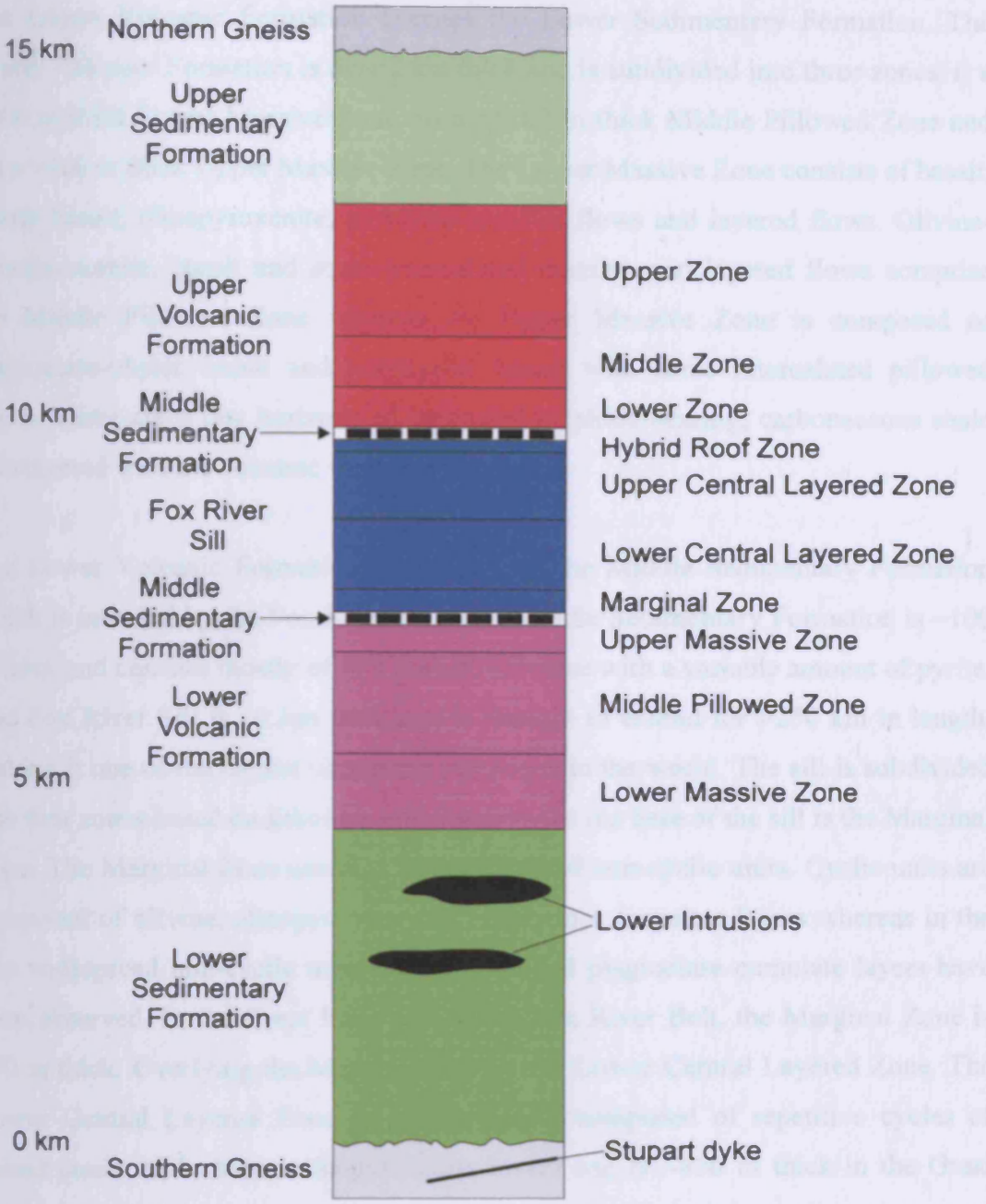

Fig. 2.11. Generalised stratigraphic column of the western Fox River Belt. Stratigraphic height is given in kilometres on the left hand side. Adapted from Scoates (1981, 1990) and Desharnais (2005).

The upper Lower Sedimentary Formation is host to a number of large differentiated sills known as the Lower Intrusions. These intrusions consist of a peridotitic base overlain by a pyroxene-rich layer with an upper gabbronorite section. The intrusions range from ~1.5 to 20 km in strike length and ~50 to 800 m in thickness. Desharnais (2005) has noted that not all of the Lower Intrusions are differentiated, instead some are zoned from peridotite at the core to pyroxenite at the margins.

The Lower Volcanic Formation overlies the Lower Sedimentary Formation. The Lower Volcanic Formation is over 2 km thick and is subdivided into three zones: i) a >700 m thick Lower Massive Zone, ii) a >1100 m thick Middle Pillowed Zone and iii) a >400 m thick Upper Massive Zone. The Lower Massive Zone consists of basalt, quartz basalt, clinopyroxenite, pyroxene-spinifex flows and layered flows. Olivine-clinopyroxenite, basalt and some intercalated massive and layered flows comprise the Middle Pillowed Zone whereas the Upper Massive Zone is composed of plagioclase-phyric basalt and porphyritic basalt with some intercalated pillowed flows. There are a few horizons of laminated sulphide-bearing, carbonaceous shale interlayered with the volcanic rocks.

The Lower Volcanic Formation is overlain by the Middle Sedimentary Formation which is intruded by the Fox River Sill. The Middle Sedimentary Formation is ~100 m thick and consists mostly of fine grained siltstone with a variable amount of pyrite. The Fox River Sill is ~2 km thick and is thought to extend for >250 km in length, making it one of the largest ultramafic intrusions in the world. The sill is subdivided into four zones based on lithology and layering. At the base of the sill is the Marginal Zone. The Marginal Zone contains both cyclic and non-cyclic units. Cyclic units are composed of olivine, clinopyroxene and plagioclase cumulate layers whereas in the less widespread non-cyclic units only olivine and plagioclase cumulate layers have been observed. In the Great Falls area of the Fox River Belt, the Marginal Zone is 250 m thick. Overlying the Marginal Zone is the Lower Central Layered Zone. The Lower Central Layered Zone is predominantly composed of repetitive cycles of paired dunite and olivine-clinopyroxenite layers and is ~850 m thick in the Great Falls area. The Upper Central Layered Zone lies above the Lower Central Layered Zone but can be distinguished by the presence of orthopyroxene in the cumulate layers and also by the more common occurrence of plagioclase cumulate rocks capping the cyclic units. The Hybrid Roof Zone is the uppermost zone in the Fox River Sill. The Hybrid Roof Zone is ~40 m thick in the Great Falls area and contains rocks characterised by the presence of quartz and granophyre. The Fox River Sill is believed to be lopolithic in cross-section because of the shallower dips in the Lower Central Layered Zone and Upper Central Layered Zone compared to the near-vertical dip of the Marginal Zone rocks.

Another volcanic formation overlies the Middle Sedimentary Formation and is termed the Upper Volcanic Formation. The Upper Volcanic Formation ranges from ~2.5 to 3.5 km thick and consists of three zones. There is the Lower Zone of layered differentiated flow units and basalt flows. The Middle Zone consists of pillowed olivine-clinopyroxenite as well as massive and layered flows whereas pillowed and massive basalt flows comprise the Upper Zone. As with the Lower Volcanic Formation, volcanic flows in the Upper Volcanic Formation are often separated by sulphide-bearing carbonaceous shale.

The Upper Sedimentary Formation is the uppermost formation in the Fox River Belt. The Upper Sedimentary Formation is very poorly exposed but is inferred to be ~1-2 km thick and consist largely of argillite, shale and carbonaceous shale (Desharnais, 2005).

The most precise published age date obtained from the igneous rocks of the Fox River Belt comes from the Fox River Sill. Heaman et al. (1986) obtained a U-Pb zircon age of 1882.9 +1.5/-1.4 Ma from a sample of varitextured gabbro at the base of a cyclic unit in the Marginal Zone of the Fox River Sill in the Great Falls area. Heaman et al. (2009) produced a U-Pb zircon age of 1900 ± 14 Ma from the Fox River dyke which is one of the Stupart dykes intruding the Southern Gneiss.

2.8.2. Ni-Cu-PGE sulphide deposits

In comparison to the Cape Smith and Thompson Belts, the Fox River Belt is not well explored for Ni-Cu-PGE sulphide deposits despite the knowledge that such deposits exist in the region. Scoates (1981) noted that sulphide minerals are common although not abundant in the volcanic rocks, with pyrrhotite as the dominant mineral. In the Fox River Sill, disseminated pyrrhotite, pentlandite, chalcopyrite, pyrite and heazlewoodite were identified by Scoates (1990) as accessory minerals in parts of the Marginal Zone, Upper Central Layered Zone and Hybrid Roof Zone. Scoates & Eckstrand (1986) and Schwann (1989) discovered three main intervals of mineralisation, with particular enrichment in the PGEs, in the Upper Central Layered Zone. These intervals were termed the Lower, Middle and Upper Mineralised Units by Schwann (1989) and are composed mainly of sulphide-bearing, medium-to-coarse

grained olivine clinopyroxenite. In 1999, a new Ni-Cu-PGE mineralised interval was discovered in the Great Falls area. The interval is termed the KO Zone and has been estimated to have a grade of 5.4 g/t Pd+Pt+Au, 2.3% Cu and 1.1% Ni (Desharnais et al., 2000). The KO Zone occurs at the contact between two cyclic units in the Marginal Zone of the Fox River Sill where a pyroxenite layer is overlain by sulphide-bearing lherzolite-olivine pyroxenite rocks (Desharnais et al., 2000). Disseminated pyrrhotite and chalcopyrite constitute the mineralisation with the sulphide minerals showing a variety of textures, including interstitial-irregular, net-textured and blebby.

2.8.3. Geodynamic setting

Scoates (1981) proposed that the Fox River Belt magmatism was the result of rifting of crust underlying an intracratonic basin at the edge of the Superior Province. Hoffman (1988) suggested that the Fox River Belt erupted in a foredeep basin whilst Halden (1991) argued for a marginal basin as the geodynamic setting of the Fox River Belt. A plume origin for the Fox River Belt has been suggested by Buchan et al. (2003) and has been supported by Desharnais (2005) who invoked the large volumes of magma and nearby presence of a radiating dyke swarm as evidence for the involvement of a mantle plume.

2.9. Thompson Nickel Belt

2.9.1. Geology of the Thompson Nickel Belt

The Thompson Nickel Belt forms a ~10-35 km wide northeast (030°) trending belt along the northwest margin of the Superior Province (Fig. 2.12) containing remnants of a Neoarchaean-Palaeoproterozoic continental margin (e.g. Bleeker, 1990; McRitchie, 1995; Layton-Matthews et al., 2007) and belongs to the Superior Boundary Zone (Weber & Scoates, 1978; Weber, 1990). The Thompson Nickel Belt separates autochthonous Archaean Superior Province rocks to the east from allochthonous Proterozoic domains of the Trans-Hudson Orogen to the west (Fig. 2.12). The Thompson Nickel Belt is exposed from ~50 km northeast of Thompson to ~125 km southwest of Thompson where it is buried beneath Palaeozoic carbonates

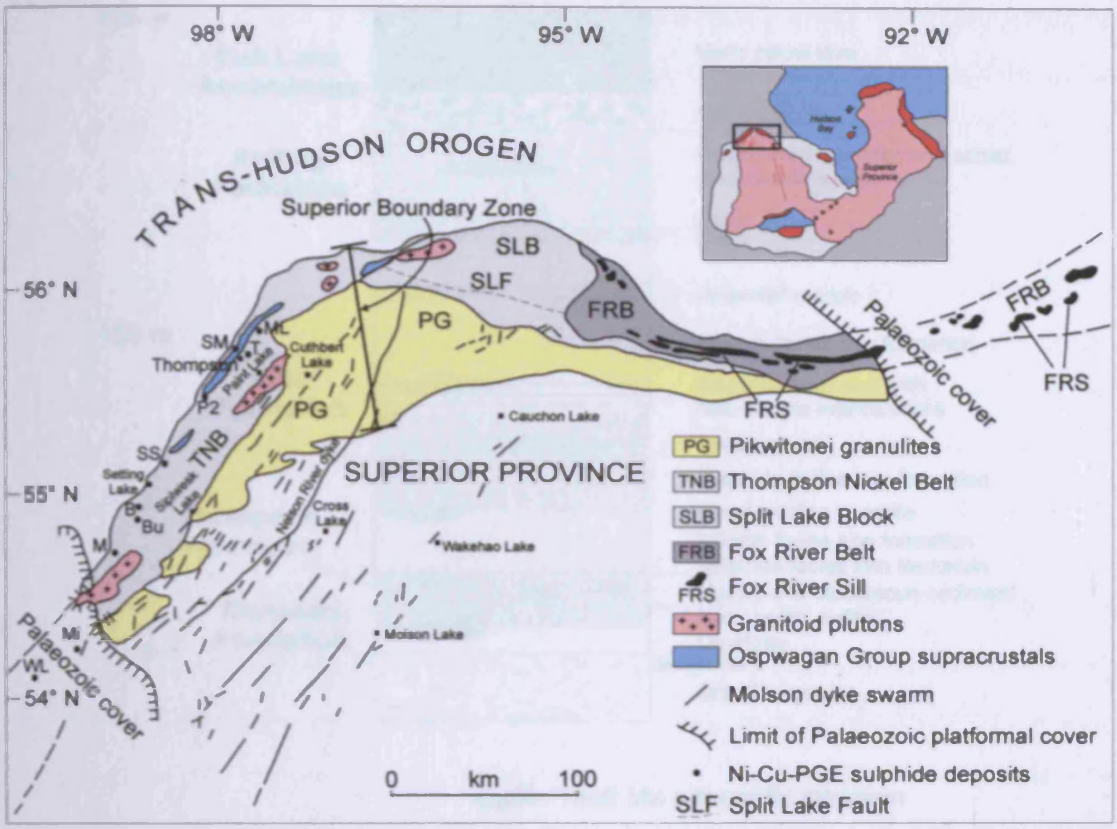

Fig. 2.12. Map of the Thompson Salient where the northwestern Archaean Superior Province adjoins the Proterozoic Trans-Hudson Orogen. Shown are the locations of the Fox River Belt, Molson dykes, Thompson Nickel Belt and some of the major ore deposits and mines within the Thompson Nickel Belt. ML Mystery Lake, SM South Manasan, T Thompson, P2 Pipe 2, SS Soab South, B Bowden, Bu Bucko, M Manibridge, Mi Minago, WL William Lake. Adapted from McRitchie (1995).

(McRitchie, 1995). Gravity and magnetic data show that the Thompson Nickel Belt continues for another ~250 km southward and then as the Superior Boundary Zone for 1000 km into South Dakota beneath 500-2000 m of Phanerozoic cover (Green et al., 1979, 1985).

The Thompson Nickel Belt is comprised of a Proterozoic supracrustal sequence of metasediments and metavolcanics known as the Ospwagan Group (Scoates et al., 1977) which is intruded by numerous ultramafic bodies (e.g. Cranstone & Turek, 1976; Peredery, 1979; Paktunc, 1984). The Ospwagan Group is subdivided into five formations (Fig. 2.13). The lowermost formation is known as the Manasan Formation and unconformably overlies the Pikwitonei granulites of the Superior Province. The Manasan Formation ranges in thickness up to 200 m and consists of quartzites and semi-pelitic to pelitic schists and gneisses. The Manasan Formation is

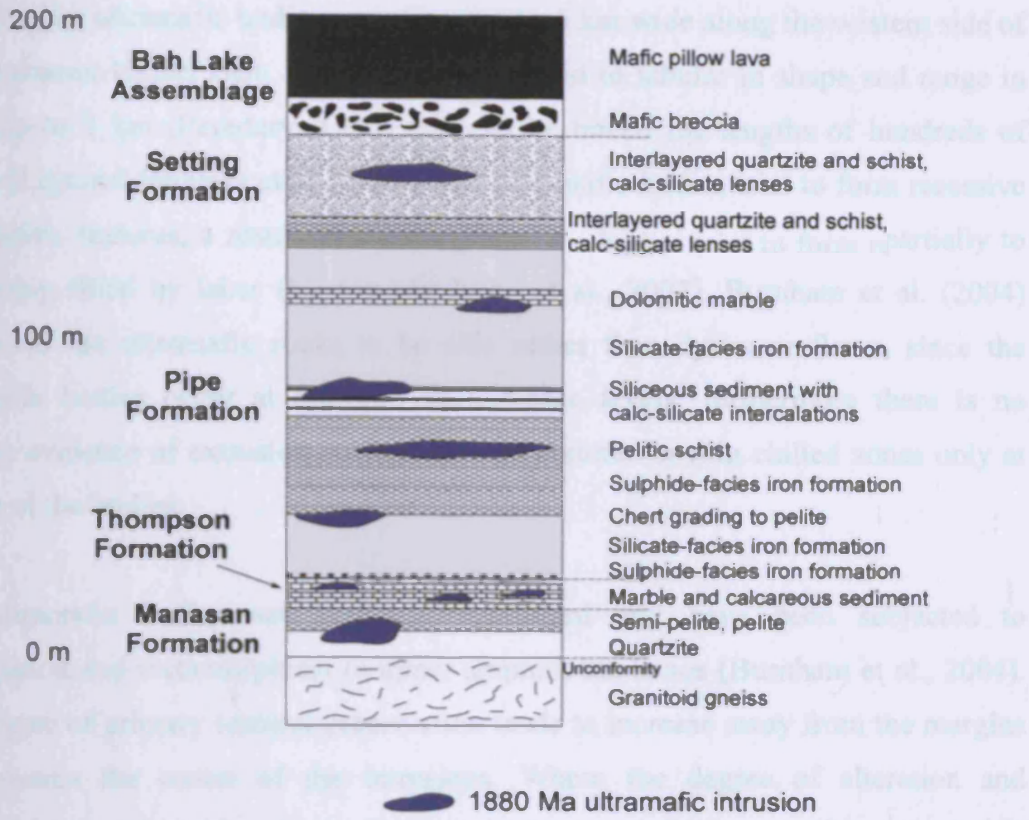

Fig. 2.13. Generalised stratigraphic column of the Ospwagan Group. Thickness of the units in metres is highlighted on the left hand side and is a minimum thickness. Adapted from Zwanzig & Bohm (2002).

overlain by the Thompson Formation which is composed mainly of calcareous semi-pelites and marbles with minor intercalations of chert. Overlying the Thompson Formation are pelitic to semi-pelitic schists and paragneisses which are interbedded with silicate-facies, sulphide-facies and cherty iron formations. These pelitic rocks and iron formations are collectively termed the Pipe Formation which appears to range in thickness between 500 and 800 m. The Pipe Formation underlies the Setting Formation which consists of quartzites, wackes and semi-pelitic to pelitic schists and paragneisses up to 200 m in thickness. The topmost formation of the Ospwagan Group consists mainly of mafic and ultramafic massive and pillowed volcanic flows. These volcanic rocks were originally known as the Ospwagan Formation but have been renamed as the Bah Lake Assemblage (Zwanzig, 2004).

A large number of ultramafic bodies intrude the Ospwagan Group at various stratigraphic levels although the highest concentration of ultramafic intrusions occurs in the Pipe and Thompson Formations (Burnham et al., 2004). Hulbert et al. (2005)

noted that the ultramafic bodies occur in a zone ~6 km wide along the western side of the Thompson Nickel Belt. The bodies are lensoid to tabular in shape and range in width up to 1 km (Peredery, 1982) and can be traced for lengths of hundreds of metres (Layton-Matthews et al., 2007). The ultramafic bodies tend to form recessive topographic features, a result of intense glacial erosion, which are now partially to completely filled by lakes (Layton-Matthews et al., 2007). Burnham et al. (2004) interpreted the ultramafic rocks to be sills rather than dykes or flows, since the ultramafic bodies occur at multiple stratigraphic levels, furthermore there is no positive evidence of extrusion such as quench textures or thin chilled zones only at the top of the bodies.

The ultramafic bodies are highly serpentinised and have been subjected to deformation and metamorphism to upper amphibolite facies (Burnham et al., 2004). The degree of primary textural preservation tends to increase away from the margins and towards the centre of the intrusions. Where the degree of alteration and deformation are low, the ultramafic intrusions commonly have a thin pyroxenitic basal zone with a thicker central zone of chromite-bearing olivine peridotites and dunites overlain by a thinner pyroxenitic upper zone (Peredery, 1982; Layton-Matthews et al., 2007). However, there are also some bodies which are more differentiated and have plagioclase- and garnet-bearing amphibolite layers (Peredery, 1982).

Hulbert et al. (2005) recorded a U-Pb zircon age of 1880 ± 5 Ma for an ultramafic body in the Setting Lake area of the Thompson Nickel Belt. These same authors found that this U-Pb age is coeval with a Re-Os isochron age of 1885 ± 49 Ma obtained from sulphide ores associated with seven mineralised ultramafic bodies in the Thompson Nickel Belt. Another ultramafic body in the Paint Lake area yielded a U-Pb age of 1876.7 ± 5.1 Ma (Heaman et al., 2009), which suggests that the ultramafic intrusions of the Thompson Nickel Belt are part of the Circum-Superior LIP. Although there are no absolute age determinations for the Bah Lake Assemblage, the volcanic rocks are not thought to be related to the ultramafic intrusions due to significant differences in geochemistry and the ages of detrital zircons and intrusive granitic rocks in the Bah Lake Assemblage (Bleeker & Hamilton, 2001; Zwanzig et al., 2003; Burnham et al., 2004; Zwanzig, 2004).

A significant amount of felsic magmatism is known to be coeval with the ultramafic magmatism in the Thompson Nickel Belt. A number of examples of quartz diorite, granodiorite, granite and monzogranite plutons from the Setting Lake and Mystery Lake areas have yielded U-Pb ages ranging between 1891 and 1871 Ma (Zwanzig et al., 2003; Percival et al., 2004, 2005; Heaman et al., 2009).

2.9.2. Ni-Cu-PGE sulphide deposits

The Thompson Nickel Belt is the second largest Ni-producing area in Canada after the Sudbury impact crater (McRitchie, 1995) and the fourth largest in the world (Naldrett, 1999). Naldrett (2004) noted that total reserves for the Thompson Nickel Belt in 2004 were 150.3 Mt at 2.32% Ni, 0.16% Cu and 0.83 g/t PGEs. The ultramafic intrusions host ~75% of the sulphide mineralisation in the Thompson Nickel Belt (Peredery, 1982). The mineralisation in the Thompson Nickel Belt is more deformed than in most other magmatic Ni-Cu-PGE deposits, and there are many examples of mobilised sulphides hosted within the metasedimentary rocks (e.g. Cumming et al., 1982). However, the mineral and chemical compositions of the ores are still similar to other deposits around the world (Lesher & Keays, 2002). The primary sulphide mineralogy is relatively simple and is dominated by pyrrhotite, pentlandite and pyrite with traces of chalcopyrite, magnetite and chromite (Layton-Matthews et al., 2007). The mineralisation textures in the Thompson Nickel Belt are quite varied and consist of disseminated (including heavy, patchy and blebby disseminated), layered, net-textured, semi-massive and massive sulphides (Peredery, 1982; Layton-Matthews et al., 2007). Hulbert et al. (2005) reported Os isotope ratios of some of the ultramafic rocks and sulphide mineralisation and found that they possess similar ratios which indicate that the source of the ores was the same as that of the ultramafic rocks.

2.9.3. Geodynamic setting

Several different models have been proposed for the geodynamic setting and mantle source of the Thompson Nickel Belt ultramafic intrusive rocks. Baragar & Scoates (1981) and Green et al. (1985) related the intrusive rocks to the initial rifting of the western portion of the Superior Province margin and onset of oceanic spreading.

Stauffer (1984) proposed that the southwestern Hearne Province was covered by a sea termed the Manikewan Ocean. Green et al. (1985) suggested that the opening of this ocean led to the intrusion of the Thompson Nickel Belt ultramafic rocks. In contrast, Weber (1990) proposed a synorogenic rifting model in which oceanic magma underplated the thin Superior Province continental margin and was erupted in a marginal or back-arc basin setting. Hoffman (1988) argued for a foredeep basin origin where the foredeep was created by Trans-Hudson thrust sheets advancing onto the Superior Province and buckling the Archaean crust. Bleeker (1990) advocated a model where the ultramafic rocks were intruded as a consequence of the collision between the Superior and Hearne Provinces.

A mantle plume model has been suggested by Buchan et al. (2003) for all the magmatism in the northwestern portion of the Superior Province. These authors proposed that a plume head impinged beneath crust just to the north of the Thompson Nickel Belt and fed the magmatism in the Thompson, Fox River and Lake Superior regions. Percival et al. (2005) have also suggested that a plume may have been the source of the Thompson Nickel Belt magmatism. In this model, a plume impinged beneath, and led to the rifting of, the Superior Province margin shortly after the margin had experienced continental arc magmatism. Subduction-related magmatism is known to have occurred >100 km west of the Thompson Nickel Belt in the Trans-Hudson Orogen at ~1.92-1.84 Ga (Lucas et al., 1996). This magmatism is preserved as the Flin Flon Belt and consists of volcanic, intrusive and plutonic rocks of varying lithological and chemical composition (Lucas et al., 1996).

The ~1891-1871 Ma felsic plutons in the Thompson Nickel Belt have been interpreted to be derived from eastward-directed subduction beneath the Superior Province (e.g. Zwanzig et al., 2003; Percival et al., 2004, 2005). However, Heaman et al. (2009) have noted the conformable relationship between a monzogranite pluton and an underlying ultramafic intrusive and suggested this relationship indicates that some of the felsic magma in the Thompson Nickel Belt was derived from the melting of continental crust during the emplacement of the ultramafic magmatism.

2.10. Winnipegosis Belt

The Winnipegosis Belt has received very little attention in the academic literature. The belt is a >150 km long, northeast trending greenstone belt consisting of sedimentary and volcanic rocks in a monoclinal, west-dipping and west-facing section (Burnham et al., 2004) (Fig. 2.14). The western margin of the Winnipegosis Belt is thought to be faulted against the sub-Palaeozoic southern extension of the Thompson Nickel Belt whilst the eastern margin is in unconformable contact with Superior Province gneisses. The stratigraphy of the Winnipegosis Belt is reported to include basal conglomerates and sandstones overlain by basalts, komatiites, carbonate iron formations and siliciclastic sedimentary rocks (Theyer, 1997; Burnham et al., 2004).

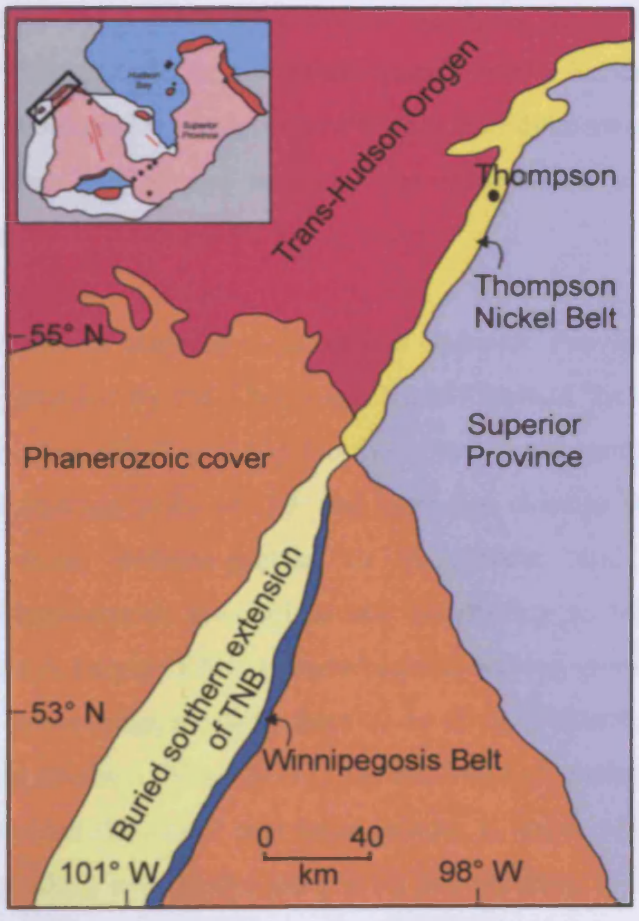

Fig. 2.14. Map showing the location of the Winnipegosis Belt relative to the unexposed, southern extension of the Thompson Nickel Belt. Adapted from Burnham et al. (2004).

The age of the Winnipegosis Belt is constrained by one U-Pb zircon date of 1864 +6/-4 Ma obtained from a coarse grained mafic unit by Hulbert et al. (1994). To date there are no reports of any Ni-Cu-PGE sulphide mineralisation associated with the rocks of the Winnipegosis Belt. There are few models for the petrogenesis of the Winnipegosis Belt. Percival et al. (2005) suggested that rifting of the Superior Province margin led to the eruption of the Winnipegosis volcanic rocks. In the discussion of Burnham et al. (2004) a plume source is advocated for the source of the magmatism.

2.11. Molson dykes

2.11.1. Geology of the Molson dykes

The Molson dykes form a large dyke swarm covering an area of ~26,000 km^2 (Heaman et al., 1986) towards the northwest margin of the Superior Province (Fig. 2.12). A detailed geological investigation of the Molson dyke swarm was carried out by Scoates & Macek (1978) and much of the information in this section is a summary of that study.

The Molson dyke swarm intrudes rocks of the Superior Province and Pikwitonei granulites and is bounded by the Thompson Nickel Belt to the northwest and the Split Lake Fault to the north (Fig. 2.12). No dykes are found south of 52° N latitude. The dykes have an average strike of 030° and have dips close to vertical. They range in composition from dolerite-gabbro to pyroxenite and contain olivine, clinopyroxene, orthopyroxene, plagioclase and hornblende as initial crystallisation phases. Ermanovics & Fahrig (1975) reported quartz-bearing granophyric portions in some dykes. The dykes range in width from <1 to 60 m (Paktunc, 1987) and can be as long as 240 km (Nelson River dyke). On the basis of width and composition, Dawson (1952) divided the dykes into three groups: i) large, >10 m wide dykes of coarse peridotite grading into olivine gabbro; ii) intermediate, 1-10 m wide dykes of gabbro or olivine gabbro; iii) minor, <1 m wide dykes of dolerite. Altogether, the Molson dyke swarm is estimated to represent a magma volume of ~50,000 km^3 (Halls & Heaman, 2000).

Using the U-Pb zircon method, Heaman et al. (1986) obtained ages for the Cross Lake and Cuthbert Lake dykes of 1883.7 +1.7/-1.5 Ma and 1883 ± 2 Ma respectively. Another dyke near Cauchon Lake has a U-Pb zircon age of 1877 +7/-4 Ma (Halls & Heaman, 2000). Heaman et al. (2009) reported three more U-Pb age dates of Molson dykes: i) 1885.2 ± 2.1 Ma for the Bear Island dyke at Sipiwesk Lake, ii) 1884.5 ± 3.8 Ma for the Molson Lake dyke, and iii) 1900 ± 5.8 Ma for the Wakehao Lake dyke. The Carrot River gabbro dyke has a U-Pb age of 1891 ± 4 Ma (Burnham et al., 2004).

Another swarm of dykes of a different age is known to be present in the northwest Superior Province. Halls & Heaman (2000) dated a second dyke at Cauchon Lake and obtained an age of 2091 ± 2 Ma. The 2091 Ma dykes occur in the northern part of the Molson dyke swarm and trend east-northeast. These dykes are also palaeomagnetically distinguishable from the younger ~1880 Ma dykes which make up the Molson dyke swarm *sensu stricto* (Zhai et al., 1994; Halls & Heaman, 2000).

2.11.2. Ni-Cu-PGE sulphide deposits

Peck et al. (1999) have described the occurrence of thin, discontinuous zones of disseminated, matrix and semi-massive sulphides towards the margins of some of the wider Molson dykes which contain Ni-Cu-PGE mineralisation. However, there are no other reports of such mineralisation in the Molson dykes in the literature.

2.11.3. Geodynamic setting

Models for the origin and geodynamic setting of the Molson dyke swarm include rifting, foredeep magmatism and back-arc spreading. Green et al. (1985) suggested that the Molson dyke swarm was emplaced due to continental rifting associated with the breakup of the Superior Province before the development of the Trans-Hudson Orogen. Hoffman (1988) proposed that the Molson dykes were intruded into a foredeep basin created by the buckling of crust during the advancement of Trans-Hudson thrust sheets over the Superior Province. Back-arc spreading prior to the collision of the Superior and Hearne Provinces has also been suggested as the setting of the Molson magmatism (Weber, 1990; Percival et al., 2005). The only plume-origin model for the Molson dykes is that of Buchan et al. (2003). In this model the

Molson dykes form part of a radiating swarm with the Pickle Crow dyke and dykes of the Hudson Bay Lowlands which emanate from a plume head located just to the north of the Thompson Salient. Heaman et al. (2009) argued against a plume origin and suggested that passive upwelling of shallow asthenosphere along the thinned margin of the Superior Province led to the intrusion of the Molson dykes and the other segments of Circum-Superior LIP magmatism.

2.12. Pickle Crow dyke

The Pickle Crow dyke is an 80 m wide, northwest trending dolerite-gabbro dyke that can be traced for ~600 km across the interior of the Superior Province from near the Thompson Salient towards Lake Superior (Buchan et al., 2003) (Fig. 2.2). There are also two dykes parallel and adjacent to the Pickle Crow dyke which have been traced for 60 and 100 km. Buchan et al. (2003) obtained an Ar-Ar hornblende age of 1876 ± 8 Ma for the Pickle Crow dyke and on the basis of this age and the trend of the dyke suggested that the dyke forms part of a radiating dyke swarm with a convergence point to the north of the Thompson Salient and may have fed the ~1880 Ma magmatism in the Lake Superior region. There are no known Ni-Cu-PGE sulphide deposits associated with the Pickle Crow dyke.

2.13. Lake Superior region

Palaeoproterozoic supracrustal rocks in the Lake Superior region form a discontinuous linear belt which extends from central Minnesota to eastern Ontario along the southern margin of the Superior Province (Fig. 2.15). The supracrustal rocks have been assigned to several groups known as the Mille Lacs and North Range Groups in Minnesota, the Animikie Group in Minnesota and Ontario, the Marquette Range Supergroup in northern Michigan and Wisconsin, and the Huronian Supergroup in Ontario. For this study only the Animikie Group and Marquette Range Supergroup are of interest as these contain igneous rocks and are potentially part of the Circum-Superior LIP. For a summary of the geology of all the Lake Superior Palaeoproterozoic supracrustal rocks see Ojakangas et al. (2001).

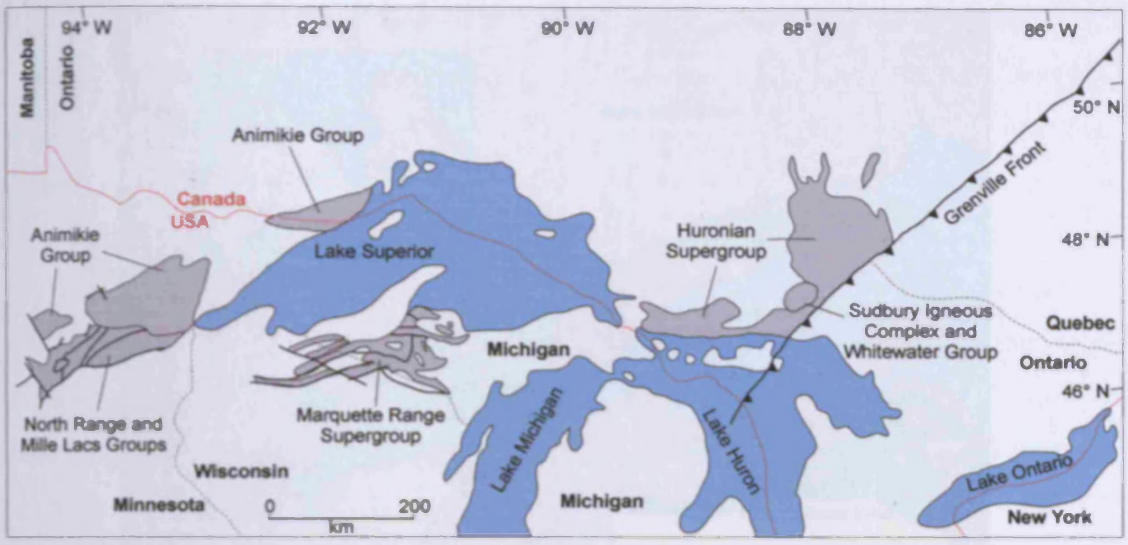

Fig. 2.15. Map of the American-Canadian border in the region of the Great Lakes. Shown is the distribution of Palaeoproterozoic stratigraphic sequences (shaded grey). Adapted from Schulz & Cannon (2007).

2.13.1. Marquette Range Supergroup

Cannon & Gair (1970) assigned iron formations and metasedimentary and metavolcanic rocks exposed to the south of Lake Superior in the northern peninsula of Michigan and adjacent areas in Wisconsin to the Marquette Range Supergroup (Fig. 2.16). The southern limit of the Marquette Range Supergroup is marked by the Niagara Fault Zone where the rocks are in contact with arc-related, volcano-plutonic rocks of the Wisconsin Magmatic Terrane which collided with the southern margin of the Superior Province during the Penokean Orogeny ~1875-1835 Ma (Van Schmus et al., 1975; Van Schmus, 1980; Schulz & Cannon, 2007).

Previous studies have focussed on the geology of the Gogebic, Marquette and Menominee iron ranges and stratigraphic successions have been determined for each range. However, the correlation of stratigraphic units between each range remains controversial and requires further precise U-Pb dating. Fig. 2.17 shows one interpretation of the stratigraphy of the different iron ranges in the Marquette Range Supergroup.

The Marquette Range Supergroup was divided into four groups by Cannon & Gair (1970). The lithologies and stratigraphy of these four groups have been summarised

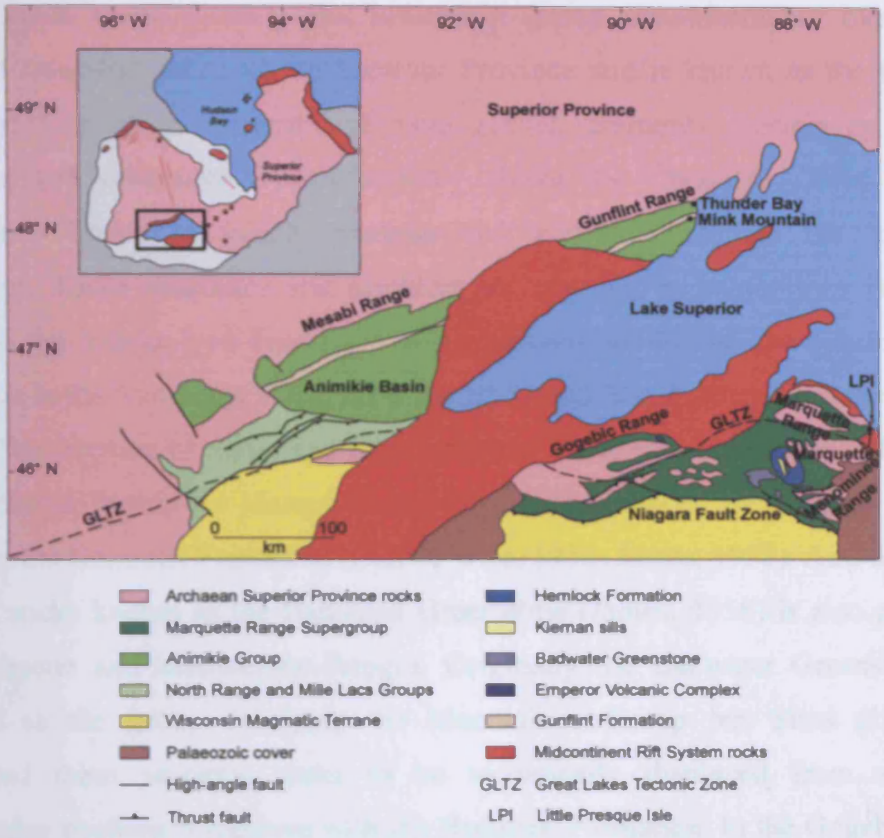

Fig. 2.16. Generalised geological map of the Lake Superior region. Shown is the distribution of the Palaeoproterozoic stratigraphic sequences (Marquette Range Supergroup, Animikie Group, North Range Group and Mille Lacs Group) and Wisconsin Magmatic Terrane, and the location of the Hemlock Formation, Kiernan sills, Badwater Greenstone, Emperor Volcanic Complex and Gunflint Formation. Adapted from Ojakangas et al. (2001).

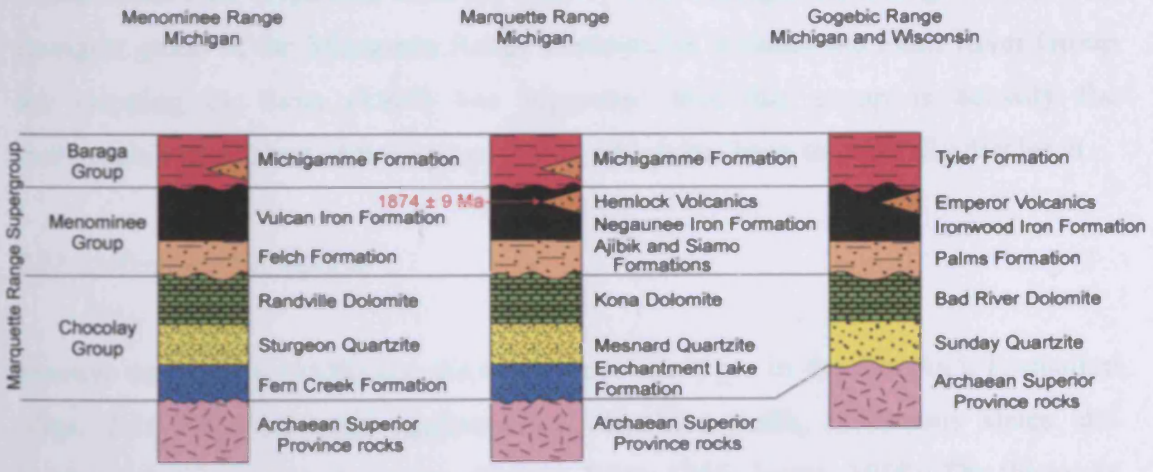

Fig. 2.17. Generalised stratigraphy of the Menominee, Marquette and Gogebic Ranges in the Marquette Range Supergroup of Michigan and Wisconsin. Thickness of units is schematic. Adapted from Schulz & Cannon (2007).

by Ojakangas et al. (2001). The lowermost group unconformably overlies the Archaean basement rocks of the Superior Province and is known as the Chocolay Group. This group is composed of basal glacial sediments overlain by arenites, quartzites and dolomites. Unconformably above the Chocolay Group lies the Menominee Group in which quartzite and argillite dominate the lowermost formations. These quartzites and argillites are overlain by major iron formations known as the Vulcan Iron Formation in the Menominee Range, the Negaunee Iron Formation in the Marquette Range, and the Ironwood Iron Formation in the Gogebic Range. The eruption of mafic and felsic volcanic rocks accompanied iron formation sedimentation. Within the Marquette and Menominee Ranges the volcanic rocks are known as the Hemlock Formation (Gair & Wier, 1956; James, 1958). Another unit of volcanic rocks known as the Badwater Greenstone (James, 1958) is also present in the Marquette and Menominee Ranges. Originally the Badwater Greenstone was assigned to the group overlying the Menominee Group but Sims (1990) has interpreted these volcanic rocks to be tectonically displaced from an initial stratigraphic position correlative with the Hemlock Formation. In the Gogebic Range the Emperor Volcanic Complex (Trent, 1976) lies at the same stratigraphic level as the Hemlock and Badwater volcanic rocks.

The Baraga Group unconformably overlies the Menominee Group and consists of quartzites which grade upwards into a greywacke and shale sequence. A few minor volcanic and iron formation units are interlayered amongst the Baraga Group. The youngest group of the Marquette Range Supergroup is called the Paint River Group but mapping by Sims (1990) has suggested that this group is actually the stratigraphic equivalent of the Baraga Group which has been tectonically displaced.

2.13.2. Hemlock Formation

Massive and pillow basalts are the dominant rock types in the Hemlock Formation (Figs. 2.16-2.17) although agglomerates, rhyolites, tuffs, tuffaceous slates and banded iron formations also occur (Gair & Wier, 1956; James, 1958). The thickness of the Hemlock Formation is extremely variable and ranges from a minimum of 700 m to a maximum of 10 km (Bayley, 1959; Wier, 1967). The age of the Hemlock Formation has been determined by U-Pb zircon dating of a rhyolite flow to be 1874 ±

9 Ma (Schneider et al., 2002). There are no Ni-Cu-PGE sulphide deposits associated with the Hemlock Formation.

2.13.3. Kiernan sills

There are two Kiernan sills intrusive into the Hemlock Formation (Fig. 2.16) which have been mapped by Gair & Wier (1956). The western sill is the larger of the two and is ~20 km long and ~700-5000 m wide. Bayley (1959) described this sill as well differentiated with a basal zone of serpentinised peridotite, a zone of metagabbro, an iron-rich transition zone, granophyric pockets, and a zone of chilled metadolerite. The eastern sill is ~10 km long and 1400 m wide and is composed of undifferentiated gabbro. No Ni-Cu-PGE sulphide mineralisation is known within the Kiernan sills.

There are currently no reliable absolute age determinations for the Kiernan sills. However, field evidence and chemical similarities suggest that the Kiernan sills are comagmatic and coeval with the extrusive Hemlock Formation (Ueng et al., 1988).

2.13.4. Badwater Greenstone

The Badwater Greenstone (Fig. 2.16) consists mainly of massive and pillow basalts (James, 1958). Agglomerates, tuffs and a small amount of sedimentary material are also present, although, unlike the Hemlock Formation, no rhyolites have been observed in the Badwater Greenstone. The thickness of the Badwater Greenstone is not well constrained but is thought to vary and could reach a maximum of 10 km (James, 1958).

No reliable age dates have been obtained from the Badwater Greenstone. Sims (1990) highlighted field evidence which suggests that the Badwater Greenstone is at the same stratigraphic level as the Hemlock Formation. Ueng et al. (1988) also considered it likely that the Badwater and Hemlock volcanic rocks are comagmatic and coeval on the basis of similarities in major element compositions. There are no known Ni-Cu-PGE sulphide deposits associated with the Badwater Greenstone.

2.13.5. Emperor Volcanic Complex

The Emperor Volcanic Complex (Figs. 2.16-2.17) is composed mainly of massive and pillow basalts, minor felsic volcanic rocks, hyaloclastite, and intrusive rocks which include mafic dykes, phacoliths and a thick mafic sill (Trent, 1976; LaBerge, 1992; Licht & Flood, 1992). The Emperor Volcanic Complex is thickest in the eastern portion of the Gogebic Range where its maximum thickness is >2 km (LaBerge, 1992). The Emperor Volcanic Complex is undated but is commonly correlated with the Hemlock Formation (e.g. Trent, 1976; Ojakangas et al., 2001). The Emperor Volcanic Complex is not associated with any Ni-Cu-PGE sulphide mineralisation.

2.13.6. Little Presque Isle lamprophyres

On Little Presque Isle close to Marquette (Fig. 2.16), two perpendicular lamprophyric dykes have yielded an Ar-Ar plateau age of 1877 ± 5 Ma (Craddock et al., 2007). These dykes strike east-west and north-south in a small, ~3 km^2 outcrop. There is no Ni-Cu-PGE sulphide mineralisation associated with these dykes.

2.13.7. Animikie Group

Southwick & Morey (1991) demonstrated that the Animikie Group unconformably overlies the Mille Lacs and North Range Groups to the south and the Superior Province basement to the north. In the more northern exposures, the Animikie Group consists of three major formations in both the Mesabi and Gunflint Ranges (Fig. 2.18). From northeastern Minnesota to the Thunder Bay area of Ontario, the three formations of the Animikie Group are the Kakabeka Quartzite Formation (oldest), Gunflint Formation and Rove Formation (youngest). The Gunflint Formation is of interest to the current study as it contains ~1880 Ma volcanic and volcaniclastic rocks (Fralick et al., 2002).

2.13.8. Gunflint Formation

The Gunflint Formation forms a ~175 km long belt north of Lake Superior with an average thickness of 120 m (Schmidt & Williams, 2003) (Fig. 2.16) and is famous for its Superior-type iron formation (Goodwin, 1956) and well preserved microfossils and stromatolites (Awramik, 1976). Fralick & Barrett (1995) divided the Gunflint Formation into two members: i) a lower member with a basal conglomerate layer and overlying cherty grainstones that pass laterally into jasper-rich grainstones; ii) an upper member containing a similar stratigraphy to that of the lower member but with the addition of black shales, volcanic ash beds and basaltic lavas. The Gunflint lavas are composed of massive and pillow basalts which outcrop in a small area near Mink Mountain in Ontario (Fig. 2.16). Fralick et al. (2002) obtained a U-Pb zircon age from volcanic ash in the upper member of 1878 ± 1.3 Ma. The basaltic nature and limited extent of lavas in the Gunflint Formation means that they are an unlikely source of the ash deposits, which probably were derived from explosive rhyolitic volcanism (Kissin & Fralick, 1994). However, the basalts are considered to be of a similar age given their similar stratigraphic position. The Gunflint Formation volcanic rocks are not associated with any Ni-Cu-PGE sulphide deposits.

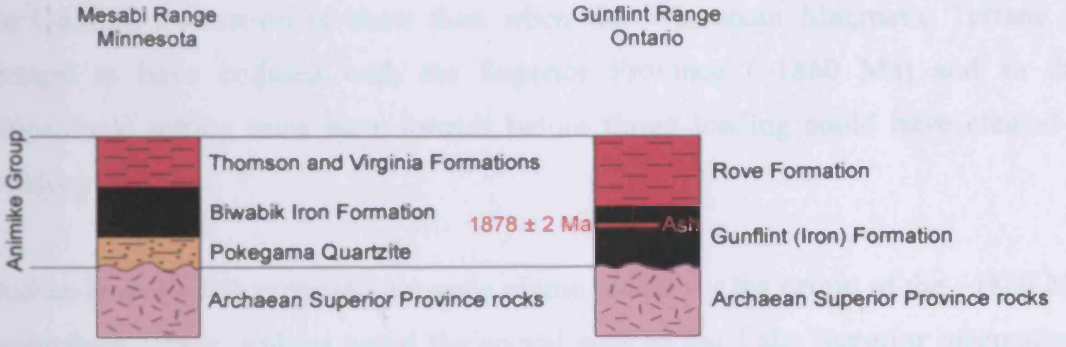

Fig. 2.18. Generalised stratigraphy of the Mesabi and Gunflint Ranges of the Animikie Group of Ontario and Minnesota. Thickness of units is schematic. Adapted from Schulz & Cannon (2007).

2.13.9. Geodynamic setting

Schulz (1987) related the Palaeoproterozoic sediments and volcanic rocks in the Lake Superior region to the initial stages of continental rifting. Southwick & Morey

(1991) and Ojakangas et al. (2001) also suggested that the volcanic rocks are related to the rifting stage of the Penokean Orogeny and erupted onto the continental shelf of the Superior Province. Hoffman (1987) refined the model of Schulz (1987) and proposed that the lower assemblages are representative of rifting deposits whereas the ~1880 Ma volcanic rocks were erupted in a foredeep basin related to the Penokean Orogeny. Schneider et al. (2002) similarly proposed that the Hemlock volcanic rocks were deposited in foredeep basins created by the oblique subduction of the Superior Province continental margin during the Penokean Orogeny.

In a geochemical study of the Hemlock and Badwater volcanic rocks and the Kiernan sills, Ueng et al. (1988) interpreted the igneous rocks to be derived from a common magma source similar to N-MORB which underwent assimilation-fractional crystallisation. Ueng et al. (1988) proposed that the magma was generated in a rifting environment which was analogous to the opening of the North Atlantic Ocean in the early Tertiary.

Van Schmus (1976), Kissin & Fralick (1994), Hemming et al. (1995), Fralick et al. (2002) and Schulz & Cannon (2007) have suggested that the ~1880 Ma Lake Superior magmatism was erupted in a spreading back-arc basin formed by extensionally-driven subsidence. Fralick et al. (2002) noted that the age obtained for the Gunflint Formation is older than when the Wisconsin Magmatic Terrane is thought to have collided with the Superior Province (~1860 Ma) and so the depositional setting must have formed before thrust loading could have created a foredeep basin.

Buchan et al. (2003) proposed a mantle plume model for the origin of the ~1880 Ma magmatism. These authors noted the coeval ages of the Lake Superior magmatism and the Pickle Crow dyke and suggested that the Pickle Crow dyke fed the magmatism around Lake Superior from a plume which impinged upon the lithosphere at a point just to the north of the Thompson Salient.

2.14. Labrador Trough

2.14.1. Geology of the Labrador Trough

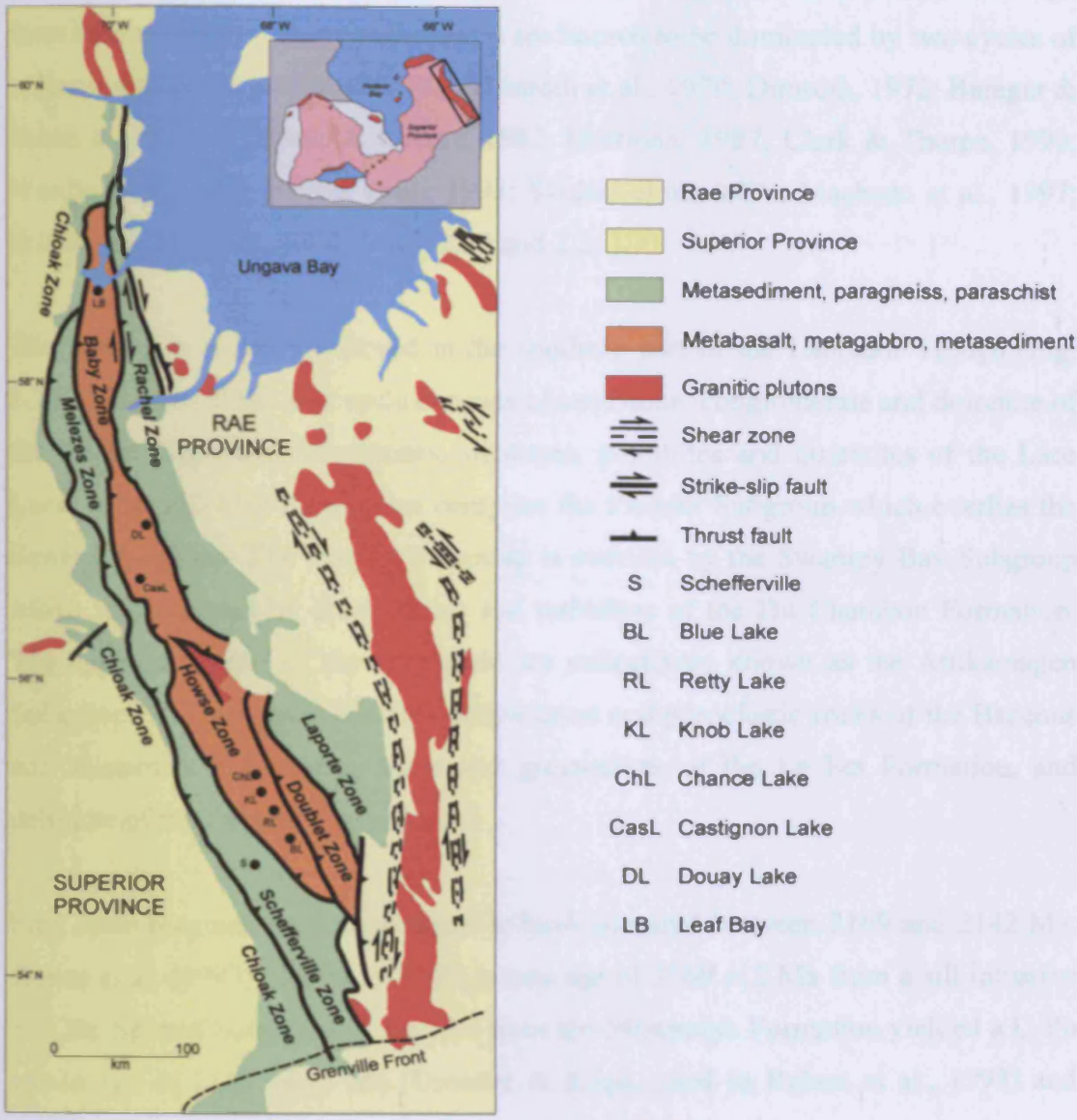

Fig. 2.19. Regional geological map of the Labrador Trough. Adapted from Machado et al. (1997).

The Labrador Trough, commonly referred to as the New Quebec Orogen, is an ~800 km long, northwest trending collisional zone along the northeast margin of the Superior Province extending from the Grenville Front to Ungava Bay (Fig. 2.19). The Labrador Trough has been divided into three major belts and further subdivided into eight tectonic zones (Wardle et al., 1990; Skulski et al., 1993). The western

division is comprised mainly of parautochthonous to allochthonous sediments of the Chioak, Melezes and Schefferville zones. The central division is largely a volcano-sedimentary belt and intrusive sills within the Howse, Baby and Doublet zones. The eastern division contains metasediments, granitoids and Archaean basement of the Laporte and Rachel zones. The geology and lithostratigraphy of the Labrador Trough have been studied by many authors and are known to be dominated by two cycles of volcano-sedimentary sequences (e.g. Dimroth et al., 1970; Dimroth, 1972; Baragar & Scoates, 1981; Le Gallais & Lavoie, 1982; Hoffman, 1987; Clark & Thorpe, 1990; Wardle et al., 1990; Rohon et al., 1993; Skulski et al., 1993; Machado et al., 1997; Williams & Schmidt, 2004) (Figs. 2.20 and 2.21).

The first cycle is best preserved in the southern part of the Labrador Trough (Fig. 2.20). The base of the first cycle consists of sandstone, conglomerate and dolomite of the Seward Subgroup. Mudstones, siltstones, dolomites and quartzites of the Lace Lake, Alder and Uve Formations comprise the Pistolet Subgroup which overlies the Seward Subgroup. The Pistolet Subgroup is overlain by the Swampy Bay Subgroup which is dominated by black shales and turbidites of the Du Chambon Formation. The uppermost units of the first cycle are collectively known as the Attikamagen Subgroup. This subgroup contains pillow lavas and pyroclastic rocks of the Bacchus and Mistamisk Formations, slates and greywackes of the Le Fer Formation, and dolomite of the Denault Formation.

First cycle magmatism is constrained to have occurred between 2169 and 2142 Ma. Rohon et al. (1993) obtained a U-Pb zircon age of 2169 ± 2 Ma from a sill intrusive into the Seward Subgroup. A rhyolite from the Mistamisk Formation yielded a U-Pb zircon age of 2142 +4/-2 Ma (Dressler & Kogh, cited in Rohon et al., 1993) and represents a minimum age for the first cycle magmatism.

Towards the west of the southern Labrador Trough, the second cycle of rocks begins with quartzites of the Wishart Formation unconformably overlying the Denault Formation. The Wishart Formation underlies shales belonging to the Ruth Formation which are overlain by a major iron formation known as the Sokoman Formation. In the Schefferville-Knob Lake area, the Sokoman Formation can reach 240 m in thickness (Williams & Schmidt, 2004). Also in the Schefferville area, the Sokoman

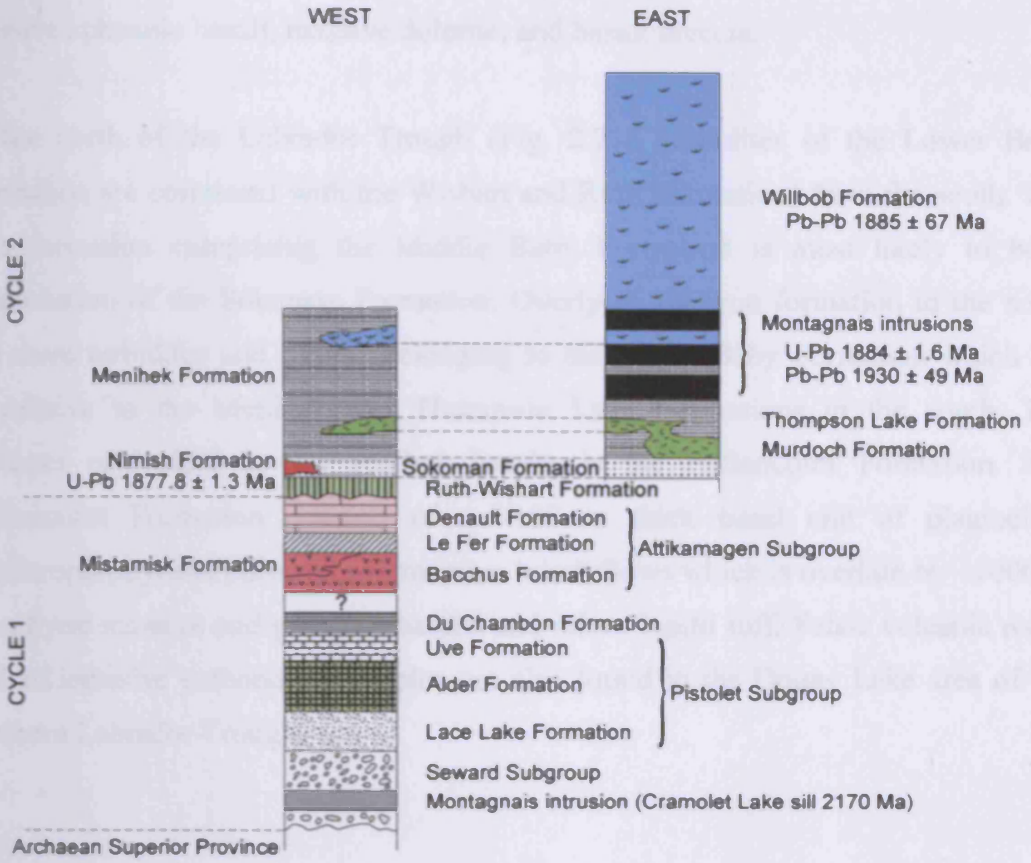

Fig. 2.20. Stratigraphy of the southern portion of the Labrador Trough. Thickness of units is schematic. Adapted from Rohon et al. (1993).

Formation is interbedded with an alkaline, mafic to felsic volcano-plutonic suite known as the Nimish Formation. A carbonatite complex of dykes, sills, diatremes and volcaniclastic rocks covering an area of ~300 km^2 near Castignon Lake is also contemporaneous with the Sokoman Formation. Turbidites of the Menihek Formation overlie the Sokoman Formation and are the uppermost preserved rocks of the second cycle sequence in the western side of the southern Labrador Trough.

In the east part of the southern Labrador Trough, the Sokoman Formation is not as well represented as it is in the west. Turbidites of the Thompson Lake Formation overlie the Sokoman Formation and are correlated with the Menihek Formation in the west. Mafic pyroclastic rocks of the Murdoch Formation are intercalated with the Thompson Lake turbidites. Overlying the Thompson Lake Formation is a ~5.5 km thick pile of basalt flows known as the Willbob Formation. The Willbob Formation

contains a variety of facies of basaltic rocks including pillow basalt, columnar basalt, massive aphanitic basalt, massive dolerite, and basalt breccia.

In the north of the Labrador Trough (Fig. 2.21), turbidites of the Lower Baby Formation are correlated with the Wishart and Ruth Formations from the south. The iron formation comprising the Middle Baby Formation is most likely to be a continuation of the Sokoman Formation. Overlying the iron formation in the north are more turbidites and basalts belonging to the Upper Baby Formation which are correlative to the Menihek and Thompson Lake Formations in the south. The northern equivalent to the Willbob basalts is the Hellancourt Formation. The Hellancourt Formation consists of a <100 m thick basal unit of plagioclase glomeroporphyritic, pillowed and massive basalt flows which is overlain by ~1000 m of aphyric massive and pillowed basalts and minor lapilli tuff. Felsic volcanic rocks and an intrusive carbonatite complex are also found in the Douay Lake area of the northern Labrador Trough.

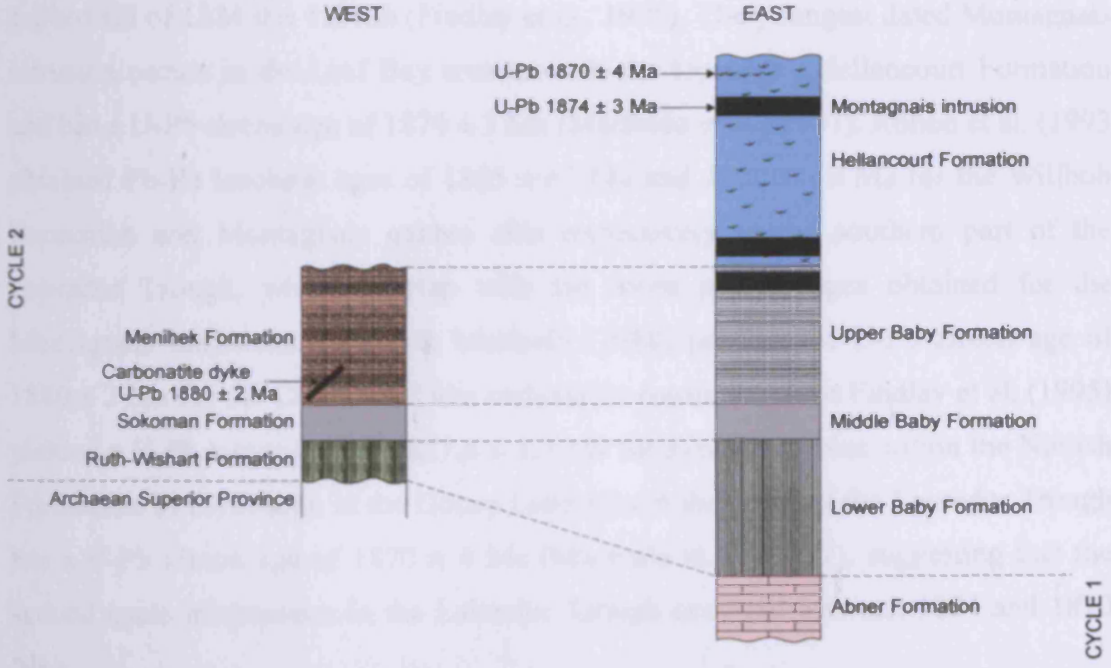

Fig. 2.21. Stratigraphy of the northern portion of the Labrador Trough. Thickness of units is schematic. Adapted from Clark & Thorpe (1990).

Numerous sills are known to intrude at various stratigraphic levels of the second cycle in both the north and south of the Labrador Trough. These sills are collectively known as the Montagnais intrusions. The sills are mostly comprised of gabbro, glomeroporphyritic gabbro and/or peridotite. Plagioclase glomeroporphyritic sills are not as common as the equigranular gabbro sills and tend to be located in the north of the Labrador Trough at the contact between the Upper Baby and Hellancourt Formations (Skulski et al., 1993). Differentiated glomeroporphyritic sills consist of olivine pyroxenite overlain by a glomeroporphyritic gabbro with a granophyric roof. The equigranular sills are mainly composed of homogenous ophitic gabbro but can be differentiated with layers of olivine gabbro, ophitic gabbro, ferrogabbro, peridotite, quartz diorite and granodiorite. In the Retty Lake-Chance Lake area of the southern Labrador Trough, the equigranular sills have gabbroic roofs and bases with central ultramafic cumulates consisting of olivine, pyroxene and amphibole. Peridotitic sills are most common in a narrow belt in the eastern part of the central Labrador Trough (Baragar & Scoates, 1981).

The second cycle magmatism is related to the Circum-Superior LIP. The oldest age of the Montagnais intrusions is from a U-Pb zircon date of a glomeroporphyritic gabbro sill of 1884.0 ± 1.6 Ma (Findlay et al., 1995). The youngest dated Montagnais intrusion occurs in the Leaf Bay area towards the top of the Hellancourt Formation and has a U-Pb zircon age of 1874 ± 3 Ma (Machado et al., 1997). Rohon et al. (1993) obtained Pb-Pb isochron ages of 1885 ± 67 Ma and 1930 ± 49 Ma for the Willbob Formation and Montagnais gabbro sills respectively in the southern part of the Labrador Trough, which overlap with the more precise ages obtained for the Montagnais intrusions. Cheve & Machado (1988) produced a U-Pb zircon age of 1880 ± 2 Ma for the Castignon Lake carbonatite complex whilst Findlay et al. (1995) yielded a U-Pb zircon age of 1877.8 ± 1.3 Ma for syenite cobbles within the Nimish Formation. A rhyodacite in the Douay Lake area in the north of the Labrador Trough has a U-Pb zircon age of 1870 ± 4 Ma (Machado et al., 1997), suggesting that the second cycle magmatism in the Labrador Trough occurred between 1884 and 1870 Ma.

2.14.2. Ni-Cu-PGE sulphide deposits

There is very little published information concerning Ni-Cu-PGE sulphide mineralisation in the Labrador Trough. The presence of such mineralisation in the Montagnais intrusions has been noted in both the north and south of the Labrador Trough. Skulski et al. (1993) and Mungall & Wares (1997) noted that in the north of the belt, sulphide mineralisation is only associated with the glomeroporphyritic gabbro Montagnais sills. Lenses of disseminated sulphides, with pyrrhotite and chalcopyrite dominating the sulphide mineralogy, occur mainly in differentiated glomeroporphyritic gabbro sills at the contact between the Baby and Hellancourt Formations. Rohon et al. (1993) has highlighted the presence of sulphide mineralisation in differentiated Montagnais sills in the southern Labrador Trough. Beaudoin et al. (1990) described the occurrence of sulphide mineralisation in a Montagnais sill at the contact between pelites of the Thompson Lake Formation and basalts of the Willbob Formation near Blue Lake. The sill near Blue Lake is composed of a peridotitic base and an upper gabbronorite unit with a granophyric zone and chilled margin. Lenses of massive sulphides occur at different levels within the sill and are composed of pyrrhotite, chalcopyrite, pentlandite and magnetite. The Blue Lake deposit is estimated to contain ~2.9 Mt of ore at a grade of 0.56% Ni, 1.02% Cu, 0.78 g/t Pd and 0.26 g/t Pt (Clark et al., 1989; Clark, 2001). Clark (2001) has located several sites in the Labrador Trough with sulphide mineralisation and has suggested that the Montagnais sills are good targets for Ni-Cu-PGE deposits, particularly for the PGEs.

2.14.3. Geodynamic setting

The volcano-sedimentary sequences within the Labrador Trough have been interpreted as recording rifting of the Superior Province margin and the production of oceanic crust (e.g. Baragar & Scoates, 1981; Le Gallais & Lavoie, 1982). Hoffman (1987) argued for a foredeep basin origin for the second cycle magmatism whilst Hoffman (1990) proposed a model in which this magmatism occurred along the western margin of the southeast Rae Province in a dextral oblique extension setting above an east-dipping subduction zone.

On the basis of geochemistry, Rohon et al. (1993) interpreted the Hellancourt/Willbob Formation basalts to have originated from a depleted mantle source in a back-arc basin. Skulski et al. (1993) agreed that the ~1880 Ma magmatism was deposited in an extensional regime. These authors noted the progressive change to deeper depositional environments within the sedimentary sequences and also the contrasting composition of volcanism (Castignon carbonatites, Nimish alkaline volcanic rocks, picritic and basaltic Hellancourt and Willbob volcanic rocks, late stage felsic and carbonatitic complexes) as convincing evidence of extension. Skulski et al. (1993) proposed that the volcanism was triggered by dextral transtension between the colliding Superior and Rae Provinces and emplaced in pull-apart basins along the thinned margin of the Superior Province via the Montagnais sills.

The only model involving a mantle plume in the petrogenesis of the ~1880 Ma Labrador Trough magmatism is that of St-Onge et al. (2000) in which the melting of a plume generated all the ~1880 Ma magmatism around the Ungava Peninsula and led to the breakaway of the Meta Incognita microcontinent now preserved in the southwest of Baffin Island.

2.15. Carbonatites

There are a number of carbonatite complexes in the Superior Province (Fig. 2.22) which have either been accurately dated at ~1880 Ma or are considered likely to be this age. These complexes have received little attention in the literature and below are only brief summaries of each complex.

2.15.1. Borden Township

The Borden Township carbonatite complex occurs in the southern portion of the Kapuskasing Structural Zone (Fig. 2.22) which is a zone of major structural weakness, effectively splitting the Superior Province in two, where lower level, amphibolite-granulite facies rocks are juxtaposed with higher level, lower grade metamorphic rocks (Percival & West, 1994; Perry et al., 2006). Bell et al. (1987) obtained a Pb-Pb isochron age of 1872 ± 13 Ma for the complex while Rukhlov &

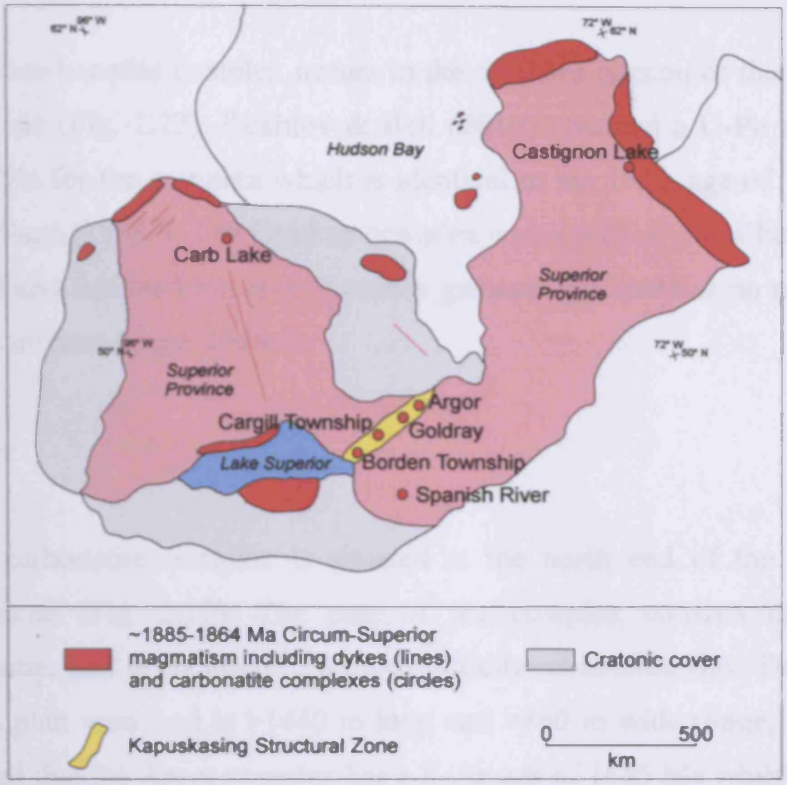

Fig. 2.22. Schematic map of the Superior Province highlighting the position of carbonatite complexes which are ~1880 Ma in age. Map adapted from Baragar & Scoates (1981).

Bell (2010) yielded a Pb-Pb age from a zircon fraction of 1882.0 ± 3.9 Ma. The carbonatite complex is arcuate in shape and consists of a series of cone sheets emplaced into brecciated and fenitised Superior Province gneisses (Sage, 1987a). Sovites and silicocarbonatites are the dominant types of carbonatite while dolomite and lamprophyre dykes are also present. The complex covers a surface area of ~4.1 km^2 and hosts apatite, Nb and U mineralisation (Sage, 1987a).

2.15.2. Cargill Township

The Cargill Township carbonatite complex is found ~150 km north of the Borden Township complex along the Kapuskasing Structural Zone (Fig. 2.22). The age of the complex may be older than the ultramafic-mafic magmatism circumscribing the Superior Province. Two U-Pb dates obtained from the carbonatite complex give ages of 1907 ± 4 Ma (Sage, 1988b) and 1896.8 ± 1.4 Ma (Rukhlov & Bell, 2010).

2.15.3. Goldray

The Goldray carbonatite complex occurs in the northern portion of the Kapuskasing Structural Zone (Fig. 2.22). Rukhlov & Bell (2010) obtained a U-Pb zircon age of 1886 ± 0.9 Ma for the complex which is identical to the U-Pb age of 1886 ± 2 Ma reported by Sage (1988c). The Goldray complex consists of sovite, silicocarbonatite, hornblendite and fenitised Superior Province gneisses but contains no mineralisation of economic interest (Sage, 1988c).

2.15.4. Argor

The Argor carbonatite complex is situated at the north end of the Kapuskasing Structural Zone (Fig. 2.22). The core of the complex consists of sovite and silicocarbonatite and is enclosed in a pyroxenitic-hornblenditic rim. The complex is dyke-like in plan view and is >1440 m long and >360 m wide (Sage, 1988a). Sage (1988a) noted that the Argor complex has a K-Ar age of 1655 Ma whilst a Pb-Pb age of 1950 Ma was reported by Sage (1992). Rukhlov & Bell (2010) produced a Pb-Pb age from zircon of 1769 ± 23 Ma, suggesting that the complex is not related to the Circum-Superior LIP. The Argor complex is also known to contain Nb deposits of economic interest (Sage, 1988a).

2.15.5. Spanish River

Unlike the above complexes, the Spanish River carbonatite complex is not situated in the Kapuskasing Structural Zone (Fig. 2.22) but occurs in a fault zone associated with the Ottawa-Bonnechere graben system (Mereu et al., 1986; Sage, 1987c; Salad Hersi & Dix, 2006). The complex has a surface area of ~2 km^2 and a core of silicocarbonatite and sovite with an outer margin of pyroxenite, ijolite and syenite surrounded by fenitised Superior Province quartz monzonite (Sage, 1987c). Previously the best age estimate for the Spanish River complex is a Rb-Sr age reported by Bell & Blenkinsop (1980) of 1838 ± 95 Ma. However, recently Rukhlov & Bell (2010) obtained a Pb-Pb zircon age of 1880.6 ± 2.4 Ma. No mineralisation of economic interest is present within the complex (Sage, 1987c).

2.15.6. Carb Lake

The Carb Lake carbonatite complex is located towards the northwest of the Superior Province (Fig. 2.22) within the Kenyon Structural Zone (Ayres et al., 1971; Gupta, 1991). The core of the complex consists of silicocarbonatite and sovite with minor narrow bands of biotitite and magnetite. The surface area of the complex is ~8 km^2. The complex has been dated by the K-Ar method at 1826 ± 97 Ma (Sage, 1987b) and by the Pb-Pb zircon method at 1865 ± 22 Ma (Rukhlov & Bell, 2010) and is prospective for Nb and REEs (Sage, 1987b).

2.15.7. Castignon Lake

The Castignon Lake carbonatite complex is located in the central Labrador Trough (Fig. 2.22). The geology of the Castignon Lake area has been described by Dimroth (1969). The carbonatite complex consists of intrusive dykes and volcanic breccias which form diatremes. There is no estimate on the overall size of the complex but the dykes range from ~0.5 m to ~30 m in thickness and can be traced for several kilometres. The age of the complex has been constrained by a U-Pb zircon age determination from a carbonatite dyke of 1880 ± 2 Ma by Cheve & Machado (1988). There are no reports of mineralisation of any economic interest associated with the carbonatite rocks of Castignon Lake.

2.16. Origin of the Circum-Superior LIP

Until recently, researchers have studied the origin and geodynamic setting of the various segments of the Circum-Superior LIP without linking all the segments together as a single entity. Various models for the formation of the Circum-Superior LIP segments have been suggested, as described in sections 2.4 to 2.15. These models include continental margin rifting, ocean floor spreading, back-arc basin rifting, volcanic arc volcanism, foredeep basin flexure, transtension in pull-apart basins along thinned continental margins, and mantle plume volcanism. More recent studies (e.g. Buchan et al., 2003; Desharnais, 2005; French et al., 2008; Heaman et al., 2009) have begun interpreting the Circum-Superior LIP as a single entity and suggesting possible modes of formation. Buchan et al. (2003) and Desharnais (2005)

advocated a mantle plume origin largely based on the presence of a possible radiating dyke swarm involving the Molson and Pickle Crow dykes. French et al. (2008) and Heaman et al. (2009) dismissed a mantle plume origin and favoured passive upwelling of N-MORB source asthenosphere along the thinned margins of the craton. Heaman et al. (2009) cited five main reasons against a mantle plume origin: i) the lack of a convincing radiating dyke swarm; ii) lack of evidence for uplift prior to volcanism; iii) lack of a hotspot track; iv) widely dispersed segments of volcanism along a continental margin; and v) presence of NMORB-like geochemical signatures and absence of ocean island basalt (OIB) geochemical signatures.

2.17. Global magmatism at ~1.88 Ga

Advancements in high precision U-Pb zircon/baddeleyite geochronology have led to the recognition of new LIPs and to the geographical extension of known LIPs, particularly in the Precambrian (Ernst & Buchan, 2001a). It is now recognised that there are many coeval LIPs or LIP fragments scattered on different cratons around the world. These coeval units are being utilised for reconstructing the continents back into the Proterozoic and Archaean (e.g. Bleeker & Ernst, 2006). There are a number of cratons which contain remnants of magmatism dated at ~1.88 Ga (Fig. 2.23), the same age as the Circum-Superior LIP. Below is a brief summary of the different localities where ~1.88 Ga magmatism is found.

Fig. 2.23. Map of the world with areas containing magmatic rocks aged ~1.88 Ga marked in red.

2.17.1. ~1.88 Ga magmatism in Australia

Magmatic activity occurring at ~1880 Ma has been recorded in the Halls Creek Orogen of northwestern Australia. The Halls Creek Orogen is an orogenic belt which formed between the East Kimberley and the composite North Australian cratons (Myers et al., 1996; Bodorkos et al., 1999; Sheppard et al., 1999; Griffin et al., 2000). The oldest rocks in the orogen are Palaeoproterozoic and are variably deformed and metamorphosed plutonic, volcanic and sedimentary rocks known collectively as the Lamboo Complex (Tyler et al., 1995). The Lamboo Complex is divided into three northeast-trending zones (Western, Central and Eastern Zones) (Tyler et al., 1995). The ~1880 Ma magmatism is preserved in the Eastern Zone of the Lamboo Complex which is comprised of the Halls Creek Group. The Halls Creek Group comprises three formations (Griffin and Tyler, 1992). The lowermost unit is the Saunders Creek Formation which is mostly composed of meta-quartz and meta-feldspathic sandstones. The uppermost formation contains quartz and feldspathic wackes, quartz and arkosic sandstones, siltstones and mudstones and is known as the Olympio Formation. The middle unit is termed the Biscay Formation and is comprised mostly of massive metabasalt lavas, mafic volcaniclastics and fragmental deposits, with minor amounts of metadolerite sills, sediments and felsic volcanic rocks (Tyler et al., 1995; Sheppard et al., 1999). Felsic volcanic rocks of the Biscay Formation have been dated by U-Pb zircon techniques and give an age of 1880 ± 3 Ma (Blake et al., 1998, cited in Sheppard et al., 1999).

The age determination for the Biscay Formation appears to be the only age date of ~1880 Ma obtained from magmatic rocks in Australia. However, there is evidence of further magmatism ~1865 Ma which is preserved within the Central Zone of the Lamboo Complex. The Tickalara Metamorphics are the oldest rocks in the Central Zone and consist of mafic metavolcanic rocks, turbiditic and calcareous metasediments, and metamorphosed tonalite and trondhjemite (Tyler et al., 1995; Sheppard et al., 1999). The maximum age of the Tickalara Metamorphics is constrained by the presence of detrital zircons in the metaturbidites which yielded a U-Pb age of 1865 ± 2 Ma (Page et al., 1995). Leucocratic granite sheets intrusive

into the Tickalara Metamorphics are dated at 1863 Ma (Tyler & Page, 1996) which must therefore be the minimum age of the Tickalara mafic metavolcanic rocks.

2.17.2. ~1.88 Ga magmatism in southern Africa

~1880 Ma magmatism is thought to be preserved in both the Kaapvaal and Zimbabwe cratons in southern Africa. These two Archaean cratons are juxtaposed along the heavily deformed and metamorphosed Limpopo Belt and together with the Limpopo and Namaqua Belts form what is referred to as the Kalahari craton (Clifford, 1970).

Hanson et al. (2004a, 2004b) obtained U-Pb baddeleyite ages of 1878.8 ± 0.5 Ma, 1873.7 ± 0.8 Ma and 1871.9 ± 1.2 Ma from doleritic sills intruding the Waterberg Group sediments in the Kaapvaal craton. Another group of ages ~1927 Ma were also obtained from the dolerite sills indicating that more than one magmatic episode is responsible for the doleritic intrusions. Palaeomagnetic studies conducted by Hanson et al. (2004a, 2004b) on the ~1878-1872 Ma samples found that the poles of the dolerite sills are antipodal to the poles of basaltic lavas and sills belonging to the Soutpansberg Group (Bumby et al., 2001, 2002) to the north of the Waterberg Group. This suggests that the Soutpansberg magmatism is coeval with and was emplaced as part of the same event as the ~1878-1872 Ma Waterberg Group magmatism but during a reversed magnetic polarity chron.

Mafic dykes known as the Sand River dykes present in the Southern Marginal Zone of the Limpopo Belt may also be ~1880 Ma in age. Barton (1979) obtained a Rb-Sr whole rock isochron age of 1876 ± 68 Ma from these dykes.

The Mashonaland sills cover an area of ~160,000 km^2 in the northeastern Zimbabwe craton (Barton & Pretorius, 1997). These sills have yielded U-Pb baddeleyite ages of 1877 ± 2.2 Ma, 1885.9 ± 1.8 Ma and 1875.6 ± 1.6 Ma (Soderlund et al., 2010). The east-west trending Mazowe River dykes may belong to the same igneous episode as the Mashonaland sills given the similar palaeomagnetic directions and a Rb-Sr whole rock age for the Mazowe River dyke of 1870 ± 600 Ma (Wilson et al., 1987).

2.17.3. ~1.88 Ga magmatism in India

Magmatism of ~1880 Ma age is found in both the Bastar and Dharwar cratons which form part of the Archaean shield complex of peninsular India. In the south of the Bastar craton the northwest-trending BD2 dolerite dyke swarm intrudes basement and supracrustal rocks. The swarm outcrops over a minimum area of ~1000 km^2 and has yielded two U-Pb ages of 1891.1 ± 0.9 Ma and 1883 ± 1.4 Ma (French et al., 2008). There are many more northwest-trending dolerite dykes with an areal extent of ~17,000 km^2 in the southern Bastar craton (Ramachandra et al., 1995) which may be the same age.

Magmatic rocks of similar age to the dykes in the Bastar craton are also found in association with the Cuddapah basin in the Dharwar craton. The Cuddapah basin is a crescent-shaped basin covering an area of 44,500 km^2 in the eastern sector of the Dharwar craton (Singh and Mishra, 2002). French et al. (2008) obtained a U-Pb baddeleyite age of 1885.4 ± 3.1 Ma from the Pulivendla sill which intrudes the Tadpatri Formation in the western part of the Cuddapah basin. There are numerous mafic dykes around the basin which are undated using reliable techniques. However, one east-west trending dyke to the southwest of the Cuddapah basin has yielded an Ar-Ar whole rock age of 1879 ± 5 Ma (Chatterjee & Bhattacharji, 2001). French et al. (2008) linked together the ~1880 Ma magmatism in the Dharwar and Bastar cratons and coined the term the Southern Bastar-Cuddapah LIP.

2.17.4. ~1.88 Ga magmatism in the Aldan Shield

The Aldan Shield is one of the accreted provinces which form the Siberian Platform. Mafic dykes are known to intrude the granite-greenstone and high-grade gneiss terranes of the Aldan Shield (Ernst et al., 1996; Jahn et al., 1998; Ernst & Buchan, 2001a). A northeasting-trending mafic dyke swarm known as the Kalaro-Nimnyrsky swarm is intrusive into the Aldan Shield, extending for >300 km and covering an area of ~215,000 km^2 (Ernst et al., 1996; Ernst & Buchan, 2001a). K-Ar dating previously constrained the age of this swarm to be ~1650-1000 Ma (Ernst & Buchan, 2001a). However, an Ar-Ar hornblende age of 1866 ± 9 Ma has been reported from these northeast-trending dykes (R. Ernst, pers. comm. 2007). These dykes may be

related to the magmatic rocks of the Akitkan Group and Selenga-Stanovoi superterrane further to the south in the Aldan Shield and which have U-Pb zircon ages ranging from 1878 ± 4 Ma to 1863 ± 9 Ma (Neymark et al., 1991; Larin et al., 2003; Buchko et al., 2006; Didenko et al., 2009).

2.17.5. ~1.88 Ga magmatism in the Baltic Shield

Magmatism of this age in the Baltic Shield is mostly found in volcanic arc complexes within the Finnish and Swedish components of the Svecofennian Orogen. These arc complexes are known as the Southern and Central Svecofennian Arc Complexes. There is a large range of igneous rocks in the Svecofennian Orogen including ultramafic to felsic lavas, mafic and felsic tuffs, mafic dykes and granodiorite, diorite and tonalite intrusions (e.g. Kahkonen, 1987; Vaisanen et al., 2002). These rocks form a number of east-west trending belts which have been subjected to high degrees of deformation and metamorphism (Suominen, 1991). The chemistry of these rocks strongly suggests a subduction-related origin for the Baltic Shield magmatism (Kahkonen, 1987; Vaisanen et al., 2002). The age range of the two arc complexes is from 1904 ± 4 Ma to 1867 ± 9 Ma (Kahkonen et al., 1989; Suominen, 1991; Nironen, 1999; Nironen et al., 2000; Vaisanen et al., 2002).

2.17.6. ~1.88 Ga magmatism in the Outer Hebrides

The geology of the Outer Hebrides is dominated by Archaean tonalitic orthogneisses of the Lewisian Complex (Macdonald & Fettes, 2007). These gneisses are divided into northern and southern domains by the South Harris Complex. The South Harris Complex contains within it the South Harris Igneous Complex which is composed of three large meta-igneous masses (a metanorite, a metadiorite and a meta-anorthosite) and numerous smaller metamorphosed basic and ultrabasic intrusions (Fettes et al., 1992). Mason et al. (2004) produced U-Pb zircon ages from the three main igneous bodies of the South Harris Igneous Complex. The age of the meta-anorthosite is 2491 +31/-27 Ma but the ages of the metanorite and metadiorite are 1890 +2/-1 Ma and 1888 ± 2 Ma respectively. Whitehouse & Bridgwater (2001) also identified a tonalite layer within the metadiorite which yielded a U-Pb zircon age of 1876 ± 5 Ma.

2.17.7. ~1.88 Ga magmatism in Greenland

The Nagssugtoqidian Orogen of southwest Greenland is a ~150 km wide east-west trending belt which consists largely of Archaean and Palaeoproterozoic orthogneisses intercalated with some Palaeoproterozoic supracrustal and magmatic rocks (Kalsbeek & Nutman, 1996). It is generally considered to link up with the Ammassalik mobile belt of eastern Greenland, the two zones being separated on the surface by the Greenland ice cap (e.g. Bridgwater et al., 1990).

The Nagssugtoqidian Orogen can be subdivided into three major lithotectonic sections: the northern, central and southern sections. All three sections are dominated by Archaean gneisses but the central section is known to contain intrusive magmatic rocks of ~1880 Ma age. These magmatic rocks belong to the Arfersiorfik and Sisimiut charnockite igneous suites of the northern and southern regions of the central zone of the orogen respectively. The Arfersiorfik igneous suite mainly consists of a large body of quartz diorite exposed over several hundred square kilometres plus outliers of quartz diorite to tonalitic gneiss sheets (van Gool et al., 2002). The Sisimiut charnockite suite is a ~30 km wide complex of tonalites, diorites, granites, leuconorites, gabbros and hornblende pyroxenites (van Gool et al., 2002).

U-Pb zircon dating of the Arfersiorfik quartz diorite has typically yielded crystallisation ages of ~1920 Ma (Kalsbeek et al., 1987; Kalsbeek & Nutman, 1996; Whitehouse et al., 1998). However, Connelly et al. (2000) have reported a U-Pb age from four zircon fractions of a quartz diorite sample of 1885 +6/-3 Ma, thus suggesting that Arfersiorfik magmatism spanned from ~1920 Ma to ~1885 Ma. A similar age range has been calculated for the Sisimiut charnockite suite. The oldest U-Pb age reported for the charnockites is 1921 ± 10 Ma (Kalsbeek & Nutman, 1996) whilst the youngest is 1873 +7/-4 Ma (Connelly et al., 2000).

The Ammassalik mobile belt is also known to contain ~1880 Ma magmatic rocks. The belt is divided into five zones on the basis of lithology and extent of Proterozoic deformation (Bridgwater et al., 1990). The centre of the belt consists of a meta-igneous complex called the Angmagssalik complex. This meta-igneous complex

contains ultrabasic rocks and layered metagabbro from leuconorite to orthopyroxene-bearing acidic rocks (Bridgwater et al., 1990). A mafic sample from the Angmagssalik complex yielded a U-Pb age of 1886 ± 2 Ma (Hansen & Kalsbeek, 1989, cited in Bridgwater et al., 1990) which makes this igneous activity coeval with that in western Greenland.

2.17.8. ~1.88 Ga magmatism on Baffin Island

Jackson (1971) first described a sequence of metamorphosed igneous and sedimentary rocks on central Baffin Island within the Palaeoproterozoic Piling Group. These rocks form the Bravo Lake Formation which extends for ~120 km across Baffin Island and varies in thickness between 1 and 2 km (St-Onge et al., 2004; Johns et al., 2006). A relatively imprecise U-Pb zircon age of 1916 ± 35 Ma from a dyke within the Bravo Lake Formation has been obtained by Wodicka (2004).

2.17.9. ~1.88 Ga magmatism in the Slave craton

The Ghost dolerite-gabbro dyke swarm forms part of the ~1880 Ma magmatic activity in the Slave craton. The Ghost dykes are found in the southwestern portion of the craton to the northeast of Great Slave Lake between Yellowknife and Ghost Lake and trend in a northeasterly direction (Henderson, 1998; Pehrsson, 2002). Davis & Bleeker (2007) obtained a U-Pb age of 1884.4 ± 3.4 Ma for the Ghost dykes.

Further north in the Slave craton than the Ghost dykes is the Wopmay Orogen which is a ~1.9 Ga north-trending orogenic belt that assembled along the western margin of the craton (Hoffman, 1973; Hoffman & Bowring, 1984). The Wopmay Orogen contains a variety of igneous rocks ranging from mafic intrusive rocks to felsic plutonic rocks, most of which are either imprecisely dated at ~1880 Ma or are slightly younger than ~1880 Ma. In the Great Bear Magmatic Zone of the Wopmay Orogen the age range of magmatic rocks is from 1876 ± 10 Ma to 1843 ± 5 Ma (Bowring et al., 1984; Ghandi et al., 2001).

The Hepburn Intrusive Suite occurs further east in the Wopmay Orogen than the magmatic rocks of the Great Bear Magmatic Zone. The Hepburn Intrusive Suite consists of approximately one hundred plutons of gabbro to granite composition (Hoffman, 1980; St-Onge et al., 1983; Hoffman & Bowring, 1984; Lalonde, 1989). The best age estimate for this intrusive suite is constrained by U-Pb zircon dating to be 1885 Ma (Hoffman & Bowring, 1984). A volcanic ash bed related to the intrusions has also yielded a U-Pb zircon age of 1882 ± 4 Ma (Bowring & Grotzinger, 1992).

A north-south zone of gabbroic sills ~200 km long and ~10 km wide intrude the Wopmay Orogen and are known as the Morel sills (Lalonde, 1988). Davis & Bleeker (2007) regarded the Morel sills to be contemporaneous with the Ghost dyke swarm. This age estimate is largely based on the syncollisional nature of the sills; the Morel sills intrude the Wopmay Orogen deposits but are not deformed (Hoffman, 1987).

The Mara River sheets of the Kilohigok basin occur eastwards from the Wopmay Orogen in the Slave craton. The sheets were described by Fahrig (1987) who assigned an age of 1675 Ma to them. However, Davis & Bleeker (2007) obtained a U-Pb age of 1870 Ma for these intrusive sheets.

2.17.10. ~1.88 Ga magmatism in the Wyoming craton

The extent of ~1880 Ma magmatism is not well constrained in the Wyoming craton. The Prairie Creek gabbroic sill intruding through muds and carbonates in the Black Hills of South Dakota has a U-Pb age of 1883 ± 5 Ma (Redden et al., 1990). This sill is part of a north-trending, vertically-dipping belt of metagabbro intrusions. However, this belt of intrusions contains at least two episodes of magmatism as Redden et al. (1990) obtained a U-Pb age of 1964 ± 15 Ma from another sill within the belt. A U-Pb age of 1884 ± 29 Ma has also been reported from an alkalic metatuff layer ~20 km west of the Prairie Creek gabbroic sill (Redden et al., 1990).

2.18. Environmental crisis

Most of the evidence for a major environmental disturbance at the time of formation of the Circum-Superior LIP comes from Condie et al. (2000) and Condie (2001) and is briefly summarised below.

Peaks in the restored cumulative area of marine intracratonic, passive margin and platform sediments indicate that sea level was relatively high at ~1.9 Ga. At the same time there is a peak in banded iron formation deposition and the chemical index of alteration for shales which is indicative of an increase in the degree of chemical weathering. There is a small peak in the amount of sedimentary phosphates and a larger peak in the number of and diversity of stromatolites at ~1.9 Ga. Massive sulphate evaporites peak just after ~1.9 Ga. The $^{87}Sr/^{86}Sr$ ratio of seawater was low at ~1.9 Ga whilst $\delta^{13}C$ and $\delta^{34}S$ isotope values were high and low respectively indicating that the burial rate of organic carbon increased relative to that of carbonate and the rate of sulphate burial increased relative to that of sulphide. A peak in the abundance of black shale deposits also occurs at ~1.9 Ga.

Condie et al. (2000) and Condie (2001) suggested that this evidence supports the existence of a superplume event at ~1.9 Ga for the following reasons. Sea level would be expected to rise in such an event because of the isostatic uplift and thermal erosion of oceanic lithosphere above plume heads and the displacement of seawater by the formation of oceanic plateaux. High sea levels would provide shallow marine basins ideal for the deposition of banded iron formations. Volcanism and hydrothermal venting associated with plumes could have provided the iron and silica needed to produce the banded iron formations. A peak in the chemical index of alteration for shales would be expected because of the increase in CO_2 in the atmosphere leading to warmer global temperatures which would enhance continental weathering rates. An increased amount of plume volcanism would decrease the relative contribution of Sr to marine carbonates from continental sources and lower the $^{87}Sr/^{86}Sr$ ratio of seawater. The abundance of black shales is consistent with the increased oceanic hydrothermal fluxes, oceanic anoxia and disruption of ocean currents associated with mantle plumes and oceanic plateaux. A high $\delta^{13}C$ value is consistent with a peak in black shale deposition. The increase in CO_2, warmer

temperatures and higher sea levels associated with mantle plume activity would promote stromatolite formation and may explain the peaks in number and diversity of stromatolites at ~1.9 Ga. A peak in the amount of sedimentary phosphates may also be expected as submarine hydrothermal systems associated with mantle plume activity could provide the phosphorus and create the anoxic conditions required for the deposition of sedimentary phosphates.

2.19. Summary

The Circum-Superior LIP extends for ~3000 km around the margins of the Superior Province in Canada (Fig. 2.1). It includes volcanic and intrusive rocks from the Cape Smith Belt, Belcher and Sleeper Islands, Fort Albany area, Sutton Inlier, Fox River Belt, Thompson Nickel Belt, Winnipegosis Belt, Lake Superior region and Labrador Trough. In addition to the cratonic margin magmatism, the Circum-Superior LIP also includes the Molson dykes, Pickle Crow dyke and a number of carbonatite complexes which are intrusive into the craton interior.

A number of different geochronological techniques (e.g. K-Ar, Pb-Pb, Rb-Sr, Re-Os, Ar-Ar, U-Pb) have been used to date rocks which potentially belong to the Circum-Superior LIP (see Table 2.1). These techniques have yielded ages for the Circum-Superior LIP rocks ranging between ~1960 and ~1826 Ma. The more precise method of U-Pb dating shows that the total age range of rocks possibly belonging to the Circum-Superior LIP is more likely to be 1907-1864 Ma (Table 2.1 and Fig. 2.24). If the carbonatite complexes are excluded from the LIP, then the age range, determined from only U-Pb age dates, decreases in length between 1900 and 1864 Ma. However, the vast majority of dated Circum-Superior LIP rocks have ages within the range of 1885 and 1870 Ma (Table 2.1 and Fig. 2.25), which is taken as the age range of the main volcanic activity of the Circum-Superior LIP in this study. The 1864 Ma Winnipegosis Belt probably represents the last manifestation of the Circum-Superior LIP.

The origin of the Circum-Superior LIP is not well understood. Previous studies have tended to look at individual segments and it is only recently that some studies have suggested the Circum-Superior LIP may be a single entity with a common origin.

Table 2.1. Age determinations for rocks belonging to the Circum-Superior LIP

	Dating method	Age (Ma)	Reference
Cape Smith Belt			
Raglan Formation gabbroic intrusion	U-Pb zircon	1887 +39/-11 (1)	Wodicka et al. (2002)
Expo-Ungava Intrusive Suite gabbro	U-Pb zircon	1882.7 ± 1.3 (2)	Randall (2005)
Chukotat Group gabbroic sill	U-Pb	1870 ± 4 (3)	St-Onge et al. (1992)
Hudson Bay			
Flaherty Formation basalts	Pb-Pb isochron	1960 ± 80 (4)	Todt et al. (1984)
Gabbroic Haig sill, Belcher Islands	U-Pb baddeleyite	1870 ± 1 (5)	M.Hamilton (pers. comm. 2008)
Gabbroic Haig sill, Sleeper Islands	U-Pb baddeleyite	1870 ± 4 (6)	M.Hamilton (pers. comm. 2008)
Hudson Bay Lowlands			
Fort Albany dolerite dyke	U-Pb baddeleyite	1870.7 ± 1.1 (7)	Hamilton & Stott (2008)
Sutton Inlier gabbroic sill	U-Pb baddeleyite	1870 ± 2 (8)	M.Hamilton (pers. comm. 2008)
Fox River Belt			
Fox River Sill Marginal Zone gabbro	U-Pb zircon	1882.9 +1.5/-1.4 (9)	Heaman et al. (1986)
Fox River gabbro dyke	U-Pb zircon	1900 ± 14 (10)	Heaman et al. (2009)
Thompson Nickel Belt			
South Setting Lake pyroxenite sill	U-Pb zircon	1880 ± 5 (11)	Hulbert et al. (2005)
Sulphide ores from mineralised intrusions	Re-Os isochron	1885 ± 49 (12)	Hulbert et al. (2005)
Paint Lake pyroxenite sill	U-Pb zircon	1876.7 ± 5.1 (13)	Heaman et al. (2009)
Winnipegosis Belt			
Coarse grained mafic unit	U-Pb zircon	1864 +6/-4 (14)	Hulbert et al. (1994)
Molson dykes			
Granophyric portion of Cross Lake dyke	U-Pb zircon	1883.7 +1.7/-1.5 (15)	Heaman et al. (1986)
Olivine pyroxenite portion of Cuthbert Lake dyke	U-Pb zircon	1883 ± 2 (16)	Heaman et al. (1986)
Cauchon Lake gabbro dyke	U-Pb zircon	1877 +7/-4 (17)	Halls & Heaman (2000)
Bear Island gabbro dyke, Sipiwesk Lake	U-Pb zircon	1885.2 ± 2.1 (18)	Heaman et al. (2009)
Wakehao Lake gabbro dyke	U-Pb zircon and baddeleyite	1900 ± 5.8 (19)	Heaman et al. (2009)
Molson Lake gabbronorite dyke	U-Pb zircon	1884.5 ± 3.8 (20)	Heaman et al. (2009)
Carrot River gabbro dyke	U-Pb	1891 ± 4 (21)	Burnham et al. (2004)
Pickle Crow dyke			
Gabbroic portion of dyke	Ar-Ar hornblende	1876 ± 8 (22)	Buchan et al. (2003)
Lake Superior region			
Hemlock Formation rhyolite	U-Pb zircon	1874 ± 9 (23)	Schneider et al. (2002)
Lamprophyric dykes on Little Presque Isle	Ar-Ar phlogopite	1877.2 ± 5.3 (24)	Craddock et al. (2007)

Table 2.1. contd.

	Dating method	Age (Ma)	Reference
Gunflint Formation volcanic ash	U-Pb zircon	1874 ± 9 (25)	Fralick et al. (2002)
Labrador Trough			
Montagnais glomeroporphyritic gabbro sill intruding the Menihek Formation	U-Pb zircon	1884.0 ± 1.6 (26)	Findlay et al. (1995)
Montagnais glomeroporphyritic gabbro sill intruding the Hellancourt Formation	U-Pb zircon	1874 ± 3 (27)	Machado et al. (1997)
Montagnais gabbro sills	Pb-Pb isochron	1930 ± 49 (28)	Rohon et al. (1993)
Willbob Formation basalts	Pb-Pb isochron	1885 ± 67 (29)	Rohon et al. (1993)
Douay Lake rhyodacite	U-Pb zircon	1870 ± 4 (30)	Machado et al. (1997)
Nimish Formation syenite cobbles	U-Pb zircon	1877.8 ± 1.3 (31)	Findlay et al. (1995)
Castignon Lake carbonatite dyke	U-Pb zircon	1880 ± 2 (32)	Cheve & Machado (1988)
Carbonatite complexes			
Borden Township	Pb-Pb isochron	1872 ± 13 (33)	Bell et al. (1987)
	Pb-Pb zircon	1882.0 ± 3.9 (34)	Rukhlov & Bell (2010)
Carb Lake	K-Ar biotite	1826 ± 97 (35)	Sage (1987b)
	Pb-Pb zircon	1865 ± 22 (36)	Rukhlov & Bell (2010)
Cargill Township	U-Pb zircon	1907 ± 4 (37)	Sage (1988b)
	U-Pb zircon	1896.8 ± 1.4 (38)	Rukhlov & Bell (2010)
Castignon Lake	U-Pb zircon	1880 ± 2 (32)	Cheve & Machado (1988)
Goldray	U-Pb zircon	1886 ± 0.9 (39)	Rukhlov & Bell (2010)
	U-Pb zircon	1884 ± 2 (40)	Sage (1988c)
Spanish River	Rb-Sr isochron	1838 ± 95 (41)	Bell & Blenkinsop (1980)
	Pb-Pb baddeleyite	1880.6 ± 2.4 (42)	Rukhlov & Bell (2010)

Numbers in parentheses correspond to the numbers written next to the age data points in Fig. 2.24.

Models that have been suggested for the origin of the Circum-Superior igneous rocks include rifting of the continental margin and ocean-floor spreading, arc volcanism, back-arc basin rifting, foredeep basin flexure, extensional pull-apart basins and the impingement of a mantle plume or plumes. The latest study by Heaman et al. (2009) advocated an origin via passive upwelling of NMORB-source asthenosphere along thinned margins of the craton.

Some of the magmatic rocks of the Circum-Superior LIP are of economic importance because of their association with Ni-Cu-PGE sulphide deposits. The Cape Smith Belt, Fox River Belt, Thompson Nickel Belt, Molson dykes and Labrador Trough are host

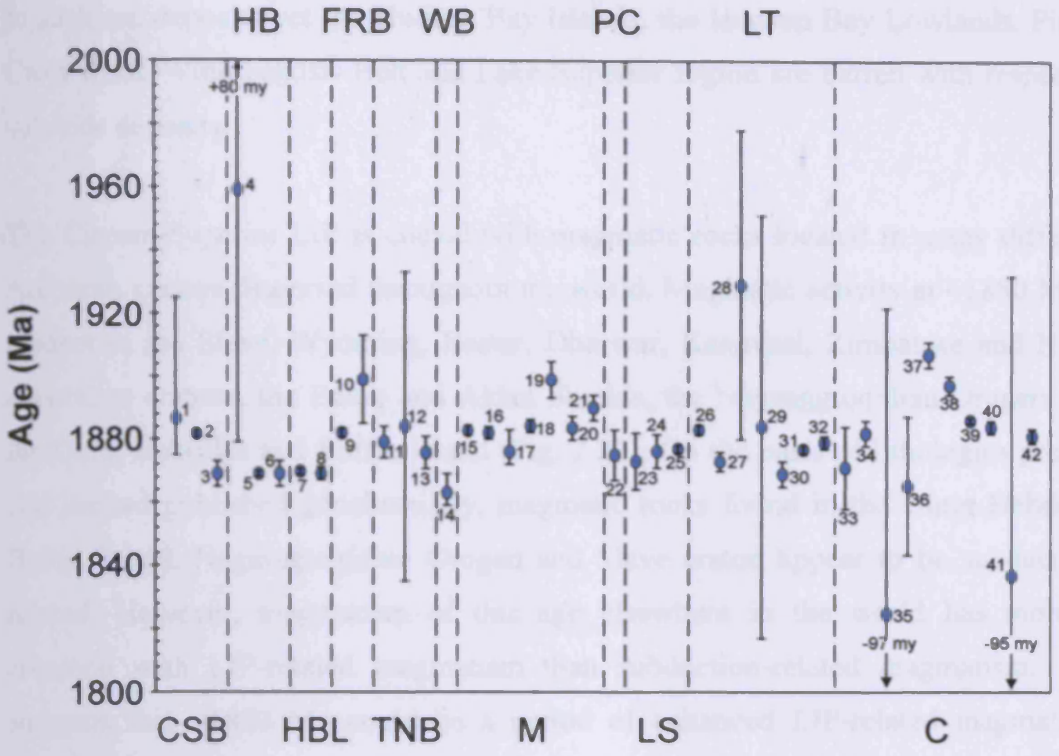

Fig. 2.24. Chart showing the ages of dated rocks considered potentially part of the Circum-Superior LIP. Error bars are also shown. The numbers (1-42) next to the age data points correspond to the numbers in parentheses in the third column of Table 2.1. Abbreviations: CSB Cape Smith Belt; HB Hudson Bay; HBL Hudson Bay Lowlands; FRB Fox River Belt; TNB Thompson Nickel Belt; WB Winnipegosis Belt; M Molson dykes; PC Pickle Crow dyke; LS Lake Superior region; LT Labrador Trough; C Carbonatites from the Superior craton interior.

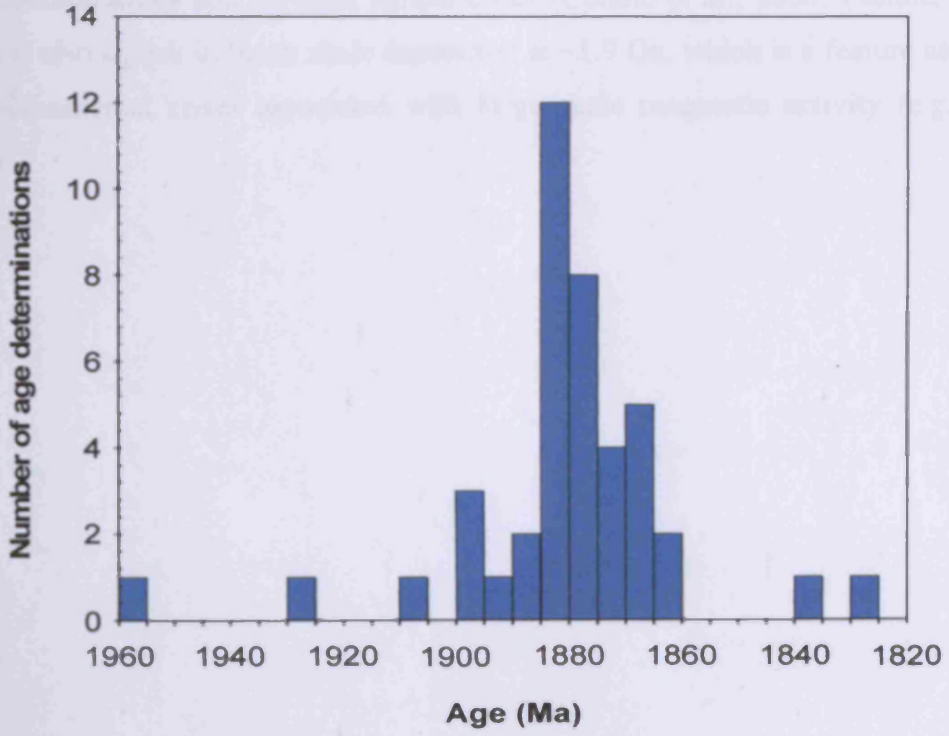

Fig. 2.25. Histogram showing the radiometrically-determined ages of rocks considered part of the Circum-Superior LIP. The width of each bar and each interval represents 5 m.y.

to such ore deposits yet the Hudson Bay islands, the Hudson Bay Lowlands, Pickle Crow dyke, Winnipegosis Belt and Lake Superior region are barren with respect to sulphide deposits.

The Circum-Superior LIP is coeval with magmatic rocks located in many different Archaean cratons dispersed throughout the world. Magmatic activity at ~1880 Ma is evident in the Slave, Wyoming, Bastar, Dharwar, Kaapvaal, Zimbabwe and North Australian cratons, the Baltic and Aldan Shields, the Nagsuggtoqidian Orogen, and the Outer Hebrides and Baffin Island (Fig. 2.23). On the basis of lithologies present and limited published geochemistry, magmatic rocks found in the Outer Hebrides, Baltic Shield, Nagssugtoqidian Orogen and Slave craton appear to be subduction-related. However, magmatism of this age elsewhere in the world has more in common with LIP-related magmatism than subduction-related magmatism. This suggests that ~1880 Ma could be a period of enhanced LIP-related magmatism, possibly on a global scale, akin to more recent times such as in the mid-Cretaceous (e.g. Larson, 1991a, 1991b). The Circum-Superior LIP and other ~1880 Ma magmatic provinces are also coeval with a significant environmental crisis. At this time in Earth's history there is evidence for high sea levels, enhanced atmospheric CO_2 concentrations and elevated temperatures (Condie et al., 2000; Condie, 2001). There is also a peak in black shale deposition at ~1.9 Ga, which is a feature common to environmental crises associated with large scale magmatic activity (e.g. Kerr, 1998).

3. Sample collection and petrography of the Circum-Superior igneous rocks

3.1. Introduction

Rock samples used in this study were collected over the summers of 2007 and 2008. Due to the widespread geographical extent of the Circum-Superior LIP and the expense and time required to reach many of the remote and geographically challenging areas where the rocks outcrop, many rock samples were resampled from various geological institutions around Canada and a limited amount of fieldwork was conducted. Descriptions of how and where rock samples were collected and a summary of their petrographic features are given in the following sections. For more detailed sample locations and thin section descriptions see Table A.1 in Appendix A.

3.2. Cape Smith Belt

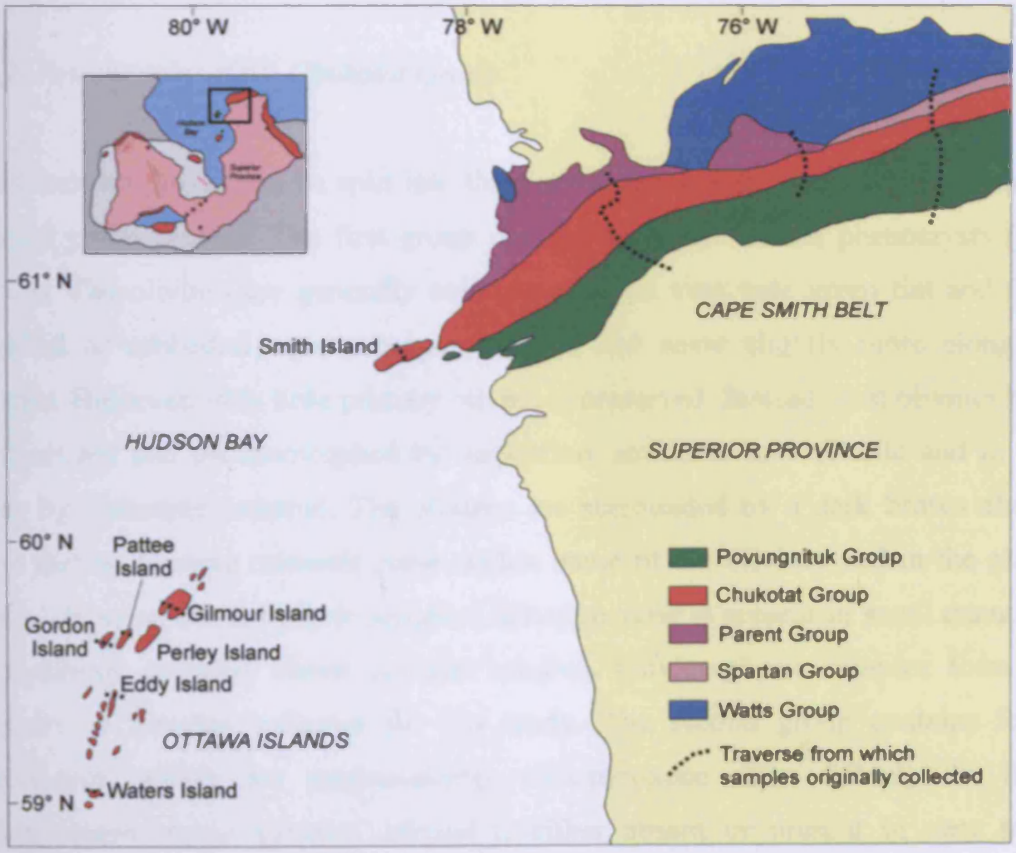

Fig. 3.1. Simplified map showing the locations of traverses from which samples of the Chukotat Group volcanic rocks used in this study were originally collected. Map outline adapted from St. Onge & Lucas (1994).

3.2.1. Sample collection

Twenty-eight rock samples were collected from the Cape Smith Belt and correspond to sample numbers MMC08-1 to MMC08-28. All twenty-eight samples are volcanic rocks belonging to the Chukotat Group on the mainland Ungava Peninsula, Smith Island and the Ottawa Islands. These samples were obtained from the archives of the Geological Survey of Canada in Ottawa and were originally collected by Dr. Robert Baragar during several traverses of the Cape Smith Belt. The locations of the traverses from which the rocks were collected are shown in Fig. 3.1. Sample MMC08-17 comes from Gordon Island, MMC08-18 from Pattee Island, MMC08-19 to MMC08-21 from Gilmour Island, MMC08-22 and MMC08-23 from Eddy Island, and MMC08-12 to MMC08-16 from Smith Island. Samples MMC08-1 to MMC08-7 come from the most westerly traverse of the Cape Smith Belt on the mainland, MMC08-24 to MMC08-28 from the central traverse, and MMC08-8 to MMC08-11 from the most easterly traverse.

3.2.2. Petrography of the Chukotat Group

The Chukotat Group can be split into three subgroups on the basis of the dominant mineral phase present. The first group contain abundant olivine phenocrysts (Fig. 3.2a-b). The olivines are generally colourless with a very pale green tint and form euhedral to subhedral equant hopper crystals and some slightly more elongated crystals. However, very little primary olivine is preserved. Instead most olivines have been altered and pseudomorphed by serpentine, actinolite and chlorite and in rare cases by carbonate material. The olivines are surrounded by a dark brown altered glass matrix. Opaque minerals occur within some of the olivines and in the glassy matrix. In some olivine-phyric samples, clinopyroxene is present in small quantities as randomly oriented brown acicular needles. Olivine-phyric samples form the majority of samples collected for this study. The second group contains fewer phenocrysts which are predominantly clinopyroxene (Fig. 3.2c-d). In these clinopyroxene-phyric samples, olivine is either absent or present in very small quantities. Clinopyroxene phenocrysts tend to be present as either equant crystals or randomly oriented elongated needle-like crystals. In some samples the clinopyroxenes are fairly well preserved whilst in others clinopyroxene is altered

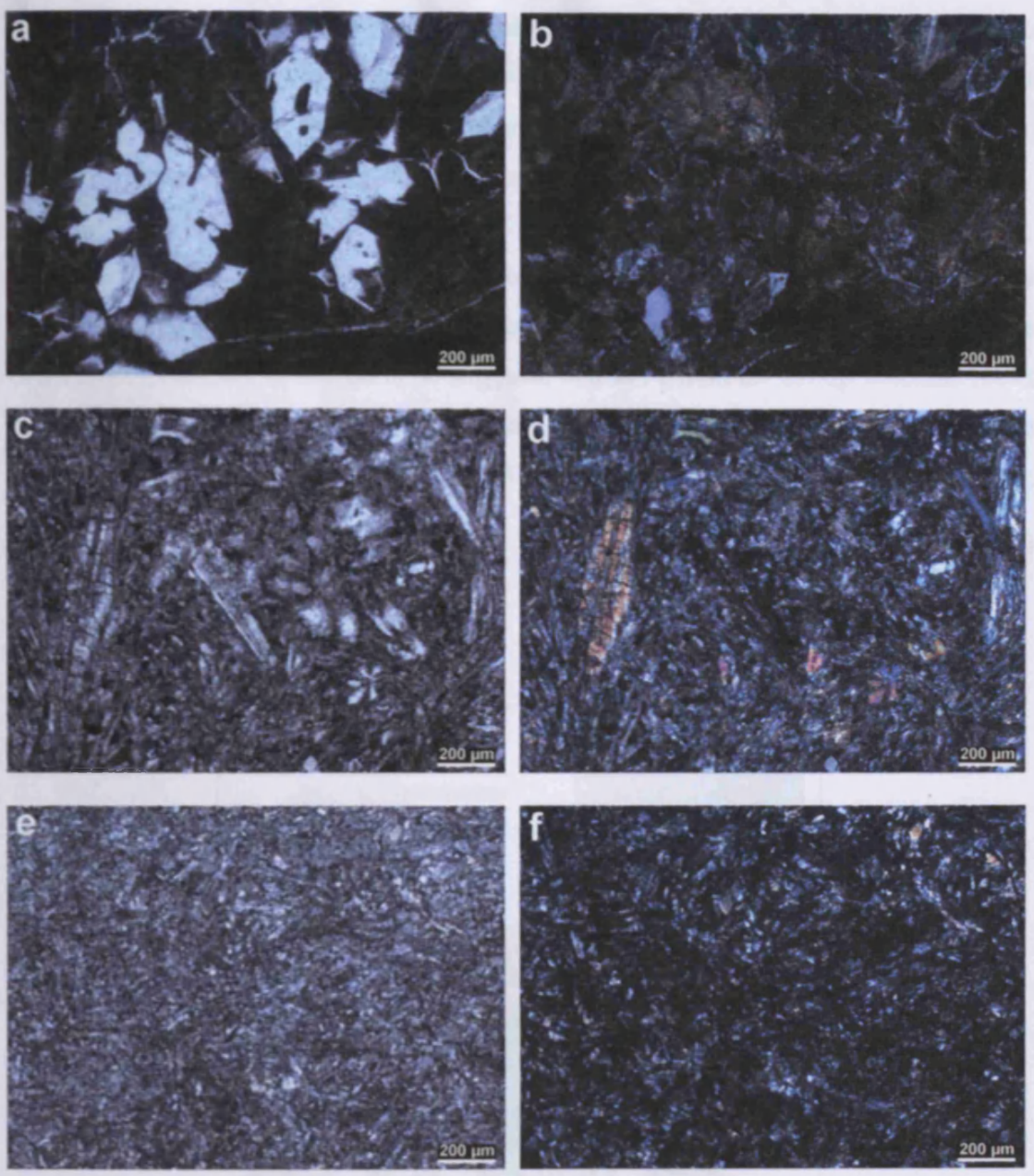

Fig. 3.2. Photomicrographs of the Chukotat Group volcanic rocks. (a) Plane-polarised photomicrograph of an olivine-phyric sample showing euhedral olivines set in a dark brown glass matrix; (b) Cross-polarised view of (a) highlighting the alteration of olivine; (c) Plane-polarised photomicrograph of a clinopyroxene-phyric sample; (d) Cross-polarised view of (c); (e) Plane-polarised photomicrograph of an aphyric sample composed mainly of small opaque minerals, clinopyroxene needles, plagioclase laths and their alteration products; (f) Cross-polarised view of (e).

mainly to actinolite and chlorite. Opaque minerals are present as small euhedral crystals and are slightly more abundant than in the olivine-phyric samples. The clinopyroxene, olivine and opaque minerals are set within a dark brown altered

glassy matrix. The third petrographical group consists of samples which are generally aphyric and composed of a brownish-green fine grained groundmass of opaque minerals, clinopyroxene needles and laths of plagioclase (Fig. 3.2e-f). Chloritised plagioclase microphenocrysts are occasionally present.

The thin sections of the Chukotat Group volcanic rocks show that the primary igneous minerals have been altered and replaced by secondary phases. The presence of serpentine, actinolite and chlorite suggests that the Chukotat Group volcanic rocks have been subjected to a grade of metamorphism up to greenschist facies. This is in agreement with previous studies on the Chukotat Group (e.g. Francis et al., 1983; Lesher, 2007).

3.3. Eastern Hudson Bay islands

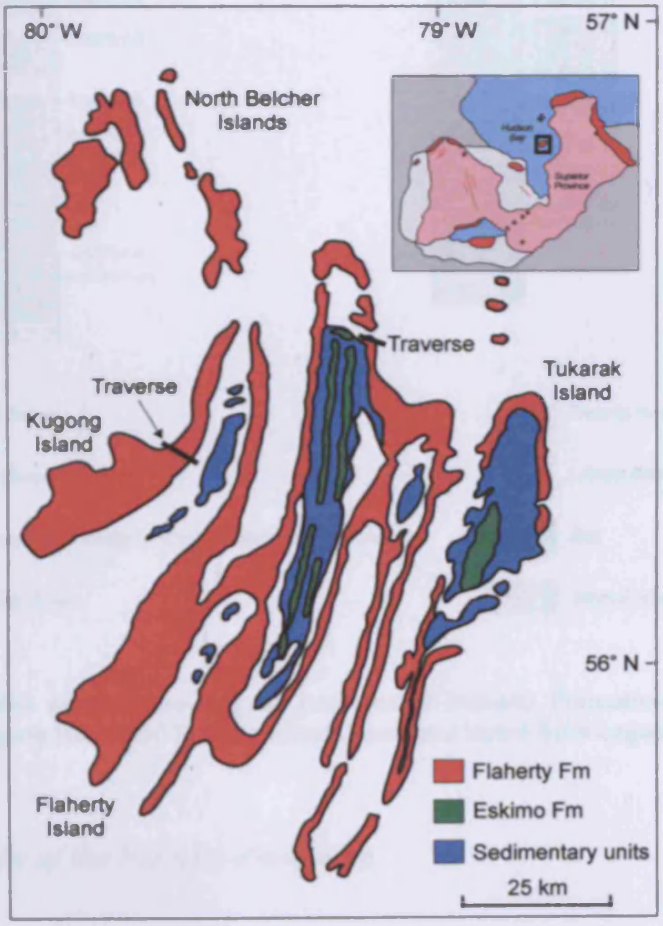

Fig. 3.3. Simplified map showing the locations of traverses from which samples of the Flaherty Formation used in this study were originally collected. Map outline adapted from Legault et al. (1994).

3.3.1. Sample collection of the Flaherty Formation from the Belcher Islands

Twenty-one rock samples of the Flaherty Formation (MMF07-1 to MMF07-21) from the Belcher Islands were collected for this study. The rocks were obtained from the archives of McGill University in Montreal and were originally collected by Dr. Don Francis and Dr. Andrew Hynes. Samples MMF07-1 to MMF07-10 were sampled from a traverse made across Kugong Island whilst samples MMF07-11 to MMF07-21 come from a traverse made partly across Flaherty Island. The locations of the traverses are shown in Fig. 3.3 and stratigraphic sections of each traverse with the sample positions are displayed in Fig. 3.4.

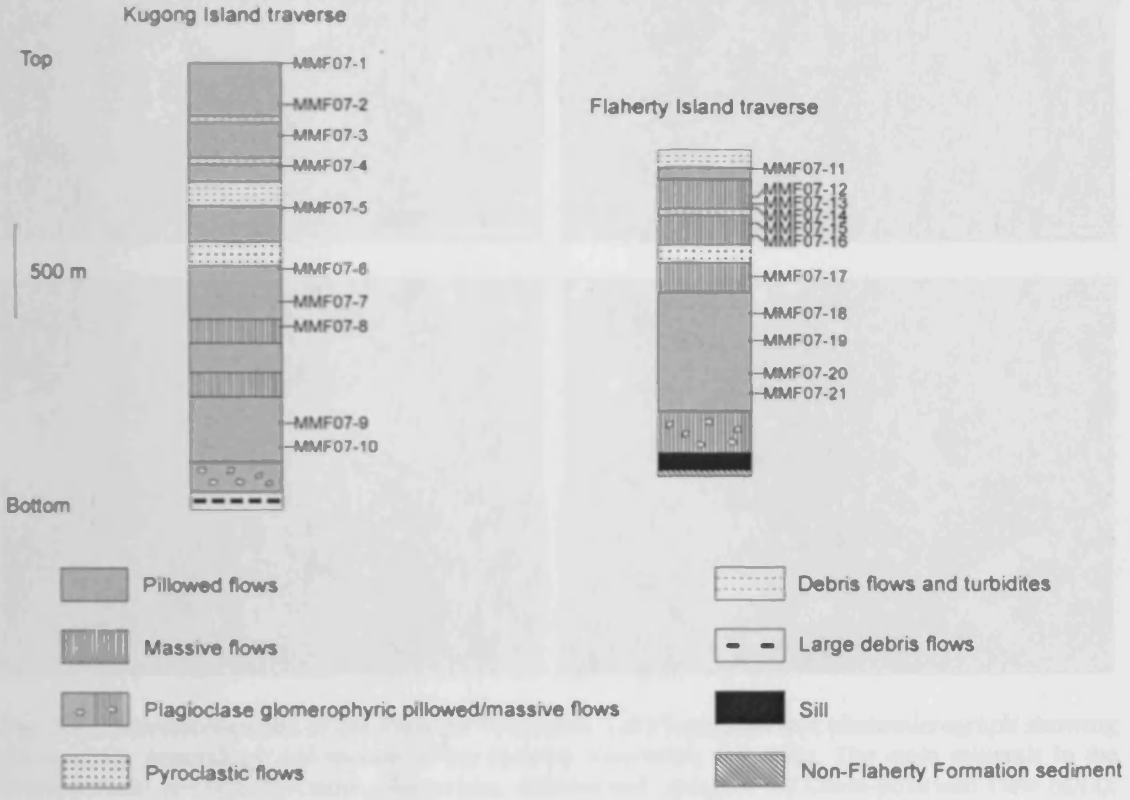

Fig. 3.4. Stratigraphic sections showing the positions of Flaherty Formation samples from both traverses across Kugong Island and Flaherty Island. Sections adapted from Legault (1994).

3.3.2. Petrography of the Flaherty Formation

The Flaherty Formation volcanic rocks are all fairly similar petrographically. Most of the samples contain approximately equal proportions of clinopyroxene and

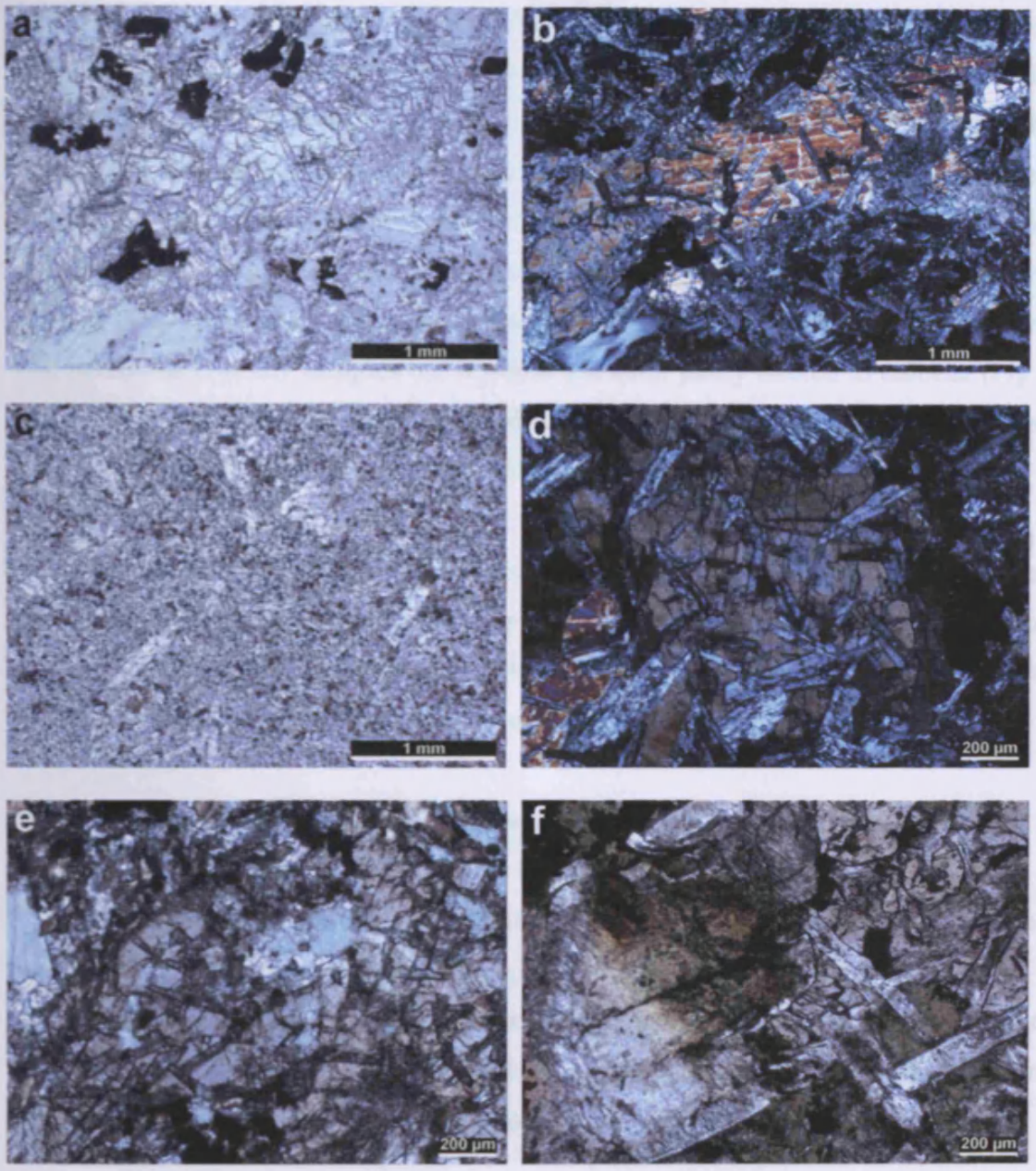

Fig. 3.5. Photomicrographs of the Flaherty Formation. (a) Plane-polarised photomicrograph showing the common mineralogy and texture of the Flaherty Formation volcanics. The main minerals in the volcanic rocks are clinopyroxene, plagioclase, chlorite and opaques; (b) Cross-polarised view of (a); (c) Plane-polarised photomicrograph of a slightly finer grained sample containing fewer phenocrysts; (d) Cross-polarised photomicrograph demonstrating the ophitic textures commonly preserved in the samples; (e) Plane-polarised photomicrograph displaying evidence of ophitic texture, sericitisation of plagioclase and chloritisation of clinopyroxene; (f) Plane-polarised photomicrograph showing that plagioclase is present as thin laths and as larger, more equant euhedral crystals.

plagioclase with a small percentage of opaque minerals (usually ~5%). The average crystal size differs between rocks with some samples coarser than others (Fig. 3.7a-c). Clinopyroxene is present usually as elongated prisms which have a maximum

length of ~2.5 mm and also as smaller, more equant crystals. Plagioclase is commonly present in the form of thin laths but can also occur as larger, more equant crystals (Fig. 3.5f). Most of the samples preserve good ophitic textures where laths of plagioclase seemingly intrude and are surrounded by larger grains of clinopyroxene (Fig. 3.5a,b,d,e). Ophitic textures are sometimes masked in the Flaherty Formation because of the dusty appearance of plagioclase (Fig. 3.5e) which has been variably altered to clay minerals and sericite in many of the samples. Clinopyroxene is fairly well preserved in many samples but in some has been partly altered to chlorite (Fig. 3.5e) giving the thin sections a greenish tint. In rare cases, ophitic textures are preserved where plagioclase laths are surrounded by grains of chlorite.

The petrography of the Flaherty Formation suggests that these volcanic rocks have undergone a certain degree of post-magmatic alteration and metamorphism. The presence of chlorite and the absence of actinolite indicate that the Flaherty Formation has been metamorphosed to subgreenschist facies.

3.3.3. Sample collection of a Haig sill from the Sleeper Islands

Ten rock samples (MMHS08-1 to MMHS08-10) were obtained for this study from one of the Haig sills exposed on the Sleeper Islands. The samples were collected by Ms. Isabelle Cadieux and stored in the archives of the Geological Survey of Canada in Ottawa. The map in Fig. 3.6 shows the location of the Haig sill on the Sleeper Islands and Fig. 3.7 displays the position of the samples within the sill.

3.3.4. Petrography of the Haig sill

Most of the samples obtained from the Haig sill are glomeroporphyritic gabbros. The most dominant petrographic features of these samples are the clots of plagioclase laths which vary in diameter up to a few centimetres. The individual crystals in these clots are generally around ~4 mm in the longest dimension. The plagioclase clots show evidence of alteration to sericite and prehnite. The plagioclase clots are surrounded by a medium grained gabbroic groundmass consisting of plagioclase, clinopyroxene, serpentine and opaque minerals. There are also traces of pumpellyite, chlorite, carbonate, apatite, quartz, amphibole, epidote and sphene. Pumpellyite

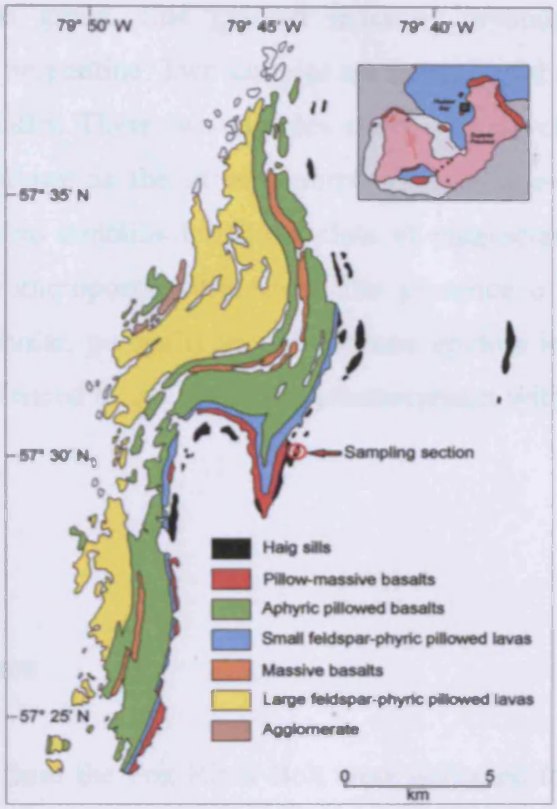

Fig. 3.6. Map showing the locality of the Haig sill from which samples used in this study were collected. Map adapted from Baragar & Lamontagne (1980).

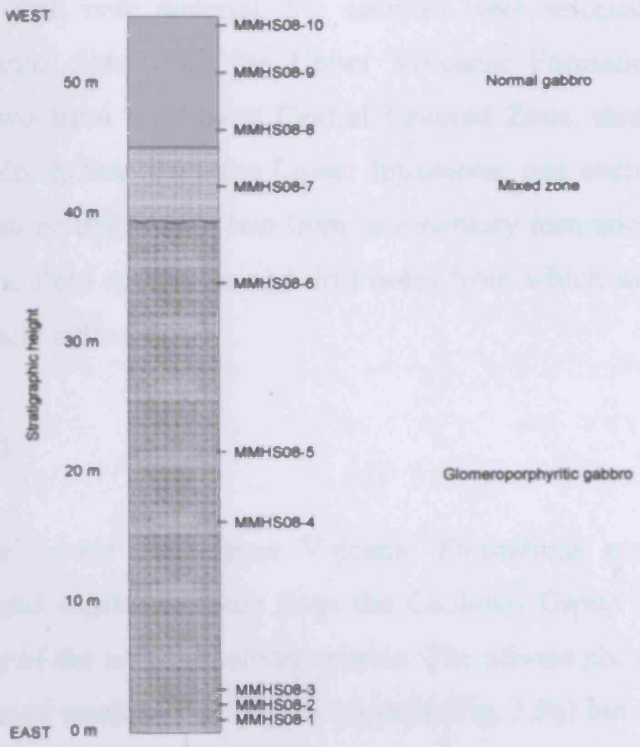

Fig. 3.7. Stratigraphic section showing the position of samples from the Haig sill. Adapted from Cadieux (1980).

commonly occurs as green, fine grained radiating crystals at the margins of clinopyroxene and in serpentine. Two samples are normal gabbros and do not contain clots of plagioclase laths. These two samples show well developed ophitic textures and the same mineralogy as the glomeroporphyritic samples. One sample comes from a mixed zone and contains far fewer clots of plagioclase crystals than those samples from the glomeroporphyritic zone. The presence of secondary alteration minerals such as prehnite, pumpellyite, chlorite and epidote indicates that the Haig sill rocks have experienced a low grade of metamorphism within the subgreenschist facies.

3.4. Fox River Belt

3.4.1. Sample collection

Thirty rock samples from the Fox River Belt were collected for this study (samples MMFR08-1 to MMFR08-30). These samples were originally collected by Dr. David Peck and Dr. Guy Desharnais and stored in the archives of the Manitoba Geological Survey in Winnipeg. Twenty of the samples were collected from outcrops whereas the other ten are drill core material. Six samples were selected from the Lower Volcanic Formation, eight from the Upper Volcanic Formation, two from the Marginal Zone, two from the Lower Central Layered Zone, three from the Upper Central Layered Zone, four from the Lower Intrusions, one each from the Stupart, Sipanigo and Bigstone dykes, and two from sedimentary formations. Fig. 3.8 shows the locations of the field specimens and drill holes from which samples used in this study were originally collected.

3.4.2. Petrography

The lavas of the Lower and Upper Volcanic Formations are almost identical petrographically and similar to those from the Chukotat Group in the Cape Smith Belt. The majority of the lavas are olivine-phyric. The olivine phenocrysts are mostly euhedral hexagons or small equant hopper crystals (Fig. 3.9a) but also occur as more elongated blades. These crystals are usually surrounded by a dark brown, often dusty, glassy groundmass (Fig. 3.9a). Very little primary olivine is present in the Fox River

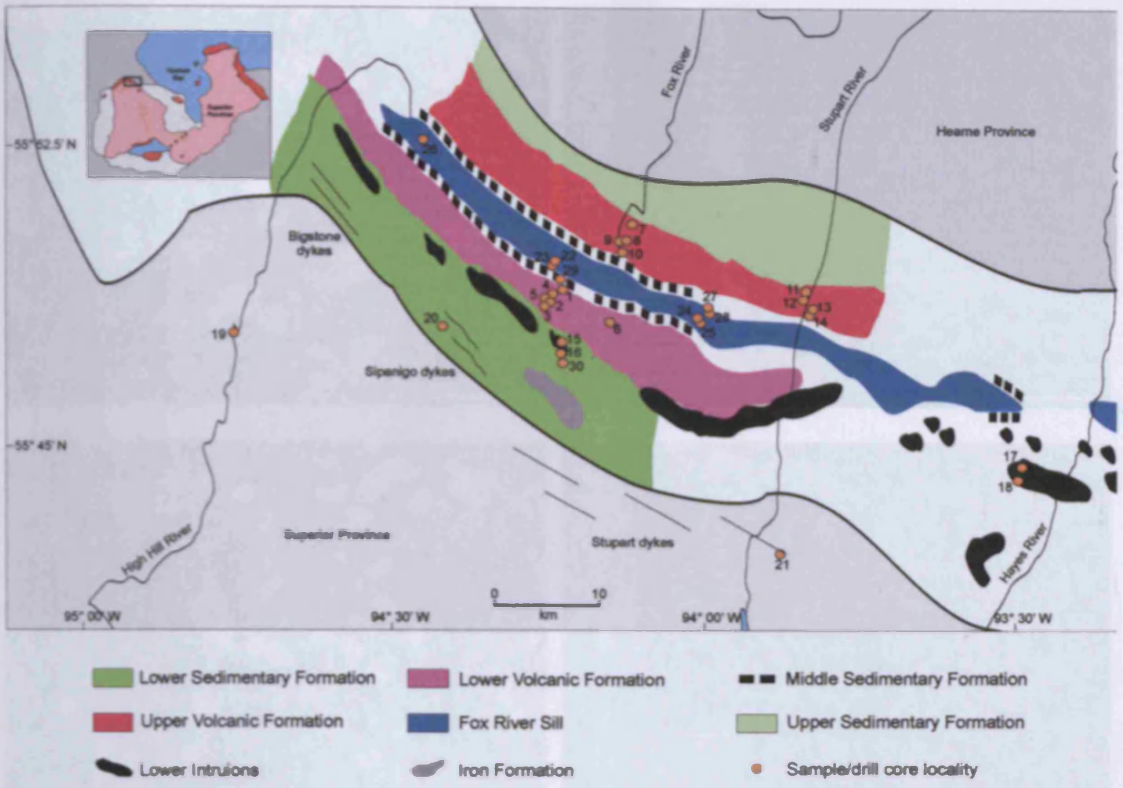

Fig. 3.8. Map showing the field and drill core localities from which samples of the Fox River Belt used in this study were originally collected. Map adapted from Scoates (1981). The numbers 1 to 30 represent samples MMFR08-1 to MMFR08-30.

Belt volcanic samples. Chlorite and serpentine are the dominant alteration minerals replacing olivines (Fig. 3.9b) although in a few samples minor amounts of secondary actinolite are observed. Olivine is the only phenocryst present in just a few samples as clinopyroxene is also usually present in the form of ornamental chains or fine needles (Fig. 3.9c-d). The abundance of clinopyroxene is variable and changes from being subordinate to the proportion of olivine, to being far greater than the proportion of olivine. Clinopyroxenes are generally less altered than olivines and there are fresh crystals in many samples. However, in some samples clinopyroxene has altered to serpentine, chlorite or tremolite. The volcanic samples which appear to contain no olivine tend to have an intersertal texture dominated by thin laths of plagioclase (Fig. 3.9e-f). The plagioclase laths are extensively altered to clays and sericite and have a very dusty appearance in thin section (Fig. 3.9e-f). Small brownish crystals also occur in these more evolved rocks and are probably altered clinopyroxenes. Opaque minerals are present in all the volcanic rocks and usually are found as small euhedral square or diamond shapes.

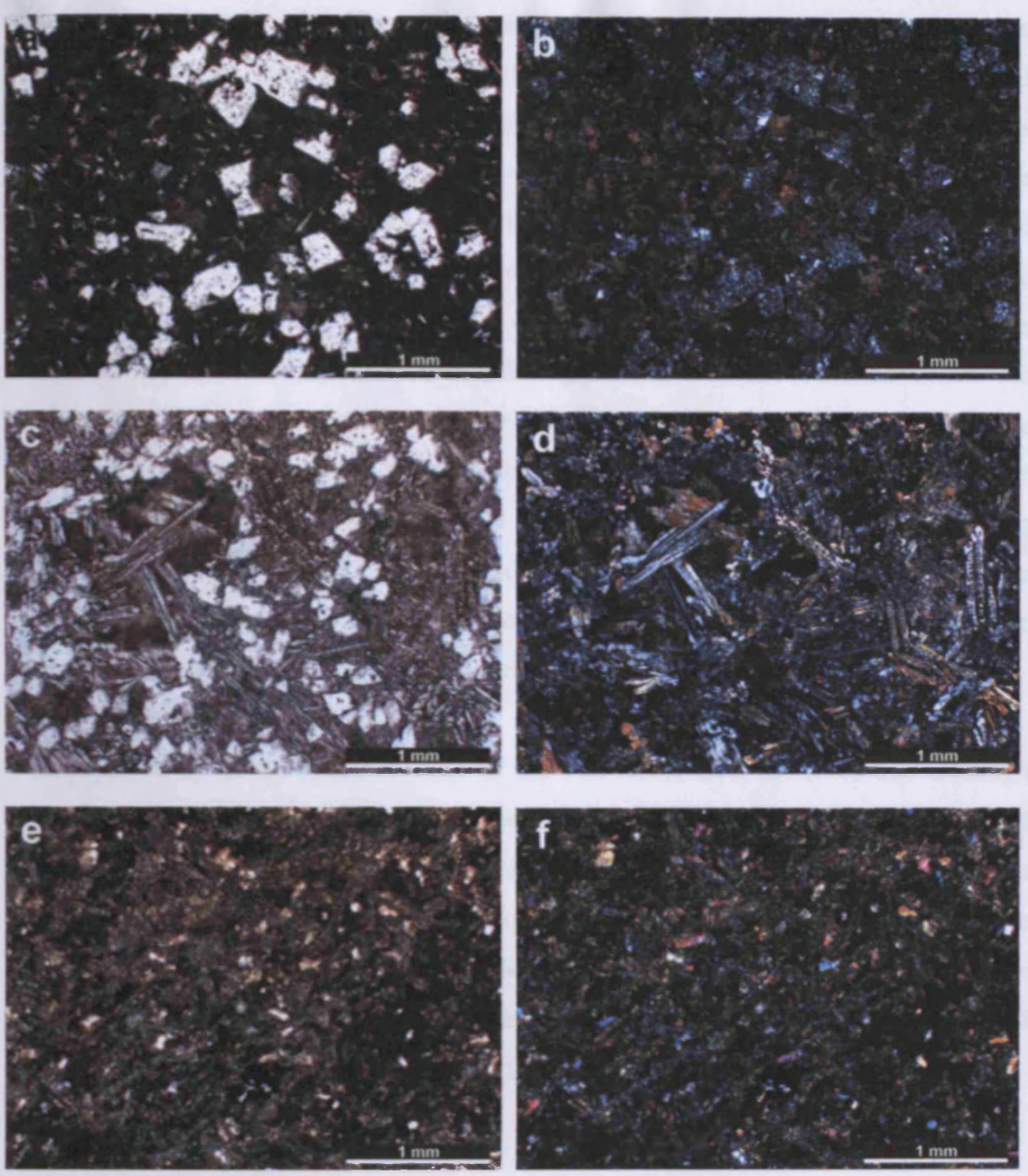

Fig. 3.9. Photomicrographs of the Fox River Belt volcanic rocks. (a) Plane-polarised photomicrograph of an olivine-phyric sample showing euhedral olivine crystals set in a dark brown glass matrix; (b) Cross-polarised view of (a) highlighting the alteration of olivine; (c) Plane-polarised photomicrograph of a sample with small euhedral olivine crystals and needles and ornamental chains of clinopyroxene set in a brown glassy matrix; (d) Cross-polarised view of (c); (e) Plane-polarised photomicrograph of a volcanic lava sample containing little to no olivine or clinopyroxene but abundant plagioclase laths which have been extensively altered; (f) Cross-polarised view of (e).

Out of the four samples from the Lower Intrusions, two are gabbros (MMFR08-15 and MMFR08-17), one is an olivine pyroxenite (MMFR08-18) and the other is a peridotite (MMFR08-16). In all four samples, clinopyroxene is present as euhedral prisms and is fairly well preserved unlike the plagioclase crystals in the gabbros which are altered to near-isotropic chlorite. The samples from the Bigstone, Sipanigo

and Stupart dykes are all gabbros containing plagioclase and green amphibole as the dominant minerals. The Fox River Sill Marginal Zone samples MMFR08-22 and MMFR08-23 are a gabbro and pyroxenite respectively. The gabbro sample consists of clinopyroxene prisms separated by altered intercumulus plagioclase whereas the pyroxenite sample contains a much higher proportion of clinopyroxene and orthopyroxene with little interstitial material. The Lower Central Layered Zone samples MMFR08-24 and MMFR08-25 are a dunite and gabbro respectively. The dunite is nearly all composed of ovoid-shaped serpentinised olivines whilst the gabbro contains prismatic clinopyroxene showing signs of alteration to amphibole and intercumulus plagioclase being replaced by epidote and chlorite. The Upper Central Layered Zone samples MMFR08-26, MMFR08-27 and MMFR08-28 are an olivine pyroxenite, peridotite and gabbro respectively. The olivine, clinopyroxene and orthopyroxene in these samples show signs of only mild alteration whereas the plagioclase in the gabbro sample is more extensively altered to sericite.

The petrography of the igneous rocks of the Fox River Belt indicates that although the samples are not pristine, they have not been subjected to high grades of metamorphism. Plagioclase appears to be one of the most affected minerals and is often altered to sericite or chlorite. Olivine is also mostly altered to serpentine. The presence of serpentine and chlorite and the lack of extensive actinolite and tremolite suggest that the rocks of the Fox River Belt have experienced a low grade of metamorphism within the subgreenschist facies.

3.5. Thompson Nickel Belt

3.5.1. Sample collection

Twenty-three rock samples (MMT08-1 to MMT08-23) from twenty-three drill hole sites in the Thompson Nickel Belt were obtained for this study from the archives of the Geological Survey of Canada in Ottawa. These samples were originally collected by Dr. Larry Hulbert. The locations of the drill hole sites are shown in Fig. 3.10.

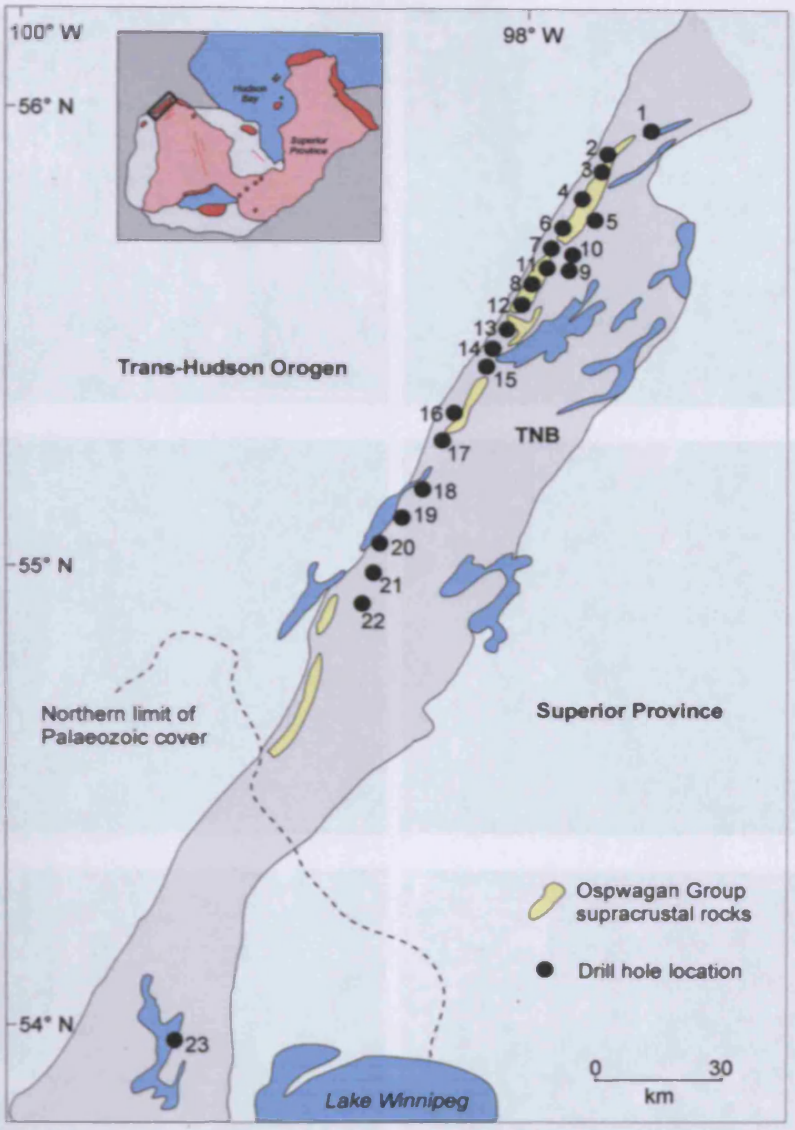

Fig. 3.10. Simplified map showing the location of drill holes in the Thompson Nickel Belt from which samples used in this study were originally collected. Map outline adapted from Hulbert et al. (2005). The numbers 1 to 23 refer to samples MMT08-1 to MMT08-23.

3.5.2. Petrography

The samples from the intrusive bodies in the Thompson Nickel Belt can be divided into dunites, peridotites and pyroxenites on the basis of relict igneous mineralogy and textures. All samples have been subjected to high degrees of metamorphism and alteration. The dunites are adcumulates almost entirely composed of pseudomorphs of serpentine after olivine although in some cases the olivine is replaced by high birefringence minerals such as talc or carbonate (Fig. 3.11b). The original morphology of olivine grains is often preserved and sometimes highlighted by the

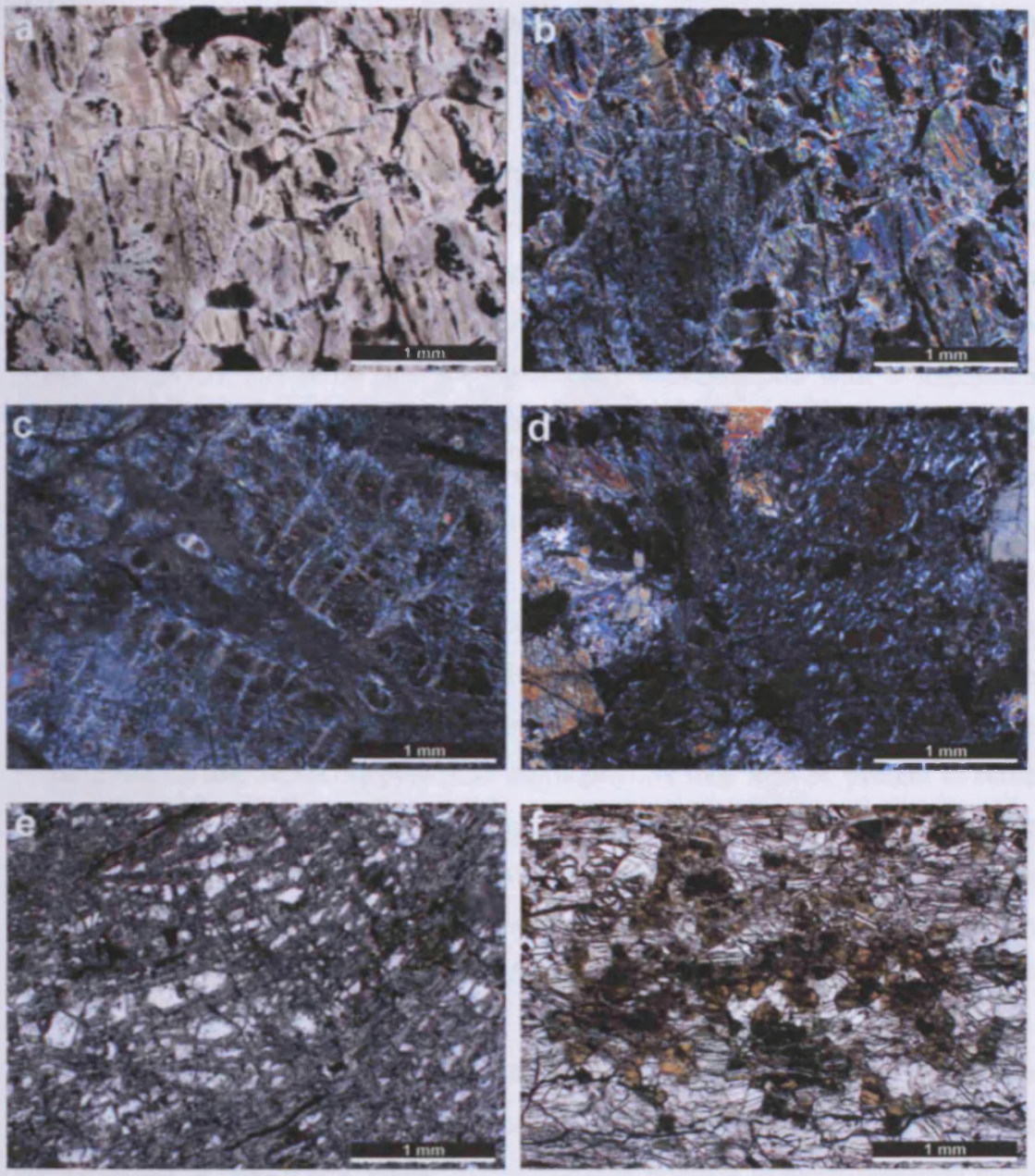

Fig. 3.11. Photomicrographs of the Thompson Nickel Belt sills. (a) Plane-polarised photomicrograph of a dunite sample composed of altered olivines and opaque minerals. The original grain boundaries are still preserved; (b) Cross-polarised view of (a); (c) Cross-polarised photomicrograph of a peridotite sample containing ovoid-shaped altered olivines set in a fine grained matrix; (d) Cross-polarised photomicrograph of a peridotite sample containing some relatively unaltered olivine nearly in extinction and amphibole in the bottom left corner; (e) Plane-polarised photomicrograph of a peridotite sample with olivine fragments set in a fine grained matrix of serpentine and chlorite; (f) Plane-polarised photomicrograph of an olivine pyroxenite sample containing yellowish altered olivines, clinopyroxene, orthopyroxene, opaque minerals and amphibole after pyroxene.

presence of opaque minerals. Olivines range up to 3 mm in size and tend usually to be ovoid in shape or more equant and meet at triple junctions (Fig. 3.11a). Very little

interstitial material is present in the dunites, but where it does occur it is composed mainly of serpentine and possibly chlorite.

The majority of samples are metamorphosed peridotite orthocumulates. These samples are mostly composed of up to ~70% pseudomorphed olivines set in a fine grained matrix (Fig. 3.11c-e). Olivines are mainly altered to serpentine or talc but in some rare cases small portions of the grains are preserved (Fig. 3.11d-e). The olivine grains are mostly subhedral and are sometimes ovoid-shaped with a maximum longest dimension of ~4 mm. The fine grained matrix is mostly composed of serpentine and chlorite with some fibrous amphibole. Rare clinopyroxene crystals are present in a few peridotite samples. Even rarer is orthopyroxene which only occurs as oikocrysts enclosing cumulus olivines. Amphibole is commonly present in small quantities as larger crystals outside of the finer grained matrix (Fig. 3.11d) and is usually tremolite. The tremolite is colourless but shows the classical ~124° cleavage and maximum low second order birefringence colours. The amphibole may be porphyroblastic and replacing pyroxene. Anthophyllite may also be present in some samples. It has lower relief and birefringence than tremolite and appears to have straight extinction in prism sections. Opaque minerals are common in the peridotite samples and occur as small euhedral crystals or as more curvilinear features which define original fractures and boundaries of altered olivine grains.

One of the Thompson Nickel Belt samples is a metamorphosed olivine pyroxenite (Fig. 3.11f). A quarter of this sample is composed of subhedral crystals which appear yellow-brown in colour and display serpentine-like textures in cross-polarised light. These grains could be altered olivines. The rock is dominated by colourless amphibole which is mainly tremolite possibly with some minor anthophyllite. This amphibole could be porphyroblastic and have replaced olivines and pyroxenes. Trace amounts of clinopyroxene and orthopyroxene are also present in the sample.

The extensive serpentinisation of samples from the Thompson Nickel Belt increases the difficulty of making interpretations about the metamorphic history of these rocks. However, the presence of tremolite and anthophyllite along with olivine and talc in some samples from the Thompson Nickel Belt indicates that this portion of the Circum-Superior LIP experienced metamorphism of amphibolite facies grade. This is

consistent with the findings of previous studies of the Thompson Nickel Belt (e.g. Burnham et al., 2004; Layton-Matthews et al., 2007) which suggested most rocks in the area experienced upper amphibolite facies metamorphism whilst some rocks underwent granulite facies metamorphism. The extensive serpentinisation seen in many samples probably occurred after the peak in metamorphism. If serpentinisation occurred prior to metamorphism, then, under such high grades of metamorphism, serpentine would have broken down to form other minerals such as olivine, talc, chlorite and tremolite.

3.6. Winnipegosis Belt

3.6.1. Sample collection

Twenty-seven rock samples (MMW07-1 to MMW07-27) from three drill hole sites close to the northern shore of Lake Winnipegosis in Manitoba were collected for this study. These samples were originally obtained by Dr. Larry Hulbert and were stored in the archives of the Geological Survey of Canada in Ottawa. Fig. 3.12 shows the locations of the three drill hole sites.

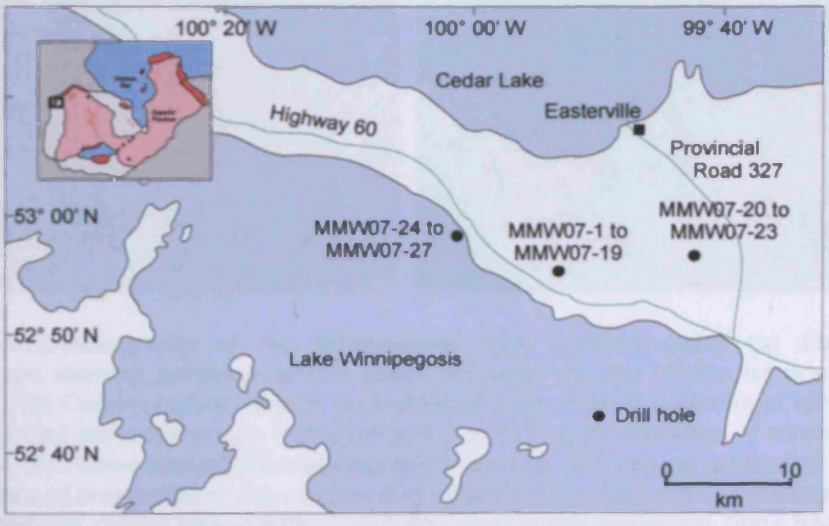

Fig. 3.12. Simplified map showing the location of drill holes in the Winnipegosis Belt from which samples used in this study were originally collected. Map outline adapted from Theyer (1997).

3.6.2. Petrography

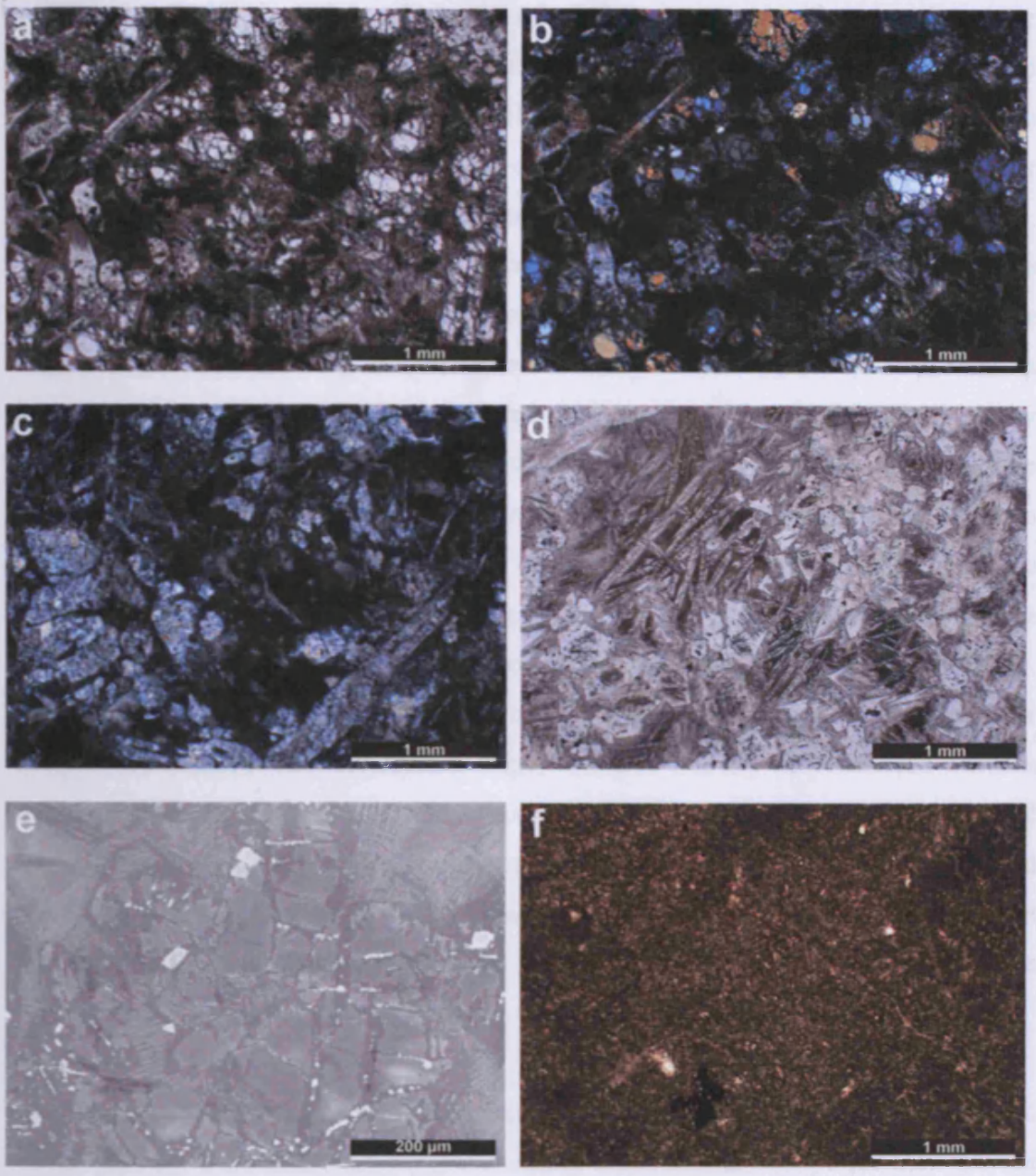

Fig. 3.13. Photomicrographs of the Winnipegosis Belt volcanic rocks. (a) Plane-polarised photomicrograph showing subhedral olivine grains and some skeletal olivine set in a dark brown glassy matrix; (b) Cross-polarised view of (a) highlighting the variable alteration of olivine crystals; (c) Cross-polarised photomicrograph highlighting the near-complete alteration of olivine crystals in most samples; (d) Plane-polarised photomicrograph displaying the euhedral habit of olivine crystals and the presence of ornamental chains composed of clinopyroxene; (e) Scanning electron microscope image of a fractured olivine crystal with Cr-rich opaque minerals distributed along fractures and as small, euhedral crystals around the olivine margins. Also shown is the plumose clinopyroxene which constitutes a large proportion of the fine grained matrix; (f) Plane-polarised photomicrograph of a fine grained volcanic rock composed of opaque minerals, clinopyroxene needles and laths of plagioclase.

The majority of samples from the Winnipegosis Belt consist of olivine crystals set in a dark brown altered glassy matrix. The estimated proportion of olivine in samples varies up to 30%. A variety of shapes of olivine crystals are found and include subhedral grains, equant hopper grains and more euhedral hexagons, diamonds and elongated blades and very fine needles (Fig. 3.13a-d). Most olivines are altered to serpentine (Fig. 3.13c) but a few samples contain fresh olivines which are either unaltered or slightly altered around their margins and in fractures (Fig. 3.13b). Opaque minerals are present but not abundant and occur along fractures in olivine crystals and as small euhedral crystals distributed throughout olivine crystals and the altered matrix material (Fig. 3.13e). In a few samples clinopyroxene is present as randomly oriented ornamental chains and thin needles (Fig. 3.13d). Analysis by scanning electron microscopy has confirmed that plumose, frond-like clinopyroxene is a major constituent of the groundmass. Scanning electron microscopy also identified the presence of trace amounts of sulphide minerals. Four of the samples from the Winnipegosis Belt are fine grained basalts which are composed of a groundmass of opaque minerals, clinopyroxene needles and laths of plagioclase (Fig. 3.13f). The plagioclase laths are altered to clay minerals and sericite. Another four samples are dunites with adcumulate textures where heavily serpentinised olivines are surrounded by minimal interstitial material. The grain boundaries of the altered olivines are highlighted by opaque minerals which are likely to have been formed during the serpentinisation of the olivines. The alteration minerals present suggest that the Winnipegosis Belt has only been subjected to a low grade of metamorphism probably within the subgreenschist facies.

Only four of the Winnipegosis Belt samples contained relatively fresh olivines. These samples were analysed using a scanning electron microscope for their olivine forsterite contents. In total, twenty-seven olivine grains were analysed. The full results are given in Table E.1 in Appendix E. The highest Fo contents measured were 90.7 and the average Fo content is 89.7.

3.7. Molson dykes

3.7.1. Sample collection

Twenty-eight rock samples were collected from the area covered by the Molson dykes and correspond to sample numbers MMM07-1 to MMM07-28. Twenty-six of the samples are from various portions of the dykes whilst the other two are samples of the country rock which the dykes intrude. These samples are stored at the archives of the University of Toronto and were originally collected by Dr. Henry Halls. All of the dyke samples come from dykes which Zhai et al. (1994) have shown to possess the same palaeomagnetic pole direction or to be antipodal to dykes which have been radiometrically age dated at ~1880 Ma. Fig. 3.14 is a map showing the localities of samples used in this study from the area of the Molson dyke swarm.

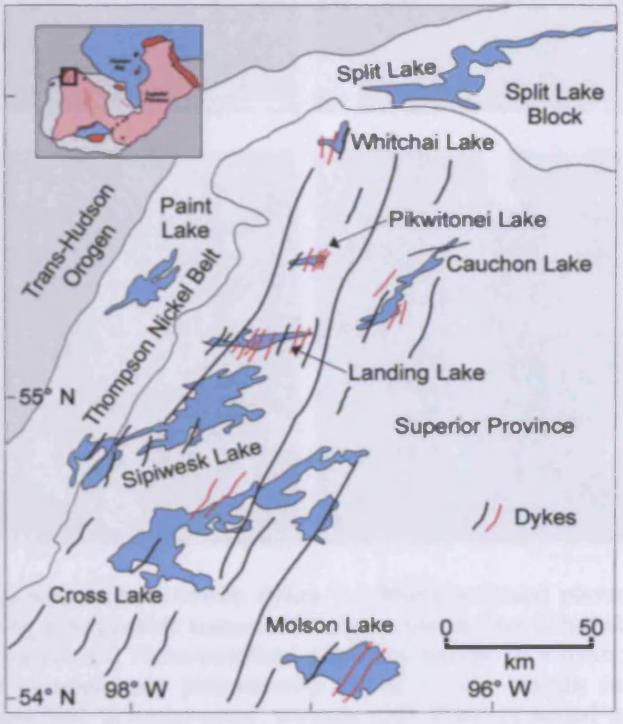

Fig. 3.14. Simplified map showing part of the Molson dyke swarm and the location of dykes from which samples used in this study were originally collected. Dykes coloured in red are those from which samples were taken. Map outline adapted from Scoates & Macek (1978).

3.7.2. Petrography

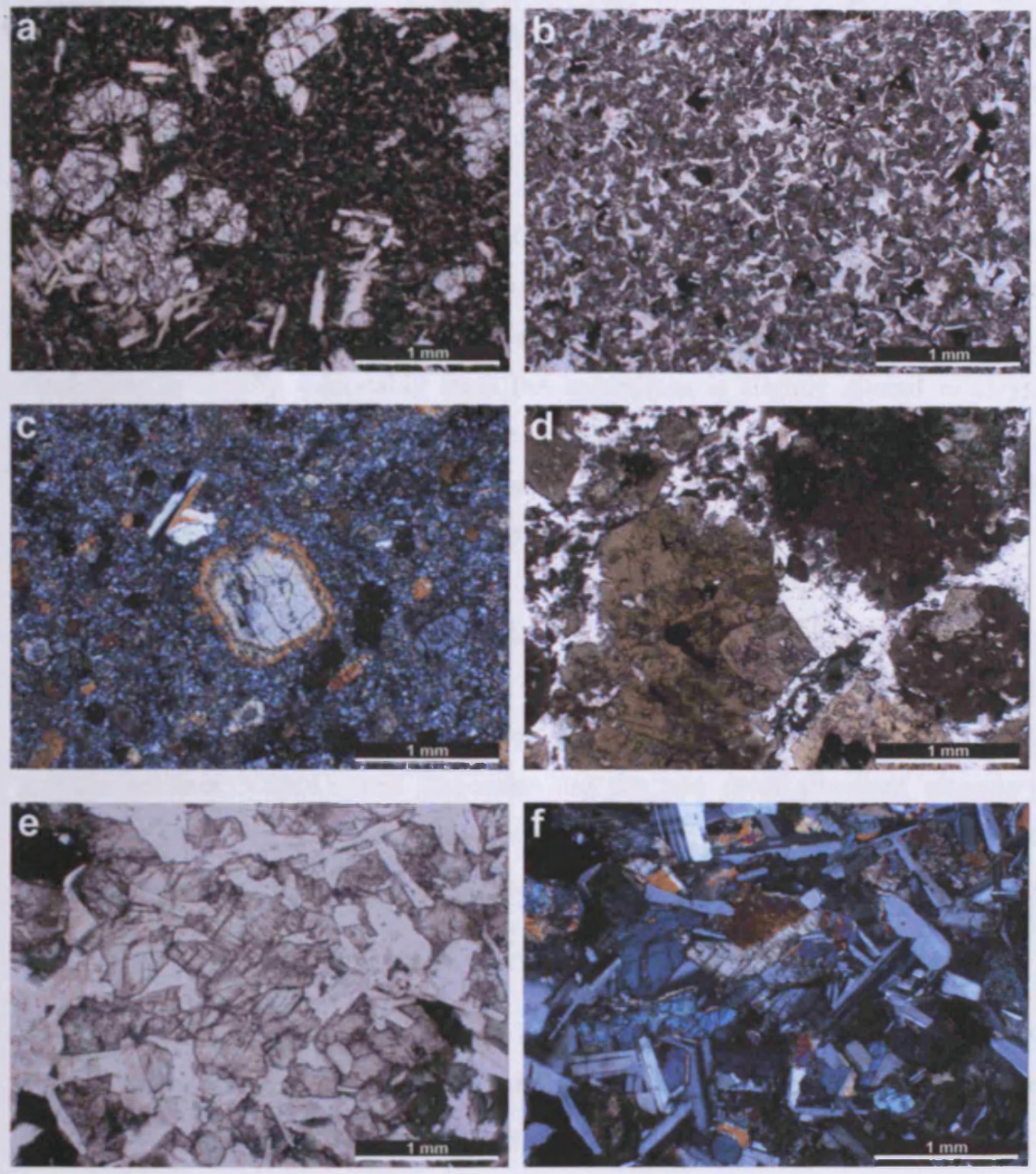

Fig. 3.15. Photomicrographs of the Molson dykes. (a) Plane-polarised photomicrograph of a dyke margin sample displaying a porphyritic texture with coarse plagioclase laths and clinopyroxene grains set in a finer grained matrix; (b) Plane-polarised photomicrograph of a dyke margin sample with a doleritic texture; (c) Cross-polarised photomicrograph of a dyke margin sample highlighting the presence of zoned, euhedral orthopyroxene crystals; (d) Plane-polarised photomicrograph of a relatively coarse dyke margin sample containing brown hornblende crystals surrounded by larger plagioclase crystals; (e) Plane-polarised photomicrograph of a gabbro from the central portion of a dyke and displaying ophitic texture; (f) Cross-polarised view of (e).

The samples from the Molson dykes are mostly fairly well preserved and have not been metamorphosed to a high grade. Olivine, clinopyroxene, orthopyroxene, plagioclase, hornblende and opaque minerals are the main minerals present in the

samples although very rarely are all these minerals present in the same sample. Samples from the margins of the dykes tend to be dolerites or fine grained gabbros (Fig. 3.15a-d). Some margin samples display a porphyritic texture with coarse laths of plagioclase and grains of clinopyroxene set in a finer grained groundmass which includes plagioclase, opaque minerals and chlorite (Fig. 3.15a). Hornblende appears to be a primary igneous mineral and often contains small inclusions of other minerals, particularly plagioclase (Fig. 3.15d). Hornblende may have crystallised late in the magmatic evolution of the Molson dykes, possibly as a result of the presence of water in the source or the introduction at some point of water into the system. Plagioclase is usually reasonably fresh but sometimes is slightly altered to clays, sericite or chlorite. Orthopyroxene is rare but when it occurs it is as zoned, euhedral crystals (Fig. 3.15c). Chlorite is the most abundant secondary mineral and can be found replacing pyroxene, hornblende and plagioclase.

Samples from further into the central portion of dykes become progressively coarser. The interior of dykes are mostly either coarse grained gabbros displaying ophitic texture (Fig. 3.15e-f) or are peridotites and pyroxenites with hypidiomorphic granular textures. Chlorite and serpentine are the two most abundant secondary minerals in samples from the interior of dykes. Chlorite forms from the alteration of olivine, pyroxene, plagioclase and hornblende whilst some olivines are also partially serpentinised.

The Molson dykes are fairly fresh and have been metamorphosed only at a low grade. The presence of serpentine and chlorite without actinolite suggests that the Molson dykes have experienced metamorphism under subgreenschist facies.

3.8. Pickle Crow dyke

3.8.1. Sample collection

Three rock samples (MMPC07-1 to MMPC07-3) were used in this study from the Pickle Crow dyke. These samples come from various positions within the dyke. MMPC07-1 comes from the western margin of the main dyke whereas MMPC07-2 and MMPC07-3 come from the interior of the dyke, 30 m and 40 m eastwards from

the western margin of the main dyke respectively. The samples were stored in the archives of the Geological Survey of Canada in Ottawa and had previously been collected by Dr. John Hanes.

3.8.2. Petrography

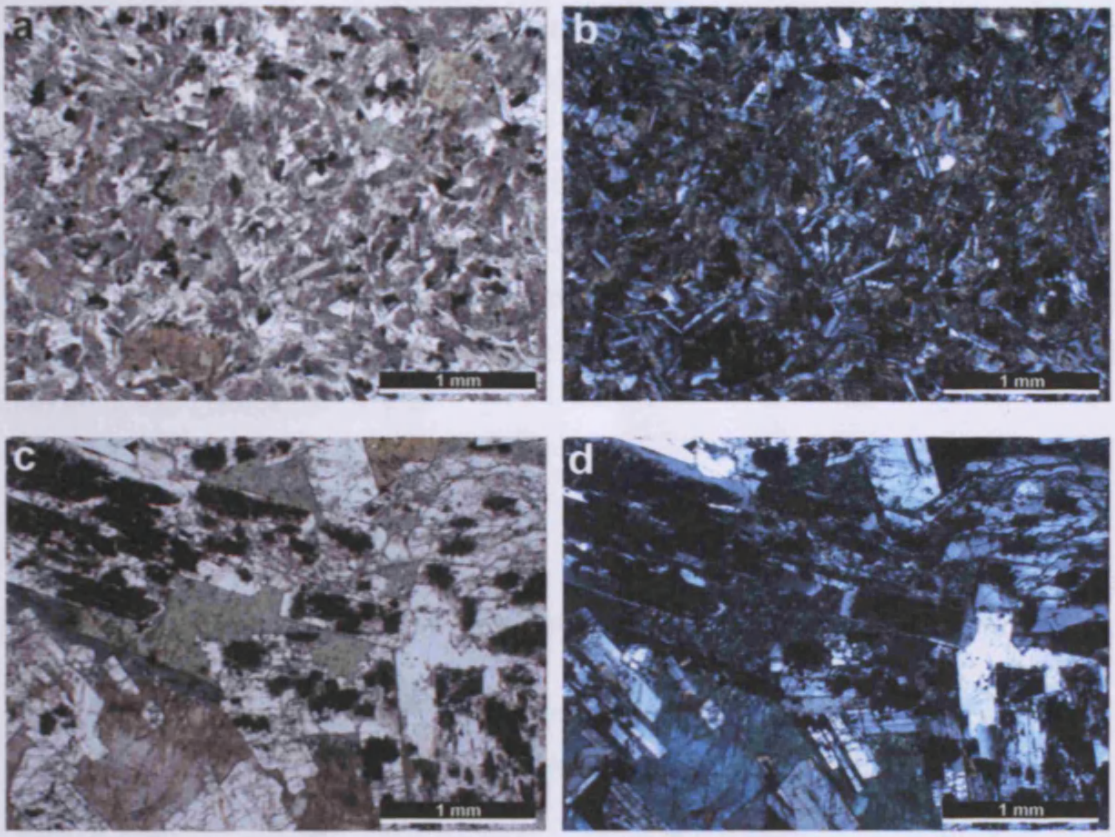

Fig. 3.16. Photomicrographs of the Pickle Crow dyke. (a) Plane-polarised photomicrograph showing the intersertal doleritic texture of the margin of the Pickle Crow dyke. The view shows opaque minerals, chlorite, plagioclase laths, dusty brown patches which may originally have been clinopyroxene, and prisms of hornblende which are variably chloritised; (b) Cross-polarised view of (a); (c) Plane-polarised photomicrograph of the coarse grained central portion of the Pickle Crow dyke which shows variably altered plagioclase, clinopyroxene, actinolite, chlorite and opaque minerals; (d) Cross-polarised view of (c).

The margin sample (MMPC07-1) of the Pickle Crow dyke is a dolerite composed of plagioclase, clinopyroxene, hornblende, chlorite and opaque minerals (Fig. 3.16a-b). Plagioclase occurs as laths up to ~0.6 mm in length and also as subrounded crystals. Remnants of ophitic texture are visible but are often obscured by the dusty green-brown material which encloses the plagioclase. The dusty green-brown material is composed of chlorite and probably other minerals formed from the alteration of

clinopyroxene and plagioclase. A few prisms of hornblende are present in the margin sample but are partially to completely replaced by chlorite.

The two samples (MMPC07-2 and MMPC07-3) from the central portion of the Pickle Crow dyke are much coarser than the margin sample. In these samples the laths of plagioclase and prisms of clinopyroxene are often >1 mm in size (Fig. 3.16c-d) and can be ~3 mm long. The central samples contain the same mineralogy as the margin sample but there are more visible examples of actinolite replacing clinopyroxene.

The original igneous minerals of the dyke samples have been altered and replaced with secondary phases. The presence of actinolite and chlorite suggest that the Pickle Crow dyke has been subjected to a grade of metamorphism which may just extend into the lower greenschist facies.

3.9. Lake Superior region

3.9.1. Sample collection of the Gunflint Formation

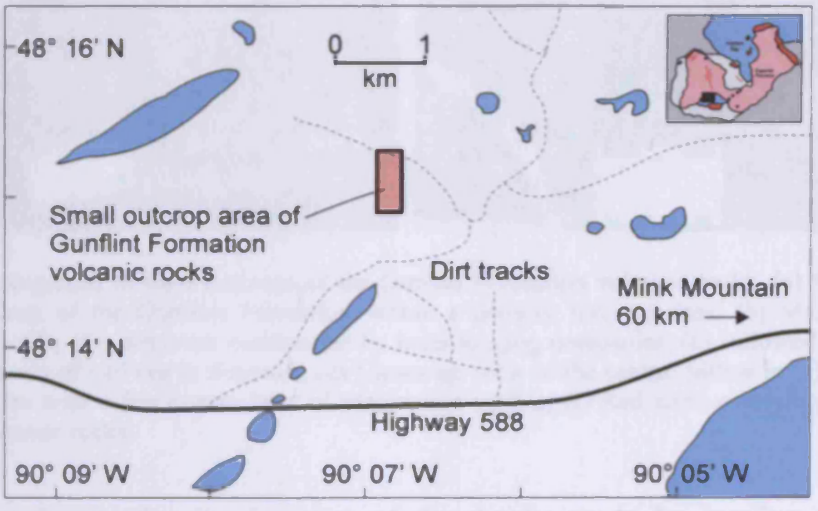

Fig. 3.17. Simplified map showing the location of outcrops from which samples of the Gunflint Formation volcanic rocks were collected.

Volcanic rocks of the Gunflint Formation are only known to outcrop in a relatively small area close to Mink Mountain (Fig. 3.17) from which seven samples (MMG08-1 to MMG08-7) were collected. This area has only been made relatively accessible in

Fig. 3.18. Photographs of field outcrops of the Gunlint Formation volcanic rocks. (a) Moss-covered pillowed outcrop of the Gunflint Formation within a densely forested area; (b) Massive outcrop located on the side of a dirt track constructed by local logging companies; (c) Pillowed outcrop with individual pillows of ~10 cm in diameter; (d) Closer-up view of the central pillow in (c); (e) Outcrop of small pillows with a few coarse laths of plagioclase visible; (f) Red chert overlying the Gunflint Formation volcanic rocks.

recent years due to the development of dirt tracks made by logging companies. Within this small area, the volcanic rocks form sparse outcrops ranging up to ~5 m in width (Fig. 3.18a-b) often overgrown by vegetation. The volcanic rocks possess reddish-orange weathered surfaces (Fig. 3.18a-e) but when broken to reveal fresh surfaces can be seen to be grey-green, dark grey or black in colour. The rocks are

fine grained with the exception of a couple of outcrops where coarse (up to 2 cm long), white plagioclase laths were observed (Fig. 3.18e). Vesicles are not abundant in the volcanic rocks but when present are often filled with a pinkish-red mineral. Both pillowed (Fig. 3.18a, c, d, e) and massive (Fig. 3.18b) outcrops were observed. The size of the pillow lavas varies, the largest observed was ~30 cm wide and the smallest <5 cm wide (Fig. 3.18e). Black material, probably devitrified glass, often fills the interstices between pillows. No bedding planes of pillow lavas were observed. The Gunflint Formation volcanic rocks are overlain by a red chert layer. A lot of chert fragments were scattered around the field area and occasionally outcrops with volcanic rock-chert contacts were observed (Fig. 3.18f).

3.9.2. Petrography of the Gunflint Formation

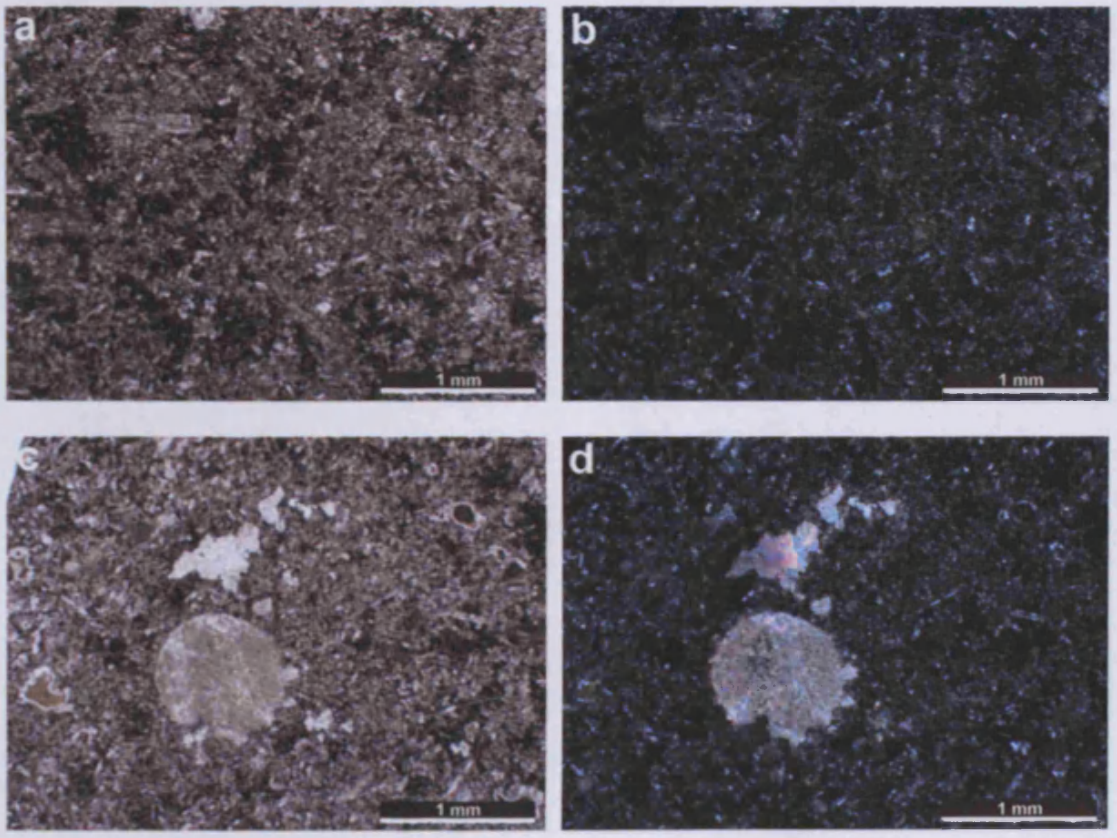

Fig. 3.19. Photomicrographs of the Gunflint Formation. (a) Plane-polarised photomicrograph showing the typical texture of the Gunflint Formation volcanic rocks. Variably altered laths of plagioclase are surrounded by a greenish-brown groundmass; (b) Cross-polarised view of (a); (c) Plane-polarised photomicrograph highlighting the amygdalar nature of some of the volcanic rocks; (d) Cross-polarised view of (c) showing amygdales filled with a high birefringence mineral, possibly carbonate.

The Gunflint Formation samples are fine grained volcanic rocks. The samples contain laths of plagioclase, ranging up to ~2 cm in length but usually <0.8 mm, set within a green chloritised matrix (Fig. 3.29a-b). Plagioclase is usually altered to sericite but in some cases it is replaced by chlorite. Occasionally, high relief epidote and opaque minerals are present within the fine grained material surrounding the altered plagioclase laths. Common to most samples is the presence of small amygdales which are ~0.5-1 mm in diameter (Fig. 3.29c-d). The amygdales usually contain carbonate and/or quartz.

3.9.3. Sample collection of the Hemlock Formation

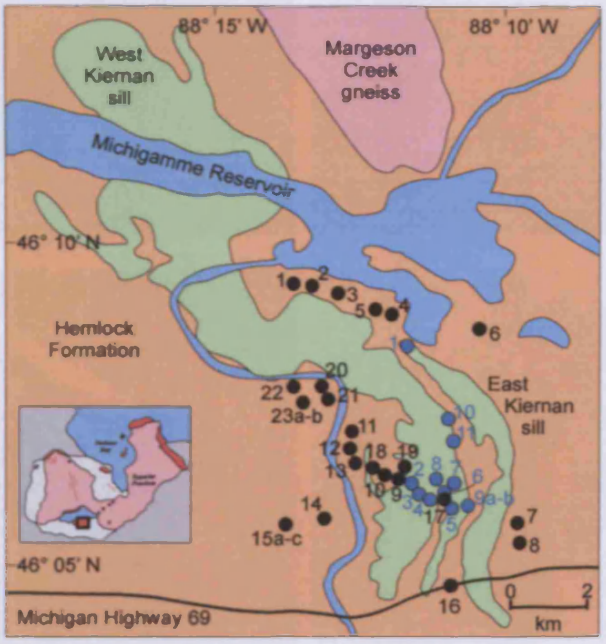

Fig. 3.20. Simplified map showing the field localities from which samples of the Hemlock Formation and Kiernan sills used in this study were collected. Map adapted from Beck & Murthy (1991). The numbers 1 to 23 in black represent samples MMH08-1 to MMH08-23. The numbers 1 to 11 in blue represent samples MMK08-1 to MMK08-11.

Twenty-six rock samples (MMH08-1 to MMH08-23b) of the Hemlock Formation were collected from the Kiernan Quadrangle area described by Gair & Wier (1956). This area is dominated by forest, swamps and lakes (Fig. 3.21a) and outcrops of exposed bedrock are not common. Exposures of the Hemlock Formation occur as small isolated outcrops in forested areas or along roadsides, ridges along roadsides, or as cliffs up to ~20 m tall along rivers. Unfortunately, many river cliffs were not

Fig. 3.21. Field photographs of the Hemlock Formation and the terrain in which it is exposed. (a) The swampy and forested terrain in which rare exposures of the Hemlock Formation occur; (b) Cliff faces composed of Hemlock Formation occur along rivers close to hydroelectric dams and unfortunately were inaccessible; (c) Massive outcrop of slaty greenstone on a roadside; (d) Pillowed outcrop along a riverside; (e) Finely layered outcrop of Hemlock Formation; (f) Moss- and lichen-covered outcrop of a felsic rock hidden in a wooded area.

accessible because of close-by hydroelectric dams (Fig. 3.21b) and safety laws restricting access to such areas. Consequently, most samples come from ridges and small outcrops on roadsides and isolated outcrops in deforested, swampy areas. Fig. 3.20 is a schematic map of sample locations.

The vast majority of samples collected are mafic volcanic rocks. Beneath the weathered exterior the fresh surfaces of the rocks range in colour from green to light grey to dark grey. The mafic volcanic rocks are generally fine grained but a few outcrops are slightly coarser in grain size and perhaps could be classified as subdoleritic. The volcanic rocks mainly form massive flows (Fig. 3.21c) but in some areas pillowed structures were observed (Fig. 3.21d). Where present, pillows reach ~80 cm in width. No chilled rims were observed and any sediment in the pillow interstices appears to have been eroded away. At two localities the Hemlock Formation was observed to be interbedded with slate-like material.

At one locality, the Hemlock Formation was observed to possess fine scale layering (Fig 3.21e). Green-light grey and green-dark grey layers up to 2 cm thick are repeated and themselves contain 1-3 mm thick layers dominated by white plagioclase crystals.

Most of the Hemlock Formation is not vesicular. However, at one sample location (MMH08-15) the Hemlock Formation contains an abundance of amygdales. Most of these amygdales are pinkish-red or colourless quartz and are surrounded by black rims. In addition to the quartz amygdales, some vesicles are filled in with a black mineral.

One sample (MMH08-6) of a felsic rock was obtained from the field area. The sample came from a small, isolated outcrop covered in moss in a wooded area (Fig. 3.21f). Where fresh surfaces were visible, the felsic rock was a pink colour and had well developed flow banding.

3.9.4. Petrography of the Hemlock Formation

The mafic volcanic rocks of the Hemlock Formation are generally fine grained (Fig. 3.22a) although some samples are slightly coarser than others and perhaps have a subdoleritic texture (Fig. 3.22b-c). The main minerals in the mafic volcanic rocks are plagioclase, chlorite, actinolite and opaque minerals. Plagioclase usually occurs as laths but also as blades and is variably altered to sericite, clays, carbonate, chlorite, epidote and clinozoisite. Actinolite appears to have formed from the alteration of

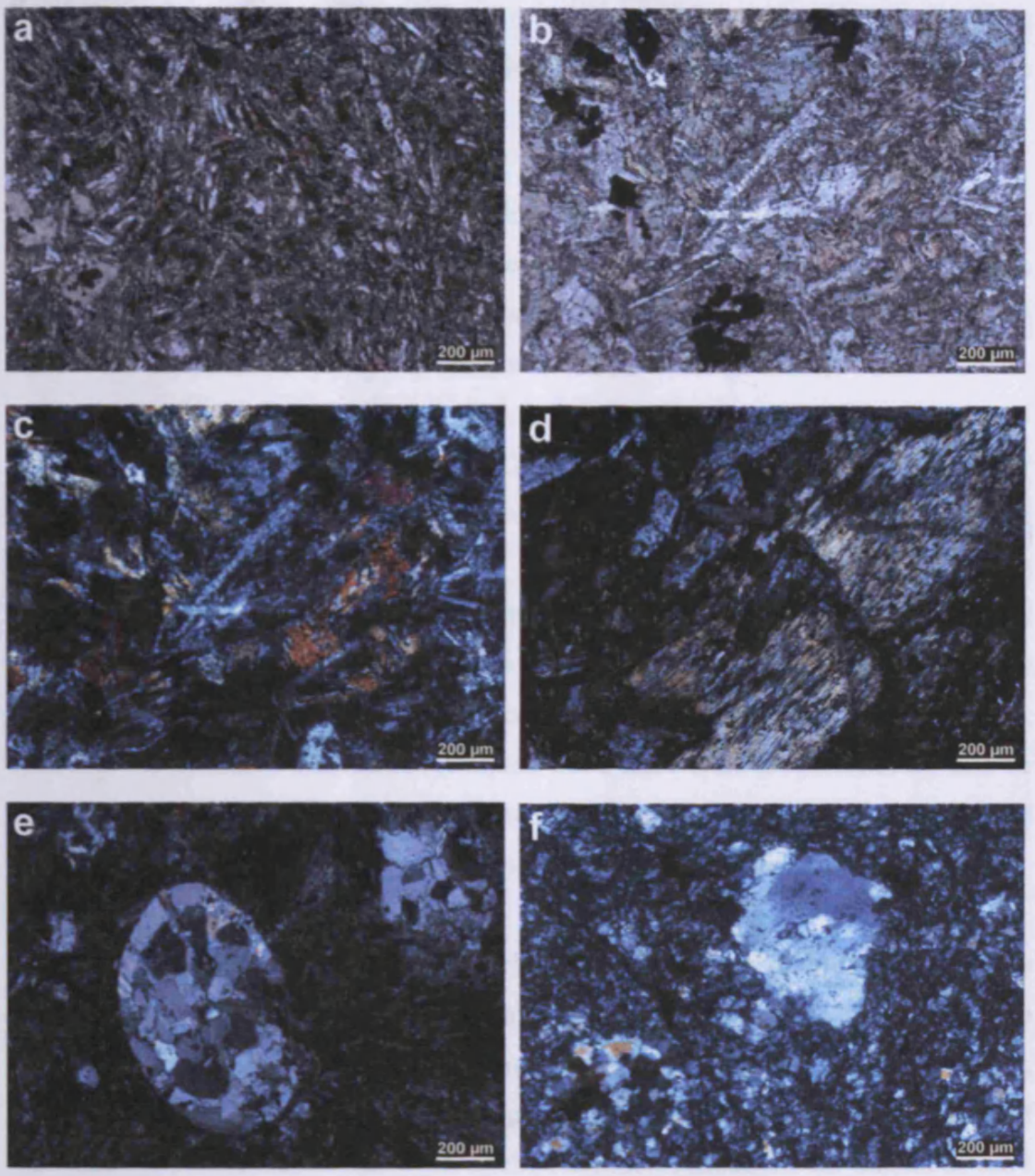

Fig. 3.22. Photomicrographs of the Hemlock Formation. (a) Plane-polarised photomicrograph showing the typical mineralogy and texture of the fine grained Hemlock Formation volcanic rocks; (b) Plane-polarised photomicrograph of a slightly coarser rock than in (a); (c) Cross-polarised view of (b); (d) Cross-polarised photomicrograph demonstrating ophitic texture where an altered grain of clinopyroxene is enclosing laths of plagioclase; (e) Cross-polarised photomicrograph of an amygdale filled with carbonate; (f) Cross-polarised photomicrograph of the felsic sample with an 'eye' of quartz surrounded by a finer grained matrix composed of quartz and feldspar.

clinopyroxene, as many crystals of actinolite appear to be pseudomorphs after clinopyroxene. This is especially the case where the actinolite has an ophitic relationship with plagioclase (Fig. 3.22d). Chlorite is also found replacing clinopyroxene and in some places occurs along with biotite which appears to form

from the breakdown of actinolite. In a few sections opaque minerals appear to have altered to a mineral with a strong brownish body colour that masks its birefringence and may possibly be sphene.

Some samples of the Hemlock Formation are amygdaloidal. The amygdales are generally quite rounded and in some places are deformed and could be used as strain markers. Some amygdales are filled with mosaic quartz and small veinlets of chlorite and biotite whilst others are mostly filled with carbonate (Fig. 3.22e).

The one felsic sample from the Hemlock Formation is composed of large crystals or 'eyes' of quartz, quartz and sericite or sericitised feldspar set in a matrix of finer grained quartz and feldspar (Fig. 3.22f). The eyes comprise ~5% of the felsic rock and reach up to ~1.5 mm in width. If an eye is composed of quartz then it will usually display mosaic texture or undulose extinction. Extended streaks of sericite are present in the finer grained matrix and may be pseudomorphous after feldspar. Quartz is the dominant mineral in the matrix but a significant proportion may also be pseudomorphs after feldspar. Opaque minerals tend to occur within cracks and could have formed after the deformation affecting the Hemlock Formation.

The formation of actinolite and chlorite at the expense of clinopyroxene is characteristic of greenschist facies metamorphism. Epidote and clinozoisite also commonly form at this metamorphic grade. Previous studies (e.g. Gair & Wier, 1956) have also assigned a metamorphic grade of greenschist facies to most rocks of the Hemlock Formation. Some rocks of the Hemlock Formation are known to have been metamorphosed to a higher grade but these rocks occur further southwest of where the samples were collected for this study (Gair & Wier, 1956).

3.9.5. Sample collection of the Kiernan sills

Twelve samples (MMK08-1 to MMK08-11) were collected from outcropping exposures of the Kiernan sills (Fig. 3.20) within the Kiernan Quadrangle area described by Gair & Wier (1956). Outcrop in this area is very poor and the search for outcrops was hindered by the forested and swampy nature of the terrain. Samples were taken from several small isolated outcrops along the roadside (Fig. 3.23a-b) or

within a few hundred metres of the roadside where small areas have been deforested (Fig. 3.23c-d).

Sample MMK08-1 is the only sample taken from the eastern Kiernan sill. This sample is a grey, coarse grained gabbroic rock from a lightly orange-stained roadside outcrop ~7 m in length (Fig. 3.23a). The maximum crystal size in this sample is 3 mm. The contact between the east Kiernan sill and the Hemlock Formation was not observed in the field.

Fig. 3.23. Photographs of the Kiernan sills. (a) Small isolated roadside outcrop of the eastern sill; (b-d) Small isolated roadside outcrops of the western sill.

All other samples come from outcrops of the western Kiernan sill. These samples are all gabbros with varying grain size up to a maximum of 3 mm. Plagioclases are white and pink in colour in most samples and occasionally green minerals, possibly of chlorite, are present. In sample MMK08-11 there is a clustering of plagioclase crystals. No contacts between the western sill and the Hemlock Formation were observed in the field.

3.9.6. Petrography of the Kiernan sills

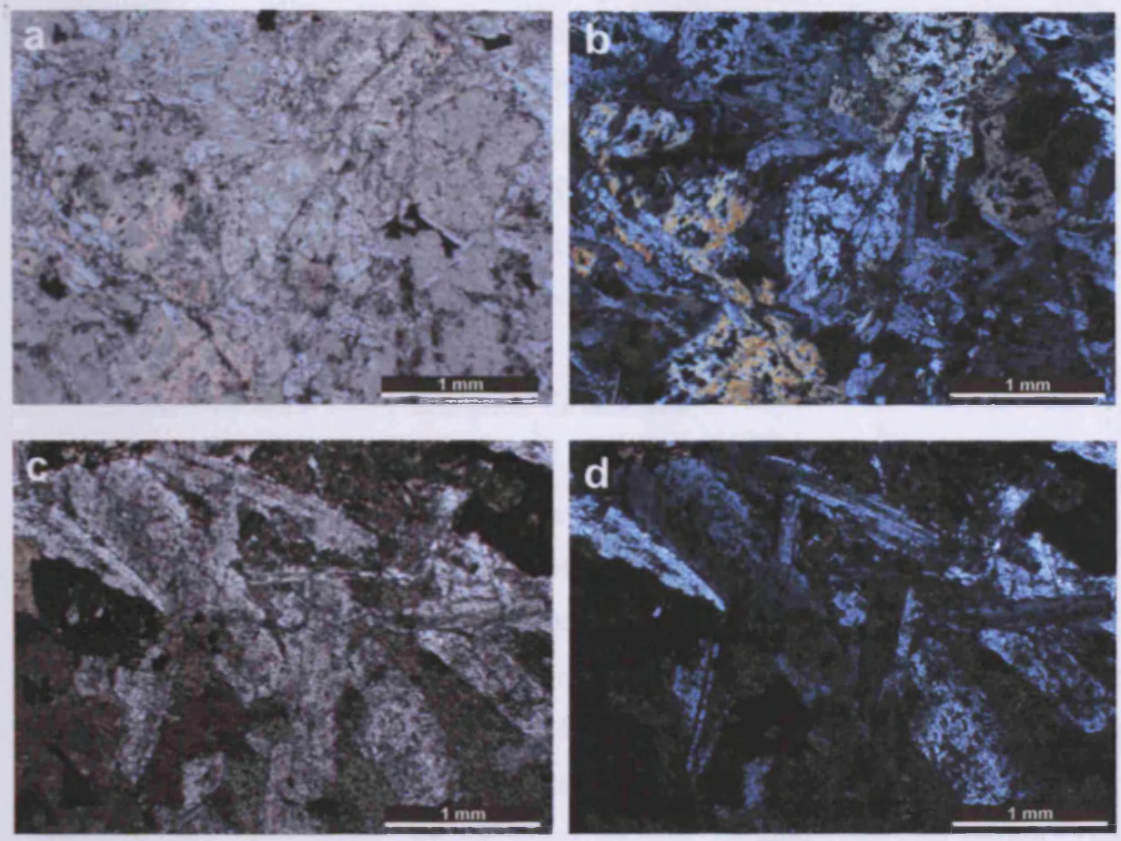

Fig. 3.24. Photomicrographs of the Kiernan sills. (a) Plane-polarised photomicrograph of a gabbro sample mostly containing plagioclase, pale green amphibole and opaque minerals; (b) Cross-polarised view of (a) better highlighting the ophitic textures where plagioclase crystals are partially to wholly surrounded by amphibole crystals; (c) Plane-polarised photomicrograph of a much coarser gabbro sample containing laths of plagioclase ~2 mm in length; (d) Cross-polarised view of (d).

All the samples collected from the Kiernan sills are gabbros with plagioclase and pale green amphibole as the dominant minerals (Fig. 3.24). The majority of samples have an average crystal size of <2 mm (Fig. 3.24a-b), however, sample MMK08-11 is coarser than the other samples and plagioclase laths tend to be >2 mm in size and sometimes form clusters (Fig. 3.24c-d). Plagioclase crystals are variably altered to sericite, carbonate, chlorite and epidote. This alteration sometimes makes it hard to recognise the original crystal morphologies and textures. The amphibole varies in colour from colourless to pale green and is usually weakly pleochroic. The first order birefringence colours of the amphibole suggest that it is actinolite. However, in a few places amphiboles with second order birefringence colours are observed and could be hornblende. Despite alteration, it is usually possible to recognise ophitic textures

with laths of plagioclase enclosed by amphibole crystals. The amphibole is most likely a secondary mineral as in a few rare cases amphibole crystals contain relicts of previous minerals in their cores, most likely to be clinopyroxene. Clinozoisite is also present in the gabbro samples and usually occurs as granular aggregates. Opaque minerals are common, although not abundant, and sometimes are rimmed by a very pale brown material with a masked birefringence. The common mineral assemblage of the Kiernan sills is similar to that of the Hemlock Formation volcanic rocks and is consistent with the sills having experienced metamorphism to greenschist facies.

3.9.7. Sample collection of the Badwater Greenstone

Nine samples of the Badwater Greenstone (MMB08-1 to MMB08-8) were collected from an area ~2 km north of the town of Crystal Falls in Iron County, Michigan. Exposed outcrops of Badwater Greenstone are rare and form <1% of the actual bedrock (James et al., 1968) and most information of the extent of the Badwater Greenstone comes from drill hole data. Much like in the search for outcrops of the Hemlock Formation and Kiernan sills, searching for exposures of the Badwater Greenstone was complicated by the abundance of swampy, forested terrain. The eight sample localities were found along the side of a dirt track (Fig. 3.25).

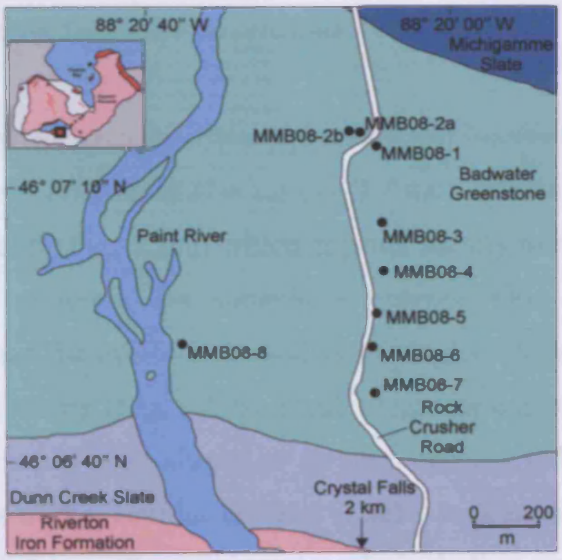

Fig. 3.25. Simplified map showing the field localities from which samples of the Badwater Greenstone used in this study were collected. Map adapted from James et al. (1968).

Fig. 3.26. Photographs of the Badwater Greenstone. (a-b) Sparse outcrops covered by vegetation and scree.

The Badwater Greenstone in the field area is a light grey rock which forms outcrops mostly covered by vegetation and scree (Fig. 3.26). The rocks are mostly fine grained with the exception of a couple of outcrops which possess plagioclase crystals 1-2 mm in length. Occasionally quartz veins are present as are patches of green minerals possibly of chlorite. All outcrops are massive with no recognisable pillow structures, although James et al. (1968) have reported pillowed outcrops from other areas. One outcrop contains vesicles, some of which are filled with black and white minerals.

3.9.8. Petrography of the Badwater Greenstone

The majority of Badwater Greenstone samples have an intersertal texture dominated by laths of plagioclase, ranging in size up to ~0.7 mm, surrounded by fine grained, brownish green material (Fig. 3.27a) which appears mostly to be actinolite, chlorite, plagioclase, opaque minerals and sometimes epidote. One sample has a more porphyritic texture than the others and consists of plagioclase laths >1 mm in length within a fine grained matrix (Fig. 3.27b). Fresh plagioclase is not observed in any of the samples, instead it has been altered to sericite, clays or chlorite or a mixture of these minerals. Some of the samples contain vesicles ranging in shape from circular to linear and are filled in with various minerals including carbonate, chlorite and quartz (Fig. 3.27c-f). The common mineral assemblage of the Badwater Greenstone

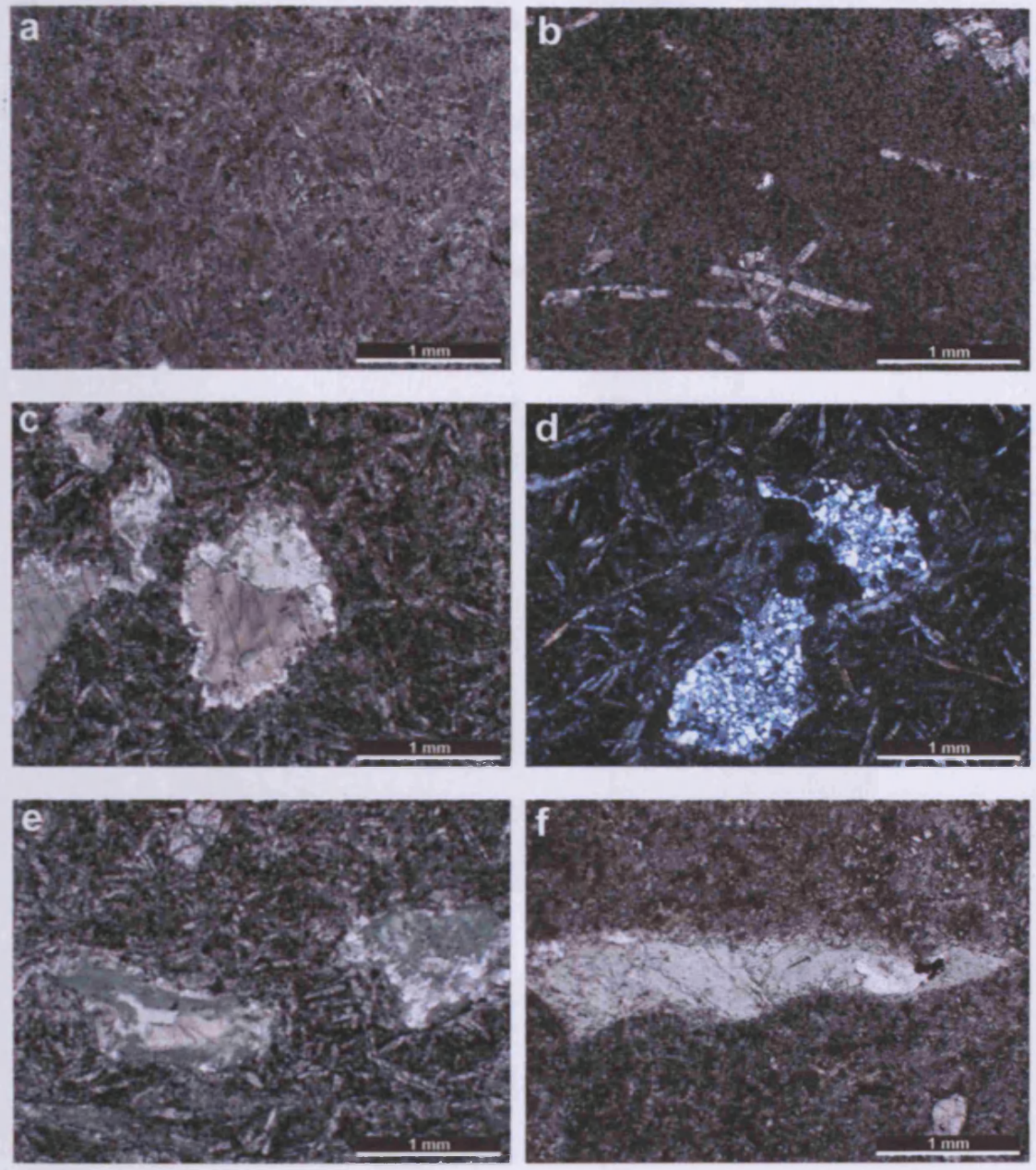

Fig. 3.27. Photomicrographs of the Badwater Greenstone. (a) Plane-polarised photomicrograph showing the fine grained intersertal texture seen in many samples of the Badwater Greenstone; (b) Plane-polarised photomicrograph of a porphyritic sample with plagioclase laths set within a finer grained matrix; (c) Plane-polarised photomicrograph of an amygdale filled mostly with carbonate with minor quartz and chlorite; (d) Cross-polarised photomicrograph of an amygdale filled with mosaic quartz; (e) Plane-polarised photomicrograph of two amygdales filled mostly with chlorite and also some carbonate and quartz; (f) Plane-polarised photomicrograph of an elongated amygdale filled with pale green chlorite.

includes actinolite, chlorite and epidote and is consistent with the volcanic rocks having experienced metamorphism to greenschist facies.

3.9.9. Sample collection of the Emperor Volcanic Complex

Seven rock samples from the Emperor Volcanic Complex (MME08-1 to MME08-7) were collected for this study. The samples were obtained from the archives of Lakehead University in Thunder Bay and had originally been collected by Dr. Stephen Kissin. Fig. 3.28 shows the localities where rock samples were collected from the Emperor Volcanic Complex.

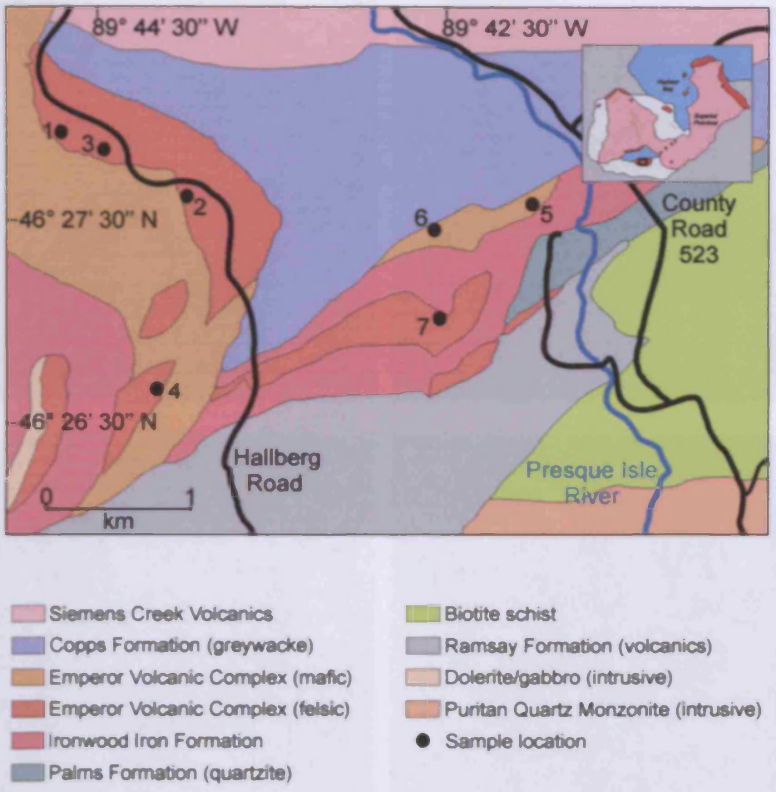

Fig. 3.28. Simplified map showing the field localities from which samples of the Emperor Volcanic Complex used in this study were originally collected. Map adapted from Klasner et al. (1998). The numbers 1 to 7 represent samples MME08-1 to MME08-7.

3.9.10. Petrography of the Emperor Volcanic Complex

There is a variety of rock types within the Emperor Volcanic Complex. Four of the samples are relatively fine grained and plagioclase-phyric (Fig. 3.29a). Plagioclase usually occurs as laths ranging in size up to ~0.6 mm and is variably altered to sericite. Occasionally the laths cluster together to form seemingly larger, rounder crystals. The plagioclase crystals are surrounded by finer grained material which

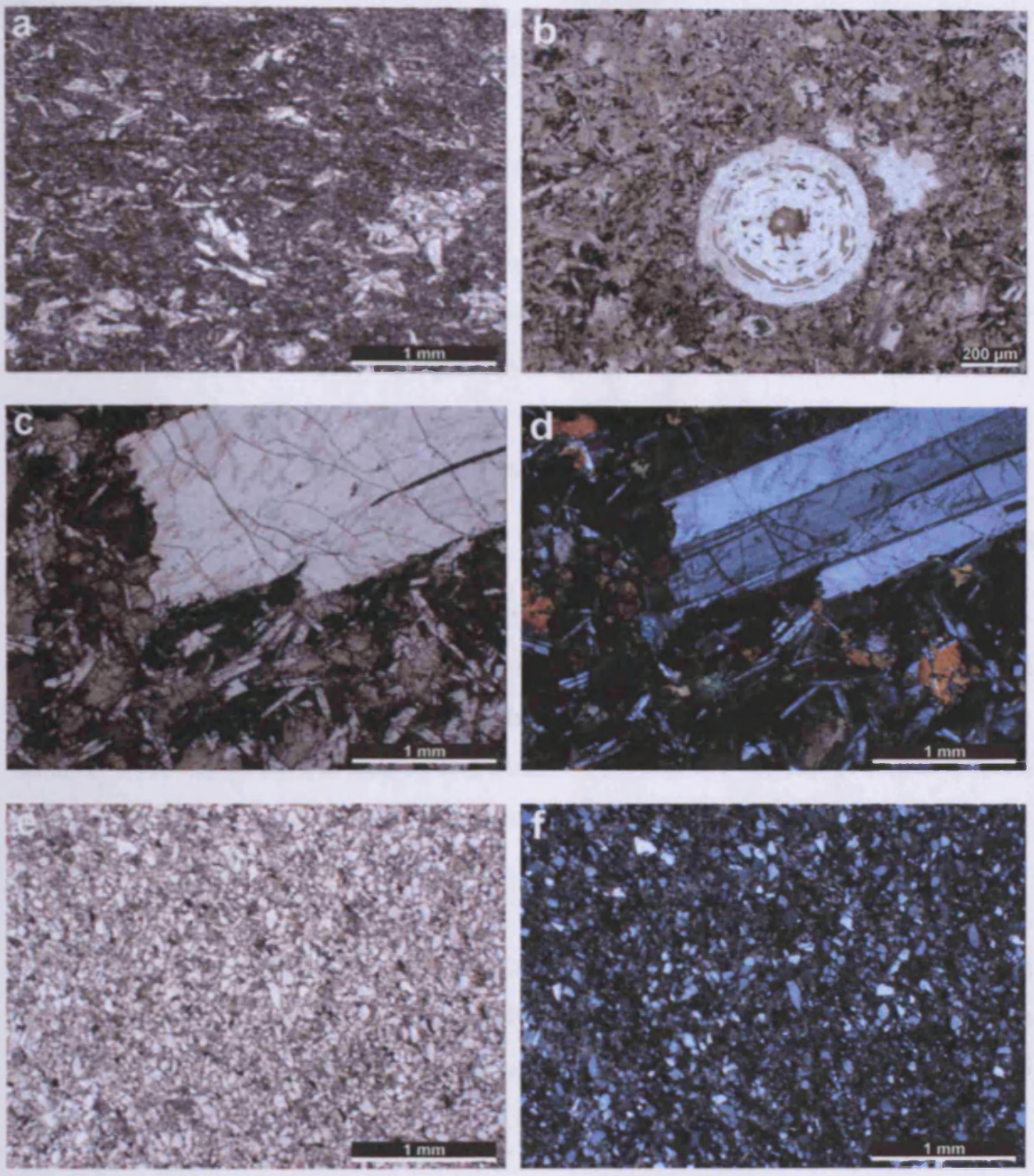

Fig. 3.29. Photomicrographs of the Emperor Volcanic Complex. (a) Plane-polarised photomicrograph of a plagioclase-phyric sample in which some of the plagioclase crystals appear to cluster together; (b) Plane-polarised photomicrograph of a rounded amygdale composed of quartz with thin veinlets of biotite; (c) Plane-polarised photomicrograph of the dolerite dyke sample exhibiting very coarse plagioclase laths and ophitic texture with smaller laths of plagioclase seemingly protruding into clinopyroxene; (d) Cross-polarised view of (c); (e) Plane-polarised photomicrograph of a more felsic volcanic rock than in (a)-(d) containing variably shaped crystals of quartz and feldspar along with a few opaque minerals set in a dusty brown matrix composed partly of carbonate; (f) Cross-polarised view of (e).

contains chlorite, altered plagioclase, epidote and opaque minerals. One of these four samples contains near-circular features which could be amygdales. The amygdales

range up to ~0.75 mm in diameter and are composed mostly of quartz with thin veinlets of greenish brown biotite (Fig. 3.29b).

One of the samples from the Emperor Volcanic Complex (MME08-2; Fig. 3.29c-d) comes from a dolerite dyke. This sample is fairly well preserved and there is only limited alteration of the minerals in thin section. Coarse laths of plagioclase which are up to ~1.2 mm wide and ~5.5 mm long are perhaps the most obvious feature of this sample. Smaller laths of plagioclase, up to ~0.7 mm in size, are partially enclosed by clinopyroxene crystals and give the rock an ophitic texture. Clinopyroxene is quite fresh in some places but in others has altered to chlorite or actinolite around the crystal margins.

Two samples are from the more felsic part of the complex. These samples (MME08-5 and MME08-6) contain an abundance of quartz and feldspar, both plagioclase and microcline, set within a dusty brown matrix (Fig. 3.29e-f). The quartz and feldspar occur as a variety of crystal shapes and sizes. The dusty brown matrix material has a speckly, high birefringence and could be carbonate and white mica formed from the alteration of feldspar.

The rocks of the Emperor Volcanic Complex have been metamorphosed to a greenschist facies grade. This is indicated by the replacement of clinopyroxene with actinolite, the presence of chlorite and epidote, and the absence of prehnite and pumpellyite.

3.10. Labrador Trough

3.10.1. Sample collection

Forty-five rock samples were collected from the Labrador Trough and correspond to sample numbers MMLT07-1 to MMLT07-45. All of the samples are from the volcanic rocks of the Hellancourt Formation and consist of field specimens and drill core material. The samples had originally been collected by Dr. James Mungall and were stored in the archives of the University of Toronto. The locations of the field specimens and drill holes are shown in Fig. 3.30.

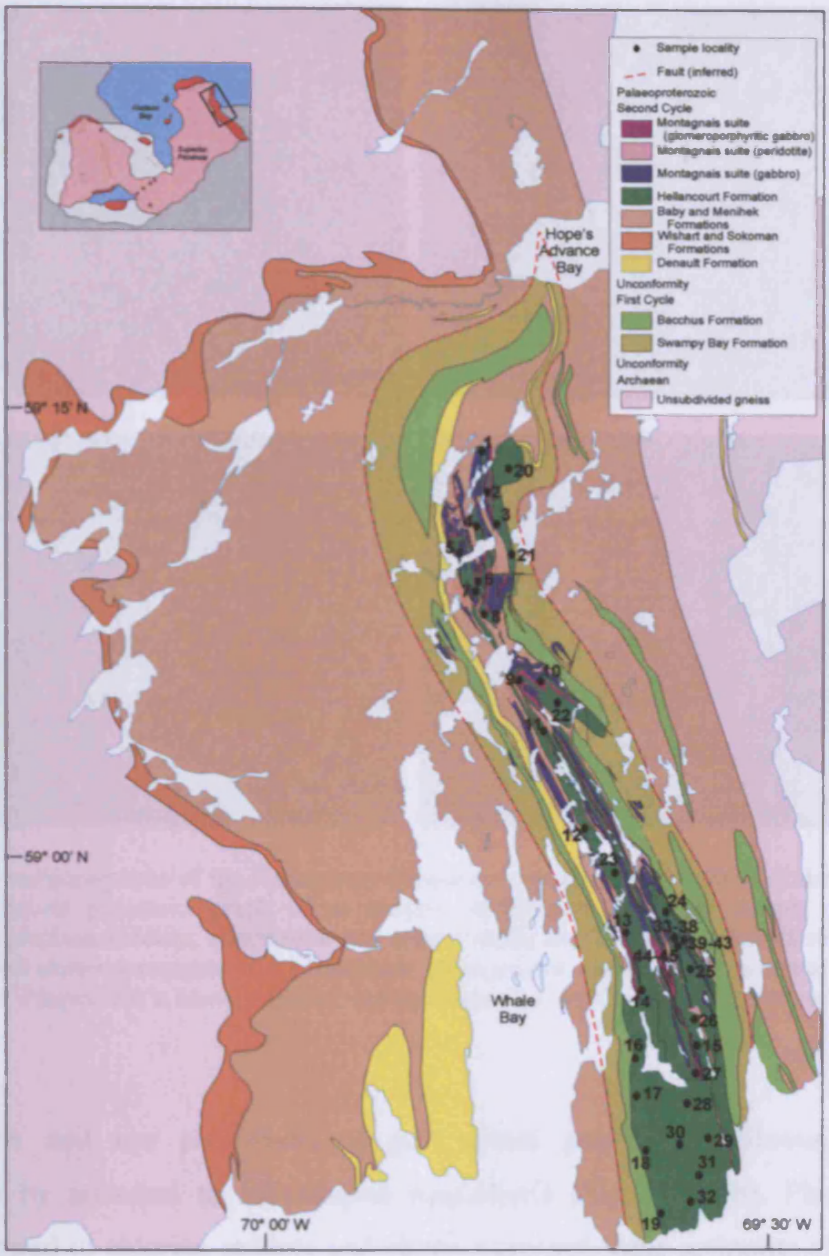

Fig. 3.30. Simplified map showing the field and drill hole localities from which samples of the Hellancourt Formation used in this study were originally collected. Map adapted from Mungall & Wares (1997). The numbers 1 to 45 represent samples MMLT07-1 to MMLT07-45.

3.10.2. Petrography of the Hellancourt Formation

The Hellancourt Formation volcanic rocks can be split into two broad groups on the basis of their petrography. The first group are samples which come from near the base of the Hellancourt Formation and contain glomerocrysts of plagioclase. The second group are generally aphyric. The aphyric samples are petrographically

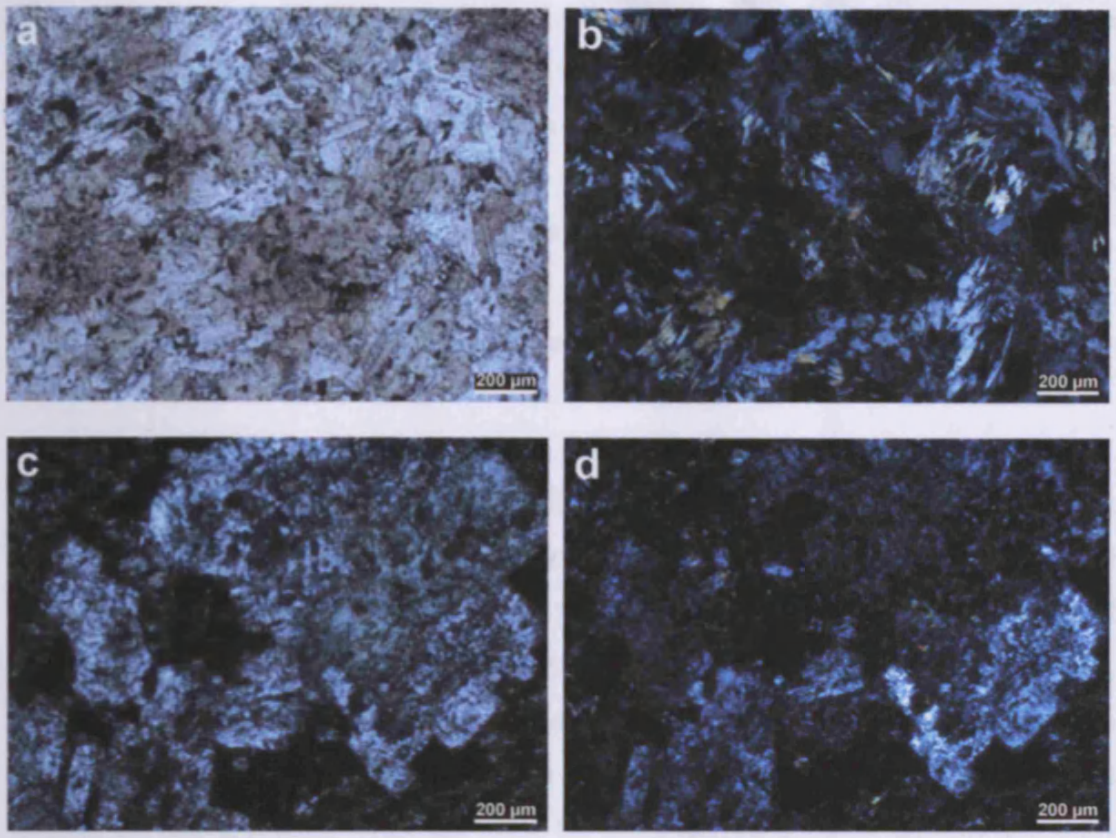

Fig. 3.31. Photomicrographs of the Hellancourt Formation volcanic rocks from the Labrador Trough. (a) Plane-polarised photomicrograph of an aphyric Hellancourt Formation sample consisting of actinolite, plagioclase, chlorite, clinozoisite and opaque minerals; (b) Cross-polarised view of (a); (c) Plane-polarised photomicrograph of a plagioclase glomerocryst consisting of anhedral crystals and euhedral laths. Plagioclase is heavily altered, mainly to chlorite; (d) Cross-polarised view of (c).

homogenous and are comprised of pale green patches of fibrous actinolite surrounded by anhedral to lath-shaped plagioclase (Fig. 3.31a-b). Plagioclase is variably altered to chlorite, epidote and clinozoisite and some actinolite also appears to have altered to near-isotropic chlorite. Opaque minerals are present but in many examples appear to have been altered to a mineral with a strong brown body colour that masks its high birefringence. The glomeroporphyritic samples display the same mineralogy as the aphyric samples and the only notable difference between the two groups is the presence of clusters of plagioclase in the first group (Fig. 3.31c-d). The glomerocrysts are made up of anhedral crystals and euhedral laths of plagioclase and are often subrounded. The maximum observed size of the glomerocrysts is 1 mm. The plagioclase glomerocrysts are not overly abundant and only comprise ~2-5% of the volume of samples. The plagioclase crystals forming the clusters are quite heavily altered to chlorite, epidote and clinozoisite.

The grade of metamorphism which the Hellancourt Formation volcanic rocks have been subjected to appears to be greenschist facies. A greenschist facies grade is highlighted by the presence of chlorite, actinolite, epidote and clinozoisite and the absence of hornblende. Although no clinopyroxene was observed in the samples, it seems probable that the actinolite is pseudomorphous after clinopyroxene.

3.11. Summary of the alteration state of the igneous rocks of the Circum-Superior LIP

Petrographical inspection of the Circum-Superior LIP rocks shows that they are not pristine and have been subjected to varying degrees of post-magmatic alteration and metamorphism. Table 3.1 summarises the extent of alteration within each segment of the Circum-Superior LIP as determined by eye. Rocks from the Hudson Bay islands, Molson dykes and Emperor Volcanic Complex are the freshest from the Circum-Superior LIP whereas the samples from the Thompson Nickel Belt are the most altered. Olivine and plagioclase are often the most altered crystals. Olivine is usually altered to serpentine as well as to actinolite and chlorite, whereas plagioclase alters to sericite, clays or chlorite. The grade of metamorphism also varies throughout the Circum-Superior LIP. Rocks from the Hudson Bay islands, Fox River Belt, Winnipegosis Belt and Molson dykes have experienced the lowest grade of metamorphism within the subgreenschist facies. The Chukotat Group, Pickle Crow dyke and Lake Superior region rocks have experienced slightly higher grades of metamorphism within the greenschist facies. The highest grade of metamorphism occurs in the Thompson Nickel Belt which appears to have experienced metamorphism to amphibolite facies.

As the rocks of the Circum-Superior LIP are not fresh and pristine, caution should be exercised when examining the geochemical compositions of the rocks to make inferences about their petrogenesis. The observed petrographical alteration of the samples is an indication that the behaviour of all the chemical elements should be screened to see if the elements have been affected by the alteration processes before such elements are used to examine the petrogenetic history of the Circum-Superior LIP.

Table 3.1. Summary of the extent of alteration of samples from the various segments of the Circum-Superior LIP

Circum-Superior LIP segment	Number of samples with 0-50% alteration	Number of samples with 50-75% alteration	Number of samples with 75-100% alteration
Chukotat Group, Cape Smith Belt	0	8	20
Flaherty Formation, Hudson Bay islands	5	12	4
Haig sill, Hudson Bay islands	2	7	1
Fox River Belt	0	9	19
Thompson Nickel Belt	0	4	19
Winnipegosis Belt	0	9	18
Molson dykes	9	11	6
Pickle Crow dyke	0	3	0
Gunflint Formation, Lake Superior region	0	2	5
Hemlock Formation, Lake Superior region	0	11	15
Kiernan sills, Lake Superior region	0	6	6
Badwater Greenstone, Lake Superior region	0	2	7
Emperor Volcanic Complex, Lake Superior region	2	3	2
Hellancourt Formation, Labrador Trough	0	13	32

4. WHOLE-ROCK GEOCHEMISTRY

4.1. Introduction

This chapter describes the whole-rock elemental and isotopic results for the igneous rocks of the Circum-Superior LIP. All of these data are displayed in Tables C.1, C.2 and D.4-D.8 in Appendices C and D. An evaluation of the accuracy and precision of the data is given in Appendices B and D. In this study, total iron was measured as and is referred to as $Fe_2O_3(T)$. Where FeO(T) is referred to, it was calculated by multiplying the total iron measured by 0.8998. All the major element concentrations are referred to as dry weight percentages.

In the sections below, the elemental and isotopic chemistry of the various segments of the Circum-Superior LIP are described in turn. To assess if secondary alteration processes have affected the igneous rocks, all the elements have been plotted against Zr. This will give an indication as to whether a particular element has been mobilised or not and if it can be used with confidence in examining the petrogenetic history of a suite of rocks. Major and trace element concentrations and their variation against fractionation indexes will be used to assess the crystallisation history of the magmatic rocks. Major and trace elements are also used to classify the igneous rocks in terms of their actual rock type and the volcanic series to which they belong. In particular, the elements SiO_2, Na_2O, K_2O, TiO_2, Zr, Nb and Y are used to assign a name and series to the Circum-Superior igneous rocks.

Chondrite-normalised rare earth element (REE) plots and primitive-mantle-normalised multi-element plots are utilised to look at the source composition of the rocks, deduce possible tectonic settings and estimate the extent of processes such as partial melting and crustal contamination. On the primitive-mantle-normalised multi-element plots the Circum-Superior igneous rocks are compared to rocks from various tectonic settings represented by the average N-MORB, enriched mid-ocean ridge basalt (E-MORB) and OIB of Sun & McDonough (1989) and basalts from the Ontong Java Plateau (Fitton & Goddard, 2004).

Trace element ratio-ratio plots are also used as indicators of the source composition and the setting in which the magmatic rocks were generated. The main trace element ratios utilised in this study are $(La/Sm)_N$, $(Gd/Yb)_N$, Zr/Nb, Nb/Th, Nb/Y and Zr/Y. These ratios form the axes of many of the diagrams shown in this chapter. On the ratio-ratio diagrams, the particular segment of the Circum-Superior LIP under consideration is represented as solid symbols and is compared to the other segments which are represented by different coloured fields on the same diagram. Isotopic ratios are used to further fingerprint the mantle sources involved in the petrogenesis of the Circum-Superior LIP.

In the following sections describing the geochemistry of the Circum-Superior LIP, many of the various segments of the LIP have been divided into varying numbers of subgroups which have been termed Group 1, Group 2 etc. The basis for the division is not consistent throughout the Circum-Superior LIP. In some segments the division is based upon petrographical differences between samples whereas in other segments it is based on major element or trace element characteristics. The various different groups and the main distinguishing features of the groups are summarised in Table 4.1.

4.2. Alteration

One of the main restrictions on using geochemistry of igneous rocks to identify magmatic processes and geodynamic settings is the potential mobility of chemical elements during rock-fluid interactions amid secondary processes such as weathering and metamorphism (e.g. Kerrich and Fryer, 1979; Dostal et al., 1980; Ludden et al., 1982; Humphries, 1984; Jochum et al., 1991; Lafleche et al., 1992; Arndt, 1994; Polat and Hofmann, 2003). Pearce (1996) noted that the ionic potential (ionic charge/ionic radius ratio) of an element strongly influences the behaviour of the element during subaerial weathering. Elements which form ions of intermediate ionic potential (0.03-0.10 pm^{-1}) are generally considered to be immobile and are retained in the solid product of weathering. Ions of low (<0.03 pm^{-1}) and high (>0.10 pm^{-1}) ionic potential are readily mobilised in solutions as hydrated cations and hydrated oxyions respectively (Pearce, 1996). The ionic potential of an element generally also influences the mobility of the element during submarine weathering and

Table 4.1. Summary of the different subgroupings within the various segments of the Circum-Superior LIP

Circum-Superior LIP section	Subgroupings	Alternative name and best distinguishing features
Chukotat Group	Group 1	*Low Th Group*: Lower Th concentrations at given Zr concentrations and no negative Nb-Ta anomalies
	Group 2	*High Th Group*: Higher Th concentrations at given Zr concentrations and negative Nb-Ta anomalies
Flaherty Formation	Group 1	*Low Th Group*: Lower Th concentrations at given Zr concentrations and positive Nb-Ta anomalies
	Group 2	*High Th Group*: Higher Th concentrations at given Zr concentrations and no positive Nb-Ta anomalies
Thompson Nickel Belt	Group 1	*Mineralised Group*: Ni-Cu-PGE sulphide mineralisation within sills
	Group 2	*Non-mineralised Group*: No Ni-Cu-PGE sulphide mineralisation within sills
Winnipegosis Belt	Group 1	*High MgO Group*: Higher MgO concentrations
	Group 2	*Low MgO Group*: Lower MgO concentrations
Molson dykes	Group 1	*High MgO Group*: Highest MgO concentrations
	Group 2	*Intermediate MgO Group*: Intermediate MgO concentrations
	Group 3	*Low MgO Group*: Lowest MgO concentrations
Hemlock Formation	Group 1	*Flat Group*: Relatively flat multi-element profiles with slight Th depletion
	Group 2	*Negative Nb-Ta Group*: Multi-element profiles with negative Nb-Ta anomalies
	Group 3	*Enriched Group*: Multi-element profiles which are enriched in the more incompatible elements relative to the less incompatible elements
	Group 4	*Positive Nb-Ta Group*: Multi-element profile with a positive Nb-Ta anomaly
Hellancourt Formation	Group 1	*Aphyric Group*: No large phenocrysts or clusters of phenocrysts
	Group 2	*Glomeroporphyritic Group*: Clusters of plagioclase phenocrysts

metamorphism (e.g. Cann, 1970; Humphris and Thompson, 1978; Menzies and Seyfried, 1979b), although higher temperatures and chloride formation may enhance the solubility of some elements (Pearce, 1996). The upper limit of metamorphism for immobile behaviour appears to be upper amphibolite facies (e.g. Ludden et al.,

1982), which is possibly due to the transition from H_2O-rich fluids to CO_2-rich fluids at this level of metamorphism (Janardhan et al., 1982).

Elements which are generally considered to be immobile up to upper greenschist/lower amphibolite facies include Sc, Ti, V, Cr, Y, Zr, Hf, Nb, Ta, Al, Ga, REEs and Th (e.g. Lahaye and Arndt, 1996; Polat and Kerrich, 2000), and consequently these elements are used on a variety of geochemical classification and tectonic discrimination diagrams (e.g. Pearce and Cann, 1971, 1973; Winchester & Floyd, 1977; Pearce and Norry, 1979; Wood, 1980; Pearce, 1982; Shervais, 1982; Meschede, 1986). Commonly mobile elements include Na, K, Rb, Cs, Mg, Ca, Sr, Ba, Cu, Zn, Si and Pb (e.g. Lesher and Stone, 1996; Zack and John, 2007). Elements which tend to show variable behaviour include Mn, Fe, Co, Ni, PGEs and U (e.g. Pearce, 1996; Hastie et al., 2007). These groupings are only generalisations and so before any inferences can be made on the petrogenetic history of an igneous rock elements should be screened for those which may have become mobilised during secondary processes and so do not reflect the original chemistry of the rock. A method used by Cann (1970) to assess element mobility is to construct bivariate diagrams with a generally accepted immobile element (e.g. Zr) on the horizontal axis and an element to be evaluated on the vertical axis. If both elements are immobile and incompatible during basaltic fractionation, and the rock samples are derived from the same mantle source, the data should yield high correlation co-efficients and straight lines with gradients close to unity. If a large degree of scatter is visible on these diagrams then this may indicate that one of the elements was mobile and its concentration altered by secondary processes. Alternatively a loss of correlation may be explained by the derivation of the igneous rocks in the same magmatic suite from a number of differing mantle sources or from a single but heterogeneous mantle source.

4.3. Chukotat Group volcanic rocks of the Cape Smith Belt

4.3.1. Alteration and element mobility

The Chukotat Group volcanic rocks have been metamorphosed to greenschist facies and several of the olivine, pyroxene and plagioclase crystals show signs of alteration

(Fig. 3.2). Loss on ignition (LOI) values of 2.06 to 4.54 wt. % are also indicative of slight alteration. Therefore an assessment of the mobility of elements within the Chukotat Group is needed, and so each element has been plotted against Zr. A representative selection of these bivariate diagrams is shown in Fig. 4.1. The elements which yield good correlations with Zr include Ti, V, Mn, Fe, Co, Ni, Ga, Y, Nb, REEs, Hf, Ta, P and Sc. These elements are relatively immobile and can be used with confidence in studying the petrogenesis of the Chukotat Group volcanic rocks. Interestingly, the light-REEs (LREEs) produce slightly more scatter on the bivariate diagrams with Zr on the abscissa compared to the heavy-REEs (HREEs) (Fig. 4.1). Cr, Cu, Zn, Rb, Si, Al, Mg and Na yield moderate correlations with Zr and should be used cautiously in this study. Rb, Sr, Cs, Ba, U, Ca, K and Th are poorly correlated with Zr (Fig. 4.1). Extreme caution should therefore be used when using these elements to study the petrogenesis of the Chukotat Group. The poor correlation of Th with Zr is surprising given that Th is generally considered to be one of the most immobile elements (Pearce, 1996). A poor correlation with Zr does not necessarily mean that Th was a mobile element. Other factors and processes such as source heterogeneity and crustal contamination may explain the scatter on such bivariate diagrams.

4.3.2. Classification

The total alkali-silica (TAS) diagram is commonly used to classify volcanic rocks and to discriminate which volcanic series rocks belong to. On this diagram (Fig. 4.2) all of the Chukotat Group samples fall within the subalkaline basalt field. According to the classification of Le Bas (2000), the Chukotat Group samples containing >12 wt. % MgO and <3 wt. % total alkalis classify as picrites. Two samples contain >18 wt. % MgO and <1 wt. % total alkalis and classify as komatiites according to the scheme of Le Bas (2000). However, in order to be a komatiite, a rock must display spinifex olivine texture (Kerr & Arndt, 2001). The weakness of the TAS diagram is that it relies on major elements which are commonly mobilised during secondary alteration processes. As a result, it seems more appropriate to put more emphasis on immobile trace elements to classify the igneous rocks of the Chukotat Group. The Zr/Ti-Nb/Y diagram was originally devised by Winchester & Floyd (1977) and modified by Pearce (1996). On this diagram (Fig. 4.3) nearly all samples plot in the

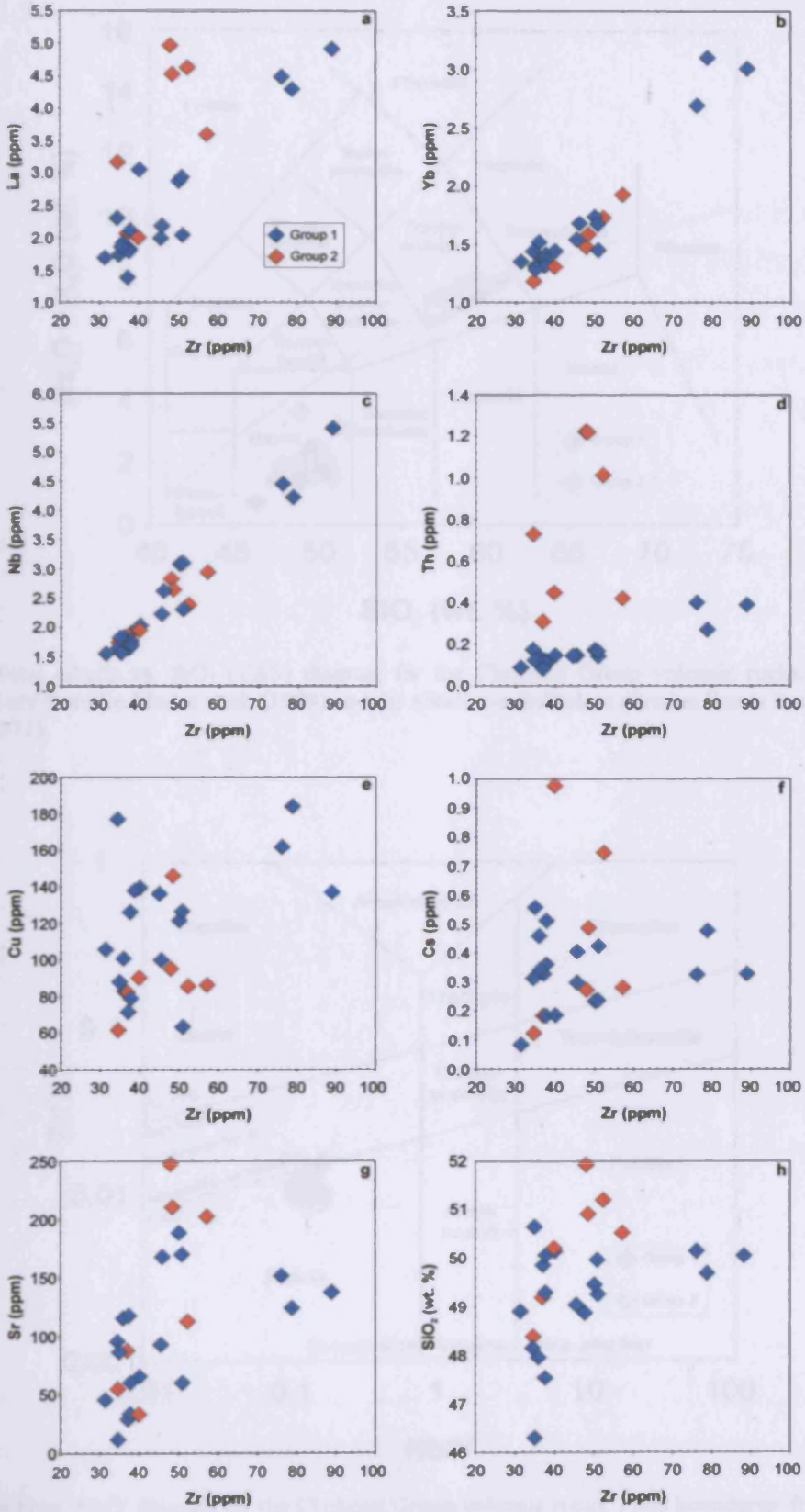

Fig. 4.1. Bivariate diagrams of selected elements vs. Zr for the Chukotat Group volcanic rocks.

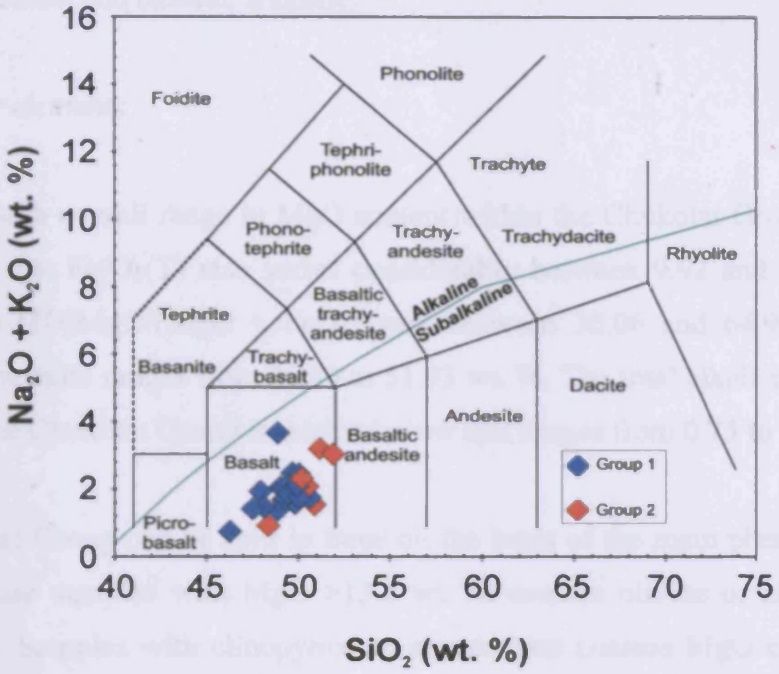

Fig. 4.2. Total alkalis vs. SiO_2 (TAS) diagram for the Chukotat Group volcanic rocks. The field boundaries are from Le Maitre et al. (1989) and the alkaline-subalkaline division line is from Irvine & Baragar (1971).

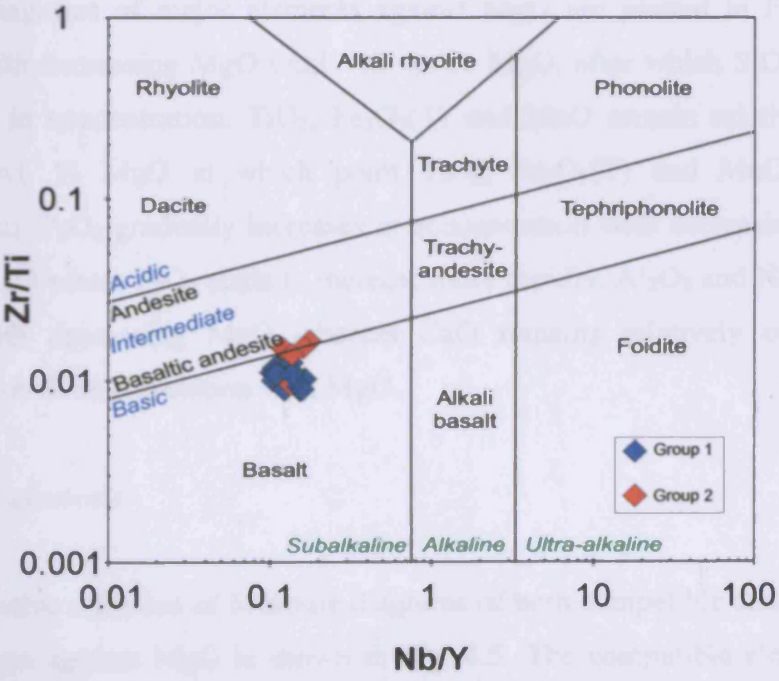

Fig. 4.3. Zr/Ti vs. Nb/Y diagram for the Chukotat Group volcanic rocks. Field boundaries from Pearce (1996).

subalkaline basalt field. There are four samples which plot on the boundary between subalkaline basalt and basaltic andesite.

4.3.3. Major elements

There is a large overall range in MgO content within the Chukotat Group from 6.62 to 19.84 wt. %. Fe_2O_3(T) also varies considerably between 9.92 and 17.13 wt. %. Mg# values (100MgO/(MgO + FeO)) vary between 30.06 and 64.91. The silica content of the suite ranges from 46.30 to 51.93 wt. %. The total alkali content (Na_2O + K_2O) of the Chukotat Group is relatively low and ranges from 0.75 to 3.67 wt. %.

The Chukotat Group can be split in three on the basis of the main phenocryst phase present. Those samples with MgO >13.8 wt. % contain olivine or altered olivine phenocrysts. Samples with clinopyroxene phenocrysts possess MgO concentrations ranging between 8.30 and 12.25 wt. %. The aphyric samples have the lowest MgO contents (6.62-7.21 wt. %) and the highest TiO_2 (1.40-1.50 wt. %), Fe_2O_3 (14.63-17.13 wt. %) and Na_2O (1.97-2.80 wt. %) concentrations.

Variation diagrams of major elements against MgO are plotted in Fig. 4.4. SiO_2 increases with decreasing MgO until ~12 wt. % MgO, after which SiO_2 then begins to decrease in concentration. TiO_2, Fe_2O_3(T) and MnO remain relatively constant until ~12 wt. % MgO at which point TiO_2, Fe_2O_3(T) and MnO increase in concentration. P_2O_5 gradually increases in concentration with decreasing MgO until ~8 wt. % MgO where P_2O_5 starts to increase more rapidly. Al_2O_3 and Na_2O generally increase with decreasing MgO whereas CaO remains relatively constant. K_2O displays no obvious correlation with MgO.

4.3.4. Trace elements

A representative selection of bivariate diagrams of both compatible and incompatible trace elements against MgO is shown in Fig. 4.5. The compatible elements Ni, Cr and Co all show good positive correlations with MgO. The highest concentrations of Ni, Cr and Co in the Chukotat Group volcanic rocks are 768, 2017 and 84 ppm respectively and decrease to minimum concentrations of 98, 170 and 46 ppm

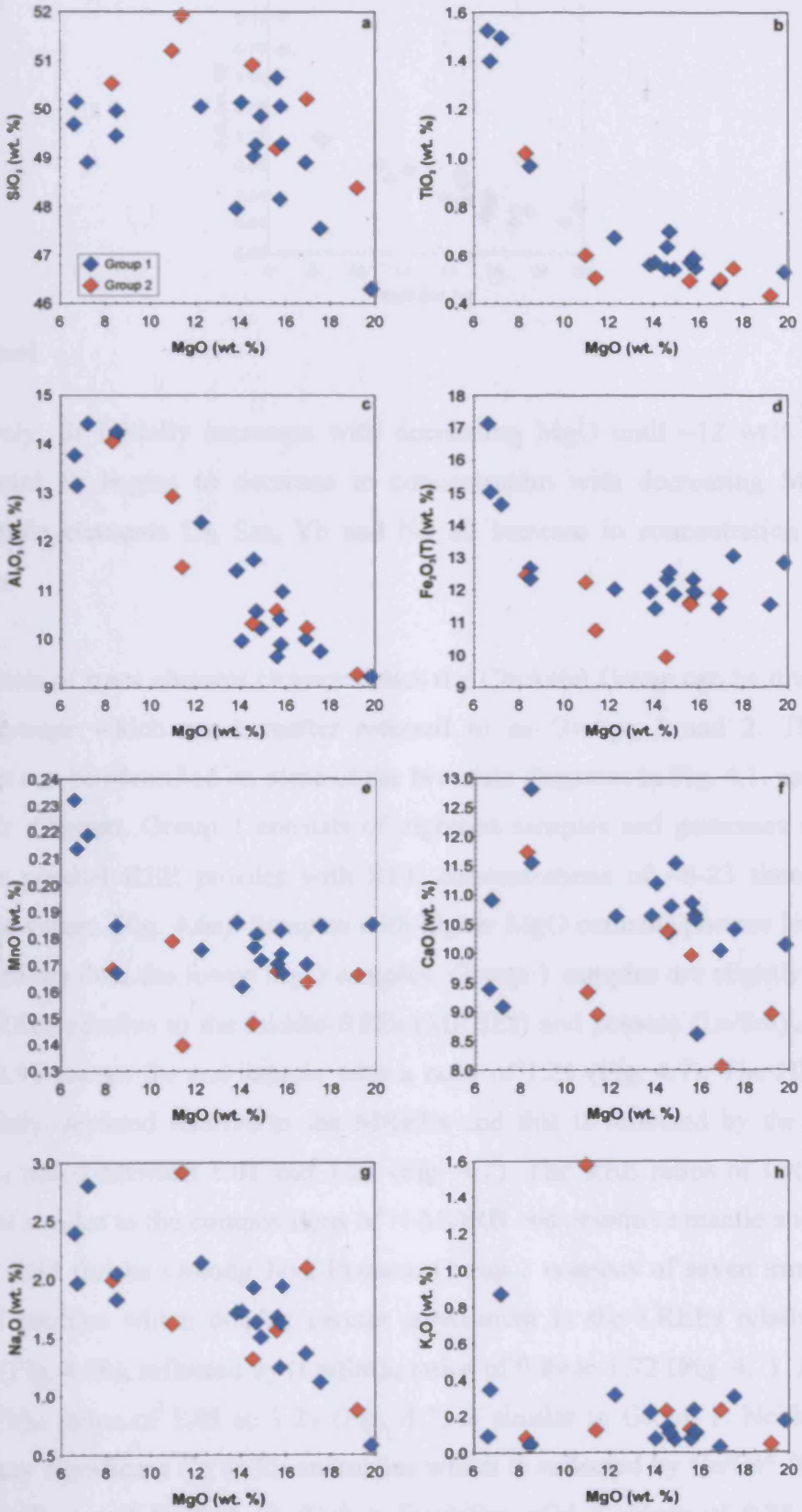

Fig. 4.4. Bivariate diagrams of major elements vs. MgO for the Chukotat Group volcanic rocks.

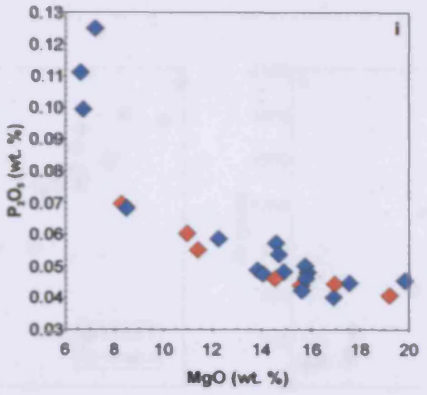

Fig. 4.4. contd.

respectively. Sr initially increases with decreasing MgO until ~12 wt% MgO, at which point Sr begins to decrease in concentration with decreasing MgO. The incompatible elements La, Sm, Yb and Nb all increase in concentration as MgO decreases.

On the basis of trace element characteristics the Chukotat Group can be divided into two subgroups which are hereafter referred to as Groups 1 and 2. These two groupings can be identified on some of the bivariate diagrams in Fig. 4.1, particularly the Th-Zr diagram. Group 1 consists of eighteen samples and possesses relatively flat, near parallel REE profiles with REE concentrations of ~6-23 times that of chondritic values (Fig. 4.6a). Samples with higher MgO contents possess lower REE concentrations than the lower MgO samples. Group 1 samples are slightly depleted in the LREEs relative to the middle-REEs (MREEs) and possess $(La/Sm)_N$ ratios of 0.63 to 0.96 except for one sample with a ratio of 1.21 (Fig. 4.7). The HREEs are also slightly depleted relative to the MREEs and this is reflected by the range in $(Gd/Yb)_N$ ratios between 1.01 and 1.25 (Fig. 4.7). The REE ratios of Group 1 are somewhat similar to the compositions of N-MORB and primitive mantle and overlap with the field for the Ontong Java Plateau. Group 2 consists of seven samples and has REE profiles which display greater enrichment in the LREEs relative to the MREEs (Fig. 4.6b), reflected by $(La/Sm)_N$ ratios of 0.89 to 1.72 (Fig. 4.7). The range in $(Gd/Yb)_N$ ratios of 1.05 to 1.23 (Fig. 4.7) is similar to Group 1. Neither group display any significant Ce or Eu anomalies which is reflected by Ce/Ce* ($Ce/Ce^* = Ce_N/\sqrt{La_N \times Pr_N}$) and Eu/Eu* ($Eu/Eu^* = Eu_N/\sqrt{Sm_N \times Gd_N}$) values of 0.88-0.99 and 0.88-1.07 respectively for all samples.

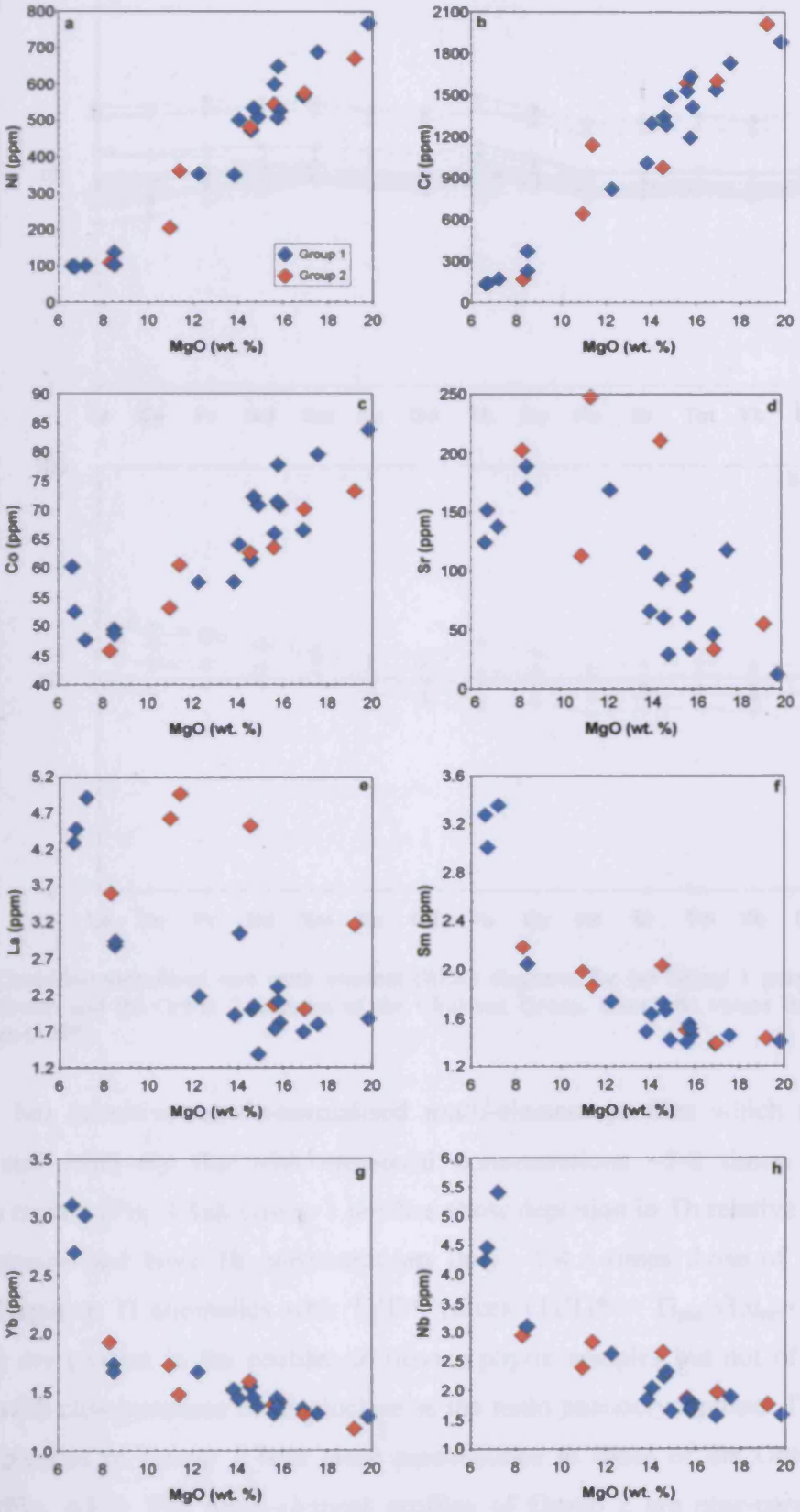

Fig. 4.5. Bivariate diagrams of selected trace elements vs. MgO for the Chukotat Group volcanic rocks.

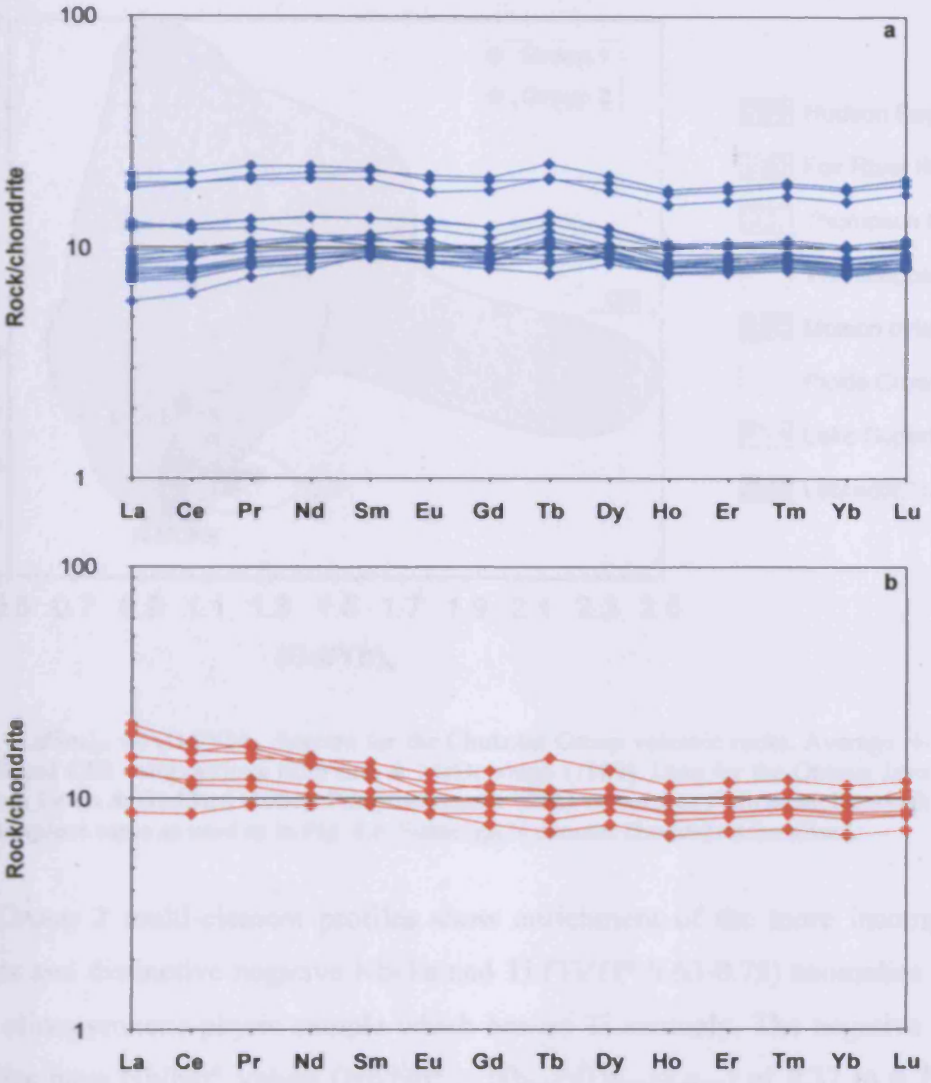

Fig. 4.6. Chondrite-normalised rare earth element (REE) diagrams for (a) Group 1 samples of the Chukotat Group and (b) Group 2 samples of the Chukotat Group. Chondrite values from Sun & McDonough (1989).

Group 1 has primitive-mantle-normalised multi-element profiles which are near-parallel and relatively flat with elemental concentrations ~2-8 times those of primitive mantle (Fig. 4.8a). Group 1 profiles show depletion in Th relative to all the other elements and have Th concentrations only ~1-4.5 times those of primitive mantle. Negative Ti anomalies with Ti/Ti* values ($Ti/Ti^* = Ti_{pm}/\sqrt{Eu_{pm} \times Gd_{pm}}$) of 0.74-0.89 are present in the profiles of olivine-phyric samples but not of those of samples with clinopyroxene or plagioclase as the main phenocryst phase. The multi-element profiles of Group 1 bear close resemblance to those of the Ontong Java Plateau (Fig. 4.8a). The multi-element profiles of Group 2 are near-parallel with elemental concentrations ~2-14 times greater than those of primitive mantle (Fig.

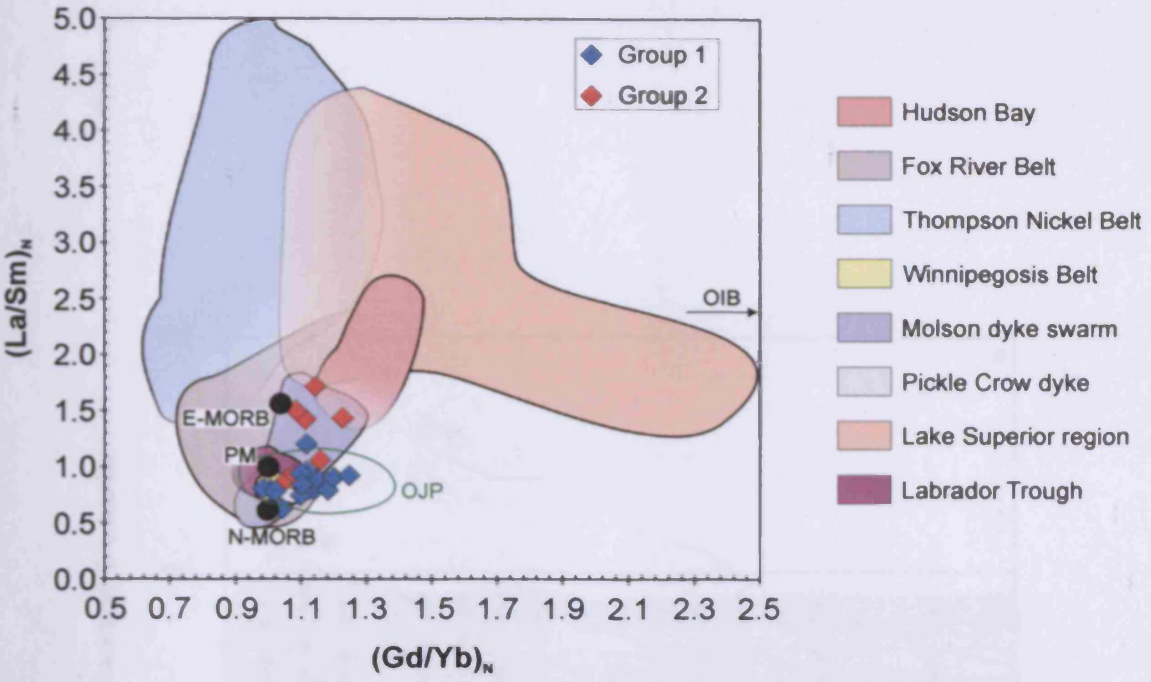

Fig. 4.7. $(La/Sm)_N$ vs. $(Gd/Yb)_N$ diagram for the Chukotat Group volcanic rocks. Average N-MORB, E-MORB and OIB compositions from Sun & McDonough (1989). Data for the Ontong Java Plateau (OJP) from Fitton & Goddard (2004). Primitive mantle (PM) values from Sun & McDonough (1989). Chondrite values same as used as in Fig. 4.6. Subscript N denotes chondrite normalised.

4.8b). Group 2 multi-element profiles show enrichment of the more incompatible elements and distinctive negative Nb-Ta and Ti (Ti/Ti* 0.63-0.75) anomalies except for the clinopyroxene-phyric sample which has no Ti anomaly. The negative Nb-Ta anomalies have Nb/Nb* values ($Nb/Nb^* = Nb_{pm}/\sqrt{Th_{pm} \times La_{pm}}$) of 0.37 to 0.79. The negative Nb-Ta anomalies of Group 2 allow the samples to be distinguished from Group 1 samples on a Zr/Nb-Nb/Th plot devised by Condie (2003). On such a plot (Fig. 4.9) the Group 2 samples plot well to the left hand side of the diagram within the arc field of Condie (2005) whilst Group 1 samples plot further to the right within the oceanic plateau field of Condie (2005) and partially overlap with the Ontong Java Plateau field. On the Nb/Y-Zr/Y diagram (Fig. 4.10), which was developed by Fitton et al. (1997) to distinguish between plume-derived lavas and N-MORB in Iceland, both groups plot within the tramlines defined by the Icelandic plume composition with the exception of one sample from Group 1 which plots just below the lower tramline. All samples fall within the Ontong Java Plateau field and lie close to the composition of primitive mantle in Fig. 4.10.

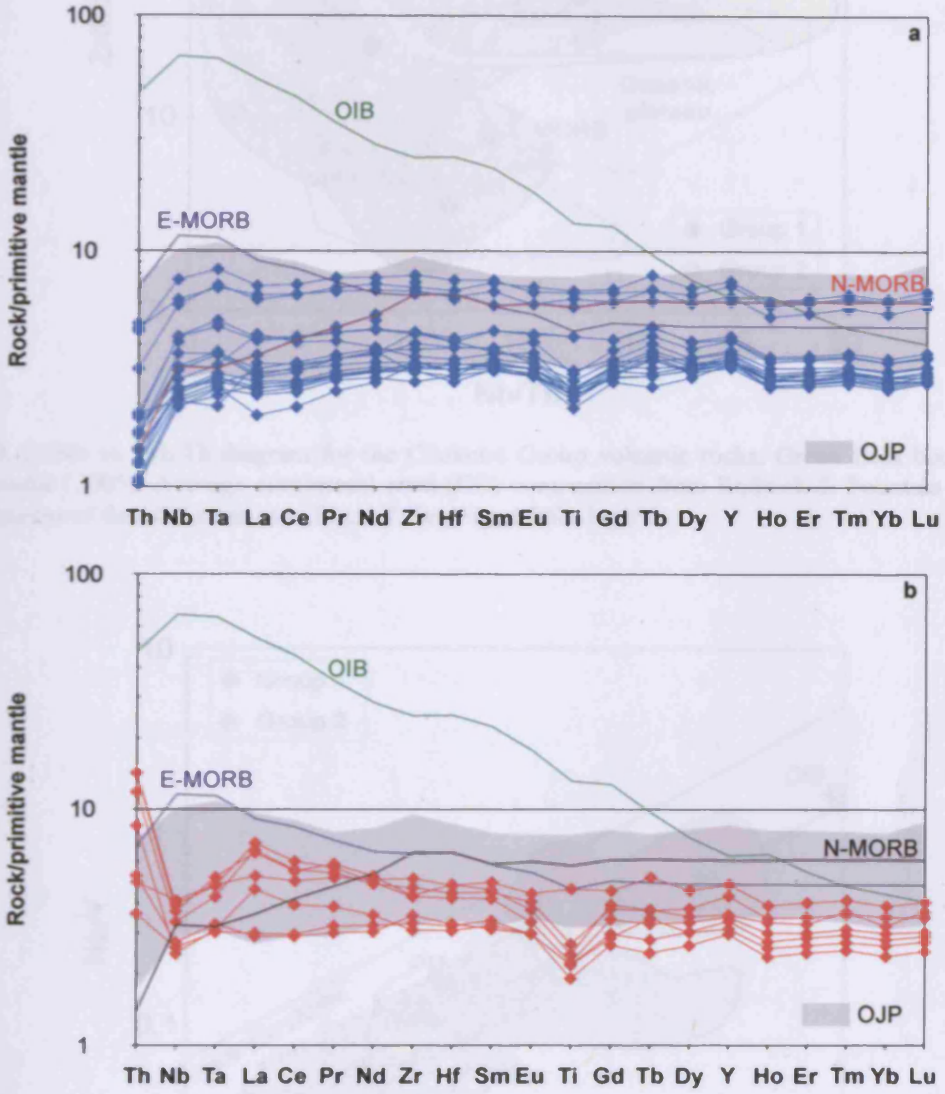

Fig. 4.8. Primitive-mantle-normalised multi-element diagrams for (a) Group 1 samples of the Chukotat Group and (b) Group 2 samples of the Chukotat Group. Data sources same as in Fig. 4.7.

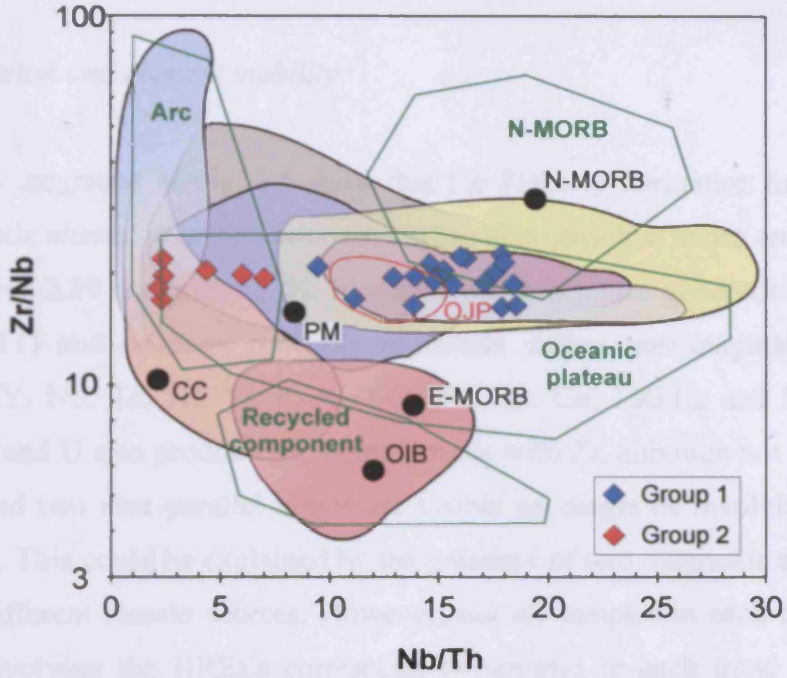

Fig. 4.9. Zr/Nb vs. Nb/Th diagram for the Chukotat Group volcanic rocks. Green field boundaries from Condie (2005). Average continental crust (CC) composition from Rudnick & Fountain (1995). Other sources of data the same as in Fig. 4.7. See Fig. 4.7 for legend.

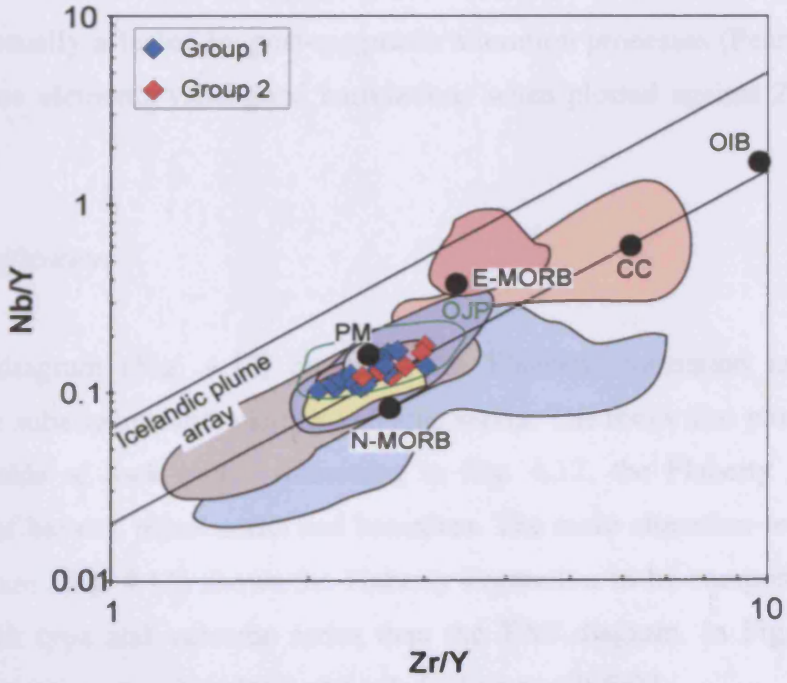

Fig. 4.10. Nb/Y vs. Zr/Y diagram for the Chukotat Group volcanic rocks. The Icelandic plume tramlines defined by Fitton et al. (1997). Other sources of data are the same as in Figs. 4.7 and 4.9. See Fig. 4.7 for legend.

4.4. Flaherty Formation of the eastern Hudson Bay islands

4.4.1. Alteration and element mobility

The photomicrographs in Fig. 3.5 show that the Flaherty Formation has undergone post-magmatic alteration and metamorphism to subgreenschist facies and LOI values range between 2.89 and 4.96 wt. %. Elements which produce good correlations with Zr (Fig. 4.11) and so were probably immobile during post-magmatic alteration include V, Y, Nb, Ta, Hf, Ti, P, Al, Fe, Mn, Ga, Co, LREEs and MREEs. The HREEs, Th and U also produce good correlations with Zr, although not as one single trend. Instead two near-parallel trends are visible on diagrams involving Zr, Th, U and HREEs. This could be explained by the presence of two magmatic suites derived from two different mantle sources. However, not all samples in each trend seen on diagrams involving the HREEs correspond to samples in each trend on diagrams involving Th and U. Elements which do not produce good correlations with Zr and are likely to have been mobilised include K, Si, Ca, Na, Cs, Rb, Ba, Sr, Zn and Cu. Post-magmatic alteration may not necessarily explain the lack of correlation between Zr and some elements. For example, the concentrations of elements Mg, Ni, Cr and Sc are not usually affected by post-magmatic alteration processes (Pearce, 1996) yet none of these elements yield good correlations when plotted against Zr (e.g. Ni-Zr Fig. 4.11f).

4.4.2. Classification

The TAS diagram (Fig. 4.12) classifies the Flaherty Formation as transitional between the subalkaline and alkaline volcanic series. The rocks also plot within three different fields of rock types. According to Fig. 4.12, the Flaherty Formation is composed of basalts, picrobasalts and basanites. The more alteration-resistant Zr/Ti-Nb/Y diagram (Fig. 4.13) shows the Flaherty Formation to be composed of a more uniform rock type and volcanic series than the TAS diagram. In Fig. 4.13 all the Flaherty Formation samples plot in the subalkaline basalt field.

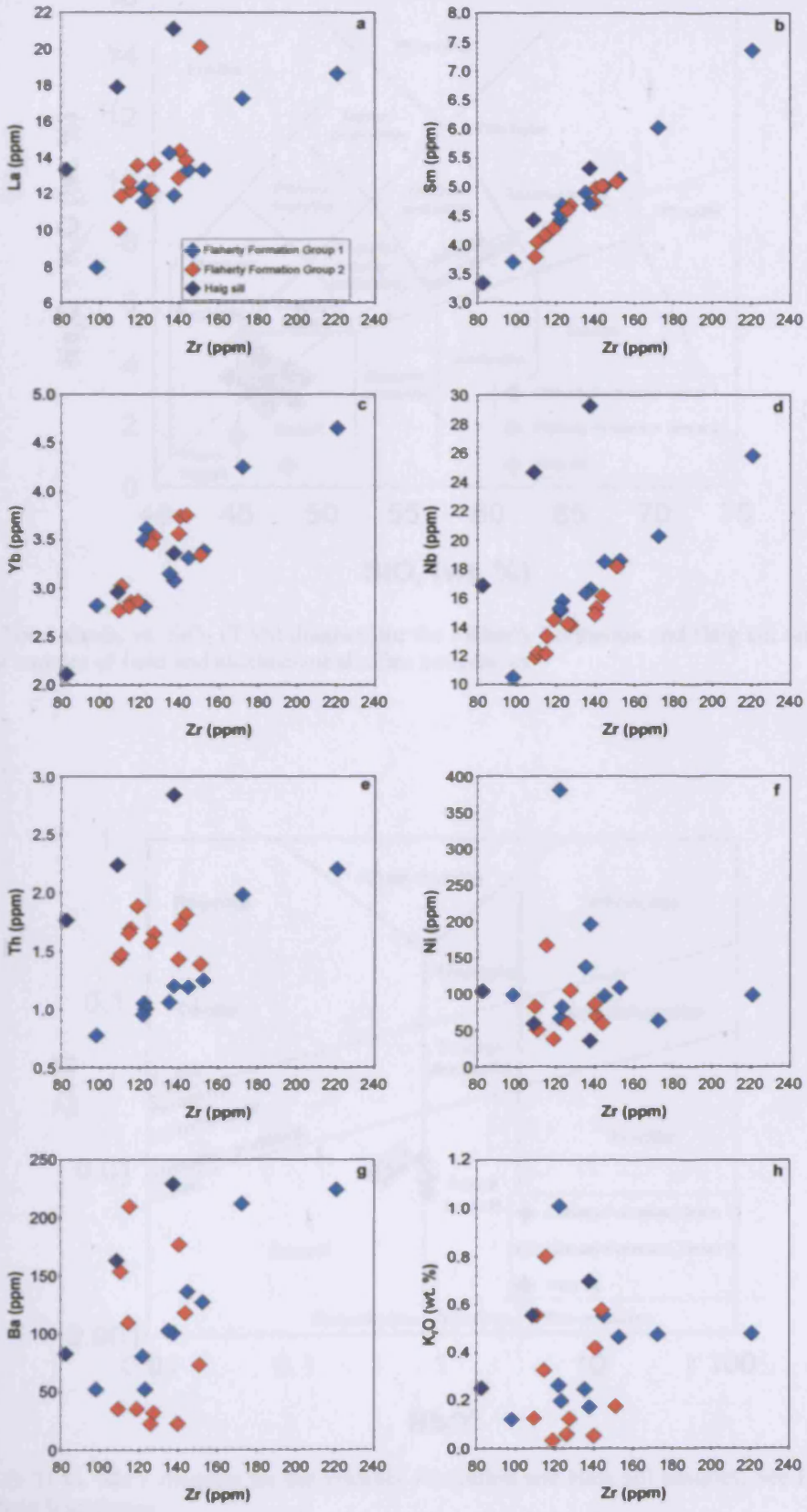

Fig. 4.11. Bivariate diagrams of selected elements vs. Zr for the Flaherty Formation and Haig sill samples.

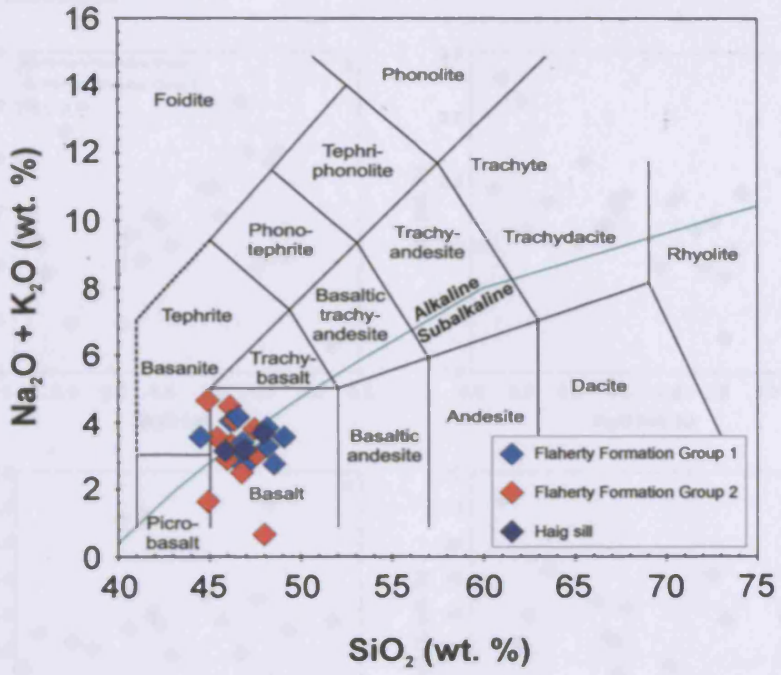

Fig. 4.12. Total alkalis vs. SiO_2 (TAS) diagram for the Flaherty Formation and Haig sill samples. See Fig. 4.2 for sources of field and alkaline-subalkaline boundaries.

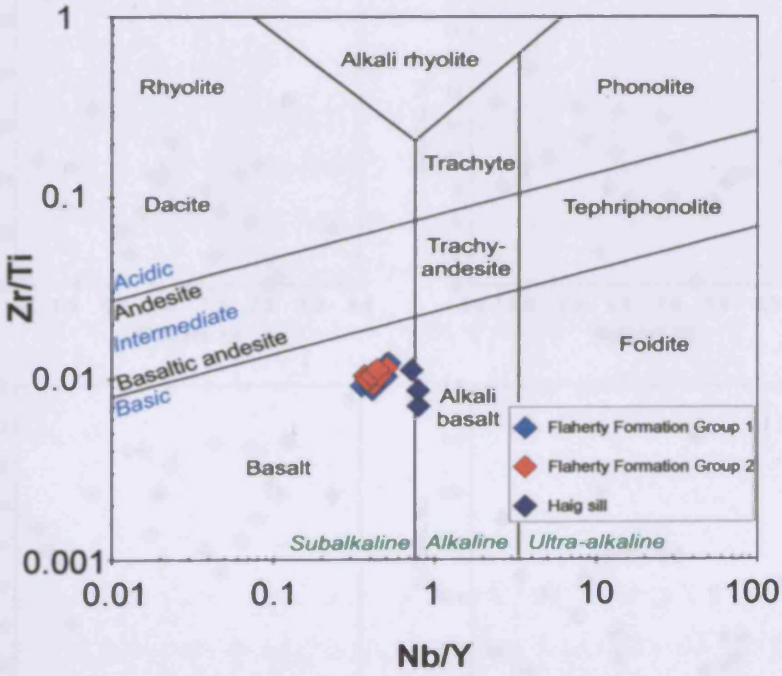

Fig. 4.13. Zr/Ti vs. Nb/Y diagram for the Flaherty Formation and Haig sill samples. See Fig. 4.3 for source of field boundaries.

4.4.3. Major elements

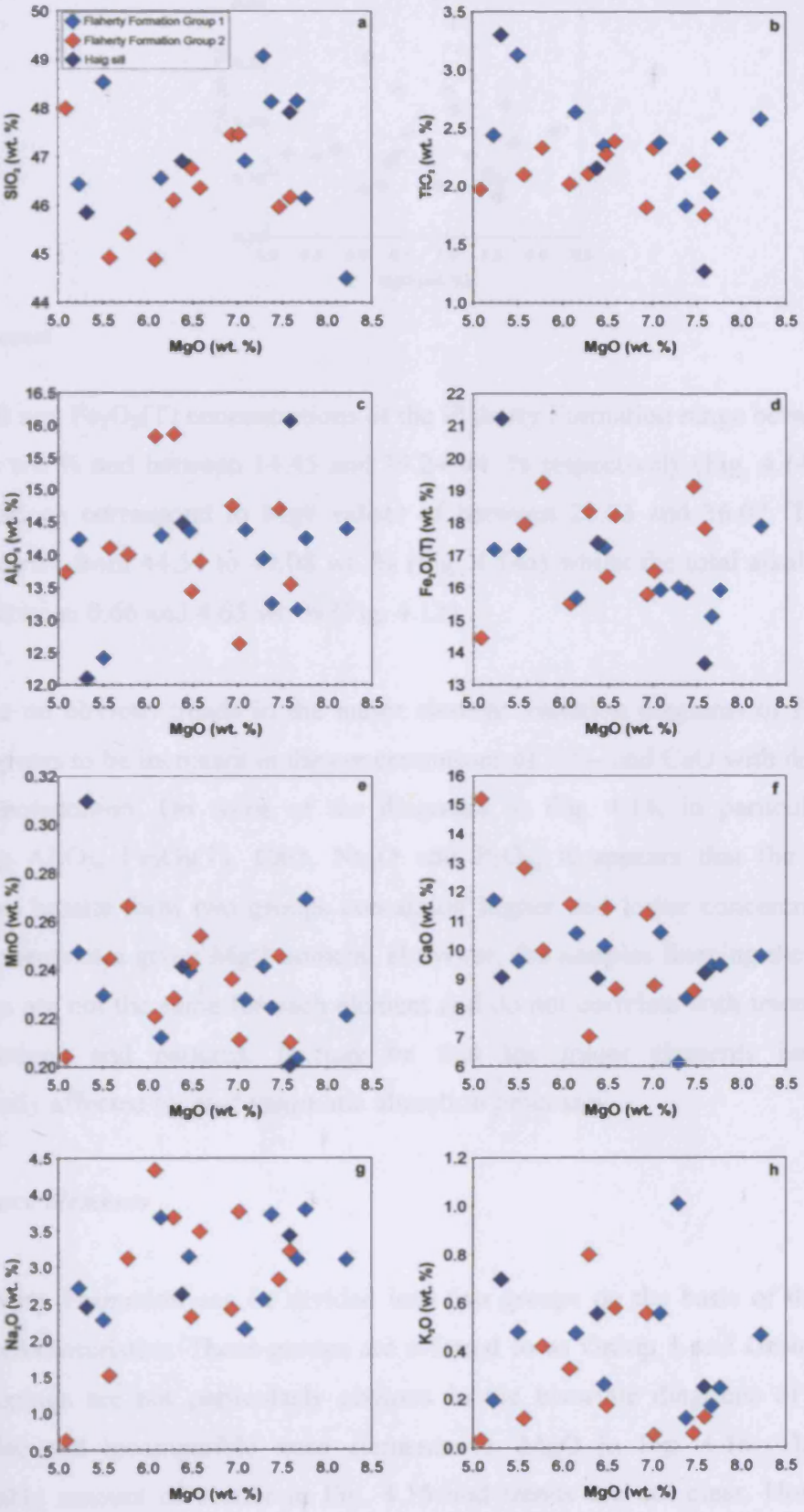

Fig. 4.14. Bivariate diagrams of major elements vs. MgO for the Flaherty Formation and Haig sill samples.

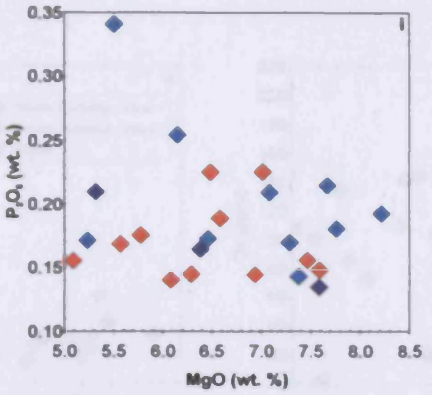

Fig. 4.14. contd.

The MgO and $Fe_2O_3(T)$ concentrations of the Flaherty Formation range between 5.09 and 8.22 wt. % and between 14.45 and 19.24 wt. % respectively (Fig. 4.14). These concentrations correspond to Mg# values of between 25.03 and 36.07. The silica content varies from 44.51 to 49.08 wt. % (Fig. 4.14a) whilst the total alkali content ranges between 0.66 and 4.65 wt. % (Fig. 4.12).

There are no obvious trends in the major element variation diagrams of Fig. 4.14. There appears to be increases in the concentrations of TiO_2 and CaO with decreasing MgO concentration. On some of the diagrams in Fig. 4.14, in particular those involving Al_2O_3, $Fe_2O_3(T)$, CaO, Na_2O and P_2O_5, it appears that the Flaherty Formation basalts form two groups containing higher and lower concentrations of these elements at a given MgO content. However, the samples forming the possible groupings are not the same for each element and do not correlate with trace element concentrations and patterns. It may be that the major elements have been significantly affected by post-magmatic alteration processes.

4.4.4. Trace elements

The Flaherty Formation can be divided into two groups on the basis of their trace element characteristics. These groups are referred to as Group 1 and Group 2. The two groupings are not particularly obvious in the bivariate diagrams of selected compatible and incompatible trace elements vs. MgO in Fig. 4.15. There is a considerable amount of scatter in Fig. 4.15 and trends are not clear. However, it appears that the incompatible elements La, Sm, Yb and Nb generally increase in

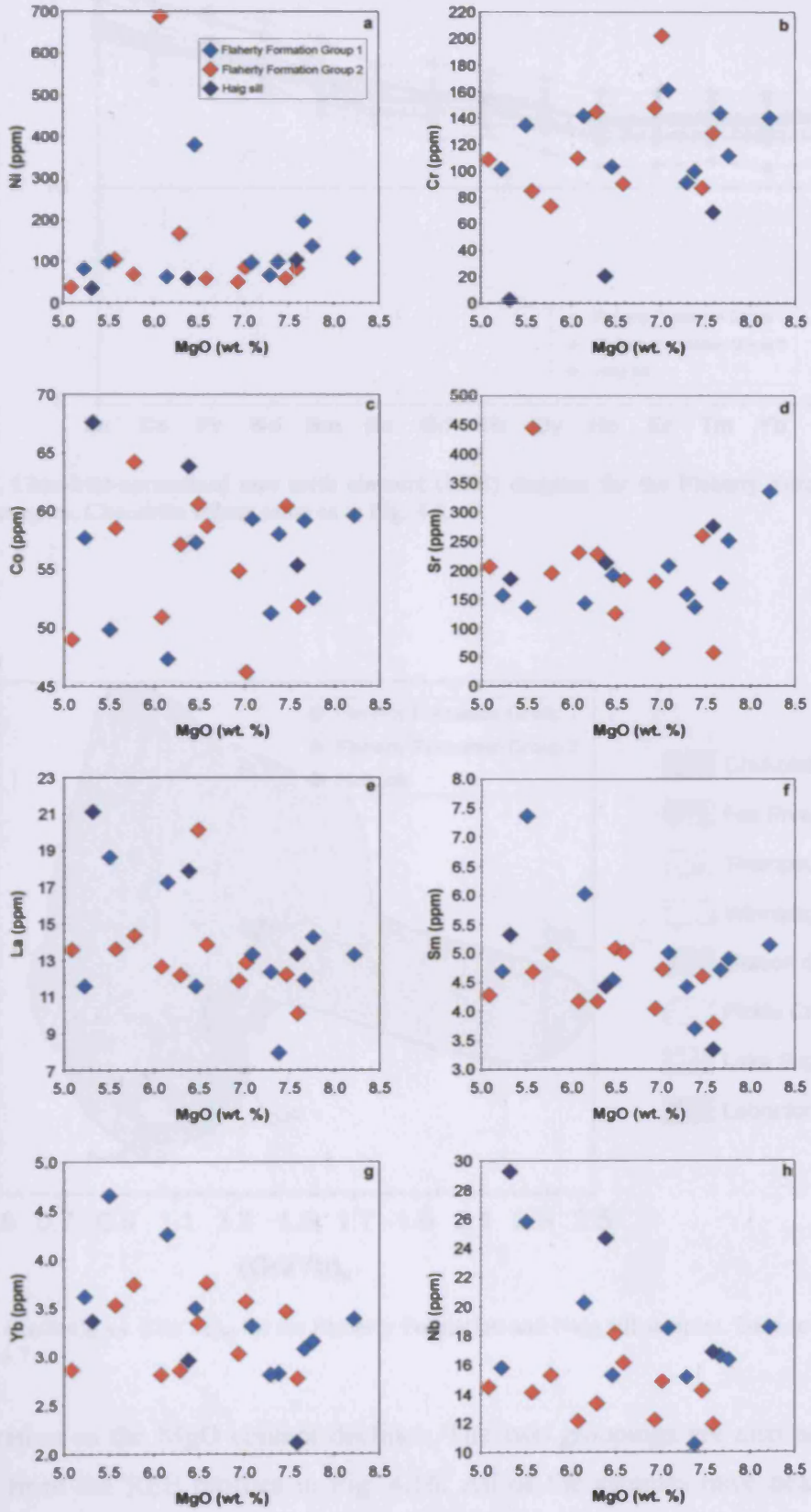

Fig. 4.15. Bivariate diagrams of selected trace elements vs. MgO for the Flaherty Formation and Haig sill samples.

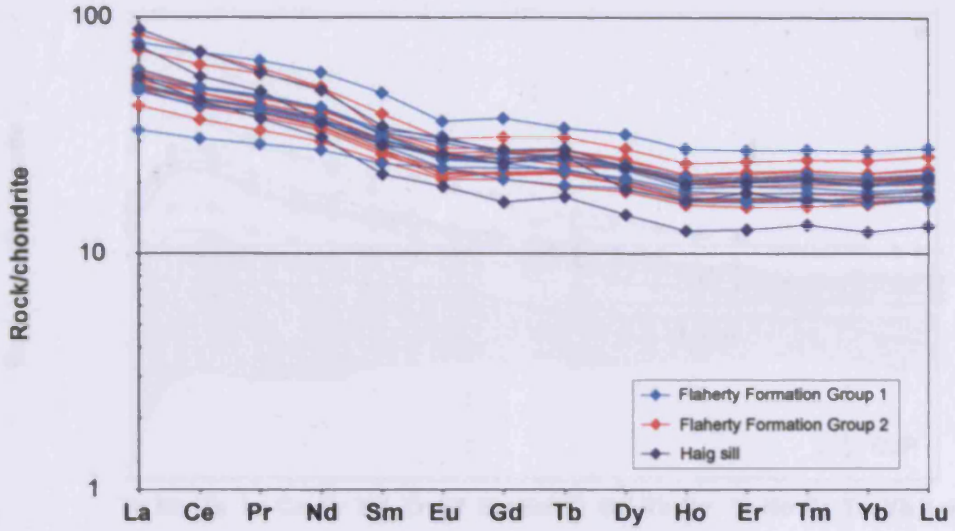

Fig. 4.16. Chondrite-normalised rare earth element (REE) diagram for the Flaherty Formation and Haig sill samples. Chondrite values same as in Fig. 4.6.

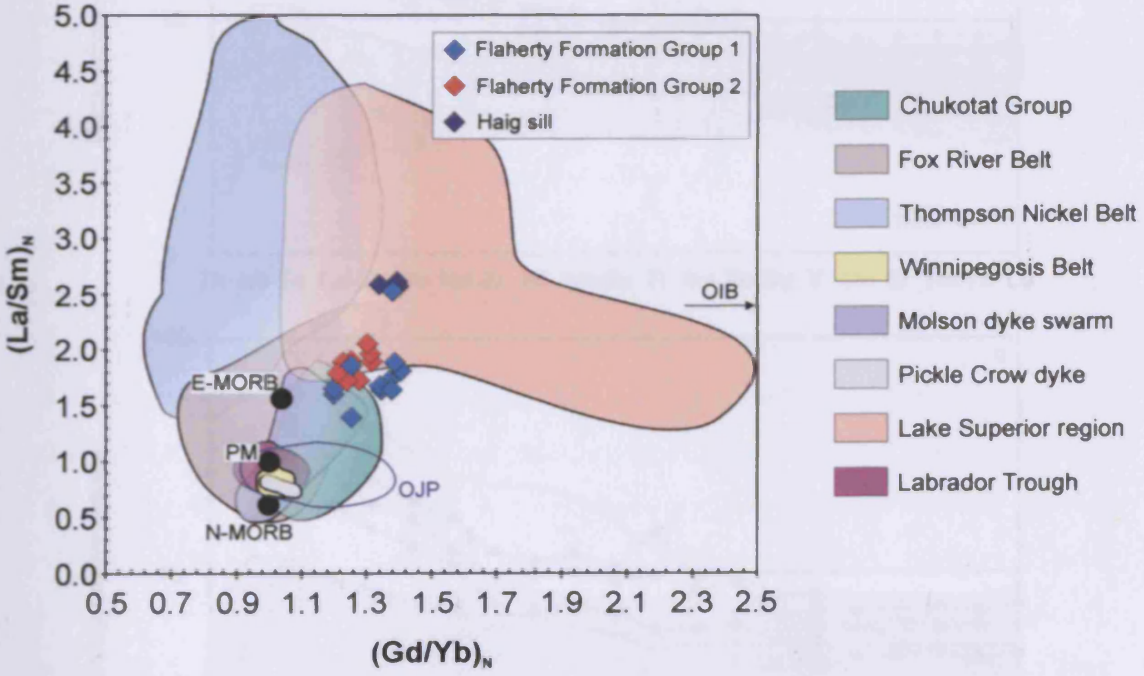

Fig. 4.17. $(La/Sm)_N$ vs. $(Gd/Yb)_N$ for the Flaherty Formation and Haig sill samples. Data sources same as in Fig. 4.7.

concentration as the MgO content declines. The two groupings are also not overly obvious from the REE profiles in Fig. 4.16. All of the samples have near-parallel profiles with REE concentrations ~16-85 times those of chondritic values. The REE profiles are all enriched in the LREEs relative to the MREEs (Fig. 4.16). This is

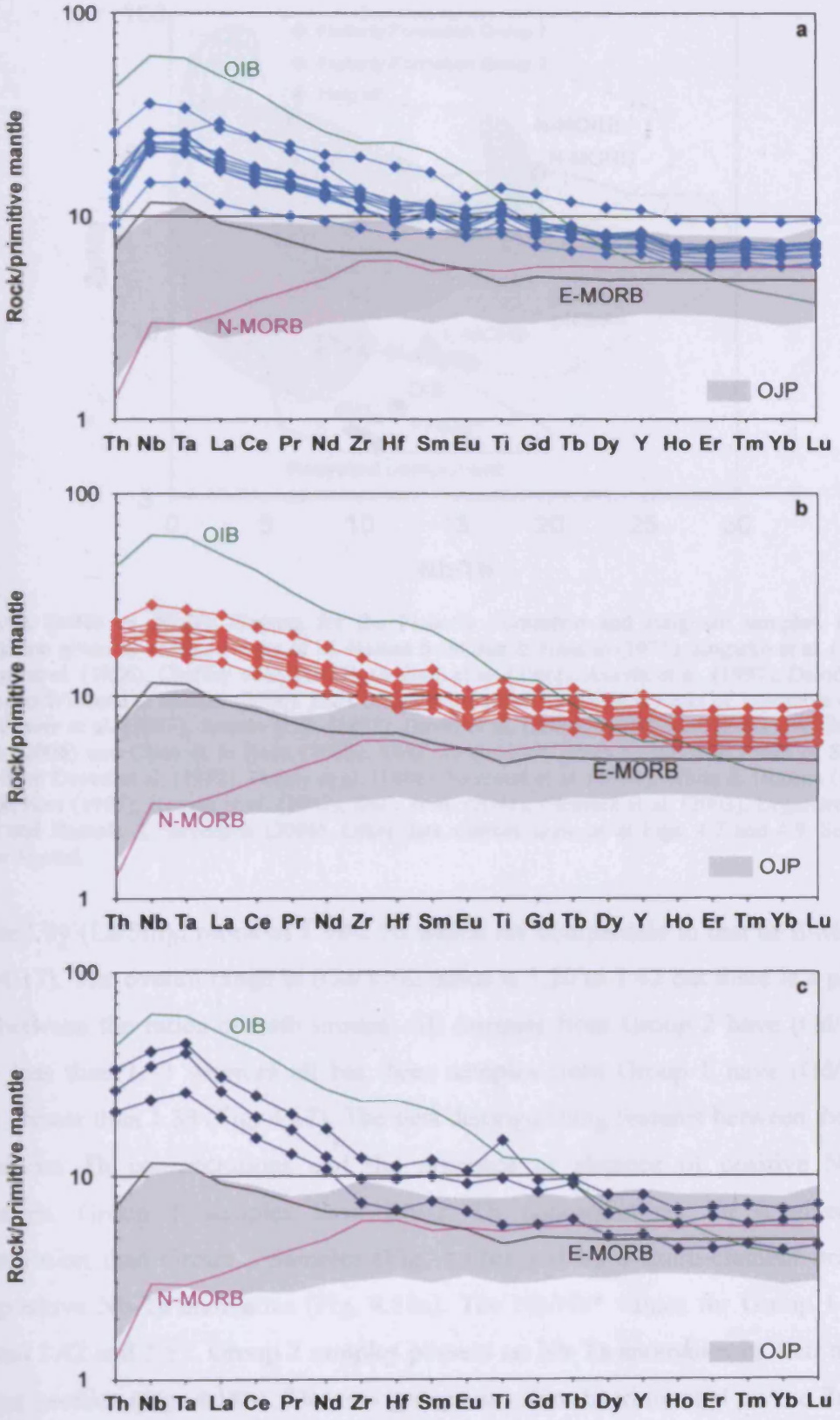

Fig. 4.18. Primitive-mantle-normalised multi-element diagrams for (a) Flaherty Formation Group 1 samples, (b) Flaherty Formation Group 2 samples and (c) Haig sill samples. Data sources same as in Fig. 4.7.

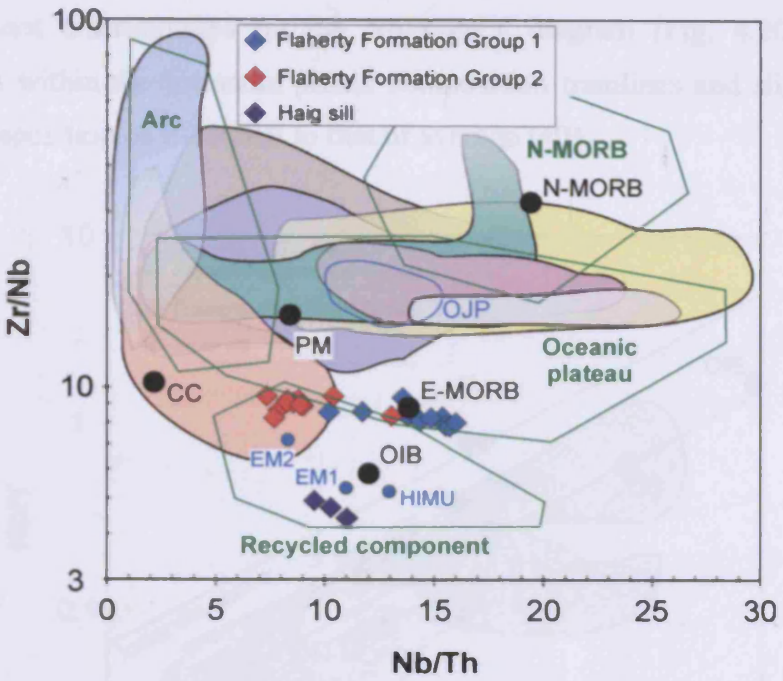

Fig. 4.19. Zr/Nb vs. Nb/Th diagram for the Flaherty Formation and Haig sill samples. HIMU composition given by volcanic rocks of St. Helena from Sun & Hanson (1975), Kogarko et al. (1984), Newsom et al. (1986), Chaffey et al. (1989), Graham et al. (1992), Asavin et al. (1997), David et al. (2000) and Willbold & Stracke (2006). EM1 composition given by volcanic rocks of Tristan da Cunha from Weaver et al. (1987), Asavin et al. (1997), David et al. (2000), Ewart et al. (2004), Willbold & Stracke (2006) and Class & le Roex (2008). EM2 composition given by volcanic rocks of Society Island from Dostal et al. (1982), Dupuy et al. (1989), Hemond et al. (1994), White & Duncan (1996), Hauri & Hart (1997), Kogiso et al. (1997), Blais et al. (2002), Clement et al. (2003), Legendre et al. (2003) and Harnois & Stevenson (2006). Other data sources same as in Figs. 4.7 and 4.9. See Fig. 4.17 for legend.

reflected by $(La/Sm)_N$ ratios of 1.39-2.56 which are comparable to that of E-MORB (Fig. 4.17). The overall range in $(Gd/Yb)_N$ ratios is 1.20 to 1.42 but there is a partial split between the ratios of both groups. All samples from Group 2 have $(Gd/Yb)_N$ ratios less than 1.33 whereas all but three samples from Group 1 have $(Gd/Yb)_N$ ratios greater than 1.33 (Fig. 4.17). The best distinguishing features between the two groups are Th concentrations and the presence or absence of positive Nb-Ta anomalies. Group 1 samples have lower Th concentrations for a given Zr concentration than Group 2 samples (Fig. 4.11e) and have multi-element profiles with positive Nb-Ta anomalies (Fig. 4.18a). The Nb/Nb* values for Group 1 vary between 1.42 and 1.57. Group 2 samples possess no Nb-Ta anomalies in their multi-element profiles (Fig. 4.18b). The two groups are also discriminated on the Zr/Nb-Nb/Th diagram (Fig. 4.19) where both have similar Zr/Nb ratios but different Nb/Th ratios. Group 1 samples plot close to the E-MORB composition whereas Group 2 samples plot closer to the EM2 end-member composition in Fig. 4.19. The two

groups are not discriminated on the Nb/Y-Zr/Y diagram (Fig. 4.20) where all samples plot within the Icelandic plume composition tramlines and slightly extend from the composition of E-MORB to that of average OIB.

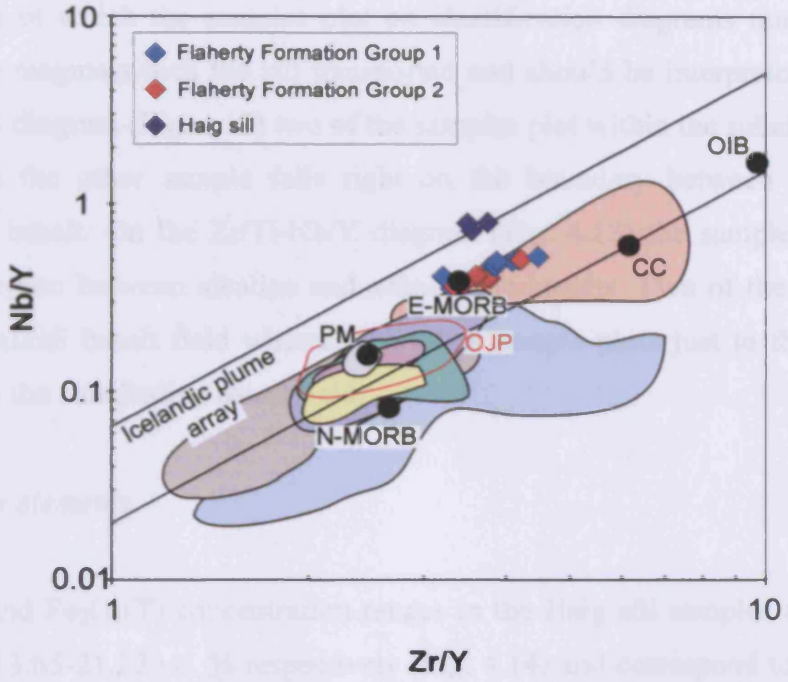

Fig. 4.20. Nb/Y vs. Zr/Y diagram for the Flaherty Formation and Haig sill samples. Data sources same as in Figs. 4.7 and 4.9. See Fig. 4.17 for legend.

4.5. Haig sill of the eastern Hudson Bay islands

4.5.1. Alteration and element mobility

Only three samples of the Haig sill from the Sleeper Islands have been analysed and so it is not possible to accurately assess the potential for element mobility in the sill. However, the reasonably low LOI values (2.25-3.23 wt. %) and petrographic observations (see section 3.3.4) suggest that the sill has only undergone a limited degree of post-magmatic alteration. Therefore it is assumed that elements with intermediate ionic potential (e.g. high field strength and rare earth elements) were immobile and provide the best means of studying the Haig sill. The three Haig sill samples have been plotted with the Flaherty Formation basalts in a selection of bivariate diagrams in Figs 4.11, 4.14 and 4.15.

4.5.2. Classification

The samples from the Haig sill do not come from chilled margins and so potentially are not truly representative of the magma which flowed through the sill. Therefore the position in which the samples plot on classification diagrams may not be the same as the magma which the sill transported and should be interpreted cautiously. On the TAS diagram (Fig. 4.12) two of the samples plot within the subalkaline basalt field whilst the other sample falls right on the boundary between alkaline and subalkaline basalt. On the Zr/Ti-Nb/Y diagram (Fig. 4.13) the samples plot in the transition region between alkaline and subalkaline basalts. Two of the samples fall just in the alkali basalt field whereas the other sample plots just to the left of the boundary in the subalkaline basalt field.

4.5.3. Major elements

The MgO and $Fe_2O_3(T)$ concentration ranges in the Haig sill samples are 5.32-7.59 wt. % and 13.65-21.22 wt. % respectively (Fig. 4.14) and correspond to Mg# values of 21.79 to 38.17. SiO_2 concentrations vary between 45.85 and 47.92 wt. % (Fig. 4.14a) and total alkali contents range from 3.16 to 3.69 wt. % (Fig. 4.12). The TiO_2 concentration of each sample varies considerably from 1.22 to 3.23 wt. % with the higher TiO_2 concentrations corresponding to the lower MgO concentrations (Fig. 4.14b).

4.5.4. Trace elements

The range in concentrations of compatible elements is generally greater than the range in incompatible elements in the Haig sill samples. The ranges in concentration of Ni and Cr are 36-104 ppm and 3-69 ppm respectively (Fig. 4.15). However, the ranges in concentration of the incompatible elements La and Nb are 13-21 ppm and 17-30 ppm respectively (Fig. 4.15).

The REE profiles of the Haig sill samples are displayed in Fig 4.16. All three samples have similar profiles with elemental abundances ~12-89 times those of chondritic values. The profiles are enriched in the LREEs relative to the MREEs and

HREEs which is reflected by $(La/Sm)_N$ and $(La/Yb)_N$ ratios of 2.56-2.60 (Fig. 4.17) and 4.34-4.53 respectively. The HREEs are depleted relative to the MREEs and $(Gd/Yb)_N$ ratios vary between 1.34 and 1.40 (Fig. 4.17). There are no significant Ce or Eu anomalies in the profiles. Primitive-mantle-normalised multi-element profiles of the Haig sill are shown in Fig. 4.18c. All profiles have elemental abundances ~4-45 times those of primitive mantle and are enriched in the more incompatible elements relative to the less incompatible elements and have $(Th/Sm)_{pm}$ ratios of 2.64-2.79. All the samples possess small positive Nb-Ta anomalies and their Nb/Nb* values vary between 1.18 and 1.32. One sample also has a positive Ti anomaly and has a Ti/Ti* value of 1.49. The three samples plot towards the bottom of the recycled component field of Condie (2005) in the Zr/Nb-Nb/Th diagram (Fig. 4.19) and just above the upper Icelandic plume tramline in the Nb/Y-Zr/Y diagram (Fig. 4.20).

4.6. Fox River Belt

4.6.1. Alteration and element mobility

Petrographic observations suggest that the rocks of the Fox River Belt have been subjected to a low grade of metamorphism and post-magmatic alteration (see section 3.4.2). LOI values for the volcanic rocks range from 1.88 to 4.84 wt. %. Rocks from the Fox River Sill have LOI contents of 2.69-12.54 wt. % whilst LOI values vary between 0.95 and 6.42 wt. % in the Lower Intrusions. The solitary Stupart dyke sample has an LOI value of 0.40 wt. %. To assess element mobility in the Fox River Belt, all elements in the igneous rocks have been plotted against Zr and a selection of these diagrams is shown in Fig. 4.21. Elements which appear to have been immobile and produce good correlations with Zr include Y, Ni, Co, Cr, V, U, Th, Ta, Hf, REEs, Nb, Ga, Ti, Al, Fe, Mn, Mg, Ca, K and P. Elements which do not produce good correlations with Zr include Ba, Sr, Cu, Cs, Rb, Zn, Si and Na. These elements may have been mobilised during secondary alteration processes.

4.6.2. Classification

The TAS diagram (Fig. 4.22) classifies the Lower Volcanic Formation as subalkaline basalts. Three of these basalts have MgO concentrations >12 wt. % and total alkali

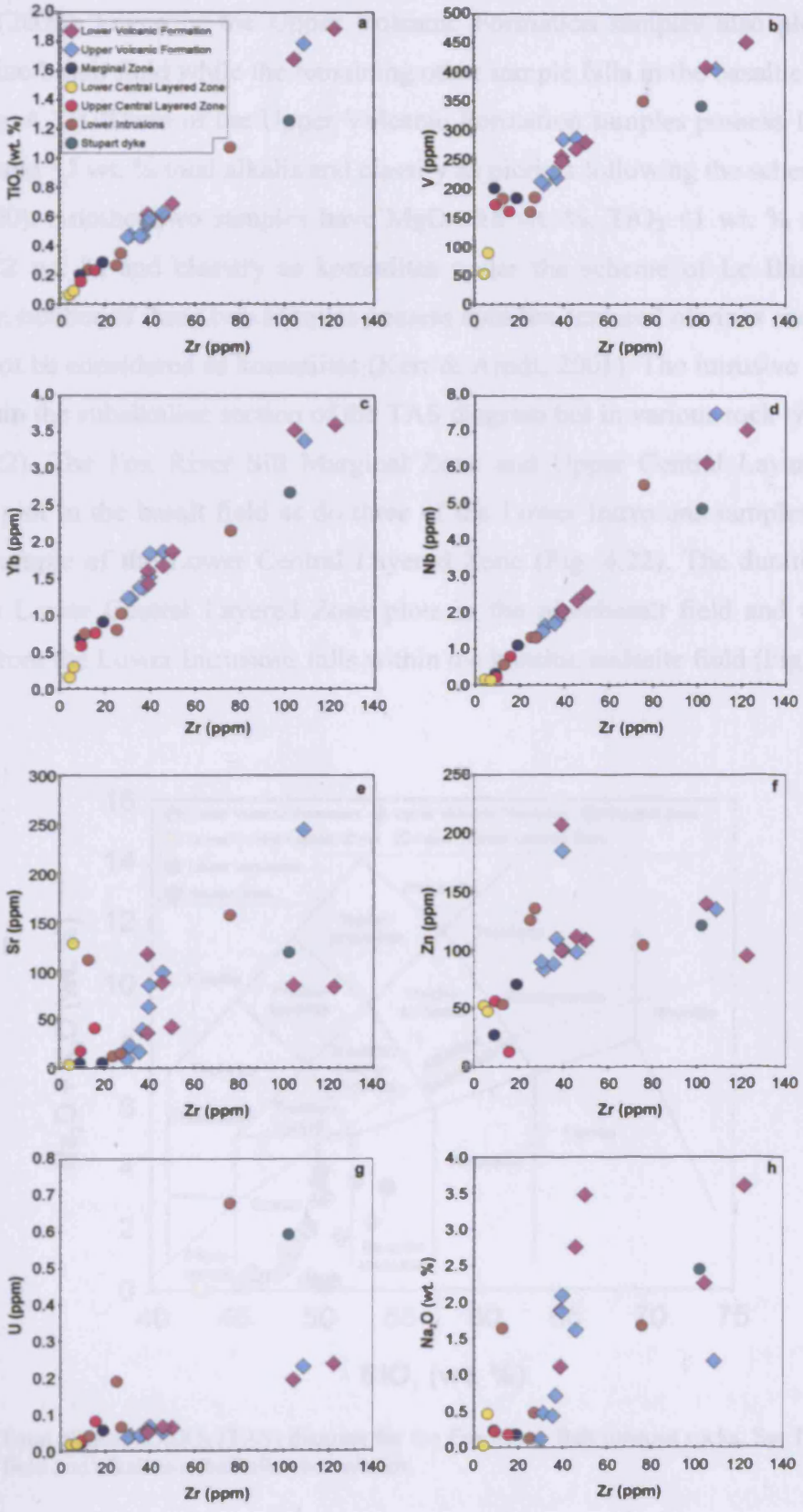

Fig. 4.21. Bivariate diagrams of selected elements vs. Zr for the Fox River Belt igneous rocks.

contents <3 wt. % and classify as picrites according to the classification scheme of Le Bas (2000). Seven of the Upper Volcanic Formation samples also plot in the subalkaline basalt field while the remaining other sample falls in the basaltic andesite field (Fig. 4.22). Three of the Upper Volcanic Formation samples possess 14-17 wt. % MgO and <3 wt. % total alkalis and classify as picrites following the scheme of Le Bas (2000). Another two samples have MgO >18 wt. %, TiO_2 <1 wt. % and total alkalis <2 wt. % and classify as komatiites under the scheme of Le Bas (2000). However, neither of these two samples possess spinifex-textured olivines and as such should not be considered as komatiites (Kerr & Arndt, 2001). The intrusive rocks all plot within the subalkaline section of the TAS diagram but in various rock type fields (Fig. 4.22). The Fox River Sill Marginal Zone and Upper Central Layered Zone samples plot in the basalt field as do three of the Lower Intrusions samples and the gabbro sample of the Lower Central Layered Zone (Fig. 4.22). The dunite sample from the Lower Central Layered Zone plots in the picrobasalt field and the other sample from the Lower Intrusions falls within the basaltic andesite field (Fig. 4.22).

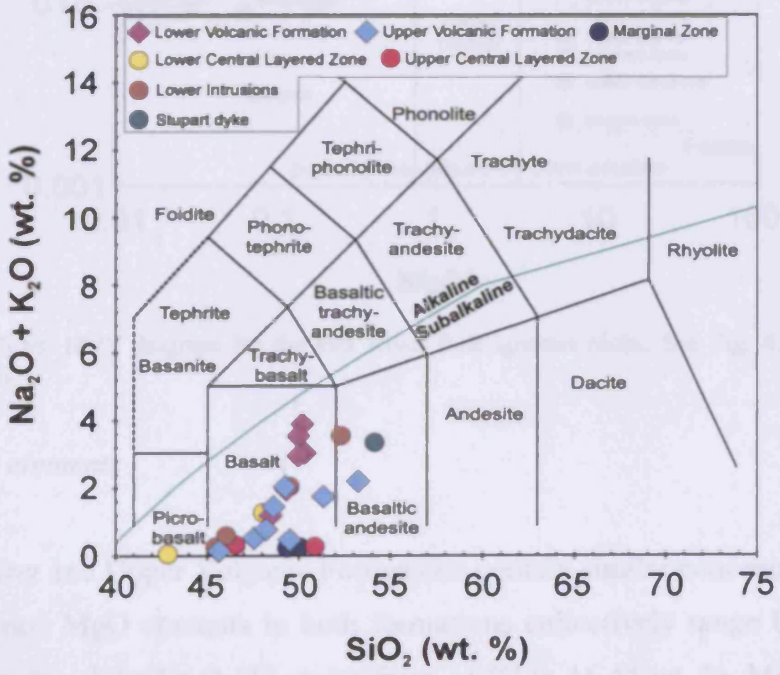

Fig. 4.22. Total alkalis vs. SiO_2 (TAS) diagram for the Fox River Belt igneous rocks. See Fig. 4.2 for sources of field and alkaline-subalkaline boundaries.

The Fox River Belt samples are plotted on the Zr/Ti-Nb/Y diagram displayed in Fig. 4.23. The volcanic rocks plot in a fairly tight cluster in the subalkaline basalt field. The intrusive rocks are more widespread and three samples do not plot within the subalkaline basalt field. The three samples, which include the Marginal Zone gabbro sample and the Lower Intrusions and Upper Central Layered Zone olivine pyroxenite samples, plot on the boundary between subalkaline basalt and basaltic andesite (Fig. 4.23). It should be noted that the intrusive rocks probably do not represent volcanic liquids and the application of classification schemes such as the TAS and Zr/Ti-Nb/Y diagrams to the intrusive samples should be done cautiously.

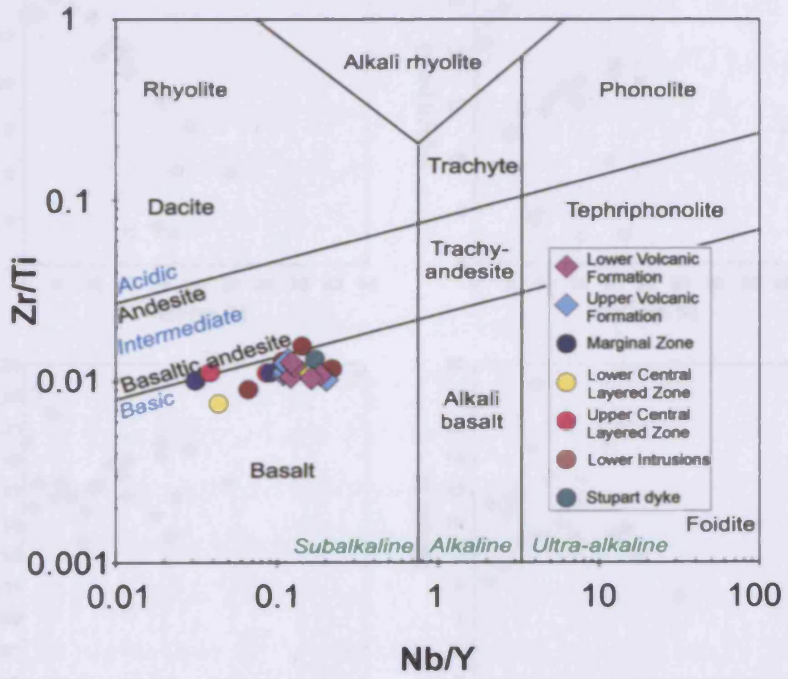

Fig. 4.23. Zr/Ti vs. Nb/Y diagram for the Fox River Belt igneous rocks. See Fig. 4.3 for source of field boundaries.

4.6.3. Major elements

Both the Lower and Upper Volcanic Formations contain similar concentrations of the major elements. MgO contents in both formations collectively range between 5.72 and 20.18 wt. % whilst Fe_2O_3(T) varies from 11.07 to 16.44 wt. %. Mg# values are between 28.46 and 62.97. The concentration of SiO_2 ranges from a minimum of 45.65 wt. % to a maximum of 53.26 wt. % and the total alkali content ranges between 0.15 and 3.89 wt. %.

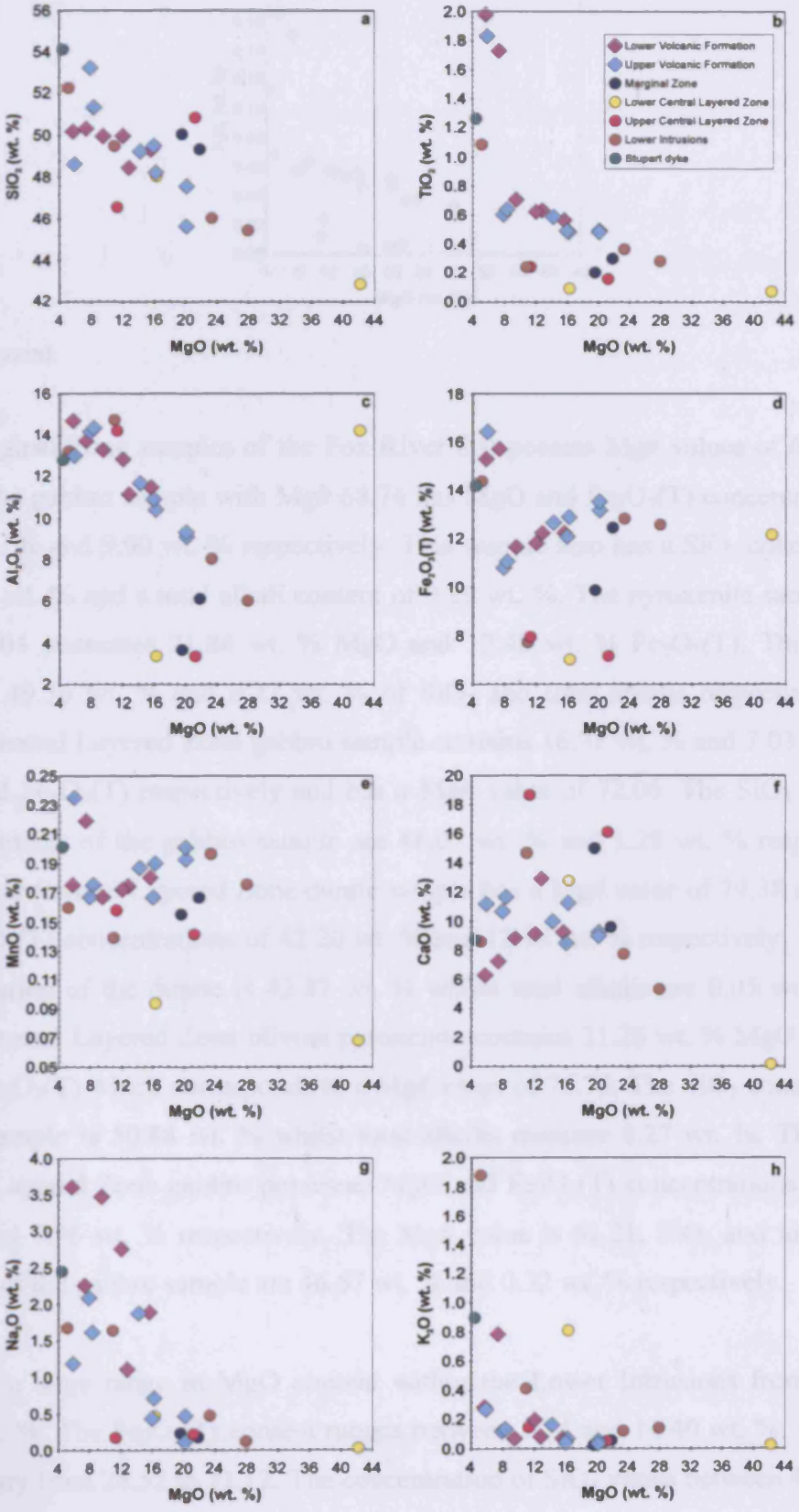

Fig. 4.24. Bivariate diagrams of major elements vs. MgO for the Fox River Belt igneous rocks.

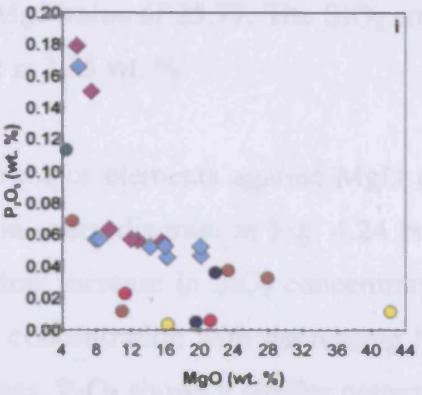

Fig. 4.24. contd.

The Marginal Zone samples of the Fox River Sill possess Mg# values of 68.74 and 66.04. The gabbro sample with Mg# 68.74 has MgO and $Fe_2O_3(T)$ concentrations of 19.59 wt. % and 9.90 wt. % respectively. This sample also has a SiO_2 concentration of 50.07 wt. % and a total alkali content of 0.26 wt. %. The pyroxenite sample with Mg# 66.04 possesses 21.84 wt. % MgO and 12.48 wt. % $Fe_2O_3(T)$. This sample contains 49.36 wt. % and 0.23 wt. % of SiO_2 and total alkalis respectively. The Lower Central Layered Zone gabbro sample contains 16.31 wt. % and 7.03 wt. % of MgO and $Fe_2O_3(T)$ respectively and has a Mg# value of 72.06. The SiO_2 and total alkali contents of the gabbro sample are 48.05 wt. % and 1.28 wt. % respectively. The Lower Central Layered Zone dunite sample has a Mg# value of 79.38 and MgO and $Fe_2O_3(T)$ concentrations of 42.20 wt. % and 12.18 wt. % respectively. The SiO_2 concentration of the dunite is 42.87 wt. % whilst total alkalis are 0.05 wt. %. The Upper Central Layered Zone olivine pyroxenite contains 21.26 wt. % MgO and 7.18 wt. % $Fe_2O_3(T)$ which corresponds to a Mg# value of 76.70. The SiO_2 concentration of this sample is 50.88 wt. % whilst total alkalis measure 0.27 wt. %. The Upper Central Layered Zone gabbro possesses MgO and $Fe_2O_3(T)$ concentrations of 11.30 wt. % and 7.96 wt. % respectively. The Mg# value is 61.21. SiO_2 and total alkali contents of the gabbro sample are 46.57 wt. % and 0.32 wt. % respectively.

There is a large range in MgO content within the Lower Intrusions from 5.17 to 27.93 wt. %. The $Fe_2O_3(T)$ content ranges between 7.74 and 14.40 wt. %. The Mg# values vary from 28.52 to 71.12. The concentration of SiO_2 varies between 45.46 and 52.30 wt. % whilst the total alkali content ranges from 0.26 to 3.55 wt. %. The Stupart dyke sample has MgO and $Fe_2O_3(T)$ concentrations of 4.44 wt. % and 14.21

wt. % respectively and a Mg# value of 25.77. The SiO_2 concentration is 54.14 wt. % and the total alkali content is 3.35 wt. %.

Variation diagrams of the major elements against MgO are shown in Fig. 4.24. A degree of scatter is seen on every diagram in Fig. 4.24 but some general trends are deducible. There is a gradual increase in SiO_2 concentration with decreasing MgO. TiO_2 slightly increases in concentration with decreasing MgO until ~8 wt. % MgO where TiO_2 rapidly increases. P_2O_5 shows a similar pattern to TiO_2 with MgO, as do Na_2O and K_2O albeit with more scatter. Al_2O_3 increases whilst MgO decreases in concentration until ~8 wt. % MgO when Al_2O_3 appears to start to decrease. Trends involving all of the samples are not clear in Fig. 4.24d but in the volcanic lavas $Fe_2O_3(T)$ slightly decreases with decreasing MgO until ~8 wt. % MgO at which point the $Fe_2O_3(T)$ concentration starts to increase. MnO and CaO do not show any obvious trends with changing MgO concentration.

4.6.4. Trace elements

Bivariate diagrams of a representative selection of compatible and incompatible trace elements against MgO are shown in Fig. 4.25. The compatible elements Ni, Cr and Co decrease in concentration with decreasing MgO. In the volcanic rocks Ni decreases from a maximum concentration of 834 ppm to a minimum of 69 ppm whilst Cr ranges from 122 to 2167 ppm. In Fig. 4.25d Sr can be seen to increase in concentration as the MgO content decreases. The incompatible elements La, Sm, Yb and Nb also increase in concentration as the value of MgO decreases (Fig. 4.25).

The REE profiles of the Fox River Belt igneous rocks are displayed in Fig. 4.26. The profiles of the two volcanic formations are reasonably similar and generally flat although the Upper Volcanic Formation samples show slightly more variation than those of the Lower Volcanic Formation (Fig. 4.26a). The Lower and Upper Volcanic Formations possess REE concentrations of ~8-27 and ~5-32 times those of chondritic values respectively. $(La/Sm)_N$ and $(Gd/Yb)_N$ ratios for the Lower Volcanic Formation vary from 0.87 to 1.11 and from 1.09 to 1.12 respectively (Fig. 4.27). The slightly greater variation in the shape of the Upper Volcanic Formation REE profiles is reflected in Fig. 4.27 with $(La/Sm)_N$ and $(Gd/Yb)_N$ ratios of 0.59-1.23 and 0.98-

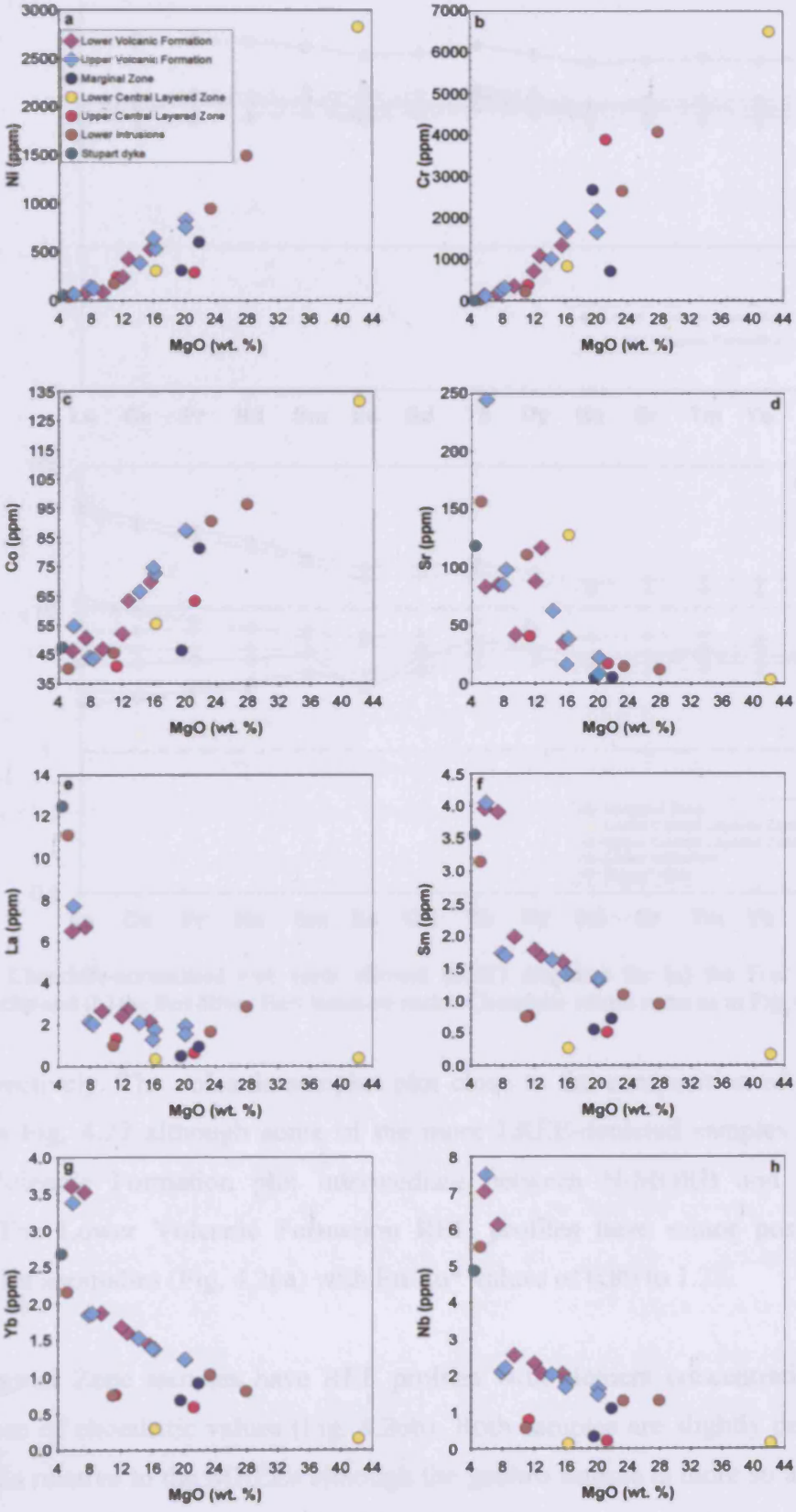

Fig. 4.25. Bivariate diagrams of selected trace elements vs. MgO for the Fox River Belt igneous rocks.

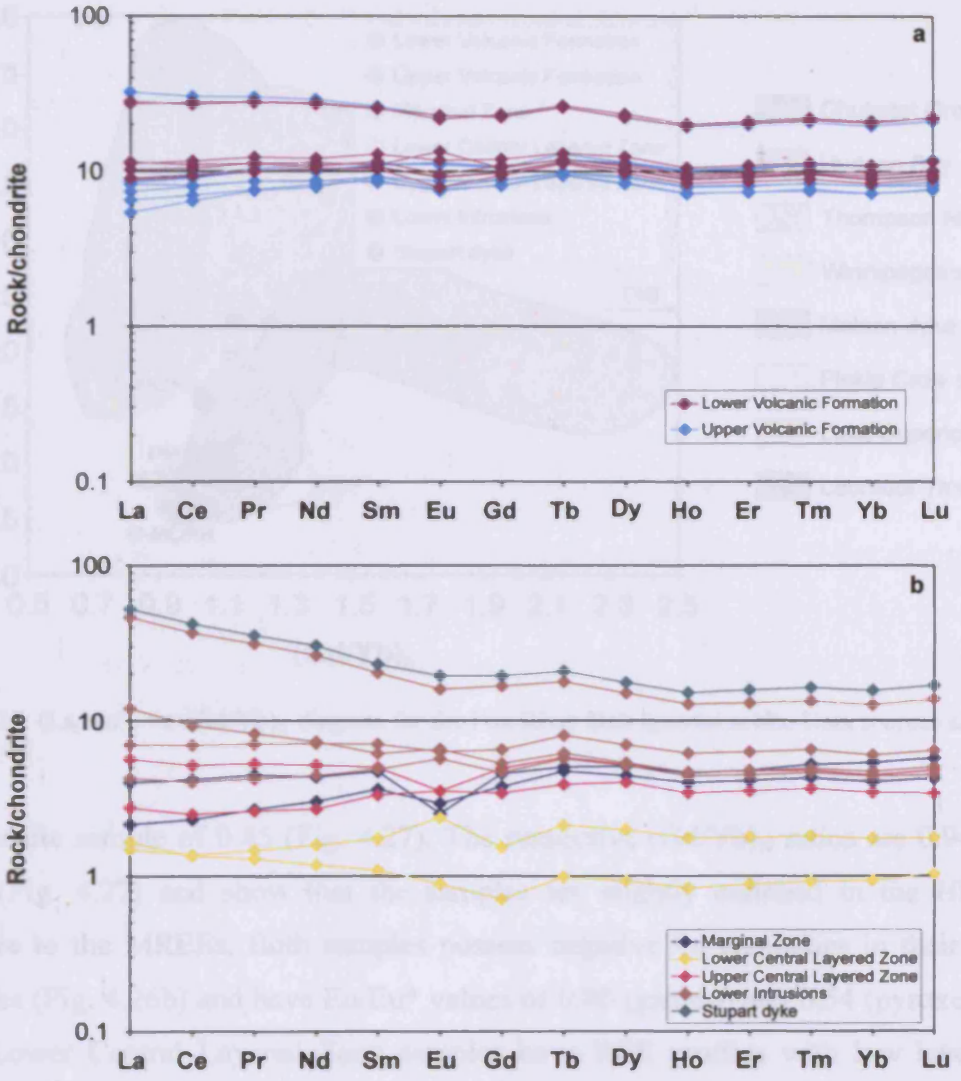

Fig. 4.26. Chondrite-normalised rare earth element (REE) diagrams for (a) the Fox River Belt volcanic rocks and (b) the Fox River Belt intrusive rocks. Chondrite values same as in Fig. 4.6.

1.17 respectively. The volcanic samples plot close to the composition of primitive mantle in Fig. 4.27 although some of the more LREE-depleted samples from the Upper Volcanic Formation plot intermediate between N-MORB and primitive mantle. The Lower Volcanic Formation REE profiles have minor positive and negative Eu anomalies (Fig. 4.26a) with Eu/Eu* values of 0.80 to 1.25.

The Marginal Zone samples have REE profiles with element concentrations ~2-6 times those of chondritic values (Fig. 4.26b). Both samples are slightly depleted in the LREEs relative to the MREEs although the gabbro sample is more so and this is reflected in its $(La/Sm)_N$ ratio of 0.59 relative to the respective value for the

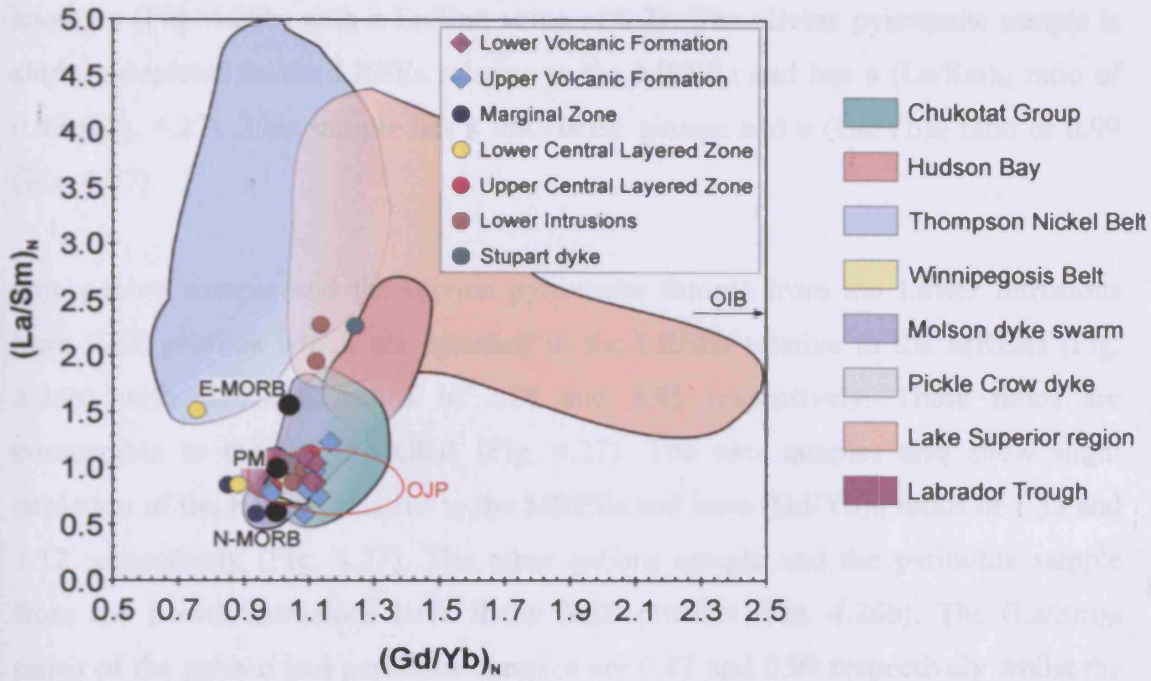

Fig. 4.27. $(La/Sm)_N$ vs. $(Gd/Yb)_N$ diagram for the Fox River Belt igneous rocks. Data sources same as in Fig. 4.7.

pyroxenite sample of 0.85 (Fig. 4.27). The respective $(Gd/Yb)_N$ ratios are 0.94 and 0.85 (Fig. 4.27) and show that the samples are slightly enriched in the HREEs relative to the MREEs. Both samples possess negative Eu anomalies in their REE profiles (Fig. 4.26b) and have Eu/Eu* values of 0.80 (gabbro) and 0.54 (pyroxenite). The Lower Central Layered Zone samples have REE profiles with low levels of element concentrations of ~0.4-1.7 times those of chondritic values. The dunite sample has a profile enriched in the LREEs relative to the MREEs (Fig. 4.26b) and has a $(La/Sm)_N$ ratio of 1.52 which is similar to that of E-MORB (Fig. 4.27). The gabbro sample is depleted in the LREEs relative to the MREEs and has a $(La/Sm)_N$ ratio of 0.85 (Fig. 4.27). The gabbro sample also has a positive Eu anomaly (Fig. 4.26b) with a Eu/Eu* value of 1.46. Both samples have low Gd concentrations and $(Gd/Yb)_N$ ratios of 0.76 (dunite) and 0.88 (gabbro) which are lower than most mantle end-member compositions (Fig. 4.27). The Upper Central Layered Zone samples possess REE concentrations of ~2.5-6 times those of chondritic values (Fig. 4.26b) with the gabbro sample having slightly higher concentrations than the olivine pyroxenite sample. The gabbro sample is slightly enriched in the LREEs and depleted in the HREEs relative to the MREEs and has $(La/Sm)_N$ and $(Gd/Yb)_N$ ratios of 1.13 and 1.11 respectively (Fig. 4.27). The gabbro sample also has a negative Eu

anomaly (Fig. 4.26b) with a Eu/Eu* value of 0.71. The olivine pyroxenite sample is slightly depleted in the LREEs relative to the MREEs and has a $(La/Sm)_N$ ratio of 0.82 (Fig. 4.27). This sample has a flat HREE pattern and a $(Gd/Yb)_N$ ratio of 0.99 (Fig. 4.27).

One gabbro sample and the olivine pyroxenite sample from the Lower Intrusions have REE profiles which are enriched in the LREEs relative to the MREEs (Fig. 4.26b) with $(La/Sm)_N$ ratios of 2.28 and 1.95 respectively. These ratios are comparable to that of E-MORB (Fig. 4.27). The two samples also show slight depletion of the HREEs relative to the MREEs and have $(Gd/Yb)_N$ ratios of 1.33 and 1.12 respectively (Fig. 4.27). The other gabbro sample and the peridotite sample from the Lower Intrusions have flatter REE profiles (Fig. 4.26b). The $(La/Sm)_N$ ratios of the gabbro and peridotite samples are 0.87 and 0.99 respectively whilst the respective $(Gd/Yb)_N$ ratios are 1.05 and 1.08 (Fig. 4.27). These ratios are similar to those of the primitive mantle composition (Fig. 4.27). The lone sample of a Stupart dyke possesses a REE profile which is enriched in the LREEs and depleted in the HREEs relative to the MREEs (Fig. 4.26b). The $(La/Sm)_N$ and $(Gd/Yb)_N$ ratios for the Stupart dyke sample are 2.27 and 1.24 respectively (Fig. 4.27).

Primitive-mantle-normalised multi-element profiles of the Fox River Belt igneous rocks are displayed in Fig. 4.28. The Lower and Upper Volcanic Formations have nearly identical multi-element profiles which are near-parallel, flat patterns with element concentrations ~2-12 times those of primitive mantle values except Th which is depleted relative to the other elements (Fig. 4.28a). The three lowest MgO samples (5.72-7.40 wt. % MgO) plot noticeably higher on Fig. 4.28a than the other samples. The three low MgO samples contain no Ti anomalies (Ti/Ti* 0.99-1.12) whereas all the other samples contain negative Ti anomalies with Ti/Ti* values of 0.69 to 0.85. The multi-element profiles of the volcanic rocks are similar to those of the Ontong Java Plateau which are generally flat and slightly depleted in Th relative to the other elements.

The multi-element profiles of the intrusive rocks (Fig. 4.28b) are somewhat different to those of the volcanic rocks with the exception of the Marginal Zone pyroxenite and Lower Intrusions peridotite samples. These two samples have relatively flat

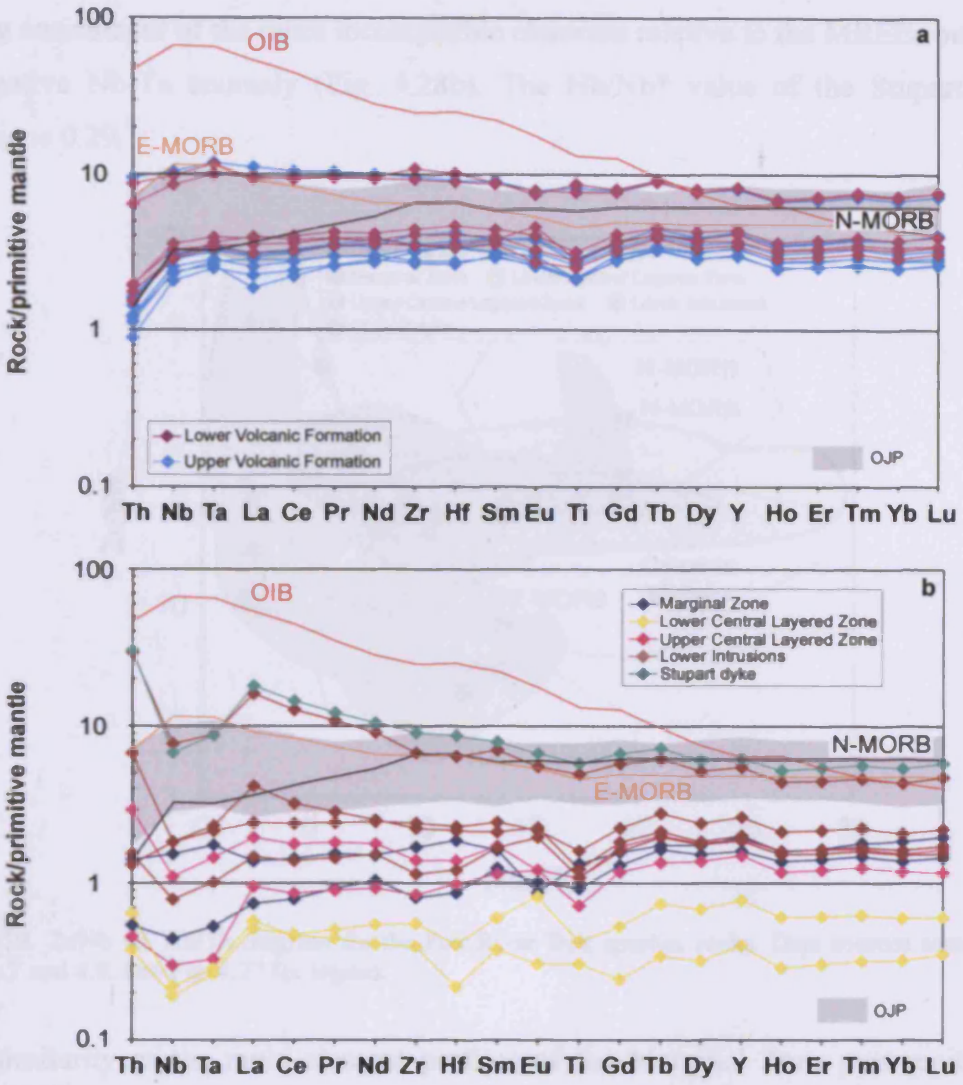

Fig. 4.28. Primitive-mantle-normalised multi-element diagrams for (a) the Fox River Belt volcanic rocks and (b) the Fox River Belt intrusive rocks. Data sources same as in Fig. 4.7.

multi-element profiles. The other Marginal Zone sample has a multi-element profile which is depleted in Th-Nb-Ta-LREEs relative to the less incompatible elements. The Lower and Upper Central Layered Zone samples have multi-element profiles which show limited fractionation between the more and less incompatible elements but contain negative Nb-Ta anomalies (Fig. 4.28b) with Nb/Nb* values ranging from 0.36 to 0.46. The Lower Central Layered Zone samples also possess negative Hf anomalies (Fig. 4.28b) with Hf/Hf* values ($Hf/Hf^* = Hf_{pm}/\sqrt{Nd_{pm} \times Sm_{pm}}$) of 0.55 and 0.70. The olivine pyroxenite and two gabbro samples from the Lower Intrusions also have multi-element profiles with negative Nb-Ta anomalies (Fig. 4.28b) and Nb/Nb* values that range from 0.35 to 0.52. The Stupart dyke sample has a multi-element profile which is similar to that of the Lower Intrusions gabbro sample which shows

strong enrichment of the more incompatible elements relative to the MREEs but with a negative Nb-Ta anomaly (Fig. 4.28b). The Nb/Nb* value of the Stupart dyke sample is 0.29.

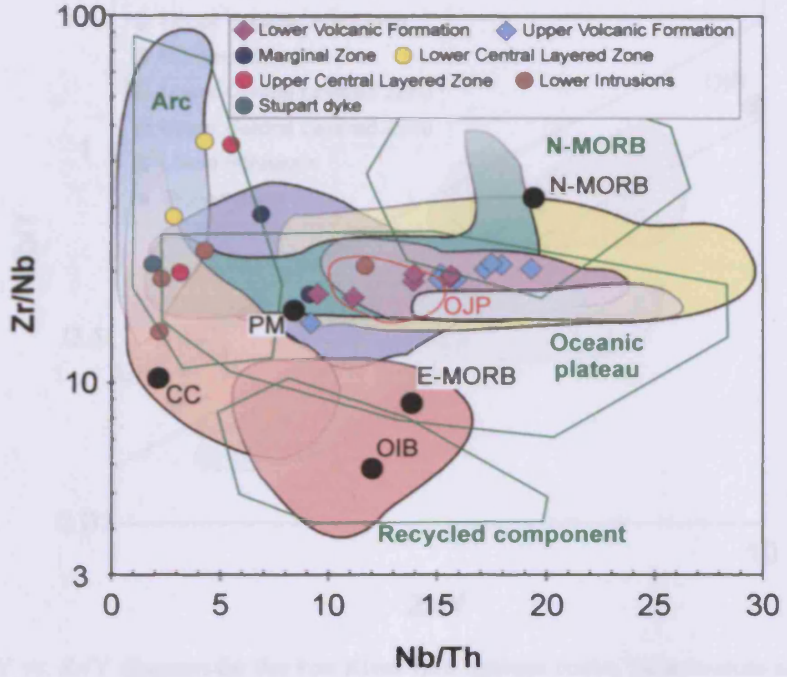

Fig. 4.29. Zr/Nb vs. Nb/Th diagram for the Fox River Belt igneous rocks. Data sources same as in Figs. 4.7 and 4.9. See Fig. 4.27 for legend.

The similarity of the multi-element profiles of the Marginal Zone pyroxenite and Lower Intrusions peridotite to the volcanic samples is mirrored on the Zr/Nb-Nb/Th diagram in Fig. 4.29. These two intrusive samples plot with the volcanic samples in the oceanic plateau field of Condie (2005) and partially overlap with the field for the Ontong Java Plateau. The remaining intrusive samples plot within the arc field of Condie (2005) in Fig. 4.29. The volcanic samples also plot within the Ontong Java Plateau field and the Icelandic plume tramlines on the Nb/Y-Zr/Y diagram in Fig. 4.30. The Marginal Zone pyroxenite and Lower Intrusions peridotite as well as the olivine pyroxenite and one of the gabbro samples from the Lower Intrusions also plot amongst the volcanic samples in Fig. 4.30. The Stupart dyke sample and Lower Central Layered Zone dunite plot at similar Zr/Y ratios to the volcanic samples but at lower Nb/Y ratios and below the lower Icelandic plume tramline (Fig. 4.30). The remaining intrusive samples plot left of the volcanic samples towards the more depleted section of Fig. 4.30 with the Lower Central Layered Zone gabbro and Upper

Central Layered Zone olivine pyroxenite falling below the lower Icelandic plume tramline.

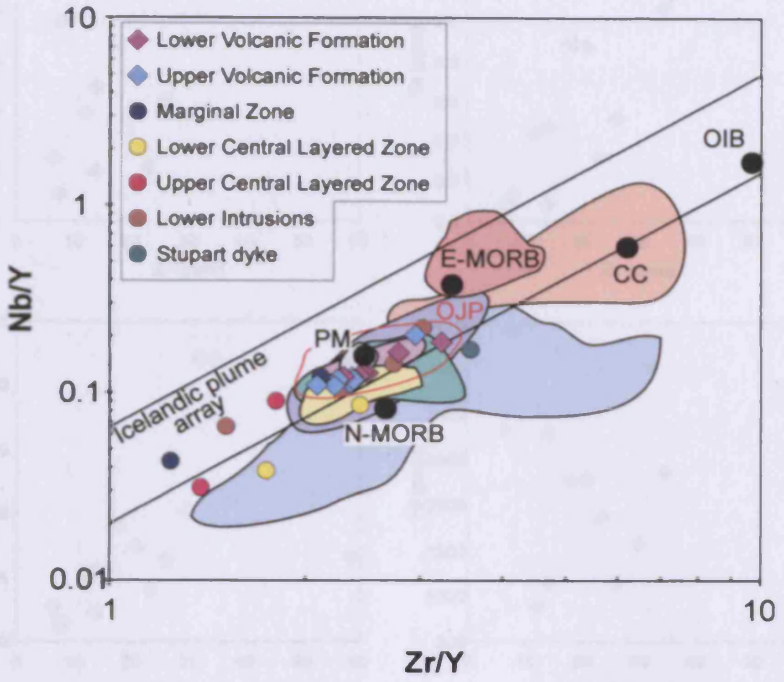

Fig. 4.30. Nb/Y vs. Zr/Y diagram for the Fox River Belt igneous rocks. Data sources same as in Figs. 4.7 and 4.9. See Fig. 4.27 for legend.

4.7. Thompson Nickel Belt

4.7.1. Alteration and element mobility

Petrographic observations (see section 3.5.2) indicate that the Thompson sills have been subjected to alteration and amphibolite facies metamorphism following the magmatic event during which they were emplaced. LOI values range from 1.13 to 13.87 wt. % and indicate that the rocks have been altered. To assess the possible effect these secondary processes may have had on the geochemistry of the rocks, all elements have been plotted against Zr and a selection of these diagrams is shown in Fig. 4.31. None of the elements give very good correlations with Zr but some produce much more scatter than others. Elements which yield reasonable correlations with Zr include Ni, Cr, Co, Ga, Y, Nb, Ta, Hf, REEs, Th, Ti, Al, Fe, Mg and P. These elements probably were immobile during secondary alteration processes. Elements which do not produce good correlations with Zr include Cu, Sr, V, Zn, Rb,

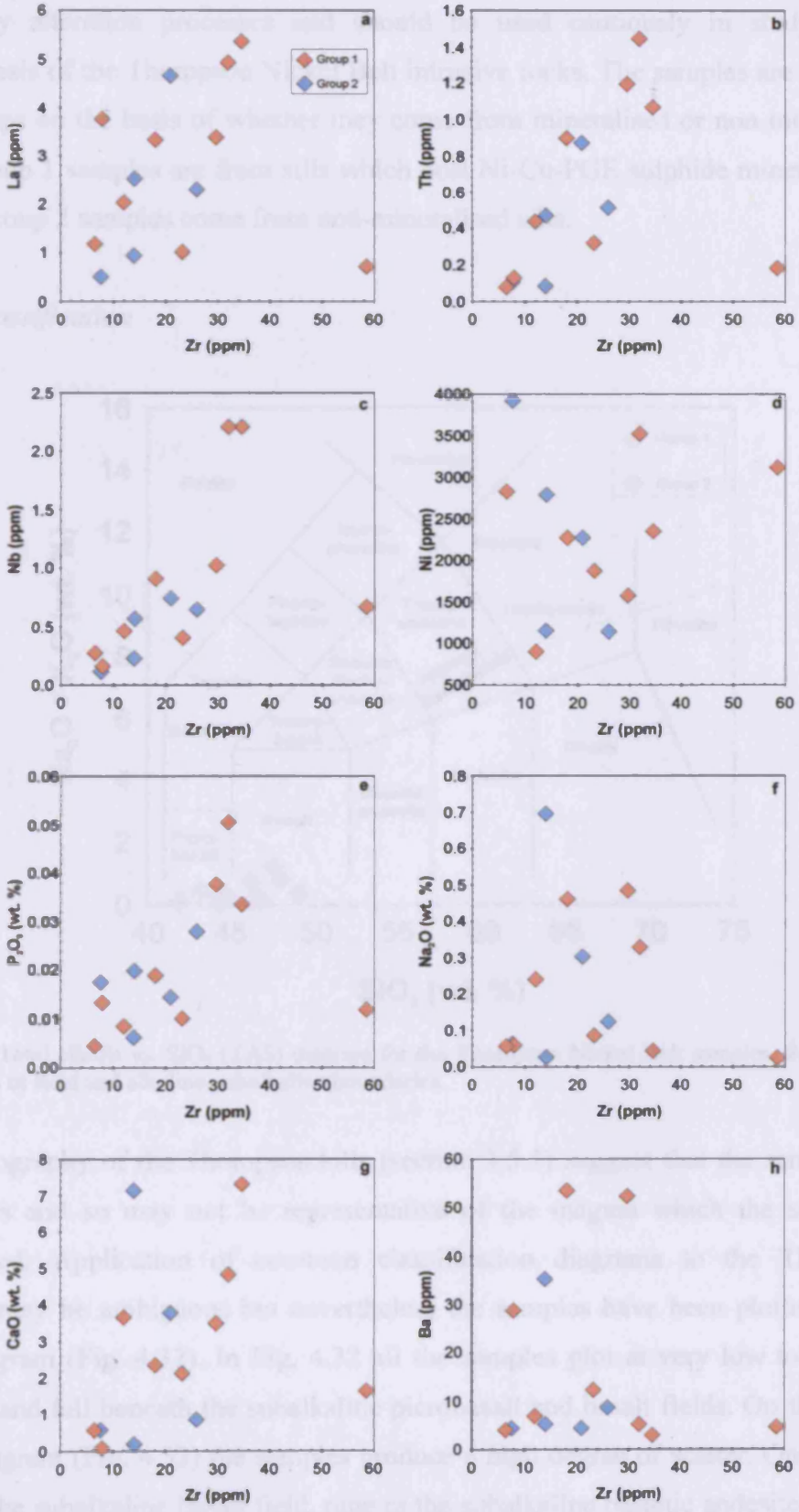

Fig. 4.31. Bivariate diagrams of selected elements vs. Zr for the Thompson Nickel Belt samples.

Cs, U, Ba, Sc, Si, Mn, Ca, Na and K. These elements may have been mobile during secondary alteration processes and should be used cautiously in studying the petrogenesis of the Thompson Nickel Belt intrusive rocks. The samples are split into two groups on the basis of whether they come from mineralised or non-mineralised sills. Group 1 samples are from sills which host Ni-Cu-PGE sulphide mineralisation whilst Group 2 samples come from non-mineralised sills.

4.7.2. Classification

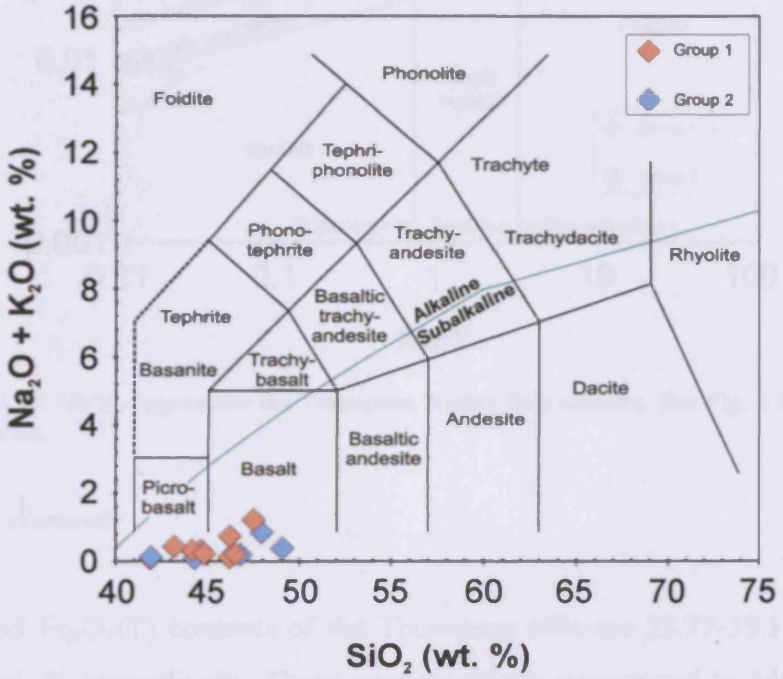

Fig. 4.32. Total alkalis vs. SiO_2 (TAS) diagram for the Thompson Nickel Belt samples. See Fig. 4.2 for sources of field and alkaline-subalkaline boundaries.

The petrography of the Thompson sills (section 3.5.2) suggest that the samples are cumulates and so may not be representative of the magma which the sills once transported. Application of common classification diagrams to the Thompson samples may be ambiguous but nevertheless the samples have been plotted on the TAS diagram (Fig. 4.32). In Fig. 4.32 all the samples plot at very low total alkali contents and fall beneath the subalkaline picrobasalt and basalt fields. On the Zr/Ti-Nb/Y diagram (Fig. 4.33) the samples produce a high degree of scatter. One sample plots in the subalkaline basalt field, nine in the subalkaline basaltic andesite-andesite field, three fall on the boundary between andesite and dacite, and one sample plots in

the alkali rhyolite field. The results of the Zr/Ti-Nb/Y diagram seem particularly unrealistic given the mineralogy of the Thompson intrusive samples.

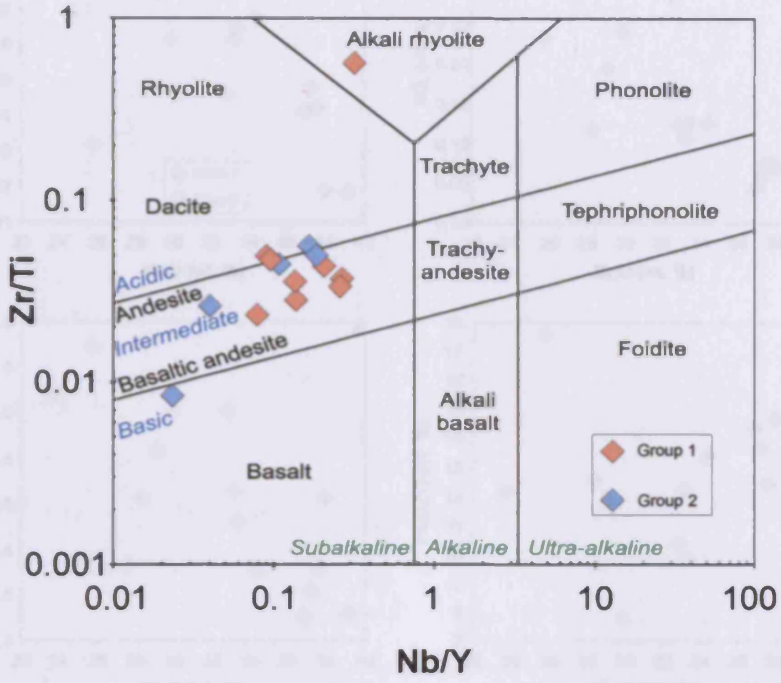

Fig. 4.33. Zr/Ti vs. Nb/Y diagram for the Thompson Nickel Belt samples. See Fig. 4.3 for the source of field boundaries.

4.7.3. Major elements

The MgO and Fe_2O_3(T) contents of the Thompson sills are 23.77-39.13 wt. % and 7.79-17.64 wt. % respectively. These concentrations correspond to Mg# values of 61.90 to 78.93. SiO_2 concentrations vary between 41.88 and 49.05 wt. % and the range in total alkali content is 0.06-1.20 wt. %. Variation diagrams of all the major elements plotted against MgO are shown in Fig. 4.34. All the major elements increase in concentration as the MgO concentration declines, with the exception of Fe_2O_3(T) which decreases as the MgO content decreases, and K_2O, which shows no obvious trend with MgO. There appears to be no obvious difference between the two groupings of the Thompson samples on the basis of major elements.

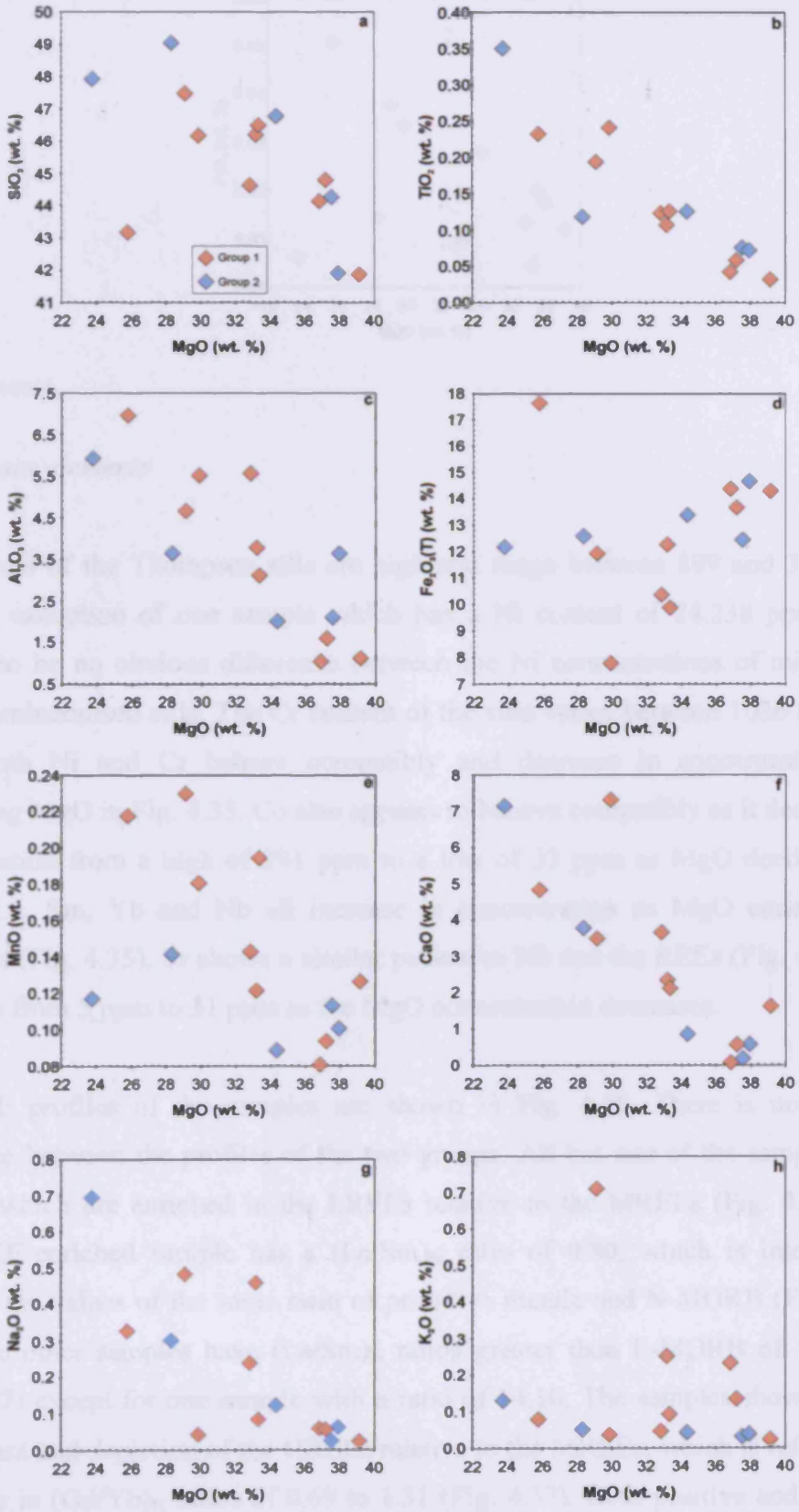

Fig. 4.34. Bivariate diagrams of major elements vs. MgO for the Thompson Nickel Belt samples.

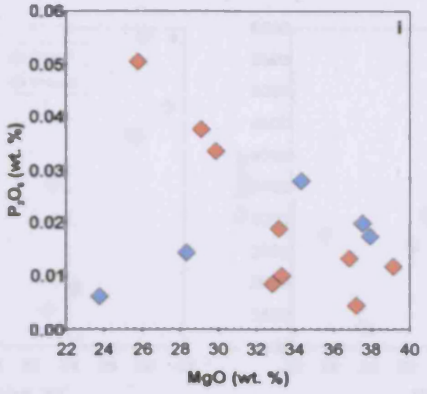

Fig. 4.34. contd.

4.7.4. Trace elements

Ni contents of the Thompson sills are high and range between 899 and 3920 ppm with the exception of one sample which has a Ni content of 24,238 ppm. There appears to be no obvious difference between the Ni concentrations of mineralised and non-mineralised sills. The Cr content of the sills varies between 1036 and 5559 ppm. Both Ni and Cr behave compatibly and decrease in concentration with decreasing MgO in Fig. 4.35. Co also appears to behave compatibly as it decreases in concentration from a high of 291 ppm to a low of 33 ppm as MgO declines (Fig. 4.35c). La, Sm, Yb and Nb all increase in concentration as MgO concentration decreases (Fig. 4.35). Sr shows a similar pattern to Nb and the REEs (Fig. 4.35) and increases from 5 ppm to 31 ppm as the MgO concentration decreases.

The REE profiles of the samples are shown in Fig. 4.36. There is no obvious difference between the profiles of the two groups. All but one of the samples have profiles which are enriched in the LREEs relative to the MREEs (Fig. 4.36). The non-LREE-enriched sample has a $(La/Sm)_N$ ratio of 0.80, which is intermediate between the values of the same ratio of primitive mantle and N-MORB (Fig. 4.37), while the other samples have $(La/Sm)_N$ ratios greater than E-MORB of 1.52-4.42 (Fig. 4.37) except for one sample with a ratio of 14.10. The samples show variable enrichment and depletion of the HREEs relative to the MREEs, which is reflected by the range in $(Gd/Yb)_N$ ratios of 0.69 to 1.31 (Fig. 4.37). Both positive and negative Eu anomalies are present in the REE profiles (Fig. 4.36) and Eu/Eu* values range between 0.48 and 1.52.

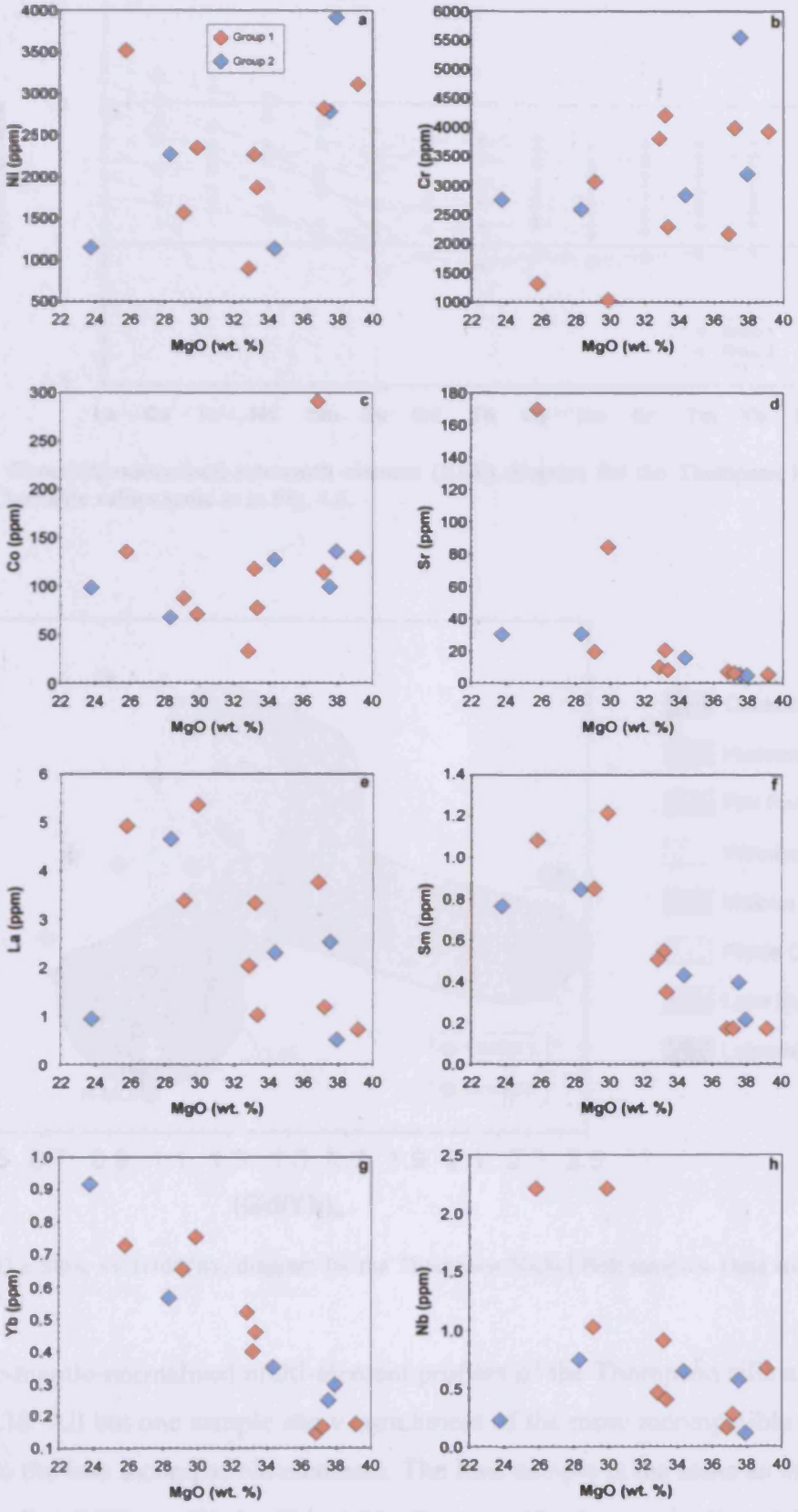

Fig. 4.35. Bivariate diagrams of selected trace elements vs. Zr for the Thompson Nickel Belt samples.

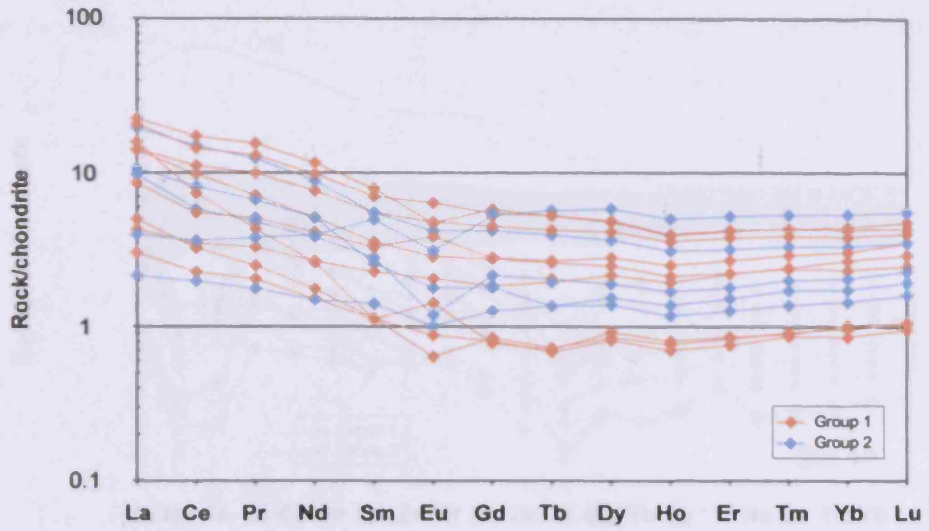

Fig. 4.36. Chondrite-normalised rare earth element (REE) diagram for the Thompson Nickel Belt samples. Chondrite values same as in Fig. 4.6.

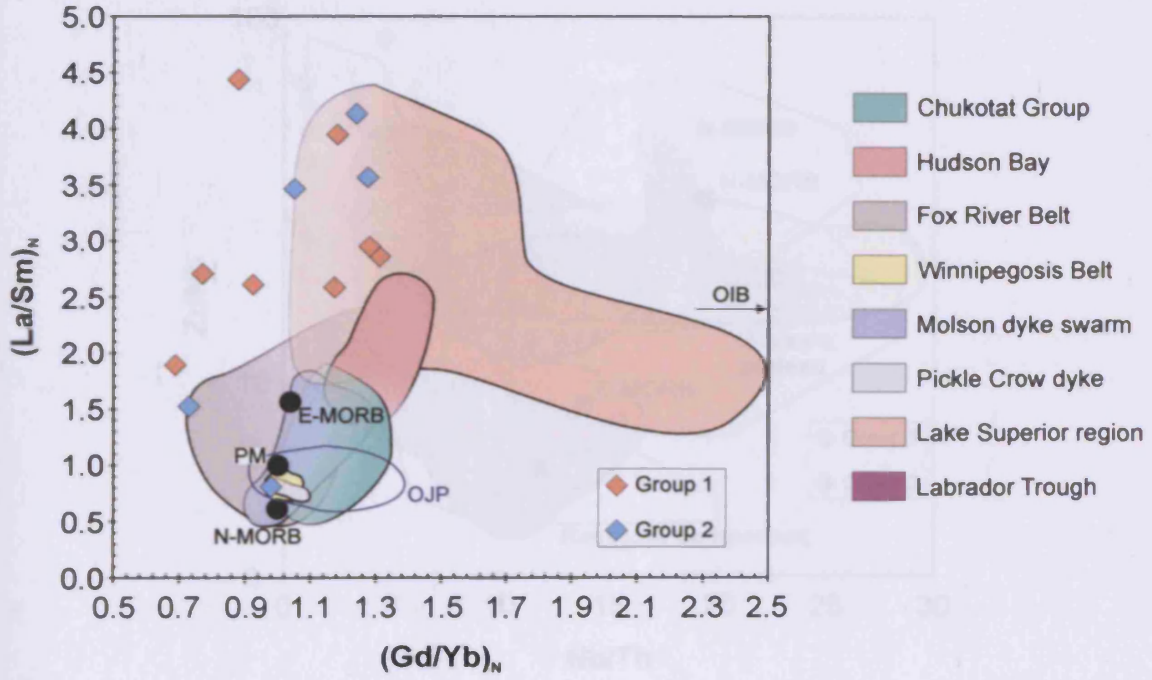

Fig. 4.37. $(La/Sm)_N$ vs. $(Gd/Yb)_N$ diagram for the Thompson Nickel Belt samples. Data sources same as in Fig. 4.7.

Primitive-mantle-normalised multi-element profiles of the Thompson sills are shown in Fig. 4.38. All but one sample show enrichment of the more incompatible elements relative to the less incompatible elements. The lone sample is the same as that with a relatively flat REE profile in Fig. 4.36. One notable feature in Fig. 4.38 is the universal presence of negative Nb-Ta anomalies. The overall range in Nb/Nb* values

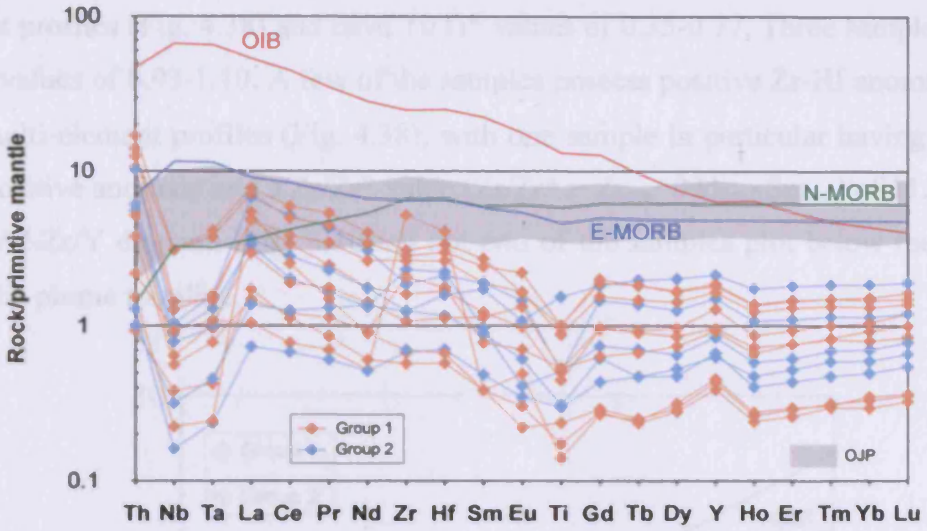

Fig. 4.38. Primitive-mantle-normalised multi-element diagram for the Thompson Nickel Belt samples. Data sources same as in Fig. 4.7.

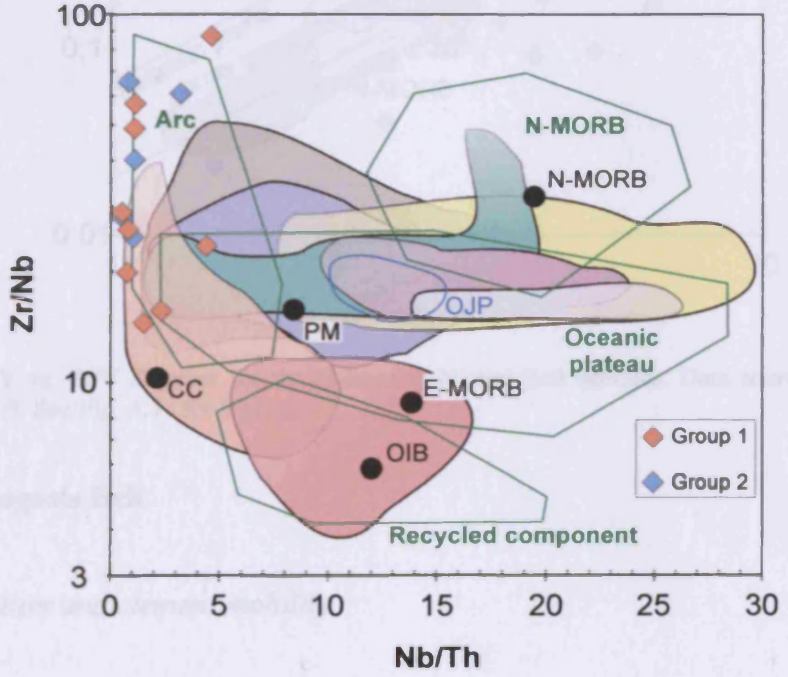

Fig. 4.39. Zr/Nb vs. Nb/Th diagram for the Thompson Nickel Belt samples. Data sources same as in Figs. 4.7 and 4.9. See Fig. 4.36 for legend.

is from 0.08 to 0.62. The low Nb concentrations give rise to low Nb/Th and high Zr/Nb ratios typical of volcanic arc environments (Fig. 4.39). The general enrichment of the more incompatible elements and the presence of the Nb-Ta anomalies are also common to continental flood basalts contaminated with crustal material. The majority of samples also have negative Ti anomalies in their multi-

element profiles (Fig. 4.38) and have Ti/Ti* values of 0.35-0.77. Three samples have Ti/Ti* values of 0.93-1.10. A few of the samples possess positive Zr-Hf anomalies in their multi-element profiles (Fig. 4.38), with one sample in particular having a very large positive anomaly and a Zr/Zr* value ($Zr/Zr^* = Zr_{pm}/\sqrt{Nd_{pm} \times Sm_{pm}}$) of 11.58. On the Nb/Y-Zr/Y diagram (Fig. 4.40) all but two of the samples plot below the lower Icelandic plume tramline.

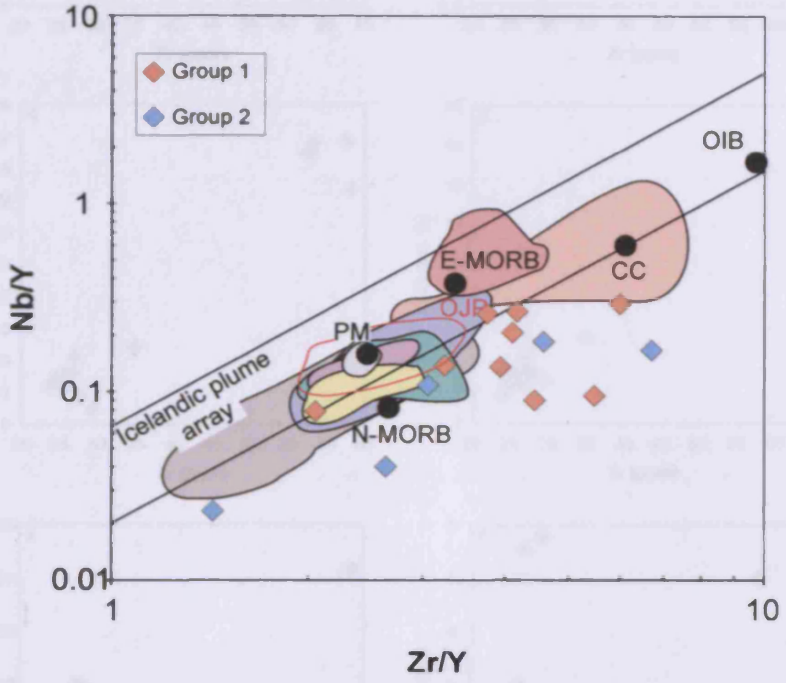

Fig. 4.40. Nb/Y vs. Zr/Y diagram for the Thompson Nickel Belt samples. Data sources same as in Figs. 4.7 and 4.9. See Fig. 4.36 for legend.

4.8. Winnipegosis Belt

4.8.1. Alteration and element mobility

The volcanic rocks of the Winnipegosis Belt have been subjected to post-magmatic alteration processes which have resulted in the presence of secondary alteration minerals (see section 3.6.2) and LOI values of 1.85-5.53 wt. % in these rocks. All elements have been plotted against Zr to assess any potential element mobilisation during secondary alteration processes. A representative selection of these bivariate diagrams is shown in Fig. 4.41. The elements which produce reasonable correlations with Zr are Sc, V, Cr, Co, Ni, Y, Ga, Nb, REEs, Hf, Ta, U, Ti, Si, Al, Mn, Mg and

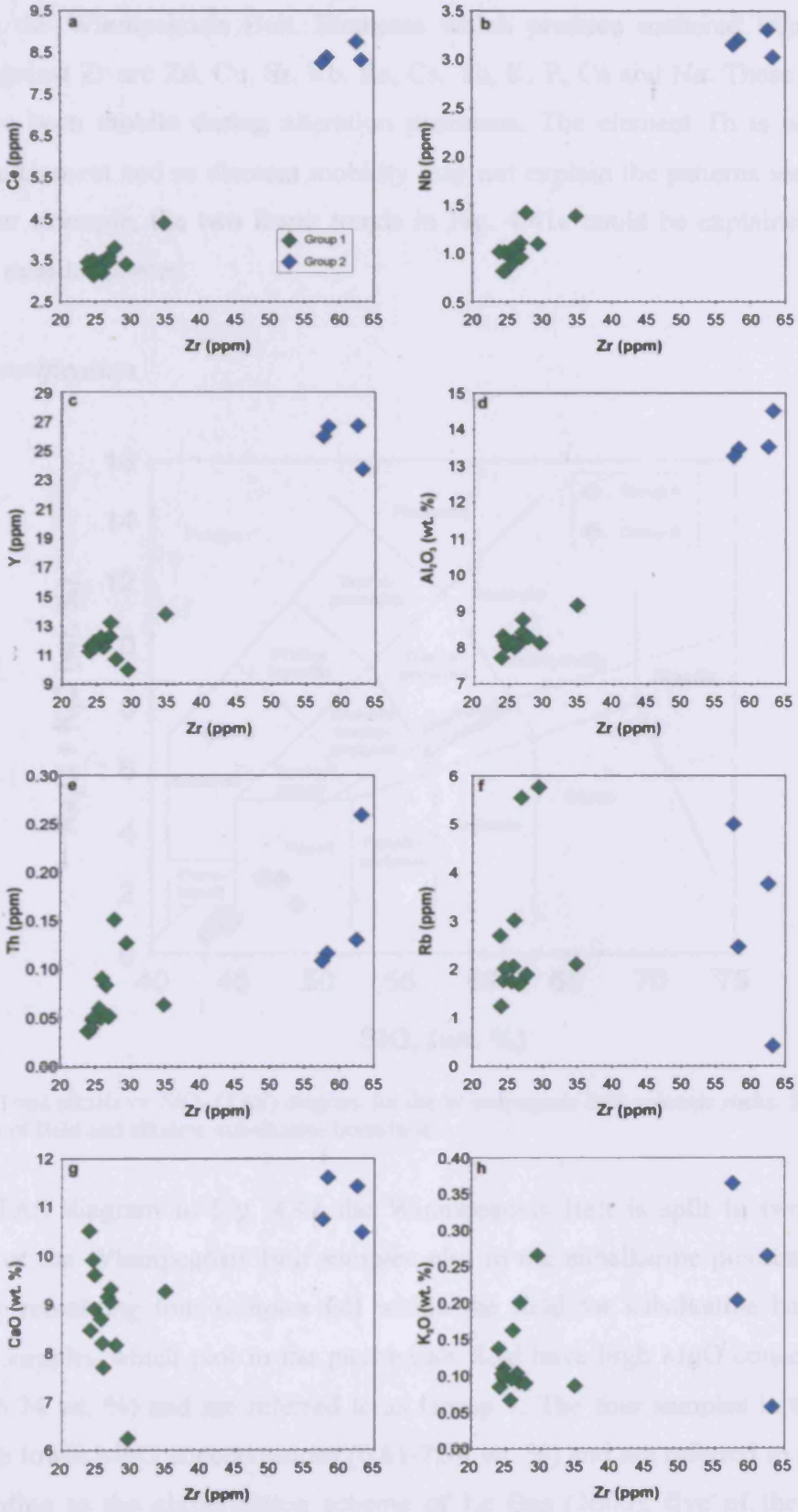

Fig. 4.41. Bivariate diagrams of selected elements vs. Zr for the Winnipegosis Belt volcanic rocks.

Fe. These elements were most likely immobile during post-magmatic processes affecting the Winnipegosis Belt. Elements which produce scattered trends when plotted against Zr are Zn, Cu, Sr, Rb, Ba, Cs, Th, K, P, Ca and Na. These elements may have been mobile during alteration processes. The element Th is usually an immobile element and so element mobility may not explain the patterns seen in Fig. 4.41e. For example, the two linear trends in Fig. 4.41e could be explained by two different mantle sources.

4.8.2. Classification

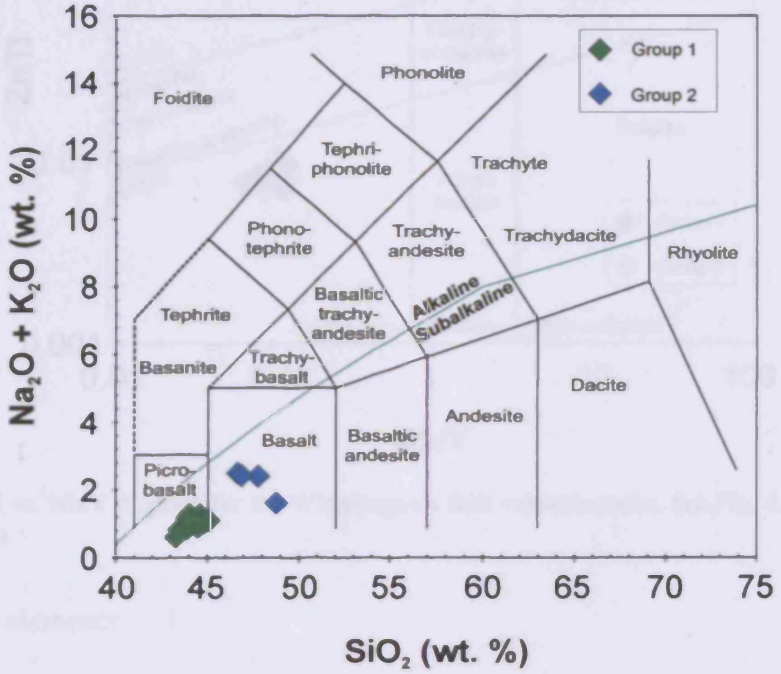

Fig. 4.42. Total alkalis vs. SiO_2 (TAS) diagram for the Winnipegosis Belt volcanic rocks. See Fig. 4.2 for sources of field and alkaline-subalkaline boundaries.

On the TAS diagram in Fig. 4.42 the Winnipegosis Belt is split in two groups, fourteen of the Winnipegosis Belt samples plot in the subalkaline picrobasalt field while the remaining four samples fall within the field for subalkaline basalt. The fourteen samples which plot in the picrobasalt field have high MgO concentrations (19.87-26.74 wt. %) and are referred to as Group 1. The four samples in the basalt field have lower MgO concentrations (6.81-7.94 wt. %) and are referred to as Group 2. According to the classification scheme of Le Bas (2000), five of the samples classify as komatiites (>18 wt. % MgO, <1 wt. % total alkalis). However, none of the

Winnipegosis Belt samples collected for this study possess olivine spinifex texture and so none are referred to as komatiites in this study. On the Zr/Ti-Nb/Y diagram (Fig. 4.43) all samples plot in the subalkaline basalt field. Therefore the Group 2 samples shall be termed basalts and the Group 1 samples termed picrites due to their high MgO content.

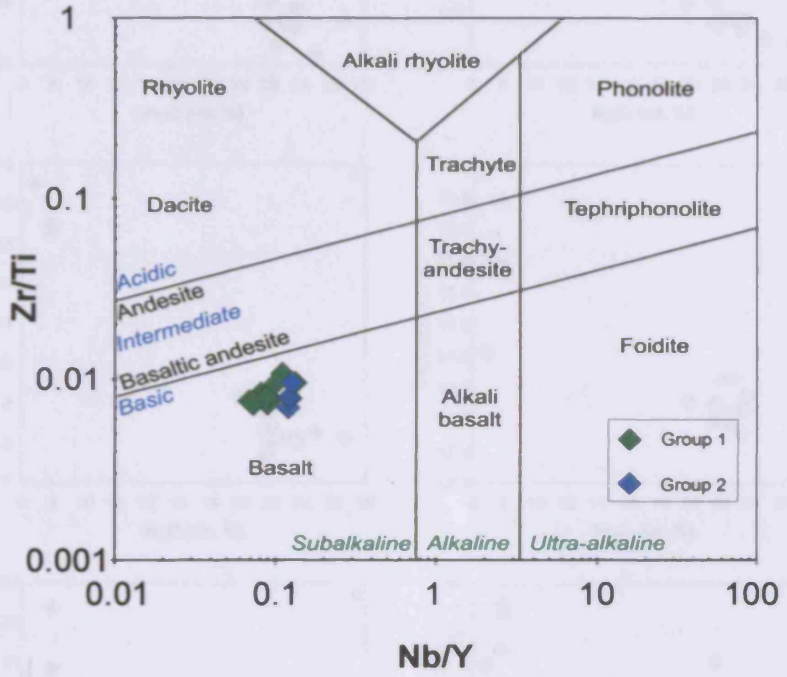

Fig. 4.43. Zr/Ti vs. Nb/Y diagram for the Winnipegosis Belt volcanic rocks. See Fig. 4.3 for source of field boundaries.

4.8.3. Major elements

Group 1 samples contain 19.87-26.74 wt. % MgO and 11.99-13.65 wt. % Fe_2O_3(T) and have Mg# values of 59.93-68.87. The SiO_2 and total alkali contents of the Group 1 samples are 45.16-46.57 wt. % and 0.65-1.34 wt. % respectively. Group 2 samples possess 6.81-7.94 wt. % MgO, 14.05-16.45 wt. % Fe_2O_3(T), 47.50-49.71 wt. % SiO_2 and 1.65-2.55 wt. % total alkalis and have Mg# values of 32.48-34.10. Variation diagrams of major element concentrations plotted against MgO are displayed in Fig. 4.44. As the concentration of MgO decreases, the concentrations of SiO_2, TiO_2, Al_2O_3, Fe_2O_3(T), MnO and P_2O_5 all increase. The concentration of CaO initially increases with declining MgO, but appears to start decreasing as the MgO content declines below ~10 wt.%. Both Na_2O and K_2O generally increase in concentration as

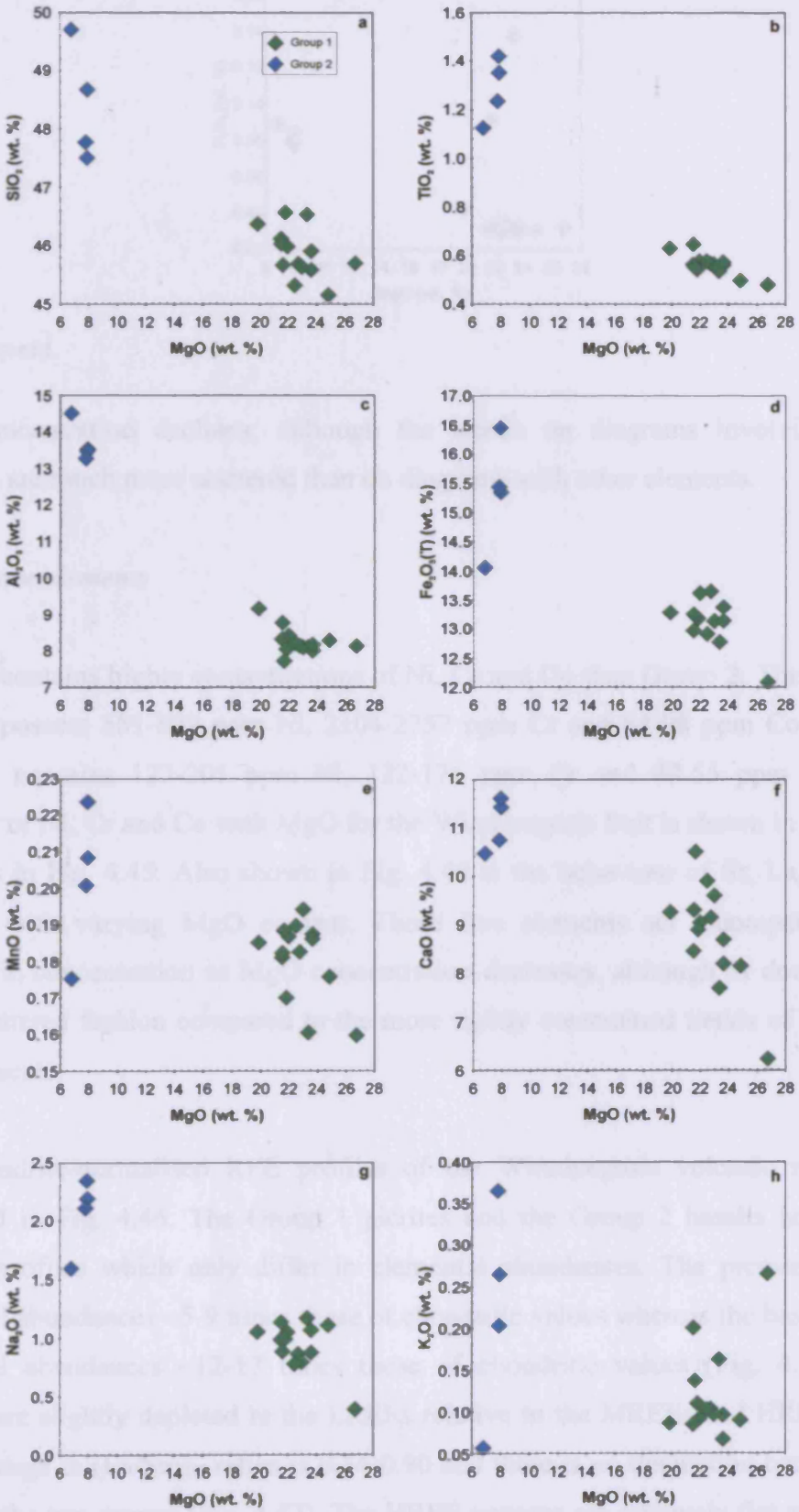

Fig. 4.44. Bivariate diagrams of major elements vs. MgO for the Winnipegosis Belt volcanic rocks.

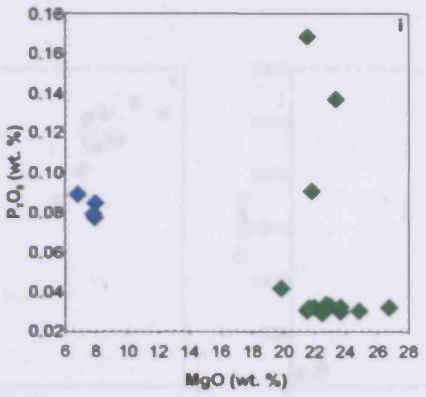

Fig. 4.44. contd.

MgO concentration declines, although the trends on diagrams involving these elements are much more scattered than on diagrams with other elements.

4.8.4. Trace elements

Group 1 contains higher concentrations of Ni, Cr and Co than Group 2. The Group 1 samples possess 581-892 ppm Ni, 2104-2757 ppm Cr and 84-98 ppm Co whereas Group 2 contains 123-201 ppm Ni, 122-176 ppm Cr and 49-55 ppm Co. The variation of Ni, Cr and Co with MgO for the Winnipegosis Belt is shown in variation diagrams in Fig. 4.45. Also shown in Fig. 4.45 is the behaviour of Sr, La, Sm, Yb and Nb with varying MgO content. These five elements act incompatibly and increase in concentration as MgO concentration decreases, although Sr does so in a more scattered fashion compared to the more tightly constrained trends of the other four elements.

The chondrite-normalised REE profiles of the Winnipegosis volcanic rocks are displayed in Fig. 4.46. The Group 1 picrites and the Group 2 basalts have near-parallel profiles which only differ in elemental abundances. The picrites contain elemental abundances ~5-9 times those of chondritic values whereas the basalts have elemental abundances ~12-17 times those of chondritic values (Fig. 4.46). The profiles are slightly depleted in the LREEs relative to the MREEs and HREEs. The overall range in $(La/Sm)_N$ ratios is 0.74-0.90 and there is no distinction between the ratios of the two groups (Fig. 4.47). The HREE patterns are relatively flat and this is emphasised by the narrow range in $(Gd/Yb)_N$ ratios of 0.99 to 1.06 (Fig. 4.47). The

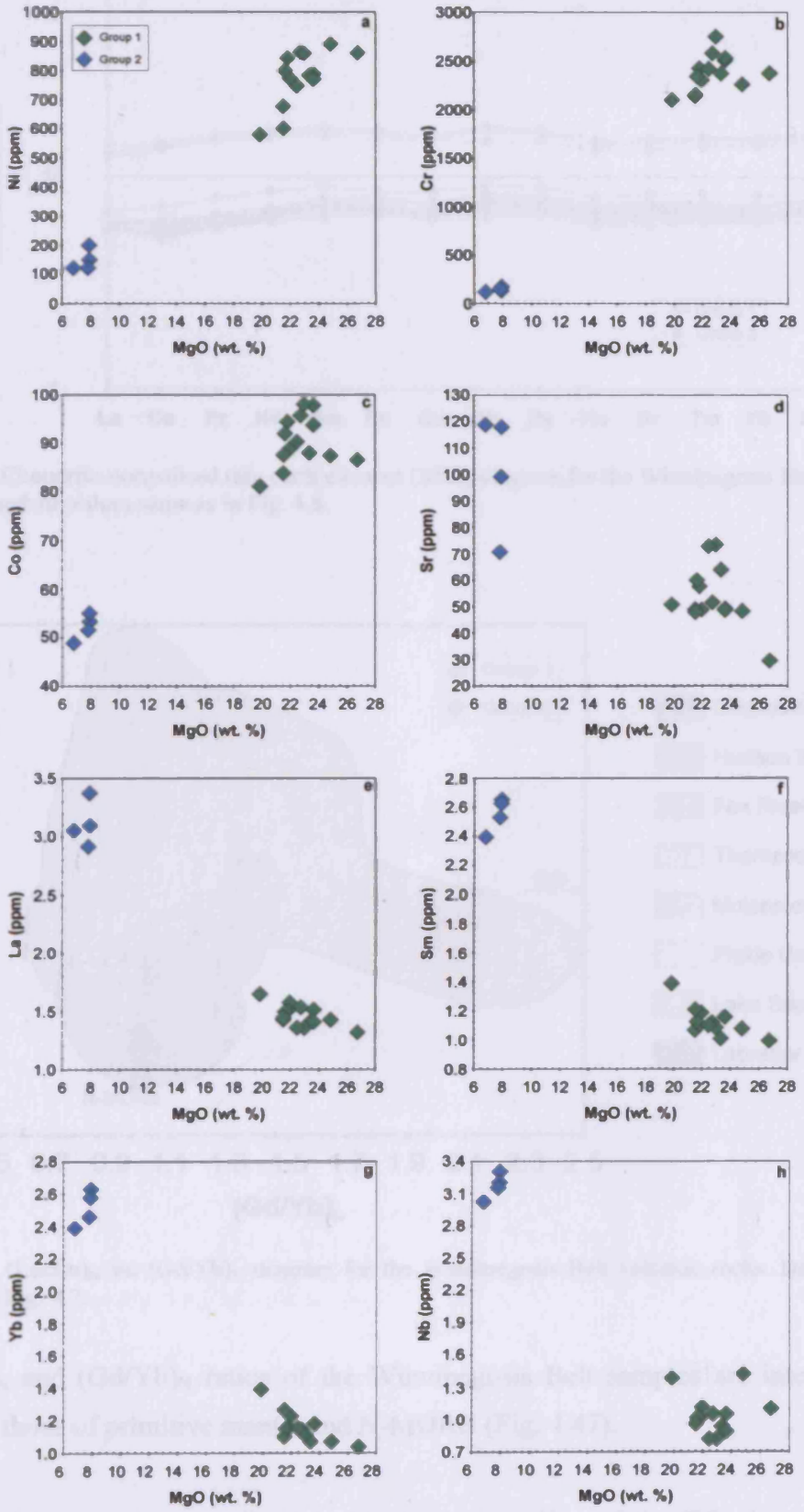

Fig. 4.45. Bivariate diagrams of selected trace elements vs. MgO for the Winnipegosis Belt volcanic rocks.

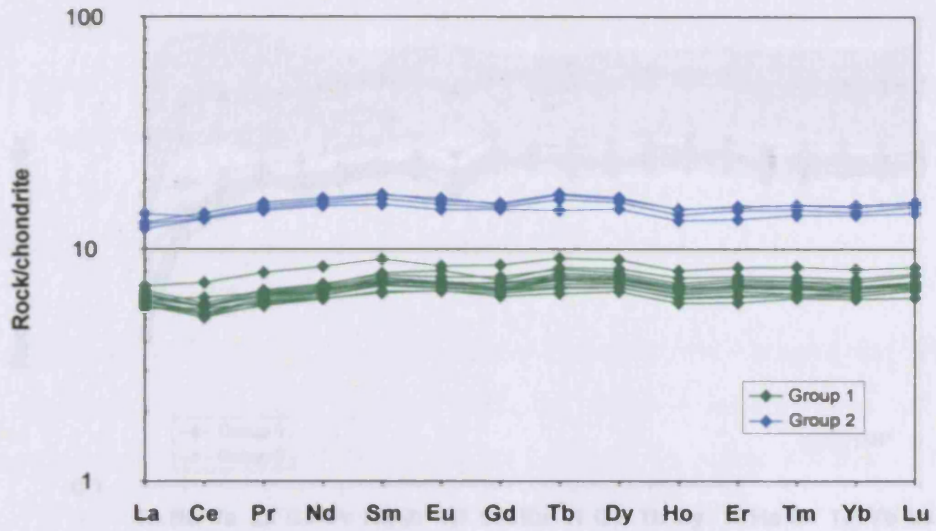

Fig. 4.46. Chondrite-normalised rare earth element (REE) diagram for the Winnipegosis Belt volcanic rocks. Chondrite values same as in Fig. 4.6.

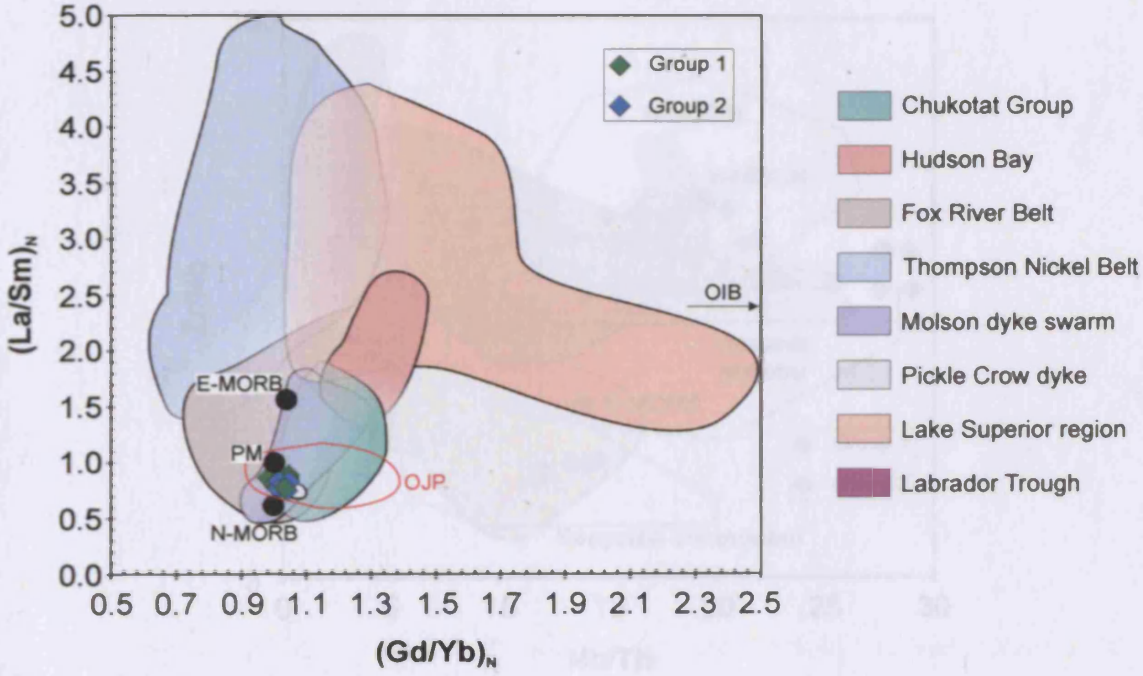

Fig. 4.47. $(La/Sm)_N$ vs. $(Gd/Yb)_N$ diagram for the Winnipegosis Belt volcanic rocks. Data sources same as in Fig. 4.7.

$(La/Sm)_N$ and $(Gd/Yb)_N$ ratios of the Winnipegosis Belt samples are intermediate between those of primitive mantle and N-MORB (Fig. 4.47).

The primitive-mantle-normalised multi-element profiles of the Winnipegosis Belt samples are shown in Fig. 4.48. The profiles contain elemental abundances ~1-6

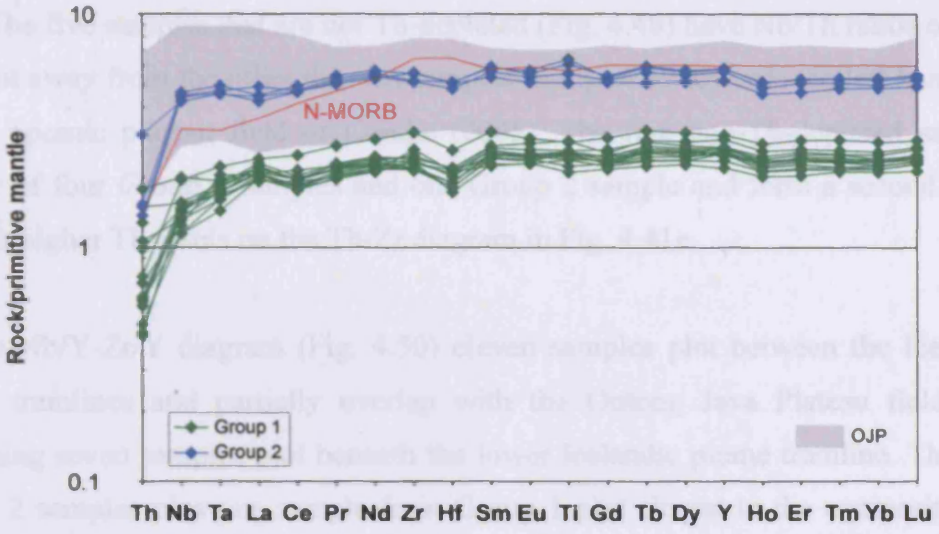

Fig. 4.48. Primitive-mantle-normalised multi-element diagram for the Winnipegosis Belt volcanic rocks. Data sources same as in Fig. 4.7.

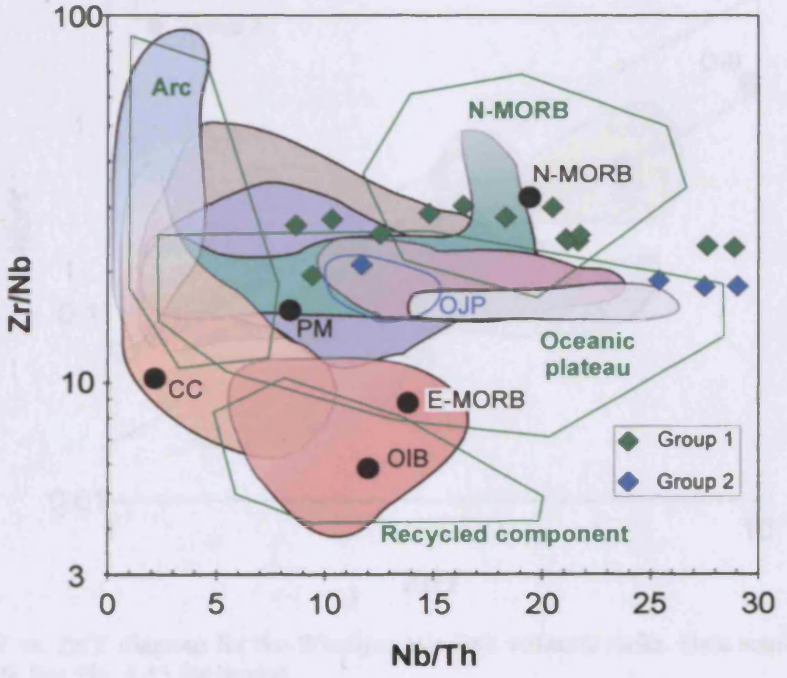

Fig. 4.49. Zr/Nb vs. Nb/Th diagram for the Winnipegosis Belt volcanic rocks. Data sources same as in Figs. 4.7 and 4.9. See Fig. 4.45 for legend.

times those of primitive mantle values. Group 2 samples plot at higher elemental abundances than Group 1 samples. All the multi-element profiles are reasonably flat with the exception of Th which is depleted relative to the other elements (Fig. 4.48) in thirteen samples. These thirteen samples have Nb/Th ratios of 14-29 and plot in both the N-MORB and oceanic plateau fields on the Zr/Nb-Nb/Th diagram in Fig.

4.49. The five samples that are not Th-depleted (Fig. 4.48) have Nb/Th ratios of 8-13 and plot away from the other thirteen samples in Fig. 4.49 towards the left hand side of the oceanic plateau field of Condie (2005). The five non-Th-depleted samples consist of four Group 1 samples and one Group 2 sample and form a second linear trend at higher Th levels on the Th-Zr diagram in Fig. 4.41e.

On the Nb/Y-Zr/Y diagram (Fig. 4.50) eleven samples plot between the Icelandic plume tramlines and partially overlap with the Ontong Java Plateau field. The remaining seven samples plot beneath the lower Icelandic plume tramline. The four Group 2 samples plus one sample from Group 1 plot closest to the composition of primitive mantle in Fig. 4.50.

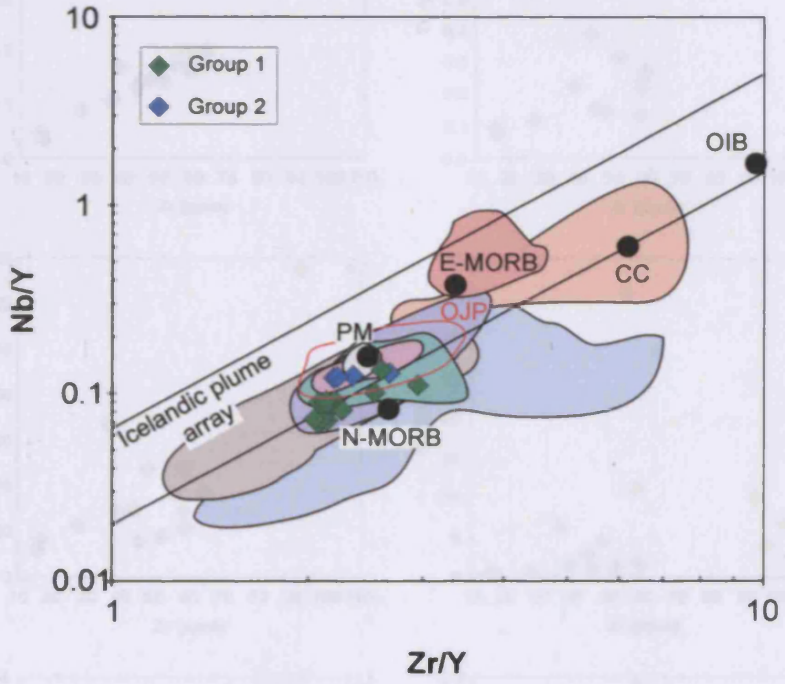

Fig. 4.50. Nb/Y vs. Zr/Y diagram for the Winnipegosis Belt volcanic rocks. Data sources same as in Figs. 4.7 and 4.9. See Fig. 4.45 for legend.

4.9. Molson dykes

4.9.1. Alteration and element mobility

The LOI values of the Molson dykes are relatively low and range from -0.22 to 1.09 wt. %. These LOI values and petrographic observations (see section 3.7.2) support

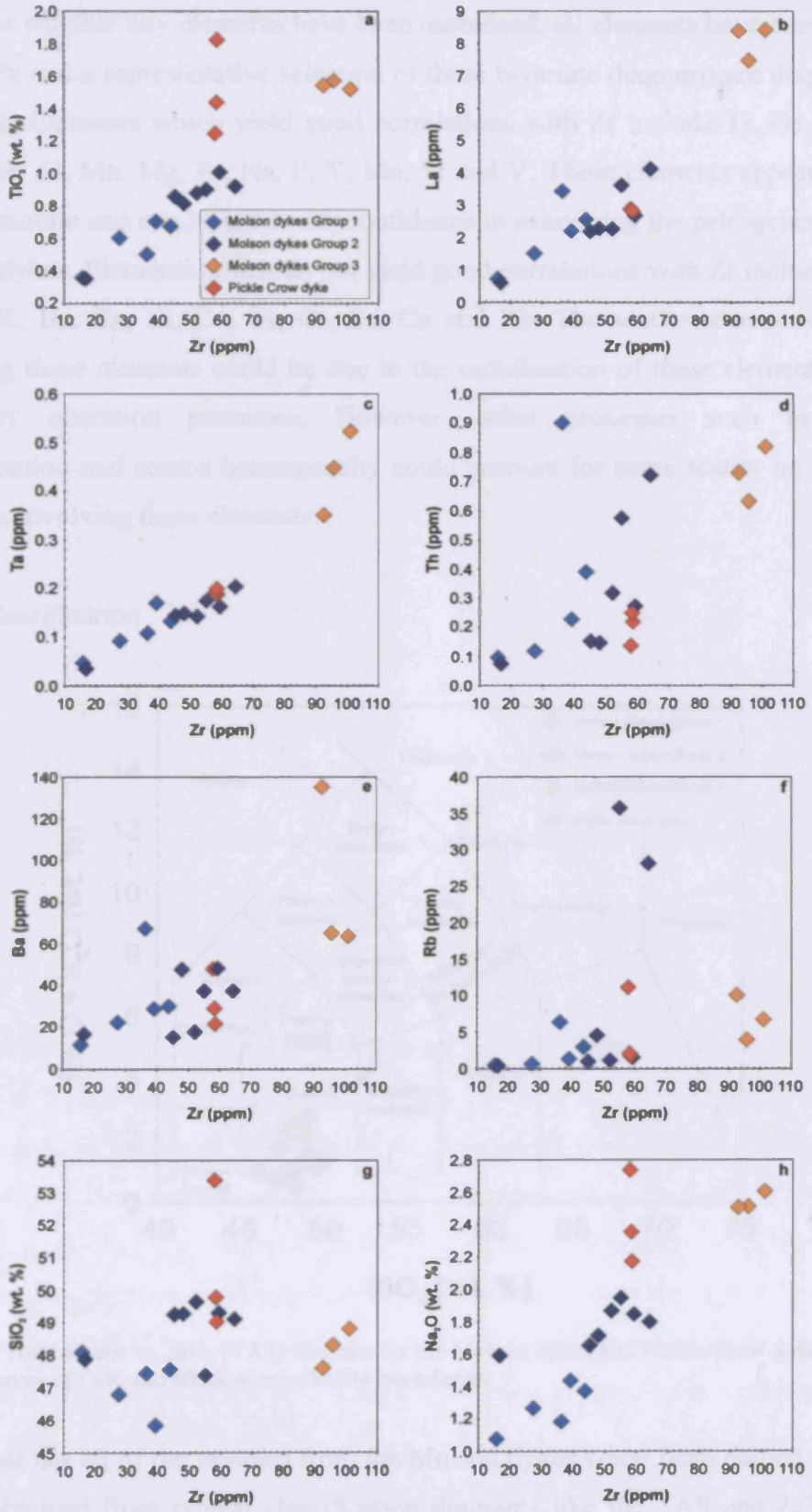

Fig. 4.51. Bivariate diagrams of selected elements vs. Zr for the Molson dykes and Pickle Crow dyke.

the notion that the Molson samples have suffered only a limited degree of alteration. To assess whether any elements have been mobilised, all elements have been plotted against Zr and a representative selection of these bivariate diagrams are displayed in Fig. 4.51. Elements which yield good correlations with Zr include Ti, Ga, Hf, Nb, Ta, REEs, Al, Mn, Mg, Fe, Na, P, Y, Mo, Sr and V. These elements appear to have been immobile and can be used with confidence in examining the petrogenesis of the Molson dykes. Elements which do not yield good correlations with Zr include Th, U, Si, Ca, K, Ba, Zn, Ni, Co, Cr, Cs, Sc, Cu and Rb. The scatter seen on diagrams involving these elements could be due to the mobilisation of these elements during secondary alteration processes. However, other processes such as crustal contamination and source heterogeneity could account for some scatter on bivariate diagrams involving these elements.

4.9.2. Classification

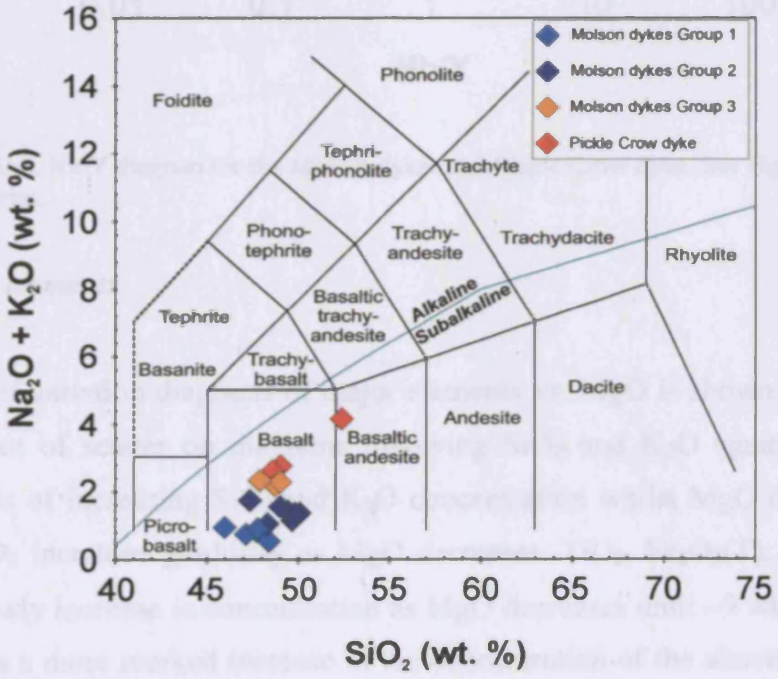

Fig. 4.52. Total alkalis vs. SiO_2 (TAS) diagram for the Molson dykes and Pickle Crow dyke. See Fig. 4.2 for sources of field and alkaline-subalkaline boundaries.

Given that not all of the samples from the Molson dykes come from chilled margins, results obtained from typical classification diagrams like the TAS and Zr/Ti-Nb/Y diagrams may be ambiguous and may not truly represent the composition of the

magma which the dykes transported. However, on both the TAS diagram (Fig. 4.52) and the Zr/Ti-Nb/Y diagram (Fig. 4.53) all of the Molson samples plot in the subalkaline basalt field.

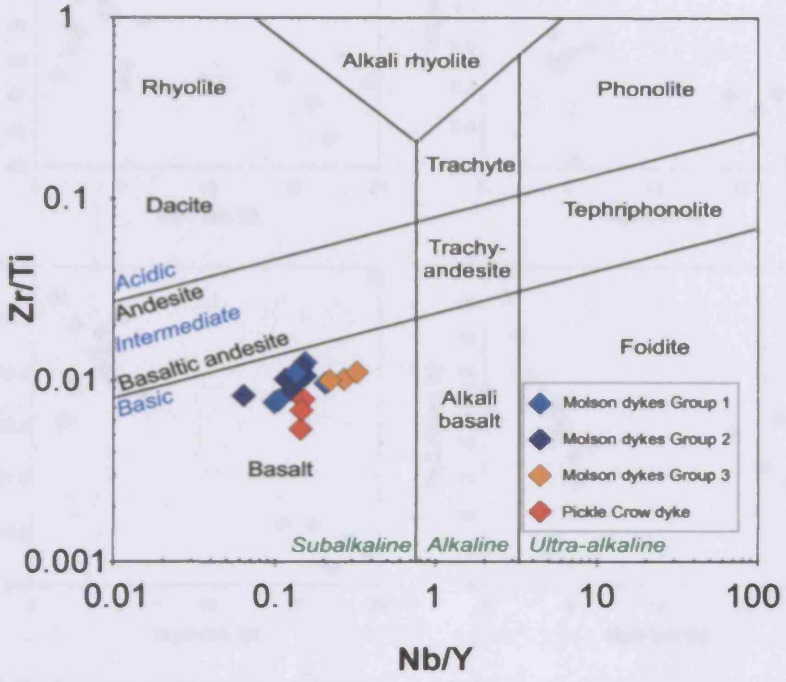

Fig. 4.53. Zr/Ti vs. Nb/Y diagram for the Molson dykes and Pickle Crow dyke. See Fig. 4.3 for source of field boundaries.

4.9.3. Major elements

A selection of variation diagrams of major elements vs. MgO is shown in Fig. 4.54. There is a lot of scatter on diagrams involving SiO_2 and K_2O against MgO but overall trends of increasing SiO_2 and K_2O concentration whilst MgO decreases are visible. Al_2O_3 increases gradually as MgO decreases. TiO_2, Fe_2O_3(T), MnO, Na_2O and P_2O_5 slowly increase in concentration as MgO decreases until ~9 wt. % at which point there is a more marked increase in the concentration of the above elements as MgO decreases. CaO appears to increase slightly in concentration as MgO declines to a concentration of ~9 wt. %, after which CaO starts to decrease in concentration.

On the basis of the diagrams in Fig. 4.54, the Molson dykes can be split into three groups. Group 1 consists of five samples containing 16.53-20.50 wt. % MgO and 10.92-12.74 wt. % Fe_2O_3(T). The Mg# values for this group range from 59.80 to

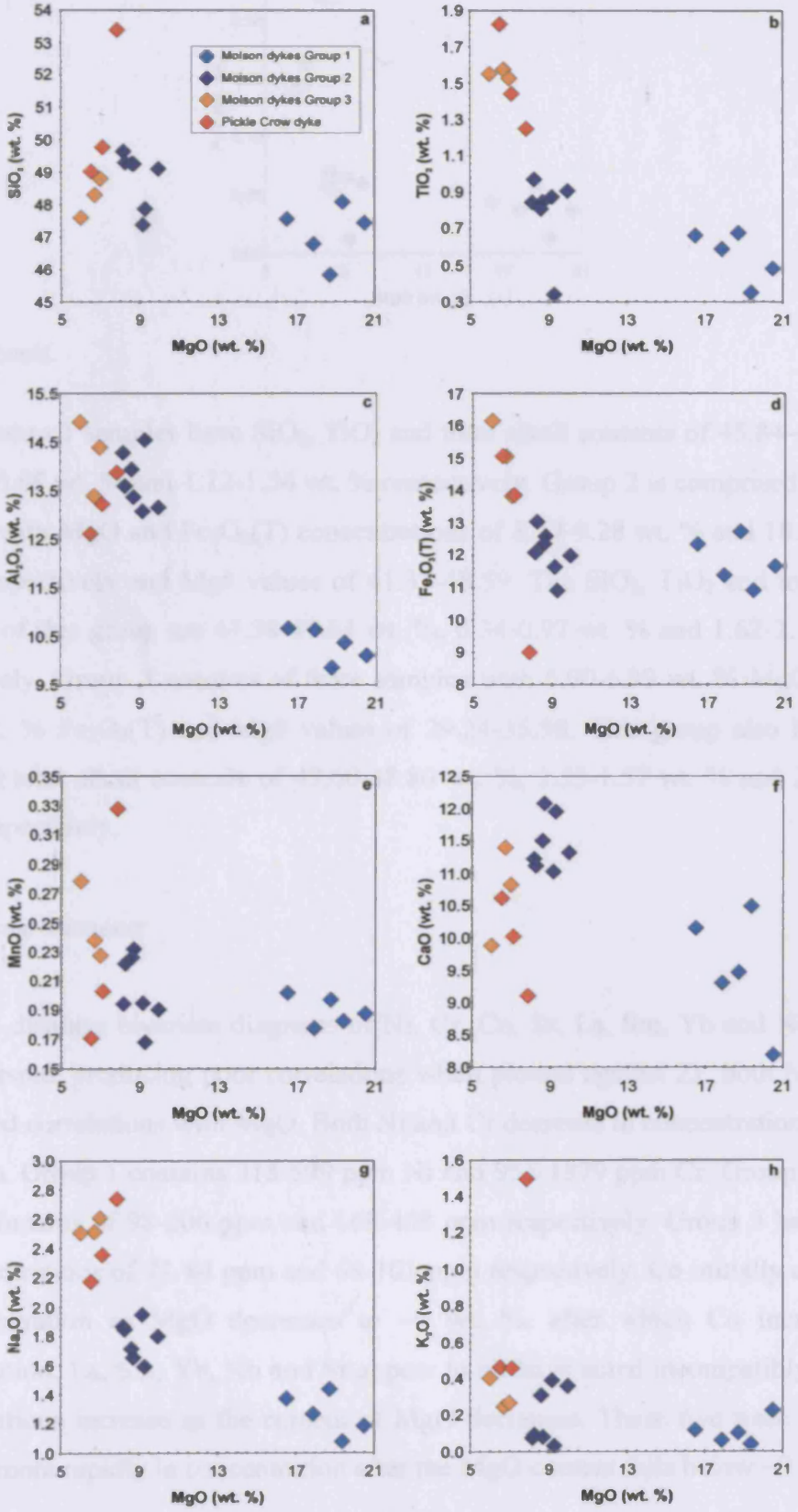

Fig. 4.54. Bivariate diagrams of major elements vs. MgO for the Molson dykes and Pickle Crow dyke.

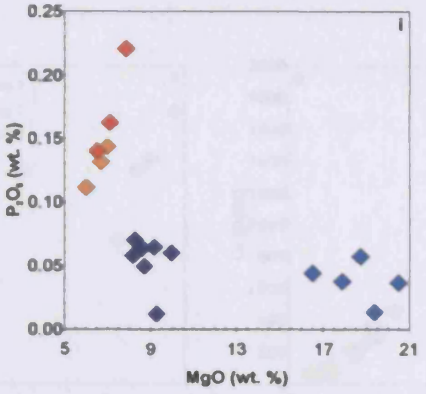

Fig. 4.54. contd.

66.36. Group 1 samples have SiO_2, TiO_2 and total alkali contents of 45.84-48.09 wt. %, 0.35-0.68 wt. % and 1.12-1.54 wt. % respectively. Group 2 is comprised of seven samples with MgO and Fe_2O_3(T) concentrations of 8.17-9.28 wt. % and 10.92-13.04 wt. % respectively and Mg# values of 41.33-48.59. The SiO_2, TiO_2 and total alkali contents of this group are 47.38-49.64 wt. %, 0.34-0.97 wt. % and 1.62-2.34 wt. % respectively. Group 3 consists of three samples with 6.00-6.99 wt. % MgO, 13.82-16.15 wt. % Fe_2O_3(T) and Mg# values of 29.24-35.98. This group also has SiO_2, TiO_2 and total alkali contents of 47.60-48.80 wt. %, 1.53-1.57 wt. % and 2.76-2.91 wt. % respectively.

4.9.4. Trace elements

Fig. 4.55 displays bivariate diagrams of Ni, Cr, Co, Sr, La, Sm, Yb and Nb against MgO. Despite producing poor correlations when plotted against Zr, both Ni and Cr yield good correlations with MgO. Both Ni and Cr decrease in concentration as MgO decreases. Group 1 contains 315-599 ppm Ni and 951-1879 ppm Cr. Group 2 has Ni and Cr contents of 98-206 ppm and 168-458 ppm respectively. Group 3 has Ni and Cr concentrations of 71-84 ppm and 68-101 ppm respectively. Co initially decreases in concentration as MgO decreases to ~9 wt. %, after which Co increases in concentration. La, Sm, Yb, Nb and Sr appear to all have acted incompatibly as their concentrations increase as the content of MgO decreases. These five trace elements increase more rapidly in concentration after the MgO content falls below ~9 wt. %.

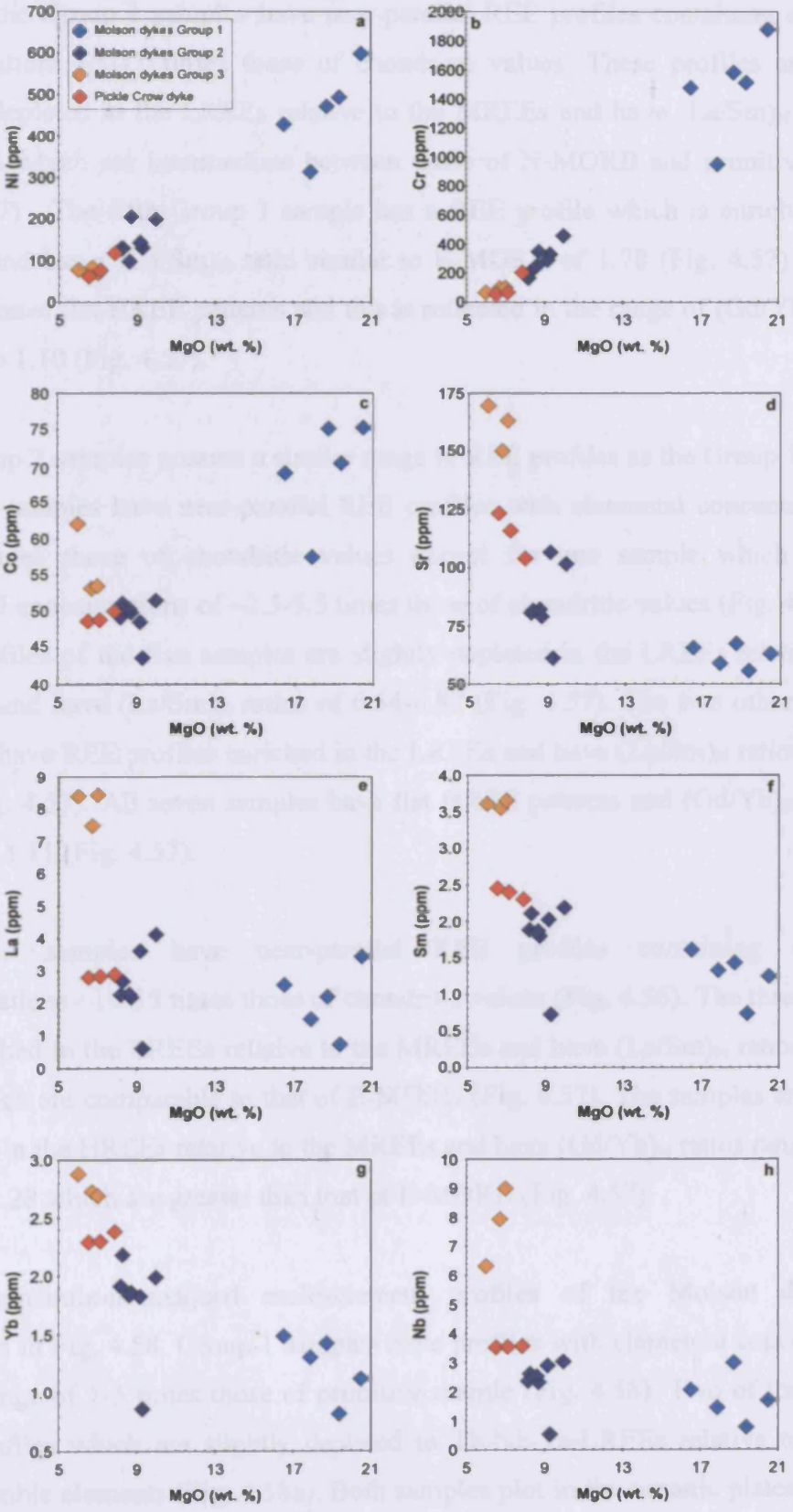

Fig. 4.55. Bivariate diagrams of selected trace elements vs. MgO for the Molson dykes and Pickle Crow dyke.

Chondrite-normalised REE patterns of the Molson dykes are shown in Fig. 4.56. Four of the Group 1 samples have near-parallel REE profiles containing elemental concentrations ~3-11 times those of chondritic values. These profiles are flat to slightly depleted in the LREEs relative to the MREEs and have $(La/Sm)_N$ ratios of 0.64-1.03 which are intermediate between those of N-MORB and primitive mantle (Fig. 4.57) . The fifth Group 1 sample has a REE profile which is enriched in the LREEs and has a $(La/Sm)_N$ ratio similar to E-MORB of 1.78 (Fig. 4.57). All five samples have flat HREE patterns and this is reflected in the range of $(Gd/Yb)_N$ ratios of 1.00 to 1.10 (Fig. 4.57).

The Group 2 samples possess a similar range in REE profiles as the Group 1 samples do. Five samples have near-parallel REE profiles with elemental concentrations of ~9-14 times those of chondritic values except for one sample which contains elemental concentrations of ~2.5-5.5 times those of chondritic values (Fig. 4.56). The REE profiles of the five samples are slightly depleted in the LREEs relative to the MREEs and have $(La/Sm)_N$ ratios of 0.54-0.82 (Fig. 4.57). The two other Group 2 samples have REE profiles enriched in the LREEs and have $(La/Sm)_N$ ratios of 1.16-1.22 (Fig. 4.57). All seven samples have flat HREE patterns and $(Gd/Yb)_N$ ratios of 0.92 and 1.11 (Fig. 4.57).

Group 3 samples have near-parallel REE profiles containing elemental concentrations ~16-35 times those of chondritic values (Fig. 4.56). The three profiles are enriched in the LREEs relative to the MREEs and have $(La/Sm)_N$ ratios of 1.36-1.50 which are comparable to that of E-MORB (Fig. 4.57). The samples are slightly depleted in the HREEs relative to the MREEs and have $(Gd/Yb)_N$ ratios ranging from 1.19 to 1.28 which are greater than that of E-MORB (Fig. 4.57).

Primitive-mantle-normalised multi-element profiles of the Molson dykes are displayed in Fig. 4.58. Group 1 samples have profiles with elemental concentrations in the range of 1-5 times those of primitive mantle (Fig. 4.58). Two of the samples have profiles which are slightly depleted in Th-Nb-Ta-LREEs relative to the less incompatible elements (Fig. 4.58a). Both samples plot in the oceanic plateau field of Condie (2005) on the Zr/Nb-Nb/Th diagram (Fig. 4.59) and one also falls within the Ontong Java Plateau field. Two other samples have flatter multi-element profiles

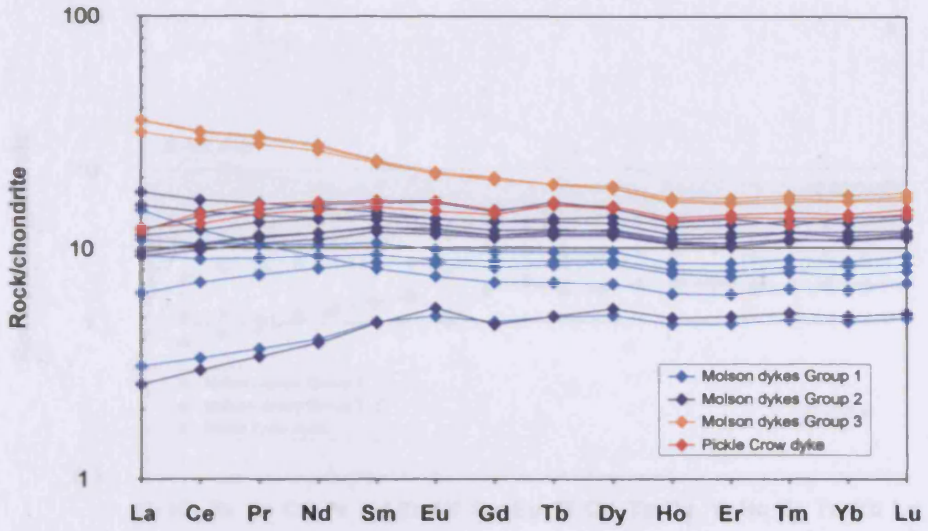

Fig. 4.56. Chondrite-normalised rare earth element (REE) diagram for the Molson dykes and Pickle Crow dyke. Chondrite values same as in Fig. 4.6.

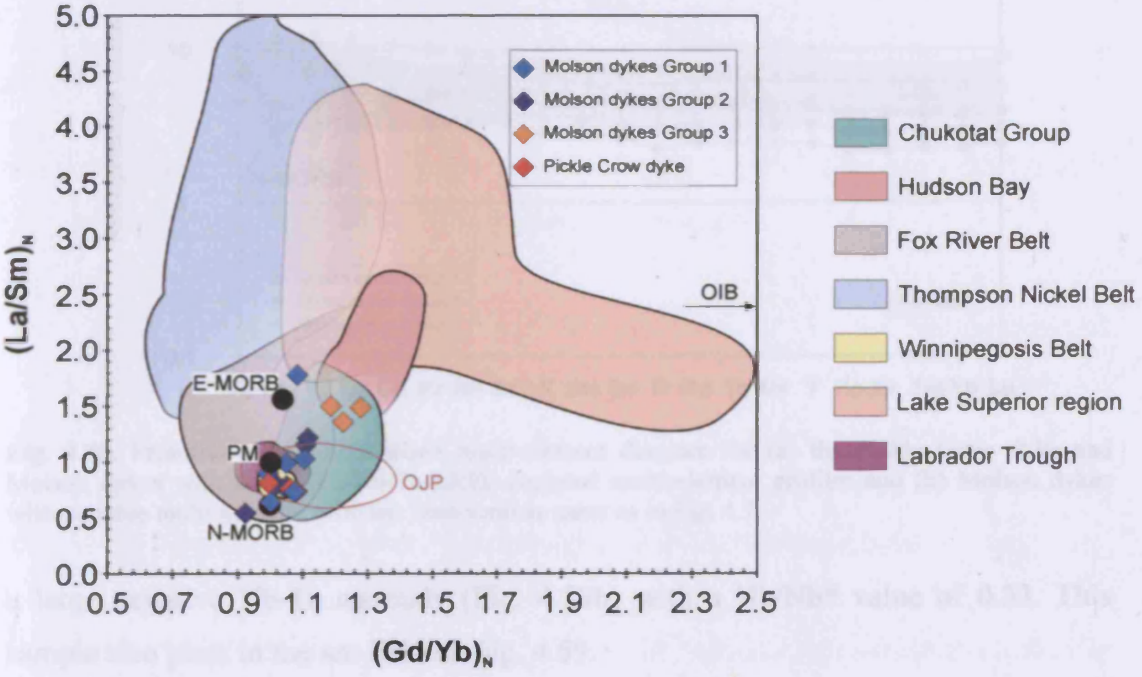

Fig. 4.57. $(La/Sm)_N$ vs. $(Gd/Yb)_N$ diagram for the Molson dykes and Pickle Crow dyke. Data sources same as in Fig. 4.7.

with the exception of small Nb-Ta anomalies (Fig. 4.58b). One of these samples has a positive Nb-Ta anomaly (Nb/Nb* 1.43) and on Fig. 4.59 plots below the Ontong Java Plateau field and towards the E-MORB composition. The other sample has a negative Nb-Ta anomaly (Nb/Nb* 0.70) and plots in the arc field on Fig. 4.59. The remaining Group 1 sample is enriched in the more incompatible elements except for

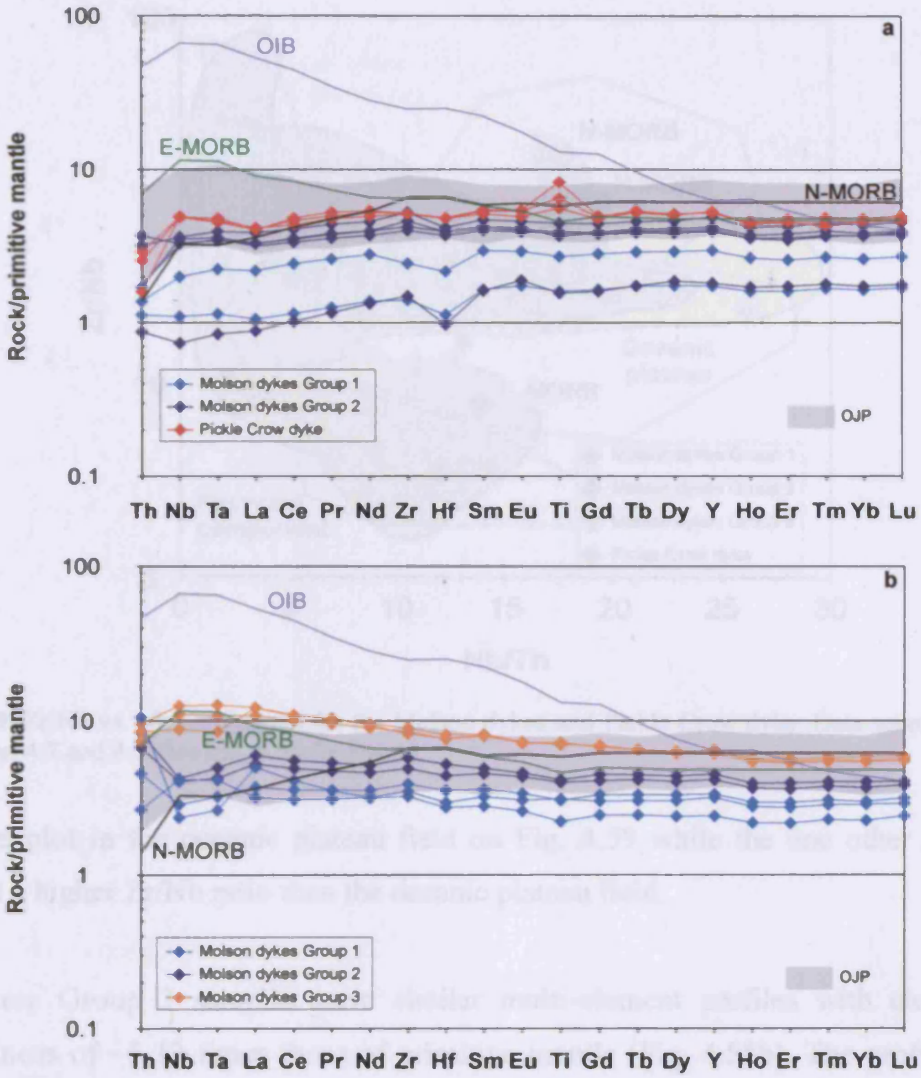

Fig. 4.58. Primitive-mantle-normalised multi-element diagram for (a) the Pickle Crow dyke and Molson dykes with flat to Th-Nb-Ta-LREE-depleted multi-element profiles and (b) Molson dykes with variable multi-element profiles. Data sources same as in Fig. 4.7.

a large negative Nb-Ta anomaly (Fig. 4.58b) with a Nb/Nb* value of 0.33. This sample also plots in the arc field on Fig. 4.59.

Two of the Group 2 samples have multi-element profiles which are slightly enriched in the more incompatible elements and possess small negative Nb-Ta anomalies (Fig. 4.58b) with Nb/Nb* values of 0.60 and 0.68. These two samples plot in the arc field on the Zr/Nb-Nb/Th diagram (Fig. 4.59). The other five Group 2 samples have multi-element profiles which have similarities to the Ontong Java Plateau in that they are flat to slightly depleted in the more incompatible elements (Fig. 4.58a). Four of these

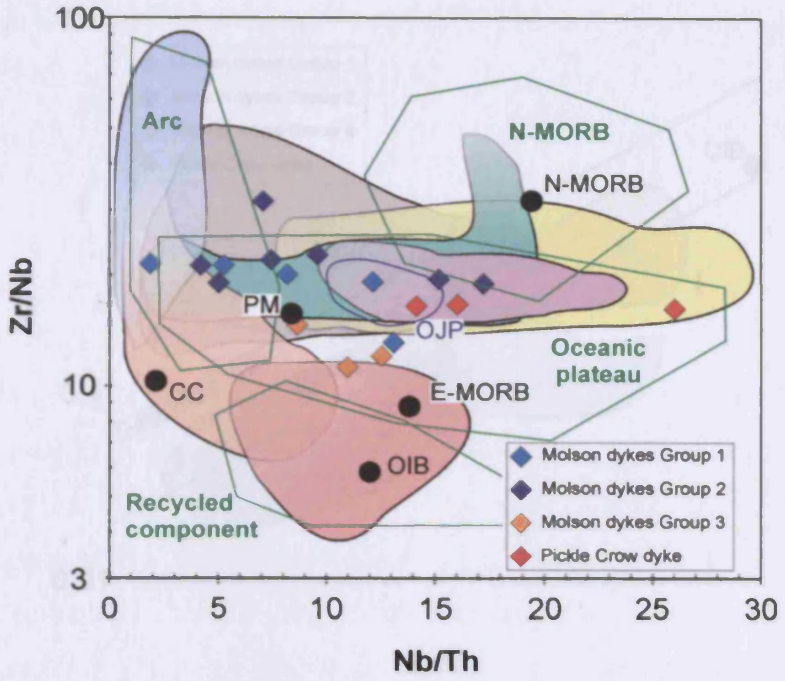

Fig. 4.59. Zr/Nb vs. Nb/Th diagram for the Molson dykes and Pickle Crow dyke. Data sources same as in Figs. 4.7 and 4.9. See Fig. 4.55 for legend.

samples plot in the oceanic plateau field on Fig. 4.59 while the one other sample plots at a higher Zr/Nb ratio than the oceanic plateau field.

The three Group 3 samples have similar multi-element profiles with elemental abundances of ~5-13 times those of primitive mantle (Fig. 4.58b). The profiles are enriched in the more incompatible elements and contain no significant Nb-Ta anomalies. On Fig. 4.59 the samples plot towards the lower part of the oceanic plateau field between the primitive mantle and E-MORB compositions.

On the Nb/Y-Zr/Y diagram (Fig. 4.60), nine of the samples plot within the Icelandic plume tramlines and six fall just below the lower tramline. Of the six samples plotting below the lower tramline, two are Group 1 samples with negative Nb-Ta anomalies. The other four are Group 2 samples. All but three of the samples plot within the Ontong Java Plateau field on Fig. 4.60. These three samples include two Group 3 samples which plot close to the E-MORB composition and one Group 2 sample which has a multi-element profile depleted in the more incompatible elements (Fig. 4.58a).

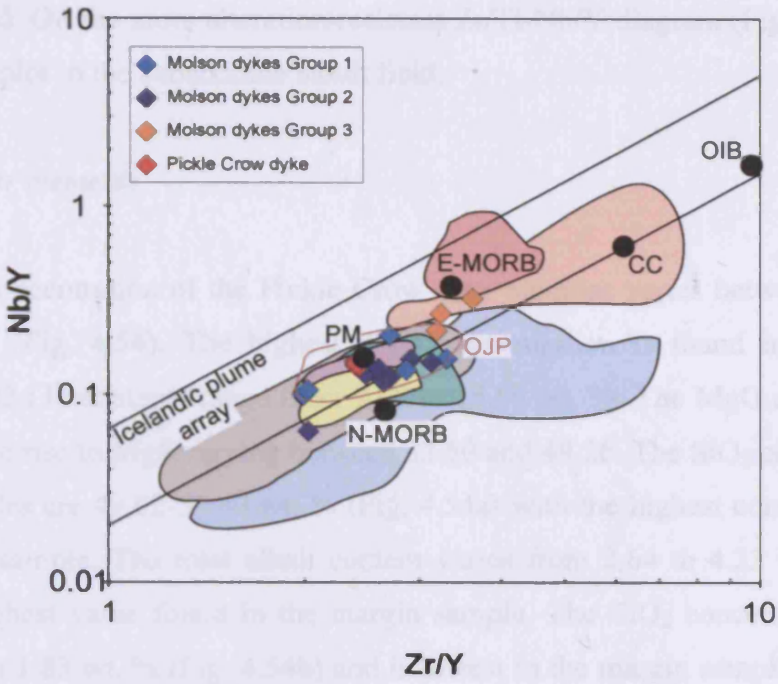

Fig. 4.60. Nb/Y vs. Zr/Y diagram for the Molson dykes and Pickle Crow dyke. Data sources same as in Figs. 4.7 and 4.9. See Fig. 4.55 for legend.

4.10. Pickle Crow dyke

4.10.1. Alteration and element mobility

Only three samples of the Pickle Crow dyke have been analysed and so it is not possible to accurately assess the potential for element mobility in the dyke. However, the reasonably low LOI values (0.91-1.98 wt. %) and petrographic observations (see section 3.8.2) suggest that the Pickle Crow dyke has only undergone a limited degree of post-magmatic alteration. Therefore it is assumed that elements with intermediate ionic potential (e.g. high field strength and rare earth elements) were immobile and provide the best means of studying the petrogenesis of the dyke. The three samples of the Pickle Crow dyke have been plotted with the samples of the Molson dykes in a selection of bivariate diagrams in Figs. 4.51, 4.54 and 4.55.

4.10.2. Classification

On the TAS diagram (Fig. 4.52) the two samples from the interior of the dyke plot in the subalkaline basalt field while the margin sample plots in the subalkaline basaltic

andesite field. On the more alteration-resistant Zr/Ti-Nb/Y diagram (Fig. 4.53) all of the samples plot in the subalkaline basalt field.

4.10.3. Major elements

The MgO concentration of the Pickle Crow dyke samples varies between 6.53 and 7.86 wt. % (Fig. 4.54). The highest MgO concentration is found in the margin sample. $Fe_2O_3(T)$ contents range from 9.00 to 15.06 wt. %. The MgO and $Fe_2O_3(T)$ contents give rise to Mg# varying between 32.50 and 49.26. The SiO_2 concentrations of the samples are 49.02-53.40 wt. % (Fig. 4.54a) with the highest content found in the margin sample. The total alkali content varies from 2.64 to 4.23 wt. %, again with the highest value found in the margin sample. The TiO_2 concentration varies from 1.25 to 1.83 wt. % (Fig. 4.54b) and is lowest in the margin sample and highest in the most interior sample.

4.10.4. Trace elements

The margin sample contains higher amounts of Ni and Cr than the other two samples. The overall ranges in Ni and Cr contents are 62-119 ppm and 57-206 ppm respectively (Fig. 4.55). All three samples contain very similar concentrations of incompatible elements. For example, the overall ranges in La and Nb concentrations are 2.81-2.90 ppm and 3.52-3.57 ppm respectively (Fig. 4.55).

The chondrite-normalised REE profiles of the Pickle Crow dyke samples are displayed in Fig. 4.56 and are all very similar. The profiles contain elemental abundances of ~12-16 times those of chondritic values and are slightly depleted in the LREEs relative to the MREEs. The $(La/Sm)_N$ ratios of the samples are 0.74-0.81 and are intermediate between those of primitive mantle and N-MORB (Fig. 4.57). $(Gd/Yb)_N$ ratios vary from 0.99 to 1.08 (Fig. 4.57). The primitive-mantle-normalised multi-element profiles of the Pickle Crow dyke are shown in Fig. 4.58a. All three samples have relatively flat patterns and element abundances ~5 times those of primitive mantle, with the exception of Th and Ti. Th is depleted relative to all the other elements and so the samples have Nb/Th ratios of 14-26 which plot in the oceanic plateau field on Fig. 4.59. Positive Ti anomalies are present in the multi-

element profiles of all three samples but are larger in the samples from the dyke interior. The Ti/Ti* value of the margin sample is 1.16 while the two interior samples have Ti/Ti* values of 1.27 and 1.59. The Pickle Crow dyke flat multi-element profiles with Th depletion are similar to the multi-element profiles of the Ontong Java Plateau (Fig. 4.58a).

On the Nb/Y-Zr/Y diagram (Fig. 4.60) all three samples plot close together within the Icelandic plume tramlines. The three samples plot close to the composition of primitive mantle and lie within the field for the Ontong Java Plateau (Fig. 4.60).

4.11. Gunflint Formation of the Lake Superior region

4.11.1. Alteration and element mobility

The Gunflint Formation lavas show evidence of significant post-magmatic alteration in their thin section petrography (see section 3.9.2) and LOI values of 5.77-9.02 wt. %. Unfortunately, only four samples of the Gunflint lavas were analysed which is too few a number to make inferences concerning element mobility. However, if the Gunflint lavas are plotted with all the other coeval igneous rocks of the Lake Superior region on bivariate diagrams with Zr as the abscissa (Fig. 4.61), then the Gunflint lavas fit well with trends formed by the other magmatic suites for many elements. Therefore elements which were probably immobile and can be used with confidence in assessing the petrogenesis of the Gunflint Formation include Sc, V, Y, Co, Ni, Ga, Nb, Ta, Cr, REEs, Hf, Th, U, Ti, Al, Fe, Mn, Mg, K and P. Elements which do not produce good correlations with Zr and were probably mobile during alteration of the Gunflint Formation and coeval Lake Superior magmatic units include Zn, Cu, Sr, Ba, Rb, Cs, Si, Ca and Na.

4.11.2. Classification

The TAS diagram (Fig. 4.62) classifies the Gunflint Formation as a heterogeneous suite of rock types. One sample plots in the subalkaline basalt field, another sample in the subalkaline basaltic andesite field and two samples in the alkaline trachybasalt

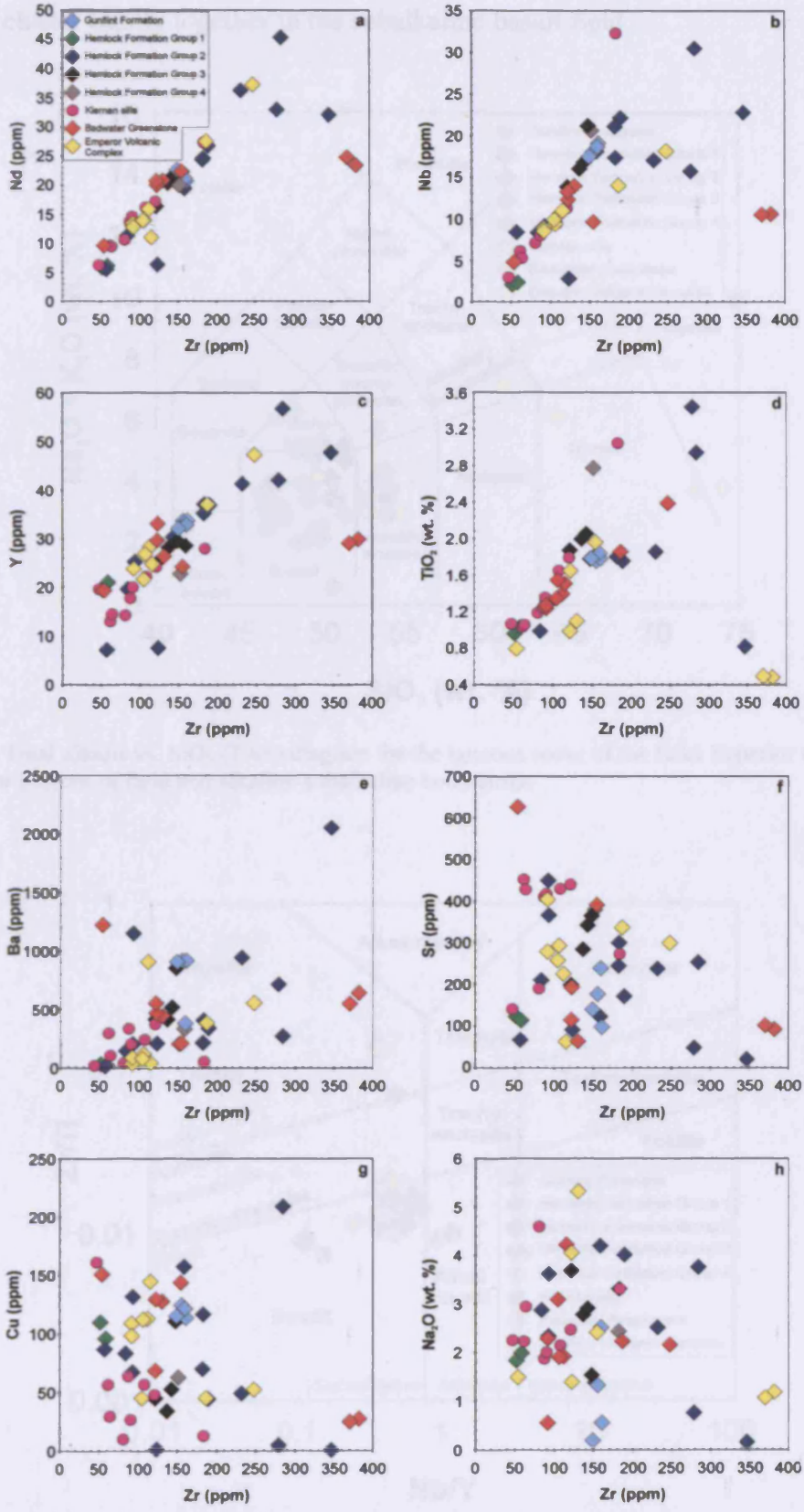

Fig. 4.61. Bivariate diagrams of selected elements vs. Zr for the igneous rocks of the Lake Superior region.

field (Fig. 4.62). Unlike in Fig. 4.62, on the Zr/Ti-Nb/Y diagram (Fig. 4.63) all the samples cluster tightly together in the subalkaline basalt field.

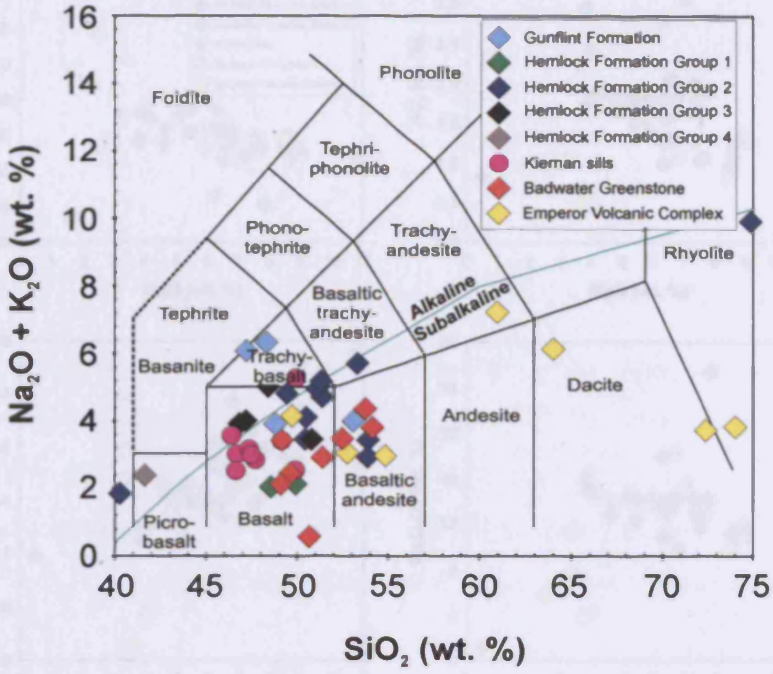

Fig. 4.62. Total alkalis vs. SiO_2 (TAS) diagram for the igneous rocks of the Lake Superior region. See Fig. 4.2 for sources of field and alkaline-subalkaline boundaries.

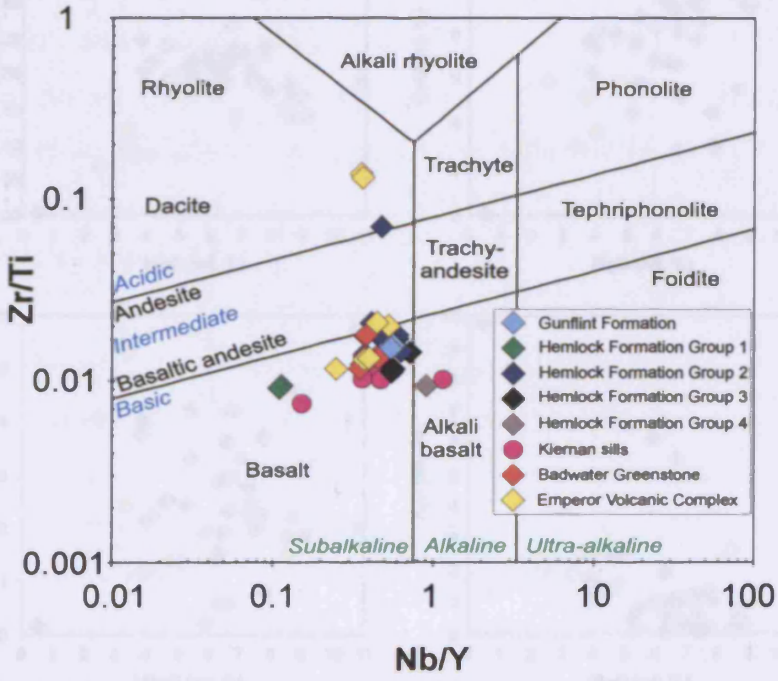

Fig. 4.63. Zr/Ti vs. Nb/Y diagram for the igneous rocks of the Lake Superior region. See Fig. 4.3 for source of field boundaries.

4.11.3. Major elements

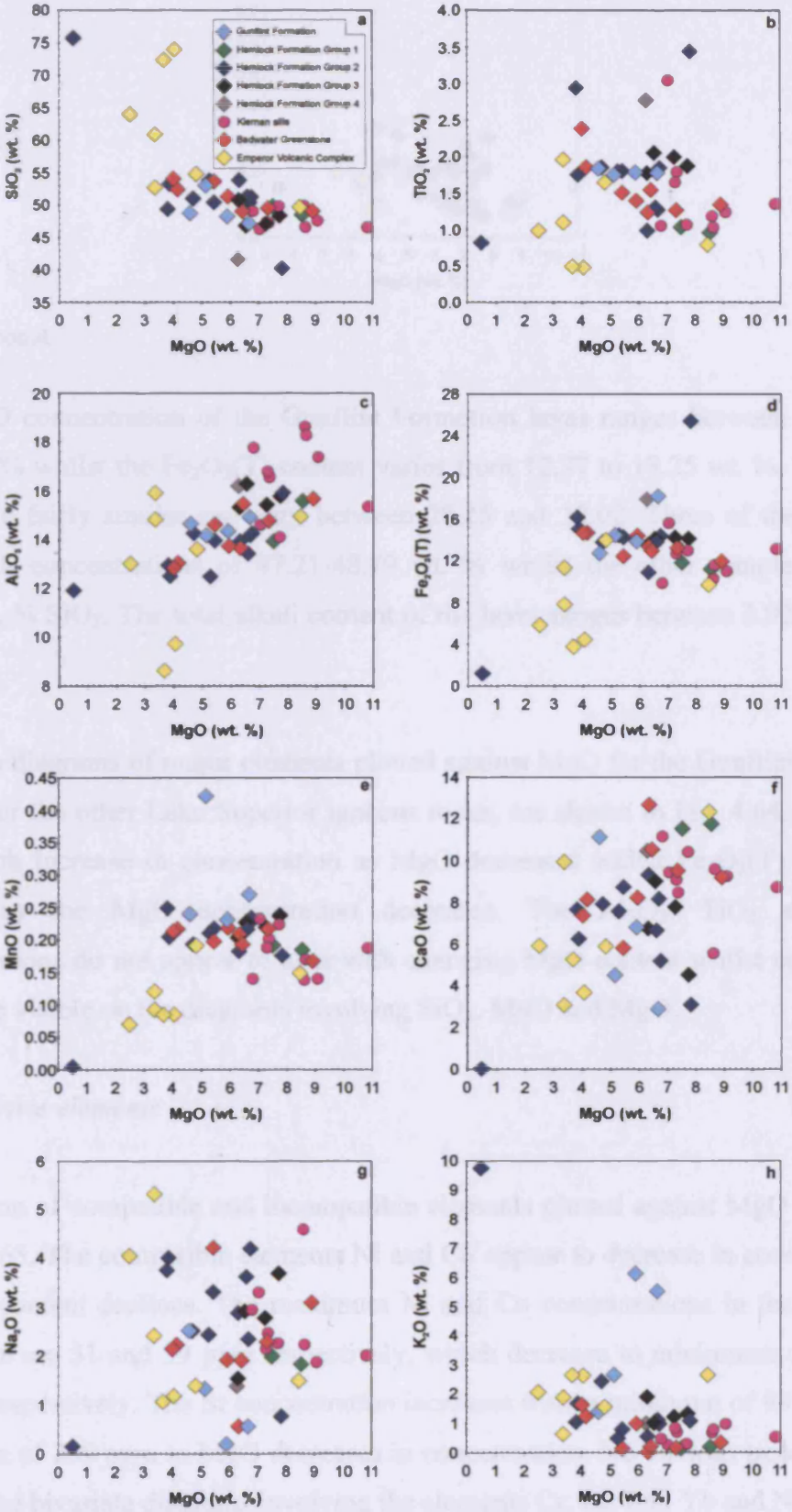

Fig. 4.64. Bivariate diagrams of major elements vs. MgO for the igneous rocks of the Lake Superior region.

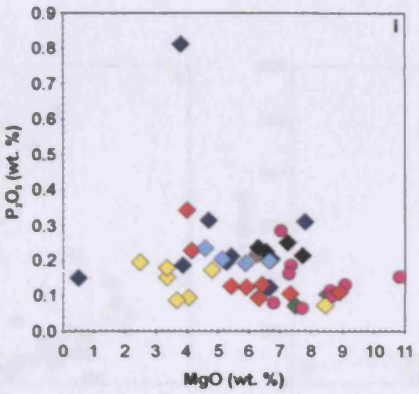

Fig. 4.64. contd.

The MgO concentration of the Gunflint Formation lavas ranges between 4.59 and 6.66 wt. % whilst the $Fe_2O_3(T)$ content varies from 12.77 to 18.25 wt. %. The Mg# values are fairly similar and vary between 28.25 and 32.02. Three of the samples have SiO_2 concentrations of 47.21-48.79 wt. % whilst the other sample contains 53.09 wt. % SiO_2. The total alkali content of the lavas ranges between 3.92 and 6.33 wt. %.

Variation diagrams of major elements plotted against MgO for the Gunflint lavas, as well as for the other Lake Superior igneous rocks, are shown in Fig. 4.64. CaO and Na_2O both increase in concentration as MgO decreases whilst $Fe_2O_3(T)$ and K_2O decline as the MgO concentration decreases. The Al_2O_3, TiO_2 and P_2O_5 concentrations do not appear to alter with changing MgO content whilst no obvious trends are visible on the diagrams involving SiO_2, MnO and MgO.

4.11.4. Trace elements

A selection of compatible and incompatible elements plotted against MgO is shown in Fig. 4.65. The compatible elements Ni and Co appear to decrease in concentration as MgO content declines. The maximum Ni and Co concentrations in the Gunflint Formation are 51 and 59 ppm respectively, which decrease to minimums of 22 and 34 ppm respectively. The Sr concentration increases from a minimum of 98 ppm to a maximum of 239 ppm as MgO decreases in concentration. No obvious trends can be seen on the bivariate diagrams involving the elements Cr, La, Sm, Yb and Nb.

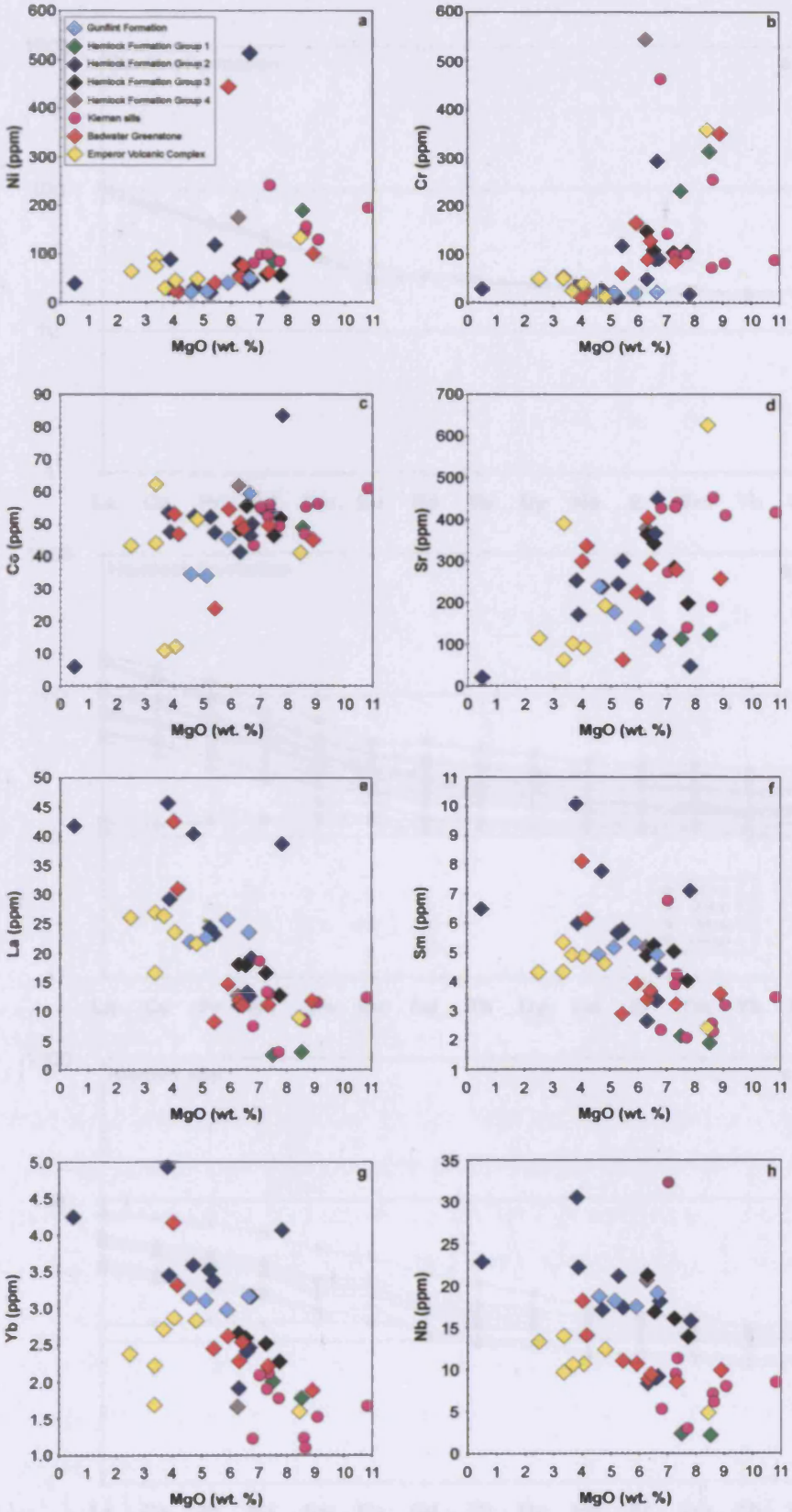

Fig. 4.65. Bivariate diagrams for selected trace elements vs. MgO for the igneous rocks of the Lake Superior region.

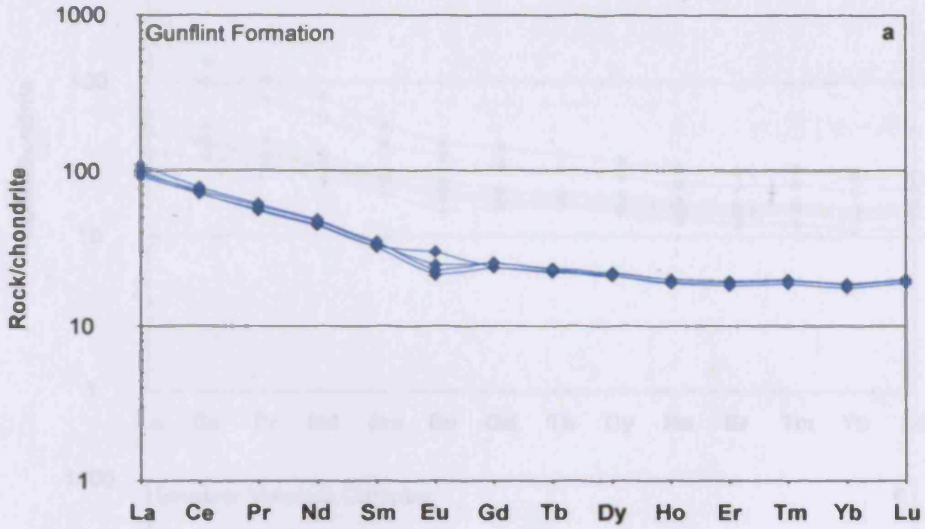
Gunflint Formation
a
Rock/chondrite
1000
100
10
1
La Ce Pr Nd Sm Eu Gd Tb Dy Ho Er Tm Yb Lu

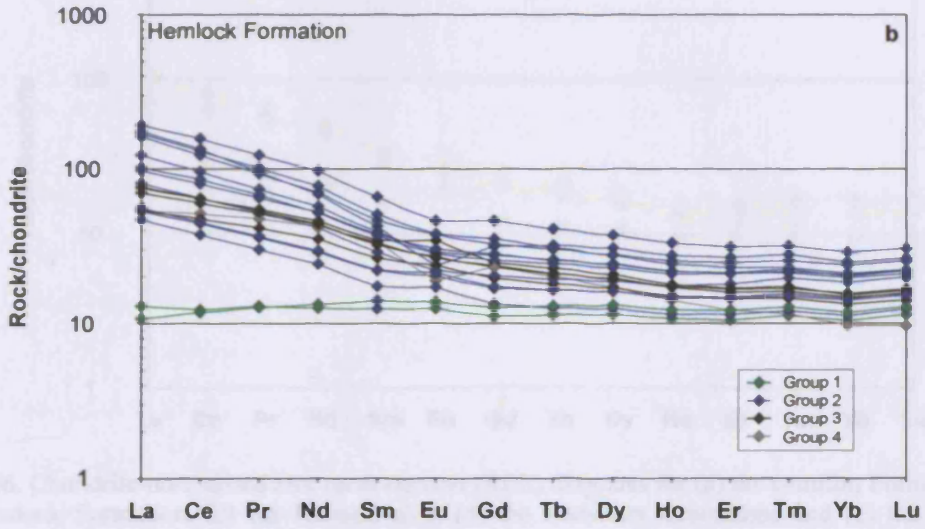
Hemlock Formation
b
Rock/chondrite
1000
100
10
1
Group 1
Group 2
Group 3
Group 4
La Ce Pr Nd Sm Eu Gd Tb Dy Ho Er Tm Yb Lu

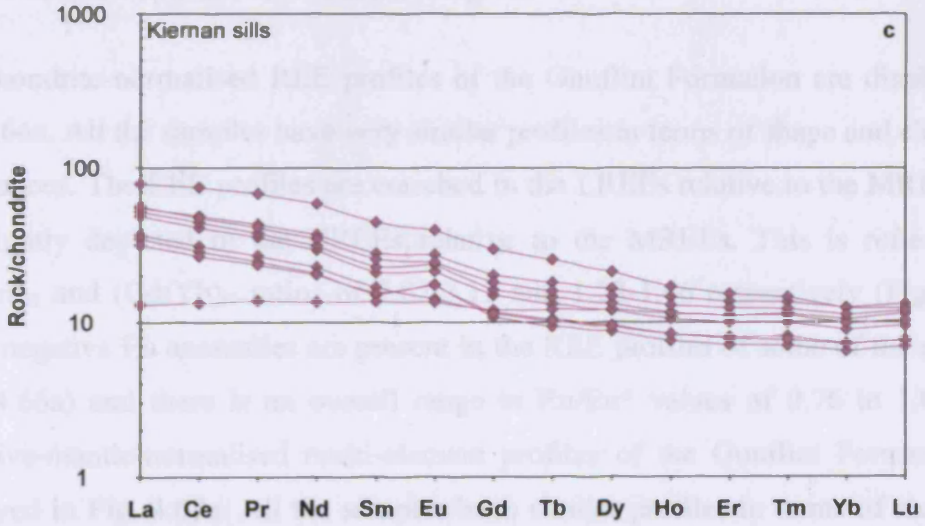
Kiernan sills
c
Rock/chondrite
1000
100
10
1
La Ce Pr Nd Sm Eu Gd Tb Dy Ho Er Tm Yb Lu

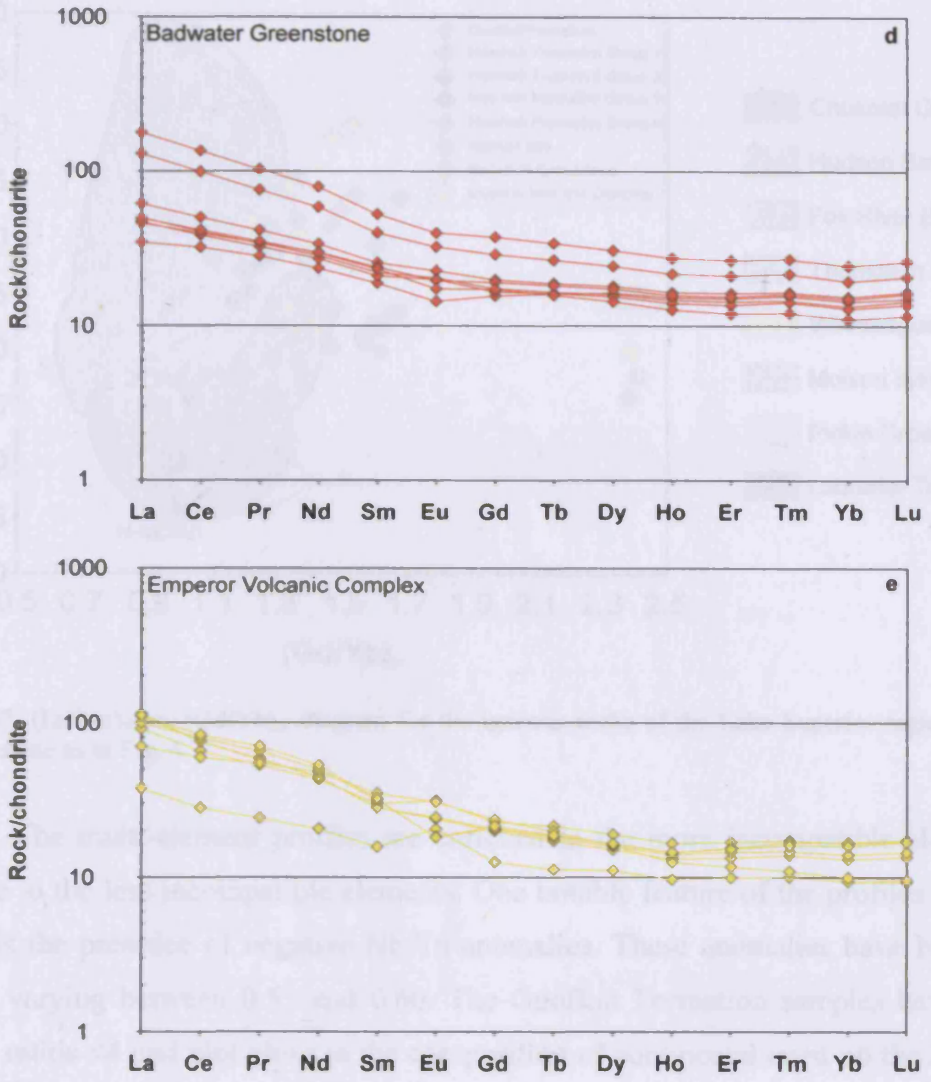

Fig. 4.66. Chondrite-normalised rare earth element (REE) diagrams for (a) the Gunflint Formation, (b) the Hemlock Formation, (c) the Kiernan sills, (d) the Badwater Greenstone and (e) the Emperor Volcanic Complex. Chondrite values same as in Fig. 4.6.

The chondrite-normalised REE profiles of the Gunflint Formation are displayed in Fig. 4.66a. All the samples have very similar profiles in terms of shape and elemental abundances. The REE profiles are enriched in the LREEs relative to the MREEs and are slightly depleted in the HREEs relative to the MREEs. This is reflected by $(La/Sm)_N$ and $(Gd/Yb)_N$ ratios of 2.82-3.11 and 1.28-1.46 respectively (Fig. 4.67). Small negative Eu anomalies are present in the REE profiles of some of the samples (Fig. 4.66a) and there is an overall range in Eu/Eu* values of 0.76 to 1.08. The primitive-mantle-normalised multi-element profiles of the Gunflint Formation are displayed in Fig. 4.68a. All the samples have similar profiles in terms of shape and elemental abundances which are ~6-60 times those of primitive mantle values (Fig.

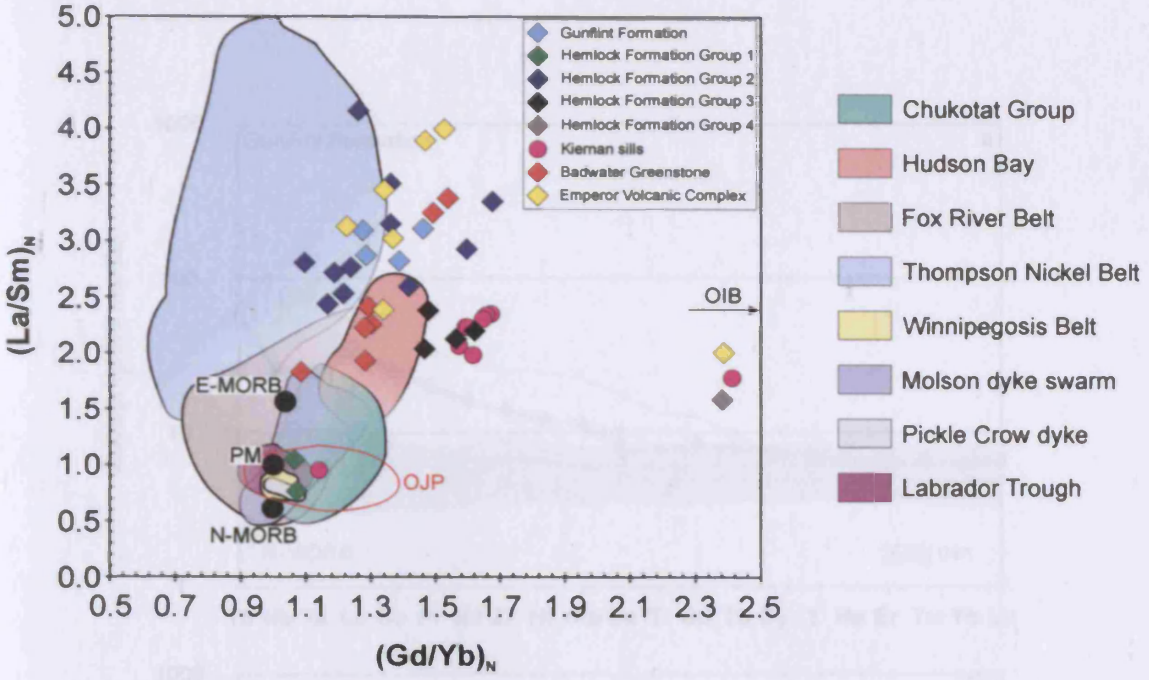

Fig. 4.67. $(La/Sm)_N$ vs. $(Gd/Yb)_N$ diagram for the igneous rocks of the Lake Superior region. Data sources same as in Fig. 4.7.

4.68a). The multi-element profiles are enriched in the more incompatible elements relative to the less incompatible elements. One notable feature of the profiles in Fig. 4.68a is the presence of negative Nb-Ta anomalies. These anomalies have Nb/Nb* values varying between 0.53 and 0.60. The Gunflint Formation samples have low Nb/Th ratios <4 and plot close to the composition of continental crust on the Zr/Nb-Nb/Th diagram in Fig. 4.69. On the Nb/Y-Zr/Y diagram (Fig. 4.70) the samples plot within the Icelandic plume tramlines and between the compositions of end-members E-MORB and continental crust.

4.12. Hemlock Formation of the Lake Superior region

4.12.1. Alteration and element mobility

Petrographical observations suggest that the Hemlock Formation samples have been metamorphosed to greenschist facies (see section 3.9.4). Although the majority of samples possess LOI values <4 wt. %, a few samples have LOI contents of up to 7.51 wt. %. All elements have been plotted against Zr in order to assess potential element mobility and a representative selection of these diagrams is shown in Fig. 4.61 along

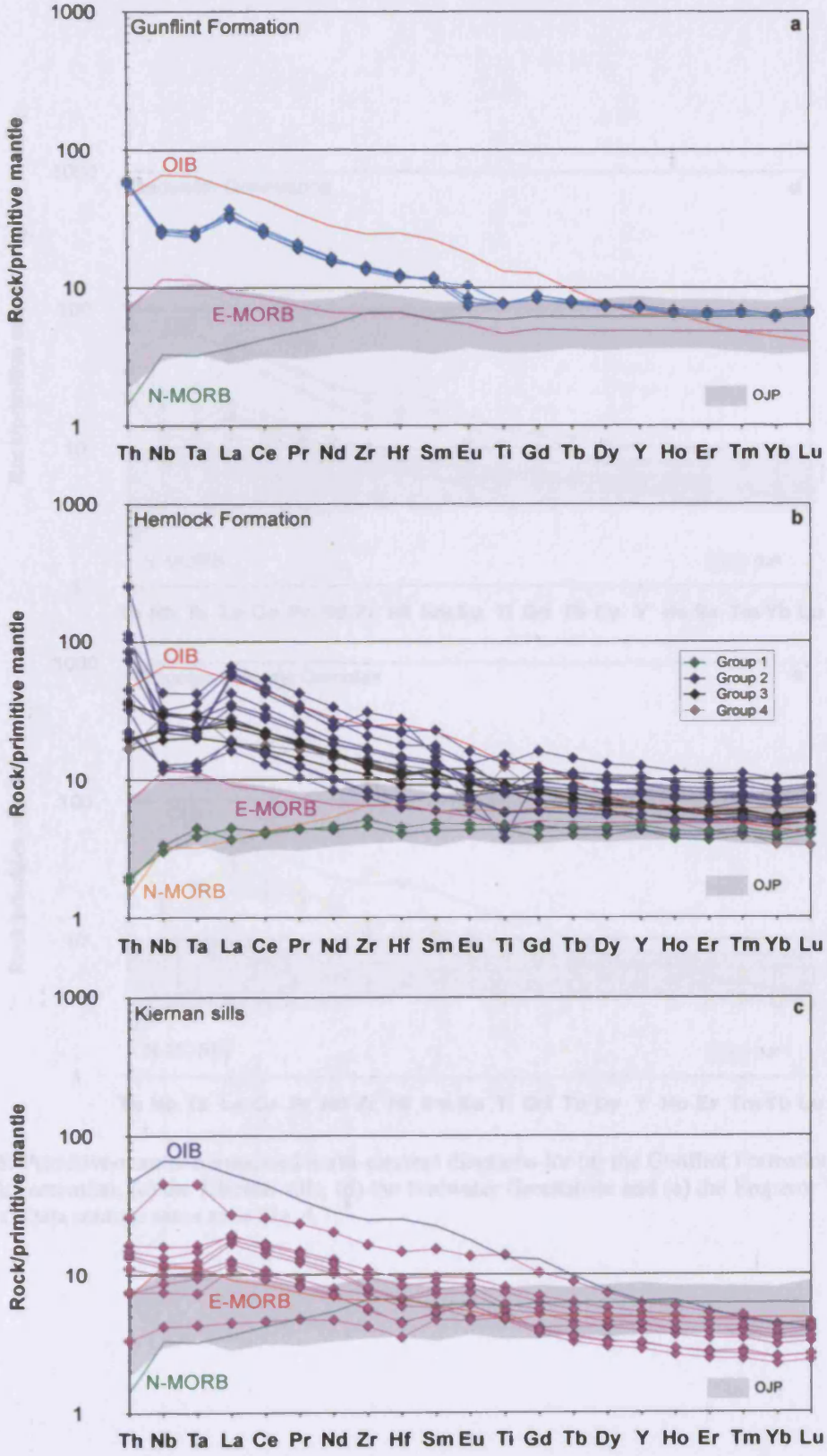
Gunflint Formation
a
Hemlock Formation
b
Kiernan sills
c
Rock/primitive mantle
1000
100
10
1
OIB
E-MORB
N-MORB
OJP
Group 1
Group 2
Group 3
Group 4
Th Nb Ta La Ce Pr Nd Zr Hf Sm Eu Ti Gd Tb Dy Y Ho Er Tm Yb Lu

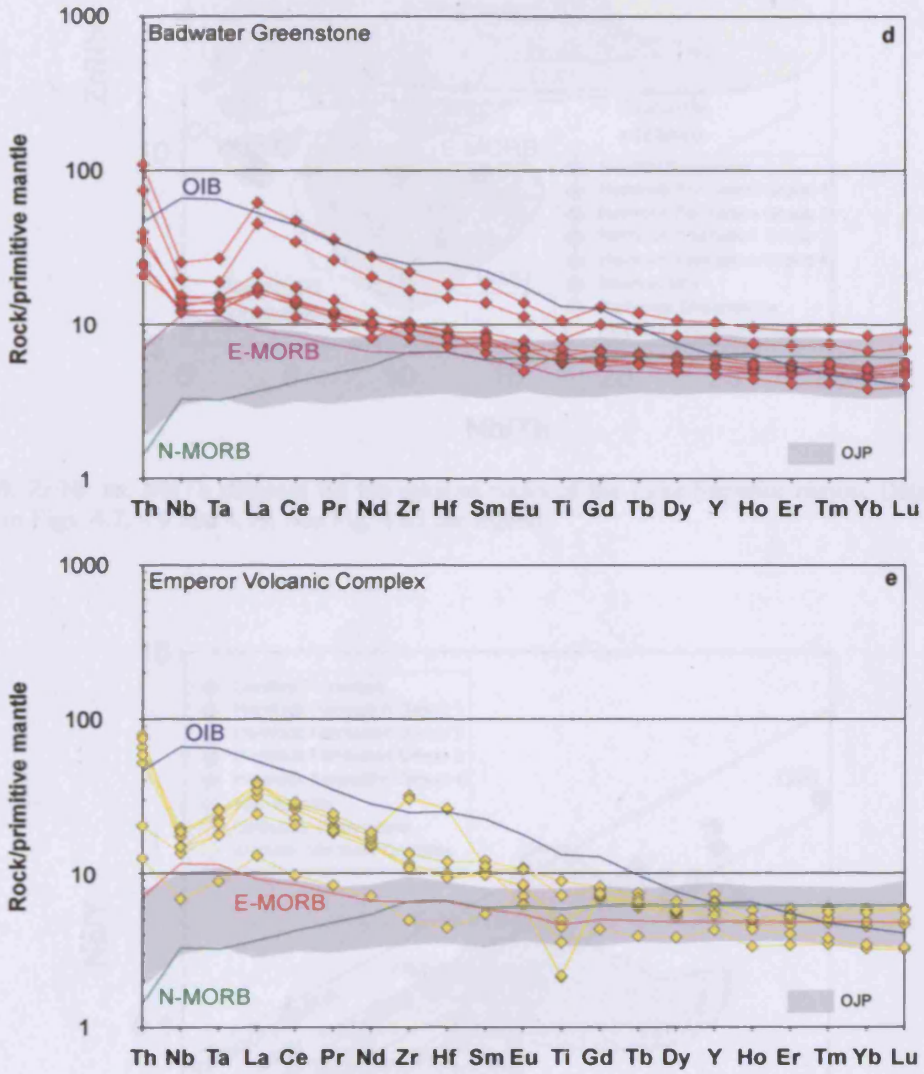

Fig. 4.68. Primitive-mantle-normalised multi-element diagrams for (a) the Gunflint Formation, (b) the Hemlock Formation, (c) the Kiernan sills, (d) the Badwater Greenstone and (e) the Emperor Volcanic Complex. Data sources same as in Fig. 4.7.

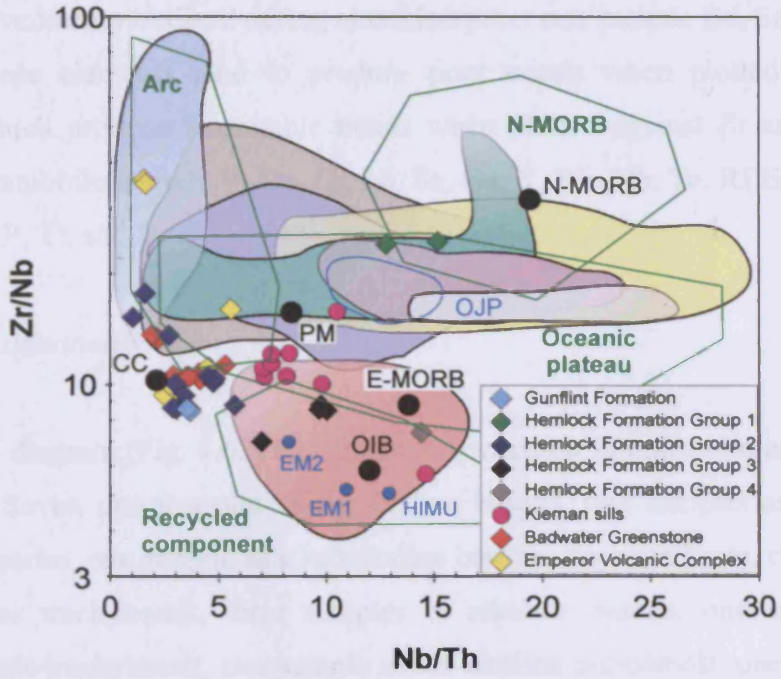

Fig. 4.69. Zr/Nb vs. Nb/Th diagram for the igneous rocks of the Lake Superior region. Data sources same as in Figs. 4.7, 4.9 and 4.19. See Fig. 4.65 for legend.

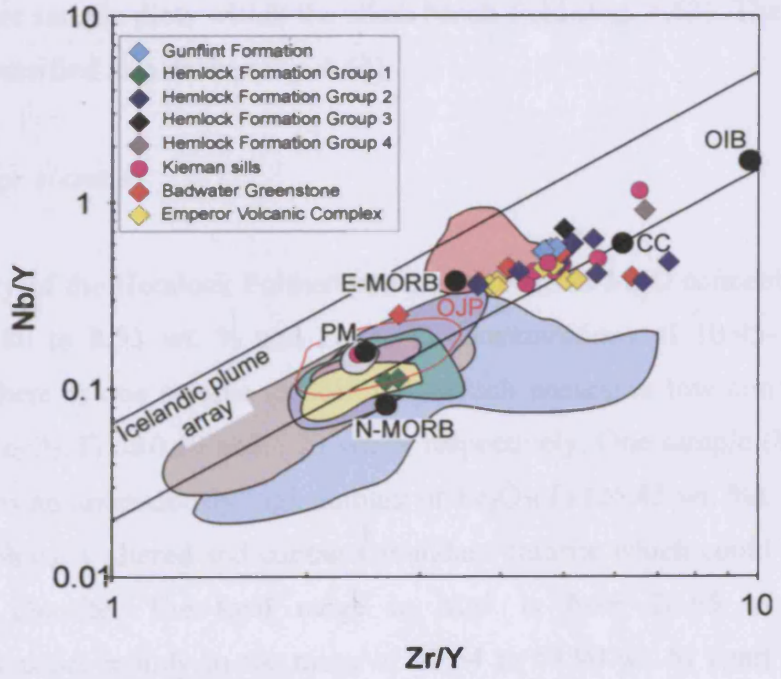

Fig. 4.70. Nb/Y vs. Zr/Y diagram for the igneous rocks of the Lake Superior region. Data sources same as in Figs. 4.7 and 4.9. See Fig. 4.65 for legend.

with samples from the other Lake Superior magmatic units. The elements which appear to have been mobilised during alteration processes include Ba, Sr, Ca, Na, Cu and Cs. These elements tend to produce poor trends when plotted against Zr. Elements which produce reasonable trends when plotted against Zr and appear to have been immobile include V, Co, Cr, Ni, Sc, Ga, Y, Rb, Nb, Ta, REEs, Ti, Al, Fe, Mn, Mg, K, P, Th and U.

4.12.2. Classification

On the TAS diagram (Fig. 4.62) the Hemlock Formation samples plot as a variety of rock types. Seven samples plot as subalkaline basalts, two samples as subalkaline basaltic andesites, one sample as a subalkaline basaltic trachyandesite, one sample as a subalkaline trachybasalt, three samples as alkaline basalts, one sample as an alkaline basalt-trachybasalt, one sample as an alkaline picrobasalt, one sample as a subalkaline rhyolite, and one sample plots to the left hand side of all the rock type fields (Fig. 4.62). On the Zr/Ti-Nb/Y diagram (Fig. 4.63) all but three of the samples plot in the subalkaline basalt field. One sample plots in the basaltic andesite field while another sample plots within the alkali basalt field (Fig. 4.63). The lowest MgO sample is classified as a dacite (Fig. 4.63).

4.12.3. Major elements

The majority of the Hemlock Formation samples possess MgO concentrations in the range of 3.80 to 8.53 wt. % and $Fe_2O_3(T)$ concentrations of 10.95-17.99 wt. %. However, there is one sample (MMH08-6) which possesses low concentrations of MgO and $Fe_2O_3(T)$ of 0.50 and 1.23 wt. % respectively. One sample (MMH08-15b) also contains an anomalously high amount of $Fe_2O_3(T)$ (25.43 wt. %). MMH08-15b is petrographically altered and contains abundant chlorite which could be an Fe-rich variety of chlorite. The total range in Mg# is from 20.65 to 45.70. SiO_2 concentrations are mainly in the range of 41.64 to 53.90 wt. % apart from the low MgO sample that contains 75.77 wt. % SiO_2 and the high $Fe_2O_3(T)$ sample that contains 40.28 wt. % SiO_2. Total alkali contents are 1.85-5.72 wt. % except for the low MgO sample that contains 9.91 wt. % total alkalis.

Major element variation diagrams with MgO as the abscissa are shown in Fig. 4.64. Although some scattering is seen on most diagrams in Fig. 4.64, general trends can usually be made out. Both SiO_2 and K_2O increase in concentration as MgO decreases whilst Al_2O_3 and CaO decrease in concentration with decreasing MgO. Fe_2O_3(T), MnO, Na_2O and P_2O_5 appear to increase in concentration as MgO decreases but then all reach minimum concentrations in the lowest MgO sample.

4.12.4. Trace elements

A selection of trace elements are plotted against MgO in bivariate diagrams displayed in Fig. 4.65. Despite some scatter on Fig. 4.65, Ni tends to decrease with decreasing MgO from a maximum value of 514 ppm to a minimum of 10 ppm although all but one sample (MMH08-21) fall in the range 10-190 ppm. Cr concentrations vary in a similar manner to Ni and range between 12 and 313 ppm with the exception of one sample (MMH08-36) with an anomalously high Cr value of 544 ppm. Two other compatible elements, Co and Sr, show no obvious correlation with MgO but are lowest in the sample with the lowest MgO concentration. La, Sm, Yb and Nb all behave incompatibly and increase in concentration as MgO concentration declines (Fig. 4.65).

On the basis of REE and multi-element profiles, the Hemlock Formation can be divided into four groups. Group 1 consists of two samples which have the lowest elemental concentrations of the Hemlock Formation (Fig. 4.66b). The two samples have flat HREE patterns and flat to slightly depleted LREE patterns (Fig. 4.66b). The $(Gd/Yb)_N$ ratio of both samples is 1.07 while the $(La/Sm)_N$ ratios are 0.76 and 1.05 (Fig. 4.67). The Group 1 samples also have flat multi-element profiles with the exception of Th which is depleted relative to the other elements (Fig. 4.68b). These two samples have the highest Nb/Th ratios in the Hemlock Formation and on the Zr/Nb-Nb/Th diagram (Fig. 4.69) plot towards the top of the oceanic plateau field and towards the bottom of the N-MORB field of Condie (2005). The multi-element profiles of Group 1 samples are similar to those of the Ontong Java Plateau basalts (Fig. 4.68b). Group 2 consists of eleven samples which have REE profiles enriched in the LREEs relative to the MREEs (Fig. 4.66b) and $(La/Sm)_N$ ratios of 2.44-4.15 (Fig. 4.67). The Group 2 samples exhibit greater depletion in the HREEs relative to

the MREEs than Group 1 samples and have $(Gd/Yb)_N$ ratios of 1.10-1.68 (Fig. 4.67). Two samples in Group 2, including the dacite sample, have negative Eu anomalies (Fig. 4.66b) and Eu/Eu* values of 0.65 and 0.67. The multi-element profiles of Group 2 have negative Nb-Ta anomalies (Fig. 4.68b) and the corresponding Nb/Nb* values vary between 0.33 and 0.86. The dacite sample also has a negative Ti anomaly (Fig. 4.68b) and a Ti/Ti* value of 0.40. On the Zr/Nb-Nb/Th diagram (Fig. 4.69) most of the Group 2 samples plot close to the composition of continental crust except for three samples which plot at slightly higher Zr/Nb ratios in or close to the volcanic arc field. The four samples in Group 3 have REE profiles which are also enriched in the LREEs and depleted in the HREEs relative to the MREEs (Fig. 4.66b). The ranges in $(La/Sm)_N$ and $(Gd/Yb)_N$ ratios of the Group 3 samples are 2.04-2.38 and 1.47-1.62 respectively (Fig. 4.67). Unlike the Group 2 samples, the multi-element profiles of Group 3 do not possess any significant Nb-Ta anomalies (Fig. 4.68b). The Group 3 samples plot distinctly away from the other Hemlock Formation samples in Fig. 4.69. Three of the samples cluster together towards the top of the recycled component field of Condie (2005) in Fig. 4.69 while the other sample plots at slightly lower Zr/Nb and Nb/Th ratios and close to the EM2 end-member composition. Group 4 consists of the sample with an anomalously high $Fe_2O_3(T)$ content (MMH08-36). This sample has a REE profile which is enriched in the LREEs and depleted in the HREEs relative to the MREEs (Fig. 4.66b). The LREE enrichment is reflected by a $(La/Sm)_N$ ratio of 1.59 and the HREE depletion is emphasised by a $(Gd/Yb)_N$ ratio of 2.38 which is greater than in any of the other Hemlock Formation samples (Fig. 4.67). The multi-element profile of the Group 4 sample has a positive Nb-Ta anomaly (Fig. 4.68b) with a Nb/Nb* value of 1.28. On the Zr/Nb-Nb/Th diagram (Fig. 4.69) this sample plots close to the composition of E-MORB.

On the Nb/Y-Zr/Y diagram (Fig. 4.70) the two Group 1 samples plot just below the lower Icelandic plume tramline but within the field for the Ontong Java Plateau. All but three of the Group 2 samples plot within the Icelandic plume tramlines and trend between the compositions of E-MORB and continental crust (Fig. 4.70). The other three Group 2 samples fall just below the lower Icelandic plume tramline at Zr/Y ratios similar to continental crust. Group 3 samples plot amongst the Group 2 samples within the tramlines and midway between the compositions of E-MORB and

continental crust (Fig. 4.70). The Group 4 sample plots within the Icelandic plume tramlines and between the compositions of continental crust and OIB (Fig. 4.70).

4.13. Kiernan sills of the Lake Superior region

4.13.1. Alteration and element mobility

Petrographic observations (see section 3.9.6) and LOI values of 2.10-4.03 wt. % suggest that the Kiernan sills were subjected to post-magmatic alteration processes which may have affected the geochemistry of the rocks. To assess which elements may have been affected, all elements have been plotted against Zr. A representative selection of these bivariate diagrams is displayed in Fig. 4.61 along with samples from the other Lake Superior magmatic suites. The elements Sc, V, Co, Y, Ga, Nb, REEs, Hf, Ta, Th, U, Ti, Al, Fe, Mn, P and Ca yield reasonable correlations when plotted against Zr. These elements were most likely immobile during any secondary alteration processes. The elements Zn, Sr, Ba, Cs, Cu, Rb, Si, K, Na, Ni, Cr and Mg do not produce good correlations with Zr and could have been mobilised during secondary alteration processes.

4.13.2. Classification

As the samples from the Kiernan sills are coarse gabbros they may not accurately represent the volcanic liquid which the sills originally transported. Therefore where they plot on classification diagrams should be treated cautiously. On the TAS diagram (Fig. 4.62), seven of the samples plot in the subalkaline basalt field. Another sample plots as an alkaline basalt while the remaining sample plots within the alkaline trachybasalt field (Fig. 4.62). On the Zr/Ti-Nb/Y diagram (Fig. 4.63) eight samples plot in the subalkaline basalt field and one sample falls within the alkali basalt field. Seven of the samples cluster tightly together in the subalkaline basalt field whilst one sample plots distinctly further to the left in the same field (Fig. 4.63).

4.13.3. Major elements

The ranges in MgO and $Fe_2O_3(T)$ concentrations in the samples of the Kiernan sills are 7.04-10.83 wt. % and 9.91-15.67 wt. % respectively. The corresponding range in Mg# is 32.29-48.10. The SiO_2 concentration varies between 46.39 and 49.94 wt. % and the range in total alkali content is 2.53-5.28 wt. %. There are no obvious trends in the major element variation diagrams displayed in Fig. 4.64. However, it appears that SiO_2, CaO and Na_2O increase in concentration as MgO concentration decreases and that as MgO declines below ~7.5 wt. % both TiO_2 and P_2O_5 increase in concentration.

4.13.4. Trace elements

The Ni and Cr contents of the Kiernan samples are 82-242 ppm and 73-463 ppm respectively. When plotted against MgO, the Ni concentration decreases with decreasing MgO concentration whereas there is no obvious trend between Cr and MgO (Fig. 4.65). Like Ni, Co also decreases in concentration as the MgO content declines (Fig. 4.65c), whereas Sr shows no obvious variation with varying MgO concentration (Fig. 4.65d). The incompatible elements La, Sm, Yb and Nb also produce no obvious trend when plotted against MgO (Fig. 4.65).

The chondrite-normalised REE profiles of the Kiernan sills are shown in Fig. 4.66c. Eight of the nine analysed samples have near-parallel REE profiles with elemental abundances ~6-79 times those of chondritic values. The profiles are enriched in the LREEs relative to the MREEs which is reflected by $(La/Sm)_N$ ratios of 1.78 to 2.34 (Fig. 4.67). The HREEs are depleted relative to the MREEs giving rise to $(Gd/Yb)_N$ ratios in the range of 1.57-1.67 with the exception of one sample with a ratio of 2.41 (Fig. 4.67). The one other analysed sample has a relatively flat REE profile (Fig. 4.66c). Its $(La/Sm)_N$ and $(Gd/Yb)_N$ ratios are 0.95 and 1.14 respectively (Fig. 4.67). Positive Eu anomalies are present in most samples (Fig. 4.66c) which is reflected in the Eu/Eu* values ranging from 1.01 to 1.38. The primitive-mantle-normalised multi-element profiles of the Kiernan samples are displayed in Fig. 4.68c. As with the REE profiles, eight of the nine samples are enriched in the more incompatible elements (Fig. 4.68c). Most of these samples have minor negative Nb-Ta anomalies

(Fig. 4.68c) and corresponding Nb/Nb* values between 0.75 and 0.92. However, one sample has a positive Nb-Ta anomaly (Fig. 4.68c) with a Nb/Nb* value of 1.71. The other one sample of the nine analysed has a flatter multi-element profile with no significant Nb-Ta anomaly (Fig. 4.68c). This sample has a profile similar to that of the Ontong Java Plateau. On the Zr/Nb-Nb/Th diagram (Fig. 4.69), the sample with a flat REE profile plots close to the Ontong Java Plateau field. The sample with a positive Nb-Ta anomaly plots in the recycled component field and close to the HIMU end-member composition (Fig. 4.69). The other Kiernan samples plot towards the bottom of the oceanic plateau field in Fig. 4.69 at Nb/Th ratios midway between the compositions of E-MORB and continental crust.

On the Nb/Y-Zr/Y diagram (Fig. 4.70) eight of the samples plot within the Icelandic plume tramlines while one sample plots on the lower tramline. The sample with a flat REE profile plots at the composition of primitive mantle (Fig. 4.70). Seven samples plot between the compositions of E-MORB and continental crust while the sample with a positive Nb-Ta anomaly plots further towards the composition of OIB (Fig. 4.70).

4.14. Badwater Greenstone of the Lake Superior region

4.14.1. Alteration and element mobility

The Badwater Greenstone has undergone greenschist facies metamorphism (see section 3.9.8) and has LOI values ranging from 2.37 to 6.73 wt. %. To assess whether alteration processes have affected the geochemistry of the Badwater Greenstone, all elements have been plotted against Zr and a representative selection of these bivariate diagrams is shown in Fig. 4.61 along with samples from the other Lake Superior magmatic suites. Elements which are well correlated with Zr include Cr, Ni, Y, Ga, REEs, Hf, Nb, Ta, Th, U, Ti, Al, Mn, Mg, Fe and P. These elements are likely to have been immobile during secondary alteration processes. Elements which do not yield good correlations with Zr include V, Zn, Sr, Ba, Cu, Rb, Cs, Si, Ca and Na. These elements may have been mobilised during secondary alteration processes and should be used cautiously in examining the petrogenesis of the Badwater Greenstone.

4.14.2. Classification

On the TAS diagram (Fig. 4.62) four samples plot in the subalkaline basalt field while three samples plot in the subalkaline basaltic andesite field. However, on the Zr/Ti-Nb/Y diagram (Fig. 4.63) all samples plot in the subalkaline basalt field.

4.14.3. Major elements

The MgO and $Fe_2O_3(T)$ concentrations in the Badwater Greenstone are 4.01-8.90 wt. % and 11.99-14.75 wt. % respectively, which yield Mg# values of 23.19 to 45.20. SiO_2 concentrations vary between 49.10 and 54.13 wt. % whilst the total alkali content ranges from a minimum of 0.58 wt. % to a maximum of 4.36 wt. %.

Variation diagrams showing major element concentrations with changing MgO concentration are displayed in Fig. 4.64. SiO_2 and $Fe_2O_3(T)$ increase in concentration as the concentration of MgO decreases. Al_2O_3 decreases and MnO remains relatively constant as MgO decreases in concentration. There is a larger degree of scatter on diagrams involving CaO, Na_2O and K_2O. However, it appears that CaO decreases whilst K_2O increases with the decline in MgO concentration. No clear general trend is present in the Na_2O-MgO diagram (Fig. 4.64g). Both TiO_2 and P_2O_5 increase in concentration with decreasing MgO but appear to more rapidly increase in concentration after MgO declines below 5 wt. %.

4.14.4. Trace elements

The Ni content of the Badwater Greenstone is mostly in the range of 23 to 101 ppm although one sample has an anomalous Ni concentration of 445 ppm. Cr concentrations vary between 12 and 350 ppm. Both Ni and Cr concentrations decrease as the concentration of MgO decreases (Fig. 4.65) as would be expected for such compatible trace elements. Scatter disguises any real trends on the diagrams involving Co and Sr in Fig. 4.65, the scatter possibly resulting from the mobilisation of Co, Sr or MgO during secondary alteration processes. The incompatible elements La, Sm, Yb and Nb are plotted against MgO in Fig. 4.65. All these incompatible

elements increase in concentration as MgO decreases although the best correlations are seen only in the Yb-MgO and Nb-MgO diagrams in Fig. 4.65.

Chondrite-normalised REE profiles of the Badwater Greenstone are displayed in Fig. 4.66d. All the profiles are near-parallel and have elemental abundances of ~11-180 times those of chondritic values (Fig. 4.66d). The profiles are enriched in the LREEs relative to the MREEs and have $(La/Sm)_N$ ratios greater than E-MORB of 1.83-3.38 (Fig. 4.67). The profiles are also depleted in the HREEs relative to the MREEs and have $(Gd/Yb)_N$ ratios mainly in the range of 1.28 to 1.56 with the exception of one sample which has a slightly lower $(Gd/Yb)_N$ ratio of 1.09 (Fig. 4.67). Very minor negative Eu anomalies are visible in some of the REE profiles in Fig. 4.66d with Eu/Eu* values reaching a minimum of 0.84. Primitive-mantle-normalised multi-element profiles of the Badwater Greenstone are shown in Fig. 4.68d. The profiles are near-parallel and contain elemental abundances of ~4-110 times those of primitive mantle values (Fig. 4.68d). The profiles are enriched in the more incompatible elements relative to the MREEs and other less incompatible elements. One other notable feature of the multi-element profiles is the presence of negative Nb-Ta anomalies. The magnitude of the anomalies is reflected by Nb/Nb* values of 0.31 to 0.75. Two of the samples also possess minor negative Ti anomalies (Fig. 4.68d) and have Ti/Ti* values of 0.76 and 0.79. On the Zr/Nb-Nb/Th diagram (Fig. 4.69) the samples plot close to the composition of continental crust and amongst many of the other samples from the Lake Superior region. All but one of the samples plot within the Icelandic plume tramlines in Fig. 4.70. Out of the samples that plot within the tramlines, one plots between the compositions of primitive mantle and E-MORB while the remaining samples trend between E-MORB and continental crust compositions (Fig. 4.70).

4.15. Emperor Volcanic Complex of the Lake Superior region

4.15.1. Alteration and element mobility

LOI values of 1.52-6.24 wt. % and petrographic observations (see section 3.9.10) suggest that the rocks of the Emperor Volcanic Complex have been affected by secondary alteration and metamorphic processes. To assess if these processes have

affected the geochemistry of rocks from the Emperor Volcanic Complex, all elements have been plotted against Zr and a representative selection of these bivariate diagrams is shown in Fig. 4.61 along with samples from the other Lake Superior magmatic suites. The elements Sc, Cr, Ni, Y, Nb, REEs, Hf, Ta, Th, U, Si, Ti, Al, Mg, Fe, Mn, Cu, Co, V and Ga yield reasonable correlations with Zr and were probably immobile during any post-magmatic processes. The elements Ba, Zn, Cs, Ca, Na, K and Rb do not produce good correlations with Zr and could have been mobilised during secondary alteration processes.

4.15.2. Classification

On the TAS diagram (Fig. 4.62) the Emperor Volcanic Complex is comprised of a diverse range of subalkaline rock types. One sample plots as a basalt, two samples as basaltic andesite, one sample as a trachyandesite, two samples as dacite, and one sample as a rhyolite (Fig. 4.62). The more alteration-resistant Zr/Ti-Nb/Y diagram (Fig. 4.63) also classifies the Emperor Volcanic Complex as a variety of rock types within the subalkaline series. On Fig. 4.63 three samples plot as basalt, one sample plots on the boundary between basalt and basaltic andesite, one sample plots as basaltic andesite, and two samples plot as dacite.

4.15.3. Major elements

The range of MgO concentrations in the Emperor Volcanic Complex is largely restricted to between 2.49 and 4.81 wt. % with one other sample possessing 8.44 wt. % MgO. The SiO_2 content of the volcanic rocks ranges between 49.72 and 74.03 wt. %. The overall range in $Fe_2O_3(T)$ content for the complex is 3.81 to 14.04 wt. %. Mg# values vary between 24.67 and 51.73. The Emperor volcanic rocks have total alkali contents ranging from 2.97 to 7.23 wt. %.

The variation of major element chemistry with respect to MgO for the Emperor igneous rocks, as well as for the other Lake Superior igneous rocks, is highlighted in Fig. 4.64. SiO_2 and Na_2O increase in concentration as MgO concentration declines. Despite some scatter, it appears that Al_2O_3, $Fe_2O_3(T)$, MnO and CaO decrease as the MgO content decreases. TiO_2 and K_2O do not show obvious trends with MgO.

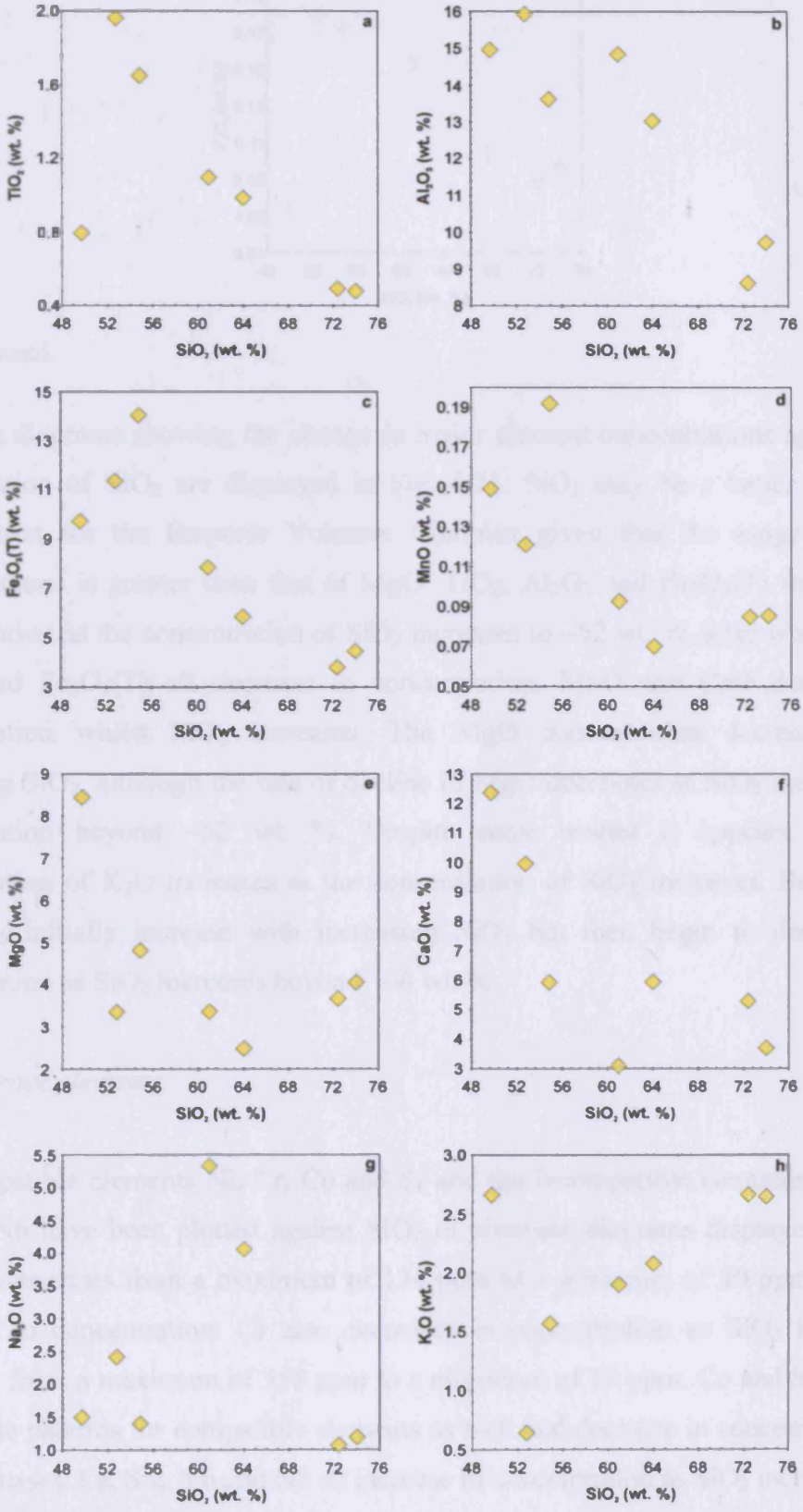

Fig. 4.71. Bivariate diagrams of major elements vs. SiO_2 for the igneous rocks of the Emperor Volcanic Complex.

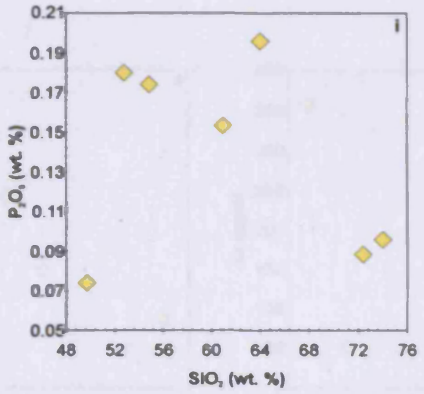

Fig. 4.71. contd.

Variation diagrams showing the change in major element concentrations against the concentration of SiO_2 are displayed in Fig. 4.71. SiO_2 may be a better index of fractionation for the Emperor Volcanic Complex given that the range in SiO_2 concentrations is greater than that of MgO. TiO_2, Al_2O_3 and $Fe_2O_3(T)$ increase in concentration as the concentration of SiO_2 increases to ~52 wt. %, after which TiO_2, Al_2O_3 and $Fe_2O_3(T)$ all decrease in concentration. MnO and CaO decrease in concentration whilst SiO_2 increases. The MgO concentration decreases with increasing SiO_2, although the rate of decline in MgO decreases as SiO_2 increases in concentration beyond ~52 wt. %. Despite some scatter it appears that the concentration of K_2O increases as the concentration of SiO_2 increases. Both Na_2O and P_2O_5 initially increase with increasing SiO_2 but then begin to decrease in concentration as SiO_2 increases beyond ~60 wt. %.

4.15.4. Trace elements

The compatible elements Ni, Cr, Co and Sr and the incompatible elements La, Sm, Yb and Nb have been plotted against SiO_2 in bivariate diagrams displayed in Fig. 4.72. Ni decreases from a maximum of 134 ppm to a minimum of 30 ppm as SiO_2 increases in concentration. Cr also decreases in concentration as SiO_2 increases, declining from a maximum of 358 ppm to a minimum of 13 ppm. Co and Sr display expectable patterns for compatible elements as well and decrease in concentration as SiO_2 increases. La, Sm, Yb and Nb all increase in concentration as SiO_2 increases.

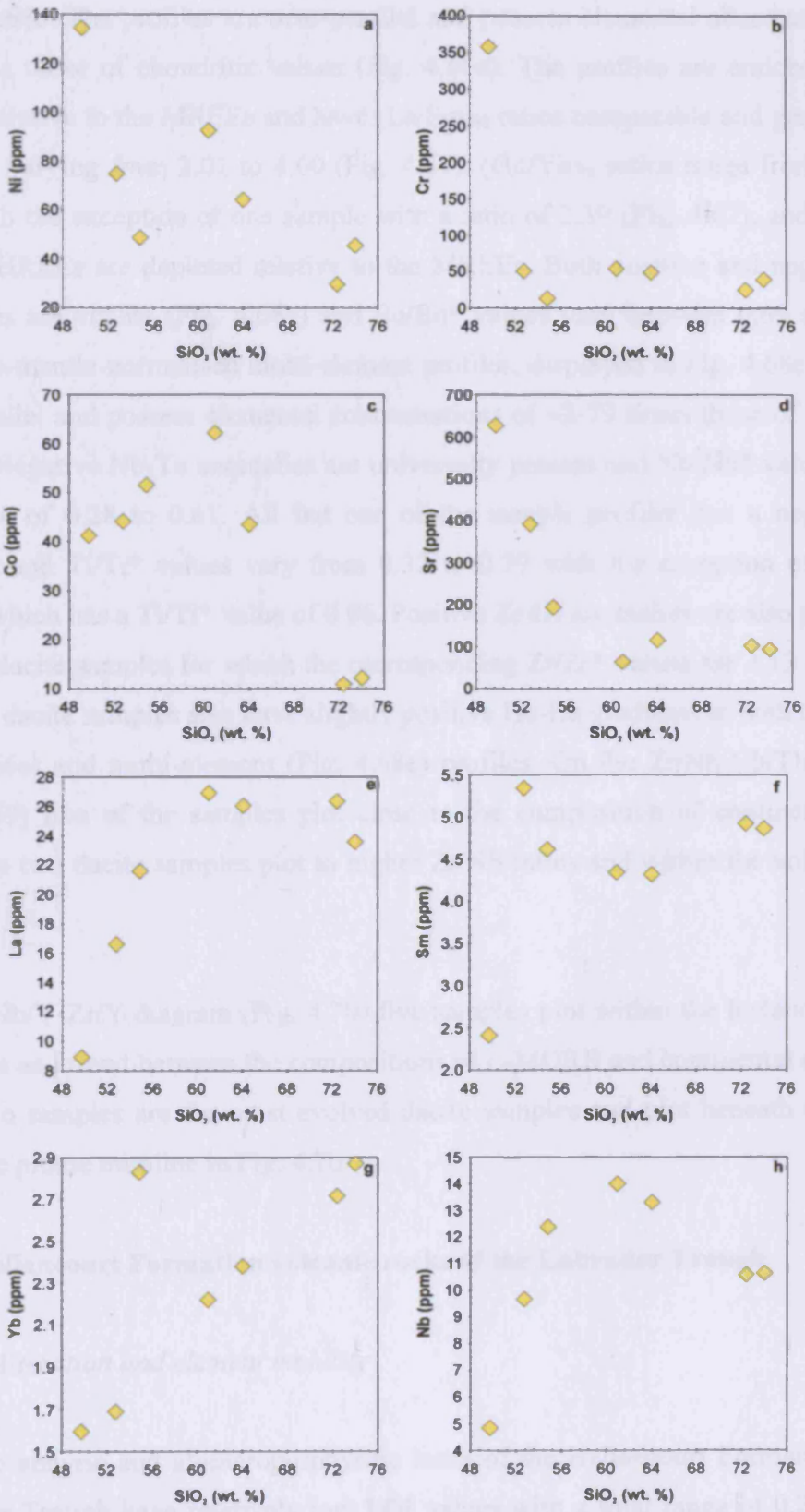

Fig. 4.72. Bivariate diagrams for selected trace elements vs. SiO_2 for the igneous rocks of the Emperor Volcanic Complex.

Chondrite-normalised REE profiles of the Emperor Volcanic Complex are displayed in Fig. 4.66e. The profiles are near-parallel and possess elemental abundances ~10-111 times those of chondritic values (Fig. 4.66e). The profiles are enriched in the LREEs relative to the MREEs and have $(La/Sm)_N$ ratios comparable and greater than OIB and varying from 2.01 to 4.00 (Fig. 4.67). $(Gd/Yb)_N$ ratios range from 1.23 to 1.52, with the exception of one sample with a ratio of 2.39 (Fig. 4.67), and indicate that the HREEs are depleted relative to the MREEs. Both positive and negative Eu anomalies are visible (Fig. 4.66e) and Eu/Eu* values vary between 0.69 and 1.46. Primitive-mantle-normalised multi-element profiles, displayed in Fig. 4.68e, are also near-parallel and possess elemental concentrations of ~2-79 times those of primitive mantle. Negative Nb-Ta anomalies are universally present and Nb/Nb* values are in the range of 0.28 to 0.61. All but one of the sample profiles has a negative Ti anomaly and Ti/Ti* values vary from 0.32 to 0.79 with the exception of the one sample which has a Ti/Ti* value of 0.96. Positive Zr-Hf anomalies are also present in the two dacite samples for which the corresponding Zr/Zr* values are 2.13 and 2.32. The two dacite samples also have slightly positive Ho-Lu gradients in both their REE (Fig. 4.66e) and multi-element (Fig. 4.68e) profiles. On the Zr/Nb-Nb/Th diagram (Fig. 4.69) five of the samples plot close to the composition of continental crust while the two dacite samples plot to higher Zr/Nb ratios and within the volcanic arc field.

On the Nb/Y-Zr/Y diagram (Fig. 4.70) five samples plot within the Icelandic plume tramlines and trend between the compositions of E-MORB and continental crust. The other two samples are the most evolved dacite samples and plot beneath the lower Icelandic plume tramline in Fig. 4.70.

4.16. Hellancourt Formation volcanic rocks of the Labrador Trough

4.16.1. Alteration and element mobility

Both the aphyric and glomeroporphyritic lavas of the Hellancourt Formation in the Labrador Trough have relatively low LOI values with a total range of 0.29 to 2.83 wt. % and have both been metamorphosed to greenschist facies (see section 3.10.2). Elements which produce good correlations with Zr (Fig. 4.73) and were probably

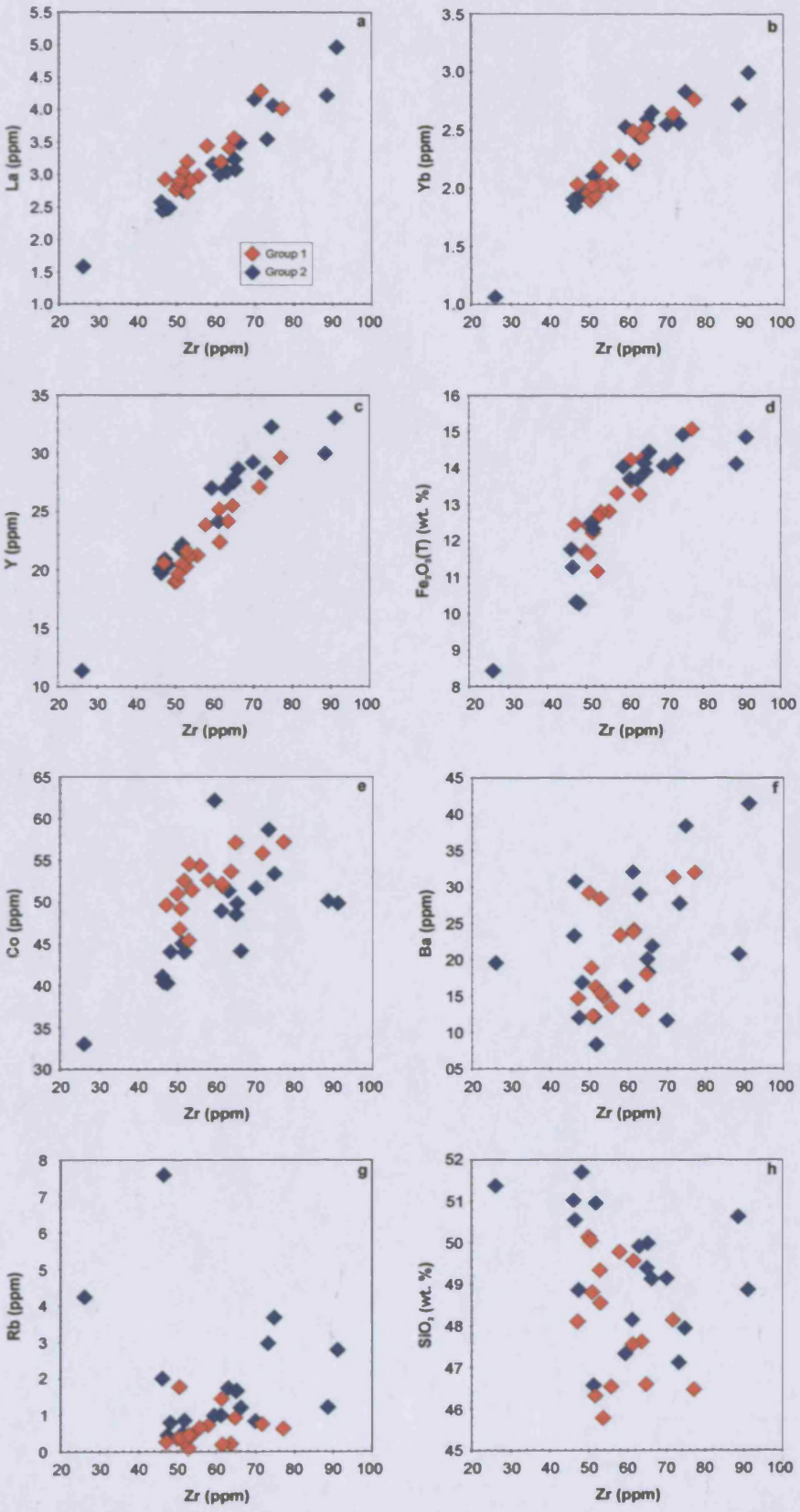

Fig. 4.73. Bivariate diagrams of selected elements vs. Zr for the Hellancourt Formation.

immobile during post-magmatic alteration processes include Sc, V, Ni, Cr, Co, Y, Ga, Hf, Nb, Ta, REEs, Th, U, Ti, Mn, Fe, Mg and P. These elements can be used with confidence to study the petrogenesis of the Labrador Trough volcanic rocks. Elements which do not produce good correlations with Zr (Fig. 4.73) include Cu, Sr, Ba, Zn, Rb, Cs, Si, Ca, Na and K. It is possible that some of the scatter seen in Fig. 4.73 could have been caused by the mobilisation of elements during secondary alteration processes. On the Co-Zr diagram (Fig. 4.73e) it is possible that there are two different trends for the aphyric and glomeroporphyritic lavas. This observation could possibly be explained by mobilisation of Co or that the two different groups, hereafter termed Group 1 (aphyric) and Group 2 (glomeroporphyritic), are derived from two different mantle sources.

4.16.2. Classification

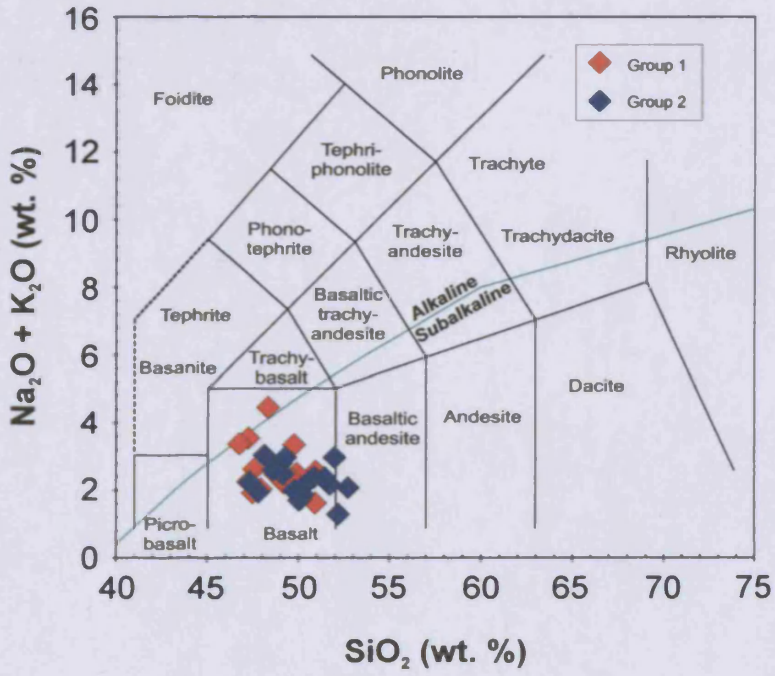

Fig. 4.74. Total alkalis vs. SiO_2 (TAS) diagram for the Hellancourt Formation. See Fig. 4.2 for sources of field and alkaline-subalkaline boundaries.

On the TAS diagram (Fig. 4.74) most of the Hellancourt Formation samples, regardless of which group they belong to, plot in the field for subalkaline basalt. However, one Group 1 sample plots as an alkaline basalt and two Group 2 samples plot in the subalkaline basaltic andesite field (Fig. 4.74). On the Zr/Ti-Nb/Y diagram

(Fig. 4.75) all of the Hellancourt Formation samples cluster together in the subalkaline basalt field.

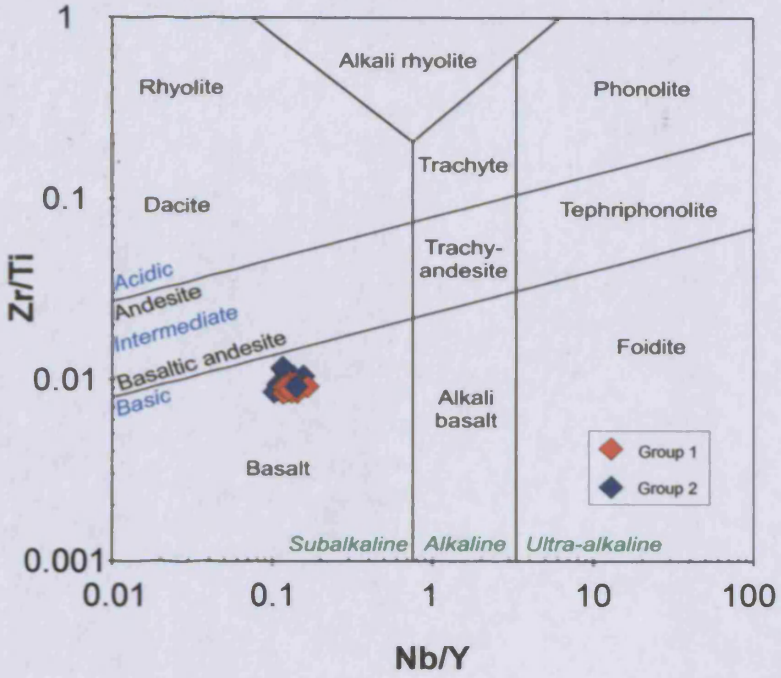

Fig. 4.75. Zr/Ti vs. Nb/Y diagram for the Hellancourt Formation. See Fig. 4.3 for source of field boundaries.

4.16.3. Major elements

The MgO content of the Group 1 lavas is slightly higher than that of the Group 2 lavas. The Group 1 lavas contain 7.29-9.86 wt. % MgO whereas the Group 2 lavas have a range in MgO of 6.03 to 8.79 wt. %. The ranges in $Fe_2O_3(T)$ concentrations for the Group 1 and Group 2 lavas are 11.17-15.09 wt. % and 10.29-14.94 wt. % respectively with the exception of the highest MgO sample of Group 2 which has an anomalous $Fe_2O_3(T)$ concentration of 8.44 wt. %. Mg# values are 36.26-47.52 for Group 1 and 32.11-47.32 for Group 2 except for the highest MgO sample with a Mg# value of 53.67. The SiO_2 contents of both groups are very similar and the overall range is from 46.73 to 52.72 wt. %. The Group 1 lavas contain higher total alkali contents up to 4.46 wt. % whilst the maximum total alkali content of the Group 2 lavas is 3.04 wt. %.

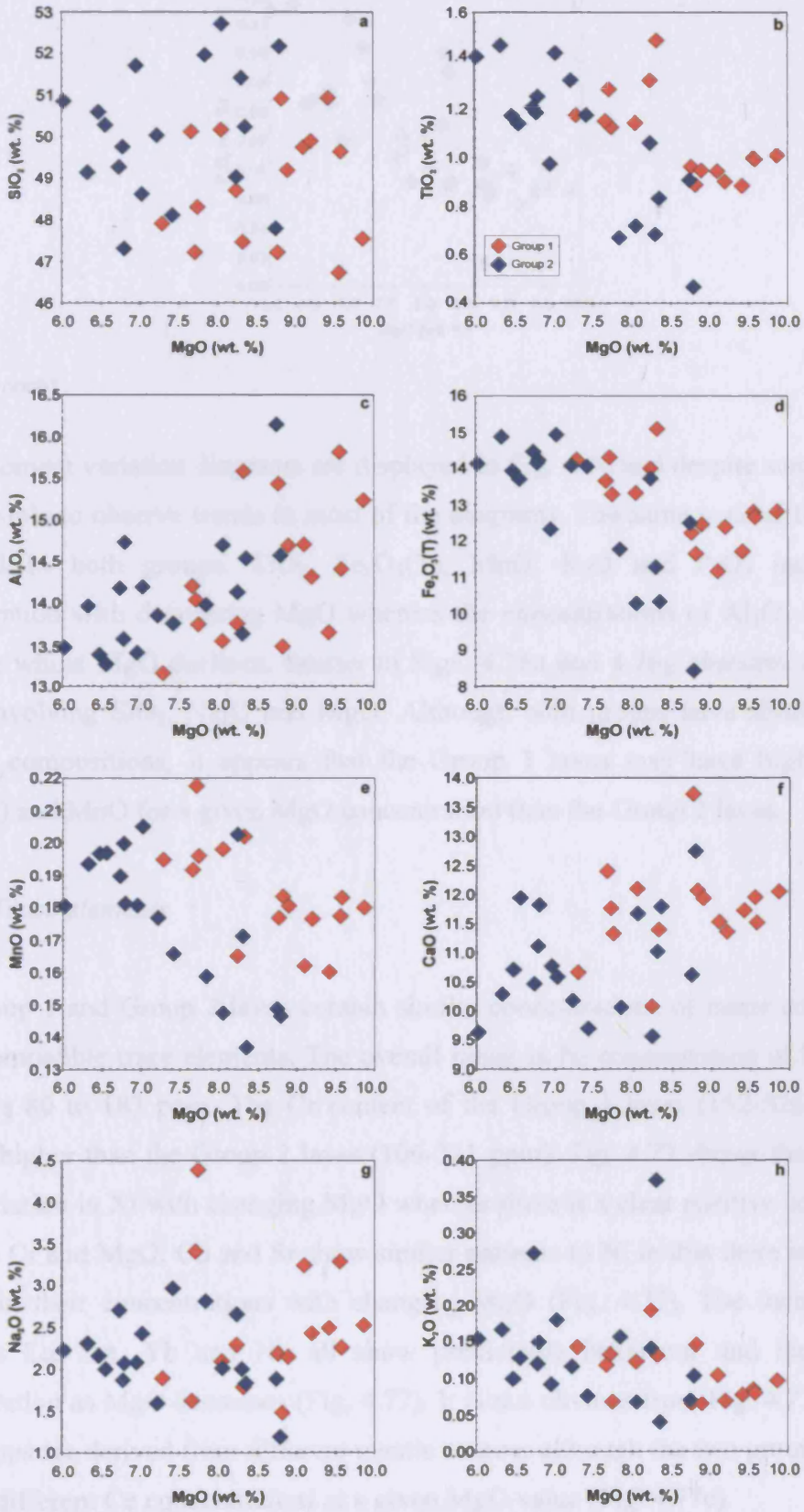

Fig. 4.76. Bivariate diagrams of major elements vs. MgO for the Hellancourt Formation.

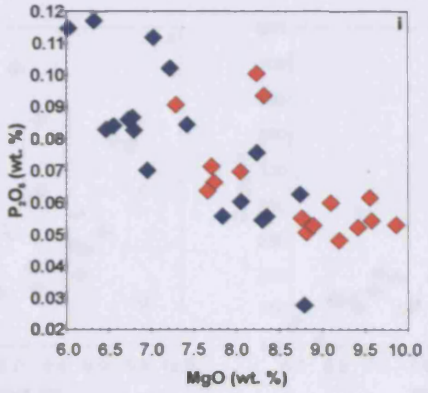

Fig. 4.76. contd.

Major element variation diagrams are displayed in Fig. 4.76 and despite some scatter it is possible to observe trends in most of the diagrams. The same general trends are observed in both groups. TiO_2, $Fe_2O_3(T)$, MnO, K_2O and P_2O_5 increase in concentration with decreasing MgO whereas the concentrations of Al_2O_3 and CaO decrease whilst MgO declines. Scatter in Figs. 4.76a and 4.76g obscures any clear trends involving SiO_2, Na_2O and MgO. Although both groups have similar major element compositions, it appears that the Group 1 lavas may have higher TiO_2, $Fe_2O_3(T)$ and MnO for a given MgO concentration than the Group 2 lavas.

4.16.4. Trace elements

The Group 1 and Group 2 lavas contain similar concentrations of many compatible and incompatible trace elements. The overall range in Ni concentration of both lava groups is 80 to 183 ppm. The Cr content of the Group 1 lavas (152-526 ppm) is slightly higher than the Group 2 lavas (106-321 ppm). Fig. 4.77 shows that there is little variation in Ni with changing MgO whereas there is a clear positive correlation between Cr and MgO. Co and Sr show similar patterns to Ni in that there is no clear change in their concentrations with changing MgO (Fig. 4.77). The incompatible elements La, Sm, Yb and Nb all show predictable behaviour and increase in concentration as MgO decreases (Fig. 4.77). It is not obvious from Fig. 4.77 that the two groups are derived from different mantle sources although the two groups appear to have different Co concentrations at a given MgO value (Fig. 4.77c).

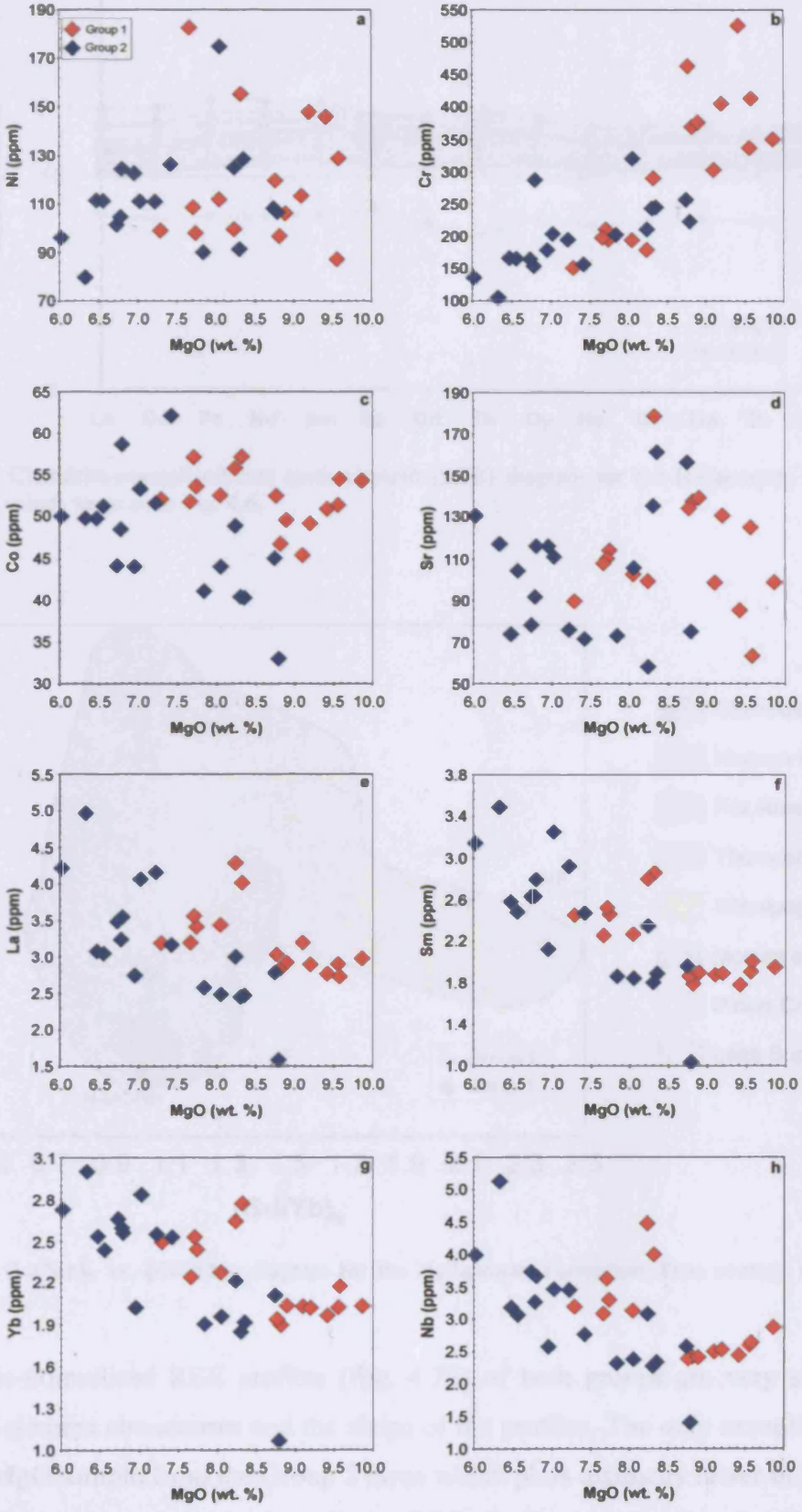

Fig. 4.77. Bivariate diagrams of selected trace elements vs. MgO for the Hellancourt Formation.

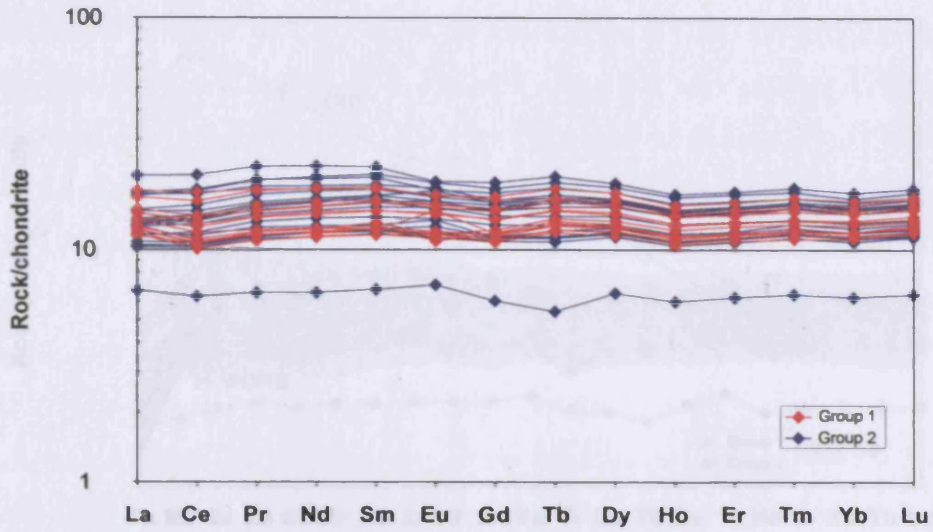

Fig. 4.78. Chondrite-normalised rare earth element (REE) diagram for the Hellancourt Formation. Chondrite values same as in Fig. 4.6.

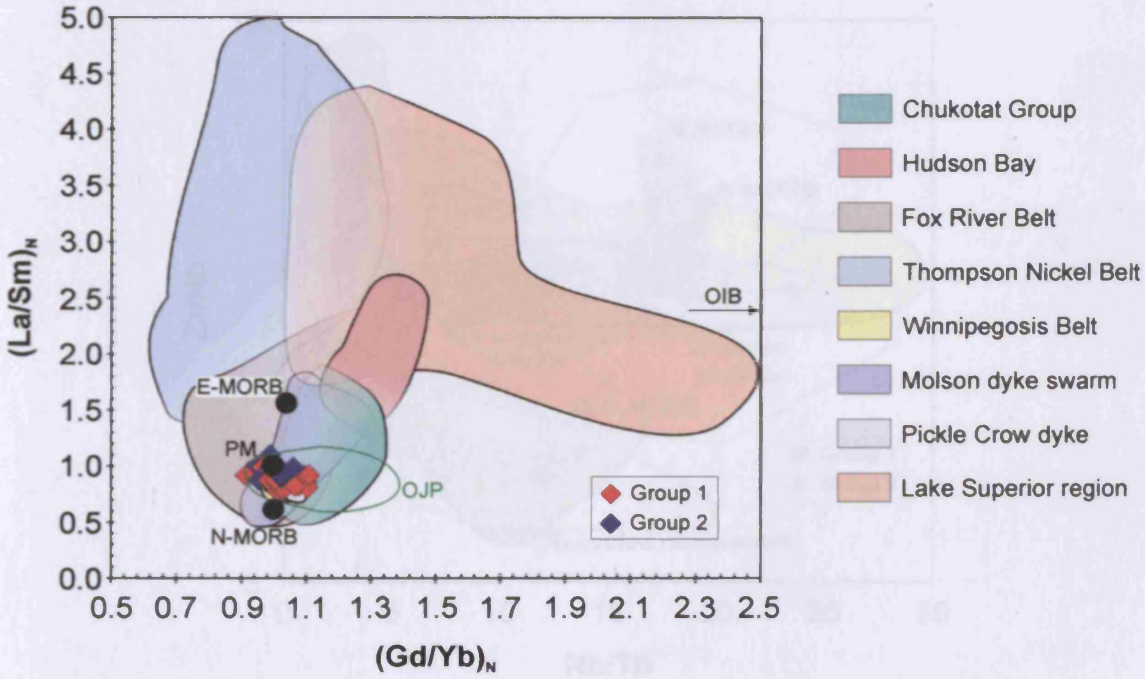

Fig. 4.79. $(La/Sm)_N$ vs. $(Gd/Yb)_N$ diagram for the Hellancourt Formation. Data sources same as in Fig. 4.7.

Chondrite-normalised REE profiles (Fig. 4.78) of both groups are very similar in terms of element abundances and the shape of the profiles. The only exception is the highest MgO sample from the Group 2 lavas which plots distinctly lower in Fig. 4.78 than the rest of the basalts. Overall the REE profiles are flat to slightly LREE-depleted. $(La/Sm)_N$ ratios are 0.77-1.10 whilst $(Gd/Yb)_N$ ratios vary between 0.91

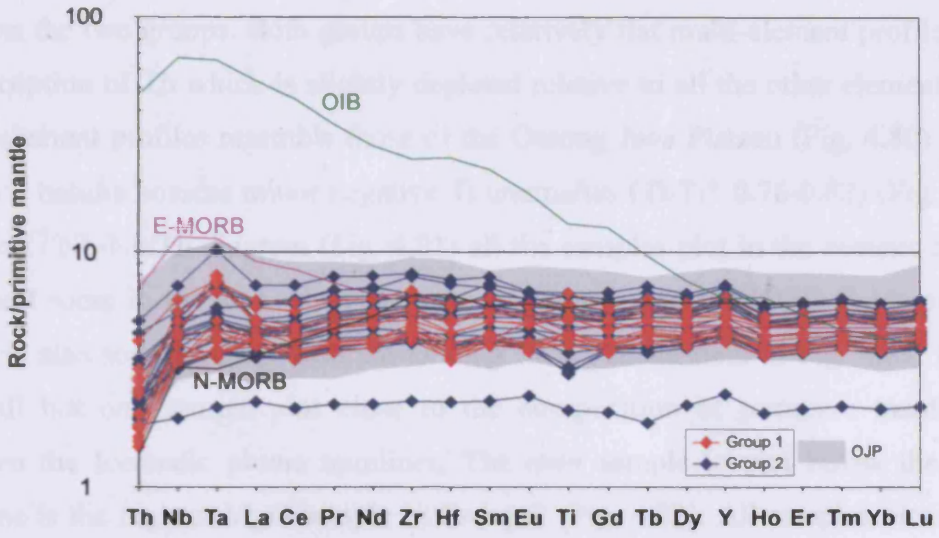

Fig. 4.80. Primitive-mantle-normalised multi-element diagram for the Hellancourt Formation. Data sources same as in Fig. 4.7.

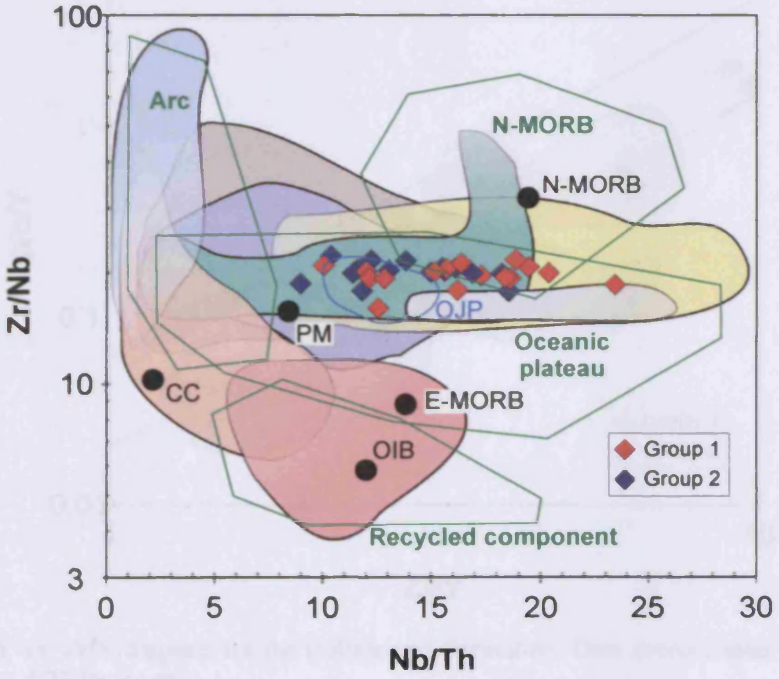

Fig. 4.81. Zr/Nb vs. Nb/Th diagram for the Hellancourt Formation. Data sources same as in Figs. 4.7 and 4.9. See Fig. 4.77 for legend.

and 1.11 (Fig. 4.79). These REE ratios plot between the primitive mantle and N-MORB compositions and within the field for the Ontong Java Plateau in Fig. 4.79. No significant Ce anomalies are present (Ce/Ce* 0.89-1.00) and the only notable Eu anomaly is found in one of the Group 1 basalts that has an Eu/Eu* value of 1.22. Primitive-mantle-normalised multi-element profiles (Fig. 4.80) are also very similar

between the two groups. Both groups have relatively flat multi-element profiles with the exception of Th which is slightly depleted relative to all the other elements. The multi-element profiles resemble those of the Ontong Java Plateau (Fig. 4.80). Three Group 2 basalts possess minor negative Ti anomalies (Ti/Ti* 0.76-0.82) (Fig. 4.80). On the Zr/Nb-Nb/Th diagram (Fig. 4.81) all the samples plot in the oceanic plateau field and some in the area where the oceanic plateau and N-MORB fields overlap. There is also some overlap with the Ontong Java Plateau field in Fig. 4.81. In Fig. 4.82 all but one sample plot close to the composition of primitive mantle and between the Icelandic plume tramlines. The only sample to plot below the lower tramline is the highest MgO sample in Group 2 (Fig. 4.82). All samples plot within the field for the Ontong Java Plateau on Fig. 4.82.

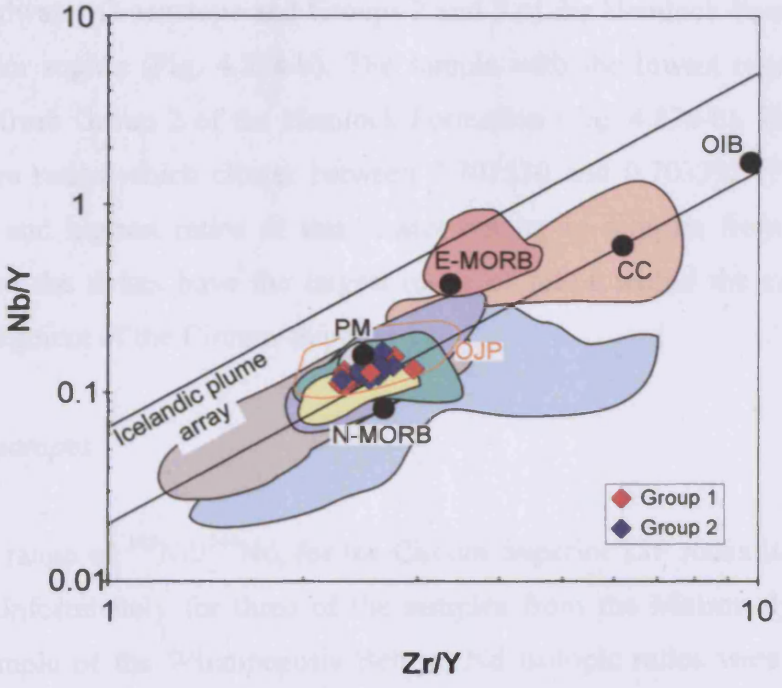

Fig. 4.82. Nb/Y vs. Zr/Y diagram for the Hellancourt Formation. Data sources same as in Figs. 4.7 and 4.9. See Fig. 4.77 for legend.

4.17. Radiogenic isotopes

Eighteen samples were selected for Sr-Nd-Pb-Hf isotopic analysis while fifteen samples were picked for Os isotopic analysis. Sr and Hf isotope ratios were successfully determined for all eighteen samples. However, four samples failed to run on the mass spectrometer for Nd isotopes while five samples failed to yield Pb

isotope ratios. Fourteen of the fifteen samples selected for Os isotopic analysis were able to be run on the mass spectrometer and gave results. Unfortunately the Os isotopic data collected are very unusual and appear not to provide any useful information on the petrogenesis of the Circum-Superior LIP. All the isotopic data collected are presented in Tables D.4-D.8 in Appendix D and are briefly described below.

4.17.1. Sr isotopes

The overall range of $^{87}Sr/^{86}Sr_i$ (the subscript i denotes that the isotopic ratio has been age-corrected to 1880 Ma) for the Circum-Superior LIP rocks is 0.701319 to 0.710950. The three samples with the highest ratios (0.7039112-0.710950) come from the Badwater Greenstone and Groups 2 and 3 of the Hemlock Formation in the Lake Superior region (Fig. 4.83a-b). The sample with the lowest ratio (0.701319) also comes from Group 2 of the Hemlock Formation (Fig. 4.83a-b). The remaining samples have ratios which cluster between 0.701530 and 0.703392 (Fig. 4.83a-b). The lowest and highest ratios of this cluster belong to samples from the Molson dykes and so the dykes have the largest range of ratios within the cluster of any individual segment of the Circum-Superior LIP.

4.17.2. Nd isotopes

The overall range of $^{143}Nd/^{144}Nd_i$ for the Circum-Superior LIP rocks is 0.509808 to 0.510475. Unfortunately for three of the samples from the Molson dykes and the Group 1 sample of the Winnipegosis Belt no Nd isotopic ratios were successfully obtained. Four samples have ratios (0.509808-0.510247) which are distinctly lower than the others (Fig. 4.83a). These four samples are from the Badwater Greenstone and Groups 2 and 3 of the Hemlock Formation. The other samples have ratios clustering between 0.510324 and 0.510475 (Fig. 4.83a). The higher ratio belongs to a sample from the Pickle Crow dyke and the lower ratio is from a Group 2 sample of the Winnipegosis Belt. The Badwater Greenstone sample and three samples from Groups 2 and 3 of the Hemlock Formation have εNd_i values ranging from +0.84 to -7.77 (Fig. 4.83b). The εNd_i values for the Pickle Crow dyke and the Winnipegosis Belt Group 2 samples are +5.29 and +2.34 respectively (Fig. 4.83b). The other

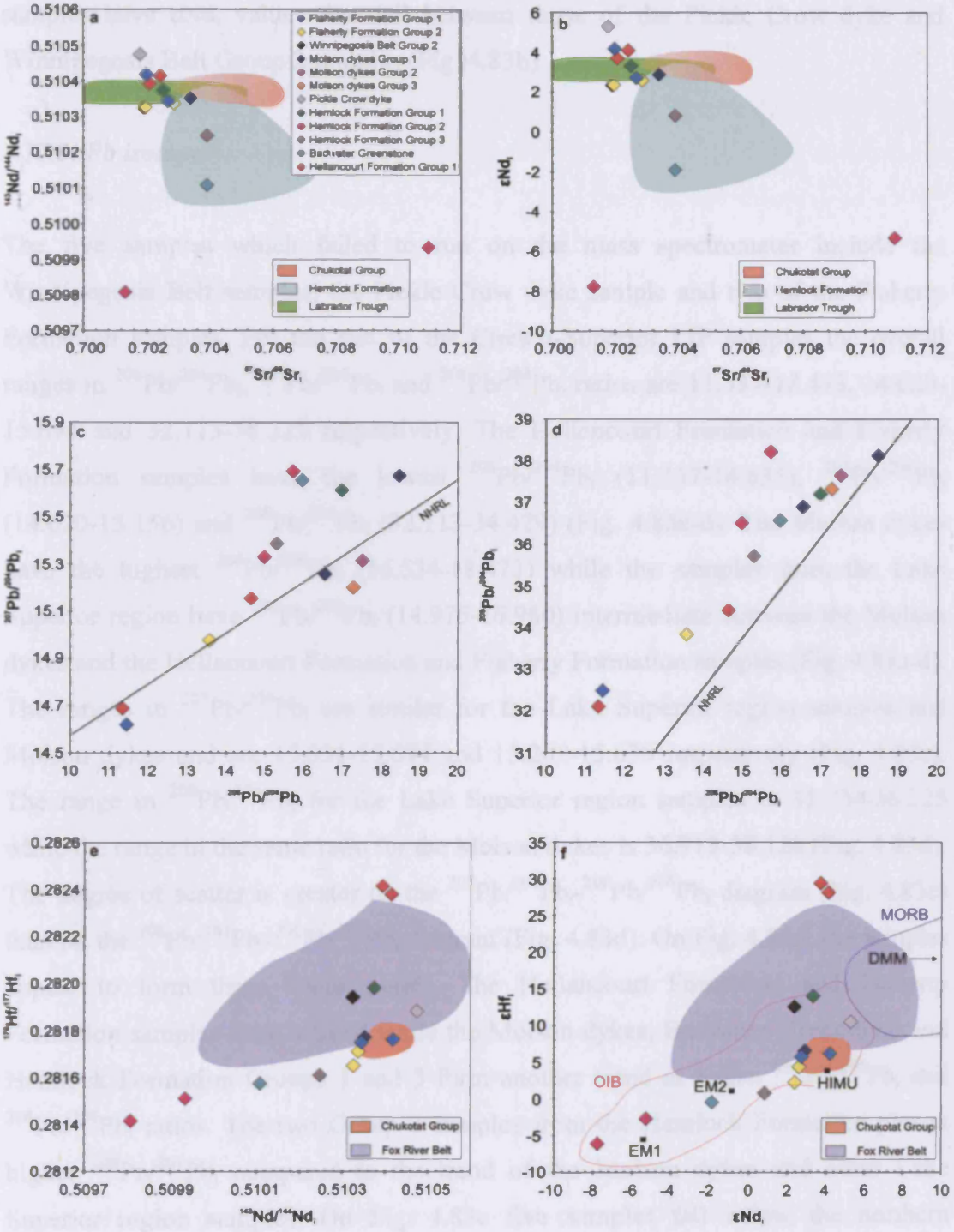

Fig. 4.83. Age-corrected radiogenic isotope diagrams for the rocks of the Circum-Superior LIP. Diamonds are the samples analysed in the current study and the legend for all diagrams is shown in (a). The coloured fields shown in (a), (b), (e) and (f) represent previously reported values from certain segments of the Circum-Superior LIP. Data sources for the fields shown in (a) and (b) are: Chukotat Group – Zindler (1982); Hemlock Formation – Beck & Murthy (1991); Labrador Trough – Rohon et al. (1993). Data sources for the fields shown in (e) and (f) are: Chukotat Group – Blichert-Toft & Arndt (1999) and Vervoort & Blichert-Toft (1999); Fox River Belt – Desharnais (2005). The northern hemisphere reference line (NHRL) in (c) and (d) is from Hart (1984). The MORB and OIB fields in (f) are from Vervoort et al. (1999). The present day compositions of the mantle end-members DMM, HIMU, EM1 and EM2 shown in (f) are from the compilation of Ernst & Buchan (2003).

samples have εNd_i values that fall between those of the Pickle Crow dyke and Winnipegosis Belt Group 2 samples (Fig. 4.83b).

4.17.3. Pb isotopes

The five samples which failed to run on the mass spectrometer include the Winnipegosis Belt samples, the Pickle Crow dyke sample and two of the Flaherty Formation samples. For the rest of the Circum-Superior LIP samples the overall ranges in $^{206}Pb/^{204}Pb_i$, $^{207}Pb/^{204}Pb_i$ and $^{208}Pb/^{204}Pb_i$ ratios are 11.337-18.473, 14.620-15.694 and 32.113-38.225 respectively. The Hellancourt Formation and Flaherty Formation samples have the lowest $^{206}Pb/^{204}Pb_i$ (11.337-14.635), $^{207}Pb/^{204}Pb_i$ (14.620-15.156) and $^{208}Pb/^{204}Pb_i$ (32.113-34.429) (Fig. 4.83c-d). The Molson dykes have the highest $^{206}Pb/^{204}Pb_i$ (16.534-18.473) while the samples from the Lake Superior region have $^{206}Pb/^{204}Pb_i$ (14.975-16.980) intermediate between the Molson dykes and the Hellancourt Formation and Flaherty Formation samples (Fig. 4.83c-d). The ranges in $^{207}Pb/^{204}Pb_i$ are similar for the Lake Superior region samples and Molson dykes and are 15.331-15.694 and 15.202-15.676 respectively (Fig. 4.83c). The range in $^{208}Pb/^{204}Pb_i$ for the Lake Superior region samples is 35.724-38.225 while the range in the same ratio for the Molson dykes is 36.913-38.128 (Fig. 4.83d). The degree of scatter is greater on the $^{207}Pb/^{204}Pb_i$-$^{206}Pb/^{204}Pb_i$ diagram (Fig. 4.83c) than on the $^{208}Pb/^{204}Pb_i$-$^{206}Pb/^{204}Pb_i$ diagram (Fig. 4.83d). On Fig. 4.83d, the samples appear to form three linear trends. The Hellancourt Formation and Flaherty Formation samples form a trend while the Molson dykes, Badwater Greenstone and Hemlock Formation Groups 1 and 3 form another trend at higher $^{206}Pb/^{204}Pb_i$ and $^{208}Pb/^{204}Pb_i$ ratios. The two Group 2 samples from the Hemlock Formation plot at higher $^{208}Pb/^{204}Pb_i$ compared to the trend of the Molson dykes and other Lake Superior region samples. On Fig. 4.83c five samples fall below the northern hemisphere reference line (NHRL) of Hart (1984). These five samples include one from the Hellancourt Formation, one from Group 1 of the Molson dykes, one from Group 1 of the Flaherty Formation and the samples of Groups 2 and 3 of the Molson dykes. However, in Fig. 4.83d all samples fall to the left (or above) the NHRL.

4.17.4. Hf isotopes

The overall range of $^{176}Hf/^{177}Hf_i$ for the Circum-Superior LIP rocks is 0.281416 to 0.282416. The four samples with the lowest ratios (0.281416-0.281610) are from the Badwater Greenstone and Groups 2 and 3 of the Hemlock Formation (Fig. 4.83e). The Molson dykes and Flaherty Formation samples have similar ratios to each other and range between 0.281710 and 0.281798 (Fig. 4.83e). The Pickle Crow dyke, Hemlock Formation Group 1 and Winnipegosis Belt samples have ratios (0.281865-0.281982) which are slightly higher than those of the Molson dykes and Flaherty Formation (Fig. 4.83e). The two highest ratios belong to the samples of the Hellancourt Formation and are 0.282381 and 0.282416 (Fig. 4.83e). The Badwater Greenstone and Hemlock Formation Groups 2 and 3 samples have εHf_i values ranging between +0.81 and -6.09 (Fig. 4.83f). The εHf_i values of the Molson dykes and Flaherty Formation range between +2.27 and +7.48 while the range for the Pickle Crow dyke, Hemlock Formation Group 1 and Winnipegosis Belt samples is from +9.86 to +14.03 (Fig. 4.83f). The high $^{176}Hf/^{177}Hf_i$ Hellancourt Formation samples have εHf_i values of +28.18 and +29.44 (Fig. 4.83f).

4.17.5. Os isotopes

Out of the fifteen samples selected for Os isotopic analysis, only one sample failed to run on the mass spectrometer. This sample (MMLT07-35) is a Hellancourt Formation Group 2 sample. The fourteen successful samples gave some unusual results. The overall range in $^{187}Os/^{188}Os_i$ is from -12.14796 to 0.11314. The corresponding range in γOs_i values is from -10669.65 to -1.56. Such extreme $^{187}Os/^{188}Os_i$ ratios and γOs_i values have not been reported in the literature for any rocks from any geographical area or geological time. Day et al. (2008) reported Os isotopic results from thirty nine analyses of samples from the 1270 Ma Muskox intrusion layered series on the northwestern edge of the Canadian Shield. Out of the thirty nine analyses, six yielded results with $^{187}Os/^{188}Os_i$ of 0.18574-2.93012 and γOs_i values of -15.7 to -1863. Day et al. (2008) ascribed the largely negative γOs_i values to post-magmatic hydrothermal Re mobilisation. It appears that the Re-Os isotope systematics of many of the Circum-Superior LIP rocks may have been

disturbed and so the calculated $^{187}Os/^{188}Os_i$ and γOs_i values may reveal little about the mantle sources and potential contaminants of the Circum-Superior LIP magmas.

4.18. Summary

Some of the main geochemical features of all the individual segments of the Circum-Superior LIP and the subgroups within the segments are summarised in Table 4.2. A feature which seems quite common throughout some of the Circum-Superior LIP is the presence of both high and low MgO rocks within individual segments. The volcanic rocks of the Chukotat Group, Fox River Belt and Winnipegosis Belt and the Molson dykes all have large variations in MgO concentrations from a minimum of 5.72 wt. % to a maximum of 26.74 wt. %. The Hellancourt Formation and Flaherty Formation have fairly restricted ranges in MgO content of 6.03-9.86 wt. % and 5.09-8.22 wt. % respectively. The most felsic rocks belonging to the Circum-Superior LIP are found in the Lake Superior region where the overall range in MgO concentrations is from 0.50 to 10.83 wt. %. The vast majority of samples from the Circum-Superior LIP plot as subalkaline basalts on the Zr/Ti-Nb/Y diagram. Out of these samples, those which have MgO >12 wt. % are referred to as picrites. None of the rocks analysed in this study are proper komatiites, even if they contain >18 wt. % MgO, as none contain olivine spinifex texture.

A trace element signature similar to that of oceanic plateaux such as the Ontong Java Plateau is common throughout a large portion of the Circum-Superior LIP. This signature has reasonably flat REE profiles and multi-element profiles with the exception of Th which is slightly depleted with respect to the other elements. Such a signature is present in the Chukotat Group, Fox River Belt, Winnipegosis Belt, Molson dykes, Pickle Crow dyke, Labrador Trough and Group 1 of the Hemlock Formation. The vast majority of samples from these areas plot close to the composition of primitive mantle and between the Icelandic plume tramlines on the Nb/Y-Zr/Y diagram. Samples with multi-element profiles possessing negative Nb-Ta anomalies are present in many of the segments of the Circum-Superior LIP. All of the Thompson Nickel Belt samples have large negative Nb-Ta anomalies with Nb/Nb* values of 0.08-0.62 while the majority of samples from the Lake Superior region (Gunflint Formation, Badwater Greenstone, Emperor Volcanic Complex, and

Table 4.2. Summary of the geochemical features of the Circum-Superior LIP

	Chukotat Group		Flaherty Formation		Haig sill	Fox River Belt	
	Group 1	Group 2	Group 1	Group 2		Volcanic rocks	Intrusive rocks
MgO (wt. %)	6.62-19.84	10.97-19.21	5.23-8.22	5.09-7.59	5.32-7.59	5.72-20.18	4.44-42.20
Fe_2O_3(T) (wt. %)	11.43-17.13	9.92-12.24	15.11-17.90	14.45-19.24	13.65-21.22	10.82-16.43	7.03-14.40
Mg#	30.06-63.20	49.91-64.91	25.29-36.07	25.03-32.80	21.79-38.17	28.46-62.97	25.77-79.38
SiO_2 (wt. %)	46.30-50.65	48.39-51.93	44.51-49.08	44.88-48.00	45.85-47.92	45.65-53.26	42.87-54.14
Total alkalis (wt. %)	0.75-3.67	0.92-3.20	2.50-3.84	0.66-4.66	3.16-3.69	0.47-3.89	0.05-3.55
$(La/Sm)_N$	0.63-1.21	0.89-1.72	1.39-2.56	1.71-2.05	2.56-2.61	0.59-1.23	0.59-2.28
$(Gd/Yb)_N$	1.01-1.25	1.05-1.23	1.20-1.42	1.21-1.32	1.34-1.40	0.98-1.17	0.76-1.33
Eu/Eu*	0.92-1.07	0.88-1.02	0.86-1.06	0.85-0.95	0.99-1.02	0.80-1.25	0.54-1.46
Nb/Th	7.01-18.54	2.17-6.02	10.39-16.00	7.33-10.20	9.53-11.01	9.18-19.31	1.88-11.69
Zr/Nb	16.24-22.58	16.96-21.94	7.81-9.42	8.22-9.44	4.41-4.91	14.51-21.10	13.74-45.38
Zr/Y	2.06-3.02	2.41-3.01	3.21-4.48	3.33-3.77	3.50-3.75	2.08-3.24	1.24-3.58
Nb/Y	0.10-0.17	0.12-0.18	0.35-0.52	0.37-0.46	0.72-0.80	0.11-0.20	0.03-0.22
Nb/Nb*	0.81-1.60	0.37-0.81	1.16-1.57	0.90-1.17	1.18-1.32	1.08-1.62	0.29-1.10
Ti/Ti*	0.74-1.05	0.63-0.75	1.04-1.20	1.07-1.27	0.92-1.49	0.69-1.12	0.60-1.14
$^{87}Sr/^{86}Sr_i$			0.701992-0.702678	0.701965-0.702858			
$^{143}Nd/^{144}Nd_i$			0.510344-0.510419	0.510326-0.510337			
εNd_i			+2.73 to +4.19	+2.38 to +2.60			
$^{206}Pb/^{204}Pb_i$			11.445	13.572			
$^{207}Pb/^{204}Pb_i$			14.620	14.978			
$^{208}Pb/^{204}Pb_i$			32.492	33.837			
$^{176}Hf/^{177}Hf_i$			0.281749-0.281762	0.281651-0.281710			
εHf_i			+5.76 to +6.21	+2.27 to +4.37			

Table 4.2. contd.

	Thompson Nickel Belt		Winnipegosis Belt		Molson dykes		
	Group 1	Group 2	Group 1	Group 2	Group 1	Group 2	Group 3
MgO (wt. %)	25.79-39.13	23.77-37.91	19.87-26.74	6.81-7.94	16.53-20.50	8.17-9.97	6.00-6.99
Fe_2O_3(T) (wt. %)	7.79-17.64	12.18-14.68	11.99-13.65	14.05-16.45	10.92-12.74	10.92-13.04	13.83-16.15
Mg#	61.90-80.99	68.45-76.98	59.93-68.87	32.48-34.10	59.80-66.36	41.33-48.59	29.24-35.98
SiO_2 (wt. %)	41.88-47.49	41.92-49.05	45.16-46.57	47.50-49.71	45.84-48.09	47.38-49.64	47.60-48.80
Total alkalis (wt. %)	0.05-0.71	0.06-0.83	0.65-1.34	1.65-2.55	1.12-1.54	1.62-2.34	2.76-2.91
$(La/Sm)_N$	1.88-14.10	0.80-4.13	0.77-0.90	0.74-0.83	0.64-1.78	0.54-1.22	1.36-1.50
$(Gd/Yb)_N$	0.69-1.67	0.73-1.27	0.99-1.06	1.02-1.06	1.00-1.10	0.92-1.11	1.19-1.28
Eu/Eu*	0.66-1.52	0.48-0.87	0.96-1.07	0.97-1.02	0.98-1.06	0.98-1.17	0.96-0.98
Nb/Th	0.60-3.59	0.85-2.65	8.64-28.87	11.69-29.02	1.88-13.11	4.21-17.23	8.65-12.55
Zr/Nb	14.48-87.67	24.78-65.71	19.51-30.19	18.18-20.88	13.13-21.49	18.97-31.77	11.24-14.65
Zr/Y	2.05-28.02	1.43-6.71	2.04-2.94	2.19-2.66	1.99-3.30	2.02-3.13	3.19-3.62
Nb/Y	0.09-0.32	0.02-0.18	0.07-0.13	0.12-0.13	0.09-0.21	0.06-0.15	0.22-0.32
Nb/Nb*	0.12-0.27	0.08-0.62	0.89-1.55	1.15-1.76	0.33-1.43	0.60-1.48	0.86-1.24
Ti/Ti*	0.19-0.93	0.35-1.10	0.94-1.09	0.99-1.16	0.88-1.02	0.90-1.01	0.98-1.04
$^{87}Sr/^{86}Sr_i$			0.702256	0.701921	0.701530-0.703392	0.701978	0.702031
$^{143}Nd/^{144}Nd_i$				0.510324	0.510352		
εNd_i				+2.35	+2.89		
$^{206}Pb/^{204}Pb_i$					16.534-18.473	17.513	17.277
$^{207}Pb/^{204}Pb_i$					15.258-15.676	15.315	15.202
$^{208}Pb/^{204}Pb_i$					36.913-38.128	37.662	37.333
$^{176}Hf/^{177}Hf_i$			0.281865	0.281942	0.281757-0.281772	0.281798	0.281788
εHf_i			+9.86	+12.59	+6.03 to +6.56	+7.48	+7.11

Table 4.2. contd.

	Pickle Crow dyke	Gunflint Formation	Hemlock Formation				Kiernan sills
			Group 1	Group 2	Group 3	Group 4	
MgO (wt. %)	6.52-7.86	4.59-6.66	7.50-8.53	0.50-7.82	6.30-7.74	6.27	6.80-10.83
Fe_2O_3(T) (wt. %)	9.00-15.06	12.77-18.25	11.26-11.87	1.23-25.43	13.62-14.28	17.99	9.91-15.67
Mg#	32.50-49.26	28.25-32.02	41.27-45.70	20.65-39.05	33.92-37.76	27.91	33.29-48.10
SiO_2 (wt. %)	49.02-53.40	47.21-53.09	48.55-49.92	40.28-75.77	46.82-50.79	41.64	46.38-49.94
Total alkalis (wt. %)	2.64-4.23	3.92-6.33	2.05-2.13	1.85-9.91	3.45-5.02	2.39	2.53-5.28
$(La/Sm)_N$	0.74-0.81	2.82-3.11	0.76-1.05	2.44-4.16	2.04-2.38	1.59	0.95-2.34
$(Gd/Yb)_N$	0.99-1.08	1.28-1.46	1.07	1.10-1.60	1.48-1.62	2.38	1.14-2.41
Eu/Eu*	1.00-1.05	0.76-1.08	1.03-1.06	0.65-1.12	0.95-1.18	0.67	1.01-1.38
Nb/Th	14.16-26.01	3.56-3.72	12.79-15.18	1.06-5.75	7.02-10.04	14.43	7.09-14.64
Zr/Nb	16.24-16.66	8.43-8.56	24.02-24.39	8.55-17.68	6.97-8.76	7.37	5.67-15.72
Zr/Y	2.39-2.43	4.61-4.86	2.64-2.77	3.68-7.26	4.69-5.00	6.67	2.39-6.54
Nb/Y	0.14-0.15	0.54-0.57	0.11	0.36-0.60	0.55-0.72	0.91	0.15-1.15
Nb/Nb*	0.95-1.01	0.53-0.60	1.09-1.16	0.33-0.86	0.92-1.10	1.28	0.75-1.71
Ti/Ti*	1.16-1.59	0.85-1.00	1.03-1.06	0.40-1.25	0.92-1.12	1.70	0.90-1.19
$^{87}Sr/^{86}Sr_i$	0.701790		0.702504	0.701319-0.710950	0.703915		
$^{143}Nd/^{144}Nd_i$	0.510475		0.510374	0.509808-0.509935	0.510247		
εNd_i	+5.29		+3.33	-5.29 to -7.77	+0.84		
$^{206}Pb/^{204}Pb_i$			16.980	14.975-15.718	15.291		
$^{207}Pb/^{204}Pb_i$			15.614	15.331-15.694	15.388		
$^{208}Pb/^{204}Pb_i$			37.211	36.518-38.225	35.724		
$^{176}Hf/^{177}Hf_i$	0.281883		0.281982	0.281416-0.281512	0.281610		
εHf_i	+10.49		+14.03	-2.69 to -6.09	+0.81		

Table 4.2. contd.

	Badwater Greenstone	Emperor Volcanic Complex	Hellancourt Formation	
			Group 1	Group 2
MgO (wt. %)	4.01-8.90	2.49-8.44	7.29-9.86	6.03-8.79
Fe_2O_3(T) (wt. %)	11.99-14.75	3.81-14.04	11.17-15.09	8.44-14.94
Mg#	23.19-45.20	24.67-51.73	36.26-47.17	32.11-53.67
SiO_2 (wt. %)	49.10-54.13	49.72-74.03	46.73-50.94	47.32-52.72
Total alkalis (wt. %)	0.58-4.36	2.97-7.23	1.62-4.46	1.29-3.04
$(La/Sm)_N$	1.83-3.38	2.01-4.00	0.84-1.10	0.77-0.99
$(Gd/Yb)_N$	1.09-1.56	1.23-2.39	0.94-1.06	0.91-1.11
Eu/Eu*	0.84-1.07	0.69-1.46	0.89-1.22	0.93-1.12
Nb/Th	1.95-5.32	1.58-5.59	11.99-23.41	8.94-18.52
Zr/Nb	10.29-13.62	9.16-35.92	15.98-21.58	17.73-22.18
Zr/Y	3.68-5.23	2.77-12.77	2.29-2.75	2.20-2.95
Nb/Y	0.35-0.46	0.25-0.53	0.12-0.17	0.10-0.15
Nb/Nb*	0.31-0.75	0.28-0.61	0.99-1.56	0.95-1.51
Ti/Ti*	0.76-1.26	0.32-0.96	0.95-1.16	0.76-1.06
$^{87}Sr/^{86}Sr_i$	0.703911		0.702081-0.702426	
$^{143}Nd/^{144}Nd_i$	0.510108		0.510394-0.510415	
εNd_i	-1.89		+3.72 to +4.12	
$^{206}Pb/^{204}Pb_i$	15.953		11.337-14.635	
$^{207}Pb/^{204}Pb_i$	15.656		14.689-15.156	
$^{208}Pb/^{204}Pb_i$	36.583		32.113-34.429	
$^{176}Hf/^{177}Hf_i$	0.281575		0.282381-0.282416	
εHf_i	-0.43		+28.17 to +29.44	

Group 2 of the Hemlock Formation) also have strongly negative Nb-Ta anomalies in their multi-element profiles. A few of the samples of the Molson dykes and Chukotat Group and most of the intrusive samples from the Fox River Belt also contain negative Nb-Ta anomalies. No such anomalies are present in the Flaherty Formation, Winnipegosis Belt, Pickle Crow dyke or Hellancourt Formation.

One interesting feature of the trace element signatures of the Chukotat Group, Fox River Belt and Hellancourt Formation is the presence in some of the samples from these segments of negative Ti anomalies. These negative Ti anomalies generally occur in the higher MgO rock samples and are absent in the lower MgO samples. However, in other segments of the Circum-Superior LIP that contain non-cumulative high MgO rocks (Winnipegosis Belt and Molson dykes) no negative Ti anomalies are present.

The Flaherty Formation basalts have trace element signatures which are somewhat different to the rest of the Circum-Superior LIP. The rocks from the Belcher Islands can effectively be split into two groups. Both groups are more enriched in Th-Nb-Ta-LREEs over the rest of the incompatible elements than the many Circum-Superior LIP samples with an oceanic-plateau-like signature. The low MgO Group 3 samples of the Molson dykes and Group 3 of the Hemlock Formation are also relatively enriched in the more incompatible elements. The two groups of the Flaherty Formation are best distinguished on the basis of Nb-Ta anomalies relative to Th and La. One group of Flaherty Formation basalts have positive Nb-Ta anomalies while the other group has no Nb-Ta anomalies. Positive Nb-Ta anomalies are also found in three samples outside of Hudson Bay; one from the Molson dykes, one from the Hemlock Formation and one from the Kiernan sills.

Further chemical differences exist between the segments of the Circum-Superior LIP in terms of HREE patterns and $(Gd/Yb)_N$ ratios. Samples from the Chukotat Group, Fox River Belt, Winnipegosis Belt, Groups 1 and 2 of the Molson dykes, Pickle Crow dyke, Group 1 of the Hemlock Formation, Hellancourt Formation and some from the Thompson Nickel Belt have flat HREE patterns and $(Gd/Yb)_N$ ratios close to unity. Samples from the Flaherty Formation, Haig sill, Group 3 of the Molson dykes, Lake Superior region (except Group 1 of the Hemlock Formation) and some

from the Thompson Nickel Belt have more negatively-sloped HREE patterns and $(Gd/Yb)_N$ ratios greater than 1.2.

In Sr-Nd isotopic space the Circum-Superior LIP samples appear to define two broad groupings. Samples from the Badwater Greenstone and Groups 2 and 3 of the Hemlock Formation have lower $^{143}Nd/^{144}Nd_i$ ratios (0.509808-0.510247) than all the other samples and are spread over a large range of $^{87}Sr/^{86}Sr_i$ ratios (0.703911-0.710950). The other broad grouping consists of samples from the Flaherty Formation, Winnipegosis Belt, Molson dykes, Pickle Crow dyke, Group 1 of the Hemlock Formation, and Hellancourt Formation. These samples have higher $^{143}Nd/^{144}Nd_i$ ratios (0.510324-0.510475) and a more restricted range of $^{87}Sr/^{86}Sr_i$ ratios (0.701530-0.703392). These ratios are similar to the very few previously published Sr and Nd isotopic ratios from the Chukotat Group and Labrador Trough. The Badwater Greenstone and Groups 2 and 3 of the Hemlock Formation also have the lowest $^{176}Hf/^{177}Hf_i$ ratios (0.281416-0.281610) in the Circum-Superior LIP. The other samples form three broad groupings in Hf isotope space. Samples from the Molson dykes and Flaherty Formation have $^{176}Hf/^{177}Hf_i$ ratios of 0.281651-0.281798 and are similar to previously published values from the Chukotat Group and some of the previously published values from the Fox River Belt. The Winnipegosis Belt, Pickle Crow dyke and Group 1 of the Hemlock Formation have slightly higher $^{176}Hf/^{177}Hf_i$ ratios (0.281865-0.281982) and overlap with some of the previously published values from the Fox River Belt. The Hellancourt Formation has the highest $^{176}Hf/^{177}Hf_i$ ratios (0.282381-0.282416) which are similar to one sample previously published from the Fox River Belt. The Circum-Superior LIP samples divide into three broad groups in Pb isotopic space. The Flaherty Formation and Hellancourt Formation have the lowest $^{206}Pb/^{204}Pb_i$ (11.337-14.635), $^{207}Pb/^{204}Pb_i$ (14.620-15.156) and $^{208}Pb/^{204}Pb_i$ (32.113-34.429) ratios. The Lake Superior region samples have higher $^{206}Pb/^{204}Pb_i$ (14.975-16.980), $^{207}Pb/^{204}Pb_i$ (15.331-15.694) and $^{208}Pb/^{204}Pb_i$ (35.724-38.225) while the Molson dykes have the highest $^{206}Pb/^{204}Pb_i$ (16.534-18.473) ratios and similar $^{207}Pb/^{204}Pb_i$ (15.202-15.676) and $^{208}Pb/^{204}Pb_i$ (36.913-38.128) ratios to the Lake Superior region samples.

5. DISCUSSION

In this chapter the major element, trace element and isotopic results are used to determine the nature of the mantle sources from which the Circum-Superior LIP was derived and the igneous processes which have affected the composition of magmas originating from these sources. Various modelling techniques are applied to ascertain the extent of partial melting, fractional crystallisation and crustal contamination as well as the depth of melting and the temperature of the mantle which melted to form the Circum-Superior LIP. The presence of negative Ti anomalies and Ni-Cu-PGE sulphide deposits in some segments of the Circum-Superior LIP is discussed and possible geochemical discriminants between fertile and barren LIPs assessed for their applicability to the Circum-Superior LIP. Possible mechanisms to explain the distribution of the majority of the magmatism around the cratonic margins of the Superior Province are discussed and the arguments of Heaman et al. (2009) concerning the formation of the Circum-Superior LIP are examined. Finally the geochemistry of the Circum-Superior LIP is compared to other worldwide ~1880 Ma magmatic provinces to assess the potential occurrence of a superplume event and the relative positions of continental fragments at this time in Earth's history.

5.1. Partial melting and primary magma compositions

Herzberg & Asimow (2008) have developed a piece of petrological software that calculates the major element composition of a primary magma from an observed lava composition. The software is known as PRIMELT2 and also calculates the degree of partial melting required to generate the primary magma, the mantle potential temperature (T_P), the primary eruption temperature, and the composition of liquidus olivine co-existing with primary liquid. PRIMELT2 can model both batch and accumulated fractional melting and uses a hybrid forward and inverse model to determine the degree of partial melting. The inverse model incrementally adds or subtracts olivine to or from a measured evolved lava composition. The inverse model assumes olivine is the only phase to have crystallised and the software will filter out samples which have experienced clinopyroxene crystallisation by examination of CaO and MgO concentrations. The results of the inverse modelling are computed in both FeO-MgO space and olivine-anorthite-diopside-silica projection space and

compared to the results of forward models derived from parameterisations of melting experiments. The degree of partial melting is determined and primary magma composition calculated when the inverse and forward models suggest a common melt fraction in both FeO-MgO and projection space. PRIMELT2 is able to model melting in projection space for harzburgite, dunite, spinel lherzolite, lherzolite, and garnet peridotite residues. The software can also filter out samples which may have originated from a pyroxenitic source or a volatile-rich source via examination of SiO_2, MgO and CaO concentrations. PRIMELT2 also allows the user to adjust the FeO and MgO concentrations of the peridotite source and the oxidation state of the source by altering $Fe^{2+}/\Sigma Fe$ and Fe_2O_3/TiO_2 ratios.

All samples in this study were run through the PRIMELT2 software. However, only nineteen samples yielded successful solutions. These results are discussed below. For all samples, the $Fe^{2+}/\Sigma Fe$ and Fe_2O_3/TiO_2 ratios were kept at 0.9 and 0.5 respectively.

5.1.1. Chukotat Group primary magmas

PRIMELT2 was able to calculate primary magma compositions for seven of the samples from the Chukotat Group volcanic rocks. The major element compositions of the primary magmas and the degrees of partial melting required to generate them are given in Table 5.1. The source composition used was that of the Kettle River fertile peridotite sample KR-4003 with FeO and MgO concentrations of 8.02 and 38.12 wt. % respectively (Herzberg & O'Hara, 2002). PRIMELT2 was only able to generate solutions for accumulated fractional melting. The MgO contents of the primary magma vary from 17.40 to 20.72 wt. % and are in equilibrium with olivine ranging in composition from $Fo_{91.4}$ to $Fo_{92.1}$. The range in the degree of partial melting required to generate the primary magmas is 32.3-34.1%.

To test the validity of the solutions obtained by PRIMELT2 for the Chukotat Group, the results have been compared to trace element melting models. The trace element composition of the mantle source is taken to be that of primitive mantle (Sun & McDonough, 1989) with 1% average continental crust (Rudnick & Fountain, 1995) extracted from it. This source has been chosen because the removal of such a small amount of melt from the pyrolite of McDonough & Sun (1995) has been shown to

Table 5.1. PRIMELT2-calculated primary magma compositions for the Chukotat Group

	MMC 08-8	MMC 08-9	MMC 08-10	MMC 08-19	MMC 08-22	MMC 08-23	MMC 08-25
Source	KR-4003	KR-4003	KR-4003	KR-4003	KR-4003	KR-4003	KR-4003
Melting style	AF	AF	AF	AF	AF	AF	AF
+/- olivine (%)	+11.98	+5.36	+13.20	+10.23	+10.06	+2.64	+8.45
SiO_2 (wt. %)	49.66	50.17	48.50	47.02	48.07	49.30	49.30
TiO_2 (wt. %)	0.53	0.54	0.62	0.50	0.54	0.50	0.55
Al_2O_3 (wt. %)	8.97	9.15	9.34	8.84	9.56	9.86	9.09
Cr_2O_3 (wt. %)	0.18	0.23	0.18	0.24	0.18	0.23	0.23
Fe_2O_3 (wt. %)	1.04	1.08	1.07	1.18	1.12	1.14	1.09
FeO (wt. %)	9.45	9.17	9.82	10.41	9.89	9.42	9.58
MnO (wt. %)	0.16	0.16	0.17	0.18	0.18	0.17	0.17
MgO (wt. %)	18.15	17.40	19.02	20.72	19.17	17.98	18.49
CaO (wt. %)	10.10	10.32	9.57	9.45	9.80	9.91	9.74
Na_2O (wt. %)	1.55	1.59	1.44	1.01	1.14	1.35	1.50
K_2O (wt. %)	0.07	0.07	0.09	0.28	0.22	0.03	0.11
NiO (wt. %)	0.11	0.10	0.13	0.13	0.10	0.08	0.12
P_2O_5 (wt. %)	0.04	0.04	0.05	0.04	0.05	0.04	0.04
T (°C)	1412	1397	1429	1460	1432	1409	1419
T_P (°C)	1533	1517	1552	1586	1555	1530	1540
Fo	91.6	91.4	91.8	92.1	91.8	91.5	91.6
F (%)	33.2	32.8	32.6	34.1	32.6	32.3	33.4

B – batch melting; AF – accumulated fractional melting; T – eruption temperature; T_P – mantle potential temperature; Fo – forsterite content of olivine in equilibrium with the melt; F – degree of partial melting.

produce a peridotite with a major element composition very similar to that of KR-4003 (Herzberg, 2004b). The same source composition has also been successfully used to model the petrogenesis of the Ontong Java Plateau (Fitton & Goddard, 2004; Tejada et al., 2004). The equation of Shaw (1970) for non-modal batch melting is used to constrain the trace element composition of the partial melts. The non-modal batch melting equation is used despite PRIMELT2 obtaining major element solutions from accumulated fractional melting because many studies have shown that batch and accumulated (pooled) fractional melting produce melts with near-identical incompatible trace element compositions especially at large degrees of melting (>30%; e.g. Rollinson, 1993; Fitton & Goddard, 2004; Hastie & Kerr, 2010). The melting equation, source composition, mineral modes, melting modes and partition co-efficients used in the trace element modelling are given in Appendix F.

The HREE patterns of the Chukotat Group primary magmas are relatively flat and their $(Gd/Yb)_N$ ratios are all less than 1.18. This suggests that either melting occurred at depths largely within the spinel stability field or that the degree of melting was high enough to consume nearly all the garnet in the source. In order to simplify the

melting model, the trace element compositions of partial melts were calculated using mineral modes for spinel lherzolite.

The results of the trace element modelling are displayed in Fig. 5.1. The multi-element profiles of the primary magmas of the Chukotat Group are similar to those generated by 32-35% partial melting of the selected source composition. The fit is good considering the uncertainties in the composition of primitive mantle and continental crust. The results of the trace element modelling may be slightly inaccurate given that a new set of mineral and melt modes and a new starting composition are not selected after all the clinopyroxene has been consumed. However, the melting models obtained by both major and trace elements are generally similar and suggest that the Chukotat Group primary magmas were generated by ~32-34% partial melting of a peridotite source with a composition similar to that of primitive mantle depleted by the extraction of a small amount of continental crust, although this source composition does not account for the negative Ti anomalies present in the Chukotat primary magmas (Fig. 5.1).

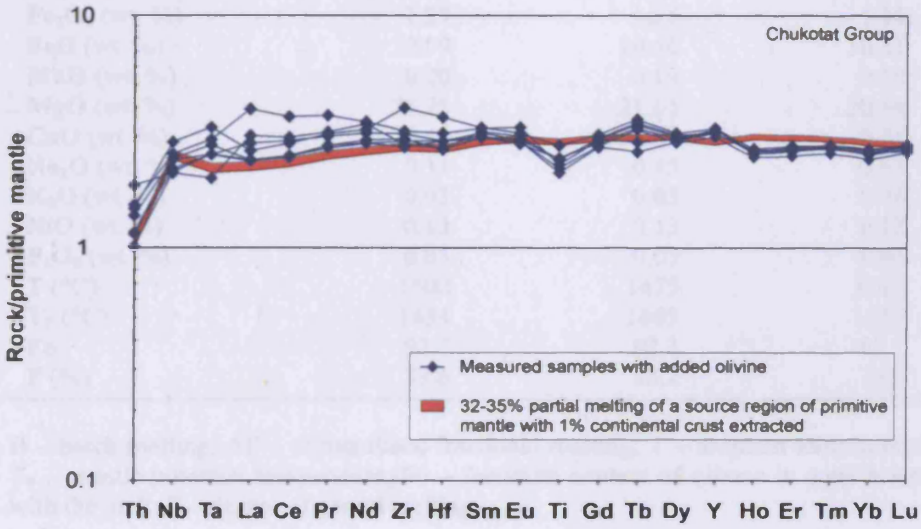

Fig. 5.1. Primitive-mantle-normalised multi-element diagram for the Chukotat Group primary magmas identified by PRIMELT2 and the results of trace element modelling. Primitive mantle values from Sun & McDonough (1989).

5.1.2. Fox River Belt primary magmas

PRIMELT2 was able to calculate primary magma compositions for three of the samples from the Fox River Belt volcanic rocks. The major element compositions of the primary magmas and the degrees of partial melting required to generate them are given in Table 5.2. The KR-4003 composition was also used as the source for the Fox River Belt rocks and primary magma solutions were only generated through accumulated fractional melting. The calculated MgO contents of the primary magmas vary between 20.40 and 23.25 wt. % and are in equilibrium with olivine ranging in composition from $Fo_{92.0}$ to $Fo_{92.7}$. The range in degree of partial melting required to generate the primary magmas is 34.3-39.6%.

Table 5.2. PRIMELT2-calculated primary magma compositions for the Fox River Belt

	MMFR08-8	MMFR08-10	MMFR08-13
Source	KR-4003	KR-4003	KR-4003
Melting style	AF	AF	AF
+/- olivine (%)	+9.45	+4.72	+15.04
SiO_2 (wt. %)	46.17	47.39	47.19
TiO_2 (wt. %)	0.45	0.48	0.42
Al_2O_3 (wt. %)	8.72	8.74	9.00
Cr_2O_3 (wt. %)	0.24	0.32	0.23
Fe_2O_3 (wt. %)	1.27	1.25	1.14
FeO (wt. %)	10.99	10.50	10.41
MnO (wt. %)	0.20	0.19	0.18
MgO (wt. %)	23.25	21.61	20.86
CaO (wt. %)	8.40	8.87	9.74
Na_2O (wt. %)	0.11	0.45	0.61
K_2O (wt. %)	0.03	0.05	0.06
NiO (wt. %)	0.13	0.13	0.12
P_2O_5 (wt. %)	0.05	0.05	0.04
T (°C)	1502	1475	1462
T_P (°C)	1634	1603	1589
Fo	92.7	92.3	92.1
F (%)	39.6	38.2	35.0

B – batch melting; AF – accumulated fractional melting; T – eruption temperature; T_P – mantle potential temperature; Fo – forsterite content of olivine in equilibrium with the melt; F – degree of partial melting.

Trace element modelling is again in agreement with the results obtained by PRIMELT2. Fig. 5.2 shows that the fit between the multi-element profiles of the Fox River Belt primary magmas and those generated by 34-40% partial melting of a source composition identical to that used for the Chukotat Group is good, although the negative Ti anomalies of the Fox River Belt primary magmas are again not

replicated. It should be noted, however, that for simplification a new set of mineral and melt modes and a new starting composition were not calculated after all the clinopyroxene is consumed. The melting equation, mineral modes, melting modes and partition co-efficients used in the calculations are the same as for the Chukotat Group and are given in Appendix F. Mineral modes for a spinel lherzolite were used because of the relatively flat HREE patterns and $(Gd/Yb)_N$ ratios close to unity of the Fox River Belt primary magmas.

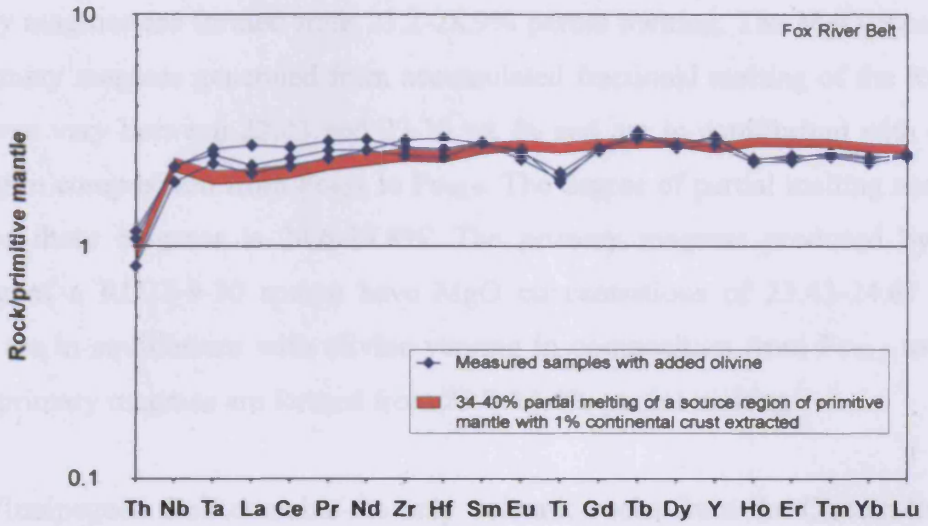

Fig. 5.2. Primitive-mantle-normalised multi-element diagram for the Fox River Belt primary magmas identified by PRIMELT2 and the results of trace element modelling. Primitive mantle values from Sun & McDonough (1989).

5.1.3. Winnipegosis Belt primary magmas

PRIMELT2 was able to successfully calculate primary magma compositions for seven of the Winnipegosis Belt samples. The seven samples gave successful solutions for accumulated fractional melting of a source composition similar to that of KR-4003 while four of the samples also gave solutions for batch melting of the same source. Four samples also gave successful solutions for accumulated fractional melting of a depleted source composition the same as that of the RC27-9-30 abyssal peridotite of Baker & Beckett (1999) which contains 8.07 wt. % FeO and 41.80 wt. % MgO. This peridotite composition has been used because previous studies have interpreted RC27-9-30 to be a depleted peridotite (Baker & Beckett, 1999; Herzberg & O'Hara, 2002; Herzberg et al., 2007; Herzberg & Asimow, 2008). Two of these

four samples yielded successful solutions for batch melting of the same source. The major element compositions of the primary magmas and the degrees of melting required to generate them are given in Table 5.3. The MgO contents of the primary magmas generated from accumulated fractional melting of the KR-4003 source vary between 19.47 and 22.01 wt. % and are in equilibrium with olivine ranging in composition from $Fo_{91.8}$ to $Fo_{92.4}$. The degree of partial melting needed to produce these primary magmas is 26.3-36.7%. The primary magmas produced by batch melting of a KR-4003 source have MgO concentrations of 20.86-23.88 wt. % which are in equilibrium with olivine varying in composition from $Fo_{92.4}$ to $Fo_{93.1}$. These primary magmas are formed from 23.2-28.9% partial melting. The MgO contents of the primary magmas generated from accumulated fractional melting of the RC27-9-30 source vary between 22.03 and 23.30 wt. % and are in equilibrium with olivine ranging in composition from $Fo_{92.6}$ to $Fo_{92.9}$. The degree of partial melting needed to produce these magmas is 24.6-29.8%. The primary magmas produced by batch melting of a RC27-9-30 source have MgO concentrations of 23.43-24.67 wt. % which are in equilibrium with olivine varying in composition from $Fo_{93.2}$ to $Fo_{93.4}$. These primary magmas are formed from 23.0-24.4% partial melting.

The Winnipegosis Belt contains the only volcanic rocks from the Circum-Superior LIP which still possess some relatively unaltered olivine crystals (Fig. 3.13). These olivine crystals were analysed by scanning electron microscopy to see if their forsterite numbers matched those calculated to be in equilibrium with primary magmas by PRIMELT2. The scanning electron microscope results are given in Appendix E. Two of the samples (MMW07-9 and MMW07-12) which gave successful PRIMELT2 solutions contain a few relatively unaltered olivine crystals thought to be phenocrysts. PRIMELT2 calculated the Fo numbers of olivine in equilibrium with MMW07-9 and MMW07-12 primary magmas (derived by accumulated fractional melting) as 92.4 and 92.3 respectively (Table 5.3). However, olivines with such high Fo numbers were not observed in the two samples. The maximum Fo numbers observed were 90.6 and 90.7 in MMW07-9 and MMW07-12 respectively (Table E.1). Whether the differences between the predicted and measured olivine Fo numbers suggest that the PRIMELT2 solutions are inaccurate is difficult to say. Only six olivine crystals in each of the two samples were suitably fresh enough for analysis. It is possible that some of the numerous olivine crystals in

Table 5.3. PRIMELT2-calculated primary magma compositions for the Winnipegosis Belt

	MMW 07-2	MMW 07-2	MMW 07-2	MMW 07-3	MMW 07-3	MMW 07-3	MMW 07-3
Source	KR-4003	KR-4003	RC 27-9-30	KR-4003	KR-4003	RC 27-9-30	RC 27-9-30
Melting style	B	AF	AF	B	AF	B	AF
+/- olivine (%)	+7.07	+0.28	+4.94	+3.00	-3.03	+7.44	+1.74
SiO_2 (wt. %)	45.57	45.88	45.66	45.38	45.66	45.20	45.44
TiO_2 (wt. %)	0.55	0.58	0.56	0.54	0.57	0.52	0.55
Al_2O_3 (wt. %)	7.84	8.38	8.01	7.88	8.35	7.54	7.97
Cr_2O_3 (wt. %)	0.33	0.34	0.33	0.38	0.39	0.37	0.38
Fe_2O_3 (wt. %)	1.27	1.36	1.29	1.32	1.40	1.26	1.34
FeO (wt. %)	10.75	11.00	10.83	10.90	11.12	10.72	10.95
MnO (wt. %)	0.18	0.18	0.18	0.18	0.19	0.18	0.18
MgO (wt. %)	23.88	22.01	23.30	23.48	21.79	24.67	23.13
CaO (wt. %)	8.44	9.01	8.61	8.86	9.39	8.49	8.97
Na_2O (wt. %)	0.97	1.04	0.99	0.83	0.89	0.80	0.84
K_2O (wt. %)	0.09	0.09	0.09	0.10	0.11	0.10	0.10
NiO (wt. %)	0.12	0.10	0.11	0.10	0.11	0.14	0.12
P_2O_5 (wt. %)	0.03	0.03	0.03	0.03	0.04	0.03	0.03
T (°C)	1512	1482	1503	1506	1478	1524	1500
T_P (°C)	1645	1611	1634	1638	1606	1659	1631
Fo	93.1	92.3	92.9	92.9	92.2	93.4	92.8
F (%)	28.9	32.1	29.8	25.9	28.3	24.4	26.4

	MMW 07-9	MMW 07-10	MMW 07-10	MMW 07-12	MMW 07-16	MMW 07-16	MMW 07-16
Source	KR-4003	KR-4003	KR-4003	KR-4003	KR-4003	KR-4003	RC 27-9-30
Melting style	AF	B	AF	AF	B	AF	B
+/- olivine (%)	+0.09	-14.20	-18.79	+5.20	+2.63	-2.76	+7.08
SiO_2 (wt. %)	46.71	45.94	46.17	46.49	45.71	45.97	45.51
TiO_2 (wt. %)	0.53	0.58	0.61	0.59	0.63	0.66	0.60
Al_2O_3 (wt. %)	8.07	9.55	9.99	8.79	8.51	8.97	8.15
Cr_2O_3 (wt. %)	0.37	0.37	0.38	0.31	0.33	0.34	0.32
Fe_2O_3 (wt. %)	1.32	1.39	1.45	1.27	1.29	1.36	1.23
FeO (wt. %)	10.70	10.23	10.36	10.70	10.60	10.77	10.45
MnO (wt. %)	0.17	0.19	0.19	0.18	0.18	0.18	0.17
MgO (wt. %)	21.91	20.86	19.47	21.56	22.19	20.62	23.43
CaO (wt. %)	8.92	9.40	9.83	8.89	9.04	9.52	8.66
Na_2O (wt. %)	0.99	1.28	1.34	1.01	1.10	1.16	1.05
K_2O (wt. %)	0.11	0.10	0.11	0.08	0.20	0.21	0.19
NiO (wt. %)	0.11	0.08	0.07	0.09	0.09	0.07	0.09
P_2O_5 (wt. %)	0.09	0.04	0.04	0.04	0.16	0.17	0.16
T (°C)	1480	1462	1437	1474	1485	1458	1505
T_P (°C)	1609	1589	1561	1602	1614	1584	1637
Fo	92.4	92.4	91.8	92.3	92.7	92.0	93.2
F (%)	36.7	23.2	24.8	34.4	24.4	26.3	23.0

the two samples now altered mostly to serpentine had higher Fo numbers which were in equilibrium with the predicted primary magma compositions.

Table 5.3. contd.

	MMW 07-16	MMW 07-18	MMW 07-18
Source	RC27-9-30	KR-4003	RC27-9-30
Melting style	AF	AF	AF
+/- olivine (%)	+2.09	-6.92	-2.45
SiO_2 (wt. %)	45.73	45.80	45.59
TiO_2 (wt. %)	0.63	0.61	0.58
Al_2O_3 (wt. %)	8.56	8.72	8.34
Cr_2O_3 (wt. %)	0.33	0.39	0.38
Fe_2O_3 (wt. %)	1.29	1.41	1.34
FeO (wt. %)	10.62	10.87	10.71
MnO (wt. %)	0.18	0.19	0.18
MgO (wt. %)	22.03	21.62	22.90
CaO (wt. %)	9.09	9.28	8.89
Na_2O (wt. %)	1.11	0.93	0.89
K_2O (wt. %)	0.20	0.07	0.07
NiO (wt. %)	0.08	0.09	0.10
P_2O_5 (wt. %)	0.16	0.04	0.03
T (°C)	1482	1475	1496
T_P (°C)	1611	1603	1627
Fo	92.6	92.3	92.8
F (%)	24.6	31.7	29.5

B – batch melting; AF – accumulated fractional melting; T – eruption temperature; T_P – mantle potential temperature; Fo – forsterite content of olivine in equilibrium with the melt; F – degree of partial melting.

Trace element modelling was applied to the Winnipegosis Belt volcanic rocks to test the validity of the PRIMELT2 solutions. In order to be consistent with models for the Chukotat Group and Fox River Belt volcanic rocks, the PRIMELT2 solutions for accumulated fractional melting are compared to trace element calculations. In the trace element modelling, mineral modes for spinel lherzolite are used because of the flat HREE patterns and corresponding $(Gd/Yb)_N$ ratios close to unity of the Winnipegosis Belt primary magmas. The same melting equation, mineral modes, melting modes and partition co-efficients are used as for the Chukotat Group and Fox River Belt and are given in Appendix F.

The trace element signatures of primary magmas derived through partial melting of a depleted peridotite source with a trace element composition identical to that of average DMM (Workman & Hart, 2005) are displayed in Fig. 5.3a. The multi-element profiles of the calculated primary melts are notably different in terms of shape and element abundances from those of the measured primary magmas (Fig. 5.3a). This suggests that the Winnipegosis Belt primary magmas were not derived

from a source with a highly depleted trace element composition. Calculated primary magmas derived through 26-38% partial melting of a fertile peridotite source, suggested by PRIMELT2 modelling, with a trace element composition identical to that of primitive mantle with 1% by mass of continental crust extracted are shown in Fig. 5.3b. However, there is some discrepancy between the multi-element profiles of calculated and measured primary magmas in Fig. 5.3b. The calculated primary magmas have multi-element profiles which are generally the same shape as the measured primary magmas but with higher element abundances. The element abundances in the measured primary magmas are more consistent with 40% partial melting, a figure higher than suggested by PRIMELT2.

The Winnipegosis Belt is the youngest portion of the Circum-Superior LIP and formed ~20 m.y. after the main phase of magmatism (see Fig. 2.24). Petrogenetic studies on Cretaceous igneous rocks in the Caribbean have suggested that mantle residual from the formation of an oceanic plateau will remain below the region of initial melting for a substantial time period (>10 m.y.) (Revillon et al., 2000; Kerr et al., 2009). A possible model for the generation of the Winnipegosis Belt volcanic rocks is therefore remelting of the same mantle source that generated the main phase of Circum-Superior magmatism. To test the applicability of this model for the Winnipegosis Belt, further trace element modelling was conducted and the results are displayed in Fig. 5.3c. The multi-element diagram in Fig. 5.3c shows that the fit between the newly calculated primary magmas and the measured primary magmas assuming degrees of melting predicted by PRIMELT2 is good. This suggests that the Winnipegosis Belt may be produced by a total of 26-38% partial melting, some of which involved the melting of the residue plus some melt from the main phase of Circum-Superior magma production. The original source composition is taken to be that of primitive mantle with 1% by mass continental crust extracted. This source was then partially melted by 12% using the same melting equation, mineral modes, melting modes and partition co-efficients as previous models. The composition of the residue from this melting event was calculated using the equation given in Appendix F. The starting composition used for the second stage of melting is taken to be that of the residue from the first melting stage with 6% of melt added to it. This technique is similar to the concept of critical melting (e.g. Maaloe, 2003) and has been used by

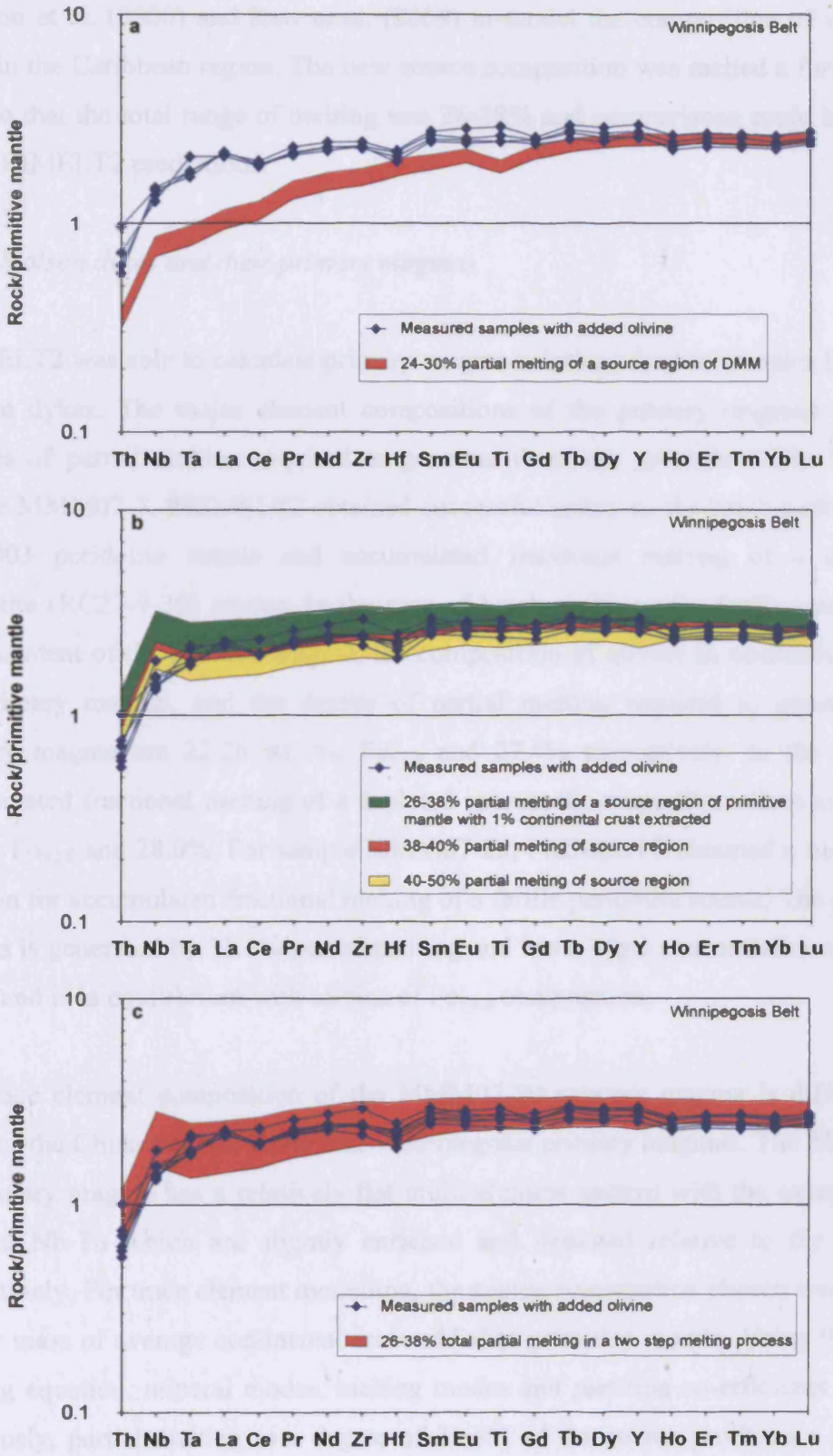

Fig. 5.3. Primitive-mantle-normalised multi-element diagrams for the Winnipegosis Belt primary magmas identified by PRIMELT2 and the results of trace element modelling. (a) Source region composition of DMM. (b) Source region composition of primitive mantle with 1% continental crust extracted. (c) Two stage melting model with remelting of the residue left from the first phase of melting of a source region composition identical to that used in (b). Primitive mantle values from Sun & McDonough (1989).

Revillon et al. (2000) and Kerr et al. (2009) to model the composition of volcanic rocks in the Caribbean region. The new source composition was melted a further 14-26% so that the total range of melting was 26-38% and comparisons could be made with PRIMELT2 predictions.

5.1.4. Molson dykes and their primary magmas

PRIMELT2 was able to calculate primary magma solutions for two samples from the Molson dykes. The major element compositions of the primary magmas and the degrees of partial melting required to generate them are given in Table 5.4. For sample MMM07-7, PRIMELT2 obtained successful solutions for batch melting of a KR-4003 peridotite source and accumulated fractional melting of a depleted peridotite (RC27-9-30) source. In the case of batch melting of a fertile source, the MgO content of the primary magma, the composition of olivine in equilibrium with the primary magma, and the degree of partial melting required to generate the primary magma are 22.26 wt. %, $Fo_{92.8}$ and 27.4% respectively. In the case of accumulated fractional melting of a depleted source, the respective values are 21.88 wt. %, $Fo_{92.6}$ and 28.0%. For sample MMM07-20, PRIMELT2 obtained a successful solution for accumulated fractional melting of a fertile peridotite source. The primary magma is generated by 31.5% partial melting and has a MgO concentration of 19.38 wt. % and is in equilibrium with olivine of $Fo_{91.8}$ composition.

The trace element composition of the MMM07-20 primary magma is different to those of the Chukotat, Fox River and Winnipegosis primary magmas. The MMM07-20 primary magma has a relatively flat multi-element pattern with the exception of Th and Nb-Ta which are slightly enriched and depleted relative to the LREEs respectively. For trace element modelling, the source composition chosen was that of 1% by mass of average continental crust added to primitive mantle. Using the same melting equation, mineral modes, melting modes and partition co-efficients as used previously, partial melting to a degree of 31.5% of the source produces a primary magma with a multi-element pattern similar in shape to the MMM07-20 primary magma but with slightly higher element abundances. This may suggest that MMM07-20 primary magma formed by a slightly higher degree of partial melting

Table 5.4. PRIMELT2-calculated primary magma compositions for the Molson dykes

	MMM07-7	MMM07-7	MMM07-20
Source	RC 27-9-30	KR-4003	KR-4003
Melting style	AF	B	AF
+/- olivine (%)	+9.63	+10.97	+8.48
SiO_2 (wt. %)	46.04	45.97	47.53
TiO_2 (wt. %)	0.65	0.65	0.63
Al_2O_3 (wt. %)	9.11	8.99	9.93
Cr_2O_3 (wt. %)	0.22	0.22	0.20
Fe_2O_3 (wt. %)	1.20	1.18	1.15
FeO (wt. %)	10.40	10.36	10.01
MnO (wt. %)	0.20	0.19	0.20
MgO (wt. %)	21.88	22.26	19.38
CaO (wt. %)	8.76	8.64	9.46
Na_2O (wt. %)	1.33	1.31	1.28
K_2O (wt. %)	0.09	0.09	0.11
NiO (wt. %)	0.08	0.08	0.08
P_2O_5 (wt. %)	0.05	0.05	0.04
T (°C)	1480	1486	1435
T_P (°C)	1608	1615	1559
Fo	92.6	92.8	91.8
F (%)	28.0	27.4	31.5

B – batch melting; AF – accumulated fractional melting; T – eruption temperature; T_P – mantle potential temperature; Fo – forsterite content of olivine in equilibrium with the melt; F – degree of partial melting.

than predicted by PRIMELT2. However, the trace element chemistry of the MMM07-20 primary magma, particularly Th, Nb, Ta and LREEs, may be affected by a small degree of crustal contamination which is not manifested in the major element chemistry. This is further discussed in section 5.3.5.

The trace element composition of the MMM07-7 primary magma is also different to those of the Chukotat, Fox River and Winnipegosis primary magmas. The MMM07-7 primary magma has a relatively flat multi-element pattern with the exception of a small positive Nb-Ta anomaly. Using a depleted trace element source composition identical to that of DMM to model partial melting does not reproduce the composition of the MMM07-7 primary magma. In order to generate the trace element source composition of MMM07-7 a variety of mixtures of mantle end-member compositions were calculated without success. If PRIMELT2 is correct in identifying MMM07-7 as being derived via only olivine crystallisation from a 27-28% partial melt, then the mantle source of the primary magma would have a flat multi-element pattern with element abundances ~0.8 times those of primitive mantle

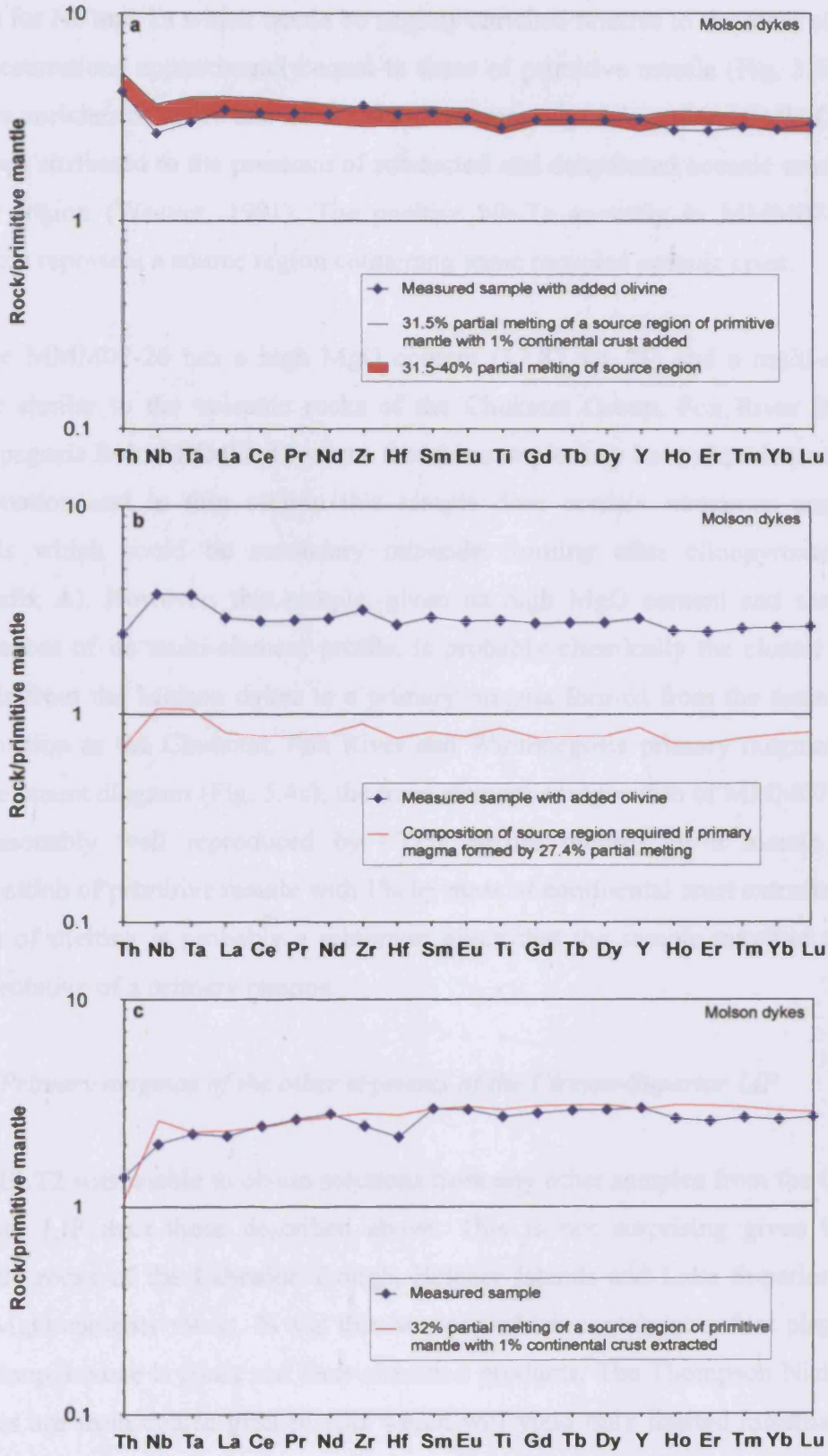

Fig. 5.4. Primitive-mantle-normalised multi-element diagrams for: (a) Molson dyke sample MMM07-20 + 8.48% olivine compared to the results of trace element modelling; (b) Molson dyke sample MMM07-7 + 9.63% olivine and the composition of the source region required by the degree of partial melting predicted by PRIMELT2; (c) Molson dyke sample MMM07-26 compared to the results of trace element modelling. Primitive mantle values from Sun & McDonough (1989).

except for Nb and Ta which would be slightly enriched relative to the other elements at concentrations approximately equal to those of primitive mantle (Fig. 5.4b). The relative enrichment of Nb and Ta is a feature commonly observed in HIMU OIB and has been attributed to the presence of subducted and dehydrated oceanic crust in the source region (Weaver, 1991). The positive Nb-Ta anomaly in MMM07-7 may therefore represent a source region containing some recycled oceanic crust.

Sample MMM07-26 has a high MgO content (17.87 wt. %) and a multi-element profile similar to the volcanic rocks of the Chukotat Group, Fox River Belt and Winnipegosis Belt. PRIMELT2 warns that this sample may have experienced augite fractionation and in thin section this sample does contain numerous amphibole crystals which could be secondary minerals forming after clinopyroxene (see Appendix A). However, this sample, given its high MgO content and shape and abundances of its multi-element profile, is probably chemically the closest sample there is from the Molson dykes to a primary magma formed from the same source composition as the Chukotat, Fox River and Winnipegosis primary magmas. On a multi-element diagram (Fig. 5.4c), the trace element composition of MMM07-26 can be reasonably well reproduced by ~32% partial melting of a mantle source composition of primitive mantle with 1% by mass of continental crust extracted. This degree of melting is probably a minimum given that the sample may not truly be representative of a primary magma.

5.1.5. Primary magmas of the other segments of the Circum-Superior LIP

PRIMELT2 was unable to obtain solutions from any other samples from the Circum-Superior LIP than those described above. This is not surprising given that the volcanic rocks of the Labrador Trough, Belcher Islands and Lake Superior region have MgO contents <9 wt. % and thin sections which contain abundant plagioclase and clinopyroxene crystals and their alteration products. The Thompson Nickel Belt samples are from coarse grained sills which will yield only limited information on the magma they once transported. Therefore it seems that the only segments of the Circum-Superior LIP where primary magmas are preserved are the Chukotat Group, Fox River Belt, Winnipegosis Belt and Molson dykes. The volcanic rocks of the Hellancourt Formation, two samples from the Hemlock Formation in the Lake

Superior region, and the Pickle Crow dyke margin have multi-element profiles with higher element abundances but similar in shape to the primary magmas of the Chukotat Group, Fox River Belt and Winnipegosis Belt. It is possible that the Hellancourt, Hemlock and Pickle Crow magmas were derived from similar primary magma compositions as the Chukotat, Fox River and Winnipegosis magmas but experienced greater degrees of fractional crystallisation.

5.1.6. Summary

The Chukotat Group, Fox River Belt, Winnipegosis Belt and Molson dykes are the only segments of the Circum-Superior LIP where primary magmas are preserved. The Chukotat, Fox River and Winnipegosis primary magmas are similar in composition and appear to have formed through slightly different degrees of partial melting of a source region with the same composition (primitive mantle – 1% continental crust). The Molson dykes appear to have sampled a more heterogeneous source region(s) although some samples have multi-element profiles of a similar shape to the Chukotat, Fox River and Winnipegosis primary magmas. The Hellancourt Formation, Pickle Crow dyke and Hemlock Formation Group 1 also have multi-element profiles similar in shape to the Chukotat, Fox River and Winnipegosis primary magmas although their MgO contents are too low for them to represent primary magmas. An interesting feature of the Chukotat and Fox River primary magmas is the presence of negative Ti anomalies which are not accounted for by the predicted composition of the source region.

5.2. Fractional crystallisation

In this section the extent to which chemical differences within the various segments of the Circum-Superior LIP can be accounted for by fractional crystallisation is discussed. To assess the extent of fractional crystallisation and the conditions under which it occurred, modelling using the MELTS computer software programme was conducted and then compared to the results derived from trace element modelling.

5.2.1. MELTS

A brief summary of the workings of MELTS is given below. This summary has been derived from Ghiorso & Sack (1995) and Asimow & Ghiorso (1998) to which the reader is referred for a more detailed description of the MELTS software. The MELTS software calculates chemical mass transfers in magmatic systems and can model crystallisation paths under certain temperature, pressure, oxygen fugacity, total enthalpy, total entropy and total volume constraints. MELTS is based on the work of Ghiorso & Sack (1995) and Asimow & Ghiorso (1998) which extended from earlier studies by Ghiorso et al. (1983), Ghiorso (1985) and Ghiorso & Kelemen (1987) on algorithms for energy minimisation. MELTS can calculate the proportions and compositions of solid and liquid phases in equilibrium assemblages by utilising thousands of experimentally-determined compositions of silicate liquids co-existing at known temperature, pressure and oxygen fugacity with apatite ± feldspar ± leucite ± olivine ± pyroxene ± quartz ± rhombohedral oxides ± spinel ± whitlockite ± water. The software can be applied to both hydrous and anhydrous magmatic systems ranging in composition from alkaline mafic magmas to rhyolite magmas over a temperature range of ~500-2000°C and pressures <2 GPa. The phase equilibria are calculated after the selection of a starting bulk composition of the system and either i) temperature and pressure, ii) enthalpy and pressure, iii) entropy and pressure, or iv) temperature and volume. The Java web applet of MELTS can be accessed on the OFM Research Inc. website (http://www.ofm-research.org/index.html).

5.2.2. Chukotat Group

The Chukotat Group picrites and basalts were modelled by MELTS with runs at 10°C temperature intervals under differing experimental conditions. A quartz-fayalite-magnetite (QFM) oxygen buffer was used in all runs whereas pressure and water content were varied (1 kbar, anhydrous; 5 kbar, anhydrous; 1 kbar, 1 wt. % H_2O). The sample MMC08-23 with 2.64% olivine added was selected as the starting composition because it was identified by PRIMELT2 as being a primary magma and it possesses a high MgO concentration and low concentrations of incompatible elements. It is not clear from the results shown on the major element variation diagrams as to which crystallisation model fits the Chukotat Group data best. This

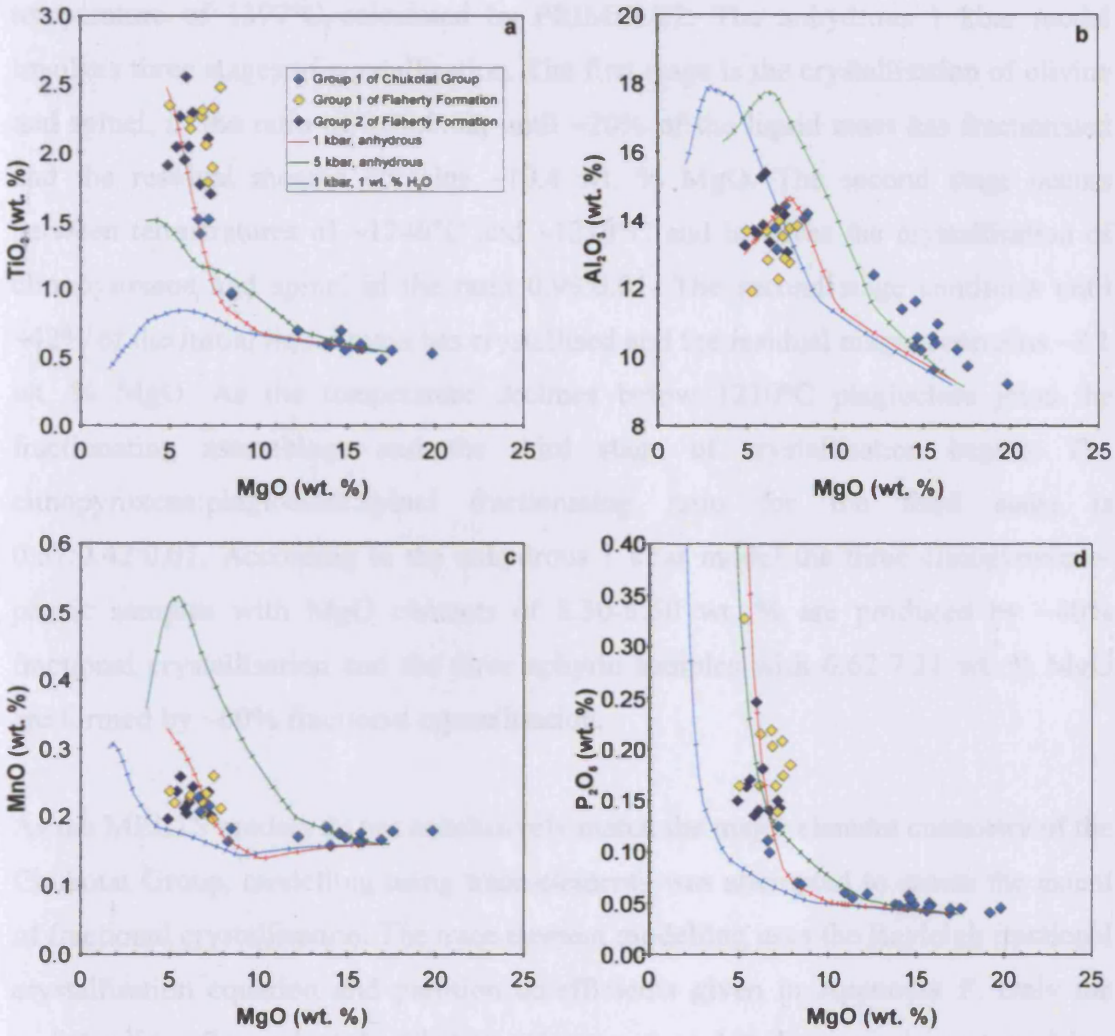

Fig. 5.5. Major element variation diagrams for the Group 1 samples of the Chukotat Group and all samples of the Flaherty Formation compared to the crystallisation pathways predicted by MELTS using the Chukotat Group primary magma as the starting composition. Red line – crystallisation pathway at 1 kbar. Green line – crystallisation pathway at 5 kbar. Blue line – crystallisation pathway at 1 kbar with 1 wt. % water. Each tick represents 5% crystallisation intervals.

may in part be due to the mobility of some of the major elements. However, on diagrams involving some of the more immobile major elements, such as TiO_2, Al_2O_3 and P_2O_5 (Fig. 5.5), the six samples with the lowest MgO contents (6.62-8.50 wt. %) plot closest to the anhydrous 1 kbar crystallisation trend whereas the other samples plot closer to the 5 kbar crystallisation trend. The 5 kbar crystallisation model is probably not suitable for the Chukotat Group because it predicts that orthopyroxene joins the crystallising assemblage after ~4% of the initial volume of liquid has crystallised. None of the samples contain orthopyroxene phenocrysts which suggests that orthopyroxene was not a crystallising phase. The anhydrous 1 kbar model predicts a liquidus temperature of 1409°C which is consistent with the eruption

temperature of 1397°C calculated by PRIMELT2. The anhydrous 1 kbar model involves three stages of crystallisation. The first stage is the crystallisation of olivine and spinel, in the ratio of 0.98:0.02, until ~20% of the liquid mass has fractionated and the residual magma contains ~10.4 wt. % MgO. The second stage occurs between temperatures of ~1240°C and ~1210°C and involves the crystallisation of clinopyroxene and spinel in the ratio 0.99:0.01. The second stage continues until ~42% of the initial liquid mass has crystallised and the residual magma contains ~8.1 wt. % MgO. As the temperature declines below 1210°C plagioclase joins the fractionating assemblage and the third stage of crystallisation begins. The clinopyroxene:plagioclase:spinel fractionating ratio for the third stage is 0.57:0.42:0.01. According to the anhydrous 1 kbar model the three clinopyroxene-phyric samples with MgO contents of 8.30-8.50 wt. % are produced by ~40% fractional crystallisation and the three aphyric samples with 6.62-7.21 wt. % MgO are formed by ~60% fractional crystallisation.

As the MELTS models do not conclusively match the major element chemistry of the Chukotat Group, modelling using trace elements was attempted to assess the extent of fractional crystallisation. The trace element modelling uses the Rayleigh fractional crystallisation equation and partition co-efficients given in Appendix F. Only the samples from Group 1 of the Chukotat Group are used in the trace element model as samples from Group 2 are likely contaminated and so their trace element signatures are not likely to be derived purely from fractional crystallisation. The trace element model is based on the three stages of crystallisation predicted by the MELTS anhydrous 1 kbar model and uses the same ratio of crystallising minerals in each stage as calculated by the MELTS model. The trace element composition of MMC08-23 with 2.64% olivine added was selected as the starting composition. The multi-element profiles of the olivine-phyric Group 1 samples are quite well reproduced by up to 20% fractional crystallisation of the selected starting composition with only olivine and spinel crystallising (Fig. 5.6a). Changing the fractionating assemblage to 99% clinopyroxene and 1% spinel, a further 8% crystallisation can reproduce the multi-element profile of the 12.25 wt. % MgO clinopyroxene-phyric sample and a total of 45% fractional crystallisation can almost reproduce the multi-element profiles of the two clinopyroxene-phyric samples with 8.49 and 8.50 wt. % MgO (Fig. 5.6b). However, the modelled multi-element profiles

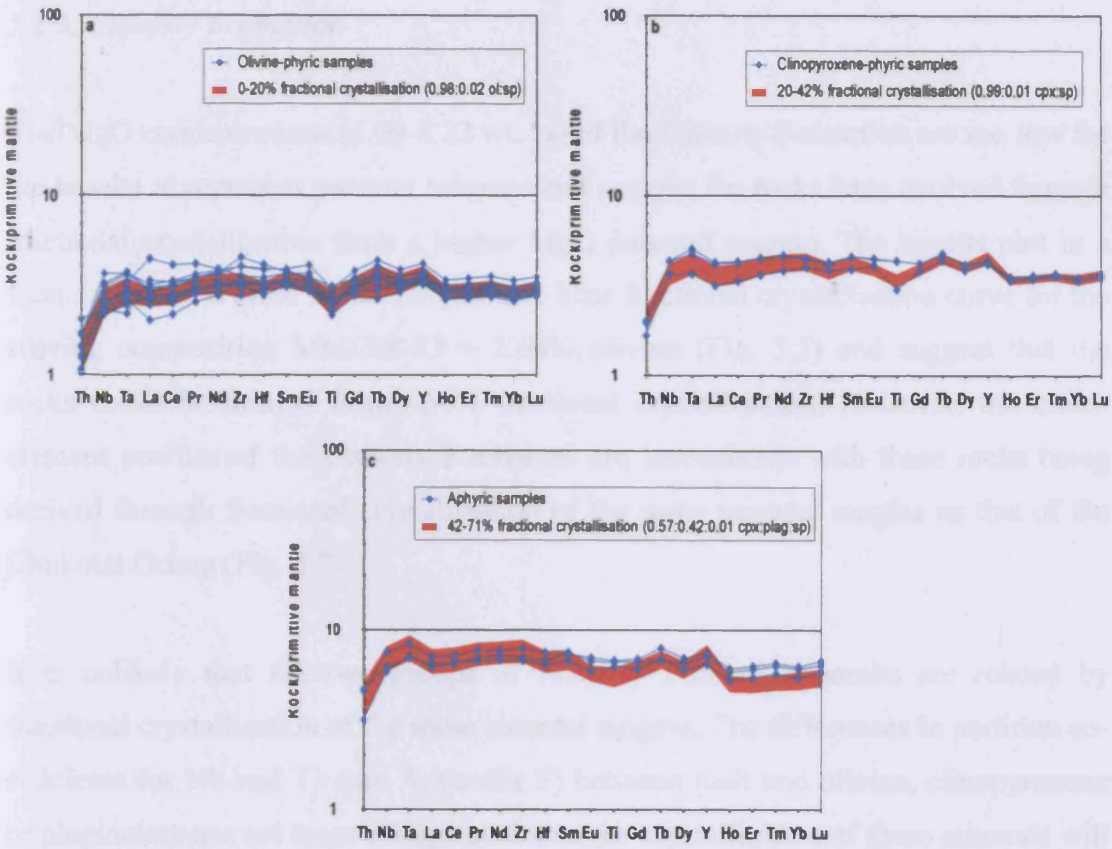

Fig. 5.6. Primitive-mantle-normalised multi-element diagrams displaying the measured Group 1 samples of the Chukotat Group compared to the results of trace element modelling using the parameters predicted by MELTS for 1 kbar fractional crystallisation. Primitive mantle values from Sun & McDonough (1989).

have negative Ti anomalies whereas the profiles of the two ~8.5 wt. % MgO samples have no Ti anomalies. A total of 70% crystallisation, with the final 18% occurring in the third crystallisation stage, is required to reproduce the general shape and abundances of the multi-element profiles of the three lowest MgO samples (Fig. 5.6c). Again however, there are Ti anomalies in the calculated multi-element profiles but no such anomalies in the actual measured profiles.

In summary, the olivine-phyric samples and the 12.25 wt. % MgO clinopyroxene-phyric sample can be related by low pressure fractional crystallisation of spinel, olivine and clinopyroxene. However, the five Group 1 samples with the lowest MgO contents have Ti concentrations which are inconsistent with being derived from higher degrees of fractional crystallisation of the same starting composition as for the higher MgO samples.

5.2.3. Flaherty Formation

The MgO concentrations (5.09-8.22 wt. %) of the Flaherty Formation are too low for the basalts to represent parental magmas and suggest the rocks have evolved through fractional crystallisation from a higher MgO parental magma. The basalts plot in a scattered fashion close to the anhydrous 1 kbar fractional crystallisation curve for the starting composition MMC08-23 + 2.64% olivine (Fig. 5.5) and suggest that the rocks could be formed from >60% fractional crystallisation. However, the multi-element profiles of the Flaherty Formation are inconsistent with these rocks being derived through fractional crystallisation of the same parental magma as that of the Chukotat Group (Fig. 5.7).

It is unlikely that the two groups of Flaherty Formation basalts are related by fractional crystallisation of the same parental magma. The differences in partition co-efficients for Nb and Ta (see Appendix F) between melt and olivine, clinopyroxene or plagioclase are not large enough such that the crystallisation of these minerals will fractionate Nb and Ta from Th and La. No unusual minerals were observed in the thin sections of the basalts which may fractionate these elements (e.g. rutile).

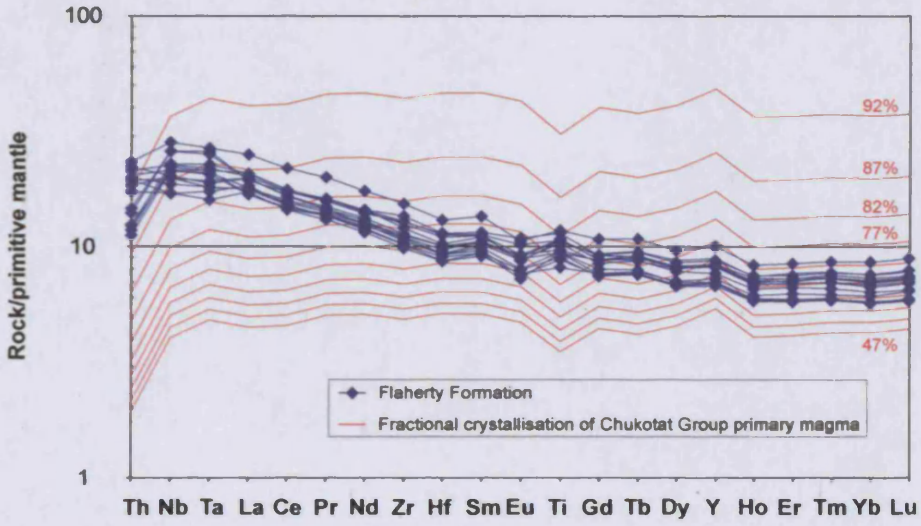

Fig. 5.7. Primitive-mantle-normalised multi-element diagram displaying the measured Flaherty Formation samples compared to the results of trace element modelling using the parameters predicted by MELTS for anhydrous 1 kbar fractional crystallisation of a parental composition identical to that used for the Chukotat Group. Partition co-efficients and fractional crystallisation equation used are given in Appendix F. Primitive mantle values from Sun & McDonough (1989).

5.2.4. Fox River Belt

The picrites and basalts of the Fox River Belt were modelled by MELTS using the same parameters as used for the Chukotat Group except for the starting composition. Instead the composition of MMFR08-8 with 9.45% olivine added was used as the starting composition. None of the computed models consistently reproduce the major element chemistry of the Fox River volcanic rocks (Fig. 5.8). However, the anhydrous 1 kbar model predicts a liquidus temperature of 1504°C which is not too dissimilar to an eruption temperature of 1502°C as predicted by PRIMELT2.

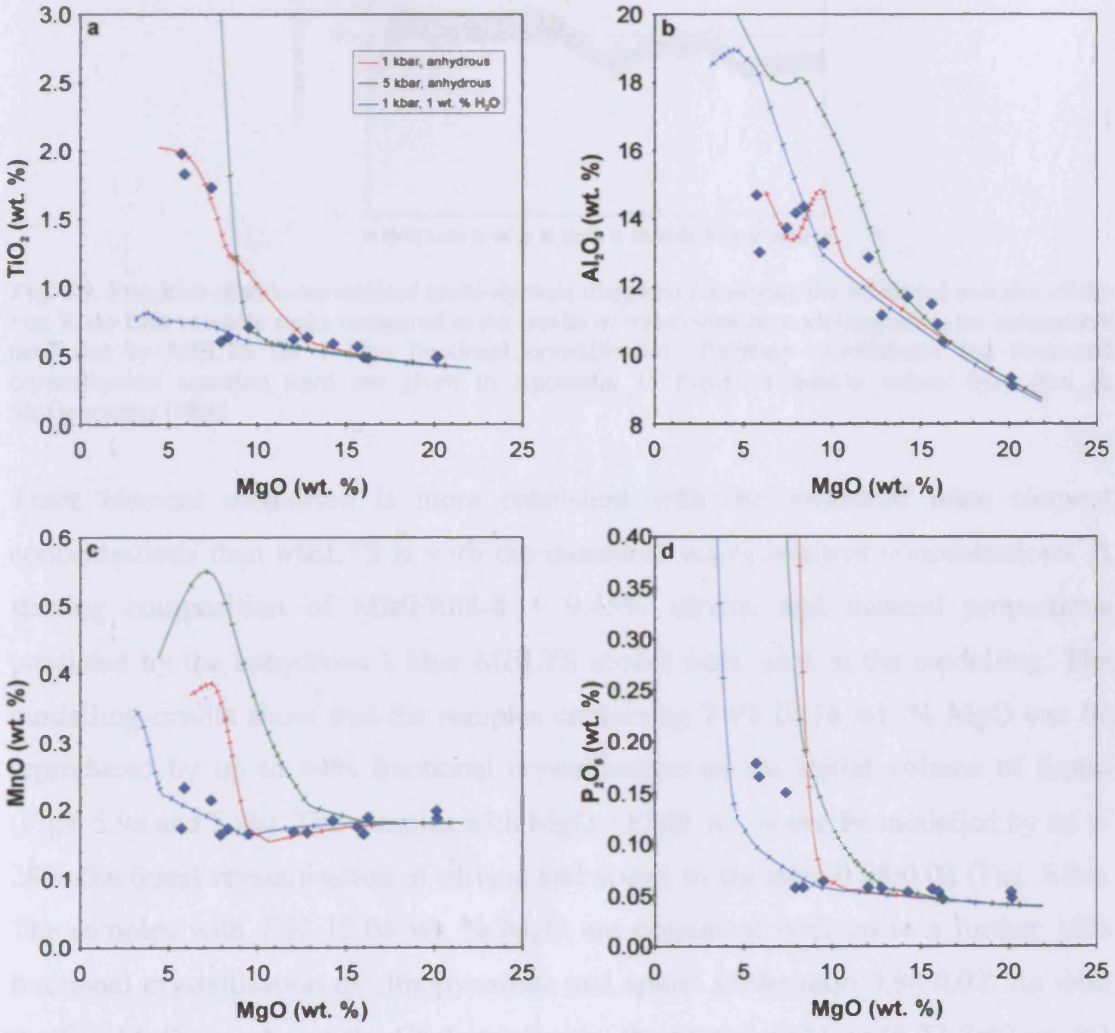

Fig. 5.8. Major element variation diagrams for the Fox River Belt volcanic rocks compared to the crystallisation pathways predicted by MELTS using the Fox River Belt primary magma as the starting composition. Red line – crystallisation pathway at 1 kbar. Green line – crystallisation pathway at 5 kbar. Blue line – crystallisation pathway at 1 kbar with 1 wt. % water. Each tick represents 5% crystallisation intervals.

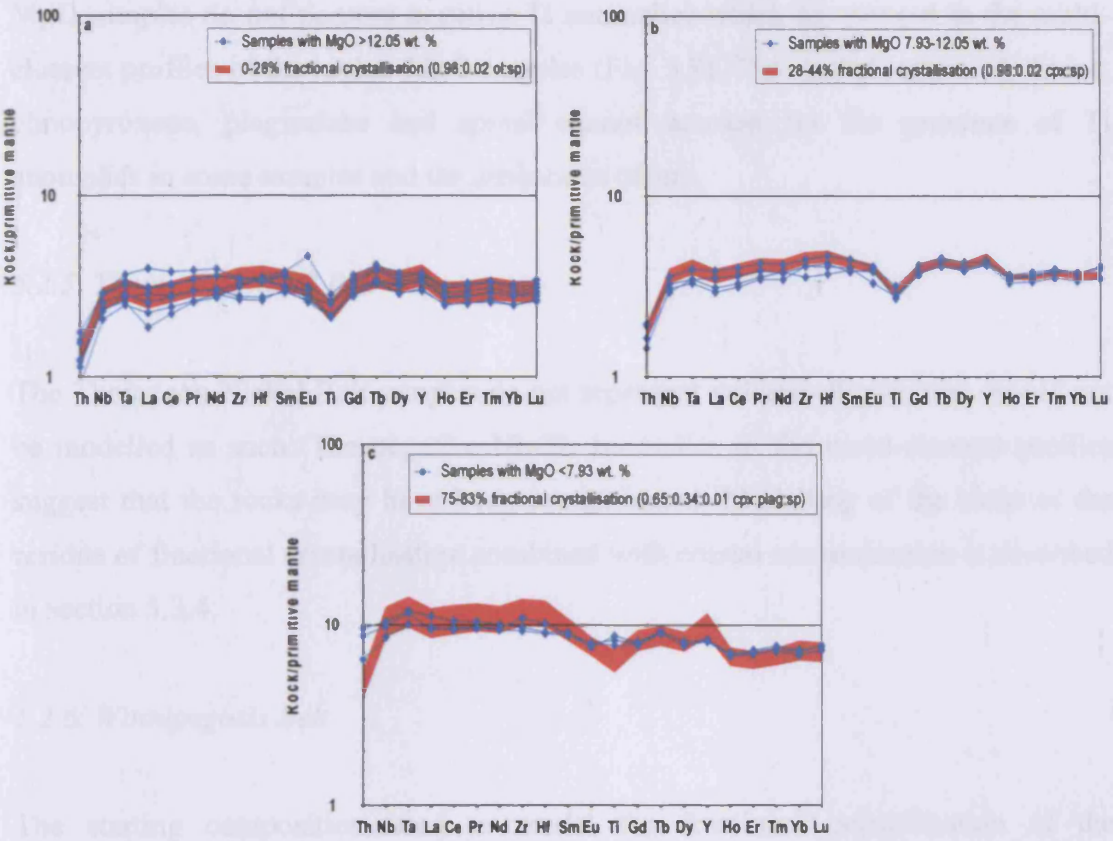

Fig. 5.9. Primitive-mantle-normalised multi-element diagrams displaying the measured samples of the Fox River Belt volcanic rocks compared to the results of trace element modelling using the parameters predicted by MELTS for 1 kbar fractional crystallisation. Partition co-efficients and fractional crystallisation equation used are given in Appendix F. Primitive mantle values from Sun & McDonough (1989).

Trace element modelling is more consistent with the measured trace element concentrations than MELTS is with the measured major element concentrations. A starting composition of MMFR08-8 + 9.45% olivine and mineral proportions predicted by the anhydrous 1 kbar MELTS model were used in the modelling. The modelling results show that the samples containing 7.93-20.18 wt. % MgO can be reproduced by up to 44% fractional crystallisation of the initial volume of liquid (Figs. 5.9a and 5.9b). The samples with MgO >12.05 wt. % can be modelled by up to 28% fractional crystallisation of olivine and spinel in the ratio 0.98:0.02 (Fig. 5.9a). The samples with 7.93-12.05 wt. % MgO are consistent with up to a further 16% fractional crystallisation of clinopyroxene and spinel in the ratio 0.98:0.02. As with the low MgO samples of the Chukotat Group, the three low MgO (5.72-7.40 wt. %) samples of the Fox River Belt volcanic rocks have trace element compositions which are inconsistent with their derivation from high degrees of fractional crystallisation of the same parental magma as the higher MgO rocks. In particular, the three low

MgO samples do not possess negative Ti anomalies which are present in the multi-element profiles of the higher MgO samples (Fig. 5.9). The crystallisation of olivine, clinopyroxene, plagioclase and spinel cannot account for the presence of Ti anomalies in some samples and the absence in others.

5.2.5. Thompson Nickel Belt

The Thompson Nickel Belt samples do not represent volcanic liquids and should not be modelled as such. The negative Nb-Ta anomalies in the multi-element profiles suggest that the rocks may have been contaminated. Modelling of the rocks as the residue of fractional crystallisation combined with crustal contamination is described in section 5.3.4.

5.2.6. Winnipegosis Belt

The starting composition used to model the fractional crystallisation of the Winnipegosis Belt volcanic rocks is MMW07-9 with an additional 0.09% olivine. The same parameters were used as in the previous MELTS modelling. The results of the MELTS modelling show that Groups 1 and 2 of the Winnipegosis Belt are best modelled by low pressure (1 kbar) and anhydrous fractional crystallisation (Fig. 5.10). The Group 1 picrites are either derived from very small degrees of fractional crystallisation or from minor amounts of olivine accumulation to the parental magma. The Group 2 basalts can be formed by ~65% fractional crystallisation of the parental magma (Fig. 5.10). The anhydrous 1 kbar MELTS model predicts an olivine liquidus temperature of 1488°C which is similar to the eruption temperature of 1480°C calculated by PRIMELT2. According to MELTS, the first stage of fractional crystallisation involves the crystallisation of olivine and spinel in the ratio 0.98:0.02 until ~66% of the initial volume of liquid remains and has a MgO content of ~10.5 wt. %. Clinopyroxene and spinel then crystallise in the ratio 0.98:0.02 until ~49% of the initial volume of liquid remains. For the final stage of crystallisation plagioclase joins clinopyroxene and spinel on the liquidus and the three respective minerals crystallise in the ratio 0.46:0.52:0.02.

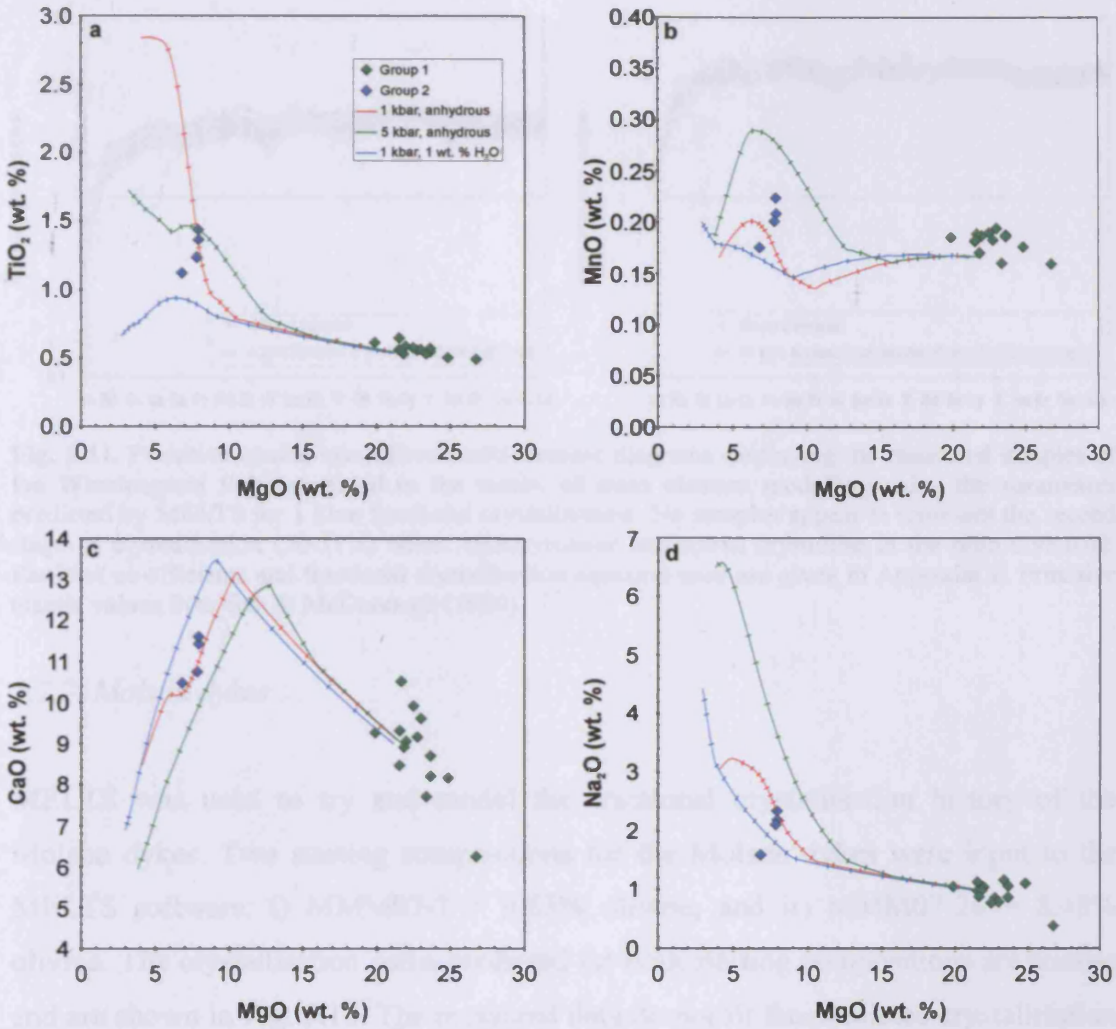

Fig. 5.10. Major element variation diagrams for the Winnipegosis Belt compared to the crystallisation pathways predicted by MELTS using the Winnipegosis Belt primary magma as the starting composition. Red line – crystallisation pathway at 1 kbar. Green line – crystallisation pathway at 5 kbar. Blue line – crystallisation pathway at 1 kbar with 1 wt. % water. Each tick represents 5% crystallisation intervals.

Trace element modelling is consistent with the results from the MELTS modelling. The multi-element profiles of the Group 1 samples range from plotting at slightly lower elemental abundances than the parental magma, indicative of minor amounts of olivine accumulation, to elemental abundances consistent with 20% fractional crystallisation (Fig. 5.11a). The four samples of Group 2 have multi-element profiles consistent with 60-65% fractional crystallisation of the parental magma (Fig. 5.11b).

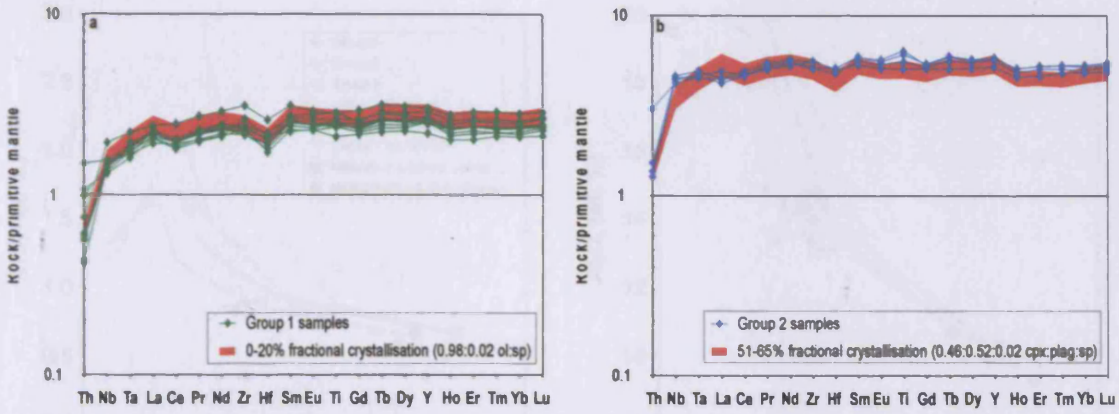

Fig. 5.11. Primitive-mantle-normalised multi-element diagrams displaying the measured samples of the Winnipegosis Belt compared to the results of trace element modelling using the parameters predicted by MELTS for 1 kbar fractional crystallisation. No samples appear to represent the second stage of crystallisation (20-51%) where clinopyroxene and spinel crystallise in the ratio 0.98:0.02. Partition co-efficients and fractional crystallisation equation used are given in Appendix F. Primitive mantle values from Sun & McDonough (1989).

5.2.7. Molson dykes

MELTS was used to try and model the fractional crystallisation history of the Molson dykes. Two starting compositions for the Molson dykes were input to the MELTS software: i) MMM07-7 + 9.63% olivine, and ii) MMM07-20 + 8.48% olivine. The crystallisation paths predicted for both starting compositions are similar and are shown in Fig. 5.12. The measured data do not fit the predicted crystallisation paths perfectly but are best replicated by anhydrous 1 kbar crystallisation. The anhydrous 1 kbar models are split into three stages. The first stages involve the crystallisation of olivine and spinel and are followed by second stages of olivine, clinopyroxene and spinel crystallisation. The second stages are short-lived and are soon followed by the third stages involving clinopyroxene, plagioclase and spinel crystallisation.

To assess the validity of the MELTS models, the trace element compositions of the Molson dykes were modelled using the parameters calculated by MELTS. The multi-element profiles of the Molson dykes are somewhat diverse and this heterogeneity cannot be explained by differing degrees of fractional crystallisation of the same parental magma. The crystallisation of olivine, clinopyroxene, plagioclase and spinel from a parental magma with a composition of MMM07-20 + 8.48% olivine can only account for the trace element composition of MMM07-20 and two Group 2 samples

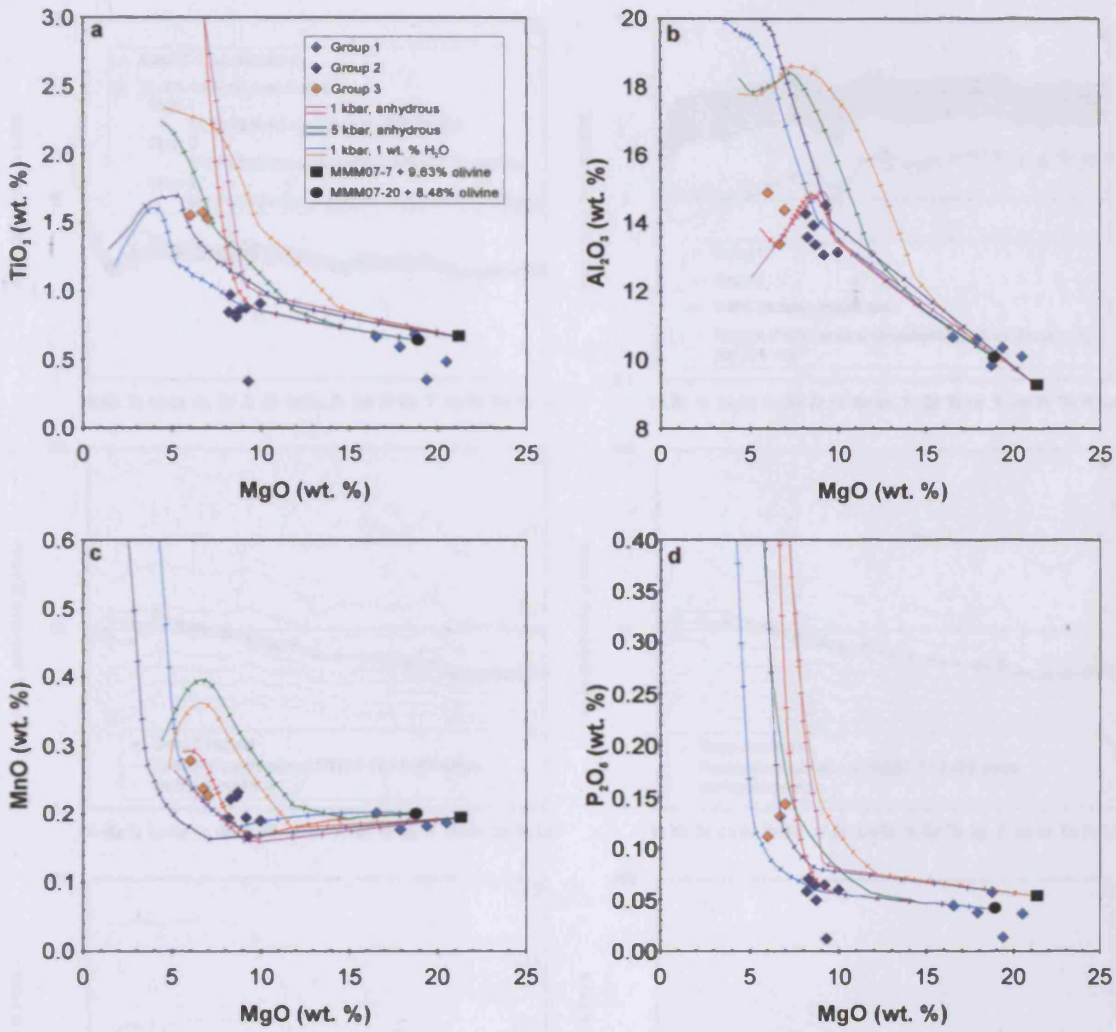

Fig. 5.12. Major element variation diagrams for the Molson dykes compared to the crystallisation pathways predicted by MELTS. Red, green and light blue lines represent crystallisation pathways at 1 kbar, 5 kbar and 1 kbar + 1 wt. % water respectively with a starting composition of MMM07-20 + 8.48% olivine. Purple, dark blue and orange lines represent crystallisation pathways at 1 kbar, 5 kbar and 1 kbar + 1 wt. % water respectively with a starting composition of MMM07-7 + 9.63% olivine. Each tick represents 5% crystallisation intervals.

(MMM07-11 and MMM07-12) (Fig. 5.13a). Olivine, clinopyroxene, plagioclase and spinel crystallisation from a parental magma composition of MMM07-7 + 9.63% olivine cannot account for the trace element composition of any of the Molson dykes aside from sample MMM07-7.

PRIMELT2 identified only MMM07-7 and MMM07-20 as potential candidates for the Molson primary magmas. Using the trace element composition of these samples plus some additional olivine as the starting compositions in the fractional crystallisation models does not reproduce the relatively flat to slightly Th-Nb-Ta-LREE-depleted multi-element profiles of two Group 1 samples and five Group 2

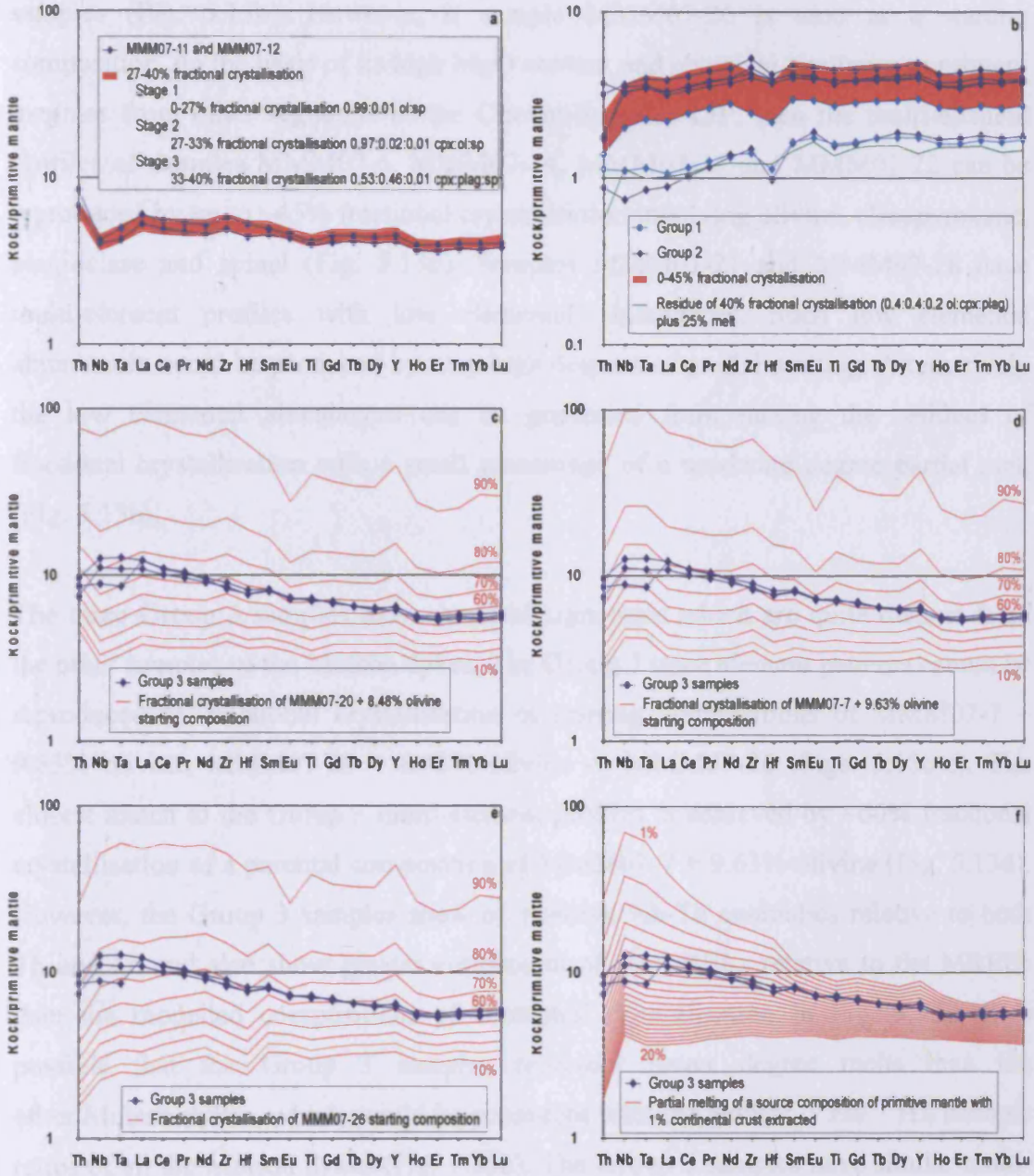

Fig. 5.13. Primitive-mantle-normalised multi-element diagrams displaying measured data from the Molson dykes with the results of trace element modelling. (a) Samples MMM07-11 and MMM07-12 compared to the product of 27-40% fractional crystallisation of a parent composition of MMM07-20 + 8.48% olivine. (b) Samples of the Molson dykes, excluding those of Group 3, those in (a) and MMM07-2, compared to the product of up to 45% fractional crystallisation, using the same fractionating assemblage stages as in (a) and a parent composition of MMM07-26, and the residue of 40% fractional crystallisation with 25% of a 15% partial melt of a source composition of primitive mantle with 1% continental crust extracted. (c) Group 3 samples compared to the product of fractional crystallisation of a parent composition of MMM07-20 + 8.48% olivine. (d) Group 3 samples compared to the product of fractional crystallisation of a parent composition of MMM07-7 + 9.63% olivine. (e) Group 3 samples compared to the product of fractional crystallisation of a parent composition of MMM07-26. (f) Group 3 samples compared to the product of 1-20% partial melting of a source composition of primitive mantle with 1% continental crust extracted. Partition co-efficients, mineral modes, melting modes and equations used are given in Appendix F. Primitive mantle values from Sun & McDonough (1989).

samples (Fig. 5.13b). However, if sample MMM07-26 is used as a starting composition, on the basis of its high MgO content and chemical similarity to primary magmas from other segments of the Circum-Superior LIP, then the multi-element profiles of samples MMM07-6, MMM07-14, MMM07-15 and MMM07-22 can be reproduced by up to ~45% fractional crystallisation involving olivine, clinopyroxene, plagioclase and spinel (Fig. 5.13b). Samples MMM07-21 and MMM07-28 have multi-element profiles with low elemental abundances. Such low elemental abundances could be produced by very high degrees of partial melting. Alternatively the low elemental abundances can be generated from mixing the residues of fractional crystallisation with a small percentage of a moderate degree partial melt (Fig. 5.13b).

The three Group 3 samples have chemical signatures which are quite distinct from the other samples of the Molson dykes. The Group 3 trace element patterns cannot be reproduced by fractional crystallisation of starting compositions of MMM07-7 + 9.63% olivine, MMM07-20 + 8.48% olivine or MMM07-26 (Figs. 5.13c-e). The closest match to the Group 3 multi-element profiles is achieved by ~60% fractional crystallisation of a parental composition of MMM07-7 + 9.63% olivine (Fig. 5.13d). However, the Group 3 samples show no positive Nb-Ta anomalies relative to both Th and La and also show greater enrichment of the LREEs relative to the MREEs than the modelled compositions of fractional crystallisation in Fig. 5.13d. It is possible that the Group 3 samples represent lower degree melts than the other Molson dykes, which would be consistent with the similar $^{176}Hf/^{177}Hf_i$ isotopic ratios of all the Molson dykes (Fig. 5.33b). The Group 3 samples have similar multi-element profiles to a 6% partial melt of a source region composition of primitive mantle with 1% continental crust extracted (Fig. 5.13f). It is difficult to ascertain how accurate this figure of 6% partial melting is because the Group 3 samples have low MgO concentrations (6.00-6.99 wt. %) and are likely to have undergone fractional crystallisation which would alter the elemental concentrations in the primary magma.

5.2.8. Pickle Crow dyke

The major element chemistry of the Pickle Crow dyke is compared to the results of MELTS modelling in Fig. 5.15 using a starting composition of the Fox River Belt primary magma (MMFR08-8 + 9.45% olivine). However, the major element chemistry of the Pickle Crow dyke does not conclusively match any of the crystallisation pathways in Fig. 5.15. Trace element modelling provides a more decisive solution to the fractional crystallisation history of the Pickle Crow dyke. The multi-element diagram in Fig. 5.14 shows that the trace element composition of the Pickle Crow dyke can be replicated, except for Ti, by ~58% fractional crystallisation of the Fox River Belt primary magma via a three stage (olivine + spinel; clinopyroxene + spinel; clinopyroxene + plagioclase + spinel) crystallisation process. The positive Ti anomalies in the multi-element profiles of the Pickle Crow dyke probably reflect the accumulation of Fe-Ti oxides.

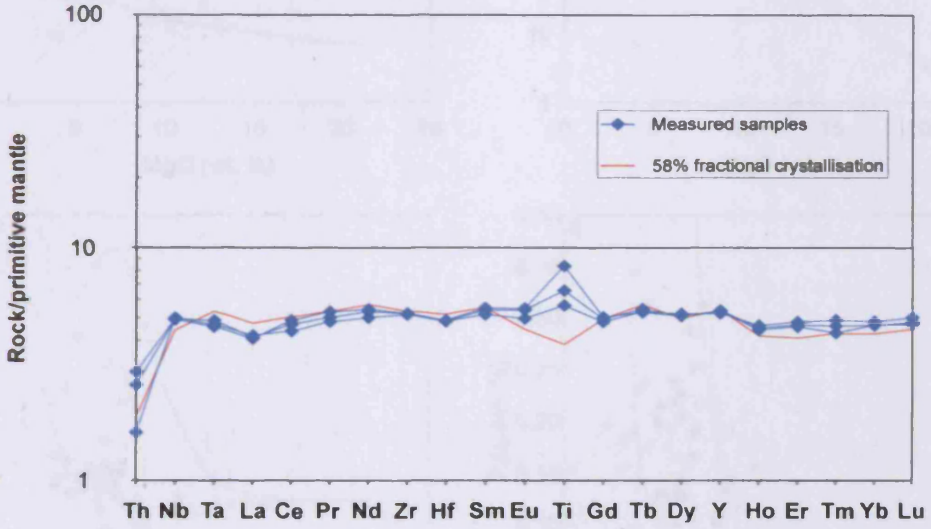

Fig. 5.14. Primitive-mantle-normalised multi-element diagram displaying the measured Pickle Crow dyke samples compared to the results of trace element modelling. The starting composition and the fractionating stages and assemblages used are the same as used for the Fox River Belt volcanic rocks in Fig. 5.9. Partition co-efficients and fractional crystallisation equation used are given in Appendix F. Primitive mantle values from Sun & McDonough (1989).

5.2.9. Lake Superior region igneous rocks

The maximum MgO content in the volcanic rocks of the Lake Superior region is 8.90 wt. % while the maximum concentration in the samples of the Kiernan sills is 10.83

wt. %. It is therefore unlikely that any of the magmatic rocks represent parental magmas. Inspection of the major element chemistry of the igneous rocks shows a considerable amount of scatter which is unlikely to be explained by a simple model of fractional crystallisation from a common parental magma such as that of the Fox River Belt primary magma (Fig. 5.15). The trace element and isotopic data (Figs. 4.68 and 4.83) show sufficient differences such that all of the rocks cannot be related by fractional crystallisation alone.

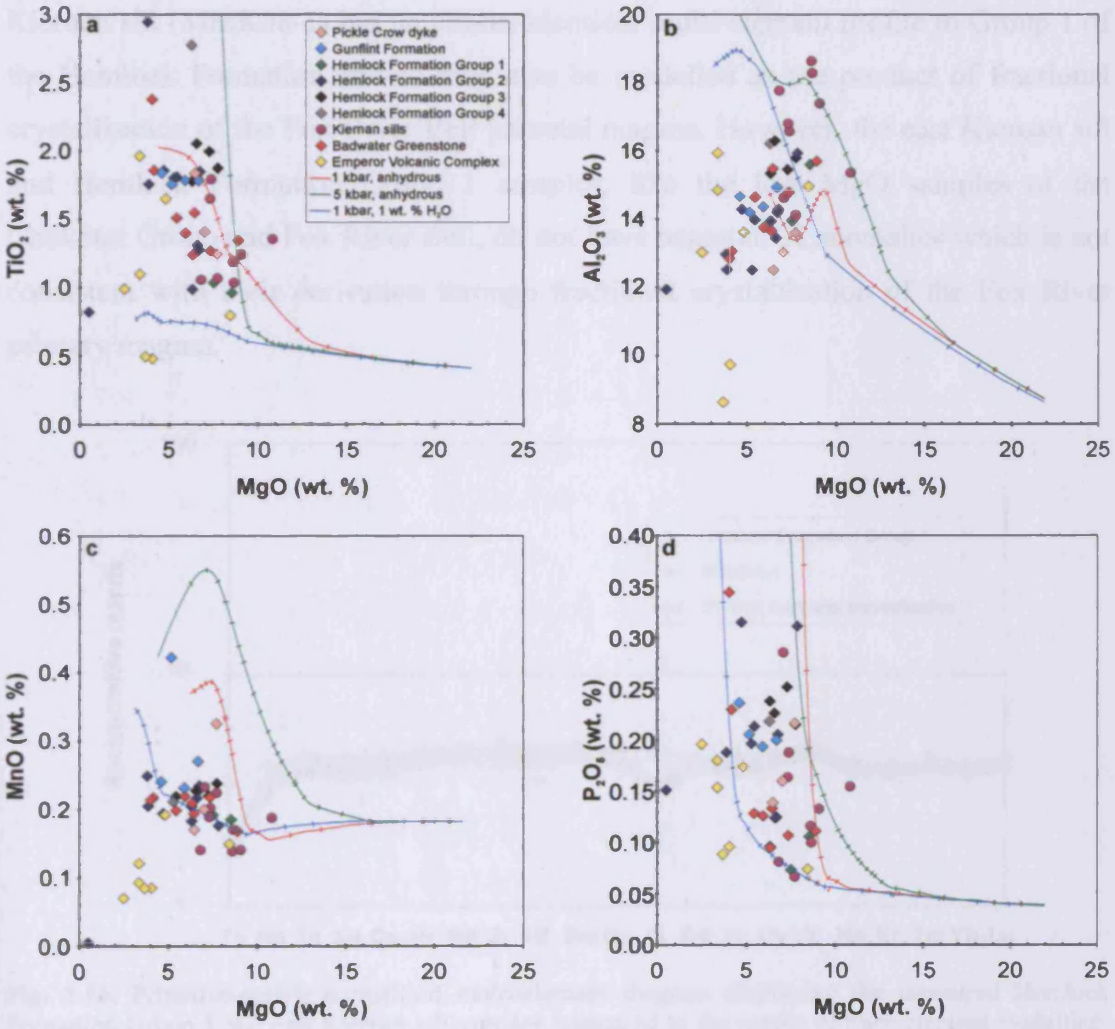

Fig. 5.15. Major element variation diagrams for the Lake Superior region igneous rocks and the Pickle Crow dyke compared to the crystallisation pathways predicted by MELTS using the Fox River Belt primary magma as the starting composition. Red line – crystallisation pathway at 1 kbar. Green line – crystallisation pathway at 5 kbar. Blue line – crystallisation pathway at 1 kbar with 1 wt. % water. Each tick represents 5% crystallisation intervals.

The Group 1 samples of the Hemlock Formation have trace element and isotopic similarities to the Fox River Belt volcanic rocks, Winnipegosis Belt and Group 1 of the Chukotat Group. Trace element modelling indicates that Group 1 of the Hemlock Formation may be formed from up to ~45% fractional crystallisation of the Fox River Belt primary magma composition of MMFR08-8 + 9.45% olivine (Fig. 5.16). At such a degree of crystallisation, the MELTS anhydrous 1 kbar model predicts that clinopyroxene and plagioclase are the dominant minerals crystallising. This is consistent with the petrography of the samples which are dominated by clinopyroxene and plagioclase or their alteration products. The sample from the east Kiernan sill (MMK08-1) has an almost identical multi-element profile to Group 1 of the Hemlock Formation and so may also be modelled as the product of fractional crystallisation of the Fox River Belt parental magma. However, the east Kiernan sill and Hemlock Formation Group 1 samples, like the low MgO samples of the Chukotat Group and Fox River Belt, do not have negative Ti anomalies which is not consistent with their derivation through fractional crystallisation of the Fox River primary magma.

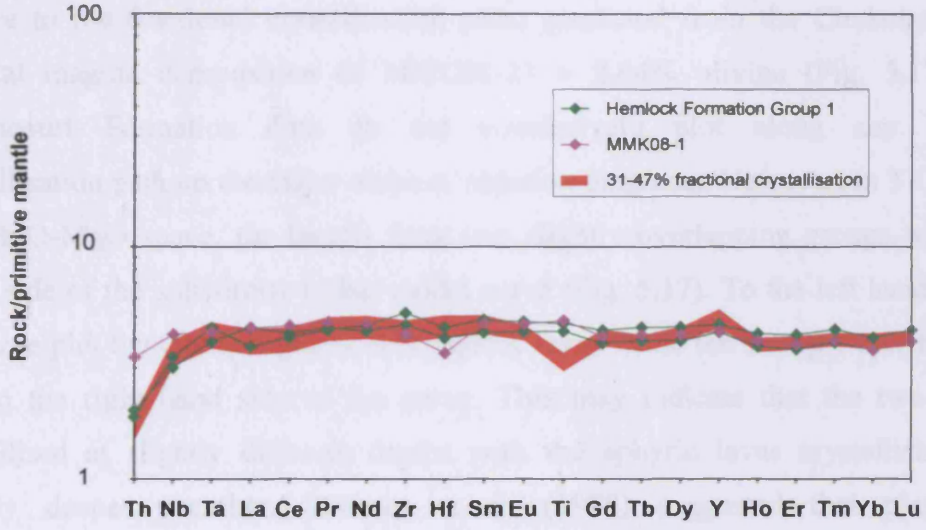

Fig. 5.16. Primitive-mantle-normalised multi-element diagram displaying the measured Hemlock Formation Group 1 and east Kiernan sill samples compared to the results of trace element modelling. The starting composition and the fractionating stages and assemblages used are the same as used for the Fox River Belt volcanic rocks in Fig. 5.9. Partition co-efficients and fractional crystallisation equation used are given in Appendix F. Primitive mantle values from Sun & McDonough (1989).

The Gunflint Formation, Badwater Greenstone, Emperor Volcanic Complex, Groups 2 and 3 of the Hemlock Formation, and the majority of samples from the Kiernan sills have trace element compositions which are enriched in Th-Nb-Ta-LREEs

relative to the less incompatible elements and/or negative Nb-Ta anomalies relative to Th and La. Such compositions cannot be modelled by fractional crystallisation alone of the Fox River Belt primary magma (Fig. 5.16) and may instead require the involvement of crustal material in their petrogenesis (see section 5.3.6). The Hemlock Formation Group 4 sample and west Kiernan sill sample MMK08-11 have positive Nb-Ta anomalies which are not replicated by olivine, clinopyroxene, plagioclase and spinel crystallisation from the Fox River Belt primary magma (Fig. 5.16). Therefore these two samples require a parental magma of different composition to the other samples in the Lake Superior region.

5.2.10. Hellancourt Formation

None of the analysed samples of the Hellancourt Formation are likely to truly represent the parental magma composition given that the highest MgO concentration is only 9.86 wt. %. Therefore the fractional crystallisation history of the Hellancourt Formation cannot be modelled by MELTS using a measured sample composition from the Labrador Trough. Instead the Hellancourt Formation basalts are plotted relative to the fractional crystallisation paths predicted from the Chukotat Group parental magma composition of MMC08-23 + 2.64% olivine (Fig. 5.17). The Hellancourt Formation data do not conclusively plot along any specific crystallisation path on the major element variation diagrams. However, in TiO_2-MgO and MnO-MgO space, the basalts form two slightly overlapping groups which lie either side of the anhydrous 1 kbar model curve (Fig. 5.17). To the left hand side of the curve plot the Group 2 glomeroporphyritic lavas while the Group 1 aphyric lavas plot to the right hand side of the curve. This may indicate that the two groups crystallised at slightly different depths with the aphyric lavas crystallising in a slightly deeper chamber. Phinney et al. (1988) suggested that plagioclase glomeroporphyritic lavas may form from trapping primitive magma at depth where they are forced to fractionate olivine and/or orthopyroxene until the residual Al- and Ca-rich magma ascends to lower pressures where the sudden depressurisation enhances the expansion and growth of the plagioclase phase. Skulski et al. (1993) noted the presence of olivine pyroxenite layers in some glomeroporphyritic sills. However, the trace element signatures of the Group 2 lavas are near-identical to those of Group 1 lavas (Fig. 4.80) and do not necessitate the crystallisation of

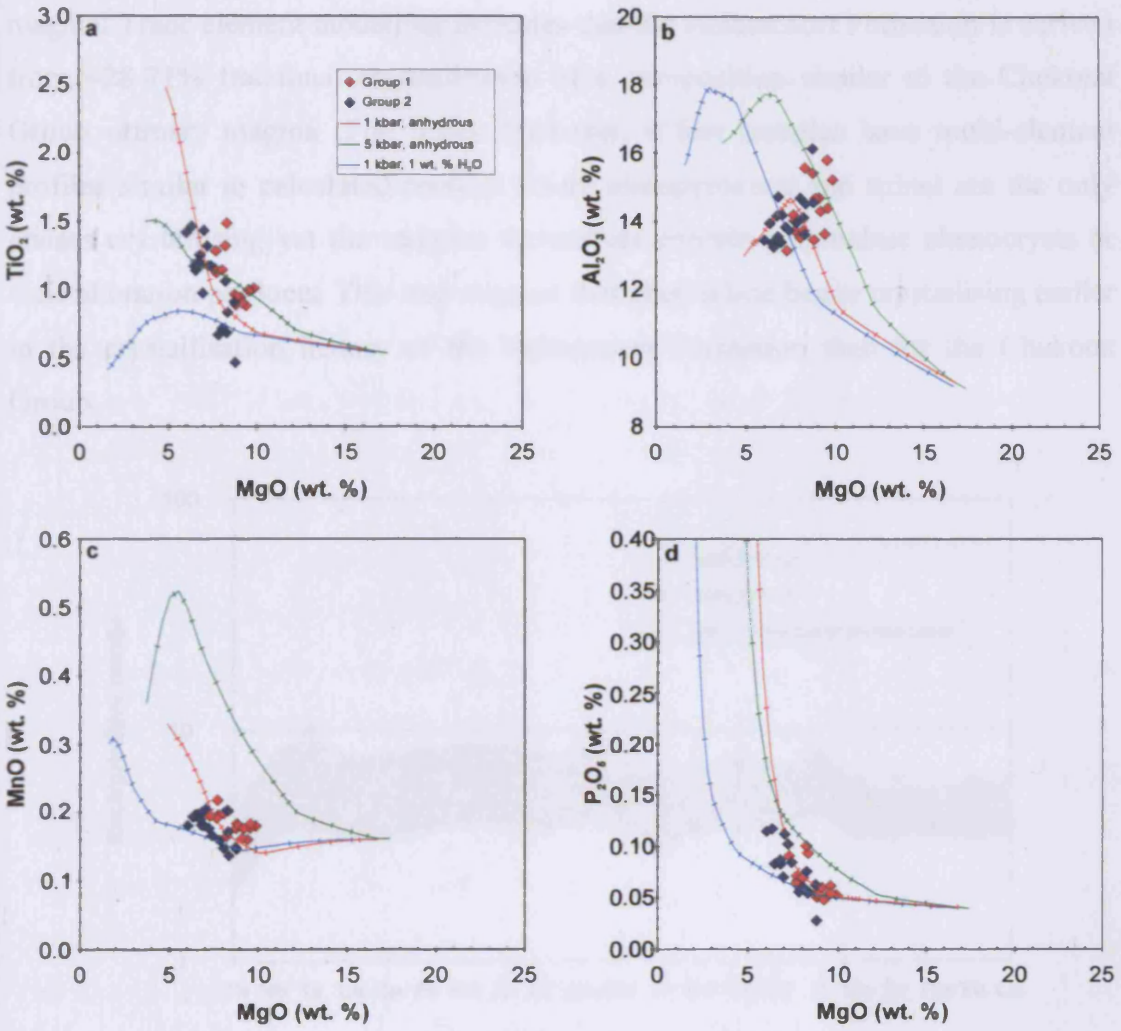

Fig. 5.17. Major element variation diagrams for the Hellancourt Formation compared to the crystallisation pathways predicted by MELTS using the Chukotat Group primary magma as the starting composition. Red line – crystallisation pathway at 1 kbar. Green line – crystallisation pathway at 5 kbar. Blue line – crystallisation pathway at 1 kbar with 1 wt. % water. Each tick represents 5% crystallisation intervals.

orthopyroxene (see below). The near-identical trace element signatures and Nd isotope signatures (Skulski et al., 1993) suggest that the two groups are derived from the same parental magma and the petrographic differences are the result of physical processes which did not alter the trace element chemical signatures.

The multi-element profiles of the Hellancourt Formation are of similar shape to those of Group 1 of the Chukotat Group but are elevated to higher elemental concentrations than the high MgO samples in the Chukotat Group. This is consistent with the derivation of the Hellancourt Formation by fractional crystallisation of a parental magma similar in composition to that of the Chukotat Group parental

magma. Trace element modelling indicates that the Hellancourt Formation is derived from ~28-71% fractional crystallisation of a composition similar to the Chukotat Group primary magma (Fig. 5.18). However, a few samples have multi-element profiles similar to calculated profiles where clinopyroxene and spinel are the only phases crystallising yet the samples themselves contain plagioclase phenocrysts or their alteration products. This may suggest that plagioclase began crystallising earlier in the crystallisation history of the Hellancourt Formation than for the Chukotat Group.

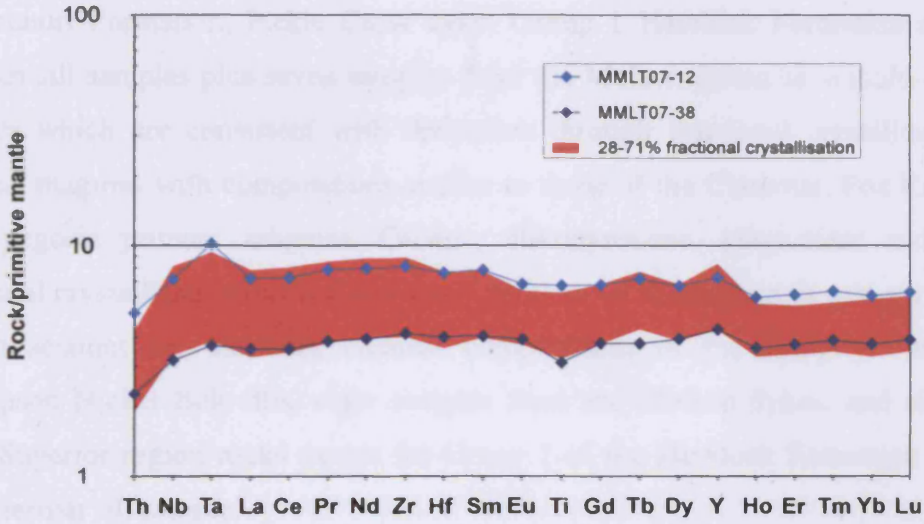

Fig. 5.18. Primitive-mantle-normalised multi-element diagram displaying the Hellancourt Formation samples with the lowest (MMLT07-38) and highest (MMLT07-12) incompatible element abundances compared to the results of trace element modelling. The starting composition and the fractionating stages and assemblages used are the same as used for the Chukotat Group in Fig. 5.6. Partition coefficients and fractional crystallisation equation used are given in Appendix F. Primitive mantle values from Sun & McDonough (1989).

As is the case with some other segments of the Circum-Superior LIP, negative Ti anomalies are present in some lavas of the Labrador Trough and absent in others. Four samples of the Group 2 lavas have negative Ti anomalies and are amongst the highest MgO samples in the Hellancourt Formation. None of the other samples possess Ti anomalies.

5.2.11. Summary

The trace element chemistry of the Circum-Superior LIP lavas appears to be a better indicator of evolution through fractional crystallisation than the major element

chemistry. It is common throughout the Circum-Superior LIP rocks which are related by fractional crystallisation that the crystallisation sequence evolves through three main stages: i) olivine + spinel; ii) clinopyroxene + spinel; iii) clinopyroxene + plagioclase + spinel. The uncontaminated Chukotat Group samples with MgO contents >8.50 wt. % are related to each other by up to 42% fractional crystallisation of the Chukotat Group primary magma. The Fox River Belt volcanic rocks with 7.93-20.18 wt. % MgO are produced by up to 44% fractional crystallisation of the Fox River Belt primary magma. All samples from the Winnipegosis Belt are related by fractional crystallisation of up to 65% of the Winnipegosis primary magma. The Hellancourt Formation, Pickle Crow dyke, Group 1 Hemlock Formation and east Kiernan sill samples plus seven samples from the Molson dykes have multi-element profiles which are consistent with derivation through fractional crystallisation of parental magmas with compositions similar to those of the Chukotat, Fox River and Winnipegosis primary magmas. Olivine, clinopyroxene, plagioclase and spinel fractional crystallisation of the Chukotat, Fox River or Winnipegosis primary magma cannot account for the trace element compositions of the Flaherty Formation, Thompson Nickel Belt sills, eight samples from the Molson dykes, and all of the Lake Superior region rocks except for Group 1 of the Hemlock Formation and the east Kiernan sill sample.

Fractional crystallisation of a common parental magma can also not explain the presence and absence of negative Ti anomalies in individual segments of the Circum-Superior LIP. Fig. 5.19 demonstrates that the magnitude of the negative Ti anomaly does not decrease rapidly enough with fractional crystallisation for the low MgO Chukotat Group (6.62-8.50 wt. % MgO) and Fox River Belt (5.72-7.40 wt. % MgO) samples to be derived through this process from the same parental magma as the higher MgO Chukotat Group and Fox River Belt samples are derived from. The four Group 2 samples of the Hellancourt Formation with negative Ti anomalies may also not share the same parental magma as all the other samples from the Hellancourt Formation. The origin of the Ti anomalies is discussed in section 5.7.

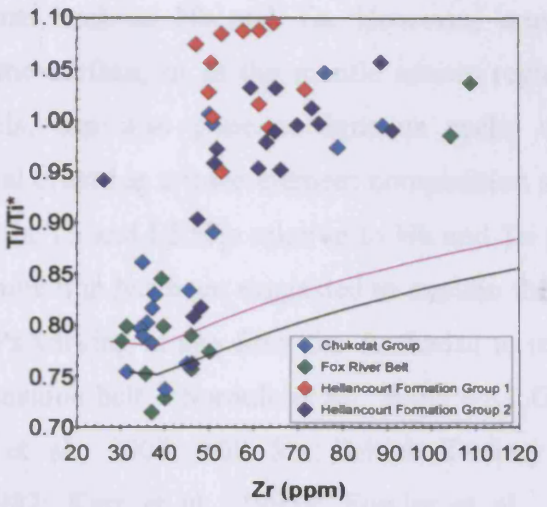

Fig. 5.19. Ti/Ti* vs. Zr diagram for the Chukotat Group, Hellancourt Formation and Fox River Belt volcanic rocks. The black line represents the modelled fractional crystallisation pathway for the Chukotat Group while the purple line represents the modelled fractional crystallisation pathway for the Fox River Belt volcanic rocks.

5.3. Contamination

5.3.1. Negative Nb-Ta anomalies

Primitive-mantle-normalised multi-element profiles with negative Nb-Ta anomalies are not universal throughout the Circum-Superior LIP but are not uncommon. The Group 2 samples of the Chukotat Group, many of the intrusions from the Fox River Belt, all of the Thompson Nickel Belt samples, some of the Molson dykes and the majority of samples from the volcanic and intrusive rocks of the Lake Superior region are depleted in Nb and Ta relative to Th and La (Figs. 4.8b, 4.28b, 4.38, 4.58b and 4.68).

Negative Nb-Ta anomalies are common in igneous rocks from volcanic arcs with a subduction-related origin (e.g. Stern, 2002). This is because Nb and Ta act as conservative elements in subduction systems and are retained in minerals such as rutile in the subducting slab instead of transferring to the melting column and contributing to the source of arc volcanism (Pearce & Peate, 1995). Other elements such as Th and the LREEs act as non-conservative elements and are readily transferred from the subducting slab to the mantle wedge in aqueous fluids and hydrous melts (Pearce & Peate, 1995). As a result, subduction-related lavas are often enriched in large ion lithophile elements such as Th and the LREEs relative to high

field strength elements such as Nb and Ta. However, crustal contamination of magma en route to the surface, or in the mantle source region before the magma reaches crustal levels, can also generate igneous rocks with negative Nb-Ta anomalies. Continental crust has a trace element composition similar to volcanic arc lavas and is enriched in Th and LREEs relative to Nb and Ta (Rudnick & Fountain, 1995). Crustal contamination has been suggested to explain the chemistry of igneous rocks from many LIPs varying in age from the Archaean to more recent times (e.g. ~2.7 Ga Abitibi greenstone belt – Sproule et al., 2002; ~1.1 Ga Keewenawan flood basalts – Vervoort et al., 2007; ~60 Ma British Tertiary igneous province – Thompson et al., 1982; Kerr et al., 1995a; Fowler et al., 2004). Therefore the negative Nb-Ta anomalies in some of the Circum-Superior LIP rocks may be the consequence of a subduction-related origin or the interaction of magma with crustal material. The following sections discuss which of these possibilities is most likely.

5.3.2. Group 2 of the Chukotat Group

The seven samples in Group 2 of the Chukotat Group have multi-element profiles with negative Nb-Ta anomalies (Fig. 4.8b). These multi-element profiles are notably different to those of the eighteen samples in Group 1 which are relatively flat and oceanic-plateau-like. If the Chukotat Group represents a volcanic arc then it would be likely that the majority of samples from it would possess negative Nb-Ta anomalies. The MgO content of the Group 2 samples also argues against a subduction setting. The maximum MgO concentration is 19.21 wt. % which is much higher than in normal volcanic arc rocks (Kerr et al., 2000). Boninites often possess high concentrations of MgO and Polat et al. (2002) have reported the presence of boninites with ~18 wt. % MgO in the ~3.7-3.8 Ga Isua greenstone belt in Greenland. However, the Group 2 samples have multi-element profiles that are different to boninites which have very depleted incompatible element abundances and positive HREE slopes (Pearce et al., 1992; Bedard, 1999). Therefore the negative Nb-Ta anomalies of the Group 2 samples are probably the result of crustal contamination.

Mungall (2007) noted the negative Nb-Ta anomalies in some Chukotat Group lavas and suggested that the Chukotat parental magmas underwent assimilation of crustal rock with concomitant fractional crystallisation (AFC) during their emplacement

through the dyke- and sill-like bodies of the Raglan Formation and Expo-Ungava Intrusive Suite. Mungall (2007) modelled the AFC evolution of the Chukotat parental magma using the PELE thermodynamic modelling software of Boudreau (1999) and a contaminant composition of that of Beauparlant Formation semi-pelite. The results of the current study are in general agreement with but disagree with some aspects of the model of Mungall (2007), namely the mechanism of contamination.

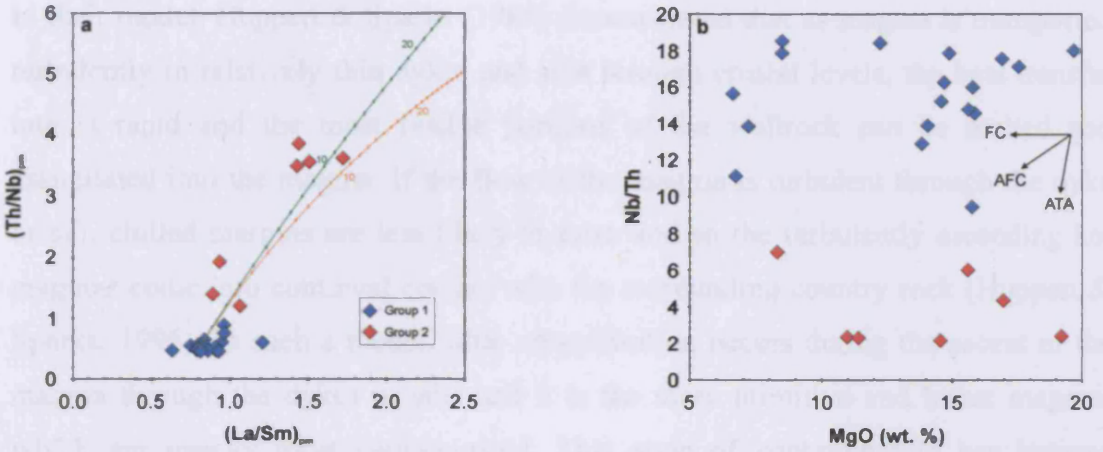

Fig. 5.20. (a) $(Th/Nb)_{pm}$ vs. $(La/Sm)_{pm}$ diagram for the Chukotat Group with calculated mixing lines for the contamination of the primary magma composition with Beauparlant Formation semi-pelite (orange line) and average Thompson Nickel Belt Archaean gneiss (green line). Each tick represents 1% addition of crustal material. (b) Nb/Th vs. MgO diagram for the Chukotat Group. Abbreviations are as follows: FC fractional crystallisation; AFC assimilation with fractional crystallisation; ATA assimilation during turbulent ascent. Primitive mantle values from Sun & McDonough (1989).

The trace element composition of the Group 2 samples can be fairly well reproduced by contaminating the Chukotat Group primary magma (MMC08-23 + 2.64% olivine) with up to ~10% of the Beauparlant Formation semi-pelite used in the study of Mungall (2007) (Fig. 5.20a). A slightly better fit to the data is produced when the Chukotat Group primary magma is contaminated with ~11% of the average composition of Archaean gneisses from the Thompson Nickel Belt (Burnham et al., 2004) (Fig. 5.20a). However, the use of a contaminant composition from a different area to the Cape Smith Belt may be conjectural. Mungall (2007) suggested that the mechanism of contamination was AFC within dykes and sills within the upper crust. AFC is a process which is usually considered to occur in large, mid-crustal magma chambers, not relatively thin dykes and sills, where magma can pond for a considerable period of time and undergo fractional crystallisation, the latent heat from which providing the energy to assimilate the wallrock of the chamber (DePaolo, 1981). A consequence of AFC is that the most evolved lavas should be the most

contaminated. Fig. 5.20b demonstrates that there is no obvious correlation between an index of fractionation (MgO) and a crustal input indicator (Nb/Th) for the Chukotat Group. Instead it is only lavas with MgO >8 wt. % that have been contaminated. Therefore the mechanism of contamination of the Group 2 samples was probably something other than AFC.

Huppert & Sparks (1985) highlighted another mechanism of magma contamination. In their model, Huppert & Sparks (1985) demonstrated that as magma is transported turbulently in relatively thin dykes and sills through crustal levels, the heat transfer rate is rapid and the most fusible portions of the wallrock can be melted and assimilated into the magma. If the flow of the magma is turbulent through the dyke or sill, chilled margins are less likely to form and so the turbulently ascending hot magmas come into continual contact with the surrounding country rock (Huppert & Sparks, 1995). In such a model, little crystallisation occurs during the ascent of the magma through the dykes or sills and it is the more primitive and hotter magmas which are usually most contaminated. This style of contamination has become known as assimilation during turbulent ascent (ATA) and has been demonstrated to have occurred in many volcanic provinces (e.g. Kerr et al., 1995a; Peate et al., 2008; Font et al., 2008).

The geochemical composition of the Chukotat Group is more consistent with ATA-style contamination than with AFC. Samples which are contaminated are randomly distributed and in the minority, suggesting that contamination occurred in local environments rather than in crustal magma chambers where large batches of magma could be contaminated homogeneously. AFC also predicts that the most evolved magmas are the most contaminated, which is not the case with the Chukotat Group where some of the contaminated magmas contain high concentrations of MgO and the most evolved samples are uncontaminated (Fig. 5.20b). The isotope data which exist for the Chukotat Group also do not support an AFC-style contamination mechanism (Fig. 5.21). The dykes and sills of the Raglan Formation and Expo Ungava Intrusive Suite intrude through the Povungnituk Group sediments and probably represent the sites of contamination of the Chukotat Group magmas.

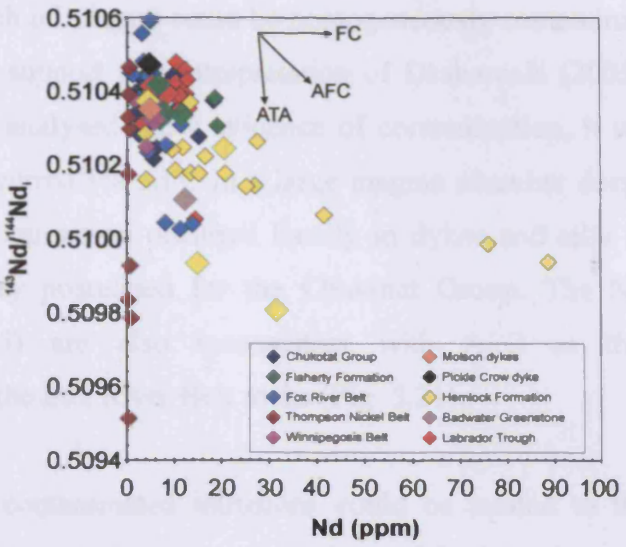

Fig. 5.21. $^{143}Nd/^{144}Nd_i$ vs. Nd diagram for the igneous rocks of the Circum-Superior LIP. Included are the results from the current study (larger diamonds with blue rims) and results from the literature (smaller diamonds with black rims). Sources of external data are Zindler (1982), Chauvel et al. (1987), Smith & Ludden (1989), Beck & Murthy (1991), Hegner & Bevier (1991), Blichert-Toft & Arndt (1999), Vervoort & Blichert-Toft (1999), Burnham et al. (2004), Desharnais (2005) and Hulbert et al. (2005). Abbreviations the same as in Fig. 5.20.

5.3.3. Fox River Belt intrusions

The majority of samples from the intrusions in the Fox River Belt show evidence for crustal contamination in their pronounced negative Nb-Ta anomalies (Fig. 4.28b). Only the Marginal Zone olivine pyroxenite from the Fox River Sill and the Lower Intrusions peridotite have multi-element profiles with no negative Nb-Ta anomalies. None of the volcanic rocks analysed in this study display obvious evidence for crustal contamination (Fig. 4.28a). However, in a more detailed study of the Fox River Belt, Desharnais (2005) discovered fifteen samples (out of ninety) from the volcanic formations with pronounced negative Nb-Ta anomalies.

Desharnais (2005) highlighted field and geochemical evidence for contamination of the Fox River Belt magmas. This included the presence of hornfelsed sediment xenoliths at the base of the Fox River Sill, trace element patterns with negative Nb-Ta anomalies and negative εNd_i and εHf_i values. Scoates (1990) also interpreted the textures of parts of the Hybrid Roof Zone of the Fox River Sill to represent remelted sediments. Desharnais (2005) noted that the distribution of the contamination signature in the contacts of many sills and within a few individual volcanic flows suggesting that the contamination did not occur in deep crustal magma chambers

where a large batch of magma could be homogeneously contaminated. The results of the current study support this interpretation of Desharnais (2005). As none of the volcanic samples analysed show evidence of contamination, it seems unlikely that contamination occurred via AFC in a large magma chamber deep in the crust. It is possible that contamination occurred locally in dykes and sills in the upper crust, similar to the way postulated for the Chukotat Group. The Nd isotope data of Desharnais (2005) are also inconsistent with AFC as the mechanism of contamination of the Fox River Belt rocks (Fig. 5.21).

To assess if the contaminated intrusions could be related to the uncontaminated volcanic rocks, the trace element compositions of the intrusive rocks were modelled using the equation for the residue of fractional crystallisation given in Appendix F and Rollinson (1993), a starting composition of the Fox River Belt primary magma MMFR08-8 + 9.45% olivine, and different possible contaminants (Archaean Superior Province biotite schist and Lower Sedimentary Formation argillite) identified by Desharnais (2005).

Fig. 5.22 shows the results of modelling the trace element compositions of the contaminated Fox River Sill intrusive samples. The Marginal Zone gabbro (MMFR08-22) can be fairly well reproduced by adding 7% biotite schist to the residue of 40% fractional crystallisation (Fig. 5.22a). The addition of the same amount of biotite schist to a residue from 10% fractional crystallisation yields a similar trace element composition to the Lower Central Layered Zone dunite (MMFR08-24) (Fig. 5.22b). The general shape of the multi-element profile of the Lower Central Layered Zone gabbro (MMFR08-25) is replicated by mixing 10% biotite schist with the residue of 70% fractional crystallisation although the calculated abundances for some elements are a bit higher than the measured abundances (Fig. 5.22b). The trace element composition of the olivine pyroxenite Upper Central Layered Zone sample (MMFR08-26) can be replicated by the addition of 7% biotite schist to the residue of 40% fractional crystallisation (Fig. 5.22c). The Upper Central Layered Zone gabbro (MMFR08-28) can be modelled as the mixture of 5% Lower Sedimentary Formation argillite with the residue of 70% fractional crystallisation (Fig. 5.22c).

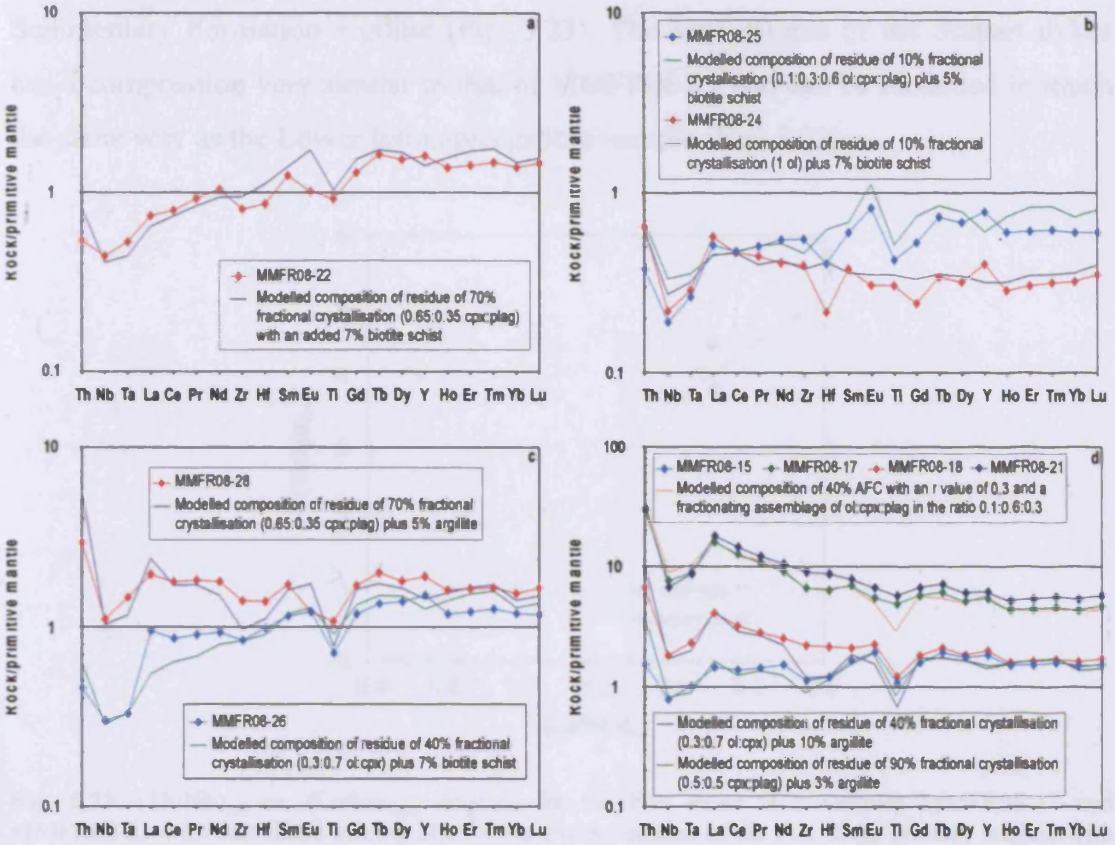

Fig. 5.22. Primitive-mantle-normalised multi-element diagrams displaying the trace element modelling results for the petrogenesis of the intrusive rocks of the Fox River Belt: (a) the Fox River Sill Marginal Zone; (b) the Fox River Sill Lower Central Layered Zone; (c) the Fox River Sill Upper Central Layered Zone; (d) the Lower Intrusions and Stupart dykes. Primitive mantle values from Sun & McDonough (1989).

The contaminated samples of the Lower Intrusions can also be successfully modelled (Fig. 5.22d). The trace element composition of the gabbro sample MMFR08-15 can be reproduced by adding 3% Lower Sedimentary Formation argillite to the residue of 90% crystallisation, although this does slightly overestimate the Th content (Fig. 5.22d). The signature of the olivine pyroxenite sample (MMFR08-18) is fairly well replicated by adding 10% argillite to the residue of 40% fractional crystallisation (Fig. 5.22d). The multi-element profile of the gabbro sample MMFR08-17 is actually able to be replicated by 40% AFC (using the equation in Appendix F given by DePaolo, 1981) with an r value (ratio of assimilation rate to the fractional crystallisation rate) of 0.3 and the Lower Sedimentary Formation argillite as the contaminant (Fig. 5.22d). However, as discussed above, the prospect of AFC as the contamination mechanism for the Fox River Belt rocks seems unlikely. It is also consistent with the geochemistry to replicate the composition of MMFR08-17 by contaminating an uncontaminated Fox River Belt magma with 20% Lower

Sedimentary Formation argillite (Fig. 5.23). The lone sample of the Stupart dykes has a composition very similar to that of MMFR08-17 and can be modelled in much the same way as the Lower Intrusions gabbro sample (Fig. 5.23).

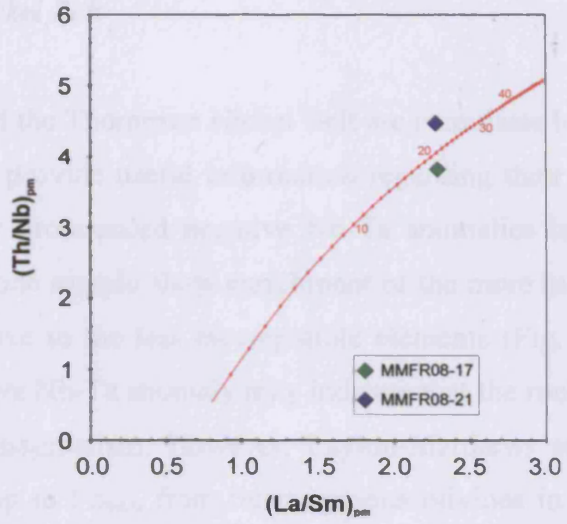

Fig. 5.23. $(Th/Nb)_{pm}$ vs. $(La/Sm)_{pm}$ diagram for the Fox River Belt samples MMFR08-17 and MMFR08-21 with calculated mixing line for the contamination of the Fox River primary magma with Lower Sedimentary Formation argillite. Each tick represents 1% addition of crustal material. Primitive mantle values from Sun & McDonough (1989).

The modelling results given above may be dependent on many variables which are estimated rather than known, but show that it is possible to derive the chemical composition of the intrusive rocks from processes affecting magmatic liquid of the composition observed in the Lower and Upper Volcanic Formations. It is surprising that very few contamination signatures have been recognised in the volcanic rocks given that the intrusive rocks are commonly contaminated. No volcanic samples in this study display negative Nb-Ta anomalies and only 17% of volcanic samples in the study of Desharnais (2005) are classed as contaminated. All but two intrusive samples in the current study are contaminated and Desharnais (2005) noted that over half of the samples from the Lower Intrusions showed evidence of contamination. Unfortunately the Nb-Ta data of Desharnais (2005) for the Marginal and the Lower and Upper Central Layered Zones are too few and of poor quality for comparison. It may be that more contaminated volcanic flows have just not been sampled due to the poor exposure in the Fox River Belt region or that erosion has for some reason preferentially removed these flows. Alternatively, the Fox River Belt magmas may have passed relatively uncontaminated through the intrusive conduits leaving behind

a solid residue from fractional crystallisation, plus some residual liquid in the mush, which still retained enough heat to assimilate the wallrock of the conduits. This does not seem unreasonable but is still speculative.

5.3.4. Thompson Nickel Belt

The igneous rocks of the Thompson Nickel Belt are cumulates but their trace element signatures may still provide useful information regarding their petrogenetic history. All samples display pronounced negative Nb-Ta anomalies in their multi-element profiles and all but one sample show enrichment of the more incompatible elements, except Nb-Ta, relative to the less incompatible elements (Fig. 4.38). The universal presence of a negative Nb-Ta anomaly may indicate that the rocks were derived from subduction-related magmatism. However, Layton-Matthews et al. (2007) reported forsterite contents up to $Fo_{94.0}$ from relict igneous olivines in metaperidotite rocks and suggested that the olivines must have crystallised from magmas containing up to 22 wt. % MgO. Such high MgO magmas are very rare in subduction settings. Therefore the Thompson Nickel Belt sills were probably emplaced in a different geodynamic setting to a volcanic arc and subsequently contaminated.

To ascertain if the contaminated cumulate rocks of the Thompson Nickel Belt could be related to the volcanic rocks of the Circum-Superior LIP, the trace element compositions were modelled using the equation for the residue of fractional crystallisation given in Appendix F and Rollinson (1993), a starting composition of the Fox River Belt primary magma MMFR08-8 + 9.45% olivine, and the average Archaean Thompson Nickel Belt gneiss composition from Burnham et al. (2004). The results of the modelling are shown in Fig. 5.24. The multi-element profiles of the Thompson samples are able to be replicated by various degrees of fractional crystallisation and contamination. One of the samples with the lowest elemental abundances is the dunite sample MMT08-21. The multi-element profile of this sample can be reproduced by adding 5% Archaean gneiss to the residue of 20% crystallisation of a fractionating assemblage with an olivine:clinopyroxene ratio of 0.9:0.1 (Fig. 5.24). Sample MMT08-7 is a peridotite and has some of the highest elemental abundances in the suite of rocks. The multi-element profile of this sample can be replicated by the addition of 40% Archaean gneiss to the residue of 80%

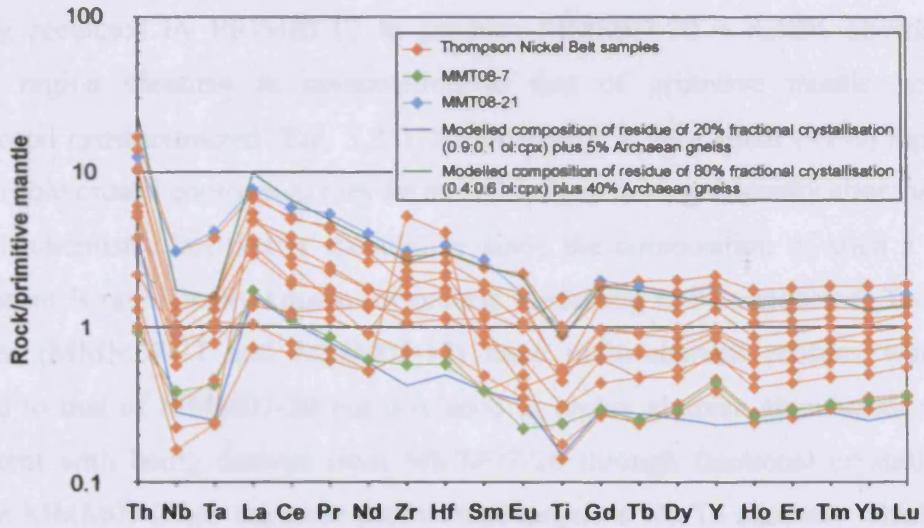

Fig. 5.24. Primitive-mantle-normalised multi-element diagram displaying the trace element modelling results for the petrogenesis of the intrusive rocks of the Thompson Nickel Belt.

crystallisation of a fractionating assemblage with an olivine:clinopyroxene ratio of 0.4:0.6 (Fig. 5.24). The trace element modelling may require the input of many variables which are not known with total confidence but shows that the Thompson Nickel Belt sills could be related to the magmatic rocks of the Circum-Superior LIP.

5.3.5. Molson dykes

Four samples from the Molson dykes display slight to pronounced negative Nb-Ta anomalies in their multi-element profiles (Fig. 4.58b). One of these samples (MMM07-20) was identified on the basis of its major element chemistry by PRIMELT2 to represent a primary magma which had only experienced olivine crystallisation (see section 5.1.4). Therefore the slight negative Nb-Ta anomaly may represent the introduction of crustal material to the source region long before the onset of melting and the ascent of magma through the crust. What may be more feasible is that the slight negative Nb-Ta anomaly represents a very small input of crustal material which was not sufficient to strongly alter the major element chemistry and be detected by PRIMELT2. Interestingly, the isotopic composition of sample MMM07-20 also does not show evidence of crustal contamination (Fig. 4.83). The trace element composition of MMM07-20 + 8.48% olivine (the primary magma composition predicted by PRIMELT2) is replicated by adding 4% average Thompson Nickel Belt Archaean gneiss to a 31.5% partial melt (the degree of partial

melting predicted by PRIMELT2 to produce MMM07-20 + 8.48% olivine) of a source region identical in composition to that of primitive mantle with 1% continental crust extracted (Fig. 5.25). Alternatively, a very small (<1%) input of a very fusible crustal component may be more likely to not significantly alter the major element chemistry but this is speculative since the composition of such a fusible component is not actually known for precise modelling to be conducted. Two other samples (MMM07-11 and MMM07-12) have multi-element profiles which are parallel to that of MMM07-20 but displaced to higher element abundances and are consistent with being derived from MMM07-20 through fractional crystallisation. Sample MMM07-2 has the most pronounced negative Nb-Ta anomaly which could be the result of contamination. Simple mixing between the Fox River Belt primary magma and ~10% of the average Thompson Nickel Belt Archaean gneiss produces a similar trace element composition to that of sample MMM07-2 (Fig. 5.25).

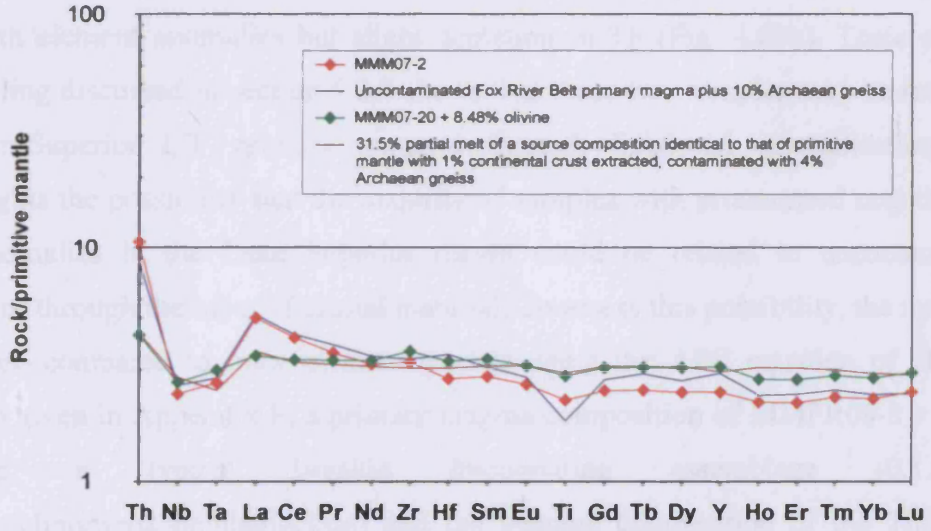

Fig. 5.25. Primitive-mantle-normalised multi-element diagram comparing the trace element modelling results of contaminating the Fox River Belt primary magma with 10% average Thompson Nickel Belt Archaean gneiss to a contaminated Molson dyke sample (MMM07-2), and contaminating a 31.5% partial melt of a hypothetical source region with 4% average Thompson Nickel Belt Archaean gneiss.

5.3.6. Lake Superior region

The vast majority of samples from the igneous rocks of the Lake Superior region have multi-element profiles with pronounced negative Nb-Ta anomalies (Fig. 4.68). The prevalence of the negative Nb-Ta signature could be an argument for a

subduction-related origin to the Lake Superior region igneous rocks. However, the field evidence suggests that these rocks may have formed in a different geodynamic setting to a volcanic arc. Abundant tephra layers are expected to be present in subduction-related settings yet very few have been observed in the current study or in previous geological reports of the area (Gair & Wier, 1956; James, 1958; Bayley, 1959; Wier, 1967; Trent, 1976). Previous geochemical studies have suggested that the negative Nb-Ta anomalies present throughout at least the Hemlock Formation are the result of extensive AFC processes (Ueng et al., 1988; Beck & Murthy, 1991). The results of the current study suggest that the majority of rocks from the Hemlock Formation, Badwater Greenstone, Emperor Volcanic Complex and Gunflint Formation can be formed as the product of AFC processes on a parental magma similar in composition to that of other segments of the Circum-Superior LIP.

The two Group 1 samples from the Hemlock Formation are considered to be uncontaminated given their relatively flat multi-element profiles with no high field strength element anomalies but slight depletion in Th (Fig. 4.68b). Trace element modelling discussed in section 5.2.9 shows that these two samples may be related to Circum-Superior LIP primary magmas through fractional crystallisation. This highlights the possibility that the majority of samples with pronounced negative Nb-Ta anomalies in the Lake Superior region could be related to uncontaminated magmas through the input of crustal material. To assess this possibility, the measured data are compared to trace element models using the AFC equation of DePaolo (1981) given in Appendix F, a primary magma composition of MMFR08-8 + 9.45% olivine, a typical basaltic fractionating assemblage (0.1:0.3:0.6 olivine:clinopyroxene:plagioclase) and the average composition of the Thompson Nickel Belt Archaean gneisses from Burnham et al. (2004) as the contaminant. The results are expressed in diagrams shown in Figs. 5.26 and 5.27.

The Group 2 samples of the Hemlock Formation have multi-element profiles which are reasonably well replicated by 55-90% AFC at an r value of 0.25 (Figs. 5.26a and 5.27). The model produces a good fit for Zr concentrations and $(La/Sm)_{pm}$ ratios (Fig. 5.27) but slightly overestimates the magnitude of the negative Nb-Ta anomalies (Fig. 5.26a), although given the uncertainty in the many variables used the fit of the model to the data is generally good. The Badwater Greenstone has $(La/Sm)_{pm}$ and Zr

values consistent with being derived from the Fox River Belt primary magma by AFC. Six samples can be derived from 45-85% AFC at an r value of 0.25 (Fig. 5.27). The other two samples require 60-70% AFC at a lower ratio of contamination rate to crystallisation rate of 0.15 (Fig. 5.27). The modelling replicates the multi-element profiles of the Badwater Greenstone reasonably well but does slightly overestimate the magnitude of the negative Nb-Ta anomalies (Fig. 5.26b). The Gunflint Formation basalts can also be modelled by ~70-75% AFC at an r value of 0.25 (Figs. 5.26c and 5.27).

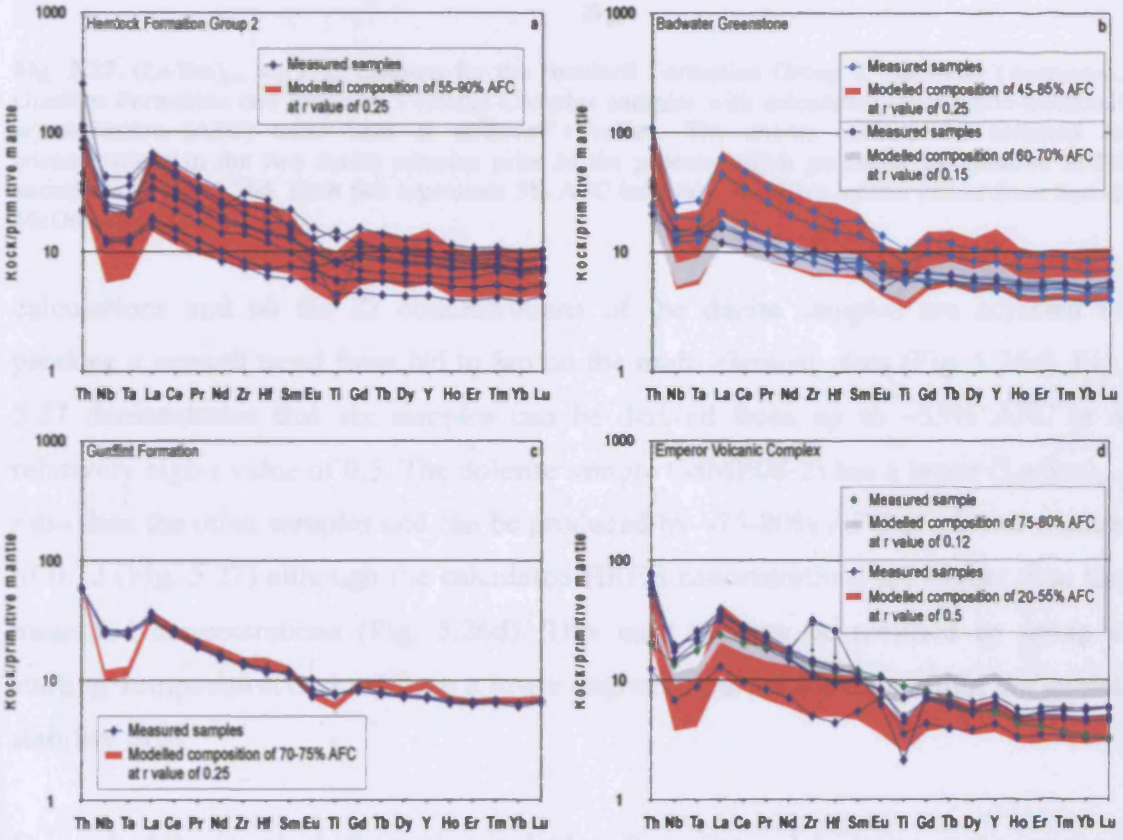

Fig. 5.26. Primitive-mantle-normalised multi-element diagrams displaying the trace element modelling results of assimilation-fractional crystallisation against the measured data for: (a) Hemlock Formation Group 2; (b) Badwater Greenstone; (c) Gunflint Formation; (d) Emperor Volcanic Complex. The arrows in (d) indicate the assumed Zr and Hf concentrations in the two dacite samples prior to the process which produced the positive Zr-Hf anomalies. Primitive mantle values from Sun & McDonough (1989).

The $(La/Sm)_{pm}$-Zr_{pm} chemistry of the Emperor Volcanic Complex may be clearer than it at first appears. The two dacite samples have anomalous positive Zr-Hf anomalies in their multi-element profiles which could be explained by the accumulation of zircon. Any role for zircon has not been considered in the AFC

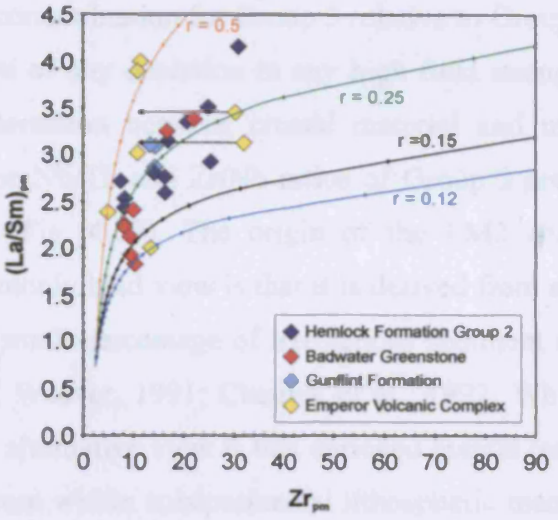

Fig. 5.27. $(La/Sm)_{pm}$ vs. Zr_{pm} diagram for the Hemlock Formation Group 2, Badwater Greenstone, Gunflint Formation and Emperor Volcanic Complex samples with calculated assimilation-fractional crystallisation (AFC) trend lines at different r values. The arrows indicate the assumed Zr concentrations in the two dacite samples prior to the process which produced the positive Zr-Hf anomalies in Fig. 5.26d. Each tick represents 5% AFC intervals. Primitive mantle values from Sun & McDonough (1989).

calculations and so the Zr concentrations of the dacite samples are adjusted to produce a smooth trend from Nd to Sm on the multi-element plots (Fig. 5.26d). Fig. 5.27 demonstrates that six samples can be derived from up to ~55% AFC at a relatively high r value of 0.5. The dolerite sample (MME08-2) has a lower $(La/Sm)_{pm}$ ratio than the other samples and can be produced by ~75-80% AFC at a lower r value of 0.12 (Fig. 5.27) although the calculated HREE concentrations are higher than the measured concentrations (Fig. 5.26d). This may perhaps be rectified by using a starting composition derived from a lower degree of partial melting within the garnet stability field.

Group 3 of the Hemlock Formation is distinct from Group 1 by being more enriched in Th-Nb-Ta-LREEs relative to the MREEs and more depleted in Y-HREEs relative to the MREEs (Fig. 4.68). This contrast in chemistry could be explained by Group 3 being derived from a lower degree of partial melting of the same source as for Group 1 and leaving garnet in the residue. However, the isotopic compositions of the two groups are different (Fig. 4.83) implying that the two groups cannot be related by differences in partial melting or fractional crystallisation. Group 3 has higher $^{87}Sr/^{86}Sr_i$ and lower $^{143}Nd/^{144}Nd_i$ and $^{176}Hf/^{177}Hf_i$ than Group 1, but not as high $^{87}Sr/^{86}Sr_i$ or as low $^{143}Nd/^{144}Nd_i$ and $^{176}Hf/^{177}Hf_i$ as Group 2. This could be the result

of a lower degree of contamination for Group 3 relative to Group 2. However, Group 3 shows no indication of any depletion in any high field strength element which is inconsistent with interaction between crustal material and magma as it ascends through the crust. The Nb/Th and Zr/Nb ratios of Group 3 are similar to the EM2 mantle end-member (Fig. 4.69). The origin of the EM2 end-member is widely debated but one commonly held view is that it is derived from a source of subducted oceanic crust with a small percentage of terrigenous sediment mixed in (Woodhead & McCulloch, 1989; Weaver, 1991; Chauvel et al., 1992; White & Duncan, 1996; Hofmann, 1997). An alternative view is that enriched mantle reservoirs such as EM1 and EM2 originate from within subcontinental lithospheric mantle (cf. Gibson et al., 2005). Unfortunately the isotopic composition of EM2 in the Palaeoproterozoic is not known. Nevertheless, given its similarity to EM2 in terms of incompatible element ratios, Group 3 of the Hemlock Formation is interpreted to have formed from a different source composition to that of Group 1, which included a small proportion of subducted sediment, and was not affected by contamination as the magmas ascended through the crust. Alternatively, Group 3 of the Hemlock Formation could have been sourced from the subcontinental lithospheric mantle. The majority of samples from the western Kiernan sill have multi-element patterns which are similar in shape to the Hemlock Formation Group 3 samples but at lower elemental abundances (Fig. 4.68). This suggests that the sill fed the Hemlock Formation Group 3 lavas and now contains slightly lower concentrations of elements than the lavas because of the preference of incompatible elements for liquid phases compared to solid cumulate phases.

The mechanism of contamination of the Lake Superior region igneous rocks is different to that for other segments of the Circum-Superior LIP. It is the most evolved samples (i.e. lowest MgO) which are the most contaminated and have the lowest Nb/Th ratios (Fig. 5.28). The Nd isotope data from the literature and the current study also indicate that the lowest $^{143}Nd/^{144}Nd_i$ ratios are found in the most evolved samples with the highest Nd concentrations (Fig. 5.21). These geochemical and isotopic features suggest that magmas of the Lake Superior region were contaminated in large magma chambers residing in the crust rather than during turbulent ascent through relatively thin conduits in the upper crust.

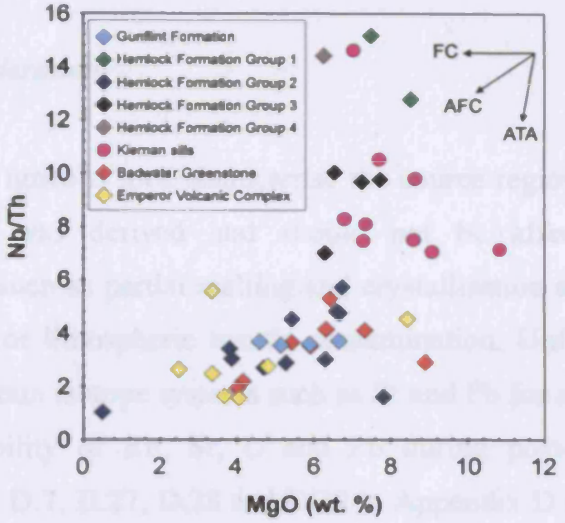

Fig. 5.28. Nb/Th vs. MgO diagram for the Lake Superior region igneous rocks. Abbreviations same as in Fig. 5.20.

5.3.7. Summary

Signatures of crustal contamination are present in the Chukotat Group, Fox River Belt, Thompson Nickel Belt, Molson dykes and Lake Superior region igneous rocks. There are no obvious signs of contamination in the Flaherty Formation, Winnipegosis Belt, Pickle Crow dyke or Hellancourt Formation. Average Archaean gneiss can satisfy the chemical composition of the contaminant but in some cases so can more localised sediment where more data are available. For example, the Beauparlant Formation semi-pelite and the Lower Sedimentary Formation argillite can be modelled as the contaminants in the Chukotat Group and Fox River Belt respectively. The mechanism of contamination of the Chukotat Group and Fox River Belt rocks appears to have been ATA as hot, primitive magmas were ascending through thin conduits in the upper crust, whereas the most evolved lavas in the Lake Superior region are the most contaminated suggesting that contamination occurred with fractional crystallisation (AFC) as the magmas were stored in large magma chambers deep in the crust.

5.4. Nature of the mantle source region(s) of the Circum-Superior LIP

5.4.1. Isotopic considerations

Isotopic ratios of an igneous rock characterise the source region of the mantle from which the magma was derived and should not be affected by subsequent fractionation events such as partial melting and crystallisation although they may be modified by crustal or lithospheric mantle contamination. Unfortunately, problems arise when using certain isotope systems such as Sr and Pb for ancient rocks because of the relative mobility of Rb, Sr, U and Pb during post-magmatic alteration processes. Equations D.7, D.27, D.28 and D.29 in Appendix D show that the Rb, Sr, U and Pb concentrations of whole rock samples are crucial when age-correcting Sr and Pb isotopic ratios. If the concentration of any of these elements has been modified by alteration processes then the calculated initial isotopic ratios can be significantly affected. The Pb isotopic ratios of the Circum-Superior LIP samples appear to have been significantly affected by post-magmatic alteration processes. This is apparent from Figs. 4.83c and 4.83d on which the Circum-Superior LIP displays large ranges in $^{206}Pb/^{204}Pb_i$, $^{207}Pb/^{204}Pb_i$ and $^{208}Pb/^{204}Pb_i$ of 11.337-18.473, 14.620-15.694 and 32.113-38.225 respectively. The ranges in all three Pb isotopic ratios are much larger than for most individual LIPs, even those such as the Caribbean-Colombian oceanic plateau which are considered to have a heterogeneous mantle source (e.g. Kerr et al., 2002; Kerr, 2003).

The large range in Pb isotope ratios is probably a result of the mobilisation of U and Pb. Fig. 5.29a shows that when U is plotted against Zr there is a considerable degree of scatter for the whole of the Circum-Superior LIP although for some segments U seems not to have been significantly altered. Pb concentrations have only been determined for the eighteen samples chosen for Pb isotopic analyses because of problems with Pb contamination in the lithium metaborate fusion method (see Appendix D). No obvious trends are observed when the Pb concentration data are plotted against Zr (Fig. 5.29b). A post-magmatic gain in U and/or loss in Pb will increase the $^{206}Pb/^{204}Pb_i$ and $^{207}Pb/^{204}Pb_i$ ratios while U loss and/or Pb gain will decrease the $^{206}Pb/^{204}Pb_i$ and $^{207}Pb/^{204}Pb_i$ ratios (see equations D.27 and D.28 in Appendix D). Additionally, Pb gain and Pb loss during alteration processes will

serve to respectively decrease and increase the $^{208}Pb/^{204}Pb_i$ ratio. The $^{208}Pb/^{204}Pb_i$ ratio may be less susceptible than the $^{206}Pb/^{204}Pb_i$ and $^{207}Pb/^{204}Pb_i$ ratios to modification because it is partially dependent on the Th/Pb ratio rather than the U/Pb ratio (see equations D.27-D.29 in Appendix D) and Th is relatively less mobile than U (e.g. Pearce, 1996; see Chapter 4).

The initial Pb isotopic ratios therefore cannot be used with confidence to infer useful information about the mantle source region(s) of the Circum-Superior LIP and this highlights the limitations of the Pb isotopic system for ancient and altered igneous rocks. Some previous studies have analysed Pb isotopic ratios of rocks from the Chukotat Group (Brevart et al., 1986; Hegner & Bevier, 1991; Arndt & Todt, 1994), Flaherty Formation (Arndt & Todt, 1994) and Labrador Trough (Rohon et al., 1993) mainly in the aim of determining the age of rocks from these areas. Unfortunately none of these studies report the U, Pb and Th concentrations required to age-correct the isotopic ratios and so no reliable comparison can be made with the results of the current study.

The Sr isotopic system is also vulnerable to post-magmatic alteration, particularly to the effects of seawater alteration (e.g. Menzies & Seyfried, 1979a). Equation D.7 in Appendix D shows that the $^{87}Sr/^{86}Sr_i$ ratio of a sample is partially dependent on the Rb and Sr concentrations of the sample. Rb and Sr can be mobilised during post-magmatic alteration processes (Pearce, 1996). The Rb and Sr concentrations of the Circum-Superior LIP samples are plotted against Zr in Fig. 5.30 on which there is a degree of scatter, possibly due to the mobilisation of Rb and Sr. Therefore the $^{87}Sr/^{86}Sr_i$ isotopic ratios of the Circum-Superior LIP samples should be interpreted with caution. On inspection of Figs. 4.83a and 4.83b the $^{87}Sr/^{86}Sr_i$ ratios of the Circum-Superior LIP do not appear to have been significantly altered with the exception of one of the Hemlock Formation Group 2 samples. Sample MMH08-12 has a low $^{87}Sr/^{86}Sr_i$ ratio of 0.701319 while the other Hemlock Formation Group 2 sample (MMH08-5) has a high $^{87}Sr/^{86}Sr_i$ ratio of 0.710950. Both samples have low $^{143}Nd/^{144}Nd_i$ ratios (Fig. 4.83a) and negative Nb-Ta anomalies (Fig. 4.68b) and have been interpreted to be crustally contaminated (see section 5.3). A low $^{87}Sr/^{86}Sr_i$ ratio is inconsistent with crustal contamination and it is most likely that the $^{87}Sr/^{86}Sr_i$ ratio has been altered because $^{143}Nd/^{144}Nd_i$ and Nb and Ta concentrations are more

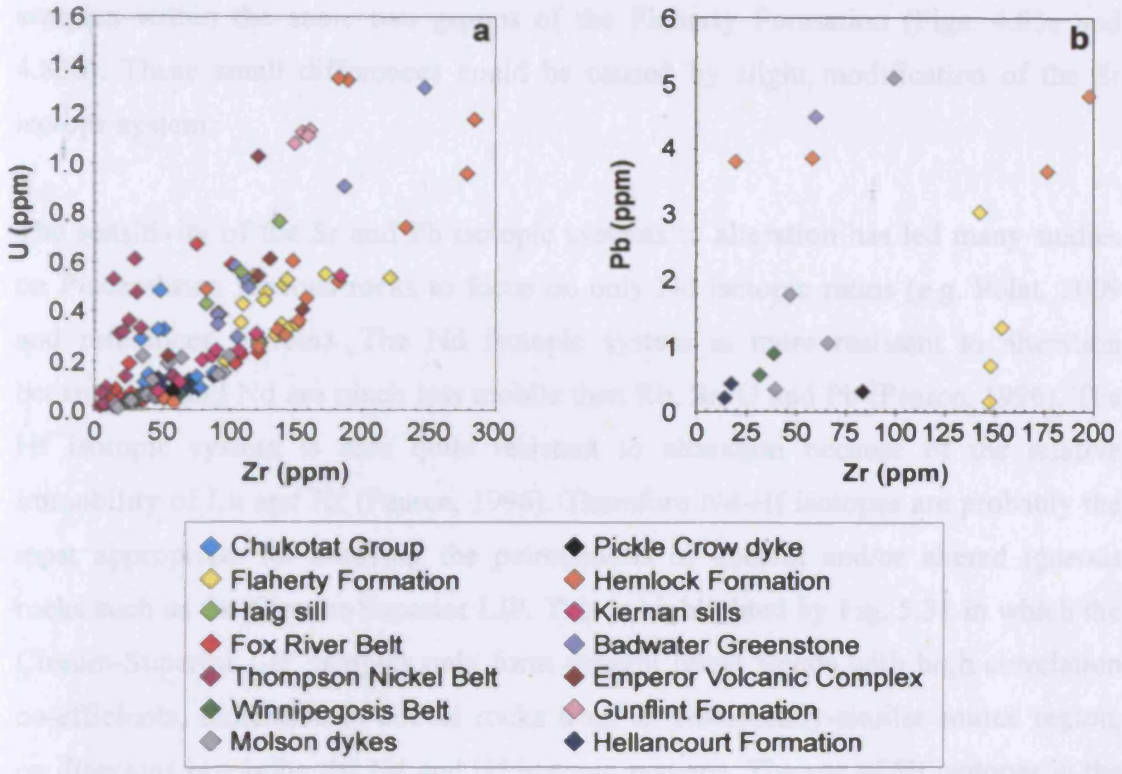

Fig. 5.29. U vs. Zr and Pb vs. Zr for the Circum-Superior LIP. In (a) all samples are plotted. In (b) only the eighteen samples selected for Sr-Nd-Pb-Hf isotopic analyses are plotted as these samples are the only ones for which Pb concentrations are available. Note the scatter on both diagrams which is possibly a result of the mobilisation of U and Pb by post-magmatic alteration processes. Consequently the Pb isotopic system may not be appropriate for studying the petrogenesis of the Circum-Superior LIP.

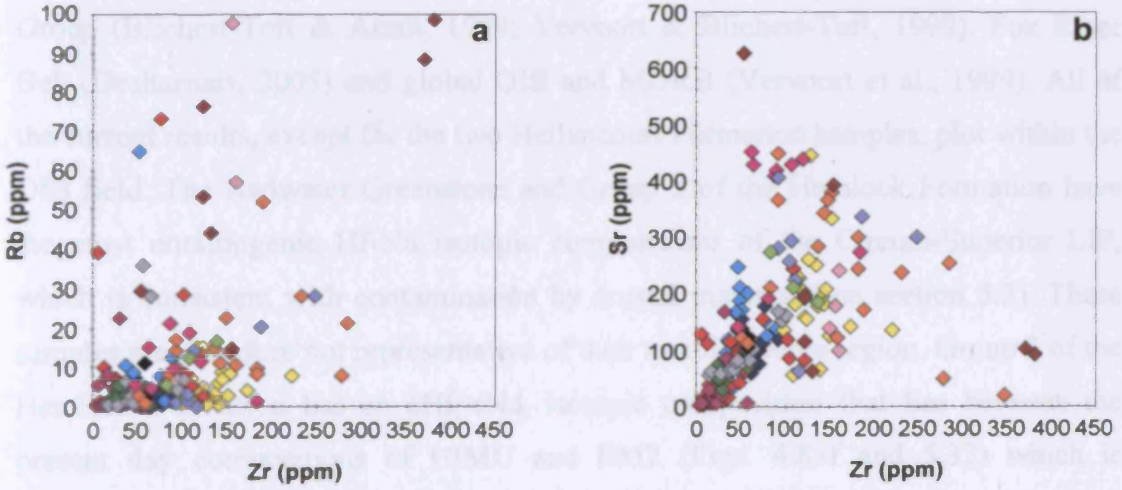

Fig. 5.30. (a) Rb vs. Zr and (b) Sr vs. Zr for the Circum-Superior LIP. Note the scatter on both diagrams, particularly in (a), which is possibly a result of the mobilisation of Rb and Sr by post-magmatic alteration processes. Consequently the Sr isotopic system should be treated cautiously when applying it to the petrogenesis of the Circum-Superior LIP. See Fig. 5.29 for legend.

resistant to alteration. There are also small differences in the $^{87}Sr/^{86}Sr_i$ ratios of samples within the same two groups of the Flaherty Formation (Figs. 4.83a and 4.83b). These small differences could be caused by slight modification of the Sr isotope system.

The sensitivity of the Sr and Pb isotopic systems to alteration has led many studies on Precambrian igneous rocks to focus on only Nd isotopic ratios (e.g. Polat, 2009 and references therein). The Nd isotopic system is more resistant to alteration because Sm and Nd are much less mobile than Rb, Sr, U and Pb (Pearce, 1996). The Hf isotopic system is also quite resistant to alteration because of the relative immobility of Lu and Hf (Pearce, 1996). Therefore Nd-Hf isotopes are probably the most appropriate for studying the petrogenesis of ancient and/or altered igneous rocks such as the Circum-Superior LIP. This is highlighted by Fig. 5.31 in which the Circum-Superior LIP samples only form straight linear trends with high correlation co-efficients, indicative of coeval rocks from an isotopically-similar source region, on diagrams involving the Nd and Hf isotopic systems. The use of Hf isotopes in the study of Precambrian LIPs is a more recent application than Nd isotopes and as such there are much less Hf than Nd isotopic data available on Precambrian LIPs.

The Hf-Nd isotopic compositions of the Circum-Superior LIP samples are shown in Figs. 4.83e and 4.83f and compared to the results of previous studies on the Chukotat Group (Blichert-Toft & Arndt, 1999; Vervoort & Blichert-Toft, 1999), Fox River Belt (Desharnais, 2005) and global OIB and MORB (Vervoort et al., 1999). All of the current results, except for the two Hellancourt Formation samples, plot within the OIB field. The Badwater Greenstone and Group 2 of the Hemlock Formation have the most unradiogenic Hf-Nd isotopic compositions of the Circum-Superior LIP, which is consistent with contamination by crustal material (see section 5.3). These samples are therefore not representative of their mantle source region. Group 3 of the Hemlock Formation has an εHf_i-εNd_i isotopic composition that lies between the present day compositions of HIMU and EM2 (Figs. 4.83f and 5.32) which is consistent with Fig. 4.69 on which the Group 3 samples fall in the recycled component field near to EM2 and suggests that the source of these samples contained recycled oceanic crust with some terrigenous sediment (cf. Weaver, 1991).

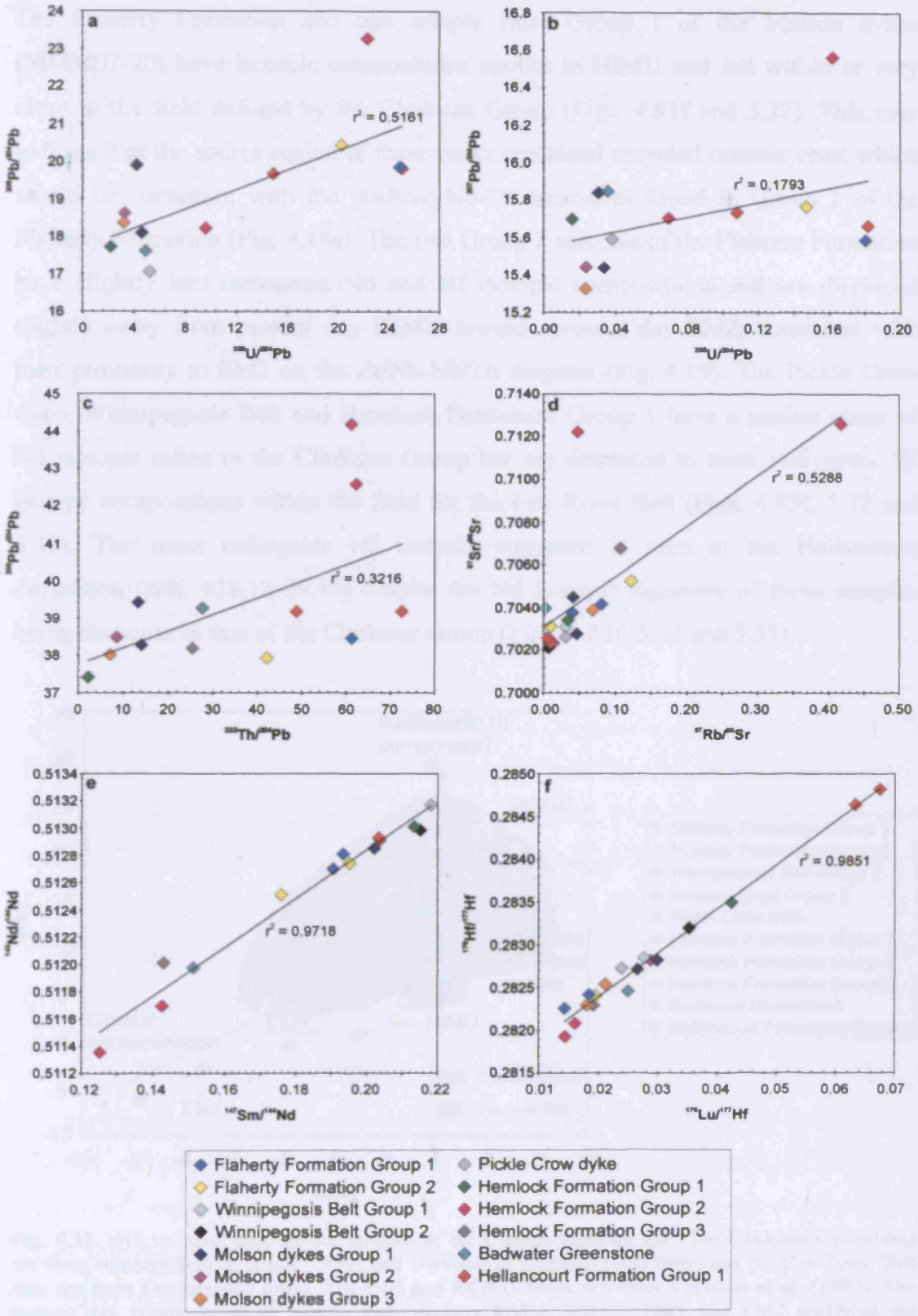

Fig. 5.31. Diagrams of measured isotopic ratios versus the corresponding parent/stable isotope ratios for the Circum-Superior LIP. (a) $^{206}Pb/^{204}Pb$ vs. $^{238}U/^{204}Pb$; (b) $^{207}Pb/^{204}Pb$ vs. $^{235}U/^{204}Pb$; (c) $^{208}Pb/^{204}Pb$ vs. $^{232}Th/^{204}Pb$; (d) $^{87}Sr/^{86}Sr$ vs. $^{87}Rb/^{86}Sr$; (e) $^{143}Nd/^{144}Nd$ vs. $^{147}Sm/^{144}Nd$; (f) $^{176}Hf/^{177}Hf$ vs. $^{176}Lu/^{177}Hf$. Correlation co-efficients are given on each diagram. Note the strong correlations in (e) and (f) highlighting that perhaps the Nd and Hf isotopic systems are the most appropriate for studying the petrogenesis of the Circum-Superior LIP.

The Flaherty Formation and one sample from Group 1 of the Molson dykes (MMM07-20) have isotopic compositions similar to HIMU and fall within or very close to the field defined by the Chukotat Group (Figs. 4.83f and 5.32). This may indicate that the source region of these rocks contained recycled oceanic crust which would be consistent with the positive Nb-Ta anomalies found in Group 1 of the Flaherty Formation (Fig. 4.18a). The two Group 2 samples of the Flaherty Formation have slightly less radiogenic Nd and Hf isotopic compositions and are displaced slightly away from present day HIMU towards present day EM2, consistent with their proximity to EM2 on the Zr/Nb-Nb/Th diagram (Fig. 4.19). The Pickle Crow dyke, Winnipegosis Belt and Hemlock Formation Group 1 have a similar range of Nd isotopic ratios to the Chukotat Group but are displaced to more radiogenic Hf isotope compositions within the field for the Fox River Belt (Figs. 4.83f, 5.32 and 5.33). The most radiogenic Hf isotopic signature is seen in the Hellancourt Formation (εHf_i +28.18-29.44) despite the Nd isotopic signature of these samples being the same as that of the Chukotat Group (Figs. 4.83f, 5.32 and 5.33).

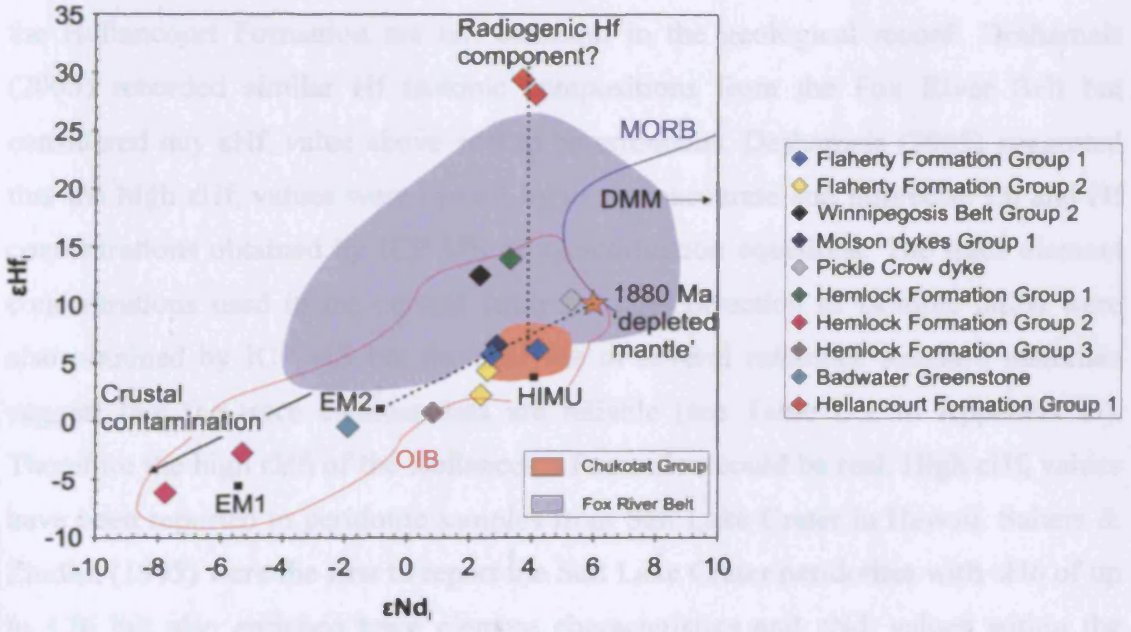

Fig. 5.32. εHf_i vs. εNd_i diagram for samples of the Circum-Superior LIP. The Chukotat Group data are from Blichert-Toft & Arndt (1999) and Vervoort & Blichert-Toft (1999) and the Fox River Belt data are from Desharnais (2005). The OIB and MORB fields are from Vervoort et al. (1999). The present day compositions of mantle end-members DMM, HIMU, EM1 and EM2 are from the compilation of Ernst & Buchan (2003). The orange star represents the estimated composition of depleted mantle at ~1880 Ma (Vervoort & Blichert-Toft, 1999). The two dashed lines represent possible mixing lines between (i) a depleted mantle component and a present day EM2-like component, and (ii) a mantle component with a radiogenic Hf isotope composition and a mantle component with a composition along the previous mixing line.

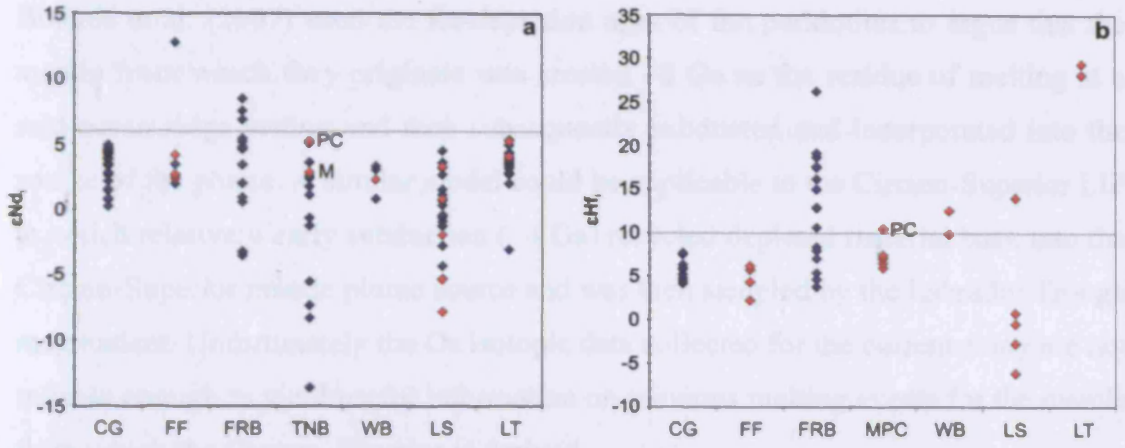

Fig. 5.33. (a) εNd_i and (b) εHf_i values of rocks from the various segments of the Circum-Superior LIP. Red diamonds represent data from the current study. Blue diamonds are data from the literature. Abbreviations as follows: CG Chukotat Group; FF Flaherty Formation; FRB Fox River Belt; TNB Thompson Nickel Belt; MPC Molson and Pickle Crow dykes; WB Winnipegosis Belt; LS Lake Superior region; LT Labrador Trough. Data sources: CG – Zindler (1982), Chauvel et al. (1987), Smith & Ludden (1989), Hegner & Bevier (1991), Blichert-Toft & Arndt (1999) and Vervoort & Blichert-Toft (1999); FF – Chauvel et al. (1987); FRB – Chauvel et al. (1987) and Desharnais (2005); TNB – Burnham et al. (2004); WB – Burnham et al. (2004); LS – Beck & Murthy (1991); LT – Smith & Ludden (1989), Rohon et al. (1993) and Skulski et al. (1993). The dashed lines represent the estimated composition of the depleted mantle at ~1880 Ma (Vervoort & Blichert-Toft, 1999).

Igneous rocks with such radiogenic Hf isotopic compositions and high εHf_i values as the Hellancourt Formation are not common in the geological record. Desharnais (2005) recorded similar Hf isotopic compositions from the Fox River Belt but considered any εHf_i value above +19 to be erroneous. Desharnais (2005) suggested that the high εHf_i values were caused by using inaccurate and imprecise Lu and Hf concentrations obtained by ICP-MS in age-correction equations. The trace element concentrations used in the current study for age-correction of isotopic ratios were also obtained by ICP-MS but the analyses of several reference standard materials suggest that the trace element data are reliable (see Table D.2 in Appendix D). Therefore the high εHf_i of the Hellancourt Formation could be real. High εHf_i values have been reported in peridotite samples from Salt Lake Crater in Hawaii. Salters & Zindler (1995) were the first to report the Salt Lake Crater peridotites with εHf_i of up to +76 but also enriched trace element characteristics and εNd_i values within the range of present day N-MORB. Bizimis et al. (2007) discovered Salt Lake Crater peridotites with even more radiogenic Hf and εHf_i of up to +114. Bizimis et al. (2007) noted that the Hf and Os isotopic compositions of the peridotites correlated with indices of the degree of depletion and suggested that the peridotites represent an ancient depleted and recycled mantle lithosphere intrinsic to the Hawaiian plume.

Bizimis et al. (2007) used the Re-depletion ages of the peridotites to argue that the mantle from which they originate was created ~2 Ga as the residue of melting at a mid-ocean ridge setting and then subsequently subducted and incorporated into the source of the plume. A similar model could be applicable to the Circum-Superior LIP in which relatively early subduction (~4 Ga) recycled depleted material back into the Circum-Superior mantle plume source and was then sampled by the Labrador Trough magmatism. Unfortunately the Os isotopic data collected for the current study are not reliable enough to yield useful information on previous melting events for the mantle from which the Circum-Superior is derived.

The positive εNd_i values of the majority of samples from the Circum-Superior LIP (Fig. 5.33a) are also indicative of mantle sources depleted by a previous melt extraction event. Samples which are uncontaminated with crustal material have a range of εNd_i values from +0.84 to +5.29. These values suggest that the mantle sources of the Circum-Superior LIP are not as depleted as the present day N-MORB-source DMM (Fig. 4.83f) nor the estimated DMM composition at ~1880 Ma (Fig. 5.32) which has an εNd_i value of +6 (Vervoort & Blichert-Toft, 1999). Vervoort & Blichert-Toft (1999) also estimated the depleted mantle at ~1880 Ma to have an εHf_i value of +10. Such a composition (εNd_i +6, εHf_i +10) is similar to that of the Pickle Crow dyke (εNd_i +5.29, εHf_i +10.49). Therefore it could be argued that the Pickle Crow dyke, Group 1 of the Molson dykes, Flaherty Formation and Group 3 of the Hemlock Formation are derived from a mixture of ~1880 Ma DMM-like and present day EM2-like mantle (Fig. 5.32). An additional end-member with a highly radiogenic Hf isotopic composition is required to explain the higher εHf_i values of the Winnipegosis Belt, Group 1 of the Hemlock Formation and the Hellancourt Formation.

5.4.2. Trace element considerations

Trace element modelling in section 5.1 has shown that the mantle source of the Chukotat Group, Fox River Belt and Winnipegosis Belt has a trace element composition similar to that of primitive mantle with 1% continental crust extracted from it. Some of the Molson dykes can also be generated from this same source composition (see sections 5.1.4 and 5.3.5). Although no obvious parental magmas

exist in the Hellancourt Formation, Pickle Crow dyke, Hemlock Formation Group 1 and east Kiernan sill, these rocks have elemental signatures consistent with being derived through fractional crystallisation of a primary magma from the same mantle source composition as for the Chukotat Group, Fox River Belt, Winnipegosis Belt and some of the Molson dykes. The igneous rocks from these segments have similar Sr and Nd isotopic ratios (Figs. 4.83a and 4.83b) which are consistent with their derivation from a mantle source of a common trace element composition. However, these rocks are not homogeneous in terms of their Hf isotope compositions (Figs. 4.83e and 4.83f). The Winnipegosis Belt, Pickle Crow dyke and Group 1 of the Hemlock Formation have a more radiogenic Hf isotopic composition than the Chukotat Group and Group 1 of the Molson dykes while the Hellancourt Formation has an even more radiogenic Hf isotopic signature than the most radiogenic Fox River Belt igneous rocks (Figs. 4.83e and 4.83f). Even though the Chukotat Group, Molson dykes, Pickle Crow dyke, Winnipegosis Belt, Hellancourt Formation and Group 1 of the Hemlock Formation have differing Hf isotope compositions, this is not manifested in their trace element compositions.

The Flaherty Formation has a markedly different trace element composition to the majority of uncontaminated samples from the various segments of the Circum-Superior LIP (see Chapter 4). However, the Nd-Hf isotopic composition of the Flaherty Formation overlaps that of the Chukotat Group (Figs. 4.83f and 5.32). One Group 1 sample of the Flaherty Formation lies in the centre of the Chukotat Group field while the other sample falls on the left hand edge of the field in Figs. 4.83f and 5.32. The two Flaherty Formation Group 2 samples plot slightly further away from the left hand edge of the Chukotat Group field and slightly closer to present day EM2 (Figs. 4.83f and 5.32). If the Flaherty Formation, particularly Group 1, has a similar isotopic composition to the Chukotat Group then why do these rocks have such contrasting trace element signatures? Different degrees of fractional crystallisation cannot explain this (see section 5.2.3). Could the Flaherty Formation be formed by lower degree melts than the Chukotat Group from the same source region? The multi-element diagram in Fig. 5.34a shows that the Flaherty Formation Group 1 samples have multi-element profiles similar to a 3% partial melt of a source composition of primitive mantle with 1% continental crust extracted. It is difficult to accurately determine the degree of partial melting which formed the Flaherty

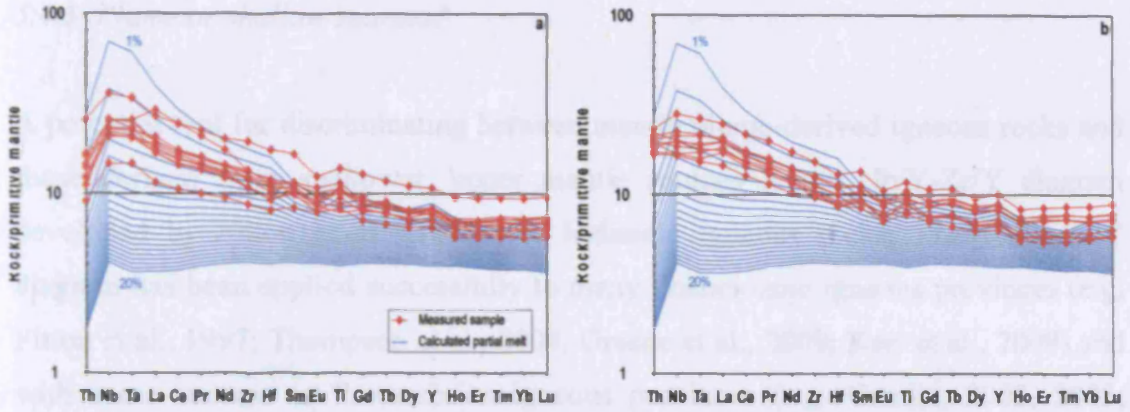

Fig. 5.34. Primitive-mantle-normalised multi-element diagrams displaying the composition of modelled partial melts compared to (a) Group 1 of the Flaherty Formation and (b) Group 2 of the Flaherty Formation. The composition of the source used in the modelling is primitive mantle with 1% continental crust extracted. The equation for non-modal batch melting, partition co-efficients, mineral modes and melting modes used in the modelling are given in Appendix F. The multi-element profiles of 1-20% partial melts are shown in the diagrams. Primitive mantle values from Sun & McDonough (1989).

Formation given that these rocks are low in MgO and lack olivine crystals and have probably undergone a considerable degree of fractional crystallisation. The Flaherty Formation Group 1 primary magma should plot at lower elemental concentrations on Fig. 5.34a than the measured samples. However, the magnitude of the positive Nb-Ta anomaly relative to La in the calculated partial melts diminishes abruptly within only a few percent partial melting such that if the Flaherty Formation Group 1 is related to the same mantle source composition as for the Chukotat Group then realistically the degree of partial melting has to be <5%. A more common interpretation of positive Nb-Ta anomalies in plume-derived rocks is the presence of recycled oceanic crust in the mantle source region (e.g. Hofmann, 1997), although it must be noted that no positive Nb-Ta anomalies are found in the Chukotat Group despite these rocks having overlapping Nd-Hf isotopic compositions with Flaherty Formation Group 1 rocks. The Flaherty Formation Group 2 samples have multi-element profiles which cannot be replicated by partial melting of a source composition of primitive mantle with 1% continental crust extracted (Fig. 5.34b). This is consistent with their Nd-Hf isotopic composition which is slightly displaced from that of the Chukotat Group towards present day EM2 (Fig. 5.32), perhaps indicating a greater terrigenous sediment component in the source of the Flaherty Formation Group 2 (cf. Weaver, 1991; Hofmann, 1997) than Group 1 of the Flaherty Formation or the Chukotat Group, or a greater contribution from the subcontinental lithospheric mantle (cf. Gibson et al., 2005).

5.4.3. Plume or shallow sources?

A potential tool for discriminating between mantle plume-derived igneous rocks and those derived from shallower, upper mantle sources is the Nb/Y-Zr/Y diagram developed by Fitton et al. (1997) for Icelandic igneous rocks. The Nb/Y-Zr/Y diagram has been applied successfully to many Phanerozoic igneous provinces (e.g. Fitton et al., 1997; Thompson et al., 2004; Greene et al., 2009; Kerr et al., 2009) and with some success to Precambrian igneous provinces (e.g. Condie, 2003, 2005; Kerrich et al., 2008; Fergusson et al., 2009; Polat, 2009; Wyman & Kerrich, 2009). The Nb/Y-Zr/Y diagram should be used cautiously for Proterozoic rocks because of the assumed higher mantle potential temperatures permitting greater degrees of partial melting which would alter the Nb/Y and Zr/Y ratios. The Nb/Y-Zr/Y diagram works on the basis that the N-MORB-source upper mantle beneath Iceland is deficient in Nb relative to the mantle source of the Icelandic plume, so basalts from the Iceland plume plot between the tramlines and N-MORB basalts plot beneath the lower tramline in Fig. 5.35a. Plume-derived rocks from various localities generally plot between the tramlines although some can plot just beneath the lower tramline (cf. Kempton et al., 2000; Condie, 2005; Kerr et al., 2009) probably because the tramlines were originally defined on the basis of Iceland volcanic rocks.

The Circum-Superior LIP rocks are plotted on the Nb/Y-Zr/Y diagram in Fig. 5.35a. The majority of samples plot between the tramlines supporting a deep mantle plume origin for these rocks. One cluster of samples occurs close to the composition of primitive mantle and within the field for the Ontong Java Plateau. This cluster includes samples of the Chukotat Group, Fox River Belt, Winnipegosis Belt, Molson dykes, Pickle Crow dyke, Hemlock Formation Group 1 and Hellancourt Formation. Some of these samples fall just below the lower tramline but most still lie within the Ontong Java Plateau field. Another set of samples cluster between the compositions of E-MORB and average continental crust in the more enriched section of the Nb/Y-Zr/Y diagram. These samples mostly consist of the eastern Hudson Bay rocks and the contaminated Lake Superior region rocks. The vast majority of these samples also lie in between the tramlines indicating they are plume-derived melts with an additional crustal component introduced either through recycling of material into the mantle source region or interaction with the crust during the ascent of magma to the

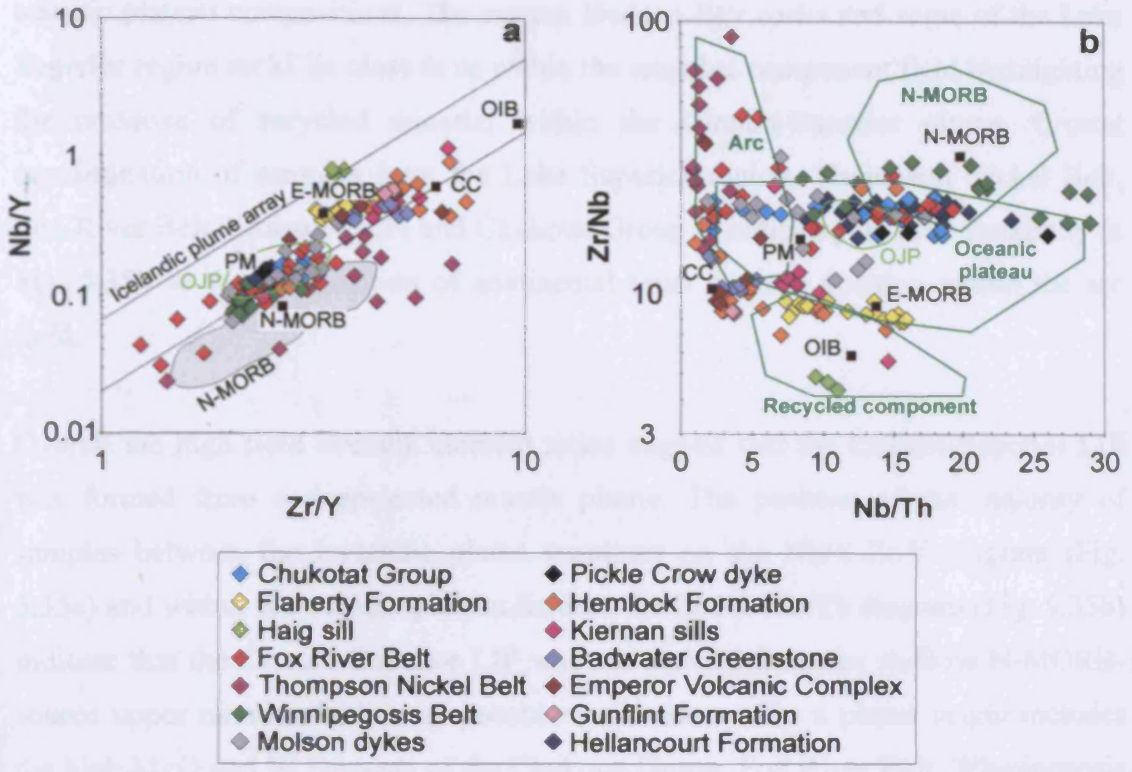

Fig. 5.35. (a) Nb/Y vs. Zr/Y and (b) Zr/Nb vs. Nb/Th diagrams for the Circum-Superior LIP. Data sources for (a) are given in Figs. 4.7, 4.9 and 4.10. Data sources for (b) are the same as for (a) except for the green field boundaries which are from Condie (2005).

surface. Out of all the samples which plot beneath the lower tramline the vast majority are contaminated intrusive rocks mainly from the Thompson Nickel Belt and Fox River Belt.

Condie (2003, 2005) also utilised the Zr/Nb-Nb/Th diagram to distinguish the source regions of igneous rocks of various ages. As is the case with the Nb/Y-Zr/Y diagram, caution should be exercised when using the Zr/Nb-Nb/Th diagram for Proterozoic rocks because of the presumed higher mantle potential temperatures and degrees of partial melting which could alter the Zr/Nb and Nb/Th ratios. The Circum-Superior LIP rocks are plotted on the Zr/Nb-Nb/Th diagram in Fig. 5.35b. The majority of samples plot in the oceanic plateau field which is consistent with a deep plume-related origin rather than a shallow, N-MORB-source origin. A few samples from the Chukotat Group, Fox River Belt, Hemlock Formation Group 1 and Hellancourt Formation fall in the overlap between the oceanic plateau and N-MORB fields and a few of the Winnipegosis Belt samples plot within the N-MORB field although the Winnipegosis Belt has an overall range in Nb/Th ratios that is more consistent with

oceanic plateau compositions. The eastern Hudson Bay rocks and some of the Lake Superior region rocks lie close to or within the recycled component field highlighting the presence of recycled material within the Circum-Superior plume. Crustal contamination of samples from the Lake Superior region, Thompson Nickel Belt, Fox River Belt, Molson dykes and Chukotat Group is indicated by their proximity in Fig. 5.35b to the composition of continental crust or their position within the arc field.

Overall the high field strength element ratios suggest that the Circum-Superior LIP was formed from a deep-seated mantle plume. The position of the majority of samples between the Icelandic plume tramlines on the Nb/Y-Zr/Y diagram (Fig. 5.35a) and within the oceanic plateau field on the Zr/Nb-Nb/Th diagram (Fig. 5.35b) indicate that the Circum-Superior LIP was not derived from the shallow N-MORB-source upper mantle. Additional geochemical evidence for a plume origin includes the high MgO and Ni contents of the Chukotat Group, Fox River Belt, Winnipegosis Belt and Molson dykes (cf. Campbell, 2007) and the relatively flat, oceanic-plateau-like multi-element profiles prevalent throughout the Circum-Superior LIP (cf. Polat, 2009 and references therein).

5.4.4. Summary

The Sr and Pb isotopic systems in the Circum-Superior LIP may have been altered by post-magmatic processes and as such may not be used with confidence in interpreting the petrogenesis of the Circum-Superior LIP. The Nd and Hf isotope systems are more resistant to secondary alteration processes and are more useful for interpreting the petrogenesis of the Circum-Superior LIP. Uncontaminated samples of the Circum-Superior LIP have εNd_i values ranging from +0.84 to +5.29, suggesting that the Circum-Superior LIP originates from a long-term depleted source region that was not as depleted as the estimated depleted mantle composition at ~1880 Ma. The εHf_i values of the Circum-Superior LIP show a greater range than the εNd_i values of +0.81 to +29.44 suggesting the involvement of mantle material both less depleted and more depleted than the estimated depleted mantle composition at ~1880 Ma. In Hf-Nd isotope space the uncontaminated Circum-Superior LIP samples appear to fall along two mixing arrays. The Pickle Crow dyke, Chukotat

Group, Flaherty Formation, Molson dykes Group 1 and Hemlock Formation Group 3 appear to lie between the estimated depleted mantle composition at ~1880 Ma and a more enriched component similar to the present day EM2. The Hemlock Formation Group 1, Winnipegosis Belt, Fox River Belt and Hellancourt Formation appear to be displaced from the former array towards a mantle component with a more radiogenic Hf isotope composition which is most strongly evident in the Hellancourt Formation. Despite the variation in Hf isotopes the trace element patterns of the Chukotat Group, Fox River Belt, Winnipegosis Belt, some Molson dykes, Pickle Crow dyke, Hemlock Formation Group 1 and Hellancourt Formation are similar and can be linked to a common mantle source region composition of primitive mantle with 1% by mass of continental crust extracted from it. The Flaherty Formation appears to have formed from source regions with different trace element compositions to that of primitive mantle with 1% continental crust extracted. Although Group 1 of the Flaherty Formation has a near-identical Nd-Hf isotopic composition to the Chukotat Group, the multi-element profiles of the Flaherty Formation Group 1 cannot easily be replicated by low degrees of partial melting of the same source region composition as for the Chukotat Group. Group 2 of the Flaherty Formation has a slightly more enriched isotopic composition than Group 1 which may indicate a greater proportion of enriched, present day EM2-like material in the source region of the Group 2 rocks. Even though a depleted mantle component may be an important part of the mantle source region of the Circum-Superior LIP, it is likely that this depleted mantle was intrinsic to a mantle plume and not N-MORB-source upper mantle given that the majority of uncontaminated extrusive samples plot between the Icelandic plume tramlines on a Nb/Y-Zr/Y diagram and in the oceanic plateau field on a Zr/Nb-Nb/Th diagram.

5.5. Depth of melting

Major and trace element ratios such as CaO/Al_2O_3, Al_2O_3/TiO_2 and $(Gd/Yb)_N$ in ultramafic lavas are useful for investigating the depth at which partial melting and melt segregation occurs. These ratios are sensitive to depth and pressure in the mantle because of the high partition co-efficients for Al_2O_3 and the HREEs in garnet, the low variation of CaO in magmas formed at different depths, and the incompatible nature of TiO_2 during melting (e.g. Herzberg, 1995; Herzberg & Zhang, 1996;

Walter, 1998; Arndt, 2003). Some studies have also noted the utility of high field strength element anomalies relative to REEs in determining the depth of melt segregation (e.g. Xie et al., 1993; McCuaig et al., 1994; Fan & Kerrich, 1997; Jayananda et al., 2008). Therefore all these ratios will be used to estimate the pressure and depth at which the magmas of the Circum-Superior LIP were generated.

5.5.1. Chukotat Group

The Chukotat primary magmas have Al_2O_3 concentrations and CaO/Al_2O_3 ratios of 8.84-9.86 wt. % and 1.01-1.13 respectively. The measured high MgO (13.84-19.84 wt. %) samples contain 9.22-11.62 wt. % Al_2O_3 (average 10.25 wt. %) and CaO/Al_2O_3 ratios of 0.79-1.13 (average 1.00). On a Al_2O_3-CaO/Al_2O_3 diagram (Fig. 5.36a) the primary magmas fall between the 4.0 and 4.5 GPa pressure contours for melting of a KR-4003 peridotite source. These pressures correspond to a depth range of ~120-135 km where garnet is the stable aluminium-bearing phase. The reliability of the CaO/Al_2O_3 ratio for the Chukotat primary magmas maybe somewhat suspect given the potential mobility of Ca and the scatter seen on a CaO-Zr plot for the Chukotat Group volcanic rocks (Fig. 5.37). Al_2O_3 and TiO_2 are less mobile than CaO and so the Al_2O_3/TiO_2 ratio may give a better indicator of whether the residue is garnet-bearing or not. However, TiO_2 appears to be unusually depleted in the Chukotat primary magmas and the high Al_2O_3/TiO_2 ratios (15.06-19.72) may not be a real indication of the depth of melting. The low TiO_2 concentrations in the Chukotat primary magmas will be discussed later. The REEs are relatively immobile and so $(Gd/Yb)_N$ ratios should be able to give an insight into the residue mineralogy and melting depth. The $(Gd/Yb)_N$ ratios of the primary magmas are 1.02-1.18 and the range for all Chukotat Group samples is 1.02-1.25. The $(Gd/Yb)_N$ ratios are low but slightly >1 which may suggest that melting occurred in the presence of a small amount of garnet, perhaps at the shallowest depths and pressures of garnet stability. Alternatively the extent of melting was maybe such that all the garnet was exhausted and incorporated into the melt. The latter may be the case because estimates derived for the degree of partial melting from major element modelling (PRIMELT2) and trace element modelling suggest that the Chukotat primary magmas formed from up to ~34% partial melting (section 5.1.1). Walter (1998) performed melting experiments on the KR-4003 peridotite composition and showed that at lower

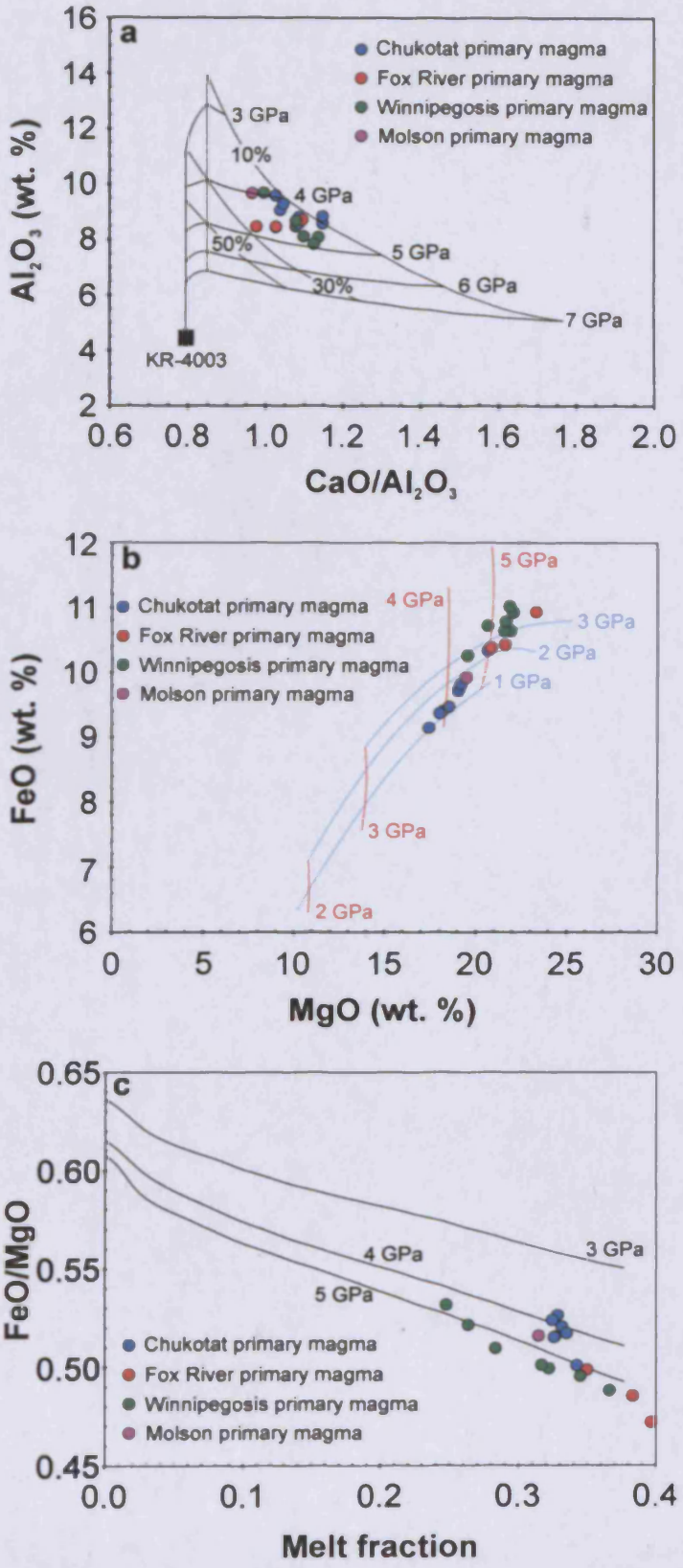

Fig. 5.36. (a) Al_2O_3 vs. CaO/Al_2O_3, (b) FeO vs. MgO and (c) FeO/MgO vs. melt fraction for the PRIMELT2-calculated primary magmas compared to the melt compositions derived from experiments on peridotite KR-4003 (Walter, 1998). In (a) the dashed lines represent percentage melting while the solid lines represent initial melting pressure. In (b) the red and blues lines represent the initial and final melting pressures respectively. In (c) the solid lines represent initial melting pressure.

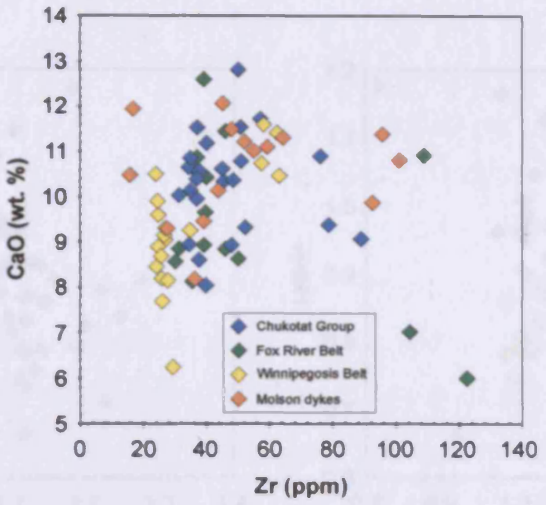

Fig. 5.37. CaO vs. Zr diagram for the Chukotat Group, Winnipegosis Belt, Fox River Belt volcanic rocks and Molson dykes.

pressures in the garnet stability field (3 GPa) garnet remains in the residue until ~10% melting and at high pressures (7 GPa) ~65% melting is required to exhaust all the garnet. A degree of melting of ~34% would probably be enough to consume most of the garnet at pressures between 4 and 5 GPa, although this is hard to say as melting is not an isobaric process and occurs over a range of pressures and depths.

Zr/Zr* and Hf/Hf* values of the Chukotat primary magmas are 0.85-1.23 and 0.82-1.12 respectively and the respective averages are 0.99 and 0.94. The respective Zr/Zr* and Hf/Hf* values of all the Chukotat Group samples are 0.85-1.23 and 0.82-1.13 and the respective averages are 1.02 and 0.98. The lack of any significant Zr or Hf anomalies does not support a deep depth of melting (>400 km where majorite garnet is stable). Furthermore there are no correlations of Zr/Zr* or Hf/Hf* with $(Gd/Yb)_N$ or MgO (Fig. 5.38).

The melt fractions and FeO and MgO concentrations of the primary magmas can also be utilised to estimate the pressure and depth of melting. Figs. 5.36b and 5.36c show that when compared to the pressure contours from parameterisations of experimental data, the Chukotat primary magmas fall close to pressures of ~3.8-5 GPa for initial melting and pressures of ~1-2 GPa for final melting. These pressures correspond to depths of ~115-150 km for the start of melting and ~30-60 km for the end of melting.

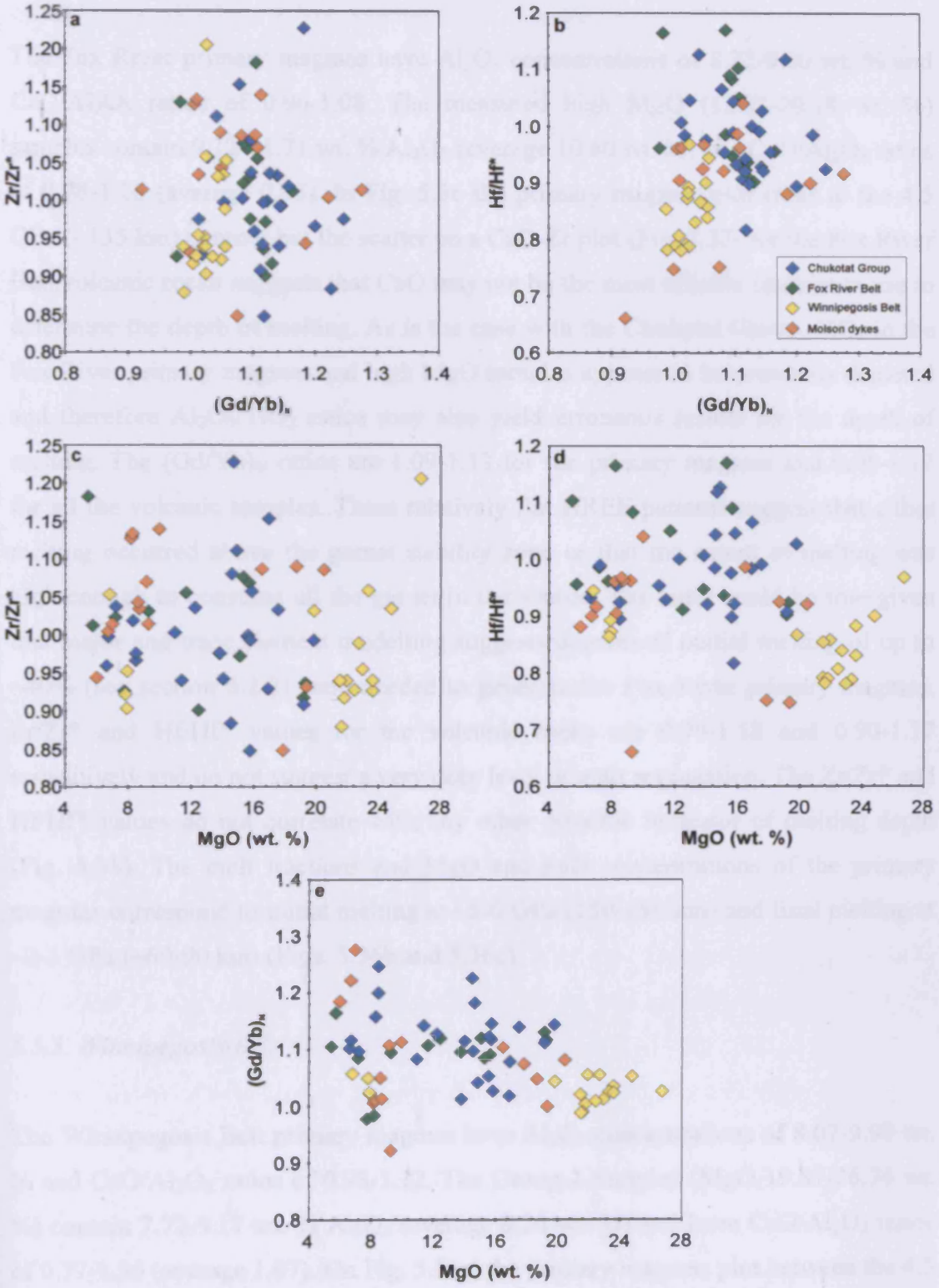

Fig. 5.38. Possible indicators of depth of melting of the Chukotat Group, Winnipegosis Belt, Fox River Belt volcanic rocks and Molson dykes. (a) Zr/Zr^* vs. $(Gd/Yb)_N$ diagram; (b) Hf/Hf^* vs. $(Gd/Yb)_N$ diagram; (c) Zr/Zr^* vs. MgO diagram; (d) Hf/Hf^* vs. $(Gd/Yb)_N$ diagram; (e) $(Gd/Yb)_N$ vs. MgO diagram. Normalising values from Sun & McDonough (1989).

5.5.2. *Fox River Belt*

The Fox River primary magmas have Al_2O_3 concentrations of 8.72-9.00 wt. % and CaO/Al_2O_3 ratios of 0.96-1.08. The measured high MgO (12.81-20.18 wt. %) samples contain 9.12-11.71 wt. % Al_2O_3 (average 10.60 wt. %) and CaO/Al_2O_3 ratios of 0.78-1.16 (average 0.95). In Fig. 5.36 the primary magmas plot close to the 4.5 GPa (~135 km) contour but the scatter on a CaO-Zr plot (Fig. 5.37) for the Fox River Belt volcanic rocks suggests that CaO may not be the most reliable element to use to determine the depth of melting. As is the case with the Chukotat Group, TiO_2 in the Fox River primary magmas and high MgO samples appears to be unusually depleted and therefore Al_2O_3/TiO_2 ratios may also yield erroneous results for the depth of melting. The $(Gd/Yb)_N$ ratios are 1.09-1.13 for the primary magmas and 0.98-1.17 for all the volcanic samples. These relatively flat HREE patterns suggest that either melting occurred above the garnet stability zone or that the extent of melting was high enough to consume all the garnet in the source. The latter could be true given that major and trace element modelling suggests degrees of partial melting of up to ~40% (see section 5.1.2) were needed to generate the Fox River primary magmas. Zr/Zr* and Hf/Hf* values for the volcanic rocks are 0.90-1.18 and 0.90-1.17 respectively and do not suggest a very deep level of melt segregation. The Zr/Zr* and Hf/Hf* values do not correlate with any other possible indicator of melting depth (Fig. 5.38). The melt fractions and MgO and FeO concentrations of the primary magmas correspond to initial melting at ~5-6 GPa (150-180 km) and final melting at ~2-3 GPa (~60-90 km) (Figs. 5.36b and 5.36c).

5.5.3. *Winnipegosis Belt*

The Winnipegosis Belt primary magmas have Al_2O_3 concentrations of 8.07-9.99 wt. % and CaO/Al_2O_3 ratios of 0.98-1.12. The Group 1 samples (MgO 19.87-26.74 wt. %) contain 7.72-9.17 wt. % Al_2O_3 (average 8.26 wt. %) and have CaO/Al_2O_3 ratios of 0.77-1.36 (average 1.07). On Fig. 5.36a, the primary magmas plot between the 4.5 and 5 GPa contours, corresponding to a melting depth of ~135-150 km. Again, the use of CaO/Al_2O_3 ratios in determining the depth of melting may be unsuitable as CaO does not form a coherent trend with Zr for the Winnipegosis Belt rocks (Fig. 5.37). The Al_2O_3/TiO_2 ratios of the primary magmas range from 14.30 to 16.38

which are greater than the value of ~13 suggested by Walter (1998) to represent the uppermost value of ultramafic melts derived from melting within the garnet stability zone. The $(Gd/Yb)_N$ ratios of all the samples, which range from 0.99 to 1.06, also indicate a lack of garnet in the source region. Zr/Zr* values are 0.92-1.03 for the primary magmas and 0.88-1.21 for all samples and do not support deep melting segregation. However, Hf/Hf* values are slightly lower and range from 0.79 to 0.90 for the primary magmas and from 0.78 to 0.97 for all the samples. Although these negative Hf anomalies are only minor, similar values of Hf/Hf* have been interpreted to represent melt segregation at depths of >400 km where majorite garnet is retained in the source (e.g. Jayananda et al., 2008). Such a depth would be in contrast to that suggested by the MgO and FeO contents of the primary magmas and their melt fractions. On Figs. 5.36b and 5.36c the primary magmas plot in space consistent with initial melting pressures of ~4.5 to 5.5 GPa which correspond to a depth of ~135-165 km. The range of final melting pressure is ~3-4 GPa (Fig. 5.36b) and this corresponds to a depth of ~90-120 km. Garnet is stable at such depths and the lack of a garnet signature in the trace element chemistry is probably due to high degree partial melting predicted by major and trace element modelling (see section 5.1.3) which would have consumed all the garnet in the source region.

5.5.4. Molson dykes

The one calculated primary magma from accumulated fractional melting of a fertile peridotite source has an Al_2O_3 concentration of 9.93 wt. % and a CaO/Al_2O_3 ratio of 0.95. The Group 1 samples (MgO 16.53-20.50 wt. %) contain 9.86-10.67 wt. % Al_2O_3 (average 10.33 wt. %) and have CaO/Al_2O_3 ratios of 0.81-1.01 (average 0.92). On the Al_2O_3-CaO/Al_2O_3 diagram (Fig. 5.36a) the primary magma plots along the 4 GPa (~120 km depth) melting contour. At such a depth garnet would be stable yet the Al_2O_3/TiO_2 ratio of 15.76 for the primary magma is slightly higher than may be expected if garnet remained in the source. The $(Gd/Yb)_N$ ratio of the primary magma is 1.10 and is also lower than may be expected for a garnet-bearing source. The $(Gd/Yb)_N$ ratios for the Group 1 and Group 2 Molson dykes range only from 0.92 to 1.11 whereas Group 3 samples have $(Gd/Yb)_N$ ratios of 1.19-1.28 and so could be derived from melting deeper in the mantle. However, Group 3 samples are evolved rocks with low MgO contents (6.00-6.99 wt. %) and so their major elements cannot

be used to constrain the pressure and depth of melting. The Zr/Zr* value (1.09) and Hf/Hf* value (0.99) of the primary magma do not suggest a deep depth of melt segregation. None of the samples have significant Zr or Hf anomalies. However, three samples, two from Group 1 and one from Group 2, have minor negative Hf anomalies (Fig. 4.58) and Hf/Hf* values of 0.66-0.75. If these minor Hf anomalies are the result of melt segregation at deep mantle levels then they are inconsistent with the flat HREE patterns of these samples. The MgO and FeO concentrations and melt fraction of the primary magma suggest that it was derived from melting starting at ~4.5 GPa (~135 km) and ending at ~2.8 GPa (~84 km) (Figs. 5.36b and 5.36c).

5.5.5. Other segments of the Circum-Superior LIP

Unfortunately none of the samples from the Flaherty Formation, Haig sill, Thompson Nickel Belt, Pickle Crow dyke, Lake Superior region and Hellancourt Formation are high MgO volcanic rocks which could represent primary magmas. Therefore the major element chemistry of these rocks cannot be used to infer the pressure and depth of partial melting. The Hellancourt Formation volcanic rocks, Group 1 of the Hemlock Formation and the Pickle Crow dyke have $(Gd/Yb)_N$ ratios close to unity (Table 2.1). Such values may suggest that these rocks formed from shallow melting in the spinel stability zone. Alternatively the rocks could be fractional crystallisation derivatives from magmas formed by deeper melting in the garnet stability zone to a degree whereby all the garnet in the source was consumed. This appears to be the case for the Chukotat, Fox River, Winnipegosis and Molson primary magmas as their major element chemistry suggests deep levels of melt segregation yet their trace element chemistry shows no sign of a strong garnet involvement. The vast majority of samples from the Flaherty Formation, Haig sill, Thompson Nickel Belt and Lake Superior region have $(Gd/Yb)_N$ ratios >1.2 which suggests that these rocks could be produced by melting within the garnet stability zone. The minimum pressure at which garnet is the dominant aluminium-bearing phase in the mantle is ~3 GPa. This corresponds to a minimum depth of melting for most of the Hudson Bay, Thompson Nickel Belt and Lake Superior region magmas of ~90 km. However, the vast majority of rocks from the Thompson Nickel Belt and Lake Superior region have been contaminated with crustal material (see section 5.3) which may increase the $(Gd/Yb)_N$ ratio without the need for melting in the garnet stability zone.

5.5.6. Summary

The primary magmas of the Circum-Superior LIP started to segregate at slightly different depths and pressures for the individual segments. Partial melting of the Chukotat Group primary magmas began at ~3.8-5 GPa and a depth range of ~115-150 km. The Fox River Belt primary magmas began segregating at ~5-6 GPa and ~150-180 km depth. The Winnipegosis Belt primary magmas started forming from melting at ~135-165 km depth and ~4.5-5.5 GPa pressure. Melting began at ~135 km depth and ~4.5 GPa pressure to produce the Molson primary magma. No garnet signature is present in the primary magmas of the Chukotat, Fox River, Winnipegosis and Molson primary magmas despite the calculated melting depths within the garnet stability zone in the mantle. This is most likely because the degree of partial melting was sufficiently high enough to consume all the garnet in the source. A garnet signature is recorded in the trace element composition (Gd/Yb_N >1.2) of the Flaherty Formation suggesting that these volcanic rocks formed at depths >90 km and from lower degrees of partial melting than many of the volcanic rocks in the other segments of the Circum-Superior LIP.

5.6. Mantle potential temperature

The temperature of the mantle as it undergoes decompression melting is often termed the mantle potential temperature (T_P). McKenzie & Bickle (1988) defined T_P as the temperature of a solid mass of adiabatically convecting mantle if it was able to reach the surface of the Earth without melting. There are a number of studies which have attempted to calculate the T_P of various mantle sources using a variety of mathematical techniques (e.g. McKenzie & Bickle, 1988; Kinzler & Grove, 1992; Langmuir et al., 1992; Asimow et al., 2001; Green et al., 2001; Herzberg & O'Hara, 2002; Wang et al., 2002; Herzberg, 2004a; McKenzie et al., 2005; Putirka, 2005; Courtier et al., 2007; Putirka et al., 2007). One of the most recent methods for calculating T_P is the PRIMELT2 software of Herzberg & Asimow (2008) briefly described in section 5.1. Once PRIMELT2 has successfully obtained a primary magma composition, in particular its MgO concentration, it utilises the equation below to calculate T_P.

$$T_P(^\circ C) = 1463 + 12.74MgO - \frac{2924}{MgO}$$

Equation 5.1

where MgO is the concentration in wt. % of the primary magma as determined by PRIMELT2.

The total uncertainty in T_P calculated by PRIMELT2 due to potential errors in determining the MgO content of primary magmas is ±60°C (2σ) (Herzberg & Asimow, 2008; Herzberg et al., 2010).

5.6.1. T_P of the Circum-Superior LIP

PRIMELT2 has been used in this study to infer the T_P of the various segments of the Circum-Superior LIP. As only the Chukotat Group, Fox River Belt, Winnipegosis Belt and Molson dykes preserve primary magma compositions, temperatures are only available for these segments and are given in Tables 5.1-5.4. For simplicity only T_P calculated by PRIMELT2 for primary magma solutions of accumulated fractional melting of a fertile peridotite source are considered. The T_P of the mantle source of the Chukotat Group is 1517-1586°C whilst the source of the Fox River Belt volcanic rocks is slightly hotter with a T_P of 1589-1634°C. One Molson dyke sample yielded a T_P of 1559°C and the range of T_P for the Winnipegosis Belt is 1584-1611°C. Herzberg (2004a) also calculated the T_P for the Chukotat Group from ten samples analysed by Hynes & Francis (1982) and Picard et al. (1990) to be 1526-1604°C.

5.6.2. Does T_P favour a mantle plume or upper mantle origin for the Circum-Superior LIP?

The mantle plume hypothesis predicts that the temperature of a plume should be significantly higher than that of the N-MORB-source upper mantle (Campbell, 2007). Mantle plumes are generally thought to originate from the core-mantle boundary (Campbell & Griffiths, 1990; Griffiths & Campbell, 1990). Boehler (1993) demonstrated that the core is over one thousand degrees hotter than the mantle overlying it. The lower mantle just above the core-mantle boundary is warmed by

heat conducted from the core, which lowers the density of the mantle causing it to rise and form mantle plumes (Campbell, 2007). Thus the calculated T_p for a suite of magmatic rocks should give an indication of whether the rocks were derived from melting of a mantle plume or ambient upper mantle.

McKenzie & Bickle (1988) originally calculated the T_p of modern N-MORB-source upper mantle to be 1280°C. A number of studies since have focussed on the temperature of the upper mantle and a range of estimated T_p of 1200 to 1600°C has been reported. Kinzler & Grove (1992) and Langmuir et al. (1992) obtained T_p ranges for the upper mantle of 1315-1475°C and 1300-1570°C respectively. Anderson (2000) used long wavelength bathymetry, subsidence, heat flow, tomography, discontinuity depths and petrology to estimate the T_p of upper mantle to be 1400 ± 200°C. Using olivine thermometry, Putirka (2005) and Putirka et al. (2007) constrained the upper mantle T_p to range between 1453 and 1475°C. However, most of these T_p estimates are considered too high (Herzberg et al., 2007; Herzberg & Asimow, 2008; Korenaga, 2008a, 2008b; Davies, 2009; Herzberg et al., 2010). Many recent studies based on phase equilibria now favour a T_p range for the upper mantle of ~1350°C (Herzberg & O'Hara, 2002; Presnall et al., 2002; Wang et al., 2002; Herzberg, 2004a; Courtier et al., 2007; Herzberg et al., 2007; Herzberg & Asimow, 2008).

Recent modelling by Herzberg & Gazel (2009) has shown that the T_p of the source of several Phanerozoic LIPs and ocean islands of suspected plume origin to typically be ~200-300°C hotter than N-MORB-source upper mantle. This is consistent with the findings of Nisbet et al. (1993). The T_P of the Circum-Superior LIP (1517-1634°C) is similar to the T_P of many of the Phanerozoic LIPs investigated by Herzberg & Gazel (2009). To ascertain if the Circum-Superior LIP is of a plume origin then the question that needs to be asked is what was the T_P of the ambient upper mantle at 1880 Ma?

There are relatively few models for the secular cooling of the Earth. Richter (1988) proposed a secular cooling model where the average upper mantle potential temperature was ~1800°C at 4 Ga and the rate of cooling has decreased throughout Earth's history (Fig. 5.39). Korenaga (2008a, 2008b) suggested a model of Earth's

thermal history drastically different to that of Richter (1988). The model of Korenaga (2008a, 2008b) utilises a low present day Urey ratio (Ur; the ratio of internal heat production within the Earth to the total surface heat flux) of 0.23 ±0.15 and predicts a peak in the T_P of the upper mantle at ~3.5 Ga and the greatest rate of cooling to be occurring at the present day (Fig. 5.39). Davies (2009) has challenged the low Ur model of Korenaga (2008a, 2008b) and suggested a secular cooling model more consistent with that of Richter (1988). In the model of Davies (2009), the greatest rate of cooling occurred earlier in Earth's history and there is only a difference of 200°C between the T_P of the present day ambient upper mantle and that of the upper mantle at 4 Ga (Fig. 5.39).

The model of Richter (1988) predicts that at 1880 Ma the T_p of the ambient upper mantle was ~1450°C and that the Circum-Superior LIP formed from mantle with an excess temperature of 67-184°C (Fig. 5.39). When compared to the model of Davies (2009), the Circum-Superior LIP formed from mantle with a T_P of ~157-274°C hotter than that of the ambient upper mantle (Fig. 5.39). However, relative to the model of Korenaga (2008a, 2008b) the Circum-Superior LIP formed from mantle that was little or no hotter than the ambient upper mantle (Fig. 5.39). Thus, the thermal models of Richter (1988) and Davies (2009) require a hot mantle plume for the origin of the Circum-Superior LIP whereas the Korenaga (2008a, 2008b) model suggests that the Circum-Superior LIP represents Proterozoic MORB formed from the melting of ambient upper mantle perhaps during the rifting of the continental margin.

The cooling curves proposed by Korenaga (2008a, 2008b) have been heavily criticised by Davies (2009) and Karato (2010). Davies (2009) argued against the assumption of Korenaga (2008a, 2008b) that the thickness of plates is determined mainly by dehydration during melting at mid-ocean ridges rather than conductive cooling and suggested that the Korenaga (2008a, 2008b) model is too sensitive to the radius of curvature of bending plates at subduction trenches. Karato (2010) showed that the constant radius of curvature of bending plates assumed by Korenaga (2008a, 2008b) was unrealistic because plate curvature depends on the flexural rigidity of plates which is affected by the plate thickness and thus invalidates the model of Korenaga (2008a, 2008b). Therefore the current study prefers the use of the thermal

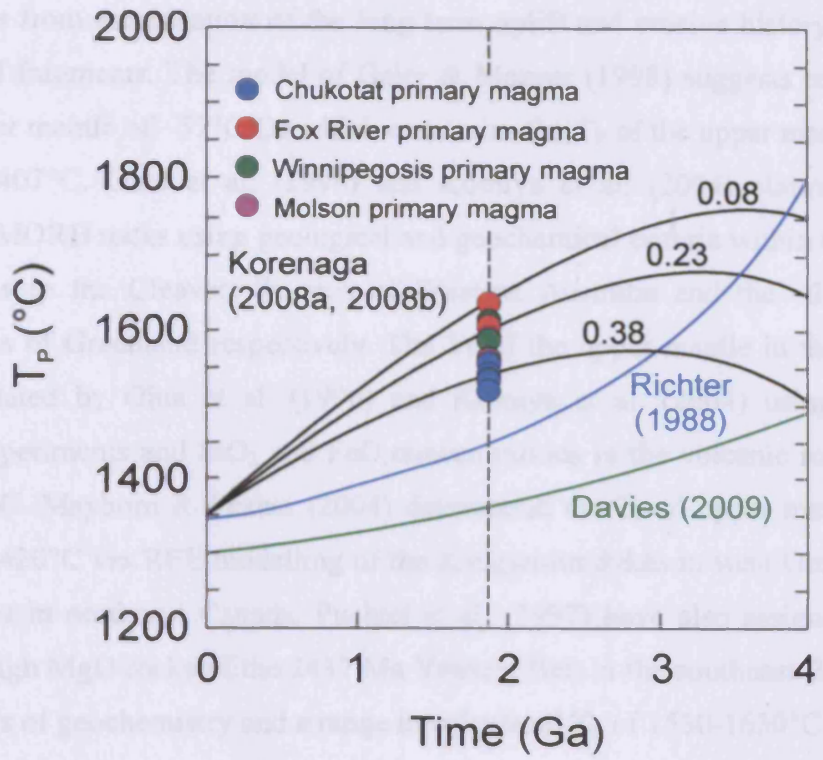

Fig. 5.39. Ambient upper mantle secular cooling models compared to the calculated mantle potential temperatures (T_P) for the primary magmas of the Circum-Superior LIP. The numbers 0.08, 0.23 and 0.38 are the present day Urey ratios used in the models of Korenaga (2008a, 2008b) to construct the secular cooling curves.

models of Richter (1988) and Davies (2009) in estimating the T_P of the ambient upper mantle at 1880 Ma and which require a mantle plume for the origin of the Circum-Superior LIP. This is also consistent with the striking similarities in the incompatible trace element chemistry between the majority of the Circum-Superior LIP primary magmas and Phanerozoic oceanic plateau lavas. However, the model of Davies (2009) is not without its problems. For example it assumes a higher Ur than is predicted by geochemical and cosmochemical estimates for the abundance of radioactive isotopes in the Earth (McDonough & Sun, 1995; Korenaga, 2008b; Butler, 2009; Davies, 2009). Davies (2009) also uses a present day T_P for ambient upper mantle of 1300°C which is slightly cooler than what many recent petrological studies suggest (~1350°C).

There are other studies that have estimated the T_P of the ambient upper mantle at certain times in the Precambrian which support a mantle plume origin for the Circum-Superior LIP. Galer & Mezger (1998) constrained the T_P of the upper mantle at ~3 Ga to be ~170°C hotter than today by calculating palaeo-ocean crust

thicknesses from examination of the long term uplift and erosive history of ancient continental fragments. The model of Galer & Mezger (1998) suggests cooling rates of the upper mantle of ~57°C/Ga which constrains the T_P of the upper mantle at 1880 Ma to ~1407°C. Ohta et al. (1996) and Komiya et al. (2004) claimed to have identified MORB rocks using geological and geochemical criteria within the ~3.3 Ga greenstones in the Cleaverville area of Western Australia and the ~3.8 Ga Isua greenstones of Greenland respectively. The T_P of the upper mantle in the Archaean was calculated by Ohta et al. (1996) and Komiya et al. (2004) using peridotite melting experiments and SiO_2 and FeO concentrations in the volcanic rocks to only be ~1480°C. Mayborn & Lesher (2004) determined the T_P of upper mantle at 2.04 Ga to be 1420°C via REE modelling of the Kangamiut dykes in west Greenland and other dykes in northeast Canada. Puchtel et al. (1997) have also assigned a plume origin to high MgO rocks of the 2437 Ma Vetreny Belt in the southeast Baltic Shield on the basis of geochemistry and a range in calculated T_P of 1530-1630°C.

5.6.3. Variation in mantle temperature beneath the Superior craton

The hottest magmas of the Circum-Superior LIP appear to be located towards the northwestern corner of the Superior craton. Whether this is an artefact of the better preservation or just fortuitous sampling of higher MgO rocks in the Thompson Salient is difficult to answer. However, it is possible that hotter parts of the mantle plume were impinging beneath the lithosphere of the northwest of the craton and feeding the Fox River, Winnipegosis and Molson magmatism whereas cooler parts of the plume impinged beneath the Cape Smith Belt in the northeastern part of the craton. Plume theory predicts that the central axis of a plume is hotter than the periphery of the plume and differences in temperature can be as much as ~150°C (Campbell, 2007). The temperature difference between the highest T_P for the Fox River Belt (1634°C) and the lowest T_P for the Chukotat Group (1517°C) is 117°C and suggests that magmas in the northwest of the craton may be sampled from the hotter, more central parts of the plume while magmas in the northeast of the craton are perhaps sampled from more peripheral regions of the plume. However, the theory that the central axis of a plume is the hottest region is questionable given evidence from the North Altantic LIP and Carribean-Colombian oceanic plateau. In these two magmatic provinces, high MgO picrites are distributed over the entire plume head

rather than a hot central core (e.g. Kerr et al., 1996; Saunders et al., 1997; Revillon et al., 1999; Starkey et al., 2009).

Herzberg & Gazel (2009) have shown that mantle plumes cool with time by studying the T_P for primary magmas from Phanerozoic LIPs and their associated ocean islands. For example, the Galapagos mantle plume has cooled from a maximum T_P of 1620°C at ~90 Ma to a T_P of 1500°C at present (Herzberg & Gazel, 2009). There is little evidence for significant cooling of the plume responsible for the Circum-Superior LIP. The difference in maximum T_P of the Fox River Belt and Winnipegosis Belt, which contain magmatic rocks with an age difference of ~20 m.y., is only 23°C. Unfortunately there is no known age-progressive hotspot chain associated with the Circum-Superior LIP (Heaman et al., 2009) to assess if the T_P decreases significantly with time.

5.6.4. Comparisons to the T_P of other LIPs

Although there are a number of Proterozoic-age dyke swarms around the world (e.g. Ernst et al., 1996), there are relatively few occurrences of Proterozoic volcanic rocks which contain high concentrations of MgO and are uncontaminated. Herzberg et al. (2010) were only able to identify six samples of Proterozoic age other than those from the Chukotat Group that satisfied the criteria of being primary magmas from which T_P could be calculated. One sample is a ~1765 Ma 12.82 wt. % MgO tholeiite from the Dubois succession in Colorado interpreted to have formed in a complex setting involving a plume and volcanic arc (Knoper & Condie, 1988; Condie, 2003). This sample formed from a mantle source with a T_P of 1510°C (Herzberg et al., 2010). A 11.74 wt. % MgO sample of the ~2056 Ma Lapland basalts (Hanski et al., 2001) is derived from a mantle source with a T_P of 1533°C (Herzberg et al., 2010). A mafic amphibolite sample containing 14.29 wt. % MgO from the ~1300 Ma Phulad 'ophiolite' in India (Volpe & Macdougall, 1990) formed from a mantle source with a T_P of 1515°C (Herzberg et al., 2010). Three ~825 Ma picrites from southern China with MgO contents of 12-15 wt. % MgO (Wang et al., 2007) originated from a mantle source with a T_P of 1449-1488°C (Herzberg et al., 2010). Therefore the Circum-Superior LIP formed from the currently known hottest mantle source in the Proterozoic. Whether this source was anomalously hot for the Proterozoic remains

unknown until further Proterozoic primary magmas are discovered and T_P values calculated.

Overall, the relatively small number of T_P values known for Proterozoic primary magmas cover a similar range to the T_P of Phanerozoic LIPs and ocean islands but are considerably lower than those of Archaean komatiites (Herzberg & Gazel, 2009; Herzberg et al., 2010). Herzberg et al. (2010) interpreted this to represent a lack of mantle plume activity in the Proterozoic largely because of their choice of secular cooling model of the upper mantle (Korenaga, 2008a, 2008b). The results of the current study suggest instead that the T_P of plumes has remained relatively steady during the Proterozoic and Phanerozoic and the rate of cooling of the Earth has decreased with time as proposed by Davies (2009).

5.6.5. Summary

The T_P of the mantle source from which the Circum-Superior LIP formed was 1517-1634°C. Such a T_P is considerably hotter than the best predictions for the T_P of ambient upper mantle at 1880 Ma. Therefore a hot mantle plume is the most likely geodynamic setting in which the magmas of the Circum-Superior LIP could have formed. The hottest T_P values are constrained to the northwestern edge of the Superior craton, perhaps suggesting that the central axis of the plume was closest to the northwestern cratonic margin.

5.7. Negative Ti anomalies

Negative Ti anomalies relative to Eu and Gd are present in the primitive-mantle-normalised multi-element profiles of some of the Circum-Superior LIP samples. They are present in some of the samples from the Chukotat Group (Fig. 4.8), Fox River Belt (Fig. 4.28), Thompson Nickel Belt (Fig. 4.38), Lake Superior region (Fig. 4.68) and Labrador Trough (Fig. 4.80). The negative Ti anomalies in the intrusive samples of the Thompson Nickel Belt are probably the result of crustal contamination while the few negative Ti anomalies in the Lake Superior region samples may be the result of crustal contamination and/or late stage Fe-Ti oxide crystallisation. The negative Ti anomalies which will be discussed in this section,

however, are those found in volcanic samples which are not low in MgO and do not show any obvious sign of crustal contamination. Such volcanic rocks include the Group 1 samples of the Chukotat Group with MgO >8.5 wt. %, the Lower and Upper Volcanic Formation samples of the Fox River Belt with MgO >7.4 wt. %, and four samples from the Hellancourt Formation containing 7.84-8.35 wt. % MgO. The presence of these Ti anomalies is unusual especially as they occur in samples which have been identified by PRIMELT2 as being derived through only a few percent of olivine crystallisation from primary magmas. Possible origins of the Ti anomalies are discussed below.

5.7.1. Analytical error

Analytical error is an unlikely explanation for the origin of the Ti anomalies. TiO_2 is measured by both ICP-OES and ICP-MS and both methods have produced very similar results for all samples analysed. The strong correlation between the two methods is highlighted by the tight trend in Fig. 5.40 with an r^2 value of 0.9979. The likelihood of both methods producing anomalous results seems low. Repeated measurements of international reference standards JB-1a and JGb-1 also show that both ICP-OES and ICP-MS methods produced highly accurate and precise results for TiO_2, the full details of which are given in Appendix B.

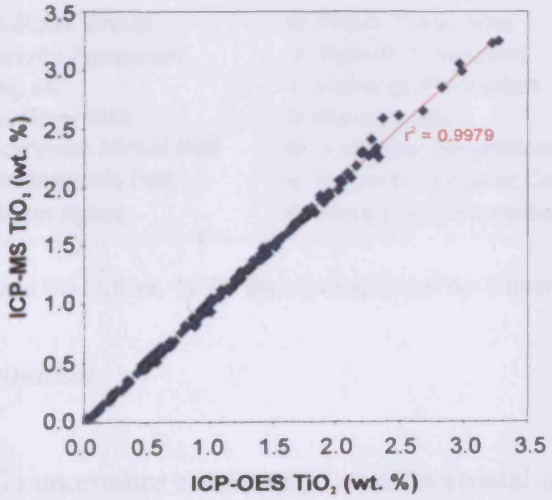

Fig. 5.40. Diagram showing the TiO_2 concentration of all the Circum-Superior LIP samples as measured by both ICP-OES and ICP-MS methods. The strong correlation (r^2 = 0.9979) indicates that both methods give almost identical results.

5.7.2. Alteration

It is unlikely that post-magmatic alteration processes are the cause of the negative Ti anomalies. Ti is generally considered to be an immobile element, hence its use in classification diagrams (Winchester & Floyd, 1977; Pearce, 1996). When Ti is plotted against Zr (Fig. 5.41a) there is little scatter which suggests that neither Ti nor Zr were mobilised by post-magmatic alteration processes. Another argument against the mobilisation of Ti is the lack of correlation between Ti/Ti* and LOI for the Circum-Superior LIP (Fig. 5.41b) especially if the high grade metamorphic, crustally contaminated Thompson Nickel Belt intrusive rocks are not considered.

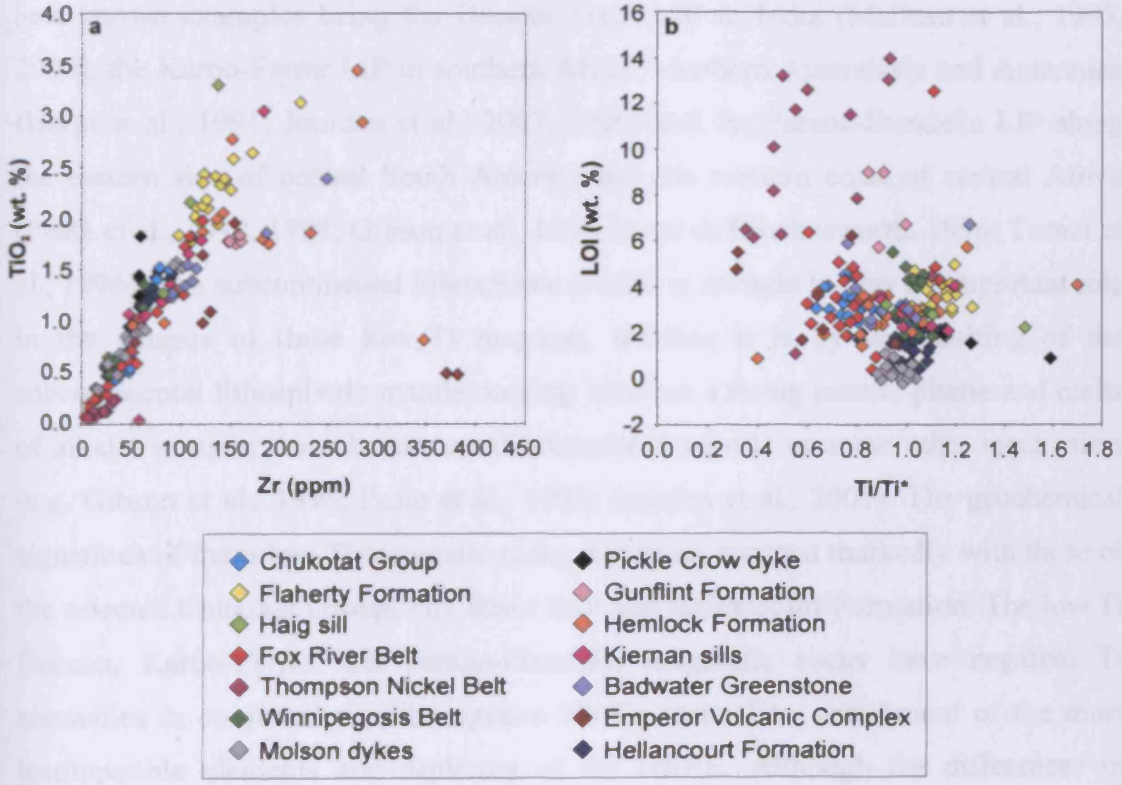

Fig. 5.41. (a) TiO_2 vs. Zr and (b) LOI vs. Ti/Ti* for all samples of the Circum-Superior LIP.

5.7.3. Crustal contamination

Negative Nb-Ta and Ti anomalies commonly occur in crustal contaminated volcanic rocks and have been used as indicators of enhanced Ni-Cu-PGE sulphide ore prospectivity in igneous provinces (e.g. Lesher et al., 2001). The samples from the Thompson Nickel Belt and Lake Superior region with negative Ti anomalies also

possess negative Nb-Ta anomalies (Figs. 4.38 and 4.68) which is consistent with crustal contamination. However, the selected samples from the Chukotat Group, Fox River Belt and Hellancourt Formation with negative Ti anomalies have multi-element profiles which are similar to the Ontong Java Plateau and are relatively flat with no negative Nb-Ta anomalies (Figs. 4.8, 4.28 and 4.80). Therefore crustal contamination seems an unlikely mechanism to explain the negative Ti anomalies in the selected Chukotat Group, Fox River Belt and Hellancourt Formation samples.

5.7.4. Subcontinental lithospheric mantle component

Low Ti picrites and basalts have been found in many LIPs with perhaps some of the best known examples being the Deccan Traps LIP in India (Melluso et al., 1995, 2006), the Karoo-Ferrar LIP in southern Africa, southern Australasia and Antarctica (Hergt et al., 1991; Jourdan et al., 2007, 2009) and the Parana-Etendeka LIP along the eastern side of central South America and the western coast of central Africa (Peate et al., 1992, 1999; Gibson et al., 1996; Peate & Hawkesworth, 1996; Turner et al., 1996). The subcontinental lithospheric mantle is thought to play an important role in the genesis of these low Ti magmas, whether it is by wet melting of the subcontinental lithospheric mantle, mixing between a rising mantle plume and melts of alkalic veins in the subcontinental lithospheric mantle or some other mechanism (e.g. Gibson et al., 1996; Peate et al., 1999; Jourdan et al., 2007). The geochemical signatures of these low Ti magmatic rocks, however, contrast markedly with those of the selected Chukotat Group, Fox River Belt and Hellancourt Formation. The low Ti Deccan, Karoo-Ferrar and Parana-Etendeka magmatic rocks have negative Ti anomalies in conjunction with negative Nb-Ta anomalies, enrichment of the most incompatible elements and depletion of the HREE. Although the differences in HREE patterns could be explained by different melting depths, the lack of enrichment in the more incompatible elements and the lack of negative Nb-Ta anomalies in the Chukotat Group, Fox River Belt and Hellancourt Formation samples are much harder to explain without invoking a role for either a crustal or lithospheric mantle component in the petrogenesis of these rocks. Furthermore, Modeland et al. (2003) have identified an enriched component in lavas of the ~2 Ga Povungnituk Group, which underlies the Chukotat Group in the Cape Smith Belt, and suggested the possibility that this enriched component represents metasomatised

lithospheric mantle. The enriched lavas of the Povungnituk Group possess no negative Nb-Ta anomalies and also no negative Ti anomalies, and so if the model of Modeland et al. (2003) is correct then it is unlikely that the subcontinental lithospheric mantle played any role in the genesis of the negative Ti anomalies seen in the Circum-Superior LIP.

5.7.5. Retention of Ti-rich minerals in the source

The depletion of Ti relative to other generally incompatible trace elements may indicate the presence of a mineral or minerals in the source which have a strong affinity for Ti. Minerals which are rich in Ti or in which Ti may substitute for another cation include sphene, magnetite, ilmenite, rutile, cassiterite, corundum, haematite, anatase, brookite and perovskite. One problem with the retention of such minerals in the source region is that many of these minerals have high K_D values for Nb and Ta because their crystal structures allow Nb and Ta to substitute in for some of the major cations (Green & Pearson, 1987; Kato et al., 1988; Foley et al., 2000). Therefore, if some of these minerals were retained in the source region, this would not only deplete the melt in Ti but also Nb and Ta. Magnetite and ilmenite do not exert as much of an influence on Nb and Ta as some of the other minerals such as sphene and rutile (Green & Pearson, 1987). However, the retention of magnetite and ilmenite in the source may lower the iron content of the melts produced, however, the selected Chukotat Group, Fox River Belt and Hellancourt Formations samples do not show any obvious evidence for anomalously low iron contents. The highest MgO samples in the Chukotat Group and Fox River Belt have similar $Fe_2O_3(T)$ concentrations to Group 1 samples of the Winnipegosis Belt which show no negative Ti anomalies. If magnetite and ilmenite were present in the source regions, then the high degrees of melting predicted to form the primary magmas of the Chukotat Group and Fox River Belt (up to 40% - see section 5.1) may well have consumed all these mineral phases but there is a lack of experimental data on melting of peridotites containing these oxide minerals to determine this.

5.7.6. Magnetite crystallisation

Volcanic rocks with negative Ti anomalies but otherwise relatively flat multi-element profiles are not common in the literature data for LIPs. However, there are some ~2.7 Ga greenstone basalts from the Superior Province which share the characteristics of the selected Circum-Superior LIP samples. Kerrich et al. (1999), Polat et al. (1999) and Polat (2009) have reported tholeiitic basalts with oceanic-plateau-like multi-element profiles except for negative Ti anomalies from the Schreiber, Hemlo, White River, Heron Bay and Winston Lake assemblages of the Wawa subprovince and the Tisdale assemblage of the Abitibi subprovince. These authors ascribe the negative Ti anomalies in the ~2.7 Ga basalts to magnetite crystallisation. This could be a possible explanation for the negative Ti anomalies of the Circum-Superior LIP because, as discussed above, magnetite can accommodate Ti while not seriously affecting other elements traditionally used in multi-element diagrams. Fig. 5.42 demonstrates the effect that magnetite crystallisation has on the Ti concentration.

Fig. 5.42 also shows the magnitude of the negative Ti anomaly of the modelled melt composition increases with progressive fractional crystallisation. This is in contrast to what is observed in the measured data from selected Circum-Superior LIP samples. The diagrams in Fig. 5.43 show that the size of the Ti anomaly in the Circum-Superior LIP samples remains unchanged with degree of fractional crystallisation, indicated by MgO and Zr concentrations, which is inconsistent with magnetite crystallisation. The presence of negative Ti anomalies in samples which are relatively primitive and rich in MgO is also unusual if magnetite crystallisation is the cause of the Ti anomalies, as significant magnetite crystallisation would not usually occur so early in the evolution of ultramafic and mafic volcanic rocks (e.g. Xu et al., 2003; Herzberg & Asimow, 2008; Pang et al., 2008). Phenocrysts of magnetite have been reported to crystallise early in basalts from the Canary Islands (Hoernle, 1987 cited in Herzberg & Asimow, 2008) but this requires high oxygen fugacity and an oxidised primary magma (e.g. Toplis, 1995; Jang et al., 2001; Herzberg & Asimow, 2008; Pang et al., 2008). However, many of the Chukotat Group and Fox River Belt samples with negative Ti anomalies have been identified by PRIMELT2 as being derived through only olivine crystallisation from a

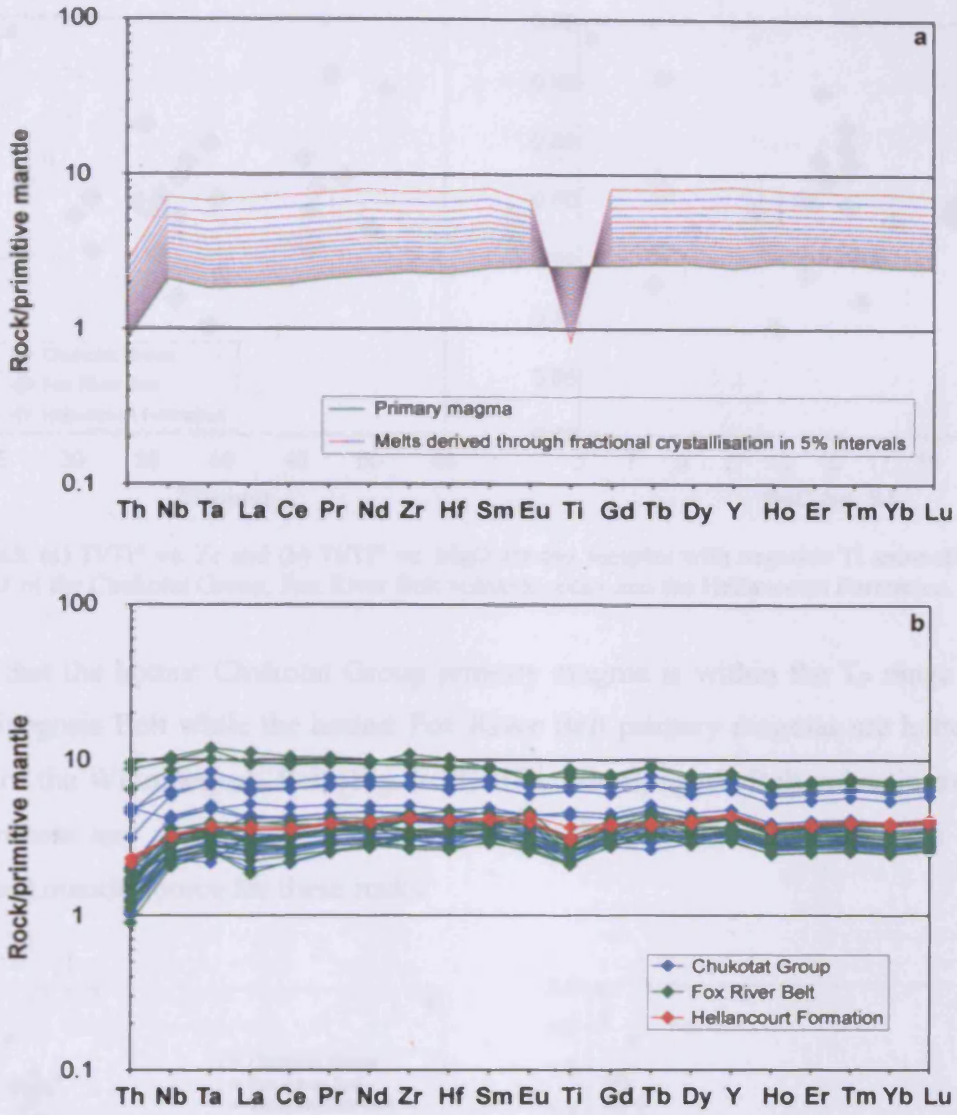

Fig. 5.42. (a) Primitive-mantle-normalised multi-element diagram displaying the results of trace element modelling for fractional crystallisation of a primary magma identical to that of a 39.6% partial melt of a source region composition of primitive mantle with 1% of continental crust extracted. The calculated results for 5% intervals of fractional crystallisation are shown. The fractionating assemblage is kept constant at 0.1 olivine, 0.3 clinopyroxene, 0.5 plagioclase, 0.1 magnetite. Partition co-efficients used given in Table F.3 in Appendix F. (b) Primitive-mantle-normalised multi-element diagram with uncontaminated volcanic samples from the Chukotat Group, Fox River Belt and Hellancourt Formation for easy comparison with (a). The Hellancourt Formation samples without negative Ti anomalies are omitted for clarity. Primitive mantle values from Sun & McDonough (1989).

primary magma melted from mantle at an oxidation state where $Fe^{2+}/\Sigma Fe$ is 0.9. If the Chukotat Group and Fox River Belt primary magmas formed in more oxidised environments where $Fe^{2+}/\Sigma Fe$ <0.9 then the higher Fe_2O_3 concentrations lower the FeO concentrations which yield lower MgO primary magmas from source regions with cooler mantle potential temperatures (T_P) (Herzberg et al., 2007; Herzberg & Asimow, 2008). The calculated T_P for the Circum-Superior LIP (see section 5.6)

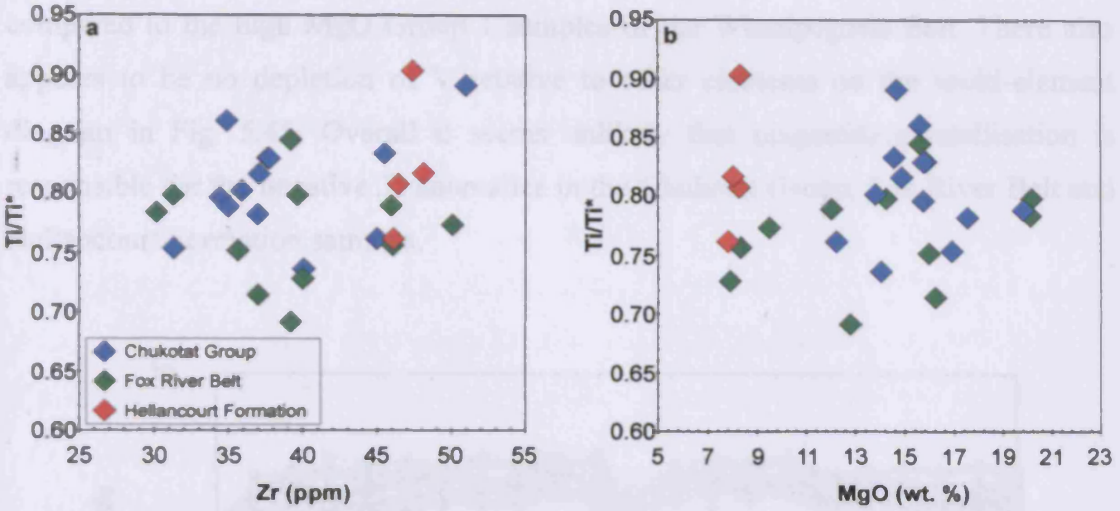

Fig. 5.43. (a) Ti/Ti* vs. Zr and (b) Ti/Ti* vs. MgO for the samples with negative Ti anomalies from Group 1 of the Chukotat Group, Fox River Belt volcanic rocks and the Hellancourt Formation.

show that the hottest Chukotat Group primary magma is within the T_P range of the Winnipegosis Belt while the hottest Fox River Belt primary magmas are hotter than those of the Winnipegosis Belt (Fig. 5.39). The Winnipegosis Belt volcanic rocks do not possess any negative Ti anomalies and so there is no suggestion of a highly oxidised mantle source for these rocks.

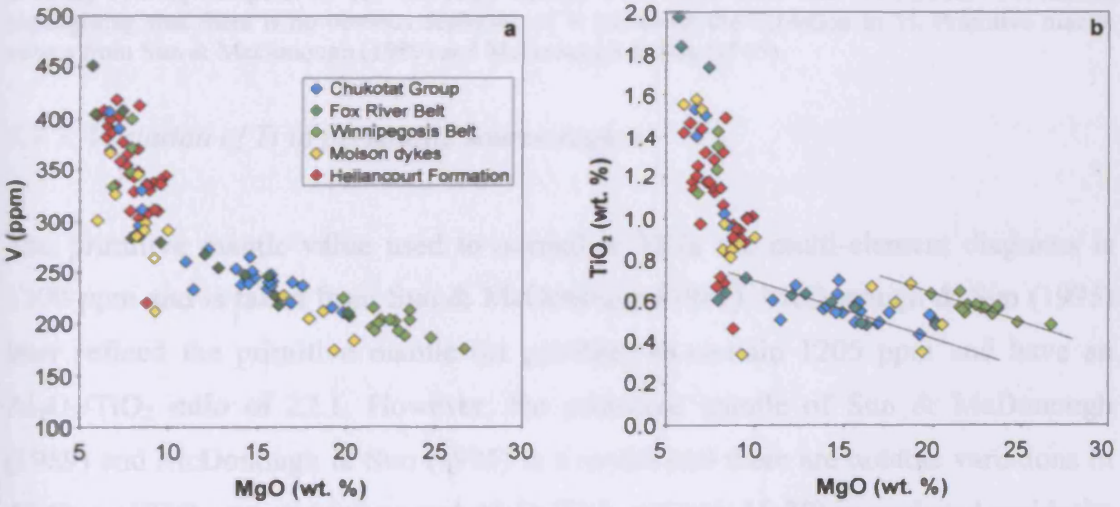

Fig. 5.44. (a) V vs. MgO and (b) TiO_2 vs. MgO variation diagrams for the Chukotat Group, Fox River Belt volcanic rocks, Winnipegosis Belt, Molson dykes and Hellancourt Formation. The two dashed lines in (b) highlight the differences in TiO_2 at a given MgO concentration for the high MgO rocks of the Circum-Superior LIP. The differences in TiO_2 are not mirrored in V concentrations.

As well as depleting the melt in Ti, the crystallisation of magnetite should lead to the depletion of V. However, in Fig. 5.44a there appears to be no obvious difference in V concentrations of the high MgO Chukotat Group and Fox River Belt samples when

compared to the high MgO Group 1 samples of the Winnipegosis Belt. There also appears to be no depletion of V relative to other elements on the multi-element diagram in Fig. 5.45. Overall it seems unlikely that magnetite crystallisation is responsible for the negative Ti anomalies in the Chukotat Group, Fox River Belt and Hellancourt Formation samples.

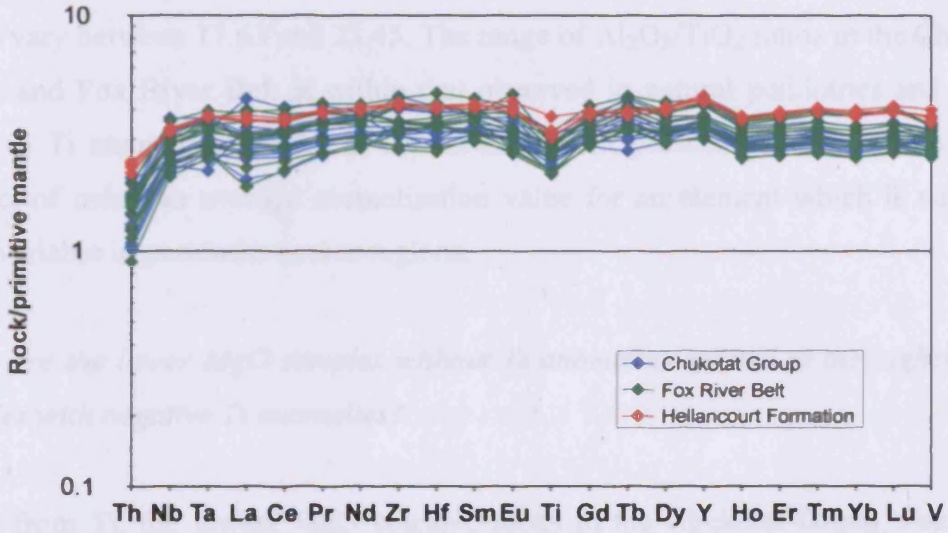

Fig. 5.45. Extended primitive-mantle-normalised multi-element diagram of the uncontaminated, Ti-anomaly-bearing samples of the Chukotat Group, Fox River Belt and Hellancourt Formation, highlighting that there is no obvious depletion of V mirroring the depletion in Ti. Primitive mantle values from Sun & McDonough (1989) and McDonough & Sun (1995).

5.7.7. Variation of Ti in peridotitic source regions

The primitive mantle value used to normalise Ti in the multi-element diagrams is 1300 ppm and is taken from Sun & McDonough (1989). McDonough & Sun (1995) later refined the primitive mantle (or pyrolite) to contain 1205 ppm and have an Al_2O_3/TiO_2 ratio of 22.1. However, the primitive mantle of Sun & McDonough (1989) and McDonough & Sun (1995) is a model and there are notable variations in Al_2O_3 and TiO_2 concentrations and Al_2O_3/TiO_2 ratios (~15-30) in analysed peridotite samples (Maaloe & Aoki, 1977; Herzberg, 1993; McDonough & Sun, 1995; Walter, 1998; Herzberg & O'Hara, 2002). If the degree of melting is high enough, clinopyroxene and any garnet in the peridotite source region will be consumed, producing a harzburgite or dunite residue, and the resulting melts will have the same Al_2O_3/TiO_2 ratios as the source. The calculated degrees of partial melting required to

generate the primary magmas of the Chukotat Group and Fox River Belt are relatively high, up to ~35% and ~40% respectively (see section 5.1), and could conceivably have consumed all the clinopyroxene and any garnet (cf. Walter, 1998). For the Chukotat Group, the primary magmas and the high MgO samples (>12.25 wt. % MgO), which although not all were suitable for PRIMELT2 solutions are still fairly primitive, have Al_2O_3/TiO_2 ratios ranging from 15.06 to 22.65. The Al_2O_3/TiO_2 ratios of the Fox River Belt primary magmas and high MgO samples (>12.05 wt. % MgO) vary between 17.63 and 23.45. The range of Al_2O_3/TiO_2 ratios in the Chukotat Group and Fox River Belt is within that observed in natural peridotites and so the negative Ti anomalies present in the multi-element profiles could therefore be an artefact of using an average normalisation value for an element which is naturally quite variable in peridotite source regions.

5.7.8. Are the lower MgO samples without Ti anomalies related to the higher MgO samples with negative Ti anomalies?

Aside from Ti, the lowest MgO volcanic rocks in the Chukotat Group, Fox River Belt and Hellancourt Formation have multi-element profiles which are near-parallel to the higher MgO samples but displaced to higher elemental abundances (Figs. 4.8, 4.28 and 4.80). The difference in element concentrations can be explained by differing degrees of fractional crystallisation of olivine, clinopyroxene, plagioclase and spinel (see section 5.2). However, trace element modelling shows that the magnitude of the negative Ti anomaly is not reduced drastically by crystallisation of the aforementioned minerals (Fig. 5.19). It is therefore hard to relate the lower MgO samples to the higher MgO samples through fractional crystallisation alone. The metasomatic addition of Ti-rich oxides (e.g. Gregoire et al., 2000; Coltorti & Gregoire, 2008) could reduce the Ti anomaly such that the Ti/Ti* value increases to ~1 but this seems unlikely given that the lower MgO magmas would have to be selectively metasomatised and that other elements such as Fe, Nb and Ta should also be affected.

Could the lower MgO samples be formed from lower degrees of melting at higher pressures than for the higher MgO samples? The partition co-efficient of Ti in clinopyroxene is known to be sensitive to pressure and decreases as the depth of

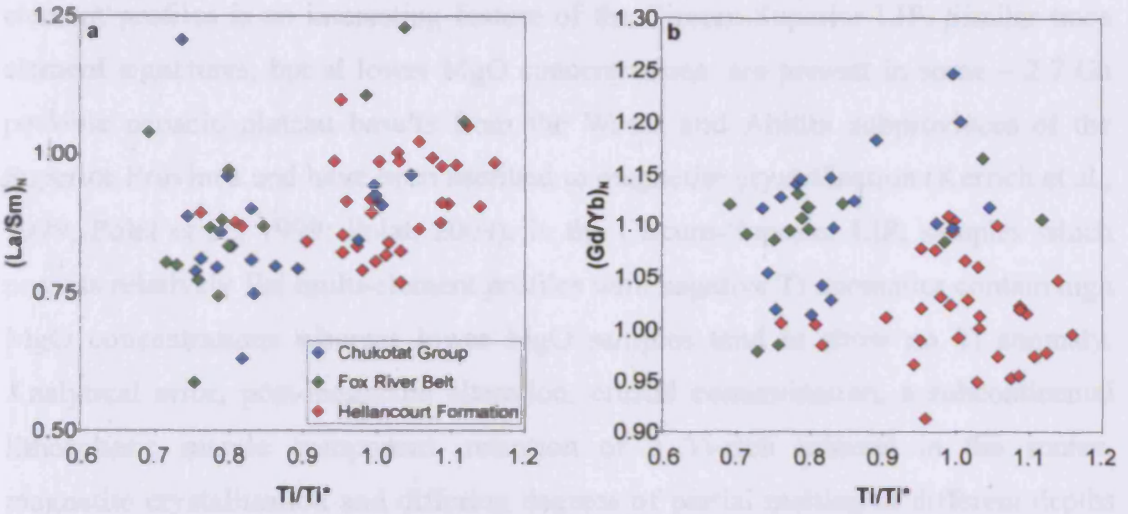

Fig. 5.46. (a) $(La/Sm)_N$ vs. Ti/Ti* and (b) $(Gd/Yb)_N$ vs. Ti/Ti* diagrams for samples from Group 1 of the Chukotat Group, Fox River Belt volcanic rocks and Hellancourt Formation.

melting increases (e.g. Adam & Green, 1994; Hill et al., 2000; Salters & Stracke, 2004). The trace element modelling in section 5.1 is simplified by use of a set of partition co-efficients (Table F.3 in Appendix F) which do not take into account changes in pressure during melting. Ti/Ti* values are compared to $(La/Sm)_N$, an indicator of degree of melting, and $(Gd/Yb)_N$, an indicator of depth of melting, in Fig. 5.46. The only notable correlation in Fig. 5.46a is in the Fox River Belt volcanic rocks where the lower MgO samples with no Ti anomalies have higher $(La/Sm)_N$ ratios than the higher MgO samples with negative Ti anomalies. However, the lower MgO Fox River Belt samples have similar $(Gd/Yb)_N$ ratios to the majority of the higher MgO samples (Fig. 5.46b) which implies that all the rocks were formed at similar depths and that differing Ti/Ti* values cannot be accounted for by partial melting at different pressures. The possibility of Ti anomalies being controlled by the degree of partial melting seems unlikely as Baker et al. (1995) and le Roex et al. (2003) have shown evidence that suggests the partition co-efficient of Ti in clinopyroxene is higher at lower melt fractions, in which case the lower MgO samples would be expected to possess negative Ti anomalies. It appears that differing degrees and depths of partial melting cannot explain the Ti enigma.

5.7.9. Summary

The presence of negative Ti anomalies in samples from the Chukotat Group, Fox River Belt and Hellancourt Formation which otherwise have relatively flat multi-

element profiles is an interesting feature of the Circum-Superior LIP. Similar trace element signatures, but at lower MgO concentrations, are present in some ~ 2.7 Ga possible oceanic plateau basalts from the Wawa and Abitibi subprovinces of the Superior Province and have been ascribed to magnetite crystallisation (Kerrich et al., 1999; Polat et al., 1999; Polat, 2009). In the Circum-Superior LIP, samples which possess relatively flat multi-element profiles with negative Ti anomalies contain high MgO concentrations whereas lower MgO samples tend to show no Ti anomaly. Analytical error, post-magmatic alteration, crustal contamination, a subcontinental lithospheric mantle component, retention of a Ti-rich mineral in the source, magnetite crystallisation and differing degrees of partial melting at different depths seem unlikely mechanisms to cause the Ti anomalies. Perhaps the best explanation for the Ti anomalies is that they are an artefact of using an averaged Ti normalisation value for primitive mantle which does not reflect the extent of the true variability of Ti in the mantle as highlighted by the variation of Ti concentrations in natural peridotites. However, this does not explain why the Ti anomalies are not present in lower MgO samples which by means of other major and trace elements could be related to the higher MgO samples by higher degrees of fractional crystallisation or lower degrees of partial melting. A very speculative explanation is that if the lower MgO samples are products of higher degrees of fractional crystallisation then these melts may have had longer residence times in magma chambers in which the incompatible trace element concentrations could have been homogenised.

5.8. Ni-Cu-PGE sulphide deposits

The Circum-Superior LIP is host to some of the world's most important Ni-Cu-PGE ore deposits, particularly in the Cape Smith Belt (Raglan Formation and Expo Ungava Intrusive Suite) (e.g. Barnes et al., 1982; Giovenazzo et al., 1989; Barnes & Picard, 1993; Naldrett, 2004; Lesher, 2007) and Thompson Nickel Belt (e.g. Cumming et al., 1982; Peredery, 1982; Naldrett, 1999, 2004; Hulbert et al., 2005; Layton-Matthews et al., 2007). Lesser known and explored ore deposits are also found in the Fox River Belt (e.g. Scoates, 1981, 1990; Scoates & Eckstrand, 1986; Schwann, 1989; Desharnais et al., 2000; Desharnais, 2005), Molson dykes (Peck et al., 1999) and Labrador Trough (e.g. Clark et al., 1989; Beaudoin et al., 1990; Mungall & Wares, 1997; Clark, 2001). However, no significant deposits have been

reported from other segments of the Circum-Superior LIP (i.e. Hudson Bay, Winnipegosis Belt, Pickle Crow dyke, Lake Superior region and craton-interior carbonatites). The Circum-Superior LIP therefore offers the opportunity to investigate why some magmatic suites contain economically important Ni-Cu-PGE deposits ('fertile') and others do not ('barren'), and whether it is possible to geochemically discriminate between so-called fertile and barren magmatic suites using the composition of volcanic rocks. Zhang et al. (2008) studied the geochemistry and economic mineralisation of ten LIPs of various ages and proposed geochemical criteria that could be used to identify those LIPs likely to be fertile and those which are likely to be barren. The criteria of Zhang et al. (2008) and those of other studies such as Lesher et al. (2001) and Maier & Barnes (2005) are applied here to the Circum-Superior LIP to assess the possibility of distinguishing between the fertile and barren segments of the Circum-Superior LIP.

5.8.1. Formation of a magmatic Ni-Cu-PGE sulphide deposit

The theory behind the genesis of Ni-Cu-PGE deposits has been discussed by numerous authors (e.g. Keays, 1995; Lesher et al., 2001; Lesher & Keays, 2002; Naldrett, 2004; Arndt et al., 2005; Mungall, 2005; Zhang et al., 2008) and is only briefly summarised in this section. To form a Ni-Cu-PGE deposit, a magma has to contain sufficient concentrations of ore metals and must be able to become saturated in sulphide. The metal content of the primary magma is important but not crucial in the genesis of the ore deposits because of the high partition co-efficients and strong affinities of Ni, Cu and PGEs for sulphide liquid relative to silicate liquid. The degree of partial melting needs to be sufficiently high to consume all of the sulphide in the source and generally needs to be greater than ~25% (see Arndt et al., 2005 and Mungall, 2005 and references therein). If the degree of partial melting is too low then the sulphide phase will remain in the melt residue and retain chalcophile elements such as Ni, Cu and PGEs.

As the magma ascends through the mantle towards the surface, decompression will result in the magma becoming increasingly more undersaturated in sulphide (Mavrogenes & O'Neill, 1999). Falling temperature has been shown to decrease the sulphur solubility of a magma but the influence of declining pressure more than

compensates for the decrease in temperature (Mavrogenes & O'Neill, 1999). An economic ore deposit may form once the magma reaches sulphide saturation in the crust and immiscible sulphide liquid droplets exsolve and segregate from the silicate magma, extracting chalcophilic elements as they form. Mavrogenes & O'Neill (1999) and O'Neill & Mavrogenes (2002) also showed that the SiO_2, TiO_2, Al_2O_3, Na_2O and particularly FeO content can affect the solubility of sulphur in ultramafic magmas whereas oxygen fugacity and sulphur fugacity are relatively unimportant.

Sulphide saturation in a magma may occur passively by cooling and crystallisation when the decline in sulphur solubility due to decreasing temperature matches the increasing sulphide concentration resulting from the decreasing volume of melt (Mungall, 2005). The passive route to sulphide saturation may be slow and will probably result in deposits poor in Ni as it would have been removed from the melt by earlier crystallising silicate mineral phases such as olivine. A quicker and more dynamic route to sulphide saturation is to introduce external sulphur to the magma by the assimilation of S-rich crustal rocks (Mungall, 2005) or subcontinental lithospheric mantle (Zhang et al., 2008).

The most favourable environments for assimilation and then the segregation and accumulation of sulphides are widened sections of magma conduits and lava channels. A hotter magma will also be capable of melting more of the country rock and if flow is turbulent then there may be greater interaction between the magma and surrounding rock. For the formation of an ore deposit it is also desirable to have a high R-factor (ratio of the mass of silicate melt to sulphide melt) (Campbell & Naldrett, 1979), which requires a large volume of magma, so that the metals are not diluted in a large volume of sulphide.

5.8.2. Geochemical discrimination between fertile and barren LIPs

Zhang et al. (2008) suggested that some mantle plumes may be predisposed to be prospective for Ni-Cu-PGE sulphide ore deposits and that the volcanic rocks erupted from such plumes display distinctive geochemical characteristics. The geochemical and isotopic differences between fertile and barren LIPs as suggested by Zhang et al. (2008) are summarised in Table 5.5.

Table 5.5. Summary of the geochemical differences between fertile and barren LIPs as suggested by Zhang et al. (2008)

Fertile LIPs	Barren LIPs
High MgO and Ni	Few high MgO and Ni samples
Low Al_2O_3 and Na_2O	High Al_2O_3 and Na_2O
High CaO/Al_2O_3	Low CaO/Al_2O_3
Enrichment of the most incompatible trace elements	No enrichment of the most incompatible trace elements
Ba enriched relative to other LILEs	Ba not significantly enriched relative to other LILEs
High Ba/Th, Ba/Nb and K/Ti and low Rb/Ba	Low Ba/Th, Ba/Nb and K/Ti and high Rb/Ba
High LREE/HREE with $(La/Yb)_N$ up to ~63	Lower LREE/HREE with $(La/Yb)_N$ up to ~17
High Os (0.01-11 ppb) and low Re/Os (0.025-10)	Low Os (0.3 ppt to 0.02 ppb) and high Re/Os (10-200)
Lower $^{87}Sr/^{86}Sr_i$	Higher $^{87}Sr/^{86}Sr_i$
FOZO-EM1 isotopic trends	FOZO-EM2 isotopic trends

The study of Zhang et al. (2008) highlighted the possibility that the presence or absence of Ni-Cu-PGE mineralisation within a LIP may be a source-related feature. Other investigations into the whole-rock geochemical discrimination between fertile and barren LIPs focus on identifying the signatures of processes thought to be important in ore genesis such as sulphide segregation and crustal contamination (e.g. Lesher et al., 2001; Maier & Barnes, 2005). Lesher et al. (2001) suggested that fertile LIPs will generally exhibit Th-U-LREE enrichment and negative Nb-Ta-Ti anomalies and utilised ratios such as $(Nb/Th)_{pm}$, $(Th/Yb)_{pm}$ and $(La/Sm)_{pm}$ in conjunction with MgO, Ni and PGE concentrations to distinguish between fertile and barren provinces. Maier & Barnes (2005) noted that ratios such as Cu/Pd are useful in assessing chalcophile element depletion and whether a magma has experienced sulphide segregation. Pd has a greater affinity for sulphide liquid than Cu (Mungall, 2005) and so a high Cu/Pd ratio may indicate that sulphide segregation has occurred and that an ore deposit may be associated with the LIP. If Cu/Pd ratios are roughly equal to that of the primitive mantle then this may suggest sulphide saturation was never reached. Where PGE concentrations are not available Maier & Barnes (2005) proposed using Cu/Zr ratios and suggested that low Cu/Zr values were the result of sulphide segregation. However, Cu is less chalcophile-like than Pd (Mungall, 2005) and so Cu/Zr ratios are less sensitive to sulphide segregation than Cu/Pd ratios.

5.8.3. Can the fertile and barren segments of the Circum-Superior LIP be distinguished on the basis of geochemistry?

This section assesses whether the geochemical criteria proposed by Zhang et al. (2008) can be successfully applied to distinguish between the fertile and barren segments of the Circum-Superior LIP.

High MgO and Ni The ore-bearing Chukotat Group and Fox River Belt contain volcanic rocks with high MgO and Ni concentrations (Fig. 5.47a). Some of the Molson dykes also contain high MgO and Ni concentrations (Fig. 5.47a). However, the Winnipegosis Belt volcanic rocks also possess high MgO and Ni concentrations (Fig. 5.47a) yet no ore deposits have been reported from these segments. The Hellancourt Formation is associated with ore deposits yet has MgO and Ni concentrations lower than many samples from the Chukotat Group and Fox River Belt and which are more similar to samples from the barren regions of Hudson Bay and Lake Superior (Fig. 5.47a). Therefore the presence of magmatic rocks with high MgO and Ni concentrations is not a reliable indicator for the presence of Ni-Cu-PGE sulphide deposits in the Circum-Superior LIP.

Low Al_2O_3 and Na_2O There appears to be no correlation between Al_2O_3 or Na_2O concentration and mineralisation state. For a given MgO concentration, there is no difference in the Al_2O_3 or Na_2O content of samples from fertile and barren segments (Figs. 5.47b and 5.47c).

High CaO/Al_2O_3 The ratio CaO/Al_2O_3 is ineffective at discriminating between mineralised and non-mineralised segments of the Circum-Superior LIP. In Fig. 5.47d samples from both mineralised and non-mineralised segments have similar CaO/Al_2O_3 ratios.

Enrichment of the most incompatible elements The enrichment of the more incompatible trace elements (e.g. Th-LREE) relative to less incompatible elements is visible in the signature of some of the samples from the Chukotat Group (Fig. 4.8b). None of the Fox River Belt volcanic rock samples analysed for this study possess such a signature (Fig. 4.28a) but most of the intrusive rock samples do (Fig. 4.28b)

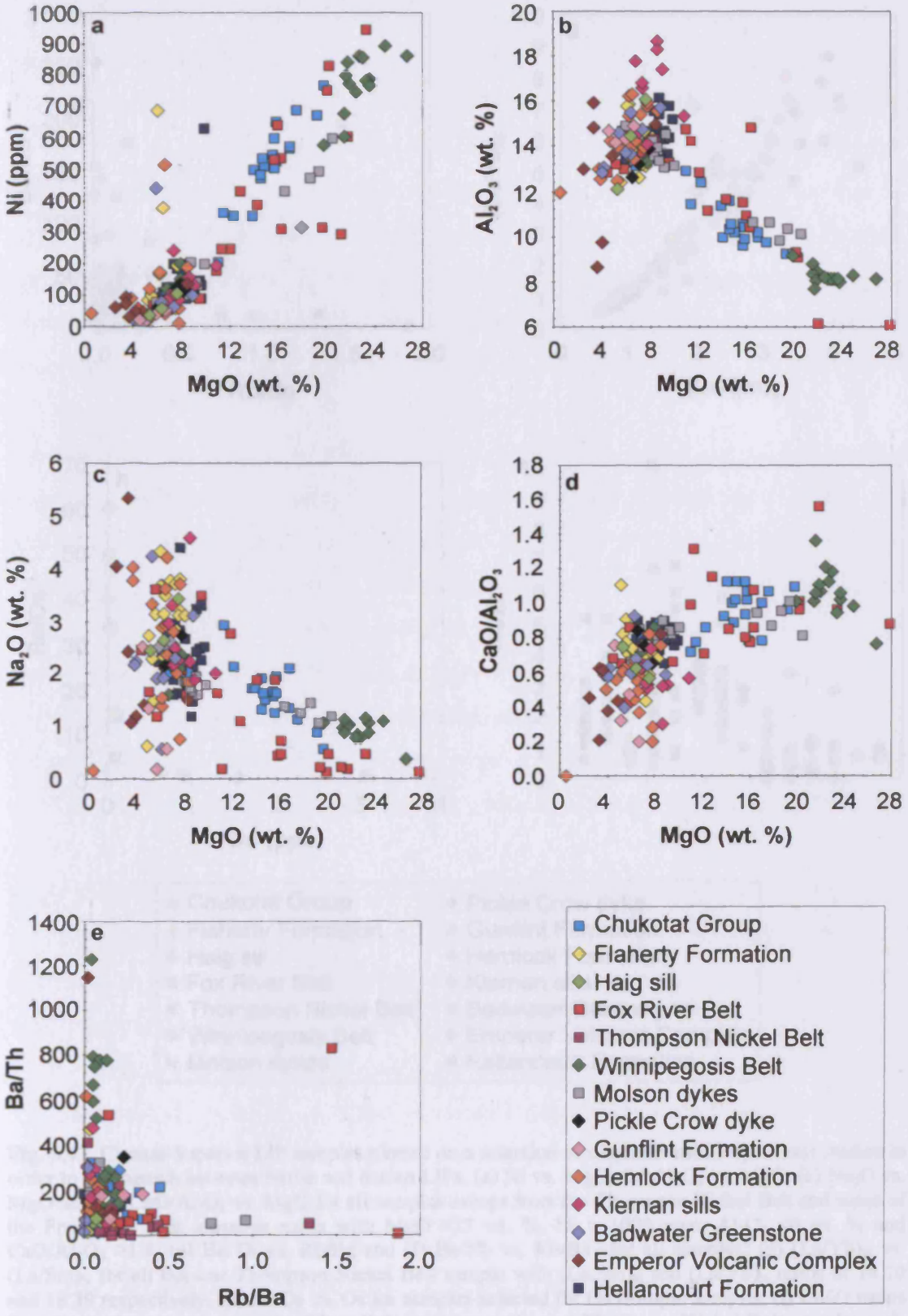
a
Ni (ppm)
MgO (wt. %)
b
Al2O3 (wt. %)
MgO (wt. %)
c
Na2O (wt. %)
MgO (wt. %)
d
CaO/Al2O3
MgO (wt. %)
e
Ba/Th
Rb/Ba
Chukotat Group
Flaherty Formation
Haig sill
Fox River Belt
Thompson Nickel Belt
Winnipegosis Belt
Molson dykes
Pickle Crow dyke
Gunflint Formation
Hemlock Formation
Kiernan sills
Badwater Greenstone
Emperor Volcanic Complex
Hellancourt Formation

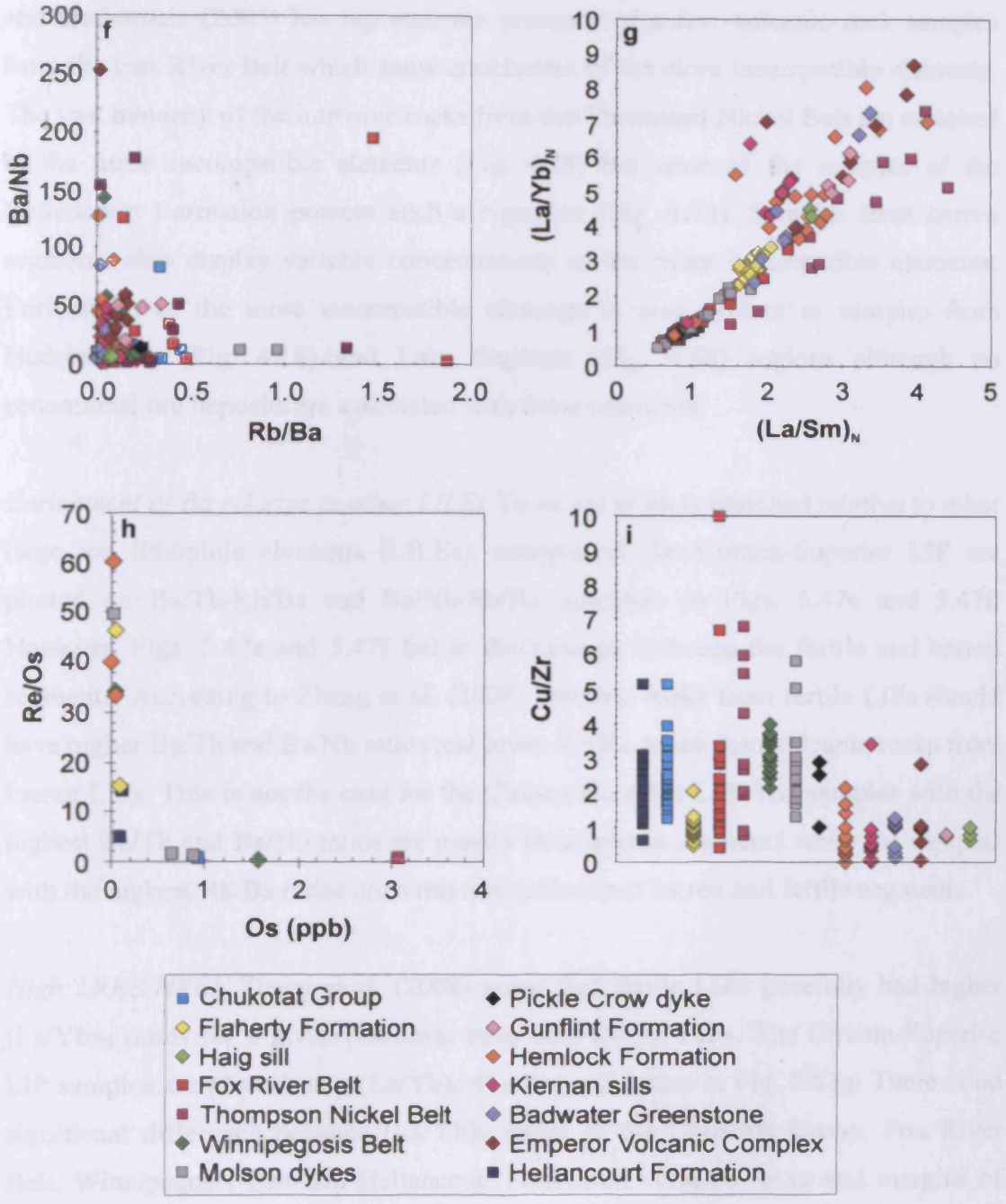

Fig. 5.47. Circum-Superior LIP samples plotted on a selection of diagrams used in previous studies in order to distinguish between fertile and barren LIPs. (a) Ni vs. MgO, (b) Al_2O_3 vs. MgO, (c) Na_2O vs. MgO and (d) CaO/Al_2O_3 vs. MgO for all samples except from the Thompson Nickel Belt and some of the Fox River Belt intrusive rocks with MgO >27 wt. %, Ni > 1000 ppm, Al_2O_3 <6 wt. % and CaO/Al_2O_3 >1.8; (e) Ba/Th vs. Rb/Ba and (f) Ba/Nb vs. Rb/Ba for all samples; (g) $(La/Yb)_N$ vs. $(La/Sm)_N$ for all but one Thompson Nickel Belt sample with $(La/Sm)_N$ and $(La/Yb)_N$ ratios of 14.10 and 18.39 respectively; (h) Re/Os vs. Os for samples selected for Os isotopic analysis; (i) Cu/Zr ratios for all samples except some Fox River Belt intrusive rocks and Thompson Nickel Belt samples with Cu/Zr ratios >10.

and Desharnais (2005) has reported the presence of a few volcanic rock samples from the Fox River Belt which show enrichment of the more incompatible elements. The vast majority of the intrusive rocks from the Thompson Nickel Belt are enriched in the more incompatible elements (Fig. 4.38) but none of the samples of the Hellancourt Formation possess such a signature (Fig. 4.80). Samples from barren segments also display variable concentrations of the more incompatible elements. Enrichment of the more incompatible elements is also evident in samples from Hudson Bay (Fig. 4.18) and Lake Superior (Fig. 4.68) regions although no economical ore deposits are associated with these segments.

Enrichment of Ba relative to other LILEs To assess if Ba is enriched relative to other large ion lithophile elements (LILEs), samples of the Circum-Superior LIP are plotted on Ba/Th-Rb/Ba and Ba/Nb-Rb/Ba diagrams in Figs. 5.47e and 5.47f. However, Figs. 5.47e and 5.47f fail to discriminate between the fertile and barren segments. According to Zhang et al. (2008) volcanic rocks from fertile LIPs should have higher Ba/Th and Ba/Nb ratios and lower Rb/Ba ratios than volcanic rocks from barren LIPs. This is not the case for the Circum-Superior LIP. The samples with the highest Ba/Th and Ba/Nb ratios are mostly from barren segments while the samples with the highest Rb/Ba ratios are a mixture rocks from barren and fertile segments.

High LREE/HREE Zhang et al. (2008) noted that fertile LIPs generally had higher $(La/Yb)_N$ ratios for a given $(La/Sm)_N$ ratio than barren LIPs. The Circum-Superior LIP samples are plotted on a $(La/Yb)_N$-$(La/Sm)_N$ diagram in Fig. 5.47g. There is no significant difference between $(La/Yb)_N$ ratios of the Chukotat Group, Fox River Belt, Winnipegosis Belt and Hellancourt Formation volcanic rocks and margins of the Molson dykes at given $(La/Sm)_N$ ratios. There are differences in the $(La/Yb)_N$ ratios of many Hudson Bay and Lake Superior region samples compared to Thompson Nickel Belt samples at similar $(La/Sm)_N$ ratios, with the ore-associated Thompson intrusive rocks having lower $(La/Yb)_N$ ratios. This contrasts with the findings of Zhang et al. (2008) although it must be noted that the Thompson Nickel Belt samples are from coarse grained intrusions which may not accurately represent the composition of the liquid magma which they transported.

Os concentrations and Re/Os ratios The Os isotope data collected for this study are somewhat unusual and so any interpretation based upon them is questionable. Nearly all the samples analysed have Os concentrations within the range for fertile LIPs (0.01-11 ppb) despite many samples coming from barren segments. The highest Os concentration is from a sample from the Thompson Nickel Belt (3.066 ppb) while the second highest concentration is from a high MgO Winnipegosis Belt sample with 1.562 ppb Os (Fig. 5.47h). Re/Os ratios provide some degree of distinction between samples from fertile and barren segments although it is by no means conclusive. All but one of the samples with Re/Os >15 are from barren segments but not all samples with Re/Os <15 are from fertile segments (Fig. 5.47h).

$^{87}Sr/^{86}Sr$ isotopic ratios The $^{87}Sr/^{86}Sr_i$ isotopic ratios of the Circum-Superior LIP obtained by this study and previous studies do not differentiate between the fertile and barren segments as there is considerable overlap between the two (Fig. 4.83).

Trends between isotopic end-members Zhang et al. (2008) have suggested that fertile LIPs tend to display trends between the proposed isotopic end-members FOZO and EM1 whereas barren LIPs trend between FOZO and EM2. It is difficult to compare the Circum-Superior LIP samples to isotopic mantle end-members such as DMM, HIMU, EM1, EM2 and FOZO as the isotopic composition of such end-members in the Palaeoproterozoic is not known. There is no obvious distinction between samples from fertile and barren segments in isotopic space (Fig. 4.83). Samples from the barren Lake Superior region exhibit higher $^{207}Pb/^{204}Pb_i$ and $^{208}Pb/^{204}Pb_i$ ratios for a given $^{206}Pb/^{204}Pb_i$ ratio and lower $^{143}Nd/^{144}Nd_i$ and $^{176}Hf/^{177}Hf_i$ ratios than samples from fertile segments although there are many other barren segment samples with similar isotopic compositions to the fertile segment samples (Fig. 4.83). Many more isotopic analyses are required from all segments of the Circum-Superior LIP to assess if any mineralisation-diagnostic trends are visible.

Negative Nb-Ta anomalies The presence of negative Nb-Ta anomalies can be indicative of crustal contamination, a process which is often considered a requirement for ore genesis. Such signatures are present in the Chukotat Group, Fox River Belt, Thompson Nickel Belt, Molson dykes and Lake Superior region (Figs. 4.8, 4.28, 4.38, 4.58 and 4.68) yet not all of these segments contain Ni-Cu-PGE

mineralisation. No negative Nb-Ta anomalies are observed in the multi-element profiles of the Hellancourt Formation (Fig. 4.80) despite its association with ore deposits.

Cu/Zr ratios The overall range in Cu/Zr ratios for the Circum-Superior LIP is 0.01-35.54 although all samples from volcanic rocks and dyke margins have ratios <6 (Fig. 5.47i). There is no obvious distinction between fertile and barren segments as samples from both display similar ranges in their Cu/Zr ratios (Fig. 5.47i).

Summary Methods utilised in previous studies such as Lesher et al. (2001), Maier & Barnes (2005) and Zhang et al. (2008) for distinguishing between fertile and barren LIPs are ineffective at discriminating between the mineralised and non-mineralised segments of the Circum-Superior LIP. Geochemical signatures expected for fertile LIPs are present in some mineralised segments but not others while some non-mineralised segments also display geochemical signatures proposed to be characteristic of fertile provinces.

5.8.4. Possible reasons for the lack of geochemical fingerprints of fertile and barren segments of the Circum-Superior LIP

Zhang et al. (2008) recognised that LIPs are often geochemically heterogeneous and that some signatures indicative of mineralisation may not reflect the presence of ore deposits. The current study reinforces the idea that whole-rock geochemistry of volcanic rocks should not be used in isolation when attempting to distinguish between fertile and barren LIPs or fertile and barren segments of an individual LIP.

The study of Zhang et al. (2008) utilises elements such as Ca, Na, K, Ba and Rb to discriminate between mineralised and non-mineralised LIPs. The use of such elements may be inappropriate for the Circum-Superior LIP and other ancient volcanic provinces due to the susceptibility of these elements to mobilisation during post-magmatic alteration processes (e.g. Pearce, 1996) (see also Chapter 4). These elements tend not to produce coherent trends when plotted against an element generally considered to be immobile like Zr (see Chapter 4). The use of mobile elements may perturb any real trends and may partly be responsible for why there is

no obvious distinction between the mineralised and non-mineralised segments of the Circum-Superior LIP. The use of Sr and Pb isotopes in studying Precambrian LIPs also has the potential to yield erroneous interpretations given that these isotope systems involve the commonly mobile elements Rb, Sr, U and Pb. Cu can be relatively mobile during post-magmatic alteration processes (e.g. Pearce, 1996) which may explain the lack of correlation between Cu and Zr in the Circum-Superior LIP rocks (see Chapter 4). If Cu was mobile then it may also have perturbed any potential signature of Cu depletion (e.g. Cu/Zr ratios) as a result of the segregation of sulphide.

Another possibility why many of the potential mineralisation indicators discussed above do not seem to apply to the Circum-Superior LIP may be that many are not good indicators of the degree of partial melting and can be affected by other igneous processes. If the degree of partial melting is not sufficiently high enough then the sulphide phase is retained in the source and this will reduce the concentration of chalcophilic elements in the melt. PGEs partition more strongly into sulphide liquid than Cu and Ni (Mungall, 2005) and so a magma's PGE concentration is more drastically affected than that of Ni and Cu if the degree of melting is insufficient to consume all of the sulphide phase.

Potential mineralisation indicators such as Al_2O_3, Na_2O, CaO/Al_2O_3, Ba/Th, Ba/Nb, K/Ti, Rb/Ba and $(La/Yb)_N$ are all influenced by the degree of partial melting but can also be altered by depth of melting, fractional crystallisation and crustal contamination such that the signature from partial melting is erased. No primary magmas have been recognised from the Flaherty Formation and Lake Superior region and so no accurate assessment can be made of the degree of partial melting which formed the magmatism in these region. The magmas of the Flaherty Formation and Lake Superior region may be formed by degrees of melting that were too low (<25%) to consume the sulphide in the source. The Hellancourt Formation also does not contain primary magmas but is associated with ore deposits and therefore could have formed from sufficiently high degrees of partial melting (>25%). However, the degree of partial melting is not the sole control on magma ore potential as major and trace element modelling indicates that the Winnipegosis Belt

volcanic rocks were derived from >25% partial melting yet no ore deposits have been reported from this segment.

The enrichment of the most incompatible elements (e.g. Th-LREE) relative to less incompatible elements and the presence of negative Nb-Ta anomalies relative to Th and La are geochemical signatures associated with magmas that have been contaminated with crustal material, a process often considered likely to lead to sulphur saturation in a magma. However, if the crustal assimilant does not contain high amounts of sulphur then sulphur saturation may not be reached given that magma is usually very sulphur undersaturated by the time it reaches crustal levels (Mavrogenes & O'Neill, 1999). The type of crustal material which a magma assimilates may therefore be an important control on the petrogenesis of an ore deposit. Sulphur-rich sediments have been reported from the Cape Smith Belt (Mungall, 2007), Fox River Belt (Desharnais, 2005), Thompson Nickel Belt (Zwanzig & Bohm, 2002) and Labrador Trough (Cameron, 1983). Interestingly, there are no known reports of sulphur-rich sedimentary rocks in the region of outcrop of the ~1880 Ma Lake Superior igneous rocks. It is possible that the reason for the lack of Ni-Cu-PGE mineralisation associated with the Lake Superior igneous rocks is that the contaminant of these rocks was not enriched enough in sulphur to drive the magma to sulphide saturation.

Negative Nb-Ta anomalies and enrichment of the most incompatible elements do not discriminate between different mechanisms of contamination. Lesher et al. (2001) and Lesher (2007) highlighted the importance of the fluid dynamics of the magma and how it interacts with the crust. Hot, turbulently flowing magma in relatively thin magma feeder conduits or lava channels is most likely to physically interact and assimilate sulphur-rich crustal rocks in a process referred to as assimilation during turbulent ascent (ATA). As discussed in section 5.3, crustal contamination within the Chukotat Group, Fox River Belt and Molson dykes is inferred to have occurred via the ATA mechanism in magma conduits at upper crustal levels. The crustal contamination mechanism inferred for the magmatism in the Lake Superior region is assimilation with concomitant fractional crystallisation (AFC) in large magma chambers situated at deep crustal levels (see section 5.3). In large magma chambers the flow of magma may not be dynamic or turbulent enough such that the magma

may not interact sufficiently with the wall rock to incorporate large amounts of sulphur (e.g. Huppert & Sparks, 1985). Maier & Barnes (2005) also note that large magma chambers often do not provide suitable traps for sulphide to accumulate and scavenge metals so that even if magma in a large chamber contains sulphides, the sulphides will not become concentrated enough to produce an economically viable ore deposit. Therefore rather than simply searching for a general crustal contamination signature when trying to locate ore deposits, it may be more beneficial to identify signatures of ATA such as low Nb/Th ratios at high MgO concentrations or low $^{143}Nd/^{144}Nd_i$ ratios at constant Nd concentrations.

The lack of a contamination signature can not be taken as an indication of a lack of mineralisation. The Hellancourt Formation basalts do not show any elemental or isotopic evidence for crustal contamination but their feeder sills, the Montagnais intrusions, are associated with sulphide mineralisation. The εNd_i values of the Hellancourt basalts obtained for the current study and in previous studies (Smith & Ludden, 1989; Rohon et al., 1993; Skulski et al., 1993) are all positive which is indicative of a depleted mantle source unaffected by crustal contamination. The only isotopic evidence for contamination comes from an intrusive dolerite dyke that has an εNd_i value of -2.99 (Skulski et al., 1993). None of the Montagnais sills samples analysed by previous studies have εNd_i <2.06 which suggests that none of these sills have been contaminated. The lack of a contamination signature could be a consequence of an unfortunate sampling bias or could indicate that crustal contamination was not required to bring the Hellancourt Formation magma to sulphur saturation.

It may be possible that the Hellancourt Formation magmas reached sulphide saturation passively through extensive cooling and fractional crystallisation. This may be consistent with the presence of reef-like horizons of PGE-rich sulphides in some of the differentiated Montganais sills (Clark, 2001), which potentially can be derived through passive sulphide saturation (Mungall, 2005). The most evolved basalt of the Hellancourt Formation (MMLT07-12) can be modelled as the product of 71% fractional crystallisation of the Chukotat Group primary magma (see section 5.2.10). Mavrogenes & O'Neill (1999) predicted that a basaltic melt formed from the partial melting of primitive mantle containing 200 ppm S would require at least 60%

fractional crystallisation to become sulphide saturated. This figure is probably a minimum as the prediction did not consider the effect of fractional crystallisation on the composition of the melt which will alter the solubility of sulphur. The example of Mavrogenes & O'Neill (1999) is also for basalt formed from mantle at a potential temperature of 1350°C which is considerably lower than any estimates for the mantle potential temperature of the Circum-Superior LIP (see section 5.6). Therefore the calculated figure for the maximum degree of fractional crystallisation of the Hellancourt Formation (71%) is probably insufficient to bring the Hellancourt magma to sulphide saturation, especially considering that the basalts of the barren Winnipegosis Belt are modelled as the products of up to 65% fractional crystallisation (section 5.2.6). The trigger for sulphide saturation in the Labrador Trough remains enigmatic.

5.8.5. Involvement of the subcontinental lithospheric mantle

Zhang et al. (2008) suggested that fertile LIPs show geochemical evidence for interaction between ascending mantle plumes and ancient cratonic lithospheric mantle. The authors demonstrated that many fertile LIPs contain an EM1-like signature and interpreted this signature to be derived from subcontinental lithospheric mantle which also enhances the Ni, Cu and PGE content of rising plumes. The geochemical and isotopic data obtained for the current study do not necessitate the involvement of subcontinental lithospheric mantle in the petrogenesis of the Circum-Superior LIP magmas. The geochemical signatures of the Circum-Superior LIP rocks can be modelled using crustal material as potential contaminants (see section 5.3). There is also no obvious indication of an EM1-like signature in any of the Circum-Superior LIP rocks let alone in rocks from the ore-bearing segments. The predicted scenario for the fertile segments is that hot, primitive magmas were selectively contaminated during their transportation through relatively thin magma conduits in the upper crust. If the proposed plume had interacted with subcontinental lithospheric mantle on its ascent then contamination of plume material would presumably have been more wholesale than if contamination occurred in upper crustal conduits and the contamination signature would be much more prevalent in the volcanic rocks.

Ellam et al. (1992) combined Re-Os and Sm-Nd isotope systematics to show that picrites of the Nuanetsi region of the Karoo flood basalt province were generated by melting of sub-lithospheric (?plume) material contaminated with subcontinental lithospheric mantle. Ellam et al. (1992) argued that the low εNd_i and γOs_i of the Karoo picrites is more consistent with interaction with subcontinental lithospheric mantle than continental crust as the latter should generate signatures of low εNd_i and high γOs_i. Unfortunately attempts to obtain $^{187}Os/^{188}Os$ ratios from samples of the Circum-Superior LIP yielded erratic results which do not allow for any coherent interpretations to be made. However, Maier & Barnes (2005) have highlighted a number of examples of magmatic sulphide deposits where $^{187}Os/^{188}Os$ results do not correlate with other geochemical and isotopic indicators, suggesting that Os isotopes are perhaps not always a powerful discriminating tool.

5.8.6. Summary

The Circum-Superior LIP contains segments which are fertile with respect to Ni-Cu-PGE sulphide deposits (Cape Smith Belt, Fox River Belt, Thompson Nickel Belt, Molson dykes and Labrador Trough) and segments which are barren (Hudson Bay, Winnipegosis Belt and Lake Superior). Methods used in previous studies on other LIPs which utilise the whole-rock geochemistry of volcanic rocks associated with ore mineralisation cannot accurately or consistently discriminate between the fertile and barren segments of the Circum-Superior LIP. Crustal contamination was probably an important process in the formation of ore deposits, particularly the mechanism by which it occurred. Contamination of magma of the Chukotat Group, Fox River Belt, Thompson Nickel Belt and Molson dykes is envisioned to have occurred during turbulent ascent in relatively thin magma conduits at upper crustal levels rather than in large magma chambers deeper in the crust where contamination of the barren Lake Superior magmas is thought to have occurred. Therefore exploration for ore deposits should probably concentrate on identifying signatures of assimilation during turbulent ascent (ATA) (e.g. high MgO and low Nb/Th, low $^{143}Nd/^{144}Nd_i$ and low Nd) rather than more general signatures of contamination (e.g. negative Nb-Ta anomalies) in order to identify regions of LIPs which are likely to have a higher economic potential, although the lack of a contamination signature should not be taken as evidence for a lack of sulphide mineralisation (e.g. Hellancourt Formation).

Zhang et al. (2008) suggested that the subcontinental lithospheric mantle has an important role in the fertility potential of LIPs but there is no clear evidence to suggest that the subcontinental lithospheric mantle played an important role in the petrogenesis of the Circum-Superior LIP, although this cannot be conclusively ruled out.

5.9. Distribution of ~1880 Ma magmatism around the cratonic margins of the Superior Province

The location of the majority of the Circum-Superior LIP magmatic rocks along the cratonic margins of the Superior Province has been used as an argument against a mantle plume origin for this LIP (French et al., 2008; Heaman et al., 2009). However, it seems inappropriate to preclude a plume origin purely on the basis of the cratonic margin location of the igneous rocks given that plumes are predicted to be large (plume head diameter >1000 km) and to originate from the core-mantle boundary (Campbell, 2007) and so may initially impinge beneath lithosphere in any tectonic environment. The discussion below focuses mainly on mechanisms consistent with the mantle plume hypothesis which may be able to explain the location of ~1880 Ma magmatic rocks around the margins of the Superior Province.

5.9.1. Flattened plume head with a large diameter under the centre of the craton

The Superior Province is ~2000 km long between its most northerly and southerly points and ~2000 km wide between its most westerly and easterly points (Fig. 2.2). Griffiths & Campbell (1990) and Campbell (2007) predicted that mantle plumes originating from the core-mantle boundary can have a maximum head diameter of ~2000-2500 km once the plume flattens beneath the lithosphere. A plume head with these dimensions is approximately the same size as the Superior Province (Fig. 5.48a) and if the plume centre point impinged beneath the centre of the craton then the margins of the plume could have melted to form the Circum-Superior LIP. However, an argument against this theory is that there is a lack of ~1880 Ma magmatic rocks located on the southern side of the Superior Province, particularly on its southeastern margin (Fig. 2.2). If a large plume head impinged beneath the centre of the craton and the plume margins melted then it seems odd that no magmatism is

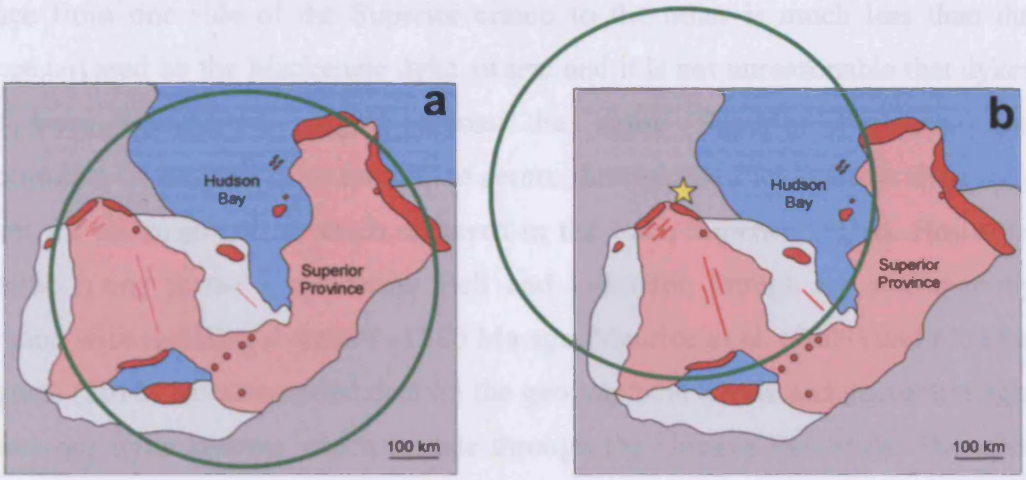

Fig. 5.48. Diagrams of the Superior Province showing the location of a mantle plume head (green circle) with a diameter of 2000 km impinging under different parts of the craton. The ~1880 Ma Circum-Superior LIP magmatic rocks are shown as red segments, lines and circles. In (a), the plume head impinges beneath the centre of the craton. In (b), the plume head impinges on lithosphere just north of the northwest craton margin. The yellow star in (b) represents the plume centre suggested by Buchan et al. (2003) which the Molson, Pickle Crow and Fort Albany dykes converge back to.

preserved on the southeast craton margin given that all the other margins of the craton have also been affected by orogenic events and still preserve ~1880 Ma magmatic rocks. A further argument is that the Molson dykes, Pickle Crow dyke and Fort Albany dykes possibly form a radiating dyke swarm which converge to a focal point just to the north of the northwest Superior Province margin (Fig. 5.48b), suggesting that the plume impinged beneath this part of the craton and not directly beneath the centre of the craton.

5.9.2. Magma transportation via dykes

As mentioned above, the Molson dykes, Pickle Crow dyke and Fort Albany dykes converge back to a focal point just north of the northwest Superior Province margin (Fig. 5.48b) which has been suggested to be the site of the plume centre responsible for the Circum-Superior LIP (Buchan et al., 2003; Hamilton & Stott, 2008). Radiating dyke swarms are commonly linked to mantle plumes and are often used to infer the location of the centre of the plume head (Ernst et al., 1995; Ernst & Buchan, 2003). The radiating dykes can transport magma for huge distances from the plume centre, the longest known on Earth being the ~1270 Ma Mackenzie dyke swarm which extends ~2500 km southeastwards throughout the Canadian Shield from its hypothesised plume centre (Ernst & Baragar, 1992; Baragar et al., 1996). The

distance from one side of the Superior craton to the other is much less than the distance covered by the Mackenzie dyke swarm and it is not unreasonable that dykes could have transported magma across the entire Superior Province. The transportation of magma from the plume centre through the Pickle Crow dyke may account for the magmatism which occurred in the Lake Superior region. However, magmatic rocks in the Cape Smith Belt and Labrador Trough are not spatially associated with radiating dykes of ~1880 Ma age. Maurice et al. (2009) and Maurice & Francis (2010) have compiled data on the geographical trends and geometric ages of numerous dyke swarms which intrude through the Ungava Peninsula. The dyke swarms have ages of 2.00-2.51 Ga and none have trends which are consistent with derivation from a plume centre near the northwest margin of the Superior Province. The presence of ~1880 Ma dykes in the Ungava Peninsula cannot totally be ruled out without further geological mapping and U-Pb geochronological work but presently there is a lack of evidence to suggest that the ~1880 Ma magmatism surrounding the Ungava Peninsula was fed by dykes radiating from a plume centre near the northwest Superior Province margin.

5.9.3. Deflection of plume material to regions of thinner lithosphere

Seismic studies have suggested that the thickness of the cratonic root of the Superior Province may be ~300 km (van der Lee & Nolet, 1997; Jaupart et al., 1998; Sol et al., 2002). The major element chemistry of the primary magmas from the Chukotat Group, Fox River Belt, Winnipegosis Belt and Molson dykes indicates that melting in these regions occurred at pressures ranging from 3.8 to 6 GPa which correspond to a range in the depth of melting of ~115-180 km (see section 5.5). Large scale melting therefore did not occur under the thickest lithosphere of the Superior Province.

Thompson & Gibson (1991) postulated that plume material ascending under continental lithosphere in particular may be diverted hundreds of kilometres away from the plume axis to areas where the lithosphere has been previously thinned (thinspots) (Fig. 5.49a). Thompson & Gibson (1991) used the British Tertiary Igneous Province, Parana flood basalts and Columbia River basalts as examples and cautioned that the location of volcanic rocks does not necessarily mark the site of where mantle plumes impinge on the base of the lithosphere. Johnston & Thorkelson

(2000) have also suggested that in regions of differing lithosphere thickness, plume material will migrate to thinspots where large amounts of decompressive melting can occur. Numerical models support the models of Thompson & Gibson (1991) and Johnston & Thorkelson (2000) and show that plume material may flow quickly and laterally along the base of the lithosphere several hundreds of kilometres away from the site of initial impingement (Sleep, 1996, 1997, 2003, 2008; Ebinger & Sleep, 1998; Sleep et al., 2002). In particular, Sleep et al. (2002) have modelled the effects of cratonic keels on plume magmatism and shown that keels will deflect plume material and focus flow up the steep gradients and focus melting along the cratonic boundaries (Fig. 5.49b).

The transport and melting of plume material beneath thinner lithosphere is consistent with the model of Maurice et al. (2009) for the evolution of the lithosphere beneath the Ungava Peninsula. In this model, the lithosphere at ~2.5 Ga is up to ~300 km thick below the Ungava Peninsula. At ~2.2 Ga the transformation of basaltic lower crust into amphibolite, granulite, garnet pyroxenite and eclogite assemblages increases the density such that the lithospheric keel becomes gravitationally unstable and detaches. This triggers decompression melting and produces several dyke swarms (Maguire, Anuc and Kogaluk Bay dykes) with enriched trace element and isotopic compositions. By ~1.9 Ga the detached Archaean lithosphere is replaced by metasomatically enriched Palaeoproterozoic lithosphere which is considerably thinner and only ~50 km thick directly below the Cape Smith Belt. The eruption and intrusion of igneous rocks related to the Povungnituk Group occurred between ~2038 Ma and ~1959 Ma (Parrish, 1989; Machado et al., 1993). The Povungnituk Group magmatism is commonly interpreted as a product of the rifting of the Superior Province margin (e.g. Baragar & Scoates, 1981; Francis et al., 1983; Picard et al., 1990; St-Onge & Lucas, 1993) and would also have led to thinning of the lithosphere directly beneath the Cape Smith Belt prior to the ~1880 Ma Circum-Superior magmatic event. The first cycle magmatism in the Labrador Trough has an age constraint of 2169-2142 Ma (Rohon et al., 1993) and may also reflect rifting and thinning of the lithosphere beneath the northeastern margin of the Superior Province ~260-290 m.y. prior to the Circum-Superior LIP magmatism. On the western side of the Ungava Peninsula on the Belcher Islands, the Flaherty Formation is separated from the younger Eskimo Formation basalts by ~3 km of sediments. The Eskimo

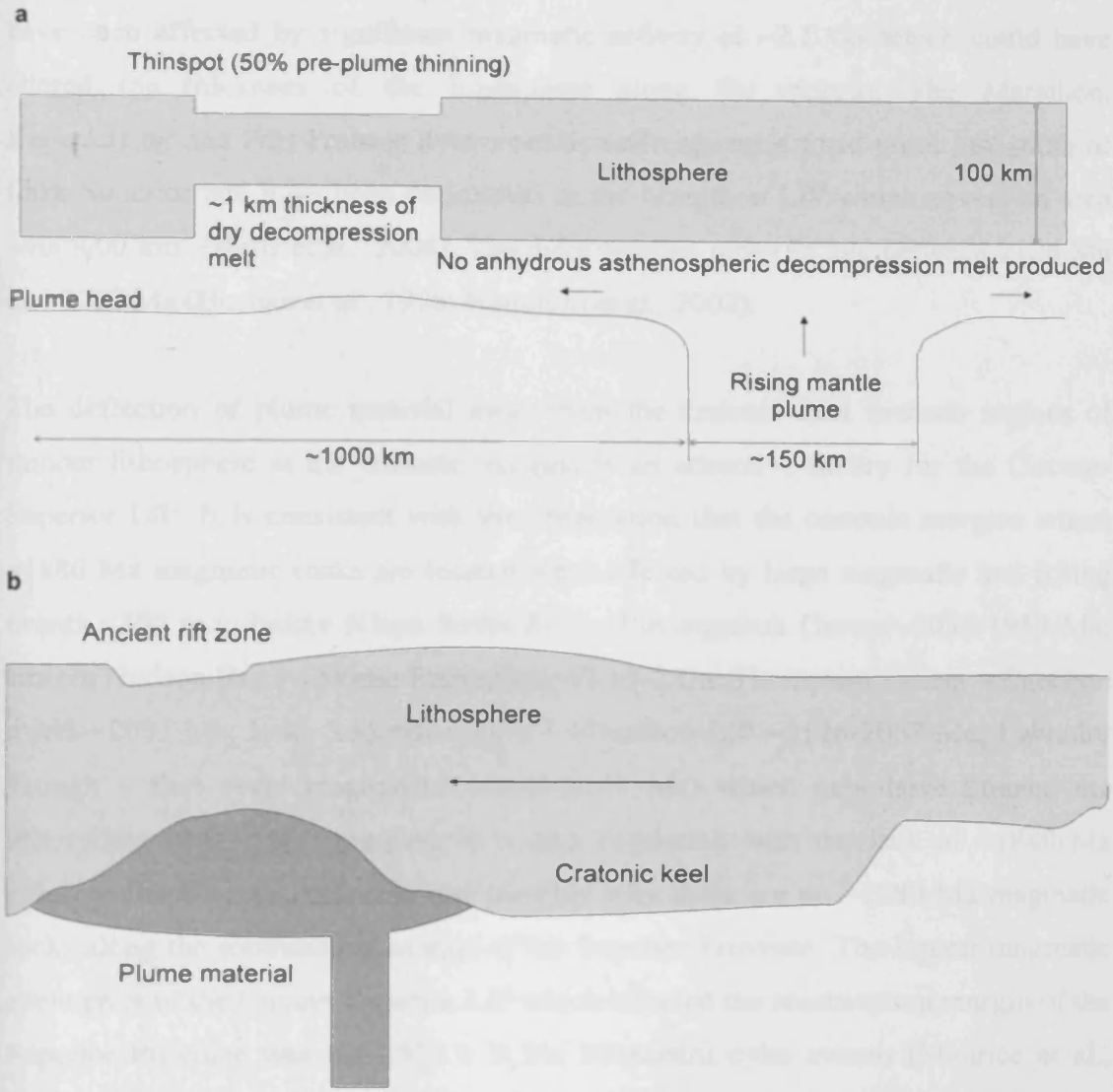

Fig. 5.49. Schematic diagrams demonstrating the influence of differing lithosphere thickness on a mantle plume. Hot plume material tends to be deflected away from thick lithosphere such as cratonic keels and towards regions of thinner lithosphere having undergone previous rifting events. Diagram (a) is from Thompson & Gibson (1991) and diagram (b) is from Sleep et al. (2002).

basalts are currently undated but have chemical similarities with 2.15-2.00 Ga Riviere du Gue, Lac Esprit and Minto dyke swarms on the western edge of mainland Ungava Peninsula (Maurice et al., 2009). There is also evidence of rifting near the northwest Superior Province margin ~200 m.y. before the onset of Circum-Superior LIP magmatism which may have thinned the lithosphere in this region. The evidence for rifting is the presence of the Cauchon dykes which have an age of 2091 ± 2 Ma (Halls & Heaman, 2000) and can be distinguished from the Molson dykes by their east-northeasterly trend and palaeomagnetic pole position (Zhai et al., 1994; Halls & Heaman, 2000). The southwestern margin of the Superior Province also appears to

have been affected by significant magmatic activity at ~2.1 Ga which could have altered the thickness of the lithosphere along the margin. The Marathon, Kapuskasing and Fort Frances dyke swarms converge on a focal point just south of Lake Superior and have been designated as the Marathon LIP which covers an area ~400,000 km^2 (Halls et al., 2008). The dyke swarms range in age between 2126 Ma and 2067 Ma (Buchan et al., 1996; Hamilton et al., 2002).

The deflection of plume material away from the cratonic keel towards regions of thinner lithosphere at the cratonic margins is an attractive theory for the Circum-Superior LIP. It is consistent with the observation that the cratonic margins where ~1880 Ma magmatic rocks are located were affected by large magmatic and rifting events <300 m.y. before (Cape Smith Belt – Povungnituk Group ~2038-1959 Ma; eastern Hudson Bay – Eskimo Formation ~?2.15-2 Ga; Thompson Salient – Cauchon dykes ~2091 Ma; Lake Superior region – Marathon LIP ~2126-2067 Ma; Labrador Trough – first cycle magmatism ~2169-2142 Ma) which may have thinned the lithosphere under these margins. It is also consistent with the lack of ~1880 Ma dykes in the Ungava Peninsula and possibly why there are no ~1880 Ma magmatic rocks along the southeastern margin of the Superior Province. The largest magmatic event prior to the Circum-Superior LIP which affected the southeastern margin of the Superior Province was the 2515 ± 3 Ma Mistassini dyke swarm (Maurice et al., 2009). The Circum-Superior LIP is therefore ~630 m.y. younger than the Mistassini dykes, a time span which perhaps was long enough to allow the lithosphere beneath the southeast Superior Province margin to thicken sufficiently such that it was unfavourable for plume material to flow along the base of this lithosphere.

The carbonatites found along the Kapuskasing Structural Zone (Fig. 2.22) could indicate that the plume responsible for the ultramafic-mafic magmatism along the cratonic margins was present under more central parts of the craton as well. Bell (2001) and Bell & Simonetti (2010) have suggested that some carbonatites are formed from low degrees of partial melting of the cooler outer margins of plumes which are volatile-rich beneath thick lithosphere. The Cargill Township and Goldray carbonatite complexes are slightly older than the ultramafic-mafic magmatism (see Table 2.1). The early emplacement of carbonatites has also been documented in other LIPs such as the Parana flood basalts and Bushveld Igneous Complex (Gibson et al.,

2006; Ernst & Bell, 2010). It is envisioned for the Circum-Superior LIP event that the Kapuskasing Structural Zone acted as a zone of mechanical weakness and a pathway to the surface for low viscosity carbonatitic magma produced by low degrees of melting of plume material. However, to test this idea detailed isotopic analyses from the carbonatite complexes are required for comparison with the ultramafic-mafic rocks along the cratonic margins. More precise ages are also required from the Argor and Carb Lake carbonatite complexes to link these with the Circum-Superior LIP.

A good relatively recent example of the control that the lithosphere has on the partial melting of plume material and the spatial distribution of plume-generated volcanic rocks is the 45 Ma to present east African magmatism. The numerical model of Ebinger & Sleep (1998) is able to explain how a single mantle plume could have supplied the Afar hotspot, Cameroon hotspot, various northern Africa hotspots and the Comoros hotspot with the lateral flow of plume material along thinned lithosphere in pre-existing rifts for hundreds of kilometres from the plume source. The deflection of plume material by a thick cratonic keel towards thinner lithosphere at a rifted craton margin has also been advocated for komatiites and basalts of the ~2.7 Ga Kambalda Sequence in the Kalgoorlie Terrane in the Yilgarn craton of Western Australia (Said & Kerrich, 2009, 2010a, 2010b; Said et al., 2010).

5.9.4. Non-plume-related edge-driven convection

An alternative explanation to the mantle plume hypothesis for the occurrence of LIPs close to the edges of Archaean cratons was advocated by King & Anderson (1995). In their model the thick cratonic lithosphere insulates the underlying asthenospheric mantle which then flows out sideways from under the craton, upwells, decompresses and melts under thinner continental lithosphere. King & Anderson (1998) developed this model further and coined the term edge-driven convection. In edge-driven convection a secondary convection cell is set up adjacent to a sharp change in lithospheric thickness (e.g. a craton margin) where locally the asthenosphere cools against the edge and sinks which creates the adjacent upwelling of mantle. These models do not require mantle temperatures as hot as for the plume model.

The edge-driven convection model may be more appropriate for some magmatic provinces than the mantle plume model (King, 2007) but it does not seem applicable to the Circum-Superior LIP. As noted by Saunders et al. (2005), the edge-driven convection model has no obvious trigger or switch off mechanism and could potentially last for several tens of millions of years, unlike the ~15 m.y. for the majority of ultramafic-mafic magmatism of the Circum-Superior LIP or ~21 m.y. if the last manifestation of magmatism (Winnipegosis Belt) is included. The presence of magmatic rocks (i.e. mafic dykes and carbonatite complexes) in the interior of the Superior Province craton is inconsistent with the edge-driven convection model which has no mechanism for generating magmatism away from the craton margins. It is also hard to envisage how the high MgO picrites of the Circum-Superior LIP can be produced without the high mantle potential temperatures of a plume, especially at the high pressures calculated in section 5.5. If the mantle source region contained high amounts of water or were composed of fertile eclogitic components, as suggested by King & Anderson (1995, 1998), then this would be inconsistent with the modelling in section 5.1 which shows that primary magmas of the Circum-Superior LIP can be derived from volatile-free peridotite source regions. Further arguments against the edge-driven convection model for the formation of several other LIPs are given in Reichow et al. (2005), Saunders et al. (2005, 2007) and Storey et al. (2007).

5.9.5. Summary

The Circum-Superior LIP is an unusual LIP in that much of it is constrained to the cratonic margins of the Superior Province. Edge-driven convection is considered an unlikely mechanism to have formed the LIP. Part of a possible radiating dyke swarm emanating from the northwest margin of the Superior Province is represented by the Molson, Pickle Crow and Fort Albany dykes. It is possible that the magmatism in the Lake Superior region was fed via the Pickle Crow dyke from a plume centre near the northwest cratonic margin. However, no ~1880 Ma dykes have been found in the Ungava Peninsula suggesting the magmatism in this region was not fed through radiating dykes, although this possibility cannot be completely ruled out without further geochronological dating of dyke swarms in the area. The favoured mechanism for the distribution of the Circum-Superior LIP is the deflection of plume

material by the thick Superior Province cratonic keel towards the cratonic margins where thinner lithosphere existed due to previous magmatic and rifting activity.

5.10. Arguments of Heaman et al. (2009) against a mantle plume origin for the Circum-Superior LIP

Heaman et al. (2009) recently suggested that the Circum-Superior LIP formed either via the upwelling of asthenosphere in pull-apart or back-arc basins or from the passive flow of asthenosphere beneath the thinned margin of the Superior Province which experienced continental rifting hundreds of million years earlier. Heaman et al. (2009) linked the upwelling of asthenosphere to changes in plate boundary stress initiated by subduction near the western margin of the Superior Province. The five arguments documented by Heaman et al. (2009) against a plume-related origin for the Circum-Superior LIP are:

i. The lack of a convincing giant radiating dyke swarm
ii. The lack of evidence for uplift prior to volcanism
iii. The lack of a subsequent hotspot track
iv. The wide distribution of ultramafic-mafic magmatic rocks along the cratonic margins of the Superior Province
v. The absence of an OIB-like geochemical signature

The merits of these five arguments are discussed below.

5.10.1. The lack of a convincing giant radiating dyke swarm

In their argument, Heaman et al. (2009) only recognised a dyke swarm formed by the Molson and Pickle Crow dykes. A more convincing radiating dyke swarm exists when the Fort Albany dykes are included (Fig. 5.48b). Together the Molson, Pickle Crow and Fort Albany dykes form a radiating fan with ~100° of arc which converges back to a focal point just to the north of the northwest margin of the Superior Province. Admittedly this is not a complete radiating dyke swarm as no dykes of the correct age and trend have been recognised in the Ungava Peninsula. It may be possible that such dykes await discovery amongst the multitude of dykes present in

the Ungava Peninsula (Buchan & Ernst, 2004; Maurice et al., 2009; Maurice & Francis, 2010) but until such a discovery, if it ever happens, there is only a partially radiating dyke swarm of ~1880 Ma age within the Circum-Superior LIP. This radiating dyke swarm most closely matches the second geometrical type of giant radiating dyke swarms identified by Ernst et al. (1995) and Ernst & Buchan (1997, 2001b) and termed a fanning pattern subdivided into separate subswarms. The Molson, Pickle Crow and Fort Albany dykes fan over an arc of ~100° which is equal to or greater than many other dyke swarms assigned to a plume origin including the ~17 Ma Columbia River dykes (60°), ~88 Ma Madagascar dykes (90°), ~100 Ma Alpha Ridge dykes (90°), ~250 Ma Siberian Traps dykes (130°), ~1270 Ma Mackenzie dykes (100°), ~2450 Ma Matachewan dykes (45°) and ~2515 Ma Mistassini dykes (35°) (Ernst & Buchan, 2001b).

A possible reason why no ~1880 Ma dykes have been located in the Ungava Peninsula is that this region lies beyond the extent of a 2000 km diameter plume head impinging beneath the northwest margin of the Superior Province (Fig. 5.48b). Dykes of an appropriate age and trend may be expected in the regions now occupied by Hudson Bay and the Hearne and Rae Provinces but the only other known ~1880 Ma dykes in the Canadian Shield are the Ghost dykes of the Slave craton (Davis & Bleeker, 2007). The Ghost dykes, however, have a markedly different geochemistry to the Molson and Pickle Crow dykes (Figs. 4.58 and 5.51b) which may be more consistent with a subduction-related origin during the collisional phase of the Wopmay Orogen (Davis & Bleeker, 2007). Other ~1880 Ma dykes occur in India and southern Africa but neither of these continental blocks is considered to have been in close proximity to the Superior Province during the existence of the supercontinent Columbia (Fig. 5.52). The geochemistry of the Indian and southern Africa dykes is also markedly different to the Molson and Pickle Crow dykes (section 5.11.1) which supports the derivation of the dykes from different mantle sources.

5.10.2. The lack of evidence for uplift prior to volcanism

The mantle plume hypothesis predicts that flood volcanism should be preceded by domal uplift of the crust of up to ~1000 m above the plume axis (Campbell, 2007).

Heaman et al. (2009) correctly noted that there is a lack of evidence for uplift in the rocks underlying the Circum-Superior LIP magmatic rocks. There is no obvious indication of crustal uplift in the underlying sedimentary sequences in terms of lithological changes, sedimentary facies changes or erosional surfaces. Condie et al. (2000) suggested that sea level at ~1.9 Ga was relatively high on the basis of a peak in the restored cumulative area of marine intracratonic, passive margin and platform sediments. If the margins of the Superior Province were sufficiently submerged prior to volcanism, then it may be that any uplift associated with the arrival of a mantle plume beneath the lithosphere might not have been significant enough to raise the site of deposition to above sea level or even to shallow water depths.

However, previous studies have argued that the sediments in the Thompson Nickel Belt and Fox River Belt and on the Belcher Islands are indicative of shallow rather than deep water coverage on the Superior Province margins (Ricketts & Donaldson, 1981; Heaman et al., 2009) such that any plume-induced crustal uplift should at least be recognisable in changes of sedimentary facies. The lack of uplift could possibly be a consequence of diverting plume material in different directions away from the initial site of plume impingement towards the thin cratonic margins as suggested in section 5.9.3. The idea of plume-induced uplift is based upon a plume head impinging beneath flat lithosphere and so the diversion of plume material to different areas possibly may not cause significant uplift of the crust in these areas. However, this is speculative as there are no known existing numerical models which take into account such a scenario. The lack of evidence for uplift is also problematic for non-plume theories such as edge-driven convection. King & Anderson (1995) argued that edge-driven convection should produce uplift along a zone parallel to the change in lithospheric thickness which creates the convection cell.

Weak evidence for crustal uplift exists on the western coast of the Ungava Peninsula and on the Hudson Bay islands. The Richmond Gulf Group is located on the eastern side of Hudson Bay and the west coast of the Ungava Peninsula. It consists of arkosic sediments of the Pachi and Qingaaluk Formations with intervening basaltic flows of the Persillon Formation (Chandler, 1988). Unconformably overlying the Richmond Gulf Group is the Nastapoka Group which consists of a lower unit of quartz-arenites and carbonates and an upper unit of ~230 m of basalt (Chandler,

1988). Chandler (1988) obtained palaeocurrent directions from trough cross-bedding in the Pachi and Qingaaluk Formations and palaeo-flow directions from pipe amygdales and vesicles in the Persillon Formation which indicate easterly to southeasterly flow down the flanks of a thermal dome with a central peak somewhere to the west. A major problem with linking this doming to the Circum-Superior magmatism is that the rocks of the Richmond Gulf and Nastapoka Groups may be too old. There is not a sufficient amount of reliable and precise age data currently available to conclusively prove this but the data which do exist suggest the Richmond Gulf and Nastapoka Groups are significantly older than the Circum-Superior LIP. Chandler & Parrish (1989) published a U-Pb age of 2025 ± 25 Ma for diagenetic apatite cement from sandstone near the base of the Richmond Gulf Group. No reliable age determinations have been made on the igneous rocks but the geochemistry of the Nastapoka basalt shows similarities to the chemical signatures of the Eskimo Formation on the Belcher Islands (Legault et al., 1994) which suggests that doming occurred prior to an earlier igneous episode than the Circum-Superior LIP. However, Ricketts et al. (1982) have suggested that the Flaherty Formation was also erupted onto an east-dipping palaeoslope. The evidence for such a palaeoslope includes an increase in the proportion of volcaniclastic rocks towards the east and the inclination of pipe vesicles and ropy flow surfaces to the east (Ricketts et al., 1982). Therefore the Flaherty Formation could possibly have been erupted along the flanks of a dome produced by plume-induced crustal uplift.

Ali et al. (2010) have challenged the notion that domal uplift prior to volcanism is a diagnostic feature of mantle plumes. Ali et al. (2010) used biolithostratigraphical, petrological, geochemical and volcanological data to support a mantle plume origin for the Emeishan LIP in China despite a lack of strong evidence for large-scale domal uplift prior to volcanism. Ali et al. (2010) concluded that the effect of a mantle plume on surface topography can be modified by the plume's thermochemical structure, how the plume transfers through the 660 km discontinuity, and how the plume interacts with lithosphere of contrasting structure, topography and rheology. Kerr & Mahoney (2007) also noted that mantle plumes containing a significant portion of compositionally dense material (thermochemical plumes) will have a reduced net buoyancy flux and will not cause significant topographic uplift. Kerr & Mahoney (2007) speculated that a thermochemical plume was responsible for the

lack of uplift associated with the Ontong Java Plateau. Therefore the lack of strong evidence for uplift prior to volcanism may not be a strong argument against a mantle plume origin for the Circum-Superior LIP.

5.10.3. The lack of a subsequent hotspot track

There is no known ~1880 Ma hotspot track associated with the Circum-Superior LIP unlike for many Phanerozoic LIPs which often have chains of volcanic islands or provinces extending away from them. Overall there is an extreme lack of hotspot tracks recognised in the Precambrian geological record. The only known published occurrence of a Precambrian hotspot track is from Australia where ~1600-1500 Ma A-type granites and felsic volcanic rocks form a ~1500 km long palaeo-curvilinear belt (Betts et al., 2007). The lack of Precambrian hotspot tracks does not seem surprising given the length of time available for lithospheric reworking, movement of tectonic plates and erosion and metamorphism of volcanic rocks to either completely remove or fragment any hotspot track. Kerr & Mahoney (2007) also noted that some thermochemical plumes with low buoyancy ratios may have thin tails which break off easily and quickly from the head as the plumes rise through the mantle, thus producing no hotspot tracks. Therefore the lack of a hotspot track associated with the Circum-Superior LIP is not a conclusive argument against a mantle plume origin for the ~1880 Ma magmatic rocks.

5.10.4. The wide distribution of ultramafic-mafic magmatic rocks along the cratonic margins of the Superior Province

Heaman et al. (2009) noted that the distribution of ultramafic-mafic magmatism along a cratonic margin for a composite strike length of >3000 km is unusual for a flood basalt province and has no modern or ancient exact analogue. The presence of LIPs on or near cratonic margins is not uncommon and examples include the 0-45 Ma east African magmatism on the northeast margin of the Tanzania craton (Ebinger & Sleep, 1998), the ~180 Ma Karoo LIP and igneous events of various other ages on the margins of the Kaapvaal and Zimbabwe cratons (Jourdan et al., 2007; Klausen et al., 2010), the ~260 Ma Emeishan LIP on the western margin of the Yangtze craton (Saunders et al., 2007), and the ~1100 Ma Keweenawan flood basalts on the southern

margin of the Superior craton (Vervoort et al., 2007). As discussed in section 5.9.3, plume material can be deflected and transported along the base of the lithosphere to regions where lithosphere is considerably thinner, perhaps as a result of a previous rifting event (e.g. Thompson & Gibson, 1991; Sleep et al., 2002; Sleep, 2008). The numerical model of Ebinger & Sleep (1998) is able to link the majority of ~0-45 Ma east African hotspots to a single plume with the transportation of plume material several hundreds of kilometres to lithospheric thinspots. Volcanic rocks of the ~200 Ma East Coast Margin Igneous Province along the eastern coast of USA and Canada have been interpreted by Sleep (1997) to have formed from a single mantle plume which impinged beneath northeast Florida despite the large extent of the province. The volcanic rocks from Nova Scotia are >2000 km away from the postulated source and were erupted from plume material transported along lithospheric conduits created by rifting (Sleep, 1997).

If the Circum-Superior LIP formed from a mantle plume which impinged beneath the northwest margin of the Superior Province then the distances which plume material would have to be transported to feed magmatism in the Cape Smith Belt and Labrador Trough are comparable to those modelled by Sleep (1997) for the East Coast Margin Igneous Province. Therefore the widespread distribution of magmatic rocks along the Superior Province margins is not a conclusive argument against a mantle plume source for the Circum-Superior LIP.

5.10.5. The absence of an OIB-like geochemical signature

Heaman et al. (2009) argued that a lack of an OIB-like geochemical signature in the Molson dykes and Thompson Nickel Belt sills is not consistent with a mantle plume origin for these rocks and the Circum-Superior LIP. OIB typically has high concentrations of incompatible trace elements and fractionated multi-element profiles with or without positive Nb-Ta anomalies (Fig. 5.50). Such trace element signatures are also absent from the Ontong Java Plateau and rare in many other Phanerozoic oceanic plateaux even though the isotopic compositions of these LIPs share similarities with OIB (Kerr, 2003; Fitton & Goddard, 2004). Therefore an OIB-like trace element signature is not necessarily abundant or present in plume-derived

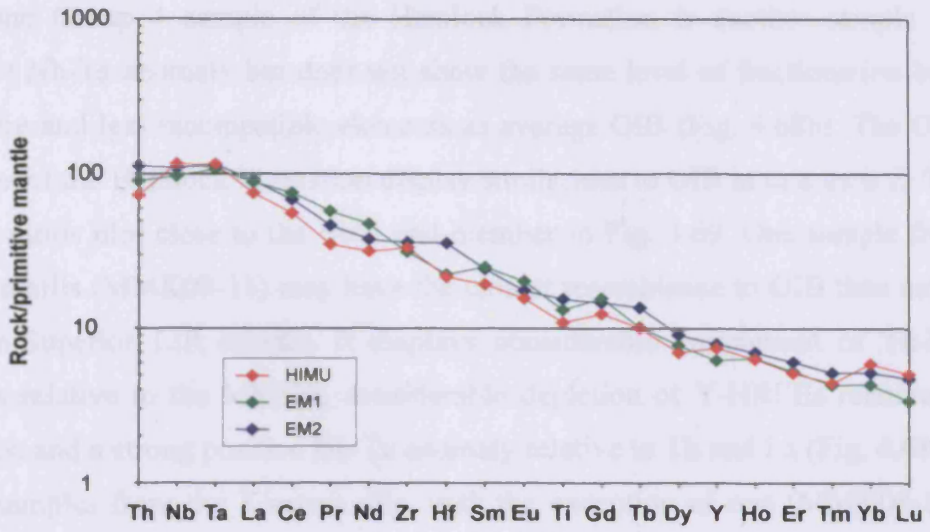

Fig. 5.50. Primitive-mantle-normalised multi-element profiles of the three different OIB end-members. Data sources for the different OIB end-members given in Fig. 4.19. Primitive mantle values from Sun & McDonough (1989).

LIPs and the lack of such a signature is not proof against a plume-related origin (cf. Kerr et al., 1995b).

Heaman et al. (2009) were correct in noting that none of the northwest margin Circum-Superior LIP samples possess a trace element signature which strongly resembles OIB. The results of the current study also show that a strong OIB-like chemical signature is not present throughout the whole of the Circum-Superior LIP. However, the current study shows that some samples from the Flaherty Formation, Haig sill, Molson dykes, Hemlock Formation and Kiernan sills have similarities to OIB. Samples from Group 1 of the Flaherty Formation have multi-element profiles with positive Nb-Ta anomalies (Fig. 4.18a) which are also seen in HIMU OIB (Weaver, 1991), although the Zr/Nb and Nb/Th ratios of Group 1 of the Flaherty Formation are more similar to E-MORB than HIMU (Fig. 4.19). Group 2 of the Flaherty Formation have similar multi-element profiles to Group 1 except for the Nb-Ta anomalies (Fig. 4.18b). The Zr/Nb and Nb/Th ratios of the Group 2 samples are similar to those of EM2 OIB (Fig. 4.19). The Haig sill also possesses positive Nb-Ta anomalies (Fig. 4.18c) and Zr/Nb and Nb/Th ratios similar to EM1 OIB (Fig. 4.19). One Molson dyke sample (MMM07-7) also has a positive Nb-Ta anomaly (Fig. 4.58b) but unlike HIMU OIB does not show any significant fractionation between the more and less incompatible elements with the exception of the Nb-Ta anomaly.

The lone Group 4 sample of the Hemlock Formation is another sample with a positive Nb-Ta anomaly but does not show the same level of fractionation between the more and less incompatible elements as average OIB (Fig. 4.68b). The Group 3 samples of the Hemlock Formation display similarities to OIB in that their Zr/Nb and Nb/Th ratios plot close to the EM2 end-member in Fig. 4.69. One sample from the Kiernan sills (MMK08-11) may have the closest resemblance to OIB than any other Circum-Superior LIP sample. It displays considerable enrichment of Th-Nb-Ta-LREEs relative to the MREEs, considerable depletion of Y-HREEs relative to the MREEs, and a strong positive Nb-Ta anomaly relative to Th and La (Fig. 4.68c). The other samples from the Kiernan sills, with the exception of one (MMK08-1), may possess an OIB-like component as the samples plot between the primitive mantle composition and the OIB field in Fig. 4.69.

None of the samples with OIB-like geochemical features, with the possible exception of the Kiernan sills sample MMK08-11, are as strongly depleted in the HREEs relative to the MREEs as OIB. This could be due to differences in the depth of melting between the Circum-Superior LIP and average OIB. The Zr/Nb and Nb/Th ratios and positive Nb-Ta anomalies in OIB have been attributed to various amounts of recycled oceanic crust, terrigenous sediment and pelagic sediment in the mantle source region (e.g. Weaver, 1991; Hofmann, 1997). The OIB-like Zr/Nb and Nb/Th ratios and positive Nb-Ta anomalies present in some of the Circum-Superior LIP samples may therefore also be due to recycled oceanic crust and terrigenous or pelagic sediment components in the source region. Alternatively, these chemical signatures could represent an origin within or contamination by material from the subcontinental lithospheric mantle (e.g. Gibson et al., 2005).

5.10.6. Summary

Four of the five arguments of Heaman et al. (2009) against a mantle plume origin for the Circum-Superior LIP are dubious. A more convincing giant radiating dyke swarm exists than recognised by Heaman et al. (2009) if the recently dated Fort Albany dykes are included, such that together with the Molson and Pickle Crow dykes a radiating swarm is formed with ~100° of arc and a focal point just north of the northwest Superior Province margin. The lack of a hotspot track is not surprising

given the age of the Circum-Superior LIP and the time that has surpassed for geological processes to remove the surface expression of plume tail magmatism. The widespread distribution of magmatism along the cratonic margin is not inconsistent with a plume origin as numerical models suggest that plume material can be transported great distances away from the initial site of plume impact to regions under thinner lithosphere such as cratonic margins which have experienced previous rifting events. The lack of OIB-like geochemical signatures in the Circum-Superior LIP highlighted by Heaman et al. (2009) is not strictly accurate. Some samples from the Hudson Bay and Lake Superior regions and the Molson dykes possess Zr/Nb and Nb/Th ratios and Nb-Ta anomalies which are similar to those seen in modern OIB, suggesting that small amounts of recycled oceanic crust and terrigenous and pelagic sediment were present in the mantle source of the Circum-Superior LIP. The lack of uplift prior to Circum-Superior volcanic activity is not consistent with the mantle plume theory. There is no obvious explanation for the lack of evidence for uplift unless it has somehow been obscured by geological processes over the last ~1880 m.y. or the plume contained a large amount of compositionally dense material. However, there is some weak evidence for crustal uplift from volcaniclastic rocks and palaeo-flow indicators in the Flaherty Formation which suggest that the Flaherty Formation was deposited on an east-dipping palaeoslope on the flank of an uplifted dome with a central peak somewhere to the west of the Belcher Islands.

5.11. Comparisons to other worldwide coeval magmatic provinces and implications for continental reconstruction and a superplume event at ~1880 Ma

As outlined in Chapter 2, the Circum-Superior LIP is coeval with magmatic provinces from a number of Archaean cratons throughout the world (Fig. 2.23). French et al. (2008) noted the worldwide occurrences of ~1880 Ma magmatism and discussed the possibility that they represent a once contiguous LIP which has since been rifted apart. If this is the case then the ~1880 Ma magmatic rocks may be useful tools in palaeocontinental reconstruction (Bleeker & Ernst, 2006). An alternative possibility is that the ~1880 Ma magmatic provinces are the eruptive products of separate mantle plumes rising through the mantle in a superplume event (Condie et al., 2000; Condie, 2001) akin to the situation in the Pacific Ocean during the mid-Cretaceous (Larson, 1991a, 1991b).

5.11.1. Geochemical comparisons between the Circum-Superior LIP and other ~1880 Ma magmatic provinces

If the Circum-Superior LIP originates from the same mantle source (plume or otherwise) as other coeval magmatic provinces then a reasonable assumption may be that the igneous rocks will at least partially share a common geochemical signature or that any differences in geochemistry are related to differing magmatic processes. Comprehensive and good quality trace element data for other ~1880 Ma magmatic provinces are not readily available and do not exist for all of the different provinces. Fig. 5.51 shows the primitive-mantle-normalised multi-element profiles for the different magmatic provinces where trace element data are available.

The Baffin Island magmatism has an OIB-like signature with marked enrichment in the more incompatible elements over the less incompatible elements and positive Nb-Ta anomalies (Fig. 5.51a). An OIB-like signature lends support to a plume origin, as does a mantle potential temperature of 1639°C calculated by PRIMELT2 from sample H798 in Johns et al. (2006). Unfortunately the age determination of the Baffin Island magmatism is very imprecise (1916 ± 35 Ma) and so the magmatic rocks may actually be considerably older than the Circum-Superior LIP. Given the age uncertainty for Baffin Island and the lack of significantly fractionated incompatible element patterns in the Circum-Superior LIP it is difficult to link the two magmatic provinces to a common origin.

The magmatic rocks of the Slave craton have multi-element profiles with negative Nb-Ta anomalies (Fig. 5.51b). This is consistent with a subduction-related origin which many studies have assigned to these rocks given their association with volcanic ash layers and felsic volcanic and plutonic rocks (e.g. Hoffman & Bowring, 1984; Lalonde, 1989; Ghandi et al., 2001). It therefore seems unlikely that the Circum-Superior LIP and the Slave craton magmatic rocks were part of a contiguous LIP formed from the same mantle source region. Likewise, the magmatic rocks of the Baltic Shield show depletion of Nb-Ta relative to Th and La (Fig. 5.51c) which is consistent with the evolution of the Svecofennian Orogen as almost continuous accretion of magmatic arc systems (Korja et al., 2006).

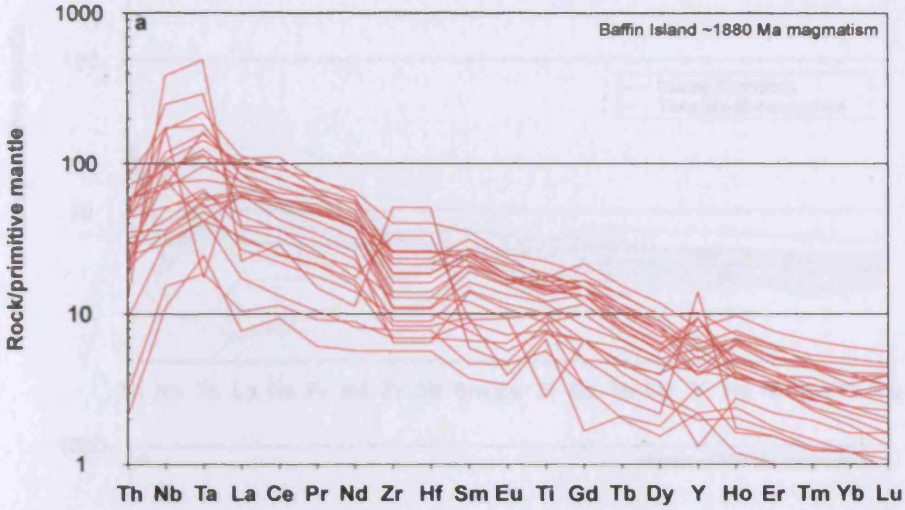
a
Baffin Island ~1880 Ma magmatism
Rock/primitive mantle
1000
100
10
1
Th Nb Ta La Ce Pr Nd Zr Hf Sm Eu Ti Gd Tb Dy Y Ho Er Tm Yb Lu

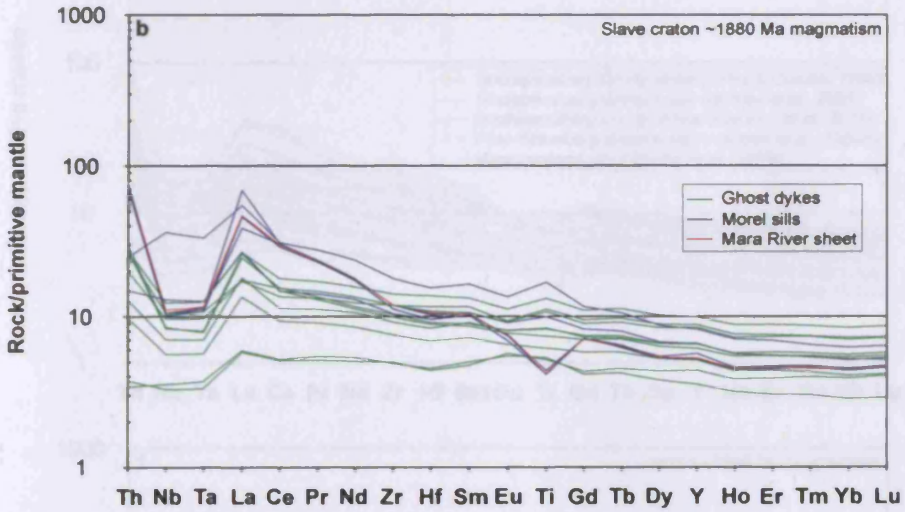
b
Slave craton ~1880 Ma magmatism
Ghost dykes
Morel sills
Mara River sheet
Rock/primitive mantle
1000
100
10
1
Th Nb Ta La Ce Pr Nd Zr Hf Sm Eu Ti Gd Tb Dy Y Ho Er Tm Yb Lu

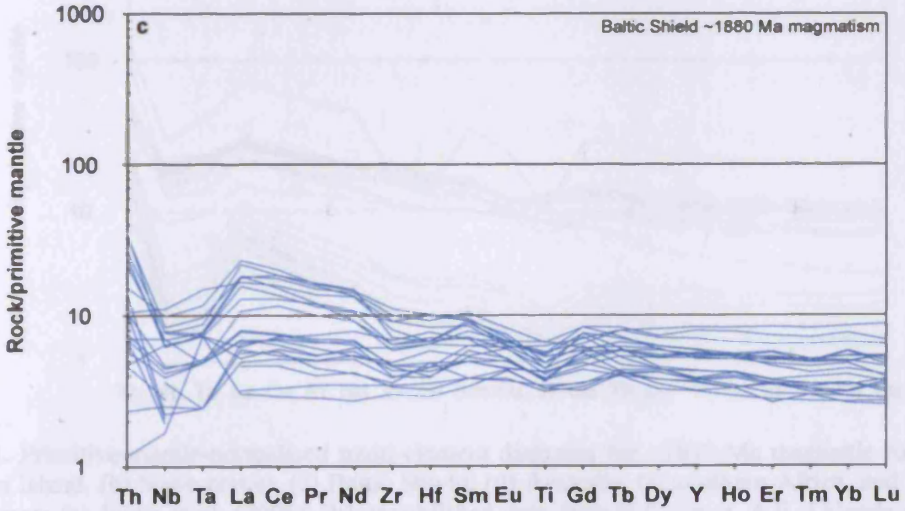
c
Baltic Shield ~1880 Ma magmatism
Rock/primitive mantle
1000
100
10
1
Th Nb Ta La Ce Pr Nd Zr Hf Sm Eu Ti Gd Tb Dy Y Ho Er Tm Yb Lu

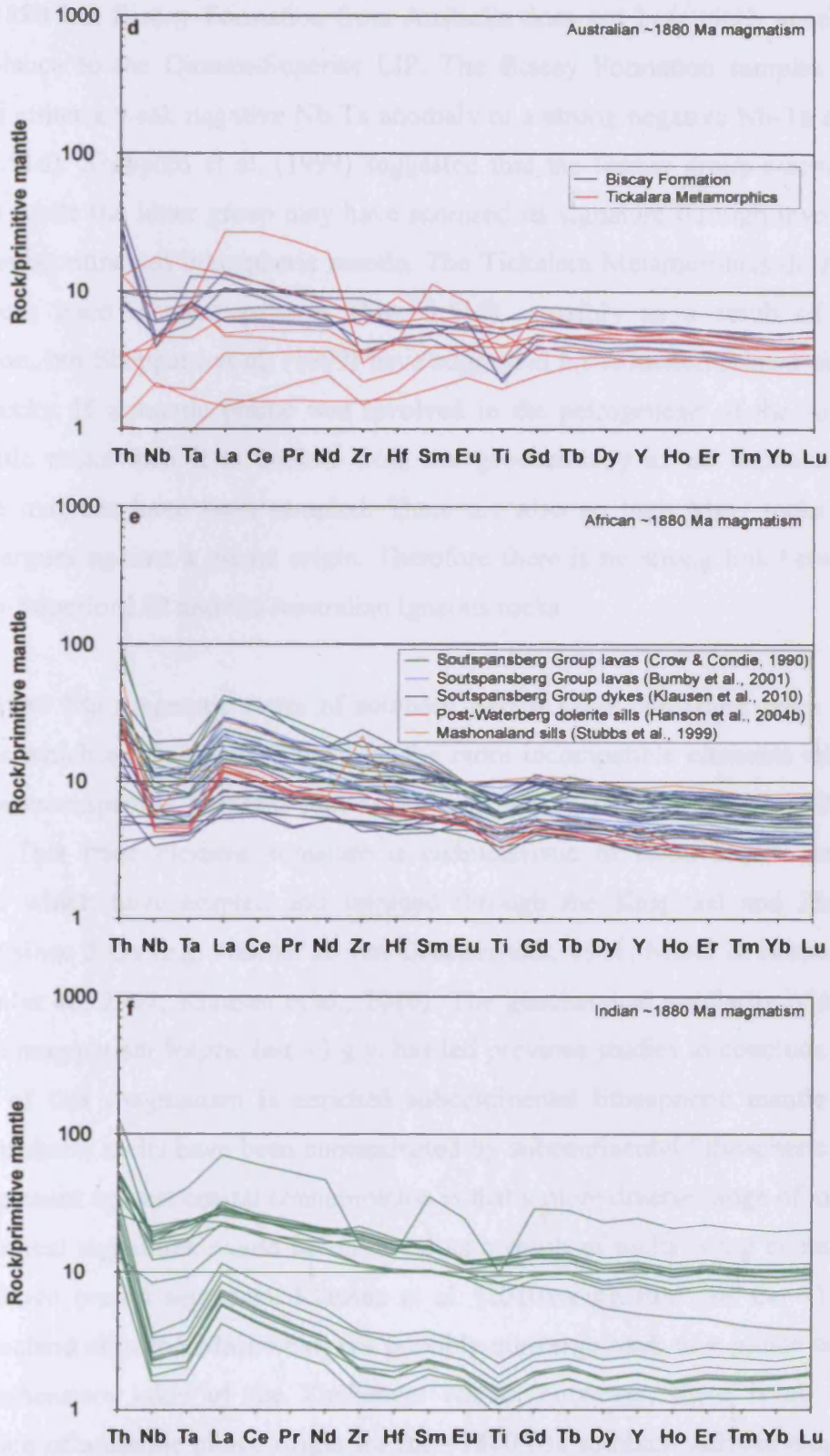

Fig. 5.51. Primitive-mantle-normalised multi-element diagrams for ~1880 Ma magmatic rocks from (a) Baffin Island, (b) Slave craton, (c) Baltic Shield, (d) Australia, (e) southern Africa, and (f) India. Data sources: (a) Johns et al. (2006); (b) unpublished data from R.E. Ernst, A.E. Lalonde and A.N. LeCheminant which are given in Appendix G; (c) Vaisanen & Westerlund (2007); (d) Sheppard et al. (1999); (e) given in diagram; (f) unpublished data from R.K. Srivastava which are given in Appendix G.

The ~1880 Ma Biscay Formation from Australia does not bear much geochemical resemblance to the Circum-Superior LIP. The Biscay Formation samples tend to possess either a weak negative Nb-Ta anomaly or a strong negative Nb-Ta anomaly (Fig. 5.51d). Sheppard et al. (1999) suggested that the former group resembled E-MORB while the latter group may have acquired its signature through involvement of the subcontinental lithospheric mantle. The Tickalara Metamorphics do not have consistent trace element patterns (Fig. 5.51d), possibly as a result of intense alteration, but Sheppard et al. (1999) have suggested a subduction-related origin for these rocks. If a mantle plume was involved in the petrogenesis of the Australian magmatic rocks then it is unclear from the geochemistry as no uncontaminated, pristine magmas have been sampled. There are also no high MgO rocks present which argues against a plume origin. Therefore there is no strong link between the Circum-Superior LIP and the Australian igneous rocks.

The ~1880 Ma magmatic rocks of southern Africa show consistent trace element patterns which are enriched in some of the more incompatible elements relative to the less incompatible elements and depleted in Nb-Ta relative to Th and La (Fig. 5.51e). This trace element signature is characteristic of flood basalts and dyke swarms which have erupted and intruded through the Kaapvaal and Zimbabwe cratons since 3 Ga (e.g. Harmer & von Gruenewaldt, 1991; Maier & Barnes, 2005; Jourdan et al., 2007; Klausen et al., 2010). The geochemical similarity of southern African magmatism for the last ~3 g.y. has led previous studies to conclude that the source of this magmatism is enriched subcontinental lithospheric mantle or that asthenospheric melts have been contaminated by subcontinental lithospheric mantle. The argument against crustal contamination is that a more diverse range of magmatic geochemical signatures would be observed as a result of melts being contaminated by different crustal segments. Klausen et al. (2010) suggested that the ~1880 Ma Mashonaland sills and Mazowe dykes possibly converge back to a plume centre on the northeastern edge of the Zimbabwe craton. However, there is no obvious indication of a mantle plume origin for the ~1880 Ma southern African magmatism including a lack of high MgO volcanic rocks.

The ~1880 Ma Indian dykes have similar multi-element profiles to the southern African magmatic rocks (Fig. 5.51f). Srivastava & Singh (2004) interpreted the

dykes to represent continental rifting and to originate from an enriched subcontinental lithospheric mantle source. As is the case in southern Africa, none of the dykes have chilled margins with high MgO concentrations suggestive of a plume origin.

There is insufficient trace element data available for the ~1880 Ma magmatism in the Wyoming craton, Greenland and Outer Hebrides. The rock types present and their major element chemistry point to subduction-related origins for the Greenland and Outer Hebrides provinces (e.g. Connelly et al., 2000; Mason et al., 2004) while Van Boening & Nabelek (2008) argued for a plume origin for the Wyoming craton intrusions.

Overall there is little geochemical similarity between the Circum-Superior LIP and other ~1880 Ma magmatic provinces. The relatively flat, oceanic-plateau-like multi-element profiles of the Circum-Superior LIP are not evident in any of the other magmatic provinces. Many of the ~1880 Ma magmatic provinces have trace element patterns which are enriched in some of the more incompatible elements and have negative Nb-Ta anomalies (Fig. 5.51). Similar signatures are present in the Circum-Superior LIP but these have been attributed to crustal contamination (see section 5.3) whereas for the other magmatic provinces such signatures appear to be more consistent with either a magmatic arc tectonic setting or an enriched subcontinental lithospheric mantle origin.

5.11.2. Implications for palaeocontinental reconstruction at ~1880 Ma

There are no published estimates of the configuration of continental fragments at ~1880 Ma. The closest are for ~1850 Ma. Rogers & Santosh (2002) have proposed that a supercontinent termed Columbia existed on Earth between ~1.9 Ga and ~1.5 Ga and contained nearly all of the then existing continental blocks. The amalgamation of continental blocks is supported by the large number of ~2.0-1.8 Ga orogenic belts found in nearly all cratons (e.g. Condie, 2002; Rogers & Santosh, 2002; Wei, 2002) including the New Quebec Orogen, Penokean Orogen and Trans-Hudson Orogen which affected the Superior craton after the formation of the Circum-Superior LIP (e.g. Lewry & Stauffer, 1990; van Kranendonk et al., 1993;

Schulz & Cannon, 2007). It may be possible that if all the continental blocks were amalgamated together or in close proximity then the ~1880 Ma magmatic provinces could have once been a contiguous LIP which has since been rifted apart. Bleeker & Ernst (2006) have suggested using geographically separate but coeval magmatic units to reconstruct the positions of the continents all the way back to the Archaean. However, the geochemistry of the Circum-Superior LIP exhibits marked differences to the other magmatic provinces which may indicate that not all of the ~1880 Ma magmatism originates from a single igneous province, thus limiting the usefulness of the ~1880 Ma magmatic rocks as tools for continental reconstruction. There are some general geochemical similarities between some of the ~1880 Ma magmatic provinces (Fig. 5.51) which does not preclude a common origin from a single mantle source. Unfortunately there is a lack of palaeomagnetic data available for the ~1880 Ma magmatic rocks to accurately determine at which latitude they were formed.

An additional argument against the ~1880 Ma magmatic provinces originally being one single province is demonstrated by the two models in Fig. 5.52 of the configuration of the continental blocks at ~1.85 Ga. For each model there is considerable distance between the cratons containing ~1880 Ma magmatic rocks, such that it is difficult to envision all of the magmatic rocks being related to a single plume. If the magmatic rocks were formed from a superplume event then the area affected by the superplume is much larger than the area proposed to have been affected by the mid-Cretaceous Pacific Ocean superplume (Fig. 5.52a; Larson, 1991a).

5.11.3. Did a superplume event occur at ~1880 Ma?

Isley & Abbott (1999) noted the occurrence of numerous banded iron formations at ~1.9 Ga and linked their formation to enhanced mantle plume volcanism during a superplume event. Condie et al. (2000) and Condie (2001) highlighted evidence for an environmental crisis at ~1.9 Ga including peaks in the chemical index of alteration of shales, amount of sedimentary phosphates, number and diversity of stromatolites, number of sulphate evaporites, abundance of black shale deposits and $\delta^{13}C$ of carbonates, and troughs in the $^{87}Sr/^{86}Sr$ ratio of seawater and $\delta^{34}S$ of sedimentary

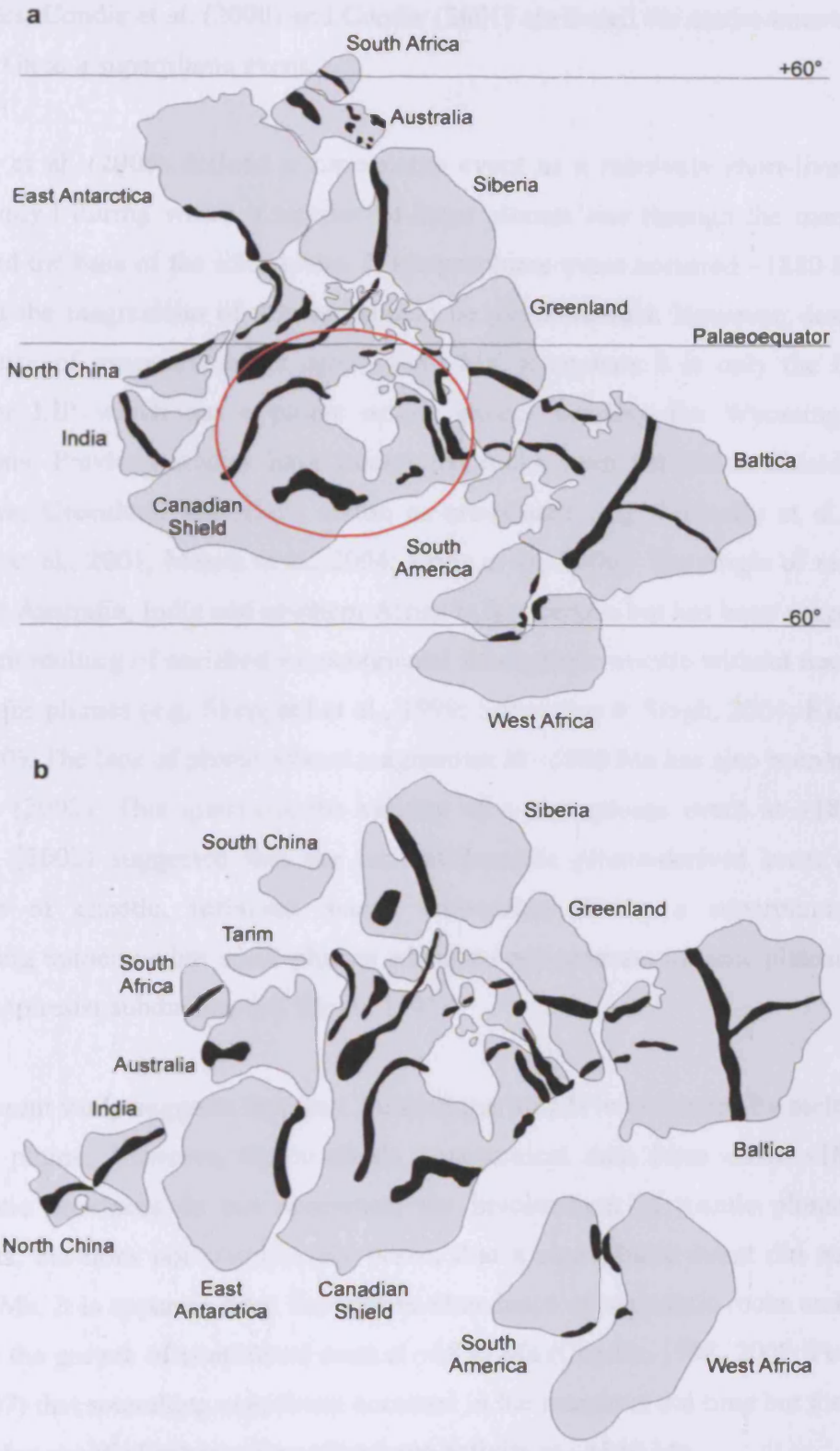

Fig. 5.52. Two possible reconstructions of the supercontinent Columbia at ~1.85 Ga from (a) Hou et al. (2008) and (b) Zhao et al. (2002). The black segments in both figures represent ~2.1-1.8 Ga orogenic belts. Precise estimates of palaeolatitude are not given in the reconstruction of Zhao et al. (2002). The red circle in (a) represents the approximate size of area affected by the mid-Cretaceous superplume of Larson (1991a).

sulphides. Condie et al. (2000) and Condie (2001) attributed the environmental crisis at ~1.9 Ga to a superplume event.

Condie et al. (2000) defined a superplume event as a relatively short-lived event (<100 m.y.) during which a number of large plumes rise through the mantle and bombard the base of the lithosphere. If a superplume event occurred ~1880 Ma then most of the magmatism of this age should be plume-related. However, despite the abundance of magmatic rocks aged ~1880 Ma, it appears it is only the Circum-Superior LIP which has a plume origin, except possibly the Wyoming craton intrusions. Previous studies have interpreted rocks from the Baltic Shield, Outer Hebrides, Greenland and Slave craton as arc-related (e.g. Connelly et al., 2000; Ghandi et al., 2001; Mason et al., 2004; Korja et al., 2006). The origin of magmatic rocks in Australia, India and southern Africa is less certain but has been suggested to represent melting of enriched subcontinental lithospheric mantle without necessarily a need for plumes (e.g. Sheppard et al., 1999; Srivastava & Singh, 2004; Klausen et al., 2010). The lack of plume-related magmatism at ~1880 Ma has also been noted by Condie (2002). This questions the validity of a superplume event at ~1880 Ma. Condie (2002) suggested that the lack of juvenile plume-derived crust may be because of chaotic, turbulent mantle convection during a superplume event producing numerous but small plumes which do not generate oceanic plateaux thick enough to resist subduction (cf. Cloos, 1993).

The current study suggests that the Circum-Superior LIP was formed by melting of a mantle plume. However, the available geochemical data from other ~1880 Ma magmatic provinces do not necessitate the involvement of mantle plumes. This suggests, but does not conclusively prove, that a superplume event did not occur ~1880 Ma. It is apparent from the relative abundance of magmatic rocks and a large peak in the growth of continental crust at ~1880 Ma (Condie, 1998, 2002; Pearson et al., 2007) that something significant occurred in the mantle at the time but there is no conclusive proof of enhanced mantle plume activity at ~1880 Ma.

5.11.4. Summary

The geochemistry of the Circum-Superior LIP does not bare close resemblance to any of the other ~1880 Ma magmatic provinces in different parts of the world. This argues against a common mantle source region and origin for all the ~1880 Ma magmatism and so there is no geochemical argument for the close proximity of the Superior craton to the other cratons in which ~1880 Ma magmatic rocks are preserved. Some of the other ~1880 Ma magmatic provinces have similar geochemical signatures and perhaps could represent fragments of a once contiguous province but at present there is a lack of palaeomagnetic data available to assess this. The prevalence of negative Nb-Ta anomalies in many of the other ~1880 Ma magmatic provinces may suggest a subduction-related origin or a subcontinental-lithospheric-mantle-related origin for these provinces. The lack of high MgO volcanic rocks and chilled margins of dykes in the other ~1880 Ma magmatic provinces also questions the validity of the proposal for enhanced mantle plume activity at ~1880 Ma. However, the occurrence of a superplume event at this time in Earth's history cannot be ruled out until more detailed petrological, geochemical and volcanological studies have been conducted on the other ~1880 Ma magmatic provinces.

5.12. Possible ideas for future work

Unfortunately no samples from the Superior Province carbonatite complexes were analysed in this study. These carbonatites therefore offer an excellent opportunity for future work. Obtaining samples of the carbonatites would be difficult because the complexes are accessible only by seasonal roads or by air and outcrops are either rare and hard to find or non-existent (Sage, 1987a, 1987b, 1987c, 1988a, 1988b, 1988c). If samples could be obtained then they could be analysed for their Nd-Hf isotopic composition and compared to the ultramafic-mafic magmatic rocks along the craton margins to see if they are derived from the same plume sources. Bell (2001) and Bell & Simonetti (2010) have noted the similarity between radiogenic isotope ratios of numerous mafic LIPs and spatially and temporally associated carbonatites. Alternatively if carbonatites and lamprophyres are sourced from shallower subcontinental lithospheric mantle sources, then analysing such rocks could highlight

the isotopic composition of the subcontinental lithospheric mantle beneath the Superior Province at ~1880 Ma.

This study found no obvious whole-rock geochemical discriminant between ore-bearing and ore-barren segments of the Circum-Superior LIP. However, no samples were analysed for PGE concentrations and so a full PGE study may be warranted. Maier & Barnes (2005) reported examples where PGEs, particularly Pd when combined with Cu and Zr in Cu/Pd and Pd/Zr ratios, were useful in the search for Ni-Cu-PGE sulphide deposits. Therefore an evaluation of PGE concentrations may be useful for determining if the magmas in the various segments of the Circum-Superior LIP experienced sulphide segregation, in which case they may be used to distinguish mineralised areas from non-mineralised areas.

Further geochemical and isotopic studies of the ~1880 Ma igneous provinces on other cratons would be useful for studies which utilise coeval igneous units in different geographical areas to reconstruct the position of the continents back through time (e.g. Bleeker & Ernst, 2006). The limited geochemical data which exist for these igneous provinces show that, although there is little similarity with the Circum-Superior LIP, there are similar geochemical signatures between certain provinces (Fig. 5.51). In combination with new palaeomagnetic data, the geochemical data could be used to test models on the configuration of the cratons at ~1880 Ma.

A useful discovery, not only for the Circum-Superior LIP but for all Precambrian LIPs, would be a method for age dating ancient and altered fine-grained volcanic rocks with the same degree of accuracy, precision and reliability as the U-Pb zircon/baddeleyite method. If such a method was possible then it would remove any doubt that ages assigned to volcanic rocks because of age determinations made on coarse-grained dykes and sills, assumed to be feeder intrusions, may not be the true ages of the volcanic rocks.

6. CONCLUSIONS AND SUMMARY

The Circum-Superior LIP is an unusual large igneous province in that the majority of it is distributed along >3000 km of the margins of the largest Archaean craton in the world, the Superior Province. The LIP consists of:

- Subalkaline picrites and basalts and numerous ultramafic intrusions of the Chukotat Group in the Cape Smith Belt and Ottawa Islands
- Subalkaline basalts of the Flaherty Formation and dolerite-gabbro Haig sills on the Belcher and Sleeper Islands in eastern Hudson Bay
- The Fort Albany dolerite dykes and dolerite-gabbro sills of the Sutton Inlier in the Hudson Bay Lowlands
- Subalkaline picrites and basalts and numerous ultramafic-mafic intrusions of the Fox River Belt
- Ultramafic sills of the Thompson Nickel Belt
- Subalkaline picrites and basalts of the Winnipegosis Belt
- Subalkaline, ultramafic-mafic dolerite-gabbro Molson dykes in the Thompson Salient
- Subalkaline, mafic dolerite-gabbro Pickle Crow dyke extending across much of the western half of the Superior Province
- Subalkaline basalts of the Gunflint Formation, subalkaline basalts and dacites of the Hemlock Formation, subalkaline gabbroic Kiernan sills, subalkaline basalts of the Badwater Greenstone, and subalkaline basalts, basaltic andesites, dacites and dolerite dykes of the Emperor Volcanic Complex, all in the Lake Superior region
- Subalkaline basalts of the Hellancourt Formation plus other mafic and felsic lavas and gabbroic-peridotitic Montagnais sills in the Labrador Trough

The majority of the ultramafic-mafic magmatism occurred between 1885 Ma and 1870 Ma. The final manifestation of Circum-Superior magmatism is represented by picrites and basalts of the Winnipegosis Belt which has an age of 1864 Ma. The earliest preserved magmatic activity may be some of the carbonatitic magmatism along the Kapuskasing Structural Zone in the centre of the craton, in particular the Cargill Township carbonatite complex which has an age range of 1897-1907 Ma.

The igneous rocks of the Circum-Superior LIP have been subjected to alteration and metamorphism since their formation. Very rarely are primary igneous minerals completely preserved. The grade of metamorphism is subgreenschist to greenschist facies in most segments although the sills in the Thompson Nickel Belt record evidence of amphibolite facies metamorphism. As a result, only immobile major and trace elements and alteration-resistant isotopic systems are suitable for studying the petrogenesis of the Circum-Superior LIP.

A common geodynamic origin for the various segments of the Circum-Superior LIP is supported by the presence of similar incompatible trace element signatures in most of the magmatic segments. This trace element signature is similar to that of modern oceanic plateaux such as the Ontong Java Plateau and can be derived from a mantle source composition similar to that of primitive mantle with 1% by mass of average continental crust extracted. Much of the geochemical variation between the different segments and within individual segments can be accounted for by differing degrees of partial melting, fractional crystallisation or crustal contamination. However, some of the igneous rocks from the various segments have different geochemical profiles with OIB-like characteristics which cannot be replicated by varying amounts of partial melting, fractional crystallisation or crustal contamination. Instead these rocks were likely derived from different mantle source compositions and highlight the heterogeneity of the mantle source region for the Circum-Superior LIP. The positive Nb-Ta anomalies of some of the rocks of the Flaherty Formation, Molson dykes and Hemlock Formation may be explained by the presence of recycled oceanic crust in the mantle source region while the Zr/Nb and Nb/Th systematics of some of the other rocks from the Flaherty Formation, Hemlock Formation and Kiernan sills are similar to the present-day EM2 mantle end-member and may be explained by the presence of some recycled terrigenous sediment in the mantle source region.

The Sr, Pb and Os radiogenic isotopes yield limited useful information on the petrogenesis of the Circum-Superior LIP and their applicability to ancient and/or altered volcanic rocks is questionable. The Nd and Hf isotopic ratios are much less influenced by post-magmatic alteration processes. Uncontaminated Circum-Superior LIP samples have positive εNd_i values suggesting derivation from a depleted mantle source but not as depleted as the estimated ~1880 Ma depleted mantle. There is a

large range in εHf_i values for uncontaminated Circum-Superior LIP samples, above and below that of the estimated ~1880 Ma depleted upper mantle. In Hf-Nd isotopic space, the uncontaminated Circum-Superior LIP samples appear to define two linear mixing trends. One trend extends from the estimated ~1880 Ma depleted upper mantle composition towards the present day EM2 end-member and includes rocks from the Hemlock Formation, Molson dykes, Flaherty Formation, Chukotat Group and Pickle Crow dyke. The other trend extends from present-day HIMU towards a radiogenic Hf isotope composition represented by the Hellancourt Formation and also includes rocks from the Winnipegosis Belt and Hemlock Formation.

An interesting feature of parts of the Circum-Superior LIP, in particular the uncontaminated high MgO rocks of the Chukotat Group, Fox River Belt and Hellancourt Formation, is the occurrence of negative Ti anomalies. Uncontaminated lower MgO rocks in these same regions do not display negative Ti anomalies in their incompatible trace element profiles. The origin of these negative Ti anomalies is unclear but may be due to the heterogeneity of the mantle source region of the Circum-Superior LIP and the use of an average normalisation value for Ti that does not reflect the large variation of Ti found in natural peridotites.

On the basis of whole-rock geochemical and isotopic compositions of volcanic rocks, it has not been possible to discriminate between segments of the Circum-Superior LIP which contain Ni-Cu-PGE sulphide deposits and those which do not. Geochemical criteria previously used to discriminate between mineralised and non-mineralised LIPs cannot be successfully applied to the Circum-Superior LIP and highlights that the whole-rock lithogeochemistry of volcanic rocks possibly associated with mineralised intrusions should not be used as an isolated tool for ore prospecting. The mechanism of crustal contamination may be an important factor in ore genesis. The barren Lake Superior region igneous rocks show geochemical evidence of crustal contamination which occurred concomitantly with fractional crystallisation in large, deep-seated magma chambers. In contrast, the fertile Chukotat Group, Fox River Belt and Molson dykes show geochemical evidence for crustal contamination as magma ascended turbulently through relatively small intrusive conduits in the upper crust where local sedimentary rocks may have been rich in sulphur. This scenario probably also occurred in the Thompson Nickel Belt.

However, the lack of any crustal contamination signature cannot be taken as evidence against the presence of ore deposits because the Hellancourt Formation show no sign of contamination yet are associated with intrusions which contain important Ni-Cu-PGE sulphide deposits.

The Circum-Superior LIP formed from anomalously hot mantle. Major element modelling shows that the MgO content of primary magmas are consistent with derivation from a mantle potential temperature up to 274°C hotter than some of the estimates for the potential temperature of the ambient upper mantle at ~1880 Ma. Major element modelling also shows that partial melting, at least beneath the Cape Smith Belt and the Thompson Salient, occurred relatively deep at pressures ranging from 3.8 to 6 GPa (~115-180 km). The lack of a garnet signature in the trace element patterns of these rocks is most likely because the degree of partial melting was high enough to consume all of the garnet in the source region.

Most previous studies on the Circum-Superior LIP have advocated the generation of this igneous province from the shallow N-MORB-source upper mantle in back-arc, foredeep or local pull-apart basins parallel to the cratonic margins. However, the conclusion of this study is that the Circum-Superior LIP was formed from a mantle plume originating from deep in the mantle and impinging beneath the Superior Province. Evidence for a mantle plume origin includes the high MgO and Ni content of many volcanic samples, the oceanic-plateau-like incompatible trace element profiles, the possible presence of a small OIB component best highlighted by positive Nb-Ta anomalies, the position of the majority of samples within the Icelandic plume tramlines or along the lower tramline on a Nb/Y-Zr/Y diagram, the position of the majority of uncontaminated samples within the oceanic plateau field on a Zr/Nb-Nb/Th diagram, the Nd-Hf isotopic ratios which differ to the estimated composition of ~1880 Ma depleted mantle, the calculated high degrees of partial melting (up to 40%), the high mantle potential temperatures, and the presence of a radiating dyke swarm with ~100° of arc formed by the Molson, Pickle Crow and Fort Albany dykes.

It is envisaged that the mantle plume initially impinged beneath the thick cratonic keel of the Superior Province and deflected towards regions of thinner lithosphere at the cratonic margins which had previously undergone rifting events. The channelling

of plume material towards the margins of the craton or the presence of compositionally dense material in the plume perhaps may be the best explanation for the lack of crustal uplift associated with the Circum-Superior LIP. The geochemistry of the Circum-Superior LIP is markedly different to the other ~1880 Ma magmatic provinces found on other cratons. This observation suggests that if a large LIP formed at ~1880 Ma, then the Circum-Superior LIP was not part of it and cannot be used in any palaeocontinental reconstruction models which attempt to link up coeval fragments of once contiguous igneous provinces. The Circum-Superior LIP may also be the only ~1880 Ma magmatic province of a mantle plume origin which suggests that another mechanism other than a superplume event was responsible for the enhanced magmatic activity that appears to have occurred on a global scale at ~1880 Ma.

REFERENCES

Abbott, D.H. & Isley, A.E. 2002. The intensity, occurrence, and duration of superplume events and eras over geological time. *Journal of Geodynamics* **34**, 265-307.

Adam, J. & Green, T.H. 1994. The effects of pressure and temperature on the partitioning of Ti, Sr and REE between amphibole, clinopyroxene and basanitic melts. *Chemical Geology* **117**, 219-233.

Aigner-Torres, M., Blundy, J., Ulmer, P. & Pettke, T. 2007. Laser ablation ICP-MS study of trace element partitioning between plagioclase and basaltic melts: an experimental approach. *Contributions to Mineralogy and Petrology* **153**, 647-667.

Anderson, D.L. 2000. The thermal state of the upper mantle; no role for mantle plumes. *Geophysical Research Letters* **27**, 3623-3636.

Arndt, N.T. 1994. Komatiites. In: Condie, K.C. (ed) *Archean crustal evolution*. Elsevier, Amsterdam. pp.11-44.

Arndt, N.T. 2003. Komatiites, kimberlites, and boninites. *Journal of Geophysical Research* **108**, doi: 10.1029/2002JB002157.

Arndt, N.T. & Todt, W. 1994. Formation of 1.9 Ga-old Trans-Hudson continental crust: Pb isotopic data. *Chemical Geology* **118**, 9-26.

Arndt, N.T., Bruegmann, G.E., Lehnert, K., Chauvel, C. & Chappell, B.W. 1987. Geochemistry, petrogenesis and tectonic environment of Circum-Superior Belt basalts, Canada. In: Pharaoh, T.C., Beckinsale, R.D. & Rickard, D. (eds) *Geochemistry and mineralization of Proterozoic volcanic suites*. Geological Society Special Publication 33. Geological Society of London, London. pp.133-145.

Arndt, N.T., Lesher, C.M. & Czamanske, G.K. 2005. Mantle-derived magmas and magmatic Ni-Cu-(PGE) deposits. *Economic Geology* **100**, 5-23.

Asavin, A.M., Kogarko, L.N., Kryuchkova, O.I., Tyurin, D.A. & Kolesov, G.M. 1997. Grand Canary, Saint Helena, and Tristan da Cunha oceanic islands: variations of trace element partition coefficients in pyroxene-melt equilibria during alkaline magma evolution. *Geochemistry International* **35**, 415-423.

Asimow, P.D. & Ghiorso, M.S. 1998. Algorithmic modifications extending MELTS to calculate subsolidus phase relations. *American Mineralogist* **83**, 1127-1132.

Asimow, P.D., Hirschmann, M.M. & Stolper, E.M. 2001. Calculation of peridotite partial melting from thermodynamic models of minerals and melts, IV. Adiabatic decompression and the composition and mean properties of mid-ocean ridge basalts. *Journal of Petrology* **42**, 963-998.

Awramik, S.M. 1976. Gunflint stromatolites: microfossil distribution in relation to stromatolite morphology. In: Walter, M.R. (ed) *Stromatolites*. Elsevier, Amsterdam. pp.311-320.

Ayres, L.D., Lumbers, S.B., Milne, V.G. & Robeson, D.W. 1971. Northwest sheet, Ontario geological map. Ontario Division of Mines Map 2201.

Baker, M.B. & Beckett, J.R. 1999. The origin of abyssal peridotites: a reinterpretation of constraints on primary bulk compositions. *Earth and Planetary Science Letters* **171**, 49-61.

Baker, M.B., Hirschmann, M.M., Ghiorso, M.S. & Stolper, E.M. 1995. Compositions of near-solidus peridotite melts from experiments and thermodynamic calculations. *Nature* **375**, 308-311.

Baragar, W.R.A. 2007a. Geology, Ottawa Islands, eastern Hudson Bay, Nunavut. Geological Survey of Canada Map 2113A.

Baragar, W.R.A. 2007b. Geology, Sleeper Islands, eastern Hudson Bay, Nunavut. Geological Survey of Canada Map 2114A.

Baragar, W.R.A. 2008. Geology, Smith Island and adjoining mainland, eastern Hudson Bay, Nunavut-Quebec. Geological Survey of Canada Map 2112A.

Baragar, W.R.A. & Lamontagne, C.G. 1980. The Circum-Ungava Belt in eastern Hudson Bay; the geology of Sleeper Islands and parts of the Ottawa and Belcher Islands. In: *Current Research Part A*. Geological Survey of Canada Paper 80-1A. Geological Survey of Canada, Ottawa. pp.89-94.

Baragar, W.R.A. & Piche, M. 1982. The Circum-Ungava Belt on eastern Hudson Bay; the geology of the Ottawa Islands and the Cape Smith region. In: *Current Research, Part A*. Geological Survey of Canada Paper 82-1A. Geological Survey of Canada, Ottawa. pp.89-94.

Baragar, W.R.A. & Scoates, R.F.J. 1981. The Circum-Superior Belt; a Proterozoic plate margin? In: Kroener, A. (ed) *Precambrian plate tectonics*. Elsevier, Amsterdam. pp.297-330.

Baragar, W.R.A. & Scoates, R.F.J. 1987. Volcanic geochemistry of the northern segments of the Circum-Superior Belt of the Canadian Shield. In: Pharaoh, T.C., Beckinsale, R.D. & Rickard, D. (eds) *Geochemistry and mineralization of Proterozoic volcanic suites*. Geological Society Special Publication 33. Geological Society of London, London. pp.113-145.

Baragar, W.R.A., Ernst, R.E., Hulbert, L.J. & Peterson, T. 1996. Longitudinal petrochemical variation in the Mackenzie dyke swarm, northwestern Canadian Shield. *Journal of Petrology* **37**, 317-359.

Barnes, S.J. & Barnes, S.-J. 1990. A new interpretation of the Katiniq nickel deposit, Ungava, northern Quebec. *Economic Geology* **85**, 1269-1272.

Barnes, S.-J. & Picard, C.P. 1993. The behaviour of platinum-group elements during partial melting, crystal fractionation, and sulphide segregation: an example from the Cape Smith Fold Belt, northern Quebec. *Geochimica et Cosmochimica Acta* **57**, 79-87.

Barnes, S.-J., Coats, C.J. & Naldrett, A.J. 1982. Petrogenesis of a Proterozoic nickel-sulfide-komatiitic association; the Katiniq sill, Ungava, Quebec. *Economic Geology* 77, 413-429.

Barton, J.M. 1979. The chemical compositions, Rb-Sr isotopic systematics and tectonic setting of certain post-kinematic mafic igneous rocks, Limpopo Mobile Belt, southern Africa. *Precambrian Research* **9**, 57-80.

Barton, J.M & Pretorius, W. 1997. The lower unconformity-bounded sequence of the Soutpansberg Group and its correlatives – remnants of a Proterozoic large igneous province. *South African Journal of Geology* **100**, 335-339.

Bayley, R.W. 1959. A metamorphosed differentiated sill in northern Michigan. *American Journal of Science* **257**, 408-430.

Beattie, P. 1994. Systematics and energetics of trace-element partitioning between olivine and silicate melts: implications for the nature of mineral/melt partitioning. *Chemical Geology* **117**, 57-71.

Beaudoin, G., Laurent, R. & Ohnenstetter, D. 1990. First report of platinum-group minerals at Blue Lake, Labrador Trough, Quebec. *Canadian Mineralogist* **28**, 409-418.

Beck, W. & Murthy, V.R. 1991. Evidence for continental crustal assimilation in the Hemlock Formation flood basalts of the early Proterozoic Penokean Orogen, Lake Superior region. In: Sims, P.K. & Carter, L.M.H. (eds) *Contributions to Precambrian geology of Lake Superior region*. US Geological Survey Bulletin 1904-I. US Government Printing Office, Washington DC. pp.I1-I25.

Bedard, J.H. 1999. Petrogenesis of boninites from the Betts Cove ophiolite, Newfoundland, Canada: identification of subducted source components. *Journal of Petrology* **40**, 1853-1889.

Bedard, J.H., Francis, D.M., Hynes, A.J. & Madeau, S. 1984. Fractionation in the feeder system at a Proterozoic rifted margin. *Canadian Journal of Earth Sciences* **21**, 489-499.

Bedini, R.M. & Bodinier, J.-L. 1999. Distribution of incompatible trace elements between the constituents of spinel peridotite xenoliths: ICP-MS data from the East African Rift. *Geochimica et Cosmochimica Acta* **63**, 3883-3900.

Bell, C.K. 1971. Boundary geology, upper Nelson River area, Manitoba and northwestern Ontario. In: Turnock, A.C. (ed) *Geoscience studies in Manitoba.* Geological Association of Canada Special Paper 9. Geological Association of Canada, Toronto. pp.11-39.

Bell, K. 2001. Carbonatites: relationships to mantle-plume activity. In: Ernst, R.E. & Buchan, K.L. (eds) *Mantle plumes: their identification through time.* Geological Society of America Special Paper 353. Geological Society of America, Boulder. pp.267-290.

Bell, K. & Blenkinsop, J. 1980. Ages and initial $^{87}Sr/^{86}Sr$ ratios from alkalic complexes of Ontario; grant 42. In: Pye, E.G. (ed) *Geoscience research grant program, summary of research, 1979-1980.* Ontario Geological Survey Miscellaneous Paper 93. Ministry of Natural Resources, Toronto. pp.16-23.

Bell, K. & Simonetti, A. 2010. Source of parental melts to carbonatites – critical isotopic constraints. *Mineralogy and Petrology* **98**, 77-89.

Bell, K., Blenkinsop, J., Kwon, S.T., Tilton, G.R. & Sage, R.P. 1987. Age and radiogenic isotopic systematics of the Borden carbonatite complex, Ontario, Canada. *Canadian Journal of Earth Sciences* **24**, 24-30.

Bergeron, R. 1957. Cape Smith-Wakeham Bay belt, New Quebec. Quebec Department of Mines Preliminary Report 355 and Preliminary Maps 1090 and 1196. 8pp.

Bergeron, R. 1959. Povungnituk range area, New Quebec. Quebec Department of Mines Preliminary Report 392 and Preliminary Map 1279. 9pp.

Betts, P.G., Giles, D., Schaefer, B.F. & Mark, G. 2007. 1600-1500 Ma hotspot track in eastern Australia: implications for Mesoproterozoic continental reconstructions. *Terra Nova* **19**, 496-501.

Bizimis, M., Griselin, M., Lassiter, J.C., Salters, V.J.M. & Sen, G. 2007. Ancient recycled mantle lithosphere in the Hawaiian plume: osmium-hafnium isotopic evidence from peridotite mantle xenoliths. *Earth and Planetary Science Letters* **257**, 259-273.

Blais, S., Guille, G., Guillou, H., Chauvel, C., Maury, R.C., Pernet, G. & Cotten, J. 2002. Maupiti: le plus ancien temoin de l'activite du point chaud de la Societe (Polynesie francaise). *Bulletin de la Societe Geologique de France* **173**, 45-55.

Bleeker, W. 1990. New structural-metamorphic constraints on early Proterozoic oblique collision along the Thompson Nickel Belt, Manitoba, Canada. In: Lewry, J.F. & Stauffer, M.L. (eds) *The early Proterozoic Trans-Hudson Orogen of North America.* Geological Association of Canada Special Paper 37. Geological Association of Canada, Toronto. pp.57-73.

Bleeker, W. 2003. The late Archean record: a puzzle in ca. 35 pieces. *Lithos* **71**, 99-134.

Bleeker, W. & Ernst, R.E. 2006. Short-lived mantle generated magmatic events and their dyke swarms: the key to unlocking Earth's paleogeographic record back to 2.6 Ga. In: Hanski, E., Mertanen, S., Ramo, T. & Vuollo, J. (eds) *Dyke swarms – time markers of crustal evolution.* Taylor & Francis, London. pp.3-26.

Bleeker, W. & Hamilton, M.A. 2001. New SHRIMP U-Pb ages for the Ospwagan Group: implications for the SE margin of the Trans-Hudson Orogen. *Geological Association of Canada-Mineralogical Association of Canada Annual Meeting 2001.* Program with Abstracts 26, pp.15.

Blichert-Toft, J. & Albarede, F. 1997. The Lu-Hf geochemistry of chondrites and the evolution of the mantle-crust system. *Earth and Planetary Science Letters* **148**, 243-258.

Blichert-Toft, J. & Arndt, N.T. 1999. Hf isotope compositions of komatiites. *Earth and Planetary Science Letters* **171**, 439-451.

Bodorkos, S., Oliver, N.H.S. & Cawood, P.A. 1999. Thermal evolution of the central Halls Creek Orogen, northern Australia. *Australian Journal of Earth Sciences* **46**, 453-465.

Boehler, R. 1993. Temperatures in the Earth's core from melting-point measurements of iron at high static pressures. *Nature* **363**, 534-536.

Bostock, H.H. 1971. Geological notes on Aquatuk River map-area, Ontario, with emphasis on the Precambrian rocks. Geological Survey of Canada Paper 70-42. Geological Survey of Canada, Ottawa. 57pp.

Boudreau, A.E. 1999. PELE – a version of the MELTS software program for the PC platform. *Computers and Geosciences* **25**, 201-203.

Bowring, S.A. & Grotzinger, J.P. 1992. Implications of new chronostratigraphy for tectonic evolution of Wopmay Orogen, northwest Canadian Shield. *American Journal of Science* **292**, 1-20.

Bowring, S.A., Van Schmus, W.R. & Hoffman, P.F. 1984. U-Pb zircon ages from Athapuscow aulacogen, east arm of Great Slave Lake, NWT, Canada. *Canadian Journal of Earth Sciences* **21**, 1315-1324.

Brevart, O., Dupre, B. & Allegre, C.J. 1986. Lead-lead age of komatiitic lavas and limitations on the structure and evolution of the Precambrian mantle. *Earth and Planetary Science Letters* 77, 293-302.

Bridgwater, D., Austrheim, H., Hansen, B.T., Mengel, F., Pedersen, S. & Winter, J. 1990. The Proterozoic Nagssugtoqidian mobile belt of southeast Greenland: a link between the eastern Canadian and Baltic Shields. *Geoscience Canada* **17**, 305-310.

Bryan, S. & Ernst, R.E. 2008. Revised definition of Large Igneous Provinces (LIPs). *Earth Science Reviews* **86**, 175-202.

Buchan, K.L. & Ernst, R.E. 2004. Diabase dyke swarms and related units in Canada and adjacent regions. Geological Survey of Canada Map 2022A.

Buchan, K.L., Halls, H.C. & Mortensen, J.K. 1996. Paleomagnetism, U-Pb geochronology, and geochemistry of Marathon dykes, Superior Province, and comparison with the Fort Frances swarm. *Canadian Journal of Earth Sciences* **33**, 1583-1595.

Buchan, K.L., Harris, B.A., Ernst, R.E. & Hanes, J.A. 2003. Ar-Ar dating of the Pickle Crow diabase dyke in the western Superior craton of the Canadian Shield of Ontario and implications for a possible plume centre associated with ca. 1880 Ma Molson magmatism of Manitoba. *Geological Association of Canada-Mineralogical Association of Canada Annual Meeting 2003*. Program with Abstracts 28, pp.17.

Buchko, I.V., Sal'nikova, E.B., Kotov, A.B., Larin, A.M., Velikoslavinskii, S.D., Sorokin, A.A., Sorokin, A.P. & Yakovleva, S.Z. 2006. Paleoproterozoic gabbroanorthosites of the Selenga-Stanovoi superterrane, southern framing of the Siberian craton. *Doklady Earth Sciences* **470**, 372-375.

Bumby, A.J., Eriksson, P.G., van der Merwe, R. & Maier, W.D. 2001. The stratigraphic relationship between the Waterberg and Soutpansberg Groups in Northern Province, South Africa: evidence from the Blouberg area. *South African Journal of Geology* **104**, 205-216.

Bumby, A.J., Eriksson, P.G., van der Merwe, R. & Steyn, G.L. 2002. A half-graben setting for the Proterozoic Soutpansberg Group (South Africa): evidence from the Blouberg area. *Sedimentary Geology* **147**, 37-56.

Burnham, O.M., Halden, N.M., Layton-Matthews, D., Lesher, C.M., Liwanag, J., Heaman, L.M., Hulbert, L.J., Machado, N., Michalak, D., Pacey, M., Peck, D.C., Potrel, A., Theyer, P., Toope, K. & Zwanzig, H.V. 2004. Geology, stratigraphy, petrogenesis, and metallogenesis of the Thompson Nickel Belt, Manitoba: final report for CAMIRO Project 97E-02. Mineral Exploration Research Centre, Laurentian University, Sudbury. 410pp.

Butler, S.L. 2009. The effects of phase boundary induced layering on the Earth's thermal history. *Geophysical Journal International* **179**, 1330-1340.

Cadieux, I. 1980. *Differentiation of a basic sill, Sleeper Islands, NWT.* BSc thesis. University of Ottawa, Ottawa. 111pp.

Cameron, E.M. 1983. Genesis of Proterozoic iron-formation: sulphur isotope evidence. *Geochimica et Cosmochimica Acta* **47**, 1069-1074.

Campbell, I.H. 2007. Testing the plume theory. *Chemical Geology* **241**, 153-176.

Campbell, I.H. & Griffiths, R.W. 1990. Implications of mantle plume structure for the evolution of flood basalts. *Earth and Planetary Science Letters* **99**, 79-93.

Campbell, I.H. & Naldrett, A.J. 1979. The influence of silicate:sulfide ratios on the geochemistry of magmatic sulfides. *Economic Geology* **74**, 1503-1506.

Cann, J.R. 1970. Rb, Sr, Y, Zr and Nb in some ocean floor basaltic rocks. *Earth and Planetary Science Letters* **10**, 7-11.

Cannon, W.F. & Gair, J.E. 1970. A revision of stratigraphic nomenclature for middle Precambrian rocks in northern Michigan. *Geological Society of America Bulletin* **81**, 2843-2846.

Card, K.D. 1990. A review of the Superior Province of the Canadian Shield, a product of Archean accretion. *Precambrian Research* **48**, 99-156.

Card, K.D. & Ciesielski, A. 1986. DNAG No. 1. Subdivisions of the Superior Province of the Canadian Shield. *Geoscience Canada* **13**, 5-13.

Chaffey, D.J., Cliff, R.A. & Wilson, B.M. 1989. Characterization of the St. Helena magma source. In: Saunders, A.D. & Norry, M.J. (eds) *Magmatism in the ocean basins.* Geological Society Special Publication 42. Geological Society of London, London. pp.257-276.

Chandler, F.W. 1984. Metallogenesis of an early Proterozoic foreland sequence, eastern Hudson Bay, Canada. *Journal of the Geological Society, London* **141**, 299-313.

Chandler, F.W. 1988. The early Proterozoic Richmond Gulf Graben, east coast of Hudson Bay, Quebec. Geological Survey of Canada Bulletin 362. Geological Survey of Canada, Ottawa. 76pp.

Chandler, F.W. & Parrish, R.R. 1989. Age of the Richmond Gulf Group and implications for rifting in the Trans-Hudson Orogen, Canada. *Precambrian Research* **44**, 277-288.

Charland, A. 1999. Geology of the West Boundary area. In: Lesher, C.M. (ed) *Komatiitic peridotite-hosted Fe-Ni-Cu-(PGE) sulphide deposits in the Raglan area, Cape Smith Belt, New Quebec.* Laurentian University, Mineral Exploration Research Centre, Guidebook Series 2. Laurentian University, Sudbury. pp.123-132.

Chatterjee, N. & Bhattacharji, S. 2001. Petrology, geochemistry and tectonic settings of the mafic dikes and sills associated with the evolution of the Proterozoic Cuddapah Basin of south India. *Proceedings of the Indian Academy of Sciences (Earth and Planetary Sciences)* **110**, 433-453.

Chauvel, C., Arndt, N.T., Kielinzcuk, S. & Thom, A. 1987. Formation of 1.9 Ga old continental crust. I: Nd isotopic data. *Canadian Journal of Earth Sciences* **24**, 396-406.

Chauvel, C., Hofmann, A.W. & Vidal, P. 1992. HIMU-EM: The French Polynesian connection. *Earth and Planetary Science Letters* **110**, 99-119.

Cheve, S.R. & Machado, N. 1988. Reinvestigation of the Castignon Lake carbonatite complex, Labrador Trough, New Quebec. *Geological Association of Canada-Mineralogical Association of Canada Annual Meeting 1988*. Program with Abstracts 13, pp.20.

Clark, T. 2001. Distribution and exploration potential of platinum-group elements in Quebec. PRO2001-06. Ministère des Ressources Naturelles, Quebec City. 13pp.

Clark, T. & Thorpe, R.I. 1990. Model lead ages from the Labrador Trough and their stratigraphic implications. In: Lewry, J.F. & Stauffer, M.L. (eds) *The early Proterozoic Trans-Hudson Orogen of North America*. Geological Association of Canada Special Paper 37. Geological Association of Canada, Toronto. pp.413-431.

Clark, T., Beaudoin, G. & Laurent, R. 1989. Les gîtes de Cu-Ni-Pd-Pt du Lac Retty, Fosse du Labrador. *Canadian Institute of Mining Bulletin* **82**, 108.

Class, C. & le Roex, A.P. 2008. Ce anomalies in Gough Island lavas – trace element characteristics of a recycled sediment component. *Earth and Planetary Science Letters* **265**, 475-486.

Clement, J.-P., Legendre, C., Caroff, M., Guillou, H., Cotten, J., Bollinger, C. & Guille, G. 2003. Epiclastic deposits and 'horseshoe-shaped' calderas in Tahiti (Society Islands) and Ua Huka (Marquesas Archipelago), French Polynesia. *Journal of Volcanology and Geothermal Research* **120**, 87-101.

Clifford, T.N. 1970. The structural framework of Africa. In: Clifford, T.N. & Gass, I.G. (eds) *African magmatism and tectonics*. Oliver & Boyd, Edinburgh. pp.1-26.

Cloos, M. 1993. Lithospheric buoyancy and collisional orogenesis: subduction of oceanic plateaus, continental margins, island arcs, spreading ridges, and seamounts. *Geological Society of America Bulletin* **105**, 715-737.

Coffin, M.F. & Eldholm, O. 1991. Large igneous provinces: JOI/USSAC workshop report. The University of Texas, Austin Institute for Geophysics Technical Report. University of Texas, Austin. pp.114.

Coffin, M.F. & Eldholm, O. 1992. Volcanism and continental break-up: a global compilation of large igneous provinces. In: Storey, B.C., Alabaster, T. & Pankhurst, R.J. (eds) *Magmatism and causes of continental break-up*. Geological Society Special Publication 68. Geological Society of London, London. pp.21-34.

Coffin, M.F. & Eldholm, O. 1993a. Large igneous provinces. *Scientific American* **269**, 42-49.

Coffin, M.F. & Eldholm, O. 1993b. Scratching the surface: estimating dimensions of large igneous provinces. *Geology* **21**, 515-518.

Coffin, M.F. & Eldholm, O. 1994. Large igneous provinces: crustal structure, dimensions, and external consequences. *Reviews of Geophysics* **32**, 1-36.

Coltorti, M. & Gregoire, M. (eds) 2008. *Metasomatism in oceanic and continental lithospheric mantle*. Geological Society Special Publication 293. Geological Society of London, London. 352pp.

Condie, K.C. 2000. Episodic continental growth models: afterthoughts and extensions. *Tectonophysics* **322**, 153-162.

Condie, K.C. 2001. *Mantle plumes and their record in Earth history*. Cambridge University Press, Cambridge. 306pp.

Condie, K.C. 2002. Breakup of a Paleoproterozoic supercontinent. *Gondwana Research* **5**, 41-43.

Condie, K.C. 2003. Incompatible element ratios in oceanic basalts and komatiites: tracking deep mantle sources and continental growth rates with time. *Geochemistry, Geophysics, Geosystems* **4**, doi: 10.1029/2002GC000333.

Condie, K.C. 2004. Supercontinents and superplume events: distinguishing signals in the geologic record. *Physics of the Earth and Planetary Interiors* **146**, 319-332.

Condie, K.C. 2005. High field strength element ratios in Archean basalts: a window to evolving sources of mantle plumes? *Lithos* **79**, 491-504.

Condie, K.C., Des Marais, D.J. & Abbott, D. 2000. Geologic evidence for a mantle superplume event at 1.9 Ga. *Geochemistry, Geophysics, Geosystems* **1**, doi: 10.1029/2003GC00095.

Connelly, J.N., van Gool, J.A.M. & Mengel, F.C. 2000. Temporal evolution of a deeply eroded orogen: the Nagssugtoqidian Orogen, west Greenland. *Canadian Journal of Earth Sciences* **37**, 1121-1142.

Courtier, A.M., Jackson, M.G., Lawrence, J.F., Wang, Z., Aeolus Lee, C.-T., Halama, R., Warren, J.M., Workman, R., Xu, W., Hirschmann, M.M., Larson, A.M., Hart, S.R., Lithgow-Bertelloni, C., Stixrude, L. & Chen, W.-P. 2007. Correlation of seismic and petrologic thermometers suggests deep thermal anomalies beneath hotspots. *Earth and Planetary Science Letters* **264**, 308-316.

Craddock, J.P., Anziano, J., Wirth, K., Vervoort, J.D., Singer, B. & Zhang, X. 2007. Structure, geochemistry and geochronology of a Penokean lamprophyre dike swarm, Archean Wawa Terrane, Little Presque Isle, Michigan, USA. *Precambrian Research* **157**, 50-70.

Cranstone, D.A. & Turek, A. 1976. Geological and geochronological relationships of the Thompson Nickel Belt, Manitoba. *Canadian Journal of Earth Sciences* **13**, 1058-1069.

Crow, C. & Condie, K.C. 1990. Geochemistry and origin of early Proterozoic volcanic rocks from the Transvaal and Soutpansberg successions, South Africa. *Precambrian Research* **47**, 17-26.

Cumming, G.L., Eckstrand, O.R. & Peredery, W.V. 1982. Geochronologic interpretations of Pb isotope ratios in nickel sulfides of the Thompson Belt, Manitoba. *Canadian Journal of Earth Sciences* **19**, 2306-2324.

David, K., Schiano, P. & Allegre, C.J. 2000. Assessment of the Zr/Hf fractionation in oceanic basalts and continental materials during petrogenetic processes. *Earth and Planetary Science Letters* **178**, 285-301.

Davidson, A. 2008. Late Paleoproterozoic to mid-Neoproterozoic history of northern Laurentia: an overview of central Rodinia. *Precambrian Research* **160**, 5-22.

Davies, G.F. 2009. Effect of plate bending on the Urey ratio and the thermal evolution of the mantle. *Earth and Planetary Science Letters* **287**, 513-518.

Davis, W.J. & Bleeker, W. 2007. New ages for Paleoproterozoic mafic intrusions in the western Slave Province and their potential relationship to tectonic events in the adjacent Wopmay Orogen. *Geological Association of Canada-Mineralogical Association of Canada Annual Meeting 2007.* Program with Abstracts 32, pp.20.

Dawson, A.S. 1952. Geology of the Partridge Crop Lake area. Publication 41-1. Manitoba Mines Branch, Winnipeg.

Day, J.M.D., Pearson, D.G. & Hulbert, L.J. 2008. Rhenium-osmium isotope and platinum-group element constraints on the origin and evolution of the 1.27 Ga Muskox layered intrusion. *Journal of Petrology* **49**, 1255-1295.

de Laeter, J.R., Bohlke, J.K., de Bievre, P., Hidaka, H., Peiser, H.S., Rosman, K.J.R. & Taylor, P.D.P. 2003. Atomic weights of the elements: review 2000. *Pure and Applied Chemistry* **75**, 683-800.

DePaolo, D.J. 1981. Trace element and isotopic effects of combined wallrock assimilation and fractional crystallization. *Earth and Planetary Science Letters* **53**, 189-202.

DePaolo, D.J. & Wasserburg, G.J. 1976. Nd isotopic variations and petrogenetic models. *Geophysical Research Letters* **3**, 249-252.

Desharnais, G. 2005. *Geochemical and isotopic investigation of magmatism in the Fox River Belt: tectonic and economic implications*. PhD thesis. University of Manitoba, Winnipeg. 207pp.

Desharnais, G., Peck, D.C., Theyer, P., Potter, L., Huminicki, M., Scoates, R.F.J., Halden, N.M. & Kohut, G. 2000. Geology and mineral occurrences of the Fox River Sill in the Great Falls area, Fox River Belt (parts of NTS 53M/16). In: *Report of Activities 2000*. Manitoba Industry, Trade and Mines, Manitoba Geological Survey, Winnipeg. pp.42-48.

Didenko, A.N., Vodovozov, V.Y., Pisarevsky, S.A., Gladkochub, D.P., Donskaya, T.V., Mazukabzov, A.M., Stanevich, A.M., Bibikova, E.V. & Kirnozova, T.I. 2009. Palaeomagnetism and U-Pb dates of the Palaeoproterozoic Akitkan Group (south Siberia) and implications for pre-Neoproterozoic tectonics. In: Reddy, S.M., Mazumder, R., Evans, D.A.D. & Collins, A.S. (eds) *Palaeoproterozoic supercontinents and global evolution*. Geological Society Special Publication 323. Geological Society of London, London. pp.145-163.

Dimroth, E. 1969. Geology of the Castignon Lake area, New Quebec territory. Preliminary Report 571. Quebec Department of Natural Resources, Mines Branch, Geological Exploration Service, Quebec. 54pp.

Dimroth, E. 1972. The Labrador Geosyncline revisited. *American Journal of Science* **272**, 487-506.

Dimroth, E., Baragar, W.R.A., Bergeron, R. & Jackson, G.D. 1970. The filling of the Circum-Ungava geosyncline. In: Baer, A.J. (ed) *Basins and geosynclines of the Canadian Shield*. Geological Survey of Canada Paper 70-40. Geological Survey of Canada, Ottawa. pp.45-142.

Doig, R. 1983. Rb-Sr isotopic study of Archean gneisses north of the Cape Smith fold belt, Ungava, Quebec. *Canadian Journal of Earth Sciences* **20**, 821-829.

Dostal, J., Dupuy, C. & Liotard, J.M. 1982. Geochemistry and origin of basaltic lavas from Society Islands, French Polynesia (south central Pacific Ocean). *Bulletin Volcanologique* **45**, 51-62.

Dostal, J., Strong, D.F. & Jamieson, R.A. 1980. Trace element mobility in the mylonite zone within the ophiolite aureole, St. Anthony complex, Newfoundland. *Earth and Planetary Science Letters* **49**, 188-192.

Dunphy, J.M., Ludden, J.N. & Francis, D.M. 1995. Geochemistry of mafic magmas from the Ungava Orogen, Quebec, Canada, and implications for mantle reservoir compositions at 2.0 Ga. *Chemical Geology* **120**, 361-380.

Dupuy, C., Barsczus, H.G., Dostal, J., Vidal, P. & Liotard, J.M. 1989. Subducted and recycled lithosphere as the mantle source of ocean island basalts from southern Polynesia, central Pacific. *Chemical Geology* 77, 1-18.

Ebinger, C.J. & Sleep, N.H. 1998. Cenozoic magmatism throughout east Africa resulting from impact of a single plume. *Nature* **395**, 788-791.

Elkins, L., Gaetani, G. & Sims, K. 2008. Partitioning of U and Th during garnet pyroxenite partial melting: constraints on the source of alkaline ocean island basalts. *Earth and Planetary Science Letters* **265**, 270-286.

Ellam, R.M., Carlson, R.W. & Shirey, S.B. 1992. Evidence from Re-Os isotopes for plume-lithosphere mixing in Karoo flood basalt genesis. *Nature* **359**, 718-721.

Ermanovics, I. & Fahrig, W.F. 1975. The petrochemistry and paleomagnetism of the Molson dikes. *Canadian Journal of Earth Sciences* **12**, 1564-1575.

Ernst, R.E. 2004. Ca. 1880 Ma Circum-Superior LIP. http://www.largeigneousprovinces.org/May.html Accessed 2/10/2006.

Ernst, R.E. & Baragar, W.R.A. 1992. Evidence from magnetic fabric for the flow pattern of magma in the Mackenzie giant radiating dyke swarm. *Nature* **356**, 511-513.

Ernst, R.E. & Bell, K. 2010. Large igneous provinces (LIPs) and carbonatites. *Mineralogy and Petrology* **98**, 55-76.

Ernst, R.E. & Buchan, K.L. 1997. Giant radiating dyke swarms: their use in identifying pre-Mesozoic large igneous provinces and mantle plumes. In: Mahoney, J.J. & Coffin, M.F. (eds) *Large igneous provinces: continental, oceanic, and planetary flood volcanism*. Geophysical Monograph 100. American Geophysical Union, Washington DC. pp.297-333.

Ernst, R.E. & Buchan, K.L. 2001a. Large mafic magmatic events through time and links to mantle-plume heads. In: Ernst, R.E. & Buchan, K.L. (eds) *Mantle plumes: their identification through time*. Geological Society of America Special Paper 352. Geological Society of America, Boulder. pp.483-575.

Ernst, R.E. & Buchan, K.L. 2001b. The use of mafic dike swarms in identifying and locating mantle plumes. In: Ernst, R.E. & Buchan, K.L. (eds) *Mantle plumes: their identification through time*. Geological Society of America Special Paper 352. Geological Society of America, Boulder. pp.247-265.

Ernst, R.E. & Buchan, K.L. 2003. Recognizing mantle plumes in the geological record. *Annual Review of Earth and Planetary Sciences* **31**, 469-523.

Ernst, R.E. & Buchan, K.L. 2004. Igneous rock association in Canada 3. Large Igneous Provinces (LIPs) in Canada and adjacent regions: 3 Ga to present. *Geoscience Canada* **31**, 103-126.

Ernst, R.E., Buchan, K.L. & Campbell, I.H. 2004. Frontiers in large igneous province research. *Lithos* **79**, 271-297.

Ernst, R.E., Buchan, K.L., West, T.D. & Palmer, H.C. 1996. Diabase (dolerite) dyke swarms of the world. Geological Survey of Canada Open File 3241. Geological Survey of Canada, Ottawa. 104pp.

Ernst, R.E., Head, J.W., Parfitt, E., Grosfils, E. & Wilson, L. 1995. Giant radiating dyke swarms on Earth and Venus. *Earth Science Reviews* **39**, 1-58.

Ewart, A., Marsh, J.S., Milner, S.C., Duncan, R.A., Kamber, B.S. & Armstrong, R.A. 2004. Petrology and geochemistry of early Cretaceous bimodal continental flood volcanism of the NW Etendeka, Namibia. Part 1: introduction, mafic lavas and re-evaluation of mantle source components. *Journal of Petrology* **45**, 59-105.

Fahrig, W.F. 1987. The tectonic setting of continental mafic dyke swarms: failed arm and early passive margin. In: Halls, H.C. & Fahrig, W.F. (eds) *Mafic dyke swarms*. Geological Association of Canada Special Paper 34. Geological Association of Canada, Toronto. pp.331-348.

Fan, J. & Kerrich, R. 1997. Geochemical characteristics of aluminium depleted and undepleted komatiites and HREE-enriched low-Ti tholeiites, western Abitibi greenstone belt: a heterogeneous mantle plume-convergent margin environment. *Geochimica et Cosmochimica Acta* **61**, 4723-4744.

Fergusson, C.L., Offler, R. & Green, T.J. 2009. Late Neoproterozoic passive margin of east Gondwana: geochemical constraints from the Anakie inlier, central Queensland, Australia. *Precambrian Research* **168**, 301-312.

Fettes, D.J., Mendum, J.R., Smith, D.I. & Watson, J.V. 1992. Geology of the Outer Hebrides. Memoir of the British Geological Survey. Her Majesty's Stationary Office, London. 197pp.

Findlay, J.M., Parrish, R.R., Birkett, T.C. & Watanabe, D.H. 1995. U-Pb ages from the Nimish Formation and Montagnais glomeroporphyritic gabbro of the central New Quebec Orogen, Canada. *Canadian Journal of Earth Sciences* **32**, 1208-1220.

Fitton, J.G. & Godard, M. 2004. Origin and evolution of magmas on the Ontong Java Plateau. In: Fitton, J.G., Mahoney, J.J., Wallace, P.J. & Saunders, A.D. (eds) *Origin and evolution of the Ontong Java Plateau.* Geological Society Special Publication 229. Geological Society of London, London. pp.151-178.

Fitton, J.G., Saunders, A.D., Norry, M.J., Hardarson, B.S. & Taylor, R.N. 1997. Thermal and chemical structure of the Iceland plume. *Earth and Planetary Science Letters* **153**, 197-208.

Foley, S.F., Barth, M.G. & Jenner, G.A. 2000. Rutile/melt partition coefficients for trace elements and an assessment of the influence of rutile on the trace element characteristics of subduction zone magmas. *Geochimica et Cosmochimica Acta* **64**, 933-938.

Font, L., Davidson, J.P., Pearson, D.G., Nowell, G.M., Jerram, D.A. & Ottley, C.J. 2008. Sr and Pb isotope micro-analysis of plagioclase crystals from Skye lavas: an insight into open-system processes in a flood basalt province. *Journal of Petrology* **49**, 1449-1471.

Fowler, S.J., Bohrson, W.A. & Spera, F.J. 2004. Magmatic evolution of the Skye igneous centre, western Scotland: modelling of assimilation, recharge and fractional crystallization. *Journal of Petrology* **45**, 2481-2505.

Fralick, P.W. & Barrett, T.J. 1995. Depositional controls on iron formation associations in Canada. In: Plint, A.G. (ed) *Sedimentary facies analysis.* International Association of Sedimentologists Special Publication 22. Blackwell Science, Oxford. pp.137-156.

Fralick, P.W., Davis, D.W. & Kissin, S.A. 2002. The age of the Gunflint Formation, Ontario, Canada: single U-Pb age determinations from reworked volcanic ash. *Canadian Journal of Earth Sciences* **39**, 1085-1091.

Francis, D.M., Ludden, J. & Hynes, A. 1983. Magma evolution in a Proterozoic rifting environment. *Journal of Petrology* **24**, 556-582.

French, J.E., Heaman, L.M., Chacko, T. & Srivastava, R.K. 2008. 1891-1883 Ma Southern Bastar-Cuddapah mafic igneous events, India: a newly recognized large igneous province. *Precambrian Research* **160**, 308-322.

Gair, J.E. & Wier, K.L. 1956. Geology of the Kiernan quadrangle, Iron County, Michigan. US Geological Survey Bulletin 1044. US Government Printing Office, Washington DC. 88pp.

Galer, S.J.G. & Mezger, K. 1998. Metamorphism, denudation and sea level in the Archean and cooling of the Earth. *Precambrian Research* **92**, 389-412.

Ghandi, S.S., Mortensen, J.K., Prasad, N. & van Breemen, O. 2001. Magmatic evolution of the southern Great Bear continental arc, northwestern Canadian Shield: geochronological constraints. *Canadian Journal of Earth Sciences* **38**, 767-785.

Ghiorso, M.S. 1985. Chemical mass transfer in magmatic processes – I. Thermodynamic relations and numerical algorithms. *Contributions to Mineralogy and Petrology* **90**, 107-120.

Ghiorso, M.S. & Kelemen, P.B. 1987. Evaluating reaction stoichiometry in magmatic systems evolving under generalized thermodynamic constraints: examples comparing isothermal and isenthalpic assimilation. In: Mysen, B.O. (ed) *Magmatic processes: physicochemical principles.* Geochemical Society Special Publication 1. The Geochemical Society, University Park. pp.319-336.

Ghiorso, M.S. & Sack, R.O. 1995. Chemical mass transfer in magmatic processes IV. A revised and internally consistent thermodynamic model for the interpolation and extrapolation of liquid-solid equilibria in magmatic systems at elevated temperatures and pressures. *Contributions to Mineralogy and Petrology* **119**, 197-212.

Ghiorso, M.S., Carmichael, I.S.E., Rivers, M.L. & Sack, R.O. 1983. The Gibbs free energy of mixing of natural silicate liquids; an expanded regular solution approximation for the calculation of magmatic intensive variables. *Contributions to Mineralogy and Petrology* **84**, 107-145.

Gibb, R.A. 1983. Model for suturing of Superior and Churchill plates: an example of double indentation tectonics. *Geology* **11**, 413-417.

Gibb, R.A. & Walcott, R.I. 1971. A Precambrian suture in the Canadian Shield. *Earth and Planetary Science Letters* **10**, 417-422.

Gibson, S.A., Thompson, R.N. & Day, J.A. 2006. Timescales and mechanisms of plume-lithosphere interactions: $^{40}Ar/^{39}Ar$ geochronology and geochemistry of alkaline igneous rocks from the Parana-Etendeka large igneous province. *Earth and Planetary Science Letters* **251**, 1-17.

Gibson, S.A., Thompson, R.N., Day, J.A., Humphris, S.E. & Dickin, A.P. 2005. Melt-generation processes associated with the Tristan mantle plume: constraints on the origin of EM-1. *Earth and Planetary Science Letters* **237**, 744-767.

Gibson, S.A., Thompson, R.N., Dickin, A.P. & Leonardos, O.H. 1996. Erratum to high-Ti and low-Ti mafic potassic magmas: key to plume-lithosphere interactions and continental flood-basalt genesis. *Earth and Planetary Science Letters* **141**, 325-341.

Gillies, S.L. 1993. *Physical volcanology of the Katinniq Peridotite Complex and associated Fe-Ni-Cu-(PGE) mineralization, Cape Smith Belt, northern Quebec.* MS thesis. University of Alabama, Tuscaloosa. 146pp.

Giovenazzo, D., Picard, C. & Guha, J. 1989. Tectonic setting of Ni-Cu-PGE deposits in the central part of the Cape Smith Belt. *Geoscience Canada* **16**, 134-136.

Goldich, S.S. 1973. Ages of Precambrian banded iron-formations. *Economic Geology* **68**, 1126-1134.

Goodwin, A.M. 1956. Facies relations in the Gunflint iron formation. *Economic Geology* **51**, 565-595.

Goodwin, A.M. 1991. *Precambrian geology: the dynamic evolution of the continental crust.* Academic Press, London. 666pp.

Govindaraju, K. 1994. Compilation of working values and sample description for 383 geostandards. *Geostandards Newsletter* **18**, Special Issue, 1-158.

Graham, D.W., Humphris, S.E., Jenkins, W.J. & Kurz, M.D. 1992. Helium isotope geochemistry of some volcanic rocks from Saint Helena. *Earth and Planetary Science Letters* **110**, 121-131.

Green, A.G., Cumming, G.L. & Cedarwell, D. 1979. Extension of the Superior-Churchill boundary zone into southern Canada. *Canadian Journal of Earth Sciences* **16**, 1691-1701.

Green, A.G., Hajnal, Z. & Weber, W. 1985. An evolutionary model of the western Churchill Province and western margin of the Superior Province in Canada and the north-central United States. *Tectonophysics* **116**, 281-322.

Green, D.H., Falloon, T.J., Eggins, S.M. & Yaxley, G.M. 2001. Primary magmas and mantle temperatures. *European Journal of Mineralogy* **13**, 437-451.

Green, T.H. & Pearson, N.J. 1987. An experimental study of Nb and Ta partitioning between Ti-rich minerals and silicate liquids at high pressure and temperature. *Geochimica et Cosmochimica Acta* **51**, 55-62.

Greene, A.R., Scoates, J.S., Weis, D., Nixon, G.T. & Kieffer, B. 2009. Melting history and magmatic evolution of basalts and picrites from the accreted Wrangellia oceanic plateau, Vancouver Island, Canada. *Journal of Petrology* **50**, 467-505.

Gregoire, M., Lorand, J.P., Reilly, S.Y. & Cottin, J.Y. 2000. Armalcolite-bearing, Ti-rich metasomatic assemblages in harzburgitic xenoliths from the Kerguelen Islands: implications for the oceanic mantle budget of high-field strength elements. *Geochimica et Cosmochimica Acta* **64**, 673-694.

Griffin, T.J. & Tyler, I.M. 1992. Geology of the southern Halls Creek Orogen: a summary of field work in 1992. Geological Survey of Western Australia Record 1992/17. Department of Minerals and Energy, Perth. 28pp.

Griffin, T.J., Page, R.W., Sheppard, S. & Tyler, I.M. 2000. Tectonic implications of Palaeoproterozoic post-collisional, high-K felsic igneous rocks from the Kimberley region of northwestern Australia. *Precambrian Research* **101**, 1-23.

Griffiths, R.W. & Campbell, I.H. 1990. Stirring and structure in mantle starting plumes. *Earth and Planetary Science Letters* **99**, 66-78.

Gupta, V.K. 1991. Shaded images of total magnetic field of Ontario. Ontario Geological Survey Maps 2584-2587.

Halden, N.M. 1991. Existence of a marginal basin within the Circum-Superior Belt: geochemical evidence from the Churchill-Superior boundary of Manitoba, Canada. *Precambrian Research* **49**, 167-183.

Halls, H.C. & Heaman, L.M. 2000. The paleomagnetic significance of new U-Pb age data from the Molson dyke swarm, Cauchon Lake area, Manitoba. *Canadian Journal of Earth Sciences* **37**, 957-966.

Halls, H.C., Davis, D.W., Stott, G.M., Ernst, R.E. & Hamilton, M.A. 2008. The Paleoproterozoic Marathon Large Igneous Province: new evidence for a 2.1 Ga long-lived mantle plume event along the southern margin of the North American Superior Province. *Precambrian Research* **162**, 327-353.

Hamilton, M.A. & Stott, G.M. 2008. Project Unit 04-018. The significance of new U/Pb baddeleyite ages from two Paleoproterozoic diabase dikes in northern Ontario. In: *Summary of Fieldwork and Other Activities 2008*. Ontario Geological Survey Open File Report 6226. Ministry of Northern Development and Mines, Toronto. pp.17-1 – 17-7.

Hamilton, M.A., Davis, D.W., Buchan, K.L. & Halls, H.C. 2002. Precise U-Pb dating of reversely magnetized Marathon diabase dykes and implications for emplacement of giant dyke swarms along the southern margin of the Superior Province, Ontario. *Current Research 2002-F6*. Geological Survey of Canada, Ottawa. 8pp.

Hanski, E., Huhma, H., Rastas, P. & Kamenetsky, V.S. 2001. The Palaeoproterozoic komatiite-picrite association of Finnish Lapland. *Journal of Petrology* **42**, 855-876.

Hanson, R.E., Crowley, J.L., Bowring, S.A., Ramezani, J., Gose, W.A., Dalziel, I.W.D., Pancake, J.A., Seidel, E.K., Blenkinsop, T.G. & Mukwakwami, J. 2004a. Coeval large-scale magmatism in the Kalahari and Laurentian cratons during Rodinia assembly. *Science* **304**, 1126-1129.

Hanson, R.E., Gose, W.A., Crowley, J.L., Ramezani, J., Bowring, S.A., Bullen, D.S., Hall, R.P., Pancake, J.A. & Mukwakwami, J. 2004b. Paleoproterozoic intraplate magmatism and basin development on the Kaapvaal craton: age, paleomagnetism and geochemistry of ~1.93 to ~1.87 Ga post-Waterberg dolerites. *South African Journal of Geology* **107**, 233-254.

Harmer, R.E. & von Gruenewaldt, G. 1991. A review of magmatism associated with the Transvaal Basin; implications for its tectonic setting. *South African Journal of Geology* **94**, 104-121.

Harnois, L. & Stevenson, R.K. 2006. Geochimie des elements majeurs et des elements-traces de basaltes et trachyphonolites de Huahine, archipel de la Societe (Polynesie francaise). *Bulletin de la Societe Geologique de France* **177**, 179-190.

Hart, S.R. 1984. A large-scale isotope anomaly in the southern hemisphere mantle. *Nature* **309**, 753-757.

Haskin, L.A., Frey, F.A., Schmitt, R.A. & Smith, R.H. 1966. Meteoric, solar and terrestrial rare-earth distributions. *Physical and Chemical Earth* **7**, 167-321.

Hastie, A.R. & Kerr, A.C. 2010. Mantle plume or slab window?: physical and geochemical constraints on the origin of the Caribbean oceanic plateau. *Earth Science Reviews* **98**, 283-293.

Hastie, A.R., Kerr, A.C., Pearce, J.A. & Mitchell, S.F. 2007. Classification of altered volcanic island arc rocks using immobile trace elements: development of the Th-Co discrimination diagram. *Journal of Petrology* **48**, 2341-2357.

Hauri, E.H. & Hart, S.R. 1997. Rhenium abundances and systematics in oceanic basalts. *Chemical Geology* **139**, 185-205.

Hauri, E.H., Wagner, T.P. & Grove, T.L. 1994. Experimental and natural partitioning of Th, U, Pb and other trace elements between garnet, clinopyroxene and basaltic melts. *Chemical Geology* **117**, 149-166.

Heaman, L.M. 2008. Precambrian large igneous provinces: an overview of geochronology, origins and impact on Earth evolution. *Journal of the Geological Society of India* **72**, 15-34.

Heaman, L.M., Machado, N., Krogh, T.E. & Weber, W. 1986. Precise U-Pb zircon ages for the Molson dyke swarm and the Fox River sill: constraints for early Proterozoic crustal evolution in northeastern Manitoba, Canada. *Contributions to Mineralogy and Petrology* **94**, 82-89.

Heaman, L.M., Peck, D.C. & Toope, K. 2009. Timing and geochemistry of 1.88 Ga Molson Igneous Events, Manitoba: insights into the formation of a craton-scale magmatic and metallogenic province. *Precambrian Research* **172**, 143-162.

Hegner, E. & Bevier, M.L. 1991. Nd and Pb isotopic constraints on the origin of the Purtuniq ophiolite and early Proterozoic Cape Smith Belt, northern Quebec, Canada. *Chemical Geology* **91**, 357-371.

Hemming, S.R., McLennan, S.M. & Hanson, G.N. 1995. Geochemical and Nd/Pb isotopic evidence for the provenance of the early Proterozoic Virginia Formation, Minnesota. Implications for the tectonic setting of the Animikie Basin. *The Journal of Geology* **103**, 147-168.

Hemond, C., Devey, C.W. & Chauvel, C. 1994. Source compositions and melting processes in the Society and Austral plumes (South Pacific Ocean): element and isotope (Sr, Nd, Pb, Th) geochemistry. *Chemical Geology* **115**, 7-45.

Henderson, J.B. 1998. Precambrian geology, Wijinnedi Lake area, district of Mackenzie, Northwest Territories. Geological Survey of Canada Open File 3609. Geological Survey of Canada, Ottawa.

Hergt, J.M., Peate, D.W. & Hawkesworth, C.J. 1991. The petrogenesis of Mesozoic Gondwana low-Ti flood basalts. *Earth and Planetary Science Letters* **105**, 134-148.

Herzberg, C. 1993. Lithospheric peridotites of the Kaapvaal craton. *Earth and Planetary Science Letters* **120**, 13-29.

Herzberg, C. 1995. Generation of plume magmas through time: an experimental perspective. *Chemical Geology* **126**, 1-16.

Herzberg, C. 2004a. Geodynamic information in peridotite petrology. *Journal of Petrology* **45**, 2507-2530.

Herzberg, C. 2004b. Partial melting below the Ontong Java Plateau. In: Fitton, J.G., Mahoney, J.J., Wallace, P.D. & Saunders, A.D. (eds) *Origin and evolution of the Ontong Java Plateau.* Geological Society Special Publication 229. Geological Society of London, London. pp.179-183.

Herzberg, C. & Asimow, P.D. 2008. Petrology of some ocean island basalts: PRIMELT2.XLS software for primary magma calculation. *Geochemistry, Geophysics, Geosystems* **9**, doi: 10.1029/2008GC002057.

Herzberg, C. & Gazel, E. 2009. Petrological evidence for secular cooling in mantle plumes. *Nature* **458**, 619-623.

Herzberg, C. & O'Hara, M.J. 2002. Plume-associated ultramafic magmas of Phanerozoic age. *Journal of Petrology* **43**, 1857-1883.

Herzberg, C. & Zhang, J. 1996. Melting experiments on anhydrous peridotite KLB-1: compositions of magmas in the upper mantle and transition zone. *Journal of Geophysical Research* **101**, 8271-8295.

Herzberg, C., Asimow, P.D., Arndt, N.T., Niu, Y., Lesher, C.M., Fitton, J.G., Cheadle, M.J. & Saunders, A.D. 2007. Temperatures in ambient mantle and plumes: constraints from basalts, picrites and komatiites. *Geochemistry, Geophysics, Geosystems* **8**, doi: 10.1029/2006GC001390.

Herzberg, C., Condie, K.C. & Korenaga, J. 2010. Thermal history of the Earth and its petrological expression. *Earth and Planetary Science Letters* **292**, 79-88.

Hill, E., Wood, B.J. & Blundy, J.D. 2000. The effect of Ca-Tschermaks component on trace element partitioning between clinopyroxene and silicate melt. *Lithos* **53**, 203-215.

Hoffman, P.F. 1973. Evolution of an early Proterozoic continental margin: the Coronation geosyncline and associated aulacogens of the northwestern Canadian Shield. *Philosophical Transactions of the Royal Society of London A* **273**, 547-581.

Hoffman, P.F. 1980. Wopmay Orogen: a Wilson cycle of early Proterozoic age in the northwest of the Canadian Shield. In: Strangway, D.W. (ed) *The continental crust and its mineral deposits.* Geological Association of Canada Special Paper 20. Geological Association of Canada, Toronto. pp.523-549.

Hoffman, P.F. 1987. Early Proterozoic foredeeps, foredeep magmatism, and Superior-type iron-formations of the Canadian Shield. In: Kroener, A. (ed) *Proterozoic lithospheric evolution.* American Geophysical Union Geodynamic Series 17. American Geophysical Union, Washington, DC. pp.85-98.

Hoffman, P.F. 1988. United plates of America, the birth of a craton: early Proterozoic assembly and growth of Laurentia. *Annual Review of Earth and Planetary Sciences* **16**, 543-603.

Hoffman, P.F. & Bowring, S.A. 1984. Short-lived 1.9 Ga continental margin and its destruction, Wopmay Orogen, northwest Canada. *Geology* **12**, 68-72.

Hofmann, A.W. 1997. Mantle geochemistry: the message from oceanic volcanism. *Nature* **385**, 218-229.

Hou, G., Santosh, M., Qian, X., Lister, G.S. & Li, J. 2008. Configuration of the late Paleoproterozoic supercontinent Columbia: insights from radiating mafic dyke swarms. *Gondwana Research* **14**, 395-409.

Hulbert, L.J., Hamilton, M.A., Horan, M.F. & Scoates, R.F.J. 2005. U-Pb zircon and Re-Os isotope geochronology of mineralized ultramafic intrusions and associated nickel ores of the Thompson Nickel Belt, Manitoba, Canada. *Economic Geology* **100**, 29-41.

Hulbert, L.J., Kyser, K., Carlson, R., Lesher, C.M. & Joudrie, C. 1994. The Winnipegosis komatiites; a new komatiite belt, central Manitoba. *Minerals Colloquium Program with Abstracts*. Geological Survey of Canada, Ottawa.

Humphries, S.E. 1984. The mobility of the rare earth elements in the crust. In: Henderson, P. (ed) *Rare earth element geochemistry*. Elsevier, Amsterdam. pp.315-341.

Humphris, S.E. & Thompson, G. 1978. Trace element mobility during hydrothermal alteration of oceanic basalts. *Geochimica et Cosmochimica Acta* **42**, 127-136.

Huppert, H.E. & Sparks, R.S.J. 1985. Komatiites I: eruption and flow. *Journal of Petrology* **26**, 694-725.

Hynes, A. & Francis, D.M. 1982. A transect of the early Proterozoic Cape Smith foldbelt, New Quebec. *Tectonophysics* **88**, 23-59.

Imai, N., Terashima, H., Itoh, S. & Ando, A. 1995. 1994 compilation values for GSJ reference samples, igneous rock series. *Geostandards Newsletter* **19**, 135-213.

Irvine, T.N. & Baragar, W.R.A. 1971. A guide to the chemical classification of the common volcanic rocks. *Canadian Journal of Earth Sciences* **8**, 523-548.

Isley, A.E. & Abbott, D.H. 1999. Plume-related mafic volcanism and the deposition of banded iron formation. *Journal of Geophysical Research* **104**, 15461-15477.

Jackson, G.D. 1960. Belcher Islands, Northwest Territories. Geological Survey of Canada Paper 60-20. Geological Survey of Canada, Ottawa. 13pp.

Jackson, G.D. 1971. Operation Penny Highlands, south-central Baffin Island. In: *Report of Activities Part A*. Geological Survey of Canada Paper 71-01A. Geological Survey of Canada, Ottawa. pp.138-140.

Jahn, B.M., Gruau, G., Capdevila, R., Cornichet, J., Nemchin, A., Pidgeon, R. & Rudnik, V.A. 1998. Archean crustal evolution of the Aldan Shield, Siberia: geochemical and isotopic constraints. *Precambrian Research* **91**, 333-363.

James, H.L. 1958. Stratigraphy of pre-Keweenawan rocks in parts of northern Michigan. US Geological Survey Professional Paper 314-C. US Government Printing Office, Washington DC. pp.27-44.

James, H.L., Dutton, C.E., Pettijohn, F.J. & Wier, K.L. 1968. Geology and ore deposits of the Iron River-Crystal Falls district, Iron County, Michigan. US Geological Survey Professional Paper 570. US Government Printing Office, Washington DC. 134pp.

Janardhan, A.S., Newton, R.C. & Hansen, E.C. 1982. The transformation of amphibolite facies gneiss to charnockite in southern Karnataka and northern Tamil Nadu, India. *Contributions to Mineralogy and Petrology* **79**, 130-149.

Jang, Y.D., Naslund, H.R. & McBirney, A.R. 2001. The differentiation trend of the Skaergaard intrusion and the timing of magnetite crystallization: iron enrichment revisited. *Earth and Planetary Science Letters* **189**, 189-196.

Jaupart, C., Mareschal, J.C., Guillou-Frottier, L. & Davaille, A. 1998. Heat flow and thickness of the lithosphere in the Canadian Shield. *Journal of Geophysical Research* **103**, 15269-15286.

Jayananda, M., Kano, T., Peucat, J.-J. & Channabasappa, S. 2008. 3.35 Ga komatiite volcanism in the western Dharwar craton, southern India: constraints from Nd isotopes and whole-rock geochemistry. *Precambrian Research* **162**, 160-179.

Jochum, K.P, Arndt, N.T. & Hofmann, A.W. 1991. Nb-Th-La in komatiites and basalts: constraints on komatiite petrogenesis and mantle evolution. *Earth and Planetary Science Letters* **107**, 272-289.

Johns, S.M., Helmstaedt, H.H. & Kyser, T.K. 2006. Paleoproterozoic submarine intrabasinal rifting, Baffin Island, Nunavut, Canada: volcanic structure and geochemistry of the Bravo Lake Formation. *Canadian Journal of Earth Sciences* **43**, 593-616.

Johnson, K.T.M. 1998. Experimental determination of partition coefficients for rare earth and high-field-strength elements between clinopyroxene, garnet, and basaltic melt at high pressures. *Contributions to Mineralogy and Petrology* **133**, 60-68.

Johnson, K.T.M., Dick, H.J.B. & Shimizu, N. 1990. Melting in the oceanic upper mantle: an ion microprobe study of diopsides in abyssal peridotites. *Journal of Geophysical Research* **95**, 2661-2678.

Johnston, S.T. & Thorkelson, D.J. 2000. Continental flood basalts: episodic magmatism above long-lived hotspots. *Earth and Planetary Science Letters* **175**, 247-256.

Jourdan, F., Bertrand, H., Feraud, G., Le Gall, B. & Watkeys, M.K. 2009. Lithospheric mantle evolution monitored by overlapping large igneous provinces: case study in southern Africa. *Lithos* **107**, 257-268.

Jourdan, F., Bertrand, H., Scharer, U., Blichert-Toft, J., Feraud, G. & Kampunzu, A.B. 2007. Major and trace element and Sr, Nd, Hf and Pb isotope compositions of the Karoo large igneous province, Botswana-Zimbabwe: lithosphere vs mantle plume contribution. *Journal of Petrology* **48**, 1043-1077.

Kahkonen, Y. 1987. Geochemistry and tectonomagmatic affinities of the metavolcanic rocks of the early Proterozoic Tampere Schist Belt, southern Finland. *Precambrian Research* **35**, 295-311.

Kahkonen, Y., Huhma, H. & Aro, K. 1989. U-Pb zircon ages and Rb-Sr whole-rock isotope studies of early Proterozoic volcanic and plutonic rocks near Tampere, southern Finland. *Precambrian Research* **45**, 27-43.

Kalsbeek, F. & Nutman, A.P. 1996. Anatomy of the early Proterozoic Nagssugtoqidian Orogen, west Greenland, explored by reconnaissance SHRIMP U-Pb zircon dating. *Geology* **24**, 515-518.

Kalsbeek, F., Pidgeon, R.T. & Taylor, P.N. 1987. Nagssugtoqidian mobile belt of west Greenland: a cryptic 1850 Ma suture between two Archaean continents – chemical and isotopic evidence. *Earth and Planetary Science Letters* **85**, 365-385.

Karato, S. 2010. Rheology of the Earth's mantle: a historical review. *Gondwana Research* **18**, 17-45.

Kato, T., Ringwood, A.E. & Irifune, T. 1988. Experimental determination of element partitioning between silicate perovskites, garnets and liquids: constraints on early differentiation of the mantle. *Earth and Planetary Science Letters* **89**, 123-145.

Keays, R.R. 1995. The role of komatiitic and picritic magmatism and S-saturation in the formation of ore deposits. *Lithos* **34**, 1-18.

Kelemen, P.B., Shimizu, N. & Dunn, T. 1993. Relative depletion of niobium in some arc magmas and the continental crust: partitioning of K, Nb, La and Ce during melt/rock reaction in the upper mantle. *Earth and Planetary Science Letters* **120**, 111-134.

Kempton, P.D. & McGill, R. 2002. Procedures for the analysis of common lead at the NERC Isotope Geosciences Laboratory and an assessment of data quality. NIGL Report Series 178. 60pp.

Kempton, P.D., Fitton, J.G., Saunders, A.D., Nowell, G.M., Taylor, R.N., Hardarson, B.S. & Pearson, G. 2000. The Iceland plume in space and time: a Sr-Nd-Pb-Hf study of the North Atlantic rifted margin. *Earth and Planetary Science Letters* **177**, 255-271.

Kempton, P.D., Nowell, G.M. & Barry, T.L. 2001. Procedure for the high precision isotopic analysis of hafnium in silicate rocks and minerals by plasma ionisation multi-collector mass spectrometry (PIMMS) and an assessment of data quality at the NERC Isotope Geosciences Laboratory. NIGL Report Series 171. 45pp.

Kerr, A.C. 1998. Oceanic plateau formation: a cause of mass extinction and black shale deposition around the Cenomanian-Turonian boundary? *Journal of the Geological Society, London* **155**, 619-626.

Kerr, A.C. 2003. Oceanic plateaus. In: Rudnick, R.L. (ed) *The crust.* In: Holland, H.G. & Turekian, K.K. (series eds) Treatise on Geochemistry Volume 3. Elsevier, Amsterdam. pp.537-565.

Kerr, A.C. & Arndt, N.T. 2001. A note on the IUGS reclassification of the high-Mg and picritic volcanic rocks. *Journal of Petrology* **42**, 2169-2171.

Kerr, A.C. & Mahoney, J.J. 2007. Oceanic plateaus: problematic plumes, potential paradigms. *Chemical Geology* **241**, 332-353.

Kerr, A.C., Kempton, P.D. & Thompson, R.N. 1995a. Crustal assimilation during turbulent magma ascent (ATA); new isotopic evidence from the Mull Tertiary lava succession, NW Scotland. *Contributions to Mineralogy and Petrology* **119**, 142-154.

Kerr, A.C., Marriner, G.F., Arndt, N.T., Tarney, J., Nivia, A., Saunders, A.D. & Duncan, R.A. 1996. The petrogenesis of Gorgona komatiites, picrites and basalts: new field, petrographic and geochemical constraints. *Lithos* **37**, 245-260.

Kerr, A.C., Marriner, G.F., Tarney, J., Nivia, A., Saunders, A.D., Thirlwall, M.F. & Sinton, C.W. 1997. Cretaceous basaltic terranes in western Colombia: elemental, chronological and Sr-Nd isotopic constraints on petrogenesis. *Journal of Petrology* **38**, 677-702.

Kerr, A.C., Pearson, D.G. & Nowell, G.M. 2009. Magma source evolution beneath the Caribbean oceanic plateau: new insights from elemental and Sr-Nd-Pb-Hf isotopic studies of ODP Leg 165 Site 1001 basalts. In: James, K.H., Lorente, M.A. & Pindell, J.L. (eds) *The origin and evolution of the Caribbean plate.* Geological Society Special Publication 328. Geological Society of London, London. pp.809-827.

Kerr, A.C., Saunders, A.D., Tarney, J., Berry, N.H. & Hards, V.L. 1995b. Depleted mantle-plume geochemical signatures: no paradox for plume theories. *Geology* **23**, 843-846.

Kerr, A.C., Tarney, J., Kempton, P.D., Spadea, P., Nivia, A., Marriner, G.F. & Duncan, R.A. 2002. Pervasive mantle plume head heterogeneity: evidence from the late Cretaceous Caribbean-Colombian oceanic plateau. *Journal of Geophysical Research* **107**, doi: 10.1029/2001JB000790.

Kerr, A.C., White, R.V. & Saunders, A.D. 2000. LIP reading: recognizing oceanic plateaux in the geological record. *Journal of Petrology* **41**, 1041-1056.

Kerrich, R. & Fryer, B.J. 1979. Archean precious-metal hydrothermal systems, Dome mine, Abitibi greenstone belt: 2. REE and oxygen isotope relations. *Canadian Journal of Earth Sciences* **16**, 440-458.

Kerrich, R. Polat, A., Wyman, D. & Hollings, P. 1999. Trace element systematics of Mg-, to Fe-tholeiitic basalt suites of the Superior Province: implications for Archean mantle reservoirs and greenstone belt genesis. *Lithos* **46**, 163-187.

Kerrich, R., Polat, A. & Xie, Q. 2008. Geochemical systematics of 2.7 Ga Kinojevis Group (Abitibi), and Manitouwadge and Winston Lake (Wawa) Fe-rich basalt-rhyolite associations: backarc rift oceanic crust? *Lithos* **101**, 1-23.

King, S.D. 2007. Hotspots and edge-driven convection. *Geology* **35**, 223-226.

King, S.D. & Anderson, D.L. 1995. An alternative mechanism of flood basalt formation. *Earth and Planetary Science Letters* **136**, 269-279.

King, S.D. & Anderson, D.L. 1998. Edge-driven convection. *Earth and Planetary Science Letters* **160**, 289-296.

Kinzler, R.J. & Grove, T.L. 1992. Primary magmas of mid-ocean ridge basalts 2. Applications. *Journal of Geophysical Research* **97**, 6907-6926.

Kissin, S.A. & Fralick, P.W. 1994. Early Proterozoic volcanics of the Animikie Group, Ontario and Michigan, and their tectonic significance. *Proceedings of the Institute on Lake Superior Geology* **40**, 18-19.

Klasner, J.S., LaBerge, G.L. & Cannon, W.F. 1998. Geologic map of the eastern Gogebic iron range, Gogebic County, Michigan. US Geological Survey Geologic Investigations Series Map I-2606.

Klausen, M.B., Soderlund, U., Olsson, J.R., Ernst, R.E., Armoogam, M., Mkhize, S.W. & Petzer, G. 2010. Petrological discrimination among Precambrian dyke swarms: eastern Kaapvaal craton (South Africa). *Precambrian Research* **183**, 501-522.

Knoper, M.W. & Condie, K.C. 1988. Geochemistry and petrogenesis of early Proterozoic amphibolites, west-central Colorado, USA. *Chemical Geology* **67**, 209-225.

Kogarko, L.N., Asavin, A.M., Barsukov, V.L., Kolesov, G.M., Kruchkova, O.I., Polyakov, A.I. & Ramendik, G.I. 1984. A geochemical model for rare-earth fractionation in alkali-basalt series in South Atlantic islands. *Geochemistry International* **21**, 27-39.

Kogiso, T.Y., Tatsumi, Y., Shimoda, G. & Barsczus, H. 1997. High μ (HIMU) ocean island basalts in southern Polynesia: new evidence for whole mantle scale recycling of subducted oceanic crust. *Journal of Geophysical Research* **102**, 8085-8103.

Komiya, T., Maruyama, S., Hirata, T., Yurimoto, H. & Nohda, S. 2004. Geochemistry of the oldest MORB and OIB in the Isua supracrustal belt, southern west Greenland: implications for the composition and temperature of early Archean upper mantle. *Island Arc* **13**, 47-72.

Korenaga, J. 2008a. Plate tectonics, flood basalts and the evolution of Earth's oceans. *Terra Nova* **20**, 419-439.

Korenaga, J. 2008b. Urey ratio and the structure and evolution of Earth's mantle. *Reviews of Geophysics* **46**, doi: 10.1029/2007RG000241.

Korja, A., Lahtinen, R. & Nironen, M. 2006. The Svecofennian orogen: a collage of microcontinents and island arcs. In: Gee, D.G. & Stephenson, R.A. (eds) *European lithosphere dynamics*. Geological Society Memoir 32. Geological Society of London, London. pp.561-578.

LaBerge, G. L. 1992. The early Proterozoic Emperor Volcanic Complex: implications for the geology of the eastern Gogebic district, northern Michigan. *Proceedings of the Institute on Lake Superior Geology* **38**, 53-55.

Lafleche, M.R., Dupuy, C. & Dostal, J. 1992. Tholeiitic volcanic rocks of the late Archean Blake River group, southern Abitibi greenstone belt: origin and geodynamic implications. *Canadian Journal of Earth Sciences* **29**, 1448-1458.

Lahaye, Y. & Arndt, N.T. 1996. Alteration of a komatiite flow from Alexo, Ontario, Canada. *Journal of Petrology* **37**, 1261-1284.

Lalonde, A.E. 1988. The Morel sills of Wopmay Orogen, NWT. *Geological Association of Canada-Mineralogical Association of Canada Annual Meeting 1988*. Program with Abstracts 13, pp.70.

Lalonde, A.E. 1989. Hepburn intrusive suite: peraluminous plutonism within a closing back-arc basin, Wopmay Orogen, Canada. *Geology* **17**, 261-264.

Langmuir, C.H., Klein, E.M. & Plank, T. 1992. Petrological systematics of mid-ocean ridge basalts: constraints on melt generation beneath ocean ridges. In: Morgan, J.P., Blackman, D.K. & Sinton, J.M. (eds) *Mantle flow and melt generation at mid-ocean ridges*. Geophysical Monograph 71. American Geophysical Union, Washington DC. pp.183-280.

Larin, A.M., Sal'nikova, E.B., Kotov, A.B., Kovalenko, V.I., Rytsk, E.Y., Yakovleva, S.Z., Berezhnaya, N.G., Kovach, V.P., Buldygerov, V.V. & Sryvtsev, N.A. 2003. The North Baikal volcanoplutonic belt: age, formation, duration, and tectonic setting. *Doklady Earth Sciences* **392**, 963-967.

Larson, R.L. 1991a. Latest pulse of Earth: evidence for a mid-Cretaceous superplume. *Geology* **19**, 547-550.

Larson, R.L. 1991b. Geological consequences of superplumes. *Geology* **19**, 963-966.

Layton-Matthews, D., Lesher, C.M., Burnham, O.M., Liwanag, J., Halden, N.M., Hulbert, L.J. & Peck, D.C. 2007. Magmatic Ni-Cu-platinum-group element deposits of the Thompson Nickel Belt. In: Goodfellow, W.D. (ed) *Mineral deposits of Canada: a synthesis of major deposit-types, district metallogeny, the evolution of geological provinces, and exploration models*. Geological Association of Canada, Mineral Deposits Division, Special Publication No. 5. Geological Association of Canada-Mineral Deposits Division, St. John's. pp.409-432.

Le Bas, M.J. 2000. IUGS reclassification of the high-Mg and picritic volcanic rocks. *Journal of Petrology* **41**, 1467-1470.

Le Gallais, C.J. & Lavoie, S. 1982. Basin evolution of the Lower Proterozoic Kaniapiskau Supergroup, central Labrador miogeocline (trough), Quebec. *Bulletin of Canadian Petroleum Geology* **30**, 150-166.

Legault, F. 1994. *The petrogenesis of Proterozoic continental volcanism in the Belcher Islands with implications for the evolution of the Circum Ungava Fold Belt.* MSc thesis. McGill University, Montreal. 84pp.

Legault, F., Francis, D.M., Hynes, A.J. & Budkewitsch, P. 1994. Proterozoic continental volcanism in the Belcher Islands: implications for the evolution of the Circum Ungava Fold Belt. *Canadian Journal of Earth Sciences* **31**, 1536-1549.

Legendre, C., Maury, R.C., Guillou, H., Cotten, J., Caroff, M., Blais, S. & Guille, G. 2003. Evolution geologique et petrologique de l'ile de Huahine (archipel de la Societe, Polynesie francaise): un volcan-bouclier intraoceanique original. *Bulletin de la Societe Geologique de France* **174**, 115-124.

Le Maitre, R.W., Bateman, P., Dudek, A., Keller, J., Lameyre, J., Le Bas, M.J., Sabine, P.A., Schmid, R., Sorenson, H., Streckeisen, A., Woolley, A.R. & Zanettin, B. 1989. *A classification of igneous rocks and glossary of terms*. Blackwell Science, Oxford. 193pp.

Lemarchand, F., Benoit, V. & Calais, G. 1987. Trace element distribution coefficients in alkaline series. *Geochimica et Cosmochimica Acta* **51**, 1071-1081.

le Roex, A.P., Bell, D.R. & Davis, P. 2003. Petrogenesis of Group 1 kimberlites from Kimberley, South Africa: evidence from bulk-rock geochemistry. *Journal of Petrology* **44**, 2261-2286.

Lesher, C.M. 2007. Deposits in the Raglan area, Cape Smith Belt, New Quebec. In: Goodfellow, W.D. (ed) *Mineral deposits of Canada: a synthesis of major deposit-types, district metallogeny, the evolution of geological provinces, and exploration models.* Geological Association of Canada, Mineral Deposits Division, Special Publication No. 5. Geological Association of Canada-Mineral Deposits Division, St. John's. pp.351-386.

Lesher, C.M. & Keays, R.R. 2002. Komatiite-associated Ni-Cu-(PGE) deposits: mineralogy, geochemistry and genesis. In: Cabri, L.J. (ed) *The geology, geochemistry, mineralogy and mineral beneficiation of platinum group minerals*. Canadian Institute of Mining, Metallurgy and Petroleum Special Volume 54. Canadian Institute of Mining, Metallurgy and Petroleum, Montreal. 852pp.

Lesher, C.M. & Stone, W.E. 1996. Exploration geochemistry of komatiites. In: Wyman, D. (ed) *Trace element geochemistry of volcanic rocks: application for massive sulphide exploration.* Geological Association of Canada Short Course Notes 12. Geological Association of Canada, Mineral Deposits Division, Winnipeg. pp.153-204.

Lesher, C.M. & Vicker, P. 1999. Geology of the Donaldson area. In: Lesher, C.M. (ed) *Komatiitic peridotite-hosted Fe-Ni-Cu-(PGE) sulphide deposits in the Raglan area, Cape Smith Belt, New Quebec.* Laurentian University, Mineral Exploration Research Centre, Guidebook Series 2. Laurentian University, Sudbury. pp.143-149.

Lesher, C.M., Burnham, O.M., Keays, R.R., Barnes, S.J. & Hulbert, L.J. 2001. Trace-element geochemistry and petrogenesis of barren and ore-associated komatiites. *Canadian Mineralogist* **39**, 673-696.

Lesher, C.M., Thibert, F., Gillies, S.L., Stilson, C.M., Thacker, J.L. & Williams, D.A. 1999. Lithology and physical volcanology of komatiitic peridotite-gabbro complexes in the Raglan Block. In: Lesher, C.M. (ed) *Komatiitic peridotite-hosted Fe-Ni-Cu-(PGE) sulphide deposits in the Raglan area, Cape Smith Belt, New Quebec.* Laurentian University, Mineral Exploration Research Centre, Guidebook Series 2. Laurentian University, Sudbury. pp.43-60.

Lewry, J.F. & Stauffer, M.R. (eds) 1990. *The early Proterozoic Trans-Hudson Orogen of North America.* Geological Association of Canada Special Paper 37. Geological Association of Canada, Toronto. 505pp.

Licht, K. & Flood, T.P. 1992. The chemistry and petrography of mafic rocks from the early Proterozoic Emperor Volcanic Complex near Marinesco, Michigan. *Proceedings of the Institute on Lake Superior Geology* **38**, 56-57.

Lucas, S.B. & St-Onge, M.R. 1992. Terrane accretion in the internal zone of the Ungava orogen, northern Quebec. Part 2: structural and metamorphic history. *Canadian Journal of Earth Sciences* **29**, 765-782.

Lucas, S.B., Stern, R.A., Syme, E.C., Reilly, B.A. & Thomas, D.J. 1996. Intraoceanic tectonics and the development of continental crust: 1.92-1.84 Ga evolution of the Flin Flon Belt, Canada. *Geological Society of America Bulletin* **108**, 602-629.

Luck, J.-M. & Allegre, C.J. 1983. ^{187}Re-^{187}Os systematics in meteorites and cosmochemical consequences. *Nature* **302**, 130-132.

Ludden, J., Gelienas, L. & Trudel, P. 1982. Acrhean metavolcanics from the Rouyn-Noranda district, Abitibi greenstone belt, Quebec: 2. Mobility of trace elements and petrogenetic constraints. *Canadian Journal of Earth Sciences* **19**, 2276-2287.

Lugmair, G.W. & Marti, K. 1978. Lunar initial $^{143}Nd/^{144}Nd$: differential evolution of the lunar crust and mantle. *Earth and Planetary Science Letters* **39**, 349-357.

Maaloe, S. 2003. Melt dynamics of a partially molten mantle with randomly oriented veins. *Journal of Petrology* **44**, 1193-1210.

Maaloe, S. & Aoki, K.-I. 1977. The major element composition of the upper mantle estimated from the composition of lherzolites. *Contributions to Mineralogy and Petrology* **63**, 161-173.

Macdonald, R. & Fettes, D.J. 2007. The tectonomagmatic evolution of Scotland. *Transactions of the Royal Society of Edinburgh: Earth Sciences* **97**, 213-295.

Machado, N. 1990. Timing of collisional events in the Trans-Hudson Orogen: evidence from U-Pb geochronology for the New Quebec Orogen, the Thompson Belt, and the Reindeer Zone (Manitoba and Saskatchewan). In: Lewry, J.F. & Stauffer, M.L. (eds) *The early Proterozoic Trans-Hudson Orogen of North America.* Geological Association of Canada Special Paper 37. Geological Association of Canada, Toronto. pp.433-441.

Machado, N., Clark, T., David, J. & Goulet, N. 1997. U-Pb ages for magmatism and deformation in the New Quebec Orogen. *Canadian Journal of Earth Sciences* **34**, 716-723.

Machado, N., David, J., Scott, D.J., Lamothe, D., Philippe, S. & Gariepy, C. 1993. U-Pb geochronology of the western Cape Smith Belt, Canada: new insights on the age of initial rifting and arc magmatism. *Precambrian Research* **63**, 211-223.

Maier, W.D. & Barnes, S.-J. 2005. Application of lithogeochemistry to exploration for PGE deposits. In: Mungall, J.E. (ed) *Exploration for platinum-group element deposits.* Mineralogical Association of Canada Short Course Series Volume 35. Mineralogical Association of Canada, Ottawa. pp.309-341.

Mallinson, T. 1999a. Geology of the Zone 2 area. In: Lesher, C.M. (ed) *Komatiitic peridotite-hosted Fe-Ni-Cu-(PGE) sulphide deposits in the Raglan area, Cape Smith Belt, New Quebec.* Laurentian University, Mineral Exploration Research Centre, Guidebook Series 2. Laurentian University, Sudbury. pp.84-90.

Mallinson, T. 1999b. Geology of the Zone 3 area. In: Lesher, C.M. (ed) *Komatiitic peridotite-hosted Fe-Ni-Cu-(PGE) sulphide deposits in the Raglan area, Cape Smith Belt, New Quebec.* Laurentian University, Mineral Exploration Research Centre, Guidebook Series 2. Laurentian University, Sudbury. pp.76-83.

Mallinson, T. 1999c. Geology of the Zone 5-8 area. In: Lesher, C.M. (ed) *Komatiitic peridotite-hosted Fe-Ni-Cu-(PGE) sulphide deposits in the Raglan area, Cape Smith Belt, New Quebec.* Laurentian University, Mineral Exploration Research Centre, Guidebook Series 2. Laurentian University, Sudbury. pp.107-116.

Mason, A.J., Parrish, R.R. & Brewer, T.S. 2004. U-Pb geochronology of Lewisian orthogneisses in the Outer Hebrides, Scotland: implications for the tectonic setting and correlation of the South Harris Complex. *Journal of the Geological Society, London* **161**, 45-54.

Maurice, C. & Francis, D. 2010. Enriched crustal and mantle components and the role of the lithosphere in generating Paleoproterozoic dyke swarms of the Ungava Peninsula, Canada. *Lithos* **114**, 95-108.

Maurice, C., David, J., O'Neil, J. & Francis, D. 2009. Age and tectonic implications of Paleoproterozoic mafic dyke swarms for the origin of 2.2 Ga enriched lithosphere beneath the Ungava Peninsula, Canada. *Precambrian Research* **174**, 163-180.

Mavrogenes, J.A. & O'Neill, H.St.C. 1999. The relative effects of pressure, temperature and oxygen fugacity on the solubility of sulfide in mafic magmas. *Geochimica et Cosmochimica Acta* **63**, 1173-1180.

Mayborn, K.R. & Lesher, C.E. 2004. Paleoproterozoic mafic dike swarms of northeast Laurentia: products of plumes or ambient mantle? *Earth and Planetary Science Letters* **225**, 305-317.

McCuaig, T.C., Kerrich, R. & Xie, Q. 1994. Phosphorus and high field strength element anomalies in Archean high-magnesian magmas as possible indicators of source mineralogy and depth. *Earth and Planetary Science Letters* **124**, 221-239.

McDonough, W.F. & Sun, S.-S. 1995. The composition of the Earth. *Chemical Geology* **120**, 223-253.

McKenzie, D. & Bickle, M.J. 1988. The volume and composition of melt generated by extension of the lithosphere. *Journal of Petrology* **29**, 625-679.

McKenzie, D. & O'Nions, R.K. 1991. Partial melt distributions from inversion of rare earth element concentrations. *Journal of Petrology* **32**, 1021-1091.

McKenzie, D., Jackson, J. & Priestley, K. 2005. Thermal structure of oceanic and continental lithosphere. *Earth and Planetary Science Letters* **233**, 337-349.

McRitchie, W.D. 1995. Mineral development potential in Manitoba – nickel in the southwest extension of the Thompson Nickel Belt. Economic Report ER95-2. Manitoba Energy and Mines, Geological Services, Winnipeg. 29pp.

Melluso, L., Beccaluva, L., Brotzu, P., Gregnanin, A., Gupta, A.K., Morbidelli, L. & Traversa, G. 1995. Constraints on the mantle sources of the Deccan Traps from the petrology and geochemistry of the basalts of Gujarat State (western India). *Journal of Petrology* **36**, 1393-1432.

Melluso, L., Mahoney, J.J. & Dallai, L. 2006. Mantle sources and crustal input as recorded in high-Mg Deccan Traps basalts of Gujarat (India). *Lithos* **89**, 259-274.

Menzies, M. & Seyfried, W.E. 1979a. Basalt–seawater interaction: trace element and strontium isotopic variations in experimentally altered glassy basalt. *Earth and Planetary Science Letters* **44**, 463-472.

Menzies, M. & Seyfried, W.E. 1979b. Experimental evidence of rare earth element immobility in greenstones. *Nature* **282**, 398-399.

Mereu, R.F., Wang, D., Kuhn, O., Forsyth, D.A., Green, A.G., Morel, P., Buchbinder, G.C.R., Crossley, D., Schwarz, E., duBerger, R., Brooks, C. & Clowes, R.M. 1986. The 1982 COCRUST seismic experiment across the Ottawa-Bonnecherre graben and Grenville Front in Ontario and Quebec. *Royal Astronomical Society Geophysical Journal* **84**, 491-514.

Merritt, C.A. 1925. Bigstone and Fox River area, northern Manitoba. In: *Summary Report 1925, Part B*. Geological Survey of Canada, Ottawa. pp.27–30.

Meschede, M. 1986. A method of discriminating between different types of mid-ocean ridge basalts and continental tholeiites with the Nb-Zr-Y diagram. *Chemical Geology* **56**, 207-218.

Modeland, S., Francis, D. & Hynes, A. 2003. Enriched mantle components in Proterozoic continental-flood basalts of the Cape Smith foldbelt, northern Quebec. *Lithos* **71**, 1-17.

Mukhopadhyay, M. & Gibb, R.A. 1981. Gravity anomalies and deep structure of eastern Hudson Bay. *Tectonophysics* **72**, 43-60.

Mungall, J.E. 2005. Magmatic geochemistry of the platinum-group elements. In: Mungall, J.E. (ed) *Exploration for platinum-group element deposits*. Mineralogical Association of Canada Short Course Series Volume 35. Mineralogical Association of Canada, Ottawa. pp.1-34.

Mungall, J.E. 2007. Crustal contamination of picritic magmas during transport through dikes: the Expo Intrusive Suite, Cape Smith Fold Belt, New Quebec. *Journal of Petrology* **48**, 1021-1039.

Mungall, J.E. & Wares, R.P. 1997. Petrology of lavas and intrusions on the Hawk Ridge property, and implications for magmatic Ni-Cu mineralization. Internal report to Troymin Resources Ltd. 42pp.

Myers, J.S., Shaw, R.D. & Tyler, I.M. 1996. Tectonic evolution of Proterozoic Australia. *Tectonics* **15**, 1431-1446.

Naldrett, A.J. 1999. World-class Ni-Cu-PGE deposits: key factors in their genesis. *Mineralium Deposita* **34**, 227-240.

Naldrett, A.J. 2004. *Magmatic sulfide deposits: geology, geochemistry and exploration*. Springer, Berlin. 727pp.

Newsom, H.E., White, W.M., Jochum, K.P. & Hofmann, A.W. 1986. Siderophile and chalcophile element abundances in oceanic basalts, Pb isotope evolution and growth of the Earth's core. *Earth and Planetary Science Letters* **80**, 299-313.

Neymark, L.A., Larin, A.M., Yakovleva, S.Z., Sryvtsev, N.A. & Buldygerov, V.V. 1991. New data on the age units of the Akitkan series of the Baikal-Patom folded region, according to the results of U-Pb dating of zircons. *Doklady Earth Sciences* **320**, 182-186.

Nielsen, R.L., Gallahan, W.E. & Newberger, F. 1992. Experimentally determined mineral-melt partition coefficients for Sc, Y and REE for olivine, orthopyroxene, pigeonite, magnetite and ilmenite. *Contributions to Mineralogy and Petrology* **110**, 488-499.

Nironen, M. 1999. Structural and magmatic evolution in the Loimaa area, southwestern Finland. *Bulletin of the Geological Society of Finland* **71**, 57-71.

Nironen, M., Elliott, B.A. & Ramo, O.T. 2000. 1.88-1.87 Ga post-kinematic intrusions of the Central Finland Granitoid Complex: a shift from C-type to A-type magmatism during lithospheric convergence. *Lithos* **53**, 37-58.

Nisbet, E.G., Cheadle, M.J., Arndt, N.T. & Bickle, M.J. 1993. Constraining the potential temperature of the Archaean mantle: a review of the evidence from komatiites. *Lithos* **30**, 291-307.

Ohta, H., Maruyama, S., Takahashi, E., Watanabe, Y. & Kato, Y. 1996. Field occurrence, geochemistry and petrogenesis of the Archean mid-oceanic ridge basalts (AMORBs) of the Cleaverville area, Pilbara craton, Western Australia. *Lithos* **37**, 199-221.

Ojakangas, R.W., Morey, G.B. & Southwick, D.L. 2001. Paleoproterozoic basin development and sedimentation in the Lake Superior region, North America. *Sedimentary Geology* **141-142**, 319-341.

Okamoto, K. 1979. Geochemical study on magmatic differentiation of Asama Volcano, central Japan. *Journal of the Geological Society of Japan* **85**, 525-535.

O'Neill, H.St.C. & Mavrogenes, J.A. 2002. The sulfide capacity and the sulfur content at sulfide saturation of silicate melts at 1400°C and 1 bar. *Journal of Petrology* **43**, 1049-1087.

Page, R.W., Hoatson, S.L., Sun, S.-S. & Fodoulis, C. 1995. High-precision geochronology of Palaeoproterozoic layered mafic-ultramafic intrusions in the East Kimberley. *Australian Geological Survey Organisation Research Newsletter* **22**, 7-8.

Paktunc, A.D. 1984. Metamorphism of the ultramafic rocks of the Thompson mine, Thompson Nickel Belt, northern Manitoba. *Canadian Mineralogist* **22**, 77-91.

Paktunc, A.D. 1987. Differentiation of the Cuthbert Lake ultramafic dikes and related mafic dikes. *Contributions to Mineralogy and Petrology* **97**, 405-416.

Pang, K.-N., Zhou, M.-F., Lindsley, D., Zhao, D. & Malpas, J. 2008. Origin of Fe-Ti oxide ores in mafic intrusions: evidence from the Panzhihua intrusion, SW China. *Journal of Petrology* **49**, 295-313.

Parrish, R.R. 1989. U-Pb geochronology of the Cape Smith Belt and Sugluk block, northern Quebec. *Geoscience Canada* **16**, 126-130.

Pearce, J.A. 1982. Trace element characteristics of lavas from destructive plate boundaries. In: Thorpe, R.S. (ed) *Andesites: orogenic andesites and related rocks*. John Wiley & Sons, Chichester. pp.525-548.

Pearce, J.A. 1996. A user's guide to basalt discrimination diagrams. In: Wyman, D. (ed) *Trace element geochemistry of volcanic rocks: application for massive sulphide exploration.* Geological Association of Canada Short Course Notes 12. Geological Association of Canada, Mineral Deposits Division, Winnipeg. pp.79-113.

Pearce, J.A. & Cann, J.R. 1971. Ophiolite origin investigated by discriminant analysis using Ti, Zr and Y. *Earth and Planetary Science Letters* **12**, 339-349.

Pearce, J.A. & Cann, J.R. 1973. Tectonic setting of basic volcanic rocks determined using trace element analyses. *Earth and Planetary Science Letters* **19**, 290-300.

Pearce, J.A. & Norry, M.J. 1979. Petrogenetic implications of Ti, Zr, Y, and Nb variations in volcanic rocks. *Contributions to Mineralogy and Petrology* **69**, 33-47.

Pearce, J.A. & Peate, D.W. 1995. Tectonic implications of the composition of volcanic arc magmas. *Annual Review of Earth and Planetary Sciences* **23**, 251-285.

Pearce, J.A., Thirlwall, M.F., Ingram, G., Murton, B.J., Arculus, R.J. & van der Laan, S.R. 1992. Isotopic evidence for the origin of boninites and related rocks drilled in the Izu-Bonin (Ogasawara) forearc, Leg 125. *Proceedings of the Ocean Drilling Program, Scientific Results* **125**, 237-261.

Peate, D.W. & Hawkesworth, C.J. 1996. Lithospheric to asthenospheric transition in low-Ti flood basalts from southern Parana, Brazil. *Chemical Geology* **127**, 1-24.

Peate, D.W., Barker, A.K., Riishuus, M.S. & Andreasen, R. 2008. Temporal variations in crustal assimilation of magma suites in the east Greenland flood basalt province: tracking the evolution of magmatic plumbing systems. *Lithos* **102**, 179-197.

Peate, D.W., Hawkesworth, C.J. & Mantovani, M.S.M. 1992. Chemical stratigraphy of the Parana lavas (South America): classification of magma types and their spatial distribution. *Bulletin of Volcanology* **55**, 119-139.

Peate, D.W., Hawkesworth, C.J., Mantovani, M.S.M., Rogers, N.W. & Turner, S.P. 1999. Petrogenesis and stratigraphy of the high-Ti/Y Urubici magma type in the Parana flood basalt province and implications for the nature of 'Dupal'-type mantle in the South Atlantic region. *Journal of Petrology* **40**, 451-473.

Pearson, D.G., Parman, S.W. & Nowell, G.M. 2007. A link between mantle melting events and continent growth seen in osmium isotopes. *Nature* **449**, 202-205.

Peck, D.C., Halden, N.M., Heaman, L.M., Corkery, M.T., Cameron, H.D.M. & Toope, K. 1999. Field, geochemical and geochronological studies of Paleoproterozoic mafic and ultramafic dykes in the northwestern Superior Province (parts of NTS 63I, 63J and 63P). In: *Report of Activities 1999*. Manitoba Industry, Trade and Mines, Geological Services, Winnipeg. pp.97-101.

Peck, D.C., Potter, L., Desharnais, G., Scoates, R.F.J., Corkery, M.T. & Bohm, C.O. 2000. Geology of the western part of the Fox River Belt (parts of NTS 53M and 53N). In: *Report of Activities 2000*. Manitoba Industry, Trade and Mines, Manitoba Geological Survey, Winnipeg. pp.38-41.

Pehrsson, S.J. 2002. Geology, Indin Lake, Northwest Territories. Geological Survey of Canada Open File 4268. Geological Survey of Canada, Ottawa.

Percival, J.A. & West, G.F. 1994. The Kapuskasing uplift: a geological and geophysical synthesis. *Canadian Journal of Earth Sciences* **31**, 1256-1286.

Percival, J.A., Whalen, J.B. & Rayner, N. 2004. Pikwitonei-Snow Lake, Manitoba transect (parts of NTS 63J, 63O and 63P), Trans-Hudson Orogen-Superior Margin Metallotect Project: initial geological, isotopic and SHRIMP U-Pb results. In: *Report of Activities 2004*. Manitoba Industry, Economic Development and Mines, Manitoba Geological Survey, Winnipeg. pp.120-134.

Percival, J.A., Whalen, J.B. & Rayner, N. 2005. Pikwitonei-Snow Lake, Manitoba transect (parts of NTS 63J, 63O and 63P), Trans-Hudson Orogen-Superior Margin Metallotect Project: new results and tectonic interpretation. In: *Report of Activities 2005*. Manitoba Industry, Economic Development and Mines, Manitoba Geological Survey, Winnipeg. pp.69-91.

Peredery, W.V. 1979. Relationship of ultramafic amphibolites to metavolcanic rocks and serpentinites in the Thompson Belt, Manitoba. *Canadian Mineralogist* **17**, 187-200.

Peredery, W.V. 1982. Geology and nickel sulphide deposits of the Thompson Belt, Manitoba. In: Hutchison, R.W., Spence, C.D. & Franklin, J.M. (eds) *Precambrian sulphide deposits*. Geological Association of Canada Special Paper 25. Geological Association of Canada, Toronto. pp.165-209.

Perry, H.K.C., Mareschal, J.-C. & Jaupart, C. 2006. Variations of strength and localized deformation in cratons: the 1.9 Ga Kapuskasing uplift, Superior Province, Canada. *Earth and Planetary Science Letters* **249**, 216-228.

Phinney, W.C., Morrison, D.A. & Maczuga, D.E. 1988. Anorthosites and related megacrystic units in the evolution of Archean crust. *Journal of Petrology* **29**, 1283-1323.

Picard, C., Lamothe, D., Piboule, M. & Oliver, R. 1990. Magmatic and geotectonic evolution of a Proterozoic oceanic basin system: the Cape Smith Thrust-Fold Belt (New Quebec). *Precambrian Research* **47**, 223-249.

Polat, A. 2009. The geochemistry of Neoarchean (ca. 2700 Ma) tholeiitic basalts, transitional to alkaline basalts, and gabbros, Wawa Subprovince, Canada: implications for petrogenetic and geodynamic processes. *Precambrian Research* **168**, 83-105.

Polat, A. & Hofmann, A.W. 2003. Alteration and geochemical patterns in the 3.7-3.8 Ga Isua greenstone belt, west Greenland. *Precambrian Research* **126**, 197-218.

Polat, A. & Kerrich, R. 2000. Archean greenstone belt magmatism and the continental growth-mantle evolution connection: constraints from Th-U-Nb-LREE systematics of the 2.7 Ga Wawa subprovince, Superior Province, Canada. *Earth and Planetary Science Letters* **175**, 41-54.

Polat, A., Hofmann, A.W. & Rosing, M.T. 2002. Boninite-like volcanic rocks in the 3.7-3.8 Ga Isua greenstone belt, west Greenland: geochemical evidence for intra-oceanic subduction zone processes in the early Earth. *Chemical Geology* **184**, 231-254.

Polat, A., Kerrich, R. & Wyman, D.A. 1999. Geochemical diversity in oceanic komatiites and basalts from the late Archean Wawa greenstone belts, Superior Province, Canada: trace element and Nd isotope evidence for a heterogeneous mantle. *Precambrian Research* **94**, 139-173.

Presnall, D.C., Gudfinnsson, G.H. & Walter, M.J. 2002. Generation of mid-ocean ridge basalts at pressures from 1 to 7 GPa. *Geochimica et Cosmochimica Acta* **66**, 2073-2090.

Puchtel, I.S., Haase, K.M., Hofmann, A.W., Chauvel, C., Kulikov, V.S., Garbe-Schonberg, C.-D. & Nemchin, A.A. 1997. Petrology and geochemistry of crustally contaminated komatiitic basalts from the Vetreny Belt, southeastern Baltic Shield: evidence for an early Proterozoic mantle plume beneath rifted Archean continental lithosphere. *Geochimica et Cosmochimica Acta* **61**, 1205-1222.

Putirka, K.D. 2005. Mantle potential temperatures at Hawaii, Iceland, and the mid-ocean ridge system, as inferred from olivine phenocrysts: evidence for thermally driven mantle plumes. *Geochemistry, Geophysics, Geosystems* **6**, doi: 10.1029/2005GC000915.

Putirka, K.D., Perfit, M., Ryerson, F.J. & Jackson, M.G. 2007. Ambient and excess mantle temperatures, olivine thermometry, and active vs. passive upwelling. *Chemical Geology* **241**, 177-206.

Quinn, H.A. 1955a. Knee Lake, Manitoba (map with marginal notes). Geological Survey of Canada Paper 55-8. Geological Survey of Canada, Ottawa.

Quinn, H.A. 1955b. Mineral prospects of the Knee Lake map-area, Manitoba. *Precambrian* **8**, 10-27.

Ramachandra, H.M., Mishra, V.P. & Deshmukh, S.S. 1995. Mafic dykes in the Bastar Precambrian: study of the Bhanupratappur-Keskal mafic dyke swarm. In: Devaraju, T.C. (ed) *Dyke swarms of peninsular India*. Geological Society of India, Bangalore. pp.183-207.

Randall, W. 2005. *U-Pb geochronology of the Expo Igneous Suite, Cape Smith Belt, and the Kyak Bay intrusion, New Quebec Orogen: implications for the tectonic evolution of the northeastern Trans-Hudson Orogen.* MSc thesis. University of Toronto, Toronto. 51pp.

Redden, J.A., Peterman, Z.E., Zartman, R.E. & DeWitt, E. 1990. U-Th-Pb geochronology and preliminary interpretation of Precambrian tectonic events in the Black Hills, South Dakota. In: Lewry, J.F. & Stauffer, M.L. (eds) *The early Proterozoic Trans-Hudson Orogen of North America.* Geological Association of Canada Special Paper 37. Geological Association of Canada, Toronto. pp.229-251.

Reichow, M.K., Saunders, A.D., White, R.V., Al'Mukhamedov, A.I., Medvedev, A.Ya. 2005. Geochemistry and petrogenesis of basalts from the West Siberian Basin: an extension of the Permo-Triassic Siberian Traps, Russia. *Lithos* **79**, 425-452.

Revillon, S., Arndt, N.T., Chauvel, C. & Hallot, E. 2000. Geochemical study of ultramafic volcanic and plutonic rocks from Gorgona Island, Colombia: the plumbing system of an oceanic plateau. *Journal of Petrology* **41**, 1127-1153.

Revillon, S., Arndt, N.T., Hallot, E., Kerr, A.C. & Tarney, J. 1999. Petrogenesis of picrites from the Caribbean Plateau and the North Atlantic magmatic province. *Lithos* **49**, 1-21.

Richter, F.M. 1988. A major change in the thermal state of the Earth at the Archean-Proterozoic boundary: consequences for the nature and preservation of continental lithosphere. *Journal of Petrology*, Special Lithosphere Issue, 39-52.

Ricketts, B.D. & Donaldson, J.A. 1981. Sedimentary history of the Belcher Group of Hudson Bay. In: Campbell, F.H.A. (ed) *Proterozoic basins of Canada.* Geological Survey of Canada Paper 81-10. Geological Survey of Canada, Ottawa. pp.235-254.

Ricketts, B.D., Ware, M.J. & Donaldson, J.A. 1982. Volcaniclastic rocks and volcaniclastic facies in the middle Precambrian (Aphebian) Belcher Group, Northwest Territories, Canada. *Canadian Journal of Earth Sciences* **19**, 1275-1294.

Rogers, J.J.W. & Santosh, M. 2002. Configuration of Columbia, a Mesoproterozoic supercontinent. *Gondwana Research* **5**, 5-22.

Rohon, M.L., Vialette, Y., Clark, T., Roger, G., Ohnenstetter, D. & Vidal, P. 1993. Aphebian mafic-ultramafic magmatism in the Labrador Trough (New Quebec): its age and nature of its mantle source. *Canadian Journal of Earth Sciences* **30**, 1582-1593.

Rollinson, H.R. 1993. *Using geochemical data: evaluation, presentation, interpretation.* Prentice Hall, London. 352pp.

Rosman, K.J.R. & Taylor, P.D.P. 1998. Isotopic compositions of the elements 1997. *Pure and Applied Chemistry* **70**, 217-235.

Royse, K.R., Kempton, P.D. & Darbyshire, D.P.F. 1998. Procedure for the analysis of rubidium-strontium and samarium-neodymium isotopes at the NERC Isotope Geosciences Laboratory. NIGL Report Series 121. 28pp.

Rudnick, R.L. & Fountain, D.M. 1995. Nature and composition of the continental crust: a lower crustal perspective. *Reviews of Geophysics* **33**, 267-309.

Rukhlov, A.S. & Bell, K. 2010. Geochronology of carbonatites from the Canadian and Baltic Shields, and the Canadian Cordillera: clues to mantle evolution. *Mineralogy and Petrology* **98**, 11-54.

Sage, R.P. 1987a. Geology of carbonatite-alkalic rock complexes in Ontario: Borden Township carbonatite complex, district of Sudbury. Ontario Geological Survey Study 33. Ministry of Northern Development and Mines, Mines and Minerals Division, Toronto. 62pp.

Sage, R.P. 1987b. Geology of carbonatite-alkalic rock complexes in Ontario: Carb Lake carbonatite complex, district of Kenora. Ontario Geological Survey Study 53. Ministry of Northern Development and Mines, Mines and Minerals Division, Toronto. 42pp.

Sage, R.P. 1987c. Geology of carbonatite-alkalic rock complexes in Ontario: Spanish River carbonatite complex, district of Sudbury. Ontario Geological Survey Study 30. Ministry of Northern Development and Mines, Mines and Minerals Division, Toronto. 62pp.

Sage, R.P. 1988a. Geology of carbonatite-alkalic rock complexes in Ontario: Argor carbonatite complex, district of Cochrane. Ontario Geological Survey Study 41. Ministry of Northern Development and Mines, Mines and Minerals Division, Toronto. 90pp.

Sage, R.P. 1988b. Geology of carbonatite-alkalic rock complexes in Ontario: Cargill Township carbonatite complex, district of Cochrane. Ontario Geological Survey Study 36. Ministry of Northern Development and Mines, Mines and Minerals Division, Toronto. 92pp.

Sage, R.P. 1988c. Geology of carbonatite-alkalic rock complexes in Ontario: Goldray carbonatite complex, district of Cochrane. Ontario Geological Survey Study 40. Ministry of Northern Development and Mines, Mines and Minerals Division, Toronto. 35pp.

Sage, R.P. 1992. Alkalic rock, carbonatite and kimberlite complexes of Ontario, Superior Province. In: Thurston, P.C., Williams, H.R., Sutcliffe, R.H. & Stott, G.M. (eds) *Geology of Ontario*. Ontario Geological Survey Special Volume 4 Part 1. Ministry of Northern Development and Mines, Toronto. pp.683-709.

Said, N. & Kerrich, R. 2009. Geochemistry of coexisting depleted and enriched Paringa basalts, in the 2.7 Ga Kalgoorlie Terrane, Yilgarn craton, Western Australia: evidence for a heterogeneous mantle plume event. *Precambrian Research* **174**, 287-309.

Said, N. & Kerrich, R. 2010a. Elemental and Nd-isotope systematics of the Upper Basalt Unit, 2.7 Ga Kambalda Sequence: quantitative modeling of progressive crustal contamination of plume asthenosphere. *Chemical Geology* **273**, 193-211.

Said, N. & Kerrich, R. 2010b. Magnesian dyke suites of the 2.7 Ga Kambalda Sequence, Western Australia: evidence for coeval melting of plume asthenosphere and metasomatised lithospheric mantle. *Precambrian Research* **180**, 183-203.

Said, N., Kerrich, R. & Groves, D. 2010. Geochemical systematics of basalts of the Lower Basalt Unit, 2.7 Ga Kambalda Sequence, Yilgarn craton, Australia: plume impingement at a rifted craton margin. *Lithos* **115**, 82-100.

Salad Hersi, O. & Dix, G.R. 2006. Precambrian fault systems as control on regional differences in relative sea level along the early Ordovician platform of eastern North America. *Journal of Sedimentary Research* **76**, 700-716.

Salters, V.J.M. & Longhi, J. 1999. Trace element partitioning during the initial stages of melting beneath mid-ocean ridges. *Earth and Planetary Science Letters* **166**, 15-30.

Salters, V.J.M. & Stracke, A. 2004. Composition of the depleted mantle. *Geochemistry, Geophysics, Geosystems* **5**, doi: 10.1029/2003GC000597.

Salters, V.J.M. & Zindler, A. 1995. Extreme $^{176}Hf/^{177}Hf$ in the sub-oceanic mantle. *Earth and Planetary Science Letters* **129**, 13-30.

Saunders, A.D., England, R.W., Reichow, M.K. & White, R.V. 2005. A mantle plume origin for the Siberian traps: uplift and extension in the West Siberian Basin, Russia. *Lithos* **79**, 407-424.

Saunders, A.D., Fitton, J.G., Kerr, A.C., Norry, M.J. & Kent, R.W. 1997. The North Atlantic Igneous Province. In: Mahoney, J.J. & Coffin, M.F. (eds) *Large igneous provinces: continental, oceanic, and*

planetary flood volcanism. Geophysical Monograph 100. American Geophysical Union, Washington DC. pp.45-93.

Saunders, A.D., Jones, S.M., Morgan, L.A., Pierce, K.L., Widdowson, M. & Xu, Y.G. 2007. Regional uplift associated with continental large igneous provinces: the roles of mantle plumes and the lithosphere. *Chemical Geology* **241**, 282-318.

Scherer, E., Munker, C. & Mezger, K. 2001. Calibration of the lutetium-hafnium clock. *Science* **293**, 683-687.

Schmidt, P.W. 1980. Paleomagnetism of igneous rocks from the Belcher Islands, Northwest Territories, Canada. *Canadian Journal of Earth Sciences* **17**, 807-822.

Schmidt, P.W. & Williams, G.E. 2003. Reversal asymmetry in Mesoproterozoic overprinting of the 1.88 Ga Gunflint Formation, Ontario, Canada: non-dipole effects or apparent polar wander? *Tectonophysics* **377**, 7-32.

Schneider, D.A., Bickford, M.E., Cannon, W.F., Schulz, K.J. & Hamilton, M.A. 2002. Age of volcanic rocks and syndepositional iron formations, Marquette Range Supergroup: implications for the tectonic setting of Paleoproterozoic iron formations of the Lake Superior region. *Canadian Journal of Earth Sciences* **39**, 999-1012.

Schulz, K.J. 1987. Early Proterozoic evolution of a rifted continental margin in the Lake Superior region. *Geological Society of America North-Central Section 21st Annual Meeting*. Abstracts with Programs 19, pp.243.

Schulz, K.J. & Cannon, W.F. 2007. The Penokean orogeny in the Lake Superior region. *Precambrian Research* **157**, 4-25.

Schwann, P.L. 1989. *Petrography, geochemistry and platinum-group element distribution in the Upper Central Layered Zone, Main Layered Series, Fox River Sill, northeastern Manitoba*. MSc thesis. Carleton University, Ottawa. 193pp.

Schwarz, E.J. & Freda, G.N. 1983. Paleomagnetism and time-stratigraphic correlation of Proterozoic redbeds of the Labrador Trough and outliers of northern Quebec. *Canadian Journal of Earth Sciences* **20**, 1725-1737.

Schwarz, E.J. & Fujiwara, Y. 1981. Paleomagnetism of the Circum-Ungava fold belt; II, Proterozoic rocks of Richmond Gulf and Manitounuk Islands. In: Campbell, F.H.A. (ed) *Proterozoic basins of Canada*. Geological Survey of Canada Paper 81-10. Geological Survey of Canada, Ottawa. pp.255-267.

Schwarz, E.J., Clark, K.R. & Fujiwara, Y. 1982. Paleomagnetism of the Sutton Lake Proterozoic inlier, Ontario, Canada. *Canadian Journal of Earth Sciences* **19**, 1330-1332.

Scoates, R.F.J. 1981. Volcanic rocks of the Fox River Belt, northeastern Manitoba. Geological Report GR81-1. Manitoba Department of Energy and Mines, Mineral Resources Division, Winnipeg. 109pp.

Scoates, R.F.J. 1990. The Fox River Sill, northeastern Manitoba – a major stratiform intrusion. Geological Report GR82-3. Manitoba Energy and Mines, Geological Services, Winnipeg. 192pp.

Scoates, R.F.J. & Eckstrand, O.R. 1986. Platinum-group elements in the Upper Central Layered Zone of the Fox River Sill, northeastern Manitoba. *Economic Geology* **81**, 1137-1146.

Scoates, R.F.J. & Macek, J.J. 1978. Molson dyke swarm. Geological Paper 78-1. Manitoba Department of Mines, Resources and Environmental Management, Mineral Resources Division, Geological Survey, Winnipeg. 53pp.

Scoates, R.F.J., Macek, J.J. & Russell, J.K. 1977. Thompson Nickel Belt project (parts of 63P-13NE, 63P-14NW, 63P-12SW and 63O-9NE). In: *Report of Activities 1977*. Manitoba Department of Mines,

Resources and Environmental Management, Mineral Resources Division, Geological Survey, Winnipeg. pp.47-54.

Scott, D.J., Helmstaedt, H. & Bickle, M.J. 1992. Purtuniq ophiolite, Cape Smith belt, northern Quebec, Canada: a reconstructed section of early Proterozoic oceanic crust. *Geology* **20**, 173-176.

Scott, D.J., St-Onge, M.R., Lucas, S.B. & Helmstaedt, H. 1989. The 1998 Ma Purtuniq ophiolite: imbricated and metamorphosed oceanic crust in the Cape Smith thrust belt, northern Quebec. *Geoscience Canada* **16**, 144-148.

Shaw, D.M. 1970. Trace element fractionation during anatexis. *Geochimica et Cosmochimica Acta* **34**, 237-243.

Sheppard, S., Tyler, I.M., Griffin, T.J. & Taylor, W.R. 1999. Palaeoproterozoic subduction-related and passive margin basalts in the Halls Creek Orogen, northwest Australia. *Australian Journal of Earth Sciences* **46**, 679-690.

Shervais, J.W. 1982. Ti-V plots and the petrogenesis of modern and ophiolitic lavas. *Earth and Planetary Science Letters* **59**, 101-118.

Shirey, S.B. & Walker, R.J. 1998. The Re-Os isotope system in cosmochemistry and high-temperature geochemistry. *Annual Review of Earth and Planetary Sciences* **26**, 423-500.

Sims, P.K. 1990. Geologic map of Precambrian rocks of Iron Mountain and Escanaba 1° × 2° quadrangles, northeastern Wisconsin and northwestern Michigan. US Geological Survey Miscellaneous Investigations Series Map I-2056.

Singh, A.P. & Mishra, D.C. 2002. Tectonosedimentary evolution of Cuddapah basin and Eastern Ghats mobile belt (India) as Proterozoic collision: gravity, seismic and geodynamic constraints. *Journal of Geodynamics* **33**, 249-267.

Skulski, T., Wares, R.P. & Smith, A.D. 1993. Early Proterozoic (1.88-1.87 Ga) tholeiitic magmatism in the New Quebec Orogen. *Canadian Journal of Earth Sciences* **30**, 1505-1520.

Sleep, N.H. 1996. Lateral flow of hot plume material ponded at sublithospheric depths. *Journal of Geophysical Research* **101**, 28065-28083.

Sleep, N.H. 1997. Lateral flow and ponding of starting plume material. *Journal of Geophysical Research* **102**, 10001-10012.

Sleep, N.H. 2003. Fate of mantle plume material trapped within a lithospheric catchment with reference to Brazil. *Geochemistry, Geophysics, Geosystems* **4**, doi: 10.1029/2002GC000464.

Sleep, N.H. 2008. Channeling at the base of the lithosphere during lateral flow of plume material beneath flow line hot spots. *Geochemistry, Geophysics, Geosystems* **9**, doi: 10.1029/2008GC002090.

Sleep, N.H., Ebinger, C.J. & Kendall, J.-M. 2002. Deflection of mantle plume material by cratonic keels. In: Fowler, C.M.R., Ebinger, C.J. & Hawkesworth, C.J. (eds) *The early Earth: physical, chemical and biological development*. Geological Society Special Publication 199. Geological Society of London, London. pp.135-150.

Smith, A.D. & Ludden, J.N. 1989. Nd isotopic evolution of the Precambrian mantle. *Earth and Planetary Science Letters* **93**, 14-22.

Smoliar, M.I., Walker, R.J. & Morgan, J.W. 1996. Re-Os ages of group IIA, IIIA, IVA, and IVB iron meteorites. *Science* **271**, 1099-1102.

Soderlund, U., Hofmann, A., Klausen, M.B., Olsson, J.R., Ernst, R.E. & Persson, P.-O. 2010. Towards a complete magmatic barcode for the Zimbabwe craton: baddeleyite U-Pb dating of regional dolerite dyke swarms and sill complexes. *Precambrian Research* **183**, 388-398.

Sol, S., Thomson, C.J., Kendall, J.-M., White, D., VanDecar, J.C. & Asudeh, I. 2002. Seismic tomographic images of the cratonic upper mantle beneath the western Superior Province of the Canadian Shield – a remnant Archean slab? *Physics of The Earth and Planetary Interiors* **134**, 53-69.

Southwick, D.L. & Morey, G.B. 1991. Tectonic imbrication and foredeep development in the Penokean Orogeny, east-central Minnesota – an interpretation based on regional geophysics and the results of test-drilling. US Geological Survey Bulletin 1904C. US Government Printing Office, Washington DC. 17pp.

Springer, G.D. 1946. Geology of the Knee Lake area-Gods Lake division. Preliminary Report 46-1. Manitoba Mineral Resources Division, Winnipeg.

Sproule, R.A., Lesher, C.M., Ayer, J.A., Thurston, P.C. & Herzberg, C.T. 2002. Spatial and temporal variations in the geochemistry of komatiites and komatiitic basalts in the Abitibi greenstone belt. *Precambrian Research* **115**, 153-186.

Srivastava, R.K. & Singh, R.K. 2004. Trace element geochemistry and genesis of Precambrian sub-alkaline mafic dikes from the central Indian craton: evidence for mantle metasomatism. *Journal of Asian Earth Sciences* **23**, 373-389.

Starkey, N.A., Stuart, F.M., Ellam, R.M., Fitton, J.G., Basu, S. & Larsen, L.M. 2009. Helium isotopes in early Iceland plume picrites: constraints on the composition of high $^{3}He/^{4}He$ mantle. *Earth and Planetary Science Letters* **277**, 91-100.

Stauffer, M.R. 1984. Manikewan: an early Proterozoic ocean in central Canada, its igneous history and orogenic closure. *Precambrian Research* **25**, 257-281.

Steiger, R.H. & Jager, E. 1977. Subcommission on geochronology: convention on the use of decay constants in geo- and cosmochronology. *Earth and Planetary Science Letters* **36**, 359-362.

Stern, R.J. 2002. Subduction zones. *Reviews of Geophysics* **40**, doi: 10.1029/2001RG000108.

Stewart, A.J. 2002. *The geochemistry and physical volcanology of the East Lake Ultramafic Zone, Cape Smith Belt, northern Quebec.* MSc thesis. McGill University, Montreal. 88pp.

Stilson, C.M., Vicker, P. & Lesher, C.M. 1999. Geology of the Boundary area. In: Lesher, C.M. (ed) *Komatiitic peridotite-hosted Fe-Ni-Cu-(PGE) sulphide deposits in the Raglan area, Cape Smith Belt, New Quebec.* Laurentian University, Mineral Exploration Research Centre, Guidebook Series 2. Laurentian University, Sudbury. pp.133-142.

St-Onge, M.R. & Lucas, S.B. 1990. Evolution of the Cape Smith Belt; early Proterozoic continental underthrusting, ophiolite obduction, and thick-skinned folding. In: Lewry, J.F. & Stauffer, M.R. (eds) *The early Proterozoic Trans-Hudson Orogen of North America.* Geological Association of Canada Special Paper 37. Geological Association of Canada, Toronto. pp.313-351.

St-Onge, M.R. & Lucas, S.B. 1992. Terrane accretion in the internal zone of the Ungava orogen, northern Quebec. Part 1: tectonostratigraphic assemblages and their tectonic implications. *Canadian Journal of Earth Sciences* **29**, 746-764.

St-Onge, M.R. & Lucas, S.B. 1993. Geology of the eastern Cape Smith Belt; parts of the Kangiqsujuaq, Cratère du Nouveau-Quebec and lacs Nuvilik map areas, Quebec. Geological Survey of Canada Memoir 438. Geological Survey of Canada, Ottawa. 110pp.

St-Onge, M.R. & Lucas, S.B. 1994. Controls on the regional distribution of iron-nickel-copper-platinum-group element sulfide mineralization in the eastern Cape Smith Belt, Quebec. *Canadian Journal of Earth Sciences* **31**, 206-218.

St-Onge, M.R., Lalonde, A.E. & King, J.E. 1983. Geology, Redrock Lake and eastern Calder River map areas, district of Mackenzie: central Wopmay Orogen, Bear Province, and the western Archean

Slave Province. In: *Current Research, Part A*. Geological Survey of Canada Paper 83-1A. Geological Survey of Canada, Ottawa. pp.147-152.

St-Onge, M.R., Lucas, S.B. & Parrish, R.R. 1992. Terrane accretion in the internal zone of the Ungava orogen, northern Quebec. Part 1: tectonostratigraphic assemblages and their tectonic interpretations. *Canadian Journal of Earth Sciences* **29**, 746-764.

St-Onge, M.R., Lucas, S.B., Scott, D.J. & Begin, N.J. 1989. Evidence for the development of oceanic crust and for continental rifting in the tectonostratigraphy of the early Proterozoic Cape Smith Belt. *Geoscience Canada* **16**, 119-122.

St-Onge, M.R., Lucas, S.B., Scott, D.J., Begin, N.J., Helmstaedt, H. & Carmichael, D.M. 1988. Thin-skinned imbrication and subsequent thick-skinned folding of rift-fill, transitional-crust, and ophiolite suites in the 1.9 Ga Cape Smith Belt, northern Quebec. In: *Current Research, Part C*. Geological Survey of Canada Paper 88-1C. Geological Survey of Canada, Ottawa. pp.1-18.

St-Onge, M.R., Scott, D.J. & Corrigan, D. 2004. Geology, Nauja Bay, Baffin Island, Nunavut. Geological Survey of Canada Open File 4482. Geological Survey of Canada, Ottawa.

St-Onge, M.R., Scott, D.J. & Lucas, S.B. 2000. Early partitioning of Quebec: microcontinent formation in the Paleoproterozoic. *Geology* **28**, 323-326.

Storey, M., Duncan, R.A. & Tegner, C. 2007. Timing and duration of volcanism in the North Atlantic Igneous Province: implications for geodynamics and links to the Iceland hotspot. *Chemical Geology* **241**, 264-281.

Stott, G.M. 1997. The Superior Province, Canada. In: de Wit, M.J. & Ashwal, L.D. (eds) *Greenstone Belts*. Oxford Monograph on Geology and Geophysics 35. Clarendon Press, Oxford. pp.480-507.

Stubbs, H.M., Hall, R.P., Hughes, D.J. & Nesbitt, R.W. 1999. Evidence for a high Mg andesitic parental magma to the east and west satellite dykes of the Great Dyke, Zimbabwe: a comparison with the continental tholeiitic Mashonaland sills. *Journal of African Earth Sciences* **28**, 325-336.

Sun, S.-S. & Hanson, G.N. 1975. Origin of Ross Island basanitoids and limitations upon the heterogeneity of mantle sources for alkali basalts and nephelinites. *Contributions to Mineralogy and Petrology* **52**, 77-106.

Sun, S.-S. & McDonough, W.F. 1989. Chemical and isotopic systematics of oceanic basalts: implications for mantle composition and processes. In: Saunders, A.D. & Norry, M.J. (eds) *Magmatism in the ocean basins*. Geological Society Special Publication 42. Geological Society of London, London. pp.313-345.

Suominen, V. 1991. The chronostratigraphy of southwestern Finland with special reference to Postjotnian and Subjotnian diabases. Geological Survey of Finland Bulletin 356. Geological Survey of Finland, Espoo. 100pp.

Tejada, M.L.G., Mahoney, J.J., Castillo, P.R., Ingle, S.P., Sheth, H.C. & Weis, D. 2004. Pin-pricking the elephant: evidence on the origin of the Ontong Java Plateau from Pb-Sr-Hf-Nd isotopic characteristics of ODP Leg 192 basalts. In: Fitton, J.G., Mahoney, J.J., Wallace, P.D. & Saunders, A.D. (eds) *Origin and evolution of the Ontong Java Plateau*. Geological Society Special Publication 229. Geological Society of London, London. pp.133-150.

Theyer, P. 1997. Stratigraphy and lithologies of selected drill core from the Lake Winnipegosis Komatiite Belt (parts of NTS 63B, 63C and 63G). In: *Report of Activities 1997*. Manitoba Industry, Trade and Mines, Manitoba Geological Survey, Winnipeg. pp.109-111.

Thibert, F. 1999. Geology of the Cross Lake area. In: Lesher, C.M. (ed) *Komatiitic peridotite-hosted Fe-Ni-Cu-(PGE) sulphide deposits in the Raglan area, Cape Smith Belt, New Quebec*. Laurentian University, Mineral Exploration Research Centre, Guidebook Series 2. Laurentian University, Sudbury. pp.61-67.

Thirlwall, M.F. 1991. Long-term reproducibility of multicollector Sr and Nd isotope ratio analysis. *Chemical Geology: Isotope Geoscience section* **94**, 85-104.

Thirlwall, M.F. & Anczkiewicz, R. 2004. Multidynamic isotope ratio analysis using MC-ICP-MS and the causes of secular drift in Hf, Nd and Pb isotope ratios. *International Journal of Spectrometry* **235**, 59-81.

Thomas, M.D. & Gibb, R.A. 1977. Gravity anomalies and deep structure of the Cape Smith foldbelt, northern Ungava, Quebec. *Geology* **5**, 169-172.

Thompson, P.M.E., Kempton, P.D., White, R.V., Kerr, A.C., Tarney, J., Saunders, A.D., Fitton, J.G. & McBirney, A. 2004. Hf-Nd isotope constraints on the origin of the Cretaceous Caribbean plateau and its relationship to the Galapagos plume. *Earth and Planetary Science Letters* **217**, 59-75.

Thompson, R.N. & Gibson, S.A. 1991. Subcontinental mantle plumes, hotspots and pre-existing thinspots. *Journal of the Geological Society, London* **148**, 973-977.

Thompson, R.N., Dickin, A.P., Gibson, I.L. & Morrison, M.A. 1982. Elemental fingerprints of isotopic contamination of Hebridean Palaeocene mantle-derived magmas by Archaean sial. *Contributions to Mineralogy and Petrology* **79**, 159-168.

Todt, W., Chauvel, C., Arndt, N.T. & Hofmann, A.W. 1984. Pb isotopic composition and age of Proterozoic komatiites and related rocks from Canada. *American Geophysical Union Fall Meeting 1984*. Program with Abstracts 65, pp.1129.

Toplis, M.J. 2005. The thermodynamics of iron and magnesium partitioning between olivine and liquid: criteria for assessing and predicting equilibrium in natural and experimental systems. *Contributions to Mineralogy and Petrology* **149**, 22-39.

Trent, V.A. 1976. The Emperor Volcanic Complex of the east Gogebic Range. In: Cohee, G.V. & Wright, W.B. (eds) *Changes in stratigraphic nomenclature by the US Geological Survey, 1975*. US Geological Survey Bulletin 1422-A. US Government Printing Office, Washington DC. pp.69-74.

Turner, S., Hawkesworth, C.J., Gallagher, K., Stewart, K., Peate, D. & Mantovani, M. 1996. Mantle plumes, flood basalts, and thermal models for melt generation beneath continents: assessment of a conductive heating model and application to the Parana. *Journal of Geophysical Research* **101**, 11503-11518.

Tyler, I.M. & Page, R.W. 1996. Palaeoproterozoic deformation, metamorphism and igneous intrusion in the Central Zone of the Lamboo Complex, Halls Creek Orogen. *Geological Society of Australia Abstracts* **41**, 450.

Tyler, I.M., Griffin, T.J., Page, R.W. & Shaw, R.D. 1995. Are there terranes within the Lamboo Complex of the Halls Creek Orogen? Geological Survey of Western Australia Annual Review 1993-94. Department of Minerals and Energy, Perth. pp.37-46.

Ueng, W.C., Fox, T.P., Larue, D.K. & Wilband, J.T. 1988. Geochemistry and petrogenesis of the early Proterozoic Hemlock volcanic rocks and the Kiernan sills, southern Lake Superior region. *Canadian Journal of Earth Sciences* **25**, 528-546.

Vaisanen, M. & Westerlund, G. 2007. Palaeoproterozoic mafic and intermediate metavolcanic rocks in the Turku area, SW Finland. *Bulletin of the Geological Society of Finland* **79**, 127-141.

Vaisanen, M., Manttari, I. & Holtta, P. 2002. Svecofennian magmatic and metamorphic evolution in southwestern Finland as revealed by U-Pb zircon SIMS geochronology. *Precambrian Research* **116**, 111-127.

Van Boening, A.M. & Nabelek, P.I. 2008. Petrogenesis and tectonic implications of Paleoproterozoic mafic rocks in the Black Hills, South Dakota. *Precambrian Research* **167**, 363-376.

van der Lee, S. & Nolet, G. 1997. Upper mantle S velocity structure of North America. *Journal of Geophysical Research* **102**, 22815-22838.

van Gool, J.A.M., Connelly, J.N., Marker, M. & Mengel, F.C. 2002. The Nagssugtoqidian Orogen of west Greenland: tectonic evolution and regional correlations from a west Greenland perspective. *Canadian Journal of Earth Sciences* **39**, 665-686.

van Kranendonk, M.J., St-Onge, M.R. & Henderson, J.R. 1993. Paleoproterozoic tectonic assembly of northeast Laurentia through multiple indentations. *Precambrian Research* **63**, 325- 347.

Van Schmus, W.R. 1976. Early and middle Proterozoic history of the Great Lakes area, North America. *Philosophical Transactions of the Royal Society of London A* **280**, 605-628.

Van Schmus, W.R. 1980. Chronology of igneous rocks associated with the Penokean Orogeny in Wisconsin. In: Morey, G.B. & Hanson, G.N. (eds) *Selected studies of Archean gneisses and Lower Proterozoic rocks, southern Canadian Shield.* Geological Society of America Special Paper 182. Geological Society of America, Boulder. pp.159-168.

Van Schmus, W.R., Thurman, E.M. & Peterman, Z.E. 1975. Geology and Rb-Sr chronology of middle Precambrian rocks in eastern and central Wisconsin. *Geological Society of America Bulletin* **86**, 1255-1265.

Vervoort, J.D. & Blichert-Toft, J. 1999. Evolution of the depleted mantle: Hf isotope evidence from juvenile rocks through time. *Geochimica et Cosmochimica Acta* **63**, 533-556.

Vervoort, J.D., Patchett, P.J., Blichert-Toft, J. & Albarede, F. 1999. Relationships between Lu-Hf and Sm-Nd isotopic systems in the global sedimentary system. *Earth and Planetary Science Letters* **168**, 79-99.

Vervoort, J.D., Wirth, K., Kennedy, B., Sandland, T. & Harpp, K.S. 2007. The magmatic evolution of the Midcontinent rift: new geochronologic and geochemical evidence from felsic magmatism. *Precambrian Research* **157**, 235-268.

Vicker, P. & Fedorowich, J.S. 1999. Geology of the Zone 13-14 area. In: Lesher, C.M. (ed) *Komatiitic peridotite-hosted Fe-Ni-Cu-(PGE) sulphide deposits in the Raglan area, Cape Smith Belt, New Quebec.* Laurentian University, Mineral Exploration Research Centre, Guidebook Series 2. Laurentian University, Sudbury. pp.117-122.

Volpe, A.M. & Macdougall, J.D. 1990. Geochemistry and isotopic characteristics of mafic (Phulad ophiolite) and related rocks in the Delhi Supergroup, Rajasthan, India: implications for rifting in the Proterozoic. *Precambrian Research* **48**, 167-191.

Walker, R.J., Carlson, R.W., Shirey, S.B. & Boyd, F.R. 1989. Os, Sr, Nd and Pb isotope systematics of southern Africa peridotite xenoliths: implications for the chemical evolution of subcontinental mantle. *Geochimica et Cosmochimica Acta* **53**, 1583-1595.

Walter, M.J. 1998. Melting of garnet peridotite and the origin of komatiite and depleted lithosphere. *Journal of Petrology* **39**, 29-60.

Wang, K., Plank, T., Walker, J.D. & Smith, E.I. 2002. A mantle melting profile across the Basin and Range, SW USA. *Journal of Geophysical Research* **107**, doi: 10.1029/2001JB000209.

Wang, X.-C., Li, X.-H., Li, W.-X. & Li, Z.-X. 2007. Ca. 825 Ma komatiitic basalts in south China: first evidence for >1500°C mantle melts by a Rodinian mantle plume. *Geology* **35**, 1103-1106.

Wardle, R.J., Ryan, B., Nunn, G.A.G. & Mengel, F.C. 1990. Labrador segment of the Trans-Hudson Orogen; crustal development through oblique convergence and collision. In: Lewry, J.F. & Stauffer, M.L. (eds) *The early Proterozoic Trans-Hudson Orogen of North America.* Geological Association of Canada Special Paper 37. Geological Association of Canada, Toronto. pp.353-369.

Wasserburg, G.J., Jacousen, S.B., DePaolo, D.J., McCulloch, M.T. & Wen, T. 1981. Precise determinations of Sm/Nd ratios, Sm and Nd isotopic abundances in standard solutions. *Geochimica et Cosmochimica Acta* **45**, 2311-2323.

Weaver, B.L. 1991. Trace element evidence for the origin of ocean-island basalts. *Geology* **19**, 123-126.

Weaver, B.L., Wood, D.A., Tarney, J. & Joron, J.L. 1987. Geochemistry of ocean island basalts from the South Atlantic: Ascension, Bouvet, St. Helena, Gough and Tristan da Cunha. In: Fitton, J.G. & Upton, B.G.J. (eds) *Alkaline igneous rocks*. Geological Society Special Publication 30. Geological Society of London, London. pp.253-267.

Weber, W. 1990. The Churchill-Superior boundary zone, southeast margin of the Trans-Hudson Orogen; a review. In: Lewry, J.F. & Stauffer, M.L. (eds) *The early Proterozoic Trans-Hudson Orogen of North America*. Geological Association of Canada Special Paper 37. Geological Association of Canada, Toronto. pp.41-55.

Weber, W. & Scoates, R.F.J. 1978. Archean and Proterozoic metamorphism in the northwestern Superior Province and the Churchill-Superior boundary, Manitoba. In: Fraser, J.A. & Heywood, W.W. (eds) *Metamorphism in the Canadian Shield*. Geological Survey of Canada Paper 78-10. Geological Survey of Canada, Ottawa. pp.5-16.

Wei, J. 2002. The late Paleoproterozoic orogeny in the North China craton. *Gondwana Research* **5**, 95-99.

White, W.M. & Duncan, R.A. 1996. Geochemistry and geochronology of the Society Islands: new evidence for deep mantle recycling. In: Basu, A. & Hart, S.R. (eds) *Earth processes: reading the isotopic code*. Geophysical Monograph 95. American Geophysical Union, Washington DC. pp.183-206.

Whitehouse, M.J. & Bridgwater, D. 2001. Geochronological constraints on Palaeoproterozoic crustal evolution and regional correlations of the northern Outer Hebridean Lewisian Complex. *Precambrian Research* **105**, 227-245.

Whitehouse, M.J., Kalsbeek, F. & Nutman, A.P. 1998. Crustal growth and crustal recycling in the Nagssugtoqidian Orogen of west Greenland: constraints from radiogenic isotope systematics and U-Pb zircon geochronology. *Precambrian Research* **91**, 365-381.

Wier, K.L. 1967. Geology of the Kelso Junction quadrangle, Iron County, Michigan. US Geological Survey Bulletin 1226. US Government Printing Office, Washington DC. 47pp.

Wieser, M.E. 2006. Atomic weights of the elements 2005. *Pure and Applied Chemistry* **78**, 2051-2066.

Willbold, M. & Stracke, A. 2006. Trace element composition of mantle end-members: implications for recycling of oceanic and upper and lower continental crust. *Geochemistry, Geophysics, Geosystems* **7**, doi: 10.1029/2005GC001005.

Williams, G.E. & Schmidt, P.W. 2004. Paleomagnetism of the 1.88 Ga Sokoman Formation in the Schefferville-Knob Lake area, Quebec, Canada, and implications for the genesis of iron oxide deposits in the central New Quebec Orogen. *Precambrian Research* **128**, 167-188.

Wilson, J.F., Jones, D.L. & Kramers, J.D. 1987. Mafic dyke swarms of Zimbabwe. In: Halls, H.C. & Fahrig, W.F. (eds) *Mafic dyke swarms*. Geological Association of Canada Special Paper 34. Geological Association of Canada, Toronto. pp.433-444.

Winchester, J.A. & Floyd, P.A. 1977. Geochemical discrimination of different magma series and their differentiation products using immobile elements. *Chemical Geology* **20**, 325-343.

Wodicka, N. 2004. Age and provenance of the Piling Group, central Baffin Island, Nunavut. *Western Churchill Metallogeny Project Worshop Abstracts*. Geological Survey of Canada, Ottawa.

Wodicka, N., Madore, L., Larbi, Y. & Vicker, P. 2002. Géochronologie U-Pb de filons-couches mafiques de la Ceinture de Cape Smith et de la Fosse du Labrador. In: *L'exploration minérale au Québec: notre savoir, vos découvertes*. Séminaire d'information sur la recherche géologique. Programme et résumés 2002-10. Ministère des Ressources Naturelles, Québec. 48pp.

Wood, D.A. 1980. The application of a Th-Hf-Ta diagram to problems of tectonomagmatic classification and to establishing the nature of crustal contamination of basaltic lavas of the British Tertiary volcanic province. *Earth and Planetary Science Letters* **50**, 11-30.

Woodhead, J.D. & McCulloch, M.T. 1989. Ancient seafloor signals in Pitcairn Island lavas and evidence for large amplitude, small length-scale mantle heterogeneities. *Earth and Planetary Science Letters* **94**, 257-273.

Workman, R.K. & Hart, S.R. 2005. Major and trace element composition of the depleted MORB mantle (DMM). *Earth and Planetary Science Letters* **231**, 53-72.

Wyman, D. & Kerrich, R. 2009. Plume and arc magmatism in the Abitibi subprovince: implications for the origin of Archean continental lithospheric mantle. *Precambrian Research* **168**, 4-22.

Xie, Q., Kerrich, R. & Fan, J. 1993. HFSE/REE fractionations recorded in three komatiite-basalt sequences, Archean Abitibi greenstone belt: implications for multiple plume sources and depths. *Geochimica et Cosmochimica Acta* **57**, 4111-4118.

Xu, Y., Mei, H., Xu, J., Huang, X., Wang, Y. & Chung, S.-L. 2003. Origin of two differentiation trends in the Emeishan flood basalts. *Chinese Science Bulletin* **48**, 390-394.

Zack, T. & John, T. 2007. An evaluation of reactive fluid flow and trace element mobility in subducting slabs. *Chemical Geology* **239**, 199-216.

Zhai, Y., Halls, H.C. & Bates, M.P. 1994. Multiple episodes of dike emplacement along the northwestern margin of the Superior Province, Manitoba. *Journal of Geophysical Research* **99**, 21717-21732.

Zhang, M., O'Reilly, S.Y., Wang, K.-L., Hronsky, J. & Griffin, W.L. 2008. Flood basalts and metallogeny: the lithospheric mantle connection. *Earth Science Reviews* **86**, 145-174.

Zhao, G., Cawood, P.A., Wilde, S.A. & Sun, M. 2002. Review of global 2.1-1.8 Ga orogens: implications for a pre-Rodinia supercontinent. *Earth Science Reviews* **59**, 125-162.

Zindler, A. 1982. Nd and Sr isotopic studies of komatiites and related rocks. In: Arndt, N.T. & Nisbet, E.G. (eds) *Komatiites*. Allen & Unwin, London. pp.399-420.

Zwanzig, H.V. 2004. Mafic-ultramafic magmatism of the Bah Lake assemblage, Ospwagan Group, Upper Ospwagan Lake, Manitoba (NTS 63O9). In: *Report of Activities 2004*. Manitoba Industry, Economic Development and Mines, Manitoba Geological Survey, Winnipeg. pp.149-155.

Zwanzig, H.V. & Bohm, C.O. 2002. Tectonostratigraphy, Sm-Nd isotope and U-Pb age data of the Thompson Nickel Belt and Kisseynew north and east margins (NTS 63J, 63P, 63Q, 64A, 64B), Manitoba. In: *Report of Activities 2002*. Manitoba Industry, Trade and Mines, Manitoba Geological Survey, Winnipeg. pp.102-114.

Zwanzig, H.V., Bohm, C.O., Protrel, A. & Machado, N. 2003. Field relations, U-Pb zircon ages and Nd model ages of granitoid intrusions along the Thompson Nickel Belt-Kisseynew Domain boundary, Setting Lake area, Manitoba (NTS 63J15 and 63O2). In: *Report of Activities 2003*. Manitoba Industry, Economic Development and Mines, Manitoba Geological Survey, Winnipeg. pp.118-129.

APPENDICES

Appendix A: List of samples with geographical co-ordinates and thin section descriptions

Appendix B: Preparation of rock samples for analysis by inductively-coupled plasma optical emission spectrometry (ICP-OES) and inductively-coupled plasma mass spectrometry (ICP-MS) and an evaluation of the accuracy and precision of the results

Appendix C: Geochemical results obtained by inductively-coupled plasma optical emission spectrometry and inductively-coupled plasma mass spectrometry

Appendix D: Preparation of rock samples for Sr-Nd-Pb-Hf-Os isotopic analysis and results

Appendix E: Scanning electron microscopy results of olivine analyses

Appendix F: Petrogenetic modelling constraints

Appendix G: Unpublished geochemical data for ~1880 Ma igneous rocks from the Bastar craton, India and the Slave craton, Canada

Appendix A: List of samples with geographical co-ordinates and thin section descriptions

Table A.1. Sample information

Sample number	Geological unit	Location	Sample type	Rock type	Thin section description	ICP	Isotopes
MMF07-1	Flaherty Formation, Belcher Islands	56° 20' 57.5'' N 79° 42' 47.3'' W	Field	Basalt	~40% clinopyroxene, ~55% plagioclase, ~5% opaques. Clinopyroxene mainly present in the groundmass. Little ophitic texture preserved. What was once clinopyroxene is altered to a colourless-green-brown pleochroic mineral with birefringence similar to calcite. Plagioclase in the form of laths up to ~0.5 mm in length and mostly altered to sericite. Calcite vein cuts across sample.	Yes	
MMF07-2	Flaherty Formation, Belcher Islands	56° 20' 54.6'' N 79° 42' 45.3'' W	Field	Basalt	~50% clinopyroxene, ~45% plagioclase, ~5% opaques. Plagioclase mostly in the form of laths but also occurs as the occasional coarser, subhedral crystal ~2 mm in length and is well sericitised. Clinopyroxene is partly altered to chlorite giving the thin section a slight greenish colour. Good ophitic texture observed. Euhedral opaque minerals also present, scattered randomly throughout section.	Yes	Sr, Nd, Pb, Hf
MMF07-3	Flaherty Formation, Belcher Islands	56° 20' 48.4'' N 79° 42' 37.0'' W	Field	Basalt	~45% clinopyroxene, ~52% plagioclase, ~3% opaques. Fine grained, lack of phenocrysts. Fewer opaques. All clinopyroxene in groundmass. Plagioclase laths reach up to ~0.5 mm in length. Subhedral plagioclase crystals also present. A lot of the plagioclase is altered to sericite. Chlorite vein cuts across sample.	Yes	
MMF07-4	Flaherty Formation, Belcher Islands	56° 20' 44.5'' N 79° 42' 33.7'' W	Field	Basalt	~47% clinopyroxene, ~47% plagioclase, ~6% opaques. Maximum crystal size ~1.5 mm. Good ophitic texture preserved. Plagioclase present as laths and show both simple and albite twinning. Plagioclase is altered to sericite, carbonate and chlorite. Clinopyroxene is in places altered to chlorite and occurs as elongated prisms. Chlorite is partly breaking down to biotite. Quartz veins run through part of the section and also contain some calcite or white mica.	Yes	
MMF07-5	Flaherty Formation, Belcher Islands	56° 20' 39.3'' N 79° 42' 24.7'' W	Field	Basalt	~45% clinopyroxene, ~50% plagioclase, ~5% opaques. Brown clinopyroxene prisms (~1 mm) are in some places altered to chlorite. Ophitic texture sometimes difficult to see due to alteration of plagioclase to sericite. Sericitisation of plagioclase gives the groundmass a cloudy appearance. Opaques form small euhedral crystals.	Yes	
MMF07-6	Flaherty Formation, Belcher Islands	56° 20' 32.4'' N 79° 42' 17.2'' W	Field	Basalt	~50% plagioclase, ~45% clinopyroxene, ~5% opaques. Maximum crystal size ~1.5 mm. Good ophitic texture preserved. Elongated prisms of clinopyroxene are a light brown or green colour depending on degree of chloritisation. Plagioclase present as laths and shows signs of alteration to sericite and clays.	Yes	
MMF07-7	Flaherty Formation, Belcher Islands	56° 20' 28.3'' N 79° 42' 16.4'' W	Field	Basalt	~45% clinopyroxene, ~50% plagioclase, ~5% opaques. Brown clinopyroxene prisms (~1 mm) are in some places altered to chlorite.	Yes	Sr, Nd, Pb, Hf

Sample number	Geological unit	Location	Sample type	Rock type	Thin section description
					Ophitic texture is still preserved. Alteratio Opaques form small euhedral crystals.
MMF07-8	Flaherty Formation, Belcher Islands	56° 20' 25.2" N 79° 42' 13.2" W	Field	Basalt	~50% clinopyroxene, ~45% plagioclase, ~ relative to other Flaherty basalts. Prisms o of plagioclase ~2.5 mm in length. Good e present. Some plagioclase completel Clinopyroxene altered to a dusty brown ma
MMF07-9	Flaherty Formation, Belcher Islands	56° 20' 13.7" N 79° 42' 02.8" W	Field	Basalt	~50% plagioclase, ~40% clinopyroxene, ~ rock aside from occasional ~2 mm long Ophitic texture poorly developed. Clinopyr by chlorite. Plagioclase occurs as laths and is more abundant in the groundmass than a veins cut across the section.
MMF07-10	Flaherty Formation, Belcher Islands	56° 20' 10.9" N 79° 41' 58.4" W	Field	Basalt	~45% clinopyroxene, ~50% plagioclase, prisms of clinopyroxene (~1.5 mm) in sor chlorite. Some plagioclase laths sericitised. few crystals of brown coloured sphene pres
MMF07-11	Flaherty Formation, Belcher Islands	56° 31' 28.0" N 79° 07' 25.5" W	Field	Basalt	~45% clinopyroxene, ~45% plagioclase, developed ophitic texture. Small microphe (<1 mm) which are more equant than elon are heavily sericitised.
MMF07-12	Flaherty Formation, Belcher Islands	56° 31' 29.6" N 79° 07' 33.9" W	Field	Basalt	~45% clinopyroxene, ~50% plagioclase texture observed. Prisms of clinopyroxene length and are partly chloritised. Laths altered to sericite. In places chlorite breaks
MMF07-13	Flaherty Formation, Belcher Islands	56° 31' 30.2" N 79° 07' 35.9" W	Field	Basalt	~50% clinopyroxene, ~45% plagioclase, ~ texture. Prisms of clinopyroxene (~1.5 plagioclase (~1 mm). Euhedral opaques. Sa groundmass. Some clinopyroxene replace greenish. Plagioclase is dusty and is beg sericite. Biotite is forming from breakdown
MMF07-14	Flaherty Formation, Belcher Islands	56° 31' 30.4" N 79° 07' 37.1" W	Field	Basalt	~45% clinopyroxene, ~45% plagioclase, ~ crystal size of ~1.5 mm. Good ophitic text clinopyroxene prisms and laths of plagiocla preserved with only some laths showing ea Opaque minerals are fairly abundant and ar crystals.
MMF07-15	Flaherty Formation, Belcher Islands	56° 31' 31.1" N 79° 07' 41.3" W	Field	Basalt	~50% clinopyroxene, ~45% plagioclase, ~ texture. A lot of clinopyroxene is well pres ~2 mm elongate prisms of clinopyroxene. ~1.5 mm long) are partly sericitised. Op

Sample number	Geological unit	Location	Sample type	Rock type	Thin section description
					crystals.
MMF07-16	Flaherty Formation, Belcher Islands	56° 31' 32.3" N 79° 07' 44.8" W	Field	Basalt	~47% clinopyroxene, ~47% plagioclase, rock with some good examples of oph occurs as small (~1 mm) subhedral equ altered to pale green chlorite. Thin laths o partly altered to sericite.
MMF07-17	Flaherty Formation, Belcher Islands	56° 31' 34.8" N 79° 07' 55.7" W	Field	Basalt	~45% clinopyroxene, ~50% plagioclas clinopyroxene prisms (~1 mm) are in som Ophitic texture well preserved as seric minimal. Opaques form small euhedral cry
MMF07-18	Flaherty Formation, Belcher Islands	56° 31' 36.9" N 79° 08' 06.8" W	Field	Basalt	~40% clinopyroxene, ~50% plagioclas examples of ophitic texture preserved. Lar (~2.5 mm) partly replaced by chlorite an Laths of plagioclase well sericitised. Opa the groundmass. Small brown biotite inclu clinopyroxene.
MMF07-19	Flaherty Formation, Belcher Islands	56° 31' 39.4" N 79° 08' 13.7" W	Field	Basalt	~50% plagioclase, ~45% clinopyroxene, texture. Large clinopyroxene crystals abundant plagioclase laths (~1 mm). Plagi down to sericite.
MMF07-20	Flaherty Formation, Belcher Islands	56° 31' 41.5" N 79° 08' 23.1" W	Field	Basalt	~45% clinopyroxene, ~45% plagioclase, prisms of clinopyroxene ~2 mm in length laths. Groundmass composed of same m inclusions found within clinopyroxenes wh chlorite. Plagioclase sericitised and in som chlorite.
MMF07-21	Flaherty Formation, Belcher Islands	56° 31' 42.1" N 79° 08' 28.7" W	Field	Basalt	~45% clinopyroxene, ~45% plagioclas ophitic texture displayed with laths of p clinopyroxene. Clinopyroxene (maximu replaced by chlorite and is a pale green co crystals of plagioclase (~2 mm) present crystals amalgamate. Sericitic alteration minerals are mostly euhedral. Little ground
MMLT07-1	Hellancourt Formation, Labrador Trough	59° 13' 03.4" N 69° 46' 54.2" W	Field	Basalt	Generally a fine grained volcanic rock con plagioclase laths and subhedral actinol scattered around. ~2% of section cons plagioclase laths (~0.5 mm in length). altered to chlorite and sericite.
MMLT07-2	Hellancourt Formation, Labrador Trough	59° 11' 43.4" N 69° 46' 36.8" W	Field	Basalt	Pale green patches of fibrous actinolite plagioclase constitute the fine grained gro common. One cluster of plagioclases

Sample number	Geological unit	Location	Sample type	Rock type	Thin section description
					plagioclase crystals are heavily altered to the original shapes of the crystals are not
MMLT07-3	Hellancourt Formation, Labrador Trough	59° 10' 44.8" N 69° 45' 59.0" W	Field	Basalt	~5% of section consists of subrounded cl anhedral crystals of plagioclase. Maximu mm. Plagioclase is quite heavily altered to clinozoisite also observed. Rest of the s plagioclase laths, subhedral actinolite and
MMLT07-4	Hellancourt Formation, Labrador Trough	59° 10' 42.2" N 69° 45' 59.0" W	Field	Basalt	Very dusty appearance. Plagioclase lat altered to sericite and clays. Near-isotro present, very little amphibole observed. minerals fairly common. There are a fe plagioclase crystals have clustered but alte
MMLT07-5	Hellancourt Formation, Labrador Trough	59° 09' 45.2" N 69° 48' 18.2" W	Field	Basalt	No thin section.
MMLT07-6	Hellancourt Formation, Labrador Trough	59° 08' 52.2" N 69° 47' 04.1" W	Field	Basalt	Generally a fine grained volcanic rock. G fine plagioclase laths, patches of fibro minerals. ~3% of section consists of subr coarser plagioclase laths which are ne sericite or chlorite.
MMLT07-7	Hellancourt Formation, Labrador Trough	59° 08' 30.8" N 69° 47' 14.0" W	Field	Basalt	~2% of section composed of clusters of are quite heavily altered to chlorite and shapes are not easily recognisable. Rest of pale green patches of fibrous amphibole lath-shaped plagioclase. Opaque minera around randomly.
MMLT07-8	Hellancourt Formation, Labrador Trough	59° 07' 59.0" N 69° 46' 47.3" W	Field	Basalt	Fairly altered rock. Fine groundmass actinolite and laths of plagioclase. Plagioc by chlorite and clays. Presence of actinol the section a green colour. Opaque mineral have altered to brown minerals with a ma wide clusters of altered plagioclase laths a
MMLT07-9	Hellancourt Formation, Labrador Trough	59° 05' 40.7" N 69° 44' 34.3" W	Field	Basalt	Most of the section consists of a fine m plagioclase laths and subhedral opaques. laths are altered to sericite and chlorit minerals are present too. ~2% of section of plagioclase (~0.5 mm in length) clustere
MMLT07-10	Hellancourt Formation, Labrador Trough	59° 05' 38.4" N 69° 43' 16.4" W	Field	Basalt	Heavily altered sample. Groundmass is ne only a few plagioclase laths remain recognised where plagioclase crystals although sericitisation has almost complete
MMLT07-11	Hellancourt Formation,	59° 04' 04.9" N	Field	Basalt	Fine grained groundmass with needles of

Sample number	Geological unit	Location	Sample type	Rock type	Thin section description
	Labrador Trough	69° 37' 01.8" W			laths of plagioclase. Some of the actino been altered to near-isotropic chlorite. T some parts to sericite and in other parts small cluster of plagioclase laths (~0.5 mi
MMLT07-12	Hellancourt Formation, Labrador Trough	59° 00' 58.7" N 69° 40' 45.5" W	Field	Basalt	~3% of sample consists of subrounded cl and anhedral plagioclase crystals. These width. The plagioclase has been altered n clusters are surrounded by a finer matri actinolite, plagioclase laths and subhedral
MMLT07-13	Hellancourt Formation, Labrador Trough	58° 57' 04.3" N 69° 38' 16.1" W	Field	Basalt	Groundmass appears to be composed of anhedral plagioclase. Some plagioclase s to chlorite. Occasional clustering of coa mm in length).
MMLT07-14	Hellancourt Formation, Labrador Trough	58° 55' 36.4" N 69° 37' 17.6" W	Field	Basalt	~4% of sample is made up of subroun laths. Clusters are a maximum of ~1 mm altered to chlorite and clays. Clusters s actinolite, plagioclase and opaque mineral
MMLT07-15	Hellancourt Formation, Labrador Trough	58° 53' 53.2" N 69° 33' 54.4" W	Field	Basalt	Fine grained sample. Groundmass compo and opaques. Two patches observed wi plagioclase crystals have aggregated to clusters. The plagioclase is quite heavily in some places replaced by quartz.
MMLT07-16	Hellancourt Formation, Labrador Trough	58° 53' 28.1" N 69° 37' 41.1" W	Field	Basalt	Heavily altered sample. Groundmass is h plagioclase clustering recognisable due coarse plagioclase laths to sericite and cla
MMLT07-17	Hellancourt Formation, Labrador Trough	58° 52' 13.3" N 69° 37' 29.4" W	Field	Basalt	No thin section.
MMLT07-18	Hellancourt Formation, Labrador Trough	58° 50' 31.9" N 69° 37' 01.8" W	Field	Basalt	Generally very fine grained. Groundm plagioclase and opaque minerals. ~3% of plagioclase crystals which are mostly a chlorite.
MMLT07-19	Hellancourt Formation, Labrador Trough	58° 48' 26.5" N 69° 36' 13.2" W	Field	Basalt	Anhedral plagioclase and actinolite groundmass. Opaque minerals also presen to alter to a brown mineral with a masked section consists of clusters of plagioclase heavily altered to sericite, clays, chlorite a
MMLT07-20	Hellancourt Formation, Labrador Trough	59° 12' 31.9" N 69° 45' 25.0" N	Field	Basalt	Fine grained volcanic rock. No phenocry green colour and is composed of fibro plagioclase. Opaque minerals present but coloured minerals with a masked birefring
MMLT07-21	Hellancourt Formation,	59° 09' 41.0" N	Field	Basalt	Aphyric volcanic rock. Laths of plagio

Sample number	Geological unit	Location	Sample type	Rock type	Thin section description
	Labrador Trough	69° 45' 05.6" W			green actinolite. Plagioclase variably al actinolite altered to a near-isotropic ch present. Minor amounts of epidote also visil
MMLT07-22	Hellancourt Formation, Labrador Trough	59° 04' 58.7" N 69° 42' 18.5" W	Field	Basalt	Fine grained rock containing no phenocrys composed of actinolite and plagioclase. Chl is not obvious what is has replaced. Opaq around, as are brown minerals with a maske
MMLT07-23	Hellancourt Formation, Labrador Trough	58° 59' 28.4" N 69° 39' 00.1" W	Field	Basalt	Aphyric. Groundmass consists of actinol plagioclase. The plagioclase is mostly alt minerals are common but not abundant.
MMLT07-24	Hellancourt Formation, Labrador Trough	58° 58' 14.5" N 69° 35' 52.5" W	Field	Basalt	Pale green patches of fibrous actinolite su lath-shaped plagioclase comprise the fi Plagioclase is variably altered to chlorite an also appears to have altered to chlorite. Opa
MMLT07-25	Hellancourt Formation, Labrador Trough	58° 56' 17.3" N 69° 34' 22.6" W	Field	Basalt	Very dusty appearance and seems to be qu almost completely replaced by sericite a commonly replaces actinolite. Opaque mine
MMLT07-26	Hellancourt Formation, Labrador Trough	58° 54' 43.9" N 69° 34' 10.7" W	Field	Basalt	Fine grained rock with no phenocrysts. Gro green actinolite and subhedral to euhedral minor amounts of opaques. Plagioclase is v whilst chlorite occasionally replaces actinoli
MMLT07-27	Hellancourt Formation, Labrador Trough	58° 52' 59.6" N 69° 34' 09.0" W	Field	Basalt	Groundmass of actinolite and plagioclase altered to sericite though the original sh preserved. Chlorite occasionally replaces ac appear to be altering to a brown-colour masked birefringence.
MMLT07-28	Hellancourt Formation, Labrador Trough	58° 52' 00.8" N 69° 34' 33.8" W	Field	Basalt	Aphyric. Groundmass consists of pale green anhedral to lath-shaped plagioclases, plu plagioclase crystals are variably altered to se minerals also appear to be altered to brown birefringence.
MMLT07-29	Hellancourt Formation, Labrador Trough	58° 50' 54.3" N 69° 33' 20.5" W	Field	Basalt	Fine grained volcanic rock with no phen comprises fine needles of pale green actino shaped plagioclase crystals. Actinolite plagioclase is commonly replaced with chl Opaque minerals commonly present.
MMLT07-30	Hellancourt Formation, Labrador Trough	58° 50' 40.5" N 69° 34' 58.3" W	Field	Basalt	No thin section.
MMLT07-31	Hellancourt Formation, Labrador Trough	58° 49' 42.0" N 69° 33' 50.3" W	Field	Basalt	Aphyric with a groundmass of actinolite n and opaque minerals. The plagioclase is va and chlorite whilst opaque minerals appear t

Sample number	Geological unit	Location	Sample type	Rock type	Thin section description
					minerals with masked birefringence.
MMLT07-32	Hellancourt Formation, Labrador Trough	58° 48' 51.5'' N 69° 34' 15.2'' W	Field	Basalt	No thin section.
MMLT07-33	Hellancourt Formation, Labrador Trough	58° 57' 23.8'' N 69° 35' 30.9'' W	Drill core (42.8 m depth)	Basalt	~3% of section consists of clustered pl heavily altered to chlorite and clays. Thes fine groundmass consisting of actinolite n and opaque minerals. In some places the g
MMLT07-34	Hellancourt Formation, Labrador Trough	58° 57' 23.8'' N 69° 35' 30.9'' W	Drill core (50.6 m depth)	Basalt	Fine groundmass consists of pale green anhedral to lath-shaped plagioclase plus minerals. Set in the groundmass are a clusters of plagioclase blades which are he clay minerals.
MMLT07-35	Hellancourt Formation, Labrador Trough	58° 57' 23.8'' N 69° 35' 30.9'' W	Drill core (76 m depth)	Basalt	Pale green fibrous actinolite, laths of opaque minerals comprise the groundm Plagioclase is variably altered to sericite, patches observed where altered plagiocla subrounded clots.
MMLT07-36	Hellancourt Formation, Labrador Trough	58° 57' 23.8'' N 69° 35' 30.9'' W	Drill core (90.3 m depth)	Basalt	~5% of section consists of clustered crystals are less than 0.5 mm in length bu ~1 mm in width. The crystals are hea chlorite. The groundmass consists of a opaque minerals.
MMLT07-37	Hellancourt Formation, Labrador Trough	58° 57' 23.8'' N 69° 35' 30.9'' W	Drill core (97 m depth)	Basalt	Pale green needles of actinolite and dust plagioclase dominate the groundmass minerals are occasionally present. A few c occur but the laths very heavily altered to s
MMLT07-38	Hellancourt Formation, Labrador Trough	58° 57' 23.8'' N 69° 35' 30.9'' W	Drill core (101 m depth)	Basalt	~2% of the section consists of subrounded of blades of plagioclase which are mostly are set in a groundmass of actinolite nee opaque minerals.
MMLT07-39	Hellancourt Formation, Labrador Trough	58° 57' 15.9'' N 69° 34' 59.7'' W	Drill core (58.2 m depth)	Basalt	Fine grained volcanic rock with no phenoc composed of fine actinolite needles and pl amounts of opaque minerals. Parts of chloritised and some of the plagiocla sericitised.
MMLT07-40	Hellancourt Formation, Labrador Trough	58° 57' 15.9'' N 69° 34' 59.7'' W	Drill core (71.5 m depth)	Basalt	Aphyric rock with a groundmass of pal surrounded by anhedral and lath-shaped minerals. Variable alteration of plagioclase
MMLT07-41	Hellancourt Formation, Labrador Trough	58° 57' 15.9'' N 69° 34' 59.7'' W	Drill core (74.3 m depth)	Basalt	Consists of a fine groundmass of actinoli minerals. The plagioclase crystals are alter places chlorite. Some of the opaque min

Sample number	Geological unit	Location	Sample type	Rock type	Thin section description
					altered to brown minerals with masked bi
MMLT07-42	Hellancourt Formation, Labrador Trough	58° 57' 15.9" N 69° 34' 59.7" W	Drill core (80.8 m depth)	Basalt	Fine grained. No phenocrysts. The grou green needles of actinolite variably al plagioclase variably altered to sericite, an
MMLT07-43	Hellancourt Formation, Labrador Trough	58° 57' 15.9" N 69° 34' 59.7" W	Drill core (121.5 m depth)	Basalt	~2% of section consists of clusters of pla subrounded and are made up of blade plagioclase is variably altered and clinozoisite. The clusters are set in a fi altered actinolite, plagioclase and opaque
MMLT07-44	Hellancourt Formation, Labrador Trough	58° 57' 10.5" N 69° 35' 20.3" W	Drill core (45.2 m depth)	Basalt	Aphyric rock. Groundmass consists of p and anhedral to lath-shaped plagioclase. C in some places appear to be altered to a masked birefringence.
MMLT07-45	Hellancourt Formation, Labrador Trough	58° 57' 10.5" N 69° 35' 20.3" W	Drill core (48.5 m depth)	Basalt	Fine grained volcanic rock with no phe consists of plagioclase, actinolite an plagioclase is variably altered to sericite,
MMM07-1	Molson dykes	55° 28' 17.9" N 95° 45' 03.4" W Cauchon Lake 55 cm from eastern margin of 5 m wide dyke	Field	Dolerite	Porphyritic texture. Quite fine grained. clinopyroxene, ~10% opaque mineral generally ~1 mm in size and altered to se textures are displayed with laths of clinopyroxene. Groundmass appears to minerals although it has a greenish colou chloritised.
MMM07-2	Molson dykes	55° 23' 51.9" N 96° 29' 55.5" W Cauchon Lake 40 cm from eastern margin of 50 m wide dyke	Field	Dolerite	Quite fine grained sample with a porphyri (up to ~1 mm in size) and prisms of gr clinopyroxene and olivine are set in a appears to be composed of the same mi altered to sericite. Groundmass also conta ~5% plagioclase, ~30% clinopyroxene, ~10% opaques, ~30% olivine. Some cryst
MMM07-3	Molson dykes	55° 24' 57.5" N 96° 28' 27.1" W Cauchon Lake 2.7 m from western margin of 15 m wide dyke	Field	Gabbro	Fairly coarse sample containing orthopyroxene and plagioclase. Maxim Gabbroic textures. Chlorite is also prese replacing the olivine and pyroxene. Plagi and chlorite. ~60% plagioclase, ~3 orthopyroxene, ~5% olivine.
MMM07-4	Molson dykes	54° 41' 08.6" N 97° 49' 15.6" W Cross Lake Eastern margin of ~1 m wide dyke	Field	Dolerite	Porphyritic texture. Large crystals of clin and possibly orthopyroxene in a finer g opaques and a green-brown material. La long but most are ~0.7 mm. Plagioclases subtly zoned. Ophitic textures common.

Sample number	Geological unit	Location	Sample type	Rock type	Thin section description
					~1.3 mm in size and are sometimes comp Plagioclases are usually fresh althou sericitised. Some patches of the groundm (?amphibole). Two green veins (?chlorite
MMM07-5	Molson dykes	54° 42' 14.6" N 97° 47' 04.4" W Cross Lake 10 cm from eastern margin of 2 m wide dyke	Field	Dolerite	Contains clinopyroxene, orthopyroxene plagioclase can be up to ~2 mm long alt more than ~0.8 mm. The laths are fairly fi sericitisation. Clinopyroxene prisms Orthopyroxene is very rare and zoned. pale green colour (?chlorite) but als plagioclase and opaque minerals.
MMM07-6	Molson dykes	55° 56' 32.1" N 96° 59' 20.0" W Whitchai Lake 2 m from western margin of 10 m wide dyke	Field	Dolerite	Fine grained, green coloured sectio clinopyroxene, ~45% green amphibole, pale brown, pleochroic, euhedral clino and opaque minerals set amongst green a of plagioclase and a green amphibole. crystals have a greenish rim possibl amphibole. Maximum crystal size ~0.4 white veins containing diamond-shaped inclusions, some of which are of plagiocla
MMM07-7	Molson dykes	55° 56' 21.4" N 96° 53' 12.5" W Whitchai Lake 35 cm from eastern margin of 20 m wide dyke	Field	Dolerite	Fine grained rock with a porphyr clinopyroxene and plagioclase are set in same minerals plus opaques. Groundmas section. The other 30% is split fairly e laths and clinopyroxene blades which ha mm. Some ophitic texture visible.
MMM07-8	Molson dykes	54° 09' 28.4" N 96° 45' 36.4" W Molson Lake	Field	Gneiss	No thin section.
MMM07-9	Molson dykes	54° 09' 28.1" N 96° 45' 38.5" W Molson Lake 29 m from western margin of 60 m wide dyke	Field	Peridotite	Hypidiomorphic granular textures where pyroxene crystals are subhedral and no Very little interstitial material prese clinopyroxene, ~10% orthopyroxene. Lim olivine has altered to serpentine and pyr chlorite.
MMM07-10	Molson dykes	54° 09' 27.8" N 96° 45' 37.5" W Molson Lake Same dyke as previous, 18 m from western margin	Field	Gabbro	Brownish green coloured thin section. Q appears to be a mosaic of crystals in replacing euhedral plagioclase. Quartz pre extinction. Coarse grained. Clinopyro plagioclase ~1.8 mm.

Sample number	Geological unit	Location	Sample type	Rock type	Thin section description
MMM07-11	Molson dykes	54° 09' 28.0" N 96° 45' 40.4" W Molson Lake Same dyke as previous, 59 m from western margin	Field	Dolerite	Fine to medium grained. Greenish co ~40% plagioclase, ~5% clinopyroxen laths ~0.5 mm, sometimes cluster tog ~1.2 mm in diameter but up to ~3 m present and together with plagioclase l few euhedral, often hexagonal cryst green but with a colourless core that inclined extinction. Could be clino amphibole. Altered clinopyroxene, opaques sat in a fine greenish matrix w plagioclase laths. Accessory biotite.
MMM07-12	Molson dykes	54° 09' 27.6" N 96° 45' 36.4" W Molson Lake Same dyke as previous, western margin	Field	Dolerite	Greenish colour to thin section. Quite Plagioclase laths (~70%) and hornblen fine greenish groundmass. Plagioclase Groundmass ~50%. Some plagioc hornblende to exhibit ophitic texture.
MMM07-13	Molson dykes	55° 34' 24.2" N 97° 01' 37.4" W Pikwitonei Lake Interior of >60 m wide dyke	Field	Pyroxenite	Coarse crystals of clinopyroxene, ortho a hypidiomorphic granular texture. Th mm. ~20% olivine, ~30% orthopyr Olivines are susceptible to serpentinisat
MMM07-14	Molson dykes	55° 34' 44.5" N 96° 34' 44.5" W Pikwitonei Lake 50 cm from eastern margin of 5 m wide dyke	Field	Dolerite	Fine grained. Small laths of plagioclase brown clinopyroxene. Trace amount either as euhedral crystals or anhedr plagioclase cluster together. Trace (?hornblende) present. ~50% clinopyrox
MMM07-15	Molson dykes	55° 34' 47.9" N 96° 57' 34.3" W Pikwitonei Lake 2m from western margin of 12.5 m wide dyke	Field	Gabbro	Gabbroic texture. ~50% plagioclase, hornblende, ~5% opaques, traces of Plagioclase mainly occurs as large subhedral grains. Laths are up to ~4. Clinopyroxene twinned in some grains places. Limited alteration. Some grain and some hornblende alters to a high Biotite associated with hornblende.
MMM07-16	Molson dykes	55° 34' 49.7" N 96° 58' 00.2" W Pikwitonei Lake 2.2 m from eastern margin of 4 m wide dyke	Field	Gabbro	Coarse grained gabbro with well develo laths of plagioclase engulfed by clino ~30% clinopyroxene, ~10% olivine Moderate alteration of plagioclase to alteration of olivine to serpentine.

Sample number	Geological unit	Location	Sample type	Rock type	Thin section description
MMM07-17	Molson dykes	55° 34' 49.4" N 96° 57' 58.9" W Pikwitonei Lake Same dyke as previous, western margin	Field	Dolerite	Large euhedral-subhedral grains of hor brown pleochroism, 124° cleavage and i hornblende is ~2 mm in longest dimen numerous inclusions, mainly small lath minerals occur within hornblende. Space l mostly filled with plagioclase which occu laths (<0.3 mm). Also present are a few hi dusty appearance. ~65% plagioclase, ~35%
MMM07-18	Molson dykes	55° 18' 07.8" N 97° 10' 54.3" W Landing Lake 10 m from eastern margin of 30 m wide dyke	Field	Gabbro	Coarse grained sample which is fairly a laths are altered to sericite, chlorite and cl dusty appearance. Clinopyroxene is also d chlorite. Difficult to estimate mineral pro rare. Maximum crystal size ~2.5 mm.
MMM07-19	Molson dykes	55° 18' 08.6" N 97° 13' 13.6" W Landing Lake Eastern margin of 0.75 m wide dyke	Field	Dolerite	Fine grained sample but fairly altered. Po plagioclase and prisms of clinopyroxene a groundmass. Plagioclase laths are mostly a clinopyroxene prisms also have a dusty actually altered to anything else. Largest mm.
MMM07-20	Molson dykes	55° 16' 38.0" N 97° 15' 24.0" W Landing Lake Western margin of 100 m wide dyke	Field	Dolerite	Fine grained, porphyritic sample. Groundm of fine plagioclase laths and green crystal the groundmass are clinopyroxene prisms (~20%) and altered olivine crystals (~30% to serpentine and has opaque minerals arc fractures. Olivine generally subhedral and plagioclase and prisms of clinopyroxene altered.
MMM07-21	Molson dykes	55° 16' 37.8" N 97° 17' 26.7" W Landing Lake 30 m from eastern margin	Field	Dolerite	Porphyritic texture. Small brown crystals show pleochroism (colourless through p birefringence and no obvious cleavag clinopyroxene but a few of the crystals h may be orthopyroxene and are zoned. Pos present as a few crystals which are surrou released during serpentinisation. Ground composed of fine grained plagioclase laths
MMM07-22	Molson dykes	55° 16' 38.3" N 97° 17' 29.3" W Landing Lake Same dyke as previous, eastern margin	Field	Dolerite	~60% hornblende, ~40% plagioclase, trace Longest plagioclase lath is ~0.4 mm but m the plagioclase is slightly altered to ser hornblende is present as small subhedral thin carbonate veins run through section.

Sample number	Geological unit	Location	Sample type	Rock type	Thin section description
MMM07-23	Molson dykes	55° 16' 37.5" N 97° 17' 27.8" W Landing Lake Same dyke as previous, 45 m from eastern margin	Field	Gabbro	Mostly composed of subhedral clin plagioclase. Some crystals of green hornbl minor amounts of olivine and opaque n size is ~3 mm. Little ophitic texture ob ~40% clinopyroxene, ~10% hornblende, minerals. Little alteration
MMM07-24	Molson dykes	55° 16' 38.4" N 97° 17' 29.0" W Landing Lake	Field	Gneiss	No thin section.
MMM07-25	Molson dykes	55° 18' 15.5" N 97° 23' 39.2" W Landing Lake 5 cm from western margin of 35 m wide dyke	Field	Dolerite	Porphyritic texture with laths of plagi prisms set in a finer groundmass. Plagiocl and extend to ~0.8 mm in length. Only s where plagioclase laths 'protrude' into laths ~35%, clinopyroxene ~15%, groundı composed of fine plagioclase laths, cl opaque minerals.
MMM07-26	Molson dykes	55° 17' 33.3" N 97° 17' 37.6" W Landing Lake Western margin of 75 m wide dyke	Field	Dolerite	Doleritic texture. Some small relicts recognisable due to opaque minerals hig and fractures. Olivines are surrounded by brown mineral with fairly high bi amphibole is dominant mineral and are m crystals (~0.75 mm) displaying 124° cl ~61% amphibole, ~2% olivine, ~2% opaq to ~0.6 mm. Matrix is a greenish col observed. Some pinkish-brown mineral pyroxene.
MMM07-27	Molson dykes	54° 08' 43.3" N 96° 44' 43.6" W Molson Lake Western margin of 36 m wide dyke	Field	Dolerite	Altered sample. Plagioclase laths are hea clays and gives the whole section a dus laths are usually <0.75 mm and occu groundmass which is nearly isotropic.
MMM07-28	Molson dykes	55° 17' 13.2" N 97° 15' 43.4" W Landing Lake 50 cm from western margin of 20 m wide dyke	Field	Dolerite	Olivine, clinopyroxene and a few plagioc grained groundmass. Olivine crystals ar subhedral (~0.4 mm in size), clinopyrox blades ~0.5 mm in size whilst plagioclase length. These crystals sit in a groundmass contain opaque minerals. Groundmass clinopyroxene ~30%, plagioclase ~10%.
MMPC07-1	Pickle Crow dyke	51° 29' 16.0" N 90° 08' 52.0" W	Field	Dolerite	~50% plagioclase mostly in the form of la length) but also as subrounded crystals. Small rectangular and small, rounder op

Sample number	Geological unit	Location	Sample type	Rock type	Thin section description
					edges present (~1%). Hornblende present prisms which are partly altered to chlorite of clinopyroxene also present (~1%). Op not abundant. ~47% of section compose which may be badly altered clinopyroxer Opaque minerals present.
MMPC07-2	Pickle Crow dyke	51° 29' 14.3" N 90° 08' 59.7" W	Field	Gabbro	Coarse grained gabbro with some ophiti plagioclase, ~35% pyroxene and an Clinopyroxene appears to alter to actino amount of primary hornblende. Prisms long. Plagioclase occurs as thick laths varying degrees of alteration to cla occasionally surrounds plagioclase.
MMPC07-3	Pickle Crow dyke	51° 29' 10.7" N 90° 09' 21.5" W	Field	Gabbro	Coarse grained gabbro very similar t mineralogy and textures as noted above.
MMW07-1	Winnipegosis Belt	52° 58' 55.9" N 99° 56' 49.9" W	Drill core (249.9 m depth)	Picrite	~20% olivine, ~80% brown glassy matrix euhedral hexagons ~0.5 mm in longest d olivine remains, nearly all altered to se concentrated along fractures in olivines.
MMW07-2	Winnipegosis Belt	52° 58' 55.9" N 99° 56' 49.9" W	Drill core (263.3 m depth)	Picrite	~20% olivine, ~5% clinopyroxene, ~7 Olivines found as small euhedral hexa crystals ~0.5 mm. Olivines are altered Opaque minerals often present around olivines. Clinopyroxene present as fine long.
MMW07-3	Winnipegosis Belt	52° 58' 55.9" N 99° 56' 49.9" W	Drill core (266.9 m depth)	Picrite	~10% olivine, ~5% clinopyroxene, ~8 Variety of crystal shapes of olivines incl subhedral forms. Longest dimensions present as very fine dendritic needles ~1 clinopyroxene are altered completely to se
MMW07-4	Winnipegosis Belt	52° 58' 55.9" N 99° 56' 49.9" W	Drill core (287.9 m depth)	Picrite	~25% olivine, ~75% brown glassy matr euhedral hexagons and elongated blades Altered to serpentine, chlorite and ac associated with fractures in olivines.
MMW07-5	Winnipegosis Belt	52° 58' 55.9" N 99° 56' 49.9" W	Drill core (288.9 m depth)	Picrite	~25% olivine, ~10% clinopyroxene, ~6 mostly present as equant hopper crystals The olivines are colourless and are compl Clinopyroxene occurs as fine ornamental which are up to ~1.5 mm in length and Opaque minerals mostly found along crack
MMW07-6	Winnipegosis Belt	52° 58' 55.9" N	Drill core	Picrite	~15% olivine, ~10% clinopyroxene, ~

Sample number	Geological unit	Location	Sample type	Rock type	Thin section description
		99° 56' 49.9" W	(301.9 m depth)		Olivine present as equant hopper crystal elongate blades up to ~0.75 mm. Serpe olivine completely. Clinopyroxene is fou needles and is also replaced by serpent common and found around the margins a crystals.
MMW07-7	Winnipegosis Belt	52° 58' 55.9" N 99° 56' 49.9" W	Drill core (308.5 m depth)	Picrite	~15% olivine, ~85% brown glassy matr altered to serpentine. Olivine crystals a variety of shapes, including euhedral hexa ~0.6 mm in size. Opaque minerals associa olivines.
MMW07-8	Winnipegosis Belt	52° 58' 55.9" N 99° 56' 49.9" W	Drill core (354.3 m depth)	Picrite	~20% olivine, ~5% clinopyroxene, ~75 Olivines tend to be euhedral hexagon cry dimension. Also found as more elongate subhedral crystals. Olivines are colourless t few fresh parts left, nearly all altered commonly found in crystals and along occurs as randomly oriented ornamental ch ~1.2 mm long. A thin serpentine vein cuts t
MMW07-9	Winnipegosis Belt	52° 58' 55.9" N 99° 56' 49.9" W	Drill core (356.2 m depth)	Picrite	~30% olivine, ~70% dark brown glassy r equant hopper crystals, thin needles, and l (up to ~1.1 mm). Most olivines are compl though a few crystals are relatively concentrated along fractures within olivi there to be sulphide minerals present.
MMW07-10	Winnipegosis Belt	52° 58' 55.9" N 99° 56' 49.9" W	Drill core (404.1 m depth)	Picrite	~25% olivine, ~75% brown glassy matri equant hopper crystals ~0.4 mm in size. colourless to very pale yellow. All the oli serpentine, actinolite and chlorite. Opaqu with fractures in serpentinised olivine cryst
MMW07-11	Winnipegosis Belt	52° 58' 55.9" N 99° 56' 49.9" W	Drill core (409.8 m depth)	Picrite	~15% olivine, ~5% clinopyroxene, ~80 Olivine occurs as euhedral hexagons and e long. The olivine is completely replaced b Opaque minerals are usually located ar margins. Clinopyroxene occurs as ~1 mm lo
MMW07-12	Winnipegosis Belt	52° 58' 55.9" N 99° 56' 49.9" W	Drill core (411.3 m depth)	Picrite	~20% olivine, ~80% dark brown glassy m small (~0.15 mm) square, diamond, rectan and also as larger (~0.75 mm) blades, hexa Variable alteration of olivines. Some are serpentine but some remain relatively fr around the margins and in cracks. Some fo

Sample number	Geological unit	Location	Sample type	Rock type	Thin section description
					now be partly composed of high birefringe associated with olivines, presumably a SEM analysis shows there are trace clinopyroxene and sulphide minerals and minerals are Cr-rich spinels.
MMW07-13	Winnipegosis Belt	52° 58' 55.9" N 99° 56' 49.9" W	Drill core (443.4 m depth)	Picrite	~20% olivine, ~5% clinopyroxene, ~1% glassy matrix. Olivines are colourless maximum long dimensions of ~0.8 mm. almost completely to serpentine. Fractures filled with opaque minerals. Clinopyro serpentine and occurs as very fine dend length.
MMW07-14	Winnipegosis Belt	52° 58' 55.9" N 99° 56' 49.9" W	Drill core (446.1 m depth)	Picrite	Very altered olivines set in a devitrified gl ~1% opaques, ~84% glassy matrix. Olivine faint dusty brown patches. There are a v equant hopper, euhedral hexagon (up to ~1 (up to ~2.5 mm) olivines. Olivines altered also to chlorite. Very thin needles and mineral are altered to same material as veins cut through section.
MMW07-15	Winnipegosis Belt	52° 58' 55.9" N 99° 56' 49.9" W	Drill core (469.3 m depth)	Picrite	~15% olivine, ~85% brown glassy ma euhedral hexagonal crystals with maximu mm. All olivine replaced by serpentine and occur in cracks within olivines. Thin veins cut through sample.
MMW07-16	Winnipegosis Belt	52° 58' 55.9" N 99° 56' 49.9" W	Drill core (475.1 m depth)	Picrite	~20% olivine, ~80% brown glassy mat colourless in PPL but clearly altered to s XPL. Olivine crystals are found as euhedr forms up to ~0.75 mm in size. Opaque mi margins of the altered olivines.
MMW07-17	Winnipegosis Belt	52° 58' 55.9" N 99° 56' 49.9" W	Drill core (499.3 m depth)	Picrite	~15% olivine, ~85% dark brown glassy m equant hopper crystals, elongated blades an mm. Some olivines are a pale green-yell altered to serpentine. Other olivines are Opaque minerals are common along fractur veins of chlorite and of serpentine run throu
MMW07-18	Winnipegosis Belt	52° 58' 55.9" N 99° 56' 49.9" W	Drill core (500.6 m depth)	Picrite	~10% olivine, ~90% brown glassy m completely altered to serpentine. The cr hopper crystals ~0.4 mm in size. Opaque m crystals in olivine and along cracks.
MMW07-19	Winnipegosis Belt	52° 58' 55.9" N	Drill core	Picrite	~20% olivine, ~80% dark brown, nearly is

Sample number	Geological unit	Location	Sample type	Rock type	Thin section description
		99° 56' 49.9" W	(503.1 m depth)		material matrix. Olivines are colourless a fairly well preserved. Serpentine is found margins and in cracks. Opaques are found and along fractures. Olivines are a var (hexagons, diamonds, squarer prisms, crystals; up to ~1 mm in longest dimens colourless needles of olivine dispersed bet analysis shows that a minor amount of cl ornamental chains, many of the euhedral o spinels, and sulphide minerals are present.
MMW07-20	Winnipegosis Belt	52° 59' 08.8" N 99° 52' 05.7" W	Drill core (354.3 m depth)	Dunite	All altered but consisted of nearly 1 essentially colourless and original grain bo Almost no interstitial material. Grains are e to have curvilinear boundaries that meet Maximum grain size is ~3 mm in the l arrays of opaque minerals highlight olivin olivines display texture and low birefring whereas others are now replaced with a hig order) mineral (?talc).
MMW07-21	Winnipegosis Belt	52° 59' 08.8" N 99° 52' 05.7" W	Drill core (398.6 m depth)	Dunite	Heavily altered sample. All olivine has obvious interstitial material remains, secti olivine with grain boundaries defined by are generally equant to elongate and have mm.
MMW07-22	Winnipegosis Belt	52° 59' 08.8" N 99° 52' 05.7" W	Drill core (421.5 m depth)	Dunite	Grain boundaries are recognisable due minerals. Very little interstitial material b which have been extensively altered to ser size ~3 mm in longest dimension.
MMW07-23	Winnipegosis Belt	52° 59' 08.8" N 99° 52' 05.7" W	Drill core (434.9 m depth)	Dunite	No thin section.
MMW07-24	Winnipegosis Belt	53° 00' 02.7" N 100° 01' 09.0" W	Drill core (237.1 m depth)	Basalt	Very fine grained rock. Consists of a groun clinopyroxene needles and plagioclase laths dusty and have been altered to clays an carbonate cut through the sample.
MMW07-25	Winnipegosis Belt	53° 00' 02.7" N 100° 01' 09.0" W	Drill core (243.4 m depth)	Basalt	Fine grained, aphyric volcanic rock. N groundmass of altered plagioclase laths, nee subhedral opaque minerals. Dusty appeara to sericitisation of plagioclase crystals.
MMW07-26	Winnipegosis Belt	53° 00' 02.7" N 100° 01' 09.0" W	Drill core (257.2 m	Basalt	Aphyric rock. Groundmass appears to be laths, opaque minerals and needles of clino

Sample number	Geological unit	Location	Sample type	Rock type	Thin section description
			depth)		a general dusty brown colour to it, probal plagioclase.
MMW07-27	Winnipegosis Belt	53° 00' 02.7" N 100° 01' 09.0" W	Drill core (268.3 m depth)	Basalt	Fine grained rock. Mostly a grou clinopyroxene and opaque minerals microphenocryst of plagioclase. Plagiocl sericite and clays.
MMB08-1	Badwater Greenstone, Marquette Range Supergroup	46° 07' 15.3" N 88° 20' 12.1" W	Field	Basalt	Fine grained rock. Laths of plagioclase (up in a finer grained matrix which includ carbonate, chlorite, epidote and opaque through part of the section.
MMB08-2a	Badwater Greenstone, Marquette Range Supergroup	46° 07' 17.5" N 88° 20' 09.4" W	Field	Basalt	Heavily altered sample. Difficult to deter Mostly green probably because of the abun
MMB08-2b	Badwater Greenstone, Marquette Range Supergroup	46° 07' 17.5" N 88° 20' 09.4" W	Field	Basalt	Intersertal texture dominated by abundan (up to ~0.7 mm long). Laths are partly alter possibly to highly birefringent carbonate. M is dusty brown and green, perhaps as it no altered plagioclase. Small opaque and (?sphene) present. Possibly a preferred laths. Also two linear vesicles (~1 mm long chlorite. Thin carbonate vein runs through s
MMB08-3	Badwater Greenstone, Marquette Range Supergroup	46° 07' 04.3" N 88° 20' 09.8" W	Field	Basalt	Phenocryst poor (<5%). The few phenocr laths or stubs of plagioclase (up to ~1 m sericite, chlorite and epidote. Set in a fine includes small opaque minerals and brown of chlorite and epidote present. Amygdale chlorite present and reach up to ~1.5 mm in
MMB08-4	Badwater Greenstone, Marquette Range Supergroup	46° 07' 00.8" N 88° 20' 09.2" W	Field	Basalt	Fine grained, consists mostly of a bro including small opaque minerals. Some sm colourless crystals which have either lo (?plagioclase altering to carbonate). Some which are colourless with patches of green filled with quartz, carbonate and chlorite. S dusty brown material with white veining veins). Thin veins of chlorite and carbonate
MMB08-5	Badwater Greenstone, Marquette Range Supergroup	46° 06' 57.6" N 88° 20' 10.0" W	Field	Basalt	Generally a little coarser than other Badw more stubby crystals. Most stubs >0.5 clinopyroxene crystals which are altered actinolite. There are also some non-lath sh sericite and chlorite.

Sample number	Geological unit	Location	Sample type	Rock type	Thin section description
MMB08-6	Badwater Greenstone, Marquette Range Supergroup	46° 06' 54.1" N 88° 20' 11.1" W	Field	Basalt	Laths and plates of plagioclase present a length. These are variably altered to ser surrounds plagioclase and includes fibr finer laths of plagioclase. Occasional an with carbonate material.
MMB08-7	Badwater Greenstone, Marquette Range Supergroup	46° 06' 49.8" N 88° 20' 09.4" W	Field	Basalt	Intersertal texture with abundant plagio ~0.6 mm in length. Laths have a dusty variably altered to sericite and carbonate. some laths. Laths are set in a green mat but contains very small opaques and bro of amygdales. Most of these are rounde but some more elongated. Some are all with mosaic textures, and some are a chlorite. The latter often have an inner c chlorite and an outermost rim of carbonat
MMB08-8	Badwater Greenstone, Marquette Range Supergroup	46° 06' 54.7" N 88° 20' 30.5" W	Field	Basalt	Very fine grained specimen with a ver laths of plagioclase, now altered to c surrounded by a glassy matrix with a gree to dark brown (?sphene) minerals prese and chlorite cut through section. One an mm in diameter and partially filled with c
MMC08-1	Chukotat Group, Cape Smith Belt	61° 23' 02.2" N 76° 57' 43.4" W	Field	Basalt	Aphyric. Brownish-green groundmass clinopyroxene and plagioclase. Thin secti
MMC08-2	Chukotat Group, Cape Smith Belt	61° 21' 19.2" N 76° 55' 49.9" W	Field	Basalt	Very phenocryst poor, with only the occ plagioclase present. Groundmass consist and plagioclase and is a brownish gr present.
MMC08-3	Chukotat Group, Cape Smith Belt	61° 15'31.0" N 77° 02' 31.3" W	Field	Basalt	Aphyric. Brownish green fine grained gr clinopyroxene needles and plagioclase l and actinolite present. One ~15 mm cryst be quartz rimmed by chlorite.
MMC08-4	Chukotat Group, Cape Smith Belt	61° 14' 46.4" N 77° 00' 54.3" W	Field	Basalt	Clinopyroxene occurs as acicular nee oriented and up to ~1.5 mm in length. Ac much of the clinopyroxene. Opaque mi euhedral crystals. ~15% clinopyroxene, ~
MMC08-5	Chukotat Group, Cape Smith Belt	61° 13' 59.3" N 76° 59' 25.6" W	Field	Picrite	<1 mm sized euhedral equant hopper o serpentine set in a dark brown altered g ~90% glass. Opaque minerals are rare. needles present, altered to serpentine and olivines.
MMC08-6	Chukotat Group, Cape	61° 12' 15.4" N	Field	Picrite	~10% olivine, <1% clinopyroxene, ~89

Sample number	Geological unit	Location	Sample type	Rock type	Thin section description
	Smith Belt	77° 00' 43.9" W			Equant hopper olivines (up to ~1 mm) and actinolite set in a dark brown altere thin acicular needles of altered to clinop matrix.
MMC08-7	Chukotat Group, Cape Smith Belt	61° 10' 25.2" N 76° 58' 59.5" W	Field	Picrite	Pale green olivines range up to ~1.5 mm serpentine, actinolite and chlorite. Opa within some of the olivines and also oc matrix. ~15% olivine, ~1% opaques, ~84
MMC08-8	Chukotat Group, Cape Smith Belt	61° 36' 42.9" N 74° 43' 12.4" W	Field	Picrite	Colourless euhedral equant olivine crys serpentine with minor amounts of chlor clinopyroxene needles (up to 1.5 mm in less altered than the olivines. ~10% olivi opaques, 88% glass.
MMC08-9	Chukotat Group, Cape Smith Belt	61° 36' 07.2" W 74° 42' 51.2" N	Field	Picrite	Colourless, equant hopper phenocrysts up in a brown altered glass matrix. Olivines Opaque minerals occur within olivines ~15% olivine, ~85% glass.
MMC08-10	Chukotat Group, Cape Smith Belt	61° 34' 51.7" N 74° 42' 09.0" W	Field	Picrite	Very pale green olivines vary in shape (~1 mm) to more elongated crystals (~1. all olivines. Opaque minerals situated wit ~15% olivine, ~85% glass, trace of opaqu
MMC08-11	Chukotat Group, Cape Smith Belt	61° 34' 14.3" N 74° 41' 18.9" W	Field	Basalt	~20% clinopyroxene, ~78% altered glass, Clinopyroxenes are equant crystals (~0 actinolite and chlorite. Olivines are larg more heavily altered to serpentine and a euhedral crystals.
MMC08-12	Chukotat Group, Cape Smith Belt	60° 48' 50.6" N 78° 23' 13.3" W	Field	Picrite	No thin section.
MMC08-13	Chukotat Group, Cape Smith Belt	60° 48' 15.3" N 78° 22' 45.0" W	Field	Picrite	Equant hopper crystals of olivine (~15%) of altered glass. Maximum size of olivine
MMC08-14	Chukotat Group, Cape Smith Belt	60° 47' 25.9" N 78° 22' 29.5" W	Field	Picrite	Olivine, clinopyroxene and opaques set in glassy matrix. ~35% olivine, ~5% cl Olivines have a slight green tint and occ mostly equant hopper crystals, with a max have been altered and replaced by serpe actinolite. Clinopyroxene are mostly ligh acicular needles up to ~2 mm in length.
MMC08-15	Chukotat Group, Cape Smith Belt	60° 46' 51.4" N 78° 21' 59.9" W	Field	Picrite	~10% olivine, ~90% glass. Olivine occur (~1 mm) set in a matrix of dark brown alt are altered and replaced by serpentine actinolite. Opaque minerals are very rare.

Sample number	Geological unit	Location	Sample type	Rock type	Thin section description
MMC08-16	Chukotat Group, Cape Smith Belt	60° 46' 08.0" N 78° 21' 33.0" W	Field	Basalt	Phenocryst-poor. Clinopyroxene (~5%) n (~1 mm) which are fairly well preserv (<1%) altered to chlorite and carbonate. V all enclosed with the dark brown altered g
MMC08-17	Chukotat Group, Cape Smith Belt	59° 39' 53.1" N 80° 33' 41.2" W	Field	Basalt	Fine grained, no crystals larger than ~ olivine are altered to chlorite and carbon as thin needles and brown equant crystals.
MMC08-18	Chukotat Group, Cape Smith Belt	59° 41' 38.3" N 80° 24' 31.9" W	Field	Basalt	~20% clinopyroxene, ~80% glass, trace occurs mostly as equant crystals (1 mm) by actinolite and chlorite. Opaques are sm dark brown altered glass matrix.
MMC08-19	Chukotat Group, Cape Smith Belt	59° 49' 15.1" N 80° 07' 34.3" W	Field	Picrite	Colourless olivines, altered to actinolite, small equant hopper crystals to larger su mm in length. Small opaques are encl ~20% olivine, ~80% brown altered glass.
MMC08-20	Chukotat Group, Cape Smith Belt	59° 49' 30.9" N 80° 04' 43.1" W	Field	Picrite	~15% olivine, ~1% clinopyroxene, ~1 Euhedral equant hopper olivines (~1 serpentine. Acicular needles of clinopyr length) randomly oriented and fairly well in olivines and in the glass matrix.
MMC08-21	Chukotat Group, Cape Smith Belt	59° 49' 02.5" N 79° 57' 55.1" W	Field	Picrite	Elongate and equant hopper crystals of length of ~1.5 mm. The olivines are alter pale green tint. Opaque minerals are set dark brown glass matrix. ~20% olivine, ~8
MMC08-22	Chukotat Group, Cape Smith Belt	59° 28' 33.4" N 80° 28' 01.7" W	Field	Picrite	Net-like veins of serpentine replace most as equant hopper crystals (~1 mm). Op matrix. ~10% olivine, ~90% glass.
MMC08-23	Chukotat Group, Cape Smith Belt	59° 28' 36.9" N 80° 28' 13.1" W	Field	Picrite	~15% olivine, ~1% clinopyroxene, ~84% by actinolite and serpentine and occurs crystals. Needles of clinopyroxene, better dispersed throughout the brown glass matr
MMC08-24	Chukotat Group, Cape Smith Belt	61° 26' 19.1" N 75° 45' 50.6" W	Field	Basalt	~20% clinopyroxene, ~80% glass, trace occurs mostly as equant crystals (1 mm) by actinolite and chlorite. Opaques are sm dark brown altered glass matrix.
MMC08-25	Chukotat Group, Cape Smith Belt	61° 25' 47.7" N 75° 45' 12.1" W	Field	Picrite	~15% olivine, ~85% glass. Olivine oc elongated crystals up to ~1 mm in length. Olivines set in a dark brown altered glass
MMC08-26	Chukotat Group, Cape Smith Belt	61° 24' 36.9" N 75° 43' 49.9" W	Field	Picrite	Equant hopper crystals of olivine (~10%) few needles of clinopyroxene (~1%) are (~1%) occur in olivine crystals and in

Sample number	Geological unit	Location	Sample type	Rock type	Thin section description
					(~88%). Olivines are altered to serpentine preserved.
MMC08-27	Chukotat Group, Cape Smith Belt	61° 23' 52.2" N 75° 42' 49.4" W	Field	Picrite	~10% olivine, ~90% glass, trace of opaqu possibly of clinopyroxene present. Olivi tint and are a mixture of equant hopper c crystals, with a maximum size of ~1 mm. serpentine and also to chlorite around the very small square shapes within olivines glass matrix.
MMC08-28	Chukotat Group, Cape Smith Belt	61° 23' 22.1" N 75° 42' 30.6" W	Field	Picrite	Net-like veins of serpentine replace m olivines are replaced with chlorite and c equant hopper crystals up to ~1 mm in le needles dispersed between olivines. Smal within some olivines whilst arrays of opa the edges of some olivines. ~15% oliv ~75% altered glass matrix.
MME08-1	Emperor Volcanic Complex, Marquette Range Supergroup	46° 27' 38.3" N 89° 44' 43.7" W	Field	Basalt	Plagioclase phenocrysts set in a finer plagioclase (up to ~0.4 mm) sometir seemingly larger, rounder crystals. Little are set in a matrix which has a dusty brow plagioclase alteration but also includes ep Rough estimate of ~20% plagioclase lat quartz and quartz plus chlorite present.
MME08-2	Emperor Volcanic Complex, Marquette Range Supergroup	46° 27' 23.8" N 89° 44' 05.1" W	Field	Dolerite	Good ophitic textures preserved. Son plagioclase present (~1.2 mm wide, ~ relatively fresh and twinned. Smaller pl 'protrude' into subhedral stubs of clino brown in colour where unaltered. Some cl some has altered to actinolite. Plagiocl epidote and has green veinlets of chlorite euhedral crystals as well as more elong ~10% coarse plagioclase laths, ~45% smal clinopyroxene/actinolite.
MME08-3	Emperor Volcanic Complex, Marquette Range Supergroup	46° 27' 34.1" N 89° 44' 30.3" W	Field	Basalt	Generally fine grained. Plagioclase laths but a few are larger. The larger laths are Laths are set in a green matrix which is Very fine, dendritic opaque minerals pre composed of amygdales. Most are colou circle shapes with ~0.75 mm diameters. T and in some examples have veins and mineral with speckly birefringence (?biotit

Sample number	Geological unit	Location	Sample type	Rock type	Thin section description
MME08-4	Emperor Volcanic Complex, Marquette Range Supergroup	46° 26' 37.2" N 89° 44' 11.0" W	Field	Basaltic andesite	Plagioclase phenocrysts ~5-10% of sectio (~0.4 mm), more rounded crystals (~0.1 larger squat prisms (~0.4 mm) set in a Plagioclase shows partial alteration to grained groundmass appears greenish alteration of feldspar to chlorite and carbo present. Veins composed of quartz, c through section.
MME08-5	Emperor Volcanic Complex, Marquette Range Supergroup	46° 27' 22.8" N 89° 42' 04.8" W	Field	Dacite	Abundant colourless crystals in a variety ~0.25 mm euhedral prisms, ~0.2 mm d blebs). These have low birefringence and of these crystals are quartz but some observed. Quartz and feldspar comprise >5 brown coloured matrix which appears to opaque minerals present, mostly as small e thin linear features and as aggregated patch
MME08-6	Emperor Volcanic Complex, Marquette Range Supergroup	46° 27' 17.6" N 89° 42' 37.4" W	Field	Dacite	Colourless 'eyes' composed mostly of qu These 'eyes' are ~0.3 mm in diameter. composed of quartz, sericite and less opaque minerals present. Quartz 'eyes' co
MME08-7	Emperor Volcanic Complex, Marquette Range Supergroup	46° 26' 55.9" N 89° 42' 34.5" W	Field	Basaltic andesite	Contains laths of plagioclase (~0.6 mm slightly altered to sericite. In some place form what initially look like larger rounde (~0.1 mm) of clinopyroxene microphenoc texture present. ~2% clinopyroxene, groundmass which is a very fine, brown co clinopyroxene and altered plagioclase. Op
MMFR08-1	Lower Volcanic Formation, Fox River Belt	55° 49' 11.0" N 94° 14' 10.0" W	Field	Basalt	Altered clinopyroxene blades and plagiocl brown glassy matrix. Maximum size Clinopyroxene commonly replaced with c laths are sericitised. Opaque minerals appearance of section obliterates textures.
MMFR08-2	Lower Volcanic Formation, Fox River Belt	55° 48' 42.6" N 94° 15' 17.3" W	Field	Picrite	~10% is composed of olivine phenocrysts chlorite, actinolite and carbonate. Occur i equant euhedral crystals to elongated bla very dusty brown matrix in which are needles (?clinopyroxene). Opaque mine euhedral. Calcite veins are present.
MMFR08-3	Lower Volcanic Formation, Fox River Belt	55° 48' 40.9" N 94° 15' 24.8" W	Field	Picrite	~15% olivine present as euhedral hexago Altered mostly to chlorite, but also mino talc. Clinopyroxene present as skeletal nee

Sample number	Geological unit	Location	Sample type	Rock type	Thin section description
					(~5%). These are randomly oriented a olivines. The longest needle is ~2.5 mm brown colour and includes some very fine
MMFR08-4	Lower Volcanic Formation, Fox River Belt	55° 48' 40.8" N 94° 15' 25.6" W	Field	Basalt	Olivine (~3%) often as euhedral to subh more rounded. Average ~0.5 mm in lon chlorite and actinolite. Small euhedral sphene. Olivines and opaques set in a d with fine clinopyroxene needles.
MMFR08-5	Lower Volcanic Formation, Fox River Belt	55° 48' 39.7" N 94° 15' 32.3" W	Field	Basalt	~2% olivine, ~13% clinopyroxene, ~2% groundmass. Small (~0.2 mm) equant g chlorite and carbonate. Long thin needles/ to ~1.5 mm) randomly oriented and muc Small euhedral opaque crystals somet Groundmass is mainly dusty brown but a very fine, wispy needle-like crystals of pos
MMFR08-6	Lower Volcanic Formation, Fox River Belt	55° 48' 15.4" N 94° 09' 26.9" W	Field	Basalt	Slightly coarser than most other Fox Ri occur as both small euhedral crystals a Plagioclase phenocrysts (~10%) mainl crystals (up to ~1.2 mm) altering to clays (~15%) present as elongate prisms. The long. Clinopyroxene alters to tremoli comprises ~70% of the section and plagioclase crystals.
MMFR08-7	Upper Volcanic Formation, Fox River Belt	55° 50' 37.6" N 94° 07' 25.9" W	Field	Basalt	Quite altered. ~65% plagioclase, ~33% cli Plagioclase occurs as laths (maximum ~0 gone to clays and chlorite. Small (~0.1 m the occasional larger (~0.5 mm) equant cr originally have been clinopyroxene, carbonate and actinolite-tremolite. Opaqu ragged patches.
MMFR08-8	Upper Volcanic Formation, Fox River Belt	55° 49' 52.2" N 94° 07' 59.7" W	Field	Picrite	Polyhedral olivine in a variety of shape comprise ~30% of section and are set in a mineral (probably clinopyroxene) and its olivine blade is ~2.2 mm in length. Olivin crystals are fresh, others have complete amphibole. Tiny opaque minerals scattered
MMFR08-9	Upper Volcanic Formation, Fox River Belt	55° 49' 44.8" N 94° 08' 01.9" W	Field	Picrite	Variety of shapes of olivine; euhedral l elongated blades, ornamental chains. Long Olivine altered to serpentine, actinolite a present as fine acicular needles which are euhedral opaques have gone to sphene.

Sample number	Geological unit	Location	Sample type	Rock type	Thin section description
					altered glass-like material. ~15% olivin opaques, ~81% glass.
MMFR08-10	Upper Volcanic Formation, Fox River Belt	55° 49' 33.5" N 94° 08' 03.7" W	Field	Picrite	~35% olivine, ~5% clinopyroxene, <1 Olivine present as subhedral grains to ~ and all altered to serpentine and actinol less altered and present as elongated pri opaques are diamond-shaped and appe Olivine and clinopyroxene set in a includes lots of fine needles possibly mic
MMFR08-11	Upper Volcanic Formation, Fox River Belt	55° 48' 19.5" N 93° 49' 43.5" W	Field	Basalt	Section dominated by fine laths of pl blades of clinopyroxene in roughly plagioclase are randomly oriented and ar Most plagioclase laths are altered to cla remain relatively unaltered and are twi range up to ~1.2 mm in size. Opaque m fine grained and dusty brown in colour.
MMFR08-12	Upper Volcanic Formation, Fox River Belt	55° 48' 11.9" N 93° 49' 45.6" W	Field	Basalt	Most of the section is composed of a dev Small phenocrysts of altered clinopyroxe ~5% of section. Laths of plagioclase, usu sericite and carbonate. Clinopyroxene subhedral crystals, many having dian diamond is ~0.5 mm. Clinopyroxene ha crystals surrounded by opaques, and chlorite. Possible ophitic textures ob abundant colourless, very thin needles ~ skeletal plagioclase. Carbonate and chlori
MMFR08-13	Upper Volcanic Formation, Fox River Belt	55° 47' 53.0" N 93° 49' 49.3" W	Field	Picrite	Olivine occurs as euhedral hopper crysta to serpentine. These are typically ~0.3 ~10% of the section. Very few opaqu euhedral and subhedral blebs within oli dark brown altered glassy matrix which al needles, possibly clinopyroxene?
MMFR08-14	Upper Volcanic Formation, Fox River Belt	55° 47' 51.5" N 93° 49' 54.7" W	Field	Picrite	~20% olivine, ~10% clinopyroxene, ~ Olivines mainly euhedral hopper crystals mm, although some elongated crystals Altered to serpentine and chlorite. Clino and occurs as skeletal needles and or oriented. Longest needle is ~2.5 mm. T mostly euhedral square-shapes. Matrix is colour.
MMFR08-15	Lower Intrusions, Fox	55° 47' 31.8" N	Drill core	Gabbro	~50% clinopyroxene, ~50% plagioclase.

Sample number	Geological unit	Location	Sample type	Rock type	Thin section description
	River Belt	94° 13' 47.5" W	(400.3 m depth)		euhedral prisms ~0.4 mm long and son Good cleavage displayed. Intercumulus fe often to near-isotropic chlorite. Very Opaque minerals present but rare.
MMFR08-16	Lower Intrusions, Fox River Belt	55° 47' 25.9" N 94° 13' 50.1" W	Drill core (130.2 m depth)	Peridotite	Equant to elongate olivine crystals serpentine. Opaque minerals are associate segments. Maximum crystal size is ~2.5 crystals visible, usually enclosing olivine grained matrix of serpentine and chlorite.
MMFR08-17	Lower Intrusions, Fox River Belt	55° 44' 39.7" N 93° 29' 58.1" W	Drill core (320 m depth)	Gabbro	~70% clinopyroxene, ~30% plagioclase. euhedral prisms ~0.4 mm long. Quite cleavage displayed. Very rare poikilitic some clinopyroxene inclusions. Intercum altered, often to near-isotropic chlorite. Ve Opaque minerals present but rare.
MMFR08-18	Lower Intrusions, Fox River Belt	55° 44' 36.1" N 93° 29' 58.5" W	Drill core (160.5 m depth)	Olivine pyroxenite	Clinopyroxene forms prismatic crystals (~ from each other by minor amounts of Clinopyroxene forms ~70% of section. Se present and altering to chlorite. Olivine c actinolite laths.
MMFR08-19	Bigstone dykes, Fox River Belt	55° 47' 55.7" N 94° 45' 45.1" W	Field	Gabbro	No thin section.
MMFR08-20	Sipanigo dykes, Fox River Belt	55° 47' 35.2" N 94° 24' 50.8" W	Field	Gabbro	Coarse grained gabbro. Plagioclase mostl between clinopyroxene and amphibole, th present. Plagioclase shows albite twinnii epidote. Lozenges of sphene present Clinopyroxene prisms (up to ~2.5 mm) green pleochroic actinolite and simply twi amounts of plagioclase and clinopyroxene.
MMFR08-21	Stupart dykes, Fox River Belt	55° 42' 22.2" N 93° 52' 24.2" W	Field	Gabbro	Green-coloured section. Dominant mine plagioclase and quartz. Minor biotite. Gr and pleochroic through various greens Probably hornblende. Not obvious if it is between the green amphibole are filled by plagioclase laths remain but most plagioc replaced by quartz often in mosaics. ~60 ~40% green amphibole. Tiny accessory zir
MMFR08-22	Marginal Zone of Fox River Sill, Fox River Belt	55° 49' 23.5" N 94° 14' 24.2" W	Field	Gabbro	~70% clinopyroxene, ~30% plagiocl clinopyroxene as euhedral equant stubs blades. Some anhedral clinopyroxene pre and good cleavage displayed. Very ra

Sample number	Geological unit	Location	Sample type	Rock type	Thin section description
					Intercumulus feldspar often heavily alter chlorite. Very rare olivine also present. So through section. Opaque minerals present
MMFR08-23	Marginal Zone of the Fox River Sill, Fox River Belt	55° 49' 21.8" N 94° 14' 25.4" W	Field	Pyroxenite	Clinopyroxene and orthopyroxene compri clinopyroxene is the dominant pyroxene well preserved and display prominent material between the pyroxenes is very du and it is difficult to say what it is. Opaqu this interstitial material.
MMFR08-24	Lower Central Layered Zone of Fox River Sill, Fox River Belt	55° 47' 57.1" N 94° 01' 11.4"W	Drill core (233.7 m depth)	Dunite	Section is dominated by ovoid-shaped oliv serpentine. The presence of opaque mine crystal boundaries. The maximum size of longest dimension. There is a minimal am between the olivine grains which has serpentine.
MMFR08-25	Lower Central Layered Zone of Fox River Sill, Fox River Belt	55° 47' 55.9" N 94° 01' 11.9" W	Drill core (132.8 m depth)	Gabbro	Clinopyroxene is the dominant mineral. T are prismatic and share uncomplica Clinopyroxene is showing incipient Occasional poikilitic orthopyroxene with i and olivine. Intercumulus plagioclase c altered to epidote and chlorite.
MMFR08-26	Upper Central Layered Zone of Fox River Sill, Fox River Belt	55° 52' 36.5" N 94° 26' 47.9" W	Drill core (431.4 m depth)	Olivine pyroxenite	Fairly well preserved rock. Clinopyroxen (~0.4 mm) separated from each other intercumulus plagioclase. Some orthopyro altering to chlorite. Olivine crystals are p laths.
MMFR08-27	Upper Central Layered Zone of Fox River Sill, Fox River Belt	55° 48' 30.5" N 94° 00' 56.9" W	Drill core (172.3 m depth)	Peridotite	No thin section.
MMFR08-28	Upper Central Layered Zone of Fox River Sill, Fox River Belt	55° 48' 30.0" N 94° 00' 57.2" W	Drill core (165.8 m depth)	Gabbro	A notable feature is the presence of aggr displaying lamination. The laths are fairl Clinopyroxene crystals have irregular intercumulus areas and may contain pla orthopyroxene crystal is observed altering
MMFR08-29	Middle Sedimentary Formation, Fox River Belt	55° 49' 13.2" N 94° 14' 02.1" W	Field	Siltstone	No thin section.
MMFR08-30	Lower Sedimentary Formation, Fox River Belt	55° 47' 25.4" N 94° 13' 50.3" W	Field	Argillite	No thin section.
MMG08-1	Gunflint Formation, Animikie Group	48° 14' 53.2" N 90° 06' 52.2" W	Field	Basalt	Fine laths of plagioclase up to ~0.3 mm in the section. Laths are quite heavily altered in a very fine grained matrix which is

Sample number	Geological unit	Location	Sample type	Rock type	Thin section description
					carbonate veins cut through the section
MMG08-2	Gunflint Formation, Animikie Group	48° 14' 54.8" N 90° 06' 48.3" W	Field	Basalt	Plagioclase laths ranging in size from ~0 the only distinguishable feature in this sec in any particular direction. Heavily altered matrix which is nearly isotropic (?chlorite)
MMG08-3	Gunflint Formation, Animikie Group	48° 14' 56.8" N 90° 06' 50.0" W	Field	Basalt	Laths of plagioclase (~0.5 mm in length) and comprise ~10% of section. Laths grained matrix which is pale green in colo features (~0.6 mm in diameter) which a mostly with carbonate.
MMG08-4	Gunflint Formation, Animikie Group	48° 14' 58.0" N 90° 06' 50.2" W	Field	Basalt	Vesicular basalt with vesicles filled with q vesicles are ~0.7 mm in diameter. Plagiocl length and together with vesicles are surro fine grained matrix.
MMG08-5	Gunflint Formation, Animikie Group	48° 15' 02.2" N 90° 06' 53.8" W	Field	Basalt	Laths of plagioclase ~0.4 mm in length variably altered to sericite. The laths are s which is dusty and green in colour. <1% rounded vesicles filled mainly with quartz.
MMG08-6	Gunflint Formation, Animikie Group	48° 15' 05.5" N 90° 06' 53.1" W	Field	Basalt	Filled vesicles occupy ~3% of the secti carbonate and some with quartz. Vesicles mm in diameter. Plagioclase laths (~15% length and are set in a green, chloritised ma
MMG08-7	Gunflint Formation, Animikie Group	48° 15' 13.1" N 90° 06' 41.0" W	Field	Basalt	Laths of plagioclase comprise ~10% of ~0.75 mm in length. They are randomly or to sericite. There are dusty brown patcl probably pseudomorphous after plagioclas a greenish matrix of chloritised materia (<1%) and are mostly circular with ~0.75 filled with carbonate but some are filled w (?chlorite) and rimmed by a high relief co birefringence.
MMH08-1	Hemlock Formation, Marquette Range Supergroup	46° 09' 27.1" N 88° 13' 49.5" W	Field	Basalt	Fine grained rock with a general gree colourless crystals with low birefringence c of the green material appears to have m could be actinolite, whilst other green mate could be chlorite. Yellow subhedral crys opaque minerals scattered around. Rock ap is best defined by actinolite needles. Sl chlorite-filled vesicles present as are veins
MMH08-2	Hemlock Formation, Marquette Range	46° 09' 27.4" N 88° 13' 44.4" W	Field	Basalt	~10% of section consists of laths of pla showing signs of alteration to sericite and

Sample number	Geological unit	Location	Sample type	Rock type	Thin section description
	Supergroup				fine grained matrix which is mostly gr chlorite is a major constituent and mayb are patches of higher order birefringen opaque minerals scattered around and oft material possibly the result of alteration of
MMH08-3	Hemlock Formation, Marquette Range Supergroup	46° 09' 26.6" N 88° 13' 39.0" W	Field	Basalt	Foliated nature best highlighted by align Mostly very fine grained and composed actinolite, rare epidote and opaques. <1% coarse grains (up to 0.75 mm) which coul round and others are diamond-shaped. The patches and are comprised of carbonate a quartz also present.
MMH08-4	Hemlock Formation, Marquette Range Supergroup	46° 09' 14.9" N 88° 13' 03.8" W	Field	Basalt	Laths and ragged plates of plagioclase (up mostly partly sericitised. Some have parti carbonate. Also present are ragged plat actinolite which probably formed from c groundmass due to alteration. ~60% pla ~10% opaques and chlorite.
MMH08-5	Hemlock Formation, Marquette Range Supergroup	46° 09' 17.4" N 88° 13' 08.1" W	Field	Basalt	Laths and ragged blades of colourless plag greenish matrix of plagioclase, carbonate, a opaques and maybe epidote. Also present which are dark brown and have a masked speckly in crossed polars (?biotite). Th appear oriented and define foliations phenocrysts ~20%, dark brown ?biotite ~2%
MMH08-6	Hemlock Formation, Marquette Range Supergroup	46° 08' 58.0" N 88° 10' 55.4" W	Field	Dacite	Section cut too thick. Quartz and feldspar quartz, quartz and sericite, and sericitised thin section. Set in a much finer grained m Eyes vary in shape from circular to more el ~1.5 mm) possibly due to deformation. S single quartz crystal showing undulose ex eyes show mosaic textures. There are sc sericite which may be stretched feldspar p eyes are composed of sericitised feldspar. very fine grained quartz with very little felc and zircon observed. Opaque minerals als presumably created during deformation eve
MMH08-7	Hemlock Formation, Marquette Range Supergroup	46° 05' 45.0" N 88° 09' 39.5" W	Field	Basalt	Plagioclase present as subrounded grains as is ~0.5 mm) Some plagioclase going to ch actinolite forms ragged prisms, typically a are set in a fine matrix of plagioclase, ac

Sample number	Geological unit	Location	Sample type	Rock type	Thin section description
					opaques and scattered epidote. Rough c ~30% actinolite, ~ 15% other minerals.
MMH08-8	Hemlock Formation, Marquette Range Supergroup	46° 05' 39.9" N 88° 09' 32.0" W	Field	Basalt	Prisms of pale green actinolite and lath ~0.5 mm long set in a fine groundmass acicular actinolite, chlorite, epidote and op
MMH08-9	Hemlock Formation, Marquette Range Supergroup	46° 06' 46.6" N 88° 12' 30.5" W	Field	Basalt	Laths of altered plagioclase and prisms of two minerals and are set in a greenish chl is altered mainly to sericite. Some ac Maximum length of plagioclase laths minerals scattered around.
MMH08-10	Hemlock Formation, Marquette Range Supergroup	46° 06' 45.6" N 88° 12' 34.2" W	Field	Basalt	Fairly coarse and ophitic texture observed mm) are well twinned, partly altered to ser have a tendency to cluster together. Prisr mm long, which in places may be alteri material (?carbonate). All set in a near i Also present are dark brown fragments w high birefringence. ~40% plagioclase, ~ isotropic material.
MMH08-11	Hemlock Formation, Marquette Range Supergroup	46° 07' 04.0" N 88° 13' 13.3" W	Field	Basalt	Few phenocrysts present. Scattered blade (up to ~1 mm in size) set in a finer, chlorit the matrix are plagioclase laths, epidot Plagioclase altered to sericite and chlorite.
MMH08-12	Hemlock Formation, Marquette Range Supergroup	46° 06' 58.1" N 88° 13' 14.4" W	Field	Basalt	Prisms of actinolite and ragged blades of of plagioclase extend for up to ~1.5 m sericite and clays and appears dusty. Grou and appears to be composed of actinolite Small (<0.1 mm) brownish crystals presen shaped. ~15% actinolite, ~15% plagioclase
MMH08-13	Hemlock Formation, Marquette Range Supergroup	46° 06' 51.9" N 88° 13' 08.6" W	Field	Basalt	Ragged blades of plagioclase (~1 mm) an green actinolite set in a fine grained m altered to chlorite and sericite. Matrix a chloritised laths of plagioclase and needle and opaque minerals.
MMH08-14	Hemlock Formation, Marquette Range Supergroup	46° 06' 34.1" N 88° 13' 32.6" W	Field	Basalt	Phenocryst-poor. Only a few laths and bl finer grained matrix. Longest blade is patches in plagioclase phenocrysts are chlo to clays and sericite. Matrix consists of ve epidote, opaques and chlorite. Veins c present.
MMH08-15a	Hemlock Formation, Marquette Range	46° 06' 27.4" N 88° 13' 56.0" W	Field	Basalt	Very altered sample. Abundance of amyg quartz but some with chlorite and biotite.

Sample number	Geological unit	Location	Sample type	Rock type	Thin section description
	Supergroup				greenish matrix which is nearly isotropic a
MMH08-15b	Hemlock Formation, Marquette Range Supergroup	46° 06' 27.4" N 88° 13' 56.0" W	Field	Basalt	Quite an altered sample. Cannot make c texture. Amygdales comprise ~10% of sec some are stretched, one is even fracture displaced. Most are composed of quartz some also contain chlorite and some biotit ~4 mm in diameter. Amygdales sit in a ch biotite and opaque minerals which appear section is quartz with patches of chlorite. textures and undulose extinction.
MMH08-15c	Hemlock Formation, Marquette Range Supergroup	46° 06' 27.4" N 88° 13' 56.0" W	Field	Basalt	No thin section.
MMH08-16	Hemlock Formation, Marquette Range Supergroup	46° 04' 53.6" N 88° 11' 50.4" W	Field	Basalt	Quite highly altered sample. Plagioclase la to sericite and often it is difficult to rec morphology. Pale green actinolite is pres altering to chlorite. Opaque minerals scatte
MMH08-17	Hemlock Formation, Marquette Range Supergroup	46° 06' 21.0" N 88° 11' 42.3" W	Field	Basalt	Ragged blades of plagioclase and pale Plagioclase blades typically <0.7 mm sericite. Some ophitic texture visible alteration. Some of the actinolite going to chloritised material. There are small (<0.1 brown minerals scattered around. Some and appear speckly in cross polars and actinolite, ~30% plagioclase, ~5% ?sphene
MMH08-18	Hemlock Formation, Marquette Range Supergroup	46° 06' 46.5" N 88° 12' 39.6" W	Field	Basalt	Plagioclase laths (~0.6 mm) are partiall chlorite. Subhedral grains of pale green, w Set in a matrix containing very fine grained chlorite, and euhedral opaque minerals.
MMH08-19	Hemlock Formation, Marquette Range Supergroup	46° 06' 45.7" N 88° 12' 28.3" W	Field	Basalt	Laths of plagioclase ~0.5-0.75 mm in leng to sericite and chlorite. Some ophiti plagioclase laths 'protrude' into plates Chlorite replaces actinolite and plagioclase occur and are associated with chlorite. Br masked birefringence minerals present (~25% actinolite, ~40% plagioclase, ~5% sp
MMH08-20	Hemlock Formation, Marquette Range Supergroup	46° 07' 50.4" N 88° 13' 30.4" W	Field	Basalt	Pale green actinolite prisms and ~1.5 mm l in a green, chloritised matrix. Matrix al plagioclase, epidote and opaque minera variably altered to sericite and chlorite.
MMH08-21	Hemlock Formation,	46° 07' 46.5" N	Field	Basalt	Aphyric. Fine groundmass-like sectio

Sample number	Geological unit	Location	Sample type	Rock type	Thin section description
	Marquette Range Supergroup	88° 13' 26.6" W			plagioclase laths and stubs and needles variably altered to chlorite. Also incl assemblage is epidote, zoisite, carbonat minerals (possibly sphene).
MMH08-22	Hemlock Formation, Marquette Range Supergroup	46° 07' 50.0" N 88° 13' 41.2" W	Field	Basalt	Intersertal texture with plagioclase laths (- set in a finer grained matrix. Evidence c chlorite. The squarer plates are more alt green. Opaques are most abundant withi appears green due to the presence of chlo matrix contains plagioclase, opaques an minerals (?sphene). ~15% plagioclase pl matrix. One quartz vein cuts through samp
MMH08-23a	Hemlock Formation, Marquette Range Supergroup	46° 07' 15.3" N 88° 20' 12.1" W	Field	Basalt	Amygdaloidal. Amygdales comprise ~30 circular and range up to ~1.5 mm in c dominant mineral filling the amygdales. T brown glassy matrix which includes opa with moderate birefringence (?actinolite).
MMH08-23b	Hemlock Formation, Marquette Range Supergroup	46° 07' 15.3" N 88° 20' 12.1" W	Field	Basalt	Plagioclase laths and rounder phenocrys and/or chlorite. The laths are up to ~0.5 rounded crystals are ~0.7 mm in diamet isotropic matrix probably dominated b carbonate veins present. All of the section colour.
MMHS08-1	Haig sills, Sleeper Islands	57° 30' 19.5" N 79° 43' 45.1" W	Field	Gabbro	Glomeroporphyritic gabbro. Subrounded p thin section. Set in a medium graine clinopyroxene, serpentine and opaques. P and prehnite. Pumpellyite replacing pa serpentine. Minor amounts of chlorite, ca plagioclase, ~10% clinopyroxene, ~20% se
MMHS08-2	Haig sills, Sleeper Islands	57° 30' 19.6" N 79° 43' 45.7" W	Field	Gabbro	Medium grained gabbro with ophitic tex mm in length altering to chlorite and pr form due to alteration of opaque minera with clinopyroxene. Thin carbonate veins plagioclase, ~35% clinopyroxene, ~5% ops
MMHS08-3	Haig sills, Sleeper Islands	57° 30' 19.6" N 79° 43' 46.2" W	Field	Gabbro	Glomeroporphyritic gabbro but finer gra Clots of plagioclase ~0.5-1 cm in diameter altered to sericite. Clinopyroxene variab Serpentine, opaques, prehnite, apatite, epid in variable amounts. ~40% plagioclase, ~ serpentine, ~5% opaques, ~2% pumpellyite
MMHS08-4	Haig sills, Sleeper Islands	57° 30' 19.9" N	Field	Gabbro	Glomeroporphyritic gabbro. Clots of pla

Sample number	Geological unit	Location	Sample type	Rock type	Thin section description
		79° 43' 48.8" W			section and are mostly green in the cent composed of plagioclase, clinopyroxen traces of prehnite, epidote and amphibol clinopyroxene, ~5% serpentine, ~5% opac
MMHS08-5	Haig sills, Sleeper Islands	57° 30' 19.9" N 79° 43' 49.1" W	Field	Gabbro	Glomeroporphyritic gabbro. ~60% plagio ~10% serpentine, ~5% opaques, traces epidote and chlorite. Clots of plagioclase are surrounded by a medium grained g laths of plagioclase in clots usually ~4 mn
MMHS08-6	Haig sills, Sleeper Islands	57° 30' 20.0" N 79° 43' 49.5" W	Field	Gabbro	Glomeroporphyritic gabbro. Clots of plag 6 mm or >2 cm in diameter and usually a a medium grained matrix. ~70% plagioc ~10% serpentine, ~5% opaques. Alsc prehnite, carbonate and amphibole.
MMHS08-7	Haig sills, Sleeper Islands	57° 30' 19.6" N 79° 43' 51.2" W	Field	Gabbro	Medium grained gabbro with occasional Plagioclase is fairly fresh but in some plac grained prehnite. ~50% plagioclase, ~3 serpentine, ~3% opaques, ~2% pumpe apatite and carbonate.
MMHS08-8	Haig sills, Sleeper Islands	57° 30' 20.3" N 79° 43' 52.1" W	Field	Gabbro	Normal gabbro with ophitic texture. Lath mm in length. ~45% plagioclase, ~3 pumpellyite, ~5% opaques, ~1% chlor prehnite. Traces of amphibole.
MMHS08-9	Haig sills, Sleeper Islands	57° 30' 20.3" N 79° 43' 52.5" W	Field	Gabbro	Normal gabbro with ophitic texture. clinopyroxene, ~30% serpentine, ~5% prehnite, apatite, carbonate, sphene, amphi trace amounts. Plagioclase laths average ~
MMHS08-10	Haig sills, Sleeper Islands	57° 30' 20.2" N 79° 43' 52.6" W	Field	Gabbro	Glomeroporphyritic gabbro with plagiocl Clots of plagioclase set in medium grainec ~15% clinopyroxene, ~10% serpentine, pumpellyite, prehnite, apatite and amphibo
MMK08-1	Kiernan sills, Marquette Range Supergroup	46° 08' 50.8" N 88° 12' 34.1" W	Field	Gabbro	Actinolite, plagioclase, opaque minera Amphiboles are subhedral and partially display ophitic textures. Plagioclase alte places to mosaics of quartz. Some of Opaque minerals mostly restricted to thir sample.
MMK08-2	Kiernan sills, Marquette Range Supergroup	46° 06' 41.6" N 88° 12' 22.6" W	Field	Gabbro	Dusty and pale green. ~45% plagioclase chlorite, clinozoisite, opaque minerals. subhedral and sometimes fibrous with first in some places going to chlorite. Some

Sample number	Geological unit	Location	Sample type	Rock type	Thin section description
					Ophitic texture. Opaque minerals are c sometimes are rimmed by a brownish min
MMK08-3	Kiernan sills, Marquette Range Supergroup	46° 06' 37.5" N 88° 12' 15.2" W	Field	Gabbro	Amphibole occurs as subhedral grair Plagioclase mostly occurs as laths whi sericite and ~1.2 mm long. Opaque miner have brownish rims with speckly birefri ~40% plagioclase, ~5% clinozoisite, chlor
MMK08-4	Kiernan sills, Marquette Range Supergroup	46° 06' 24.2" N 88° 11' 52.4" W	Field	Gabbro	Good examples of ophitic texture with plagioclase laths seemingly intruding subh actinolite. Some actinolite appears to have Clinozoisite occurs as granular aggregate actinolite, ~10% clinozoisite, opaque mine
MMK08-5	Kiernan sills, Marquette Range Supergroup	46° 06' 21.0" N 88° 11' 42.3" W	Field	Gabbro	Plagioclase, green amphibole, opaque min Actinolite is colourless to pale green and good examples of ophitic textures between Laths of plagioclase generally ~1 mm lo clusters. Opaque minerals commonly have
MMK08-6	Kiernan sills, Marquette Range Supergroup	46° 06' 22.2" N 88° 11' 41.5" W	Field	Gabbro	Ophitic textures visible with sericitised pl by subhedral pale green amphibole (actin mainly occurs as laths up to ~1.5 mm in le granular aggregates. ~50% plagioclase, opaque minerals and clinozoisite.
MMK08-7	Kiernan sills, Marquette Range Supergroup	46° 06' 24.7" N 88° 11' 38.2" W	Field	Gabbro	Amphibole (actinolite) often as large Sometimes fibrous, generally colourless c texture disguised by alteration of plagioc chlorite and epidote. Laths of plagioclas minerals present with rims of colourless bright, speckly birefringence. ~60% plagio
MMK08-8	Kiernan sills, Marquette Range Supergroup	46° 06' 24.1" N 88° 11' 43.5" W	Field	Gabbro	Pale green actinolite, plagioclase, epic minerals. Some ophitic texture still vis plagioclase. Mosaic quartz occasionally re altered plagioclase usually ~1.5 mm in size actinolite, ~10% other minerals.
MMK08-9a	Kiernan sills, Marquette Range Supergroup	46° 06' 20.0" N 88° 11' 26.5" W	Field	Gabbro	Somewhat different to other Kiernan sam identify minerals with much certainty. Mos crystals (~1 mm) surrounded by a near-i very pale green in PPL (?chlorite). Opaque as very small euhedral-subhedral crystals.
MMK08-9b	Kiernan sills, Marquette Range Supergroup	46° 06' 20.0" N 88° 11' 26.5" W	Field	Gabbro	Pale green tint. Plagioclase, green amphil altered opaque minerals. Amphibole as pal subhedral grains with birefringence up to

Sample number	Geological unit	Location	Sample type	Rock type	Thin section description
					hornblende. Ophitic texture visible. Plagic variably altered to sericite. Maximum Clinozoisite occurs as small aggregates. amphibole.
MMK08-10	Kiernan sills, Marquette Range Supergroup	46° 07' 03.8" N 88° 11' 28.6" W	Field	Gabbro	Dusty and pale green. Alteration of plagioc a dusty appearance. Actinolite is a very pal pleochroic. Ophitic textures still visible. S replacing plagioclase. Clinozoisite is fou plagioclase, ~40% amphibole, ~10% minerals.
MMK08-11	Kiernan sills, Marquette Range Supergroup	46° 06' 46.9" N 88° 11' 27.6" W	Field	Gabbro	Coarser than other Kiernan samples. Laths >2 mm long and sometimes cluster togethe through greens and very light brown. Possi Plagioclase altered to sericite, chlorite examples of ophitic texture preserved. Tv through slide. Very few opaque minerals, with possible relict pyroxene.
MMT08-1	Ultramafic intrusions, Thompson Nickel Belt	55° 58' 25.9" N 97° 22' 52.4" W Moak Lake	Drill core (183.4 m depth)	Peridotite	Serpentinised olivine grains comprise ~70% subhedral crystals with maximum long Opaque minerals highlight the outlines and olivine crystals. Very rare clinopyroxen grained matrix appears to be comprised o fibrous amphibole.
MMT08-2	Ultramafic intrusions, Thompson Nickel Belt	55° 49' 21.5" N 97° 47' 31.7" W North Manasan	Drill core (59.3 m depth)	Peridotite	Altered olivine crystals are the dominant comprising ~75% of the sample. These are to serpentine and have outlines and fractu minerals. Maximum crystal size is ~2 mm A few colourless amphibole crystals scatt pseudomorphs. Fine matrix material com opaques and chlorite.
MMT08-3	Ultramafic intrusions, Thompson Nickel Belt	55° 48' 58.1" N 97° 45' 24.0" W Mystery Lake	Drill core (137.6 m depth)	Peridotite	Serpentinised subhedral olivine grains are n presence of opaque minerals along boundari ovoid shaped and range up to ~2.5 mm. Cli rare. Even rarer are remnants of p clinopyroxene surrounds olivine. Colourle first order birefringence and ~124° cl minerals mainly located along fractures in the section is a fine grained matrix of serpe amphibole.
MMT08-4	Ultramafic intrusions, Thompson Nickel Belt	55° 45' 23.2" N 97° 53' 09.2" W	Drill core (466.1 m	Peridotite	Olivine occurs mostly as equant, ~0.3 mm no fractures. There are some fragmented oli

Sample number	Geological unit	Location	Sample type	Rock type	Thin section description
		Thompson Airport	depth)		are ovoid shaped, larger (~2 mm) and co olivines are variably altered to serpentine serpentine with cores of opaque min orthopyroxene occur. All these crystals a matrix of serpentine, chlorite and amphibo
MMT08-5	Ultramafic intrusions, Thompson Nickel Belt	55° 43' 57.4" N 97° 47' 31.3" W Thompson	Drill core (438.5 m depth)	Peridotite	Limited serpentinisation. Contains phlogopite, opaques and amphibole. Oli which are typically ~2.5 mm in size. present are associated with fractures in Orthopyroxene is mainly found as oikoc grains. Phlogopite is present in trace amo to colourless pleochroism and high birefrir rimmed by chlorite. Amphibole present is
MMT08-6	Ultramafic intrusions, Thompson Nickel Belt	55° 41' 39.0" N 97° 55' 39.0" W Birchtree	Drill core (6.4 m depth)	Peridotite	Sample consists of ~70% equant (~0.4 m are variably altered to serpentine. Rare also present. The other ~30% of the samp which is serpentinised and contains numer
MMT08-7	Ultramafic intrusions, Thompson Nickel Belt	55° 37' 12.3" N 98° 00' 46.4" W Ospwagan Lake	Drill core (177.1 m depth)	Peridotite	~60% serpentine pseudomorphs after original grain outlines and fracture patte concentrated along the fractures. Colou crystals with high first order birefringenc present in trace amounts. Fine grained mat and chlorite.
MMT08-8	Ultramafic intrusions, Thompson Nickel Belt	55° 34' 51.8" N 98° 03' 52.5" W Ospwagan Lake	Drill core (162.1 m depth)	Peridotite	Very altered rock. Very little primary min the section is composed of serpentine ps Grains still tend to retain their original Most are ovoid-shaped and ~2 mm in the minerals highlight the crystal margins and set in a fine grained matrix of serpentine an
MMT08-9	Ultramafic intrusions, Thompson Nickel Belt	55° 34' 30.2" N 97° 54' 57.2" W Nichols Lake	Drill core (786.4 m depth)	Peridotite	Serpentinised olivine grains containing abu set in a fine matrix of serpentine, chlo amphibole. Olivine grains are equant (~0.5 of the section. Some rare orthopyroxene cry
MMT08-10	Ultramafic intrusions, Thompson Nickel Belt	55° 35' 40.9" N 97° 54' 01.7" W Nichols Lake	Drill core (177.7 m depth)	Dunite	All altered but consisted of nearly 100% ol but with brown staining. Original grain bo although fractures are less obvious. Almo Grains are equant to elongate and tend to h that meet in triple point junctions. There grains. Maximum grain size is ~3 mm in th are ~1.25 mm. Linear arrays of opaque grain boundaries. Some olivines dis

Sample number	Geological unit	Location	Sample type	Rock type	Thin section description
					birefringence typical of serpentine where with a high birefringence (high third order trace amount of a colourless, moderate extinction, high pink birefringence minera some of the olivines.
MMT08-11	Ultramafic intrusions, Thompson Nickel Belt	55° 35' 30.3" N 98° 02' 26.5" W Muskeg City	Drill core (220.2 m depth)	Dunite	Originally composed near completely completely altered to serpentine. Original recognisable due to presence of opaque m crystals are equant and have curvilinear b junctions. The maximum size of crystal interstitial material present between the oli
MMT08-12	Ultramafic intrusions, Thompson Nickel Belt	55° 30' 45.5" N 98° 07' 46.3" W Mid Lake	Drill core (615.6 m depth)	Dunite	Section is dominated by ovoid-shaped oli now consist of serpentine. The prese highlights the original crystal boundarie crystals is ~3 mm in the longest dimen amount of interstitial material between th mostly been converted to serpentine.
MMT08-13	Ultramafic intrusions, Thompson Nickel Belt	55° 29' 23.7" N 98° 07' 46.5" W Pipe 2	Drill core (1640.7 m depth)	Peridotite	Very altered rock, little primary miner consists of pseudomorphs possibly after ol but tend to retain original morphology, in fracture patterns. Most are ovoid shapes mm in longest dimension. Occasionally s elongate crystals with curvilinear bound along grain boundaries and fractures. Alt fine grained matrix which contains chlorit amphibole.
MMT08-14	Ultramafic intrusions, Thompson Nickel Belt	55° 27' 51.0" N 98° 08' 54.7" W South of Pipe	Drill core (110.1 m depth)	Olivine pyroxenite	~25% serpentinised olivine, ~5% relati opaques, ~45% amphibole, ~20% serpentir and orthopyroxene. Variable alteration which are altering to serpentine display y are mostly euhedral crystals which range These occur mainly along fractures and gr Some orthopyroxene present as oikocrysts
MMT08-15	Ultramafic intrusions, Thompson Nickel Belt	55° 27' 16.8" N 98° 07' 01.7" W Otter Lake	Drill core (275.2 m depth)	Peridotite	Very serpentinised rock. There are few (~10%) and these contain yellowish green orthopyroxene present. Actinolite and tren not overly abundant. Green minerals whic within the section and could be a form of sp
MMT08-16	Ultramafic intrusions, Thompson Nickel Belt	55° 16' 42.2" N 98° 23' 37.2" W McPhail Lake	Drill core (158.0 m depth)	Peridotite	A few relicts of olivine remain in this sa gone to serpentine. In some places serpe original boundaries. Altered olivine cryst

Sample number	Geological unit	Location	Sample type	Rock type	Thin section description
					mm in longest dimension. Subhedral grai are also present. Minor orthopyroxene crystals. ~40% of section is composed of a
MMT08-17	Ultramafic intrusions, Thompson Nickel Belt	55° 39' 06.3" N 97° 59' 35.5" W Soab Lake	Drill core (143.7 m depth)	Peridotite	~30% of the section is composed of a fine There are a few relicts of olivine gra serpentine, even destroying original gra carbonate are associated with some of Largest olivine grain is ~4 mm long. Subh blades of amphibole with ~124° orthopyroxene is present and mainly occu other crystals.
MMT08-18	Ultramafic intrusions, Thompson Nickel Belt	55° 08' 34.6" N 98° 28' 09.4" W Setting Lake area	Drill core (131.2 m depth)	Peridotite	Olivine grains are equant to elonga boundaries. The largest crystal is ~4 mm Nearly all the olivines are altered to serpe now outline the original crystal mar orthopyroxene and clinopyroxene present colourless amphibole with ~124° cleavage grained matrix composed mostly of serpen
MMT08-19	Ultramafic intrusions, Thompson Nickel Belt	55° 05' 20.3" N 98° 29' 23.8" W Setting Lake	Drill core (434.3 m depth)	Peridotite	Heavily serpentinised sample. Serpentine p comprise ~70% of the section. The grains to ~3 mm in longest dimension. Opaque m crystal morphologies. The surrounding fi composed mostly of serpentine.
MMT08-20	Ultramafic intrusions, Thompson Nickel Belt	55° 03' 14.9" N 98° 31' 03.3" W Setting Lake South	Drill core (260.4 m depth)	Peridotite	Serpentinised olivines are mostly equant i size. Opaque minerals outline the crystal Colourless amphibole is also present in tr prisms. A fine grained matrix of serpenti ~35% of the sample.
MMT08-21	Ultramafic intrusions, Thompson Nickel Belt	54° 55' 41.7" N 98° 39' 46.7" W Wabowden Lake	Drill core (1227 m depth)	Dunite	Consists of nearly 100% altered olivine. Th with brown staining. The olivine crystals have curvilinear boundaries meeting in tr olivine has been replaced by serpentine bu are recognisable due to the presence maximum size of olivine crystals is ~2 mm
MMT08-22	Ultramafic intrusions, Thompson Nickel Belt	54° 52' 40.4" N 98° 39' 13.6" W Bucko Lake	Drill core (98.5 m depth)	Peridotite	Equant to elongate olivine crystals ar serpentine. Opaque minerals are associated segments. Maximum crystal size is ~3 m crystals visible, usually enclosing oli amphibole present too. ~30% of section is serpentine, chlorite and fibrous amphibole.
MMT08-23	Ultramafic intrusions,	53° 48' 58.8" N	Drill core	Dunite	All altered but originally consisted of m

Sample number	Geological unit	Location	Sample type	Rock type	Thin section description
	Thompson Nickel Belt	99° 22' 20.1'' W William Lake	(568.5 m depth)		crystals are mostly ovoid and extend up dimension. The olivine has been altered minerals surround the original crystal mar material.

Appendix B: Preparation of rock samples for analysis by inductively-coupled plasma optical emission spectrometry (ICP-OES) and inductively-coupled plasma mass spectrometry (ICP-MS) and an evaluation of the accuracy and precision of the results

B.1. Preparation of rock samples into powder

Rock samples were prepared into powder using the rock preparation laboratories at Cardiff University. Weathered surfaces, veins and alteration patches were removed from the rock samples using a diamond-bladed mechanical rock saw. Samples were then crushed to a coarse grit by a steel jaw crusher. Approximately 80 ml of each sample was reduced to a fine powder in an agate planetary ball mill. Afterwards, approximately 2 g of each powdered sample was ignited for two hours in a furnace at 900°C to drive off volatile substances and determine loss on ignition (LOI) values. The LOI of a sample was calculated using the equation below.

$$LOI(wt.\%) = \frac{Mass\ of\ wet\ powder - Mass\ of\ ignited\ powder}{Mass\ of\ wet\ powder} \times 100$$

Equation B.1

B.2. Preparation of solutions for ICP-OES and ICP-MS analysis

Samples in this study were prepared for ICP analysis using the lithium metaborate fusion method. To prepare the samples, 0.1 ± 0.001 g of each ignited sample was mixed with 0.6 ± 0.004 g of lithium metaborate flux in a platinum crucible. A few drops of lithium iodide wetting agent were added to each mixture which was then fused using the Claisse Fluxy automated fusion system. Each mixture was then dissolved in a 50 ml solution of 20 ml of 10% HNO_3 and 30 ml of 18.2 Ω deionised water obtained using a Milli-Q purification system. After the mixture had fully dissolved, 1 ml of 100 ppm Rh spike was added to the solution which was then made up to 100 ml with 18.2 Ω deionised water. Approximately 20 ml of each solution was run on the ICP-OES to obtain major element and some trace element abundances. An aliquot of 1 ml of each solution was added to 1 ml of In and Tl and 8 ml of 2% HNO_3

and run on the ICP-MS to obtain trace element abundances. The instruments at Cardiff University used to analyse elemental abundances are a Jobin Yvon Horiba Ultima 2 inductively-coupled plasma optical emission spectrometer and a Thermo Elemental X7 series inductively-coupled plasma mass spectrometer. The samples were run on the mass spectrometers by Dr. Iain McDonald and Dr. Ley Woolley.

B.3. Evaluation of the accuracy and precision of the geochemical data

B.3.1. Standards

In order to assess the accuracy and precision of the whole-rock elemental data obtained by ICP-OES and ICP-MS external and internal standards were analysed. The external standards used were JB-1a and JGb-1. JB-1a and JGb-1 are a basalt and a gabbro respectively and both are issued by the Geological Survey of Japan. The certified element concentrations in JB-1a and JGb-1 are given in Tables B.5-B.8 and are published in Imai et al. (1995). These two standards were run in every batch of samples analysed mainly to assess the accuracy of the results but also to help determine the precision of the results. Three internal standards were also run in every sample batch. These three samples were MMF07-17, MMLT07-28 and MMLT07-41 and were used to assess the precision of the elemental data.

B.3.2. Accuracy

All of the results from the different runs of standards JB-1a and JGb-1 are given in Tables B.1-B.4 along with the percentage errors of the measured values compared with the certified values. The percentage error for each element was calculated using the following equation:

$$\%\,error = \frac{Difference\ between\ measured\ and\ certified\ concentrations\ of\ element}{Certified\ concentration\ of\ element} \times 100$$

Equation B.2

Table B.1. ICP-OES element concentrations for the external standard JB-1a in the four batches of samples analysed and their percentage differences from the accepted values

	Run 1	% error	Run 2	% error	Run 3	% error	Run 4	% error
Major elements (wt. %)								
SiO_2	52.44	0.06	52.22	0.36	52.06	0.67	52.00	0.78
TiO_2	1.31	2.13	1.32	3.27	1.31	2.09	1.31	2.04
Al_2O_3	14.32	0.93	14.21	1.65	14.40	0.37	14.49	0.29
$Fe_2O_3(T)$	9.24	2.14	9.25	2.26	9.08	0.36	9.12	0.80
MnO	0.15	2.32	0.15	0.43	0.15	0.59	0.15	1.80
MgO	7.97	1.74	8.17	4.39	7.86	0.40	7.89	0.71
CaO	9.26	0.54	9.15	1.73	9.31	0.02	9.28	0.31
Na_2O	2.65	2.79	2.80	2.54	2.68	1.93	2.76	1.02
K_2O	1.45	3.58	1.44	2.55	1.37	1.93	1.43	2.35
P_2O_5	0.24	7.73	0.27	5.39	0.27	5.36	0.25	3.14
Trace elements (ppm)								
Sc	28.49	2.11	27.82	0.28	27.93	0.10	27.84	0.20
V	197.41	10.27	196.09	10.87	228.81	4.01	205.77	6.47
Cr	436.62	5.21	409.84	1.24	401.65	3.22	415.06	0.01
Co	39.42	0.21	40.61	2.81	36.42	7.80	36.91	6.57
Ni	149.28	6.63	141.65	1.18	123.88	11.51	146.28	4.49
Cu	62.09	11.88					54.72	1.41
Zn	77.53	5.46	207.65	153.23	85.79	4.62		
Sr	443.83	0.19	440.98	0.46	444.75	0.39	445.11	0.48
Y	25.75	7.29	23.41	2.48	23.91	0.36	23.96	0.17
Zr	142.92	2.11	149.58	2.45	142.74	2.23	143.88	1.45
Ba	503.98	1.40	500.92	0.79	502.39	1.09	494.18	0.57

Table B.2. ICP-OES element concentrations for the external standard JGb-1 in the four batches of samples analysed and their percentage differences from the accepted values

	Run 1	% error	Run 2	% error	Run 3	% error	Run 4	% error
Major elements (wt. %)								
SiO_2	43.39	0.62	43.36	0.70	42.97	1.58	44.04	0.86
TiO_2	1.63	2.10	1.64	2.36	1.64	2.66	1.61	0.32
Al_2O_3	16.78	4.04	17.30	1.10	17.50	0.08	17.58	0.51
$Fe_2O_3(T)$	15.35	1.94	15.27	1.39	15.41	2.30	15.85	5.24
MnO	0.20	3.72	0.19	0.19	0.20	4.03	0.19	1.05
MgO	7.95	1.24	8.09	3.06	7.80	0.60	7.53	4.08
CaO	11.49	3.46	11.69	1.73	11.90	0.01	12.07	1.42
Na_2O	1.83	52.22	1.22	1.88	1.25	3.85	1.22	1.33
K_2O	0.25	2.63	0.24	1.17	0.26	7.98	0.22	7.94
P_2O_5	0.04	25.14	0.05	14.22	0.05	16.65	0.05	15.31
Trace elements (ppm)								
Sc	34.69	3.11	34.88	2.56	35.66	0.38	34.27	4.29
V	635.55	0.09	660.07	3.95	670.74	5.63	661.43	4.16
Cr	59.63	3.17	59.24	2.48	56.98	1.41	50.68	12.32
Co	59.10	1.66	62.54	4.06	61.01	1.51	57.45	4.42
Ni	20.88	17.81	29.34	15.51	41.72	64.24	39.14	54.10
Cu	88.42	3.18					83.65	2.39
Zn	103.92	4.66	170.72	56.62	104.53	4.10		
Sr	321.15	1.79	308.60	5.63	322.15	1.48	321.51	1.68
Y	10.54	1.34	9.71	6.68	10.86	4.46	10.76	3.44
Zr	34.18	4.22	31.75	3.20	35.37	7.82	36.66	11.76
Ba	61.85	3.81	60.77	5.49	61.97	3.62	65.26	1.50

Table B.3. ICP-MS element concentrations for the external standard JB-1a in the four batches of samples analysed and their percentage differences from the accepted values

	Run 1	% error	Run 2	% error	Run 3	% error	Run 4	% error
Major elements (wt. %)								
TiO_2	1.28	0.08	1.33	4.29	1.32	2.85	1.28	0.33
MnO	0.14	7.43	0.15	0.98	0.15	3.21	0.15	1.39
$Fe_2O_3(T)$			9.14	0.45	7.95	12.60	9.00	1.05
Trace elements (ppm)								
V	199.04	2.91	199.55	2.66	213.61	4.20	200.34	2.27
Cr	405.01	3.32	400.61	2.20	399.19	1.83	416.94	6.36
Co	35.99	6.77	39.28	1.77	37.94	1.71	37.64	2.50
Ni	137.05	1.40	139.14	0.10	139.63	0.46	144.11	3.68
Cu	69.14	21.95	60.34	6.41	54.51	3.86	61.16	7.87
Zn			80.46	2.00	83.65	1.89	79.64	2.99
Ga	17.95	0.27	17.59	1.72	17.72	1.00	17.88	0.11
Rb	38.38	2.09	38.39	2.07	39.75	1.40	42.47	8.35
Sr	440.33	0.38	449.89	1.79	430.18	2.67	454.67	2.87
Y	23.83	0.71	23.38	2.58	23.91	0.36	24.20	0.85
Zr	141.85	1.49	143.17	0.58	142.28	1.20	143.80	0.14
Nb	26.91	0.03	27.86	3.57	27.12	0.82	27.53	2.33
Mo			1.18	24.68				
Cs	1.26	3.97	1.21	7.56	1.24	5.65	1.32	0.54
Ba	501.34	0.53	484.48	3.87	483.68	4.03	494.80	1.82
La	37.43	0.45	37.35	0.67	37.96	0.96	38.25	1.73
Ce	64.94	1.46	63.70	3.34	67.20	1.98	64.65	1.89
Pr	7.22	1.12	7.01	4.01	7.37	0.95	7.24	0.77
Nd	25.58	1.60	25.16	3.23	26.36	1.39	26.10	0.38
Sm	4.92	2.92	4.92	2.95	5.26	3.72	5.06	0.28
Eu	1.52	3.84	1.48	1.53	1.48	1.62	1.52	4.04
Gd	4.67	0.02	4.60	1.49	4.53	3.10	4.70	0.68
Tb	0.73	5.07	0.67	3.05	0.68	0.79	0.70	1.66
Dy	4.09	2.48	3.90	2.14	4.10	2.76	4.00	0.23
Ho	0.74	4.08	0.72	1.69	0.79	10.58	0.73	2.78
Er	2.14	1.70	2.03	6.91	2.14	1.82	2.09	4.23
Tm	0.33	1.52	0.31	4.84	0.33	1.18	0.32	1.92
Yb	2.08	0.76	2.07	1.26	2.03	3.19	2.05	2.61
Lu	0.32	3.03	0.32	3.05	0.31	4.90	0.31	5.84
Hf	3.45	1.23	3.28	3.68	3.46	1.41	3.38	0.89
Ta	1.60	17.25	1.57	18.57	1.66	13.94	1.60	17.13
Th	8.92	1.27	8.89	1.52	8.69	3.79	8.58	4.96
U	1.66	5.73	1.59	1.31	1.67	6.66	1.66	5.42

Tables B.1 and B.3 display the results obtained for JB-1a using ICP-OES and ICP-MS respectively. The vast majority of elements have percentage errors less than 5% for both analytical methods. This suggests that the sample analyses for all the batches can be considered accurate. Fig. B.1 further highlights the accuracy of the data as there is good overlap between the measured and certified element concentrations. Fig B.1 also shows that for the majority of elements both ICP-OES and ICP-MS methods

Table B.4. ICP-MS element concentrations for the external standard JGb-1 in the four batches of samples analysed and their percentage differences from the accepted values

	Run 1	% error	Run 2	% error	Run 3	% error	Run 4	% error
Major elements (wt. %)								
TiO_2	1.63	1.87	1.63	1.75	1.64	2.21	1.63	1.68
MnO	0.19	2.12	0.18	4.15	0.20	7.54	0.19	0.15
$Fe_2O_3(T)$			14.91	0.00	13.77	7.67	15.01	0.64
Trace elements (ppm)								
V	629.14	0.92	637.47	0.39	664.57	4.66	632.55	0.39
Cr	59.88	3.60	59.52	2.98	55.37	4.21	56.11	2.92
Co	59.66	0.74	59.85	0.42	61.62	2.54	58.73	2.29
Ni	18.31	27.91	29.08	14.49	41.42	63.07	40.97	61.29
Cu	81.21	5.23	90.90	6.06	91.57	6.85	95.45	11.37
Zn			106.45	2.34	112.26	2.99	118.99	9.17
Ga	19.73	10.22	17.80	0.58	18.67	4.33	18.84	5.26
Rb	5.79	15.75	5.77	15.95	5.23	23.80	6.41	6.75
Sr	328.23	0.38	307.02	6.11	330.94	1.20	338.85	3.62
Y	10.38	0.20	9.66	7.13	10.10	2.92	11.18	7.50
Zr	33.67	2.65	32.21	1.79	34.83	6.19	32.95	0.44
Nb	2.46	12.25	2.72	3.02	2.28	18.49	2.37	15.33
Mo			0.37	37.55				
Cs	0.18	30.38	0.68	162.89	0.27	5.60	0.29	9.85
Ba	60.63	5.71	65.18	1.37	71.96	11.91	61.82	3.86
La	3.81	5.86	3.35	6.85	3.36	6.53	3.43	4.59
Ce	7.83	4.14	7.64	6.44	8.05	1.41	7.81	4.36
Pr	1.14	0.80	1.08	4.04	1.15	1.59	1.14	0.47
Nd	5.09	6.97	5.33	2.51	5.16	5.69	5.12	6.33
Sm	1.44	3.29	1.49	0.30	1.45	2.96	1.42	4.73
Eu	0.60	3.71	0.59	4.24	0.62	0.74	0.60	3.56
Gd	1.53	5.09	1.40	12.94	1.63	1.54	1.48	7.79
Tb	0.28	3.10	0.29	1.17	0.25	12.34	0.22	22.65
Dy	1.73	10.71	1.53	2.06	1.70	9.14	1.66	6.20
Ho	0.34	3.03	0.30	9.45	0.35	5.02	0.32	2.79
Er	1.01	2.79	1.09	4.49	0.96	7.96	0.94	9.94
Tm	0.15	5.00	0.14	14.02	0.15	5.16	0.15	8.75
Yb	0.99	6.98	0.98	7.95	0.92	12.79	0.91	13.71
Lu	0.15	1.33	0.14	9.84	0.15	2.91	0.14	7.97
Hf	0.72	18.18	0.91	3.47	0.84	4.66	0.80	9.47
Ta	0.13	26.11	0.13	28.26	0.17	5.32	0.14	24.41
Th	0.57	19.38	0.75	56.00	0.38	21.58	0.38	21.42
U	0.10	24.62	0.10	24.65	0.10	22.20	0.10	23.55

give similar results, indicating that both analytical methods produce relatively accurate data. However, for V, Ni and Zn, the ICP-MS method is more consistent at producing accurate results than the ICP-OES method. One element that gave consistently high errors (>10%) in each sample batch was Ta. This could be explained by the large uncertainty in the certified JB-1a value (1.93 ± 0.49 ppm) (Imai et al., 1995).

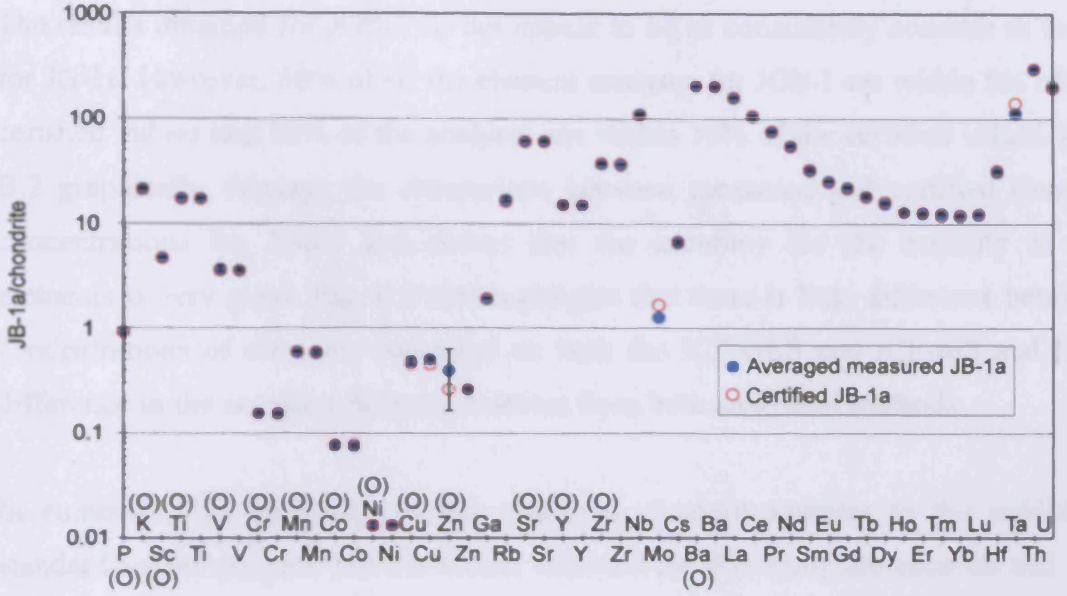

Fig. B.1. Chondrite-normalised plot displaying the averaged measured element concentrations and the certified element concentrations for geostandard JB-1a. The black error bars represent the percentage relative standard deviation (RSD) and precision of the elemental analyses. (O) represents measurement by ICP-OES. All other elements measured by ICP-MS. Chondrite normalising factors from Sun & McDonough (1989) and McDonough & Sun (1995).

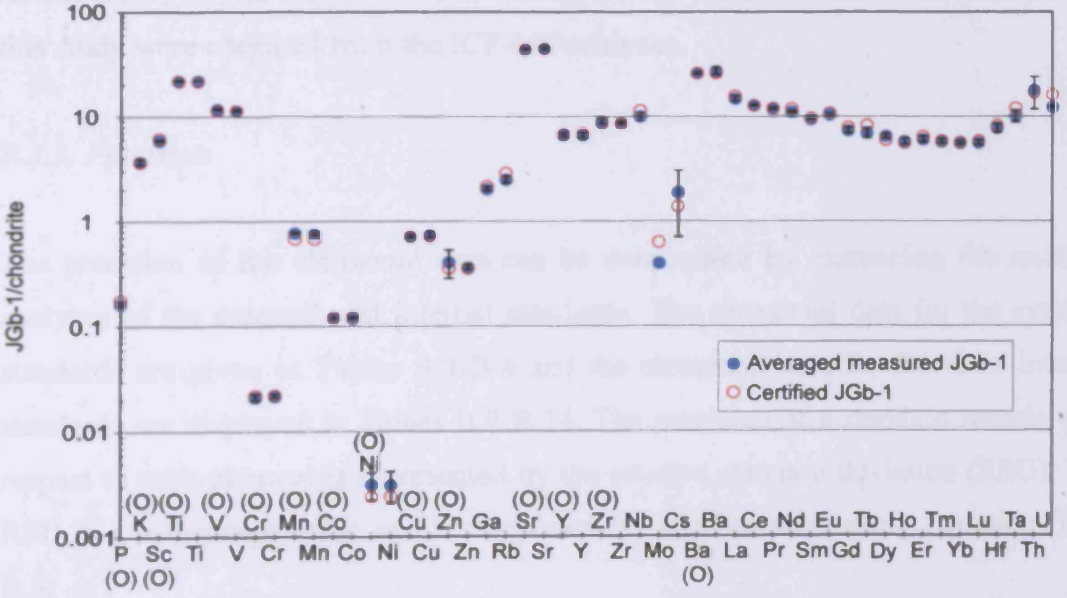

Fig. B.2. Chondrite-normalised plot displaying the averaged measured element concentrations and the certified element concentrations for geostandard JGb-1. The black error bars represent the percentage RSD and precision of the elemental analyses. (O) represents measurement by ICP-OES. All other elements measured by ICP-MS. Chondrite normalising factors from same sources as in Fig. B.1.

The results for JGb-1 from both analytical methods are given in Tables B.2 and B.4. The results obtained for JGb-1 do not appear to be as consistently accurate as those for JB-1a. However, 60% of all the element analyses for JGb-1 are within 5% of the certified values and 80% of the analyses are within 10% of the certified values. Fig. B.2 graphically displays the comparison between measured and certified element concentrations for JGb-1 and shows that the accuracy for the majority of the elements is very good. Fig. B.2 also highlights that there is little difference between concentrations of elements measured on both the ICP-OES and ICP-MS and little difference in the accuracy of measurements from both analytical methods.

In summary, the similarity of the measured standard samples to the published standard values suggest that the results obtained for this study are accurate and can be relied upon during interpretation. The ICP-OES and ICP-MS methods gave very similar results for nearly all the elements which were measured on both machines. Therefore the concentration values of TiO_2, MnO, Fe_2O_3, Sc, Cr, Co, Cu, Sr, Y, Zr and Ba used in this study were averages of the ICP-OES and ICP-MS data for each respective element. However, as the ICP-MS method gave slightly more consistent results for V, Ni and Zn in JB-1a, the concentration values for these elements used in this study were obtained from the ICP-MS analyses.

B.3.3. Precision

The precision of the elemental data can be determined by examining the multiple analyses of the external and internal standards. The elemental data for the external standards are given in Tables B.1-B.4 and the elemental data for the three internal standards are displayed in Tables B.9-B.14. The precision of a standard sample with respect to each element is represented by the relative standard deviation (RSD). The RSD is a percentage value and is calculated for each element using Equations B.3-B.5.

$$\bar{x} = \frac{\sum x}{n}$$

Equation B.3

where $\bar{x}$ is the average element concentration, x is the element concentration and n is the number of element concentration measurements.

$$s = \frac{\sqrt{\sum \left(x - \bar{x} \right)^2}}{n-1}$$

Equation B.4

where s is the standard deviation.

$$RSD(\%) = \frac{100s}{\bar{x}}$$

Equation B.5

The RSD for all the elements in the external and internal standards are given in Tables B.5-B.14. The error bars in Figs. B.1-B.5 also represent the RSD of elements in the standard samples. The data in Tables B.5 and B.7 and Fig. B.1 show that the sample analyses for JB-1a are precise. The vast majority of elements have RSD less than 5%. Fe_2O_3(T) and Cu are the only ICP-MS-measured elements with RSD >5% but are still fairly precise with RSD <10%. P_2O_5, V, Ni, Cu and Zn are the only ICP-OES-measured elements with RSD >5% but again these elements, with the exception of Zn, have RSD values <10%. The ICP-OES-determined Zn has an anomalous RSD of 58.92%. Fig. B.1 also highlights that aside from Zn, the ICP-OES results have a similar precision to those obtained from ICP-MS. Tables B.6 and B.8 and Fig. B.2 display the RSD for all elements in JGb-1 and show that the data are not as consistently precise as the data for JB-1a. However, the data for JGb-1 are still fairly precise with nearly all elements having RSD values <10%. The only exceptions to this are ICP-OES-measured Na_2O, Ni and Zn and ICP-MS-measured Ni, Cs, Tb, Ta

Table B.5. Comparison between the accepted and averaged measured element concentrations by ICP-OES and the standard deviation and relative standard deviation (RSD) of the external JB-1a standard

	Certified JB-1a	Average JB-1a	Standard deviation	RSD (%)
SiO_2 (wt. %)	52.41	52.18	0.20	0.38
TiO_2 (wt. %)	1.28	1.31	0.01	0.58
Al_2O_3 (wt. %)	14.45	14.35	0.12	0.83
Fe_2O_3(T) (wt. %)	9.05	9.18	0.09	0.94
MnO (wt. %)	0.15	0.15	0.00	1.73
MgO (wt. %)	7.83	7.97	0.14	1.78
CaO (wt. %)	9.31	9.25	0.07	0.77
Na_2O (wt. %)	2.73	2.72	0.07	2.50
K_2O (wt. %)	1.40	1.42	0.03	2.40
P_2O_5 (wt. %)	0.26	0.26	0.02	6.52
Sc (ppm)	27.90	28.02	0.32	1.13
V (ppm)	205.00	207.02	15.15	7.32
Cr (ppm)	392.00	415.79	14.94	3.59
Co (ppm)	38.60	38.34	2.00	5.23
Ni (ppm)	139.00	140.27	11.37	8.10
Cu (ppm)	56.70	58.40	5.21	8.93
Zn (ppm)	82.10	123.65	72.86	58.92
Sr (ppm)	442.00	443.66	1.87	0.42
Y (ppm)	24.00	24.26	1.03	4.23
Zr (ppm)	144.00	144.78	3.24	2.24
Ba (ppm)	504.00	500.37	4.31	0.86

Table B.6. Comparison between the accepted and averaged measured element concentrations by ICP-OES and the standard deviation and relative standard deviation (RSD) of the external JGb-1 standard

	Certified JGb-1	Average JGb-1	Standard deviation	RSD (%)
SiO_2 (wt. %)	43.66	43.44	0.44	1.02
TiO_2 (wt. %)	1.60	1.63	0.02	1.03
Al_2O_3 (wt. %)	17.49	17.29	0.36	2.07
Fe_2O_3(T) (wt. %)	15.06	15.47	0.26	1.68
MnO (wt. %)	0.19	0.19	0.00	2.50
MgO (wt. %)	7.85	7.84	0.24	3.05
CaO (wt. %)	11.90	11.79	0.25	2.14
Na_2O (wt. %)	1.20	1.38	0.30	21.74
K_2O (wt. %)	0.24	0.24	0.02	6.55
P_2O_5 (wt. %)	0.06	0.05	0.00	6.05
Sc (ppm)	35.80	34.88	0.59	1.68
V (ppm)	635.00	656.95	15.03	2.29
Cr (ppm)	57.80	56.63	4.14	7.31
Co (ppm)	60.10	60.02	2.22	3.70
Ni (ppm)	25.40	32.77	9.56	29.16
Cu (ppm)	85.70	86.04	3.37	3.92
Zn (ppm)	109.00	126.39	38.39	30.37
Sr (ppm)	327.00	318.35	6.52	2.05
Y (ppm)	10.40	10.47	0.53	5.02
Zr (ppm)	32.80	34.49	2.09	6.05
Ba (ppm)	64.30	62.47	1.94	3.11

Table B.7. Comparison between the accepted and averaged measured element concentrations by ICP-MS and the standard deviation and relative standard deviation (RSD) of the external JB-1a standard

	Certified JB-1a	Average JB-1a	Standard deviation	RSD (%)
TiO_2 (wt. %)	1.28	1.30	0.03	2.18
MnO (wt. %)	0.15	0.15	0.01	4.45
Fe_2O_3(T) (wt. %)	9.10	8.70	0.65	7.47
V (ppm)	205.00	203.13	7.00	3.45
Cr (ppm)	392.00	405.44	8.06	1.99
Co (ppm)	38.60	37.71	1.35	3.59
Ni (ppm)	139.00	139.98	2.97	2.12
Cu (ppm)	56.70	61.29	6.02	9.82
Zn (ppm)	82.10	81.25	2.12	2.61
Ga (ppm)	17.90	17.79	0.16	0.91
Rb (ppm)	39.20	39.75	1.93	4.85
Sr (ppm)	442.00	443.77	10.85	2.44
Y (ppm)	24.00	23.83	0.34	1.43
Zr (ppm)	144.00	142.77	0.88	0.61
Nb (ppm)	26.90	27.35	0.42	1.55
Mo (ppm)	1.57	1.18		
Cs (ppm)	1.31	1.26	0.05	3.61
Ba (ppm)	504.00	491.07	8.52	1.73
La (ppm)	37.60	37.75	0.43	1.14
Ce (ppm)	65.90	65.12	1.48	2.28
Pr (ppm)	7.30	7.21	0.15	2.08
Nd (ppm)	26.00	25.80	0.54	2.08
Sm (ppm)	5.07	5.04	0.16	3.16
Eu (ppm)	1.46	1.50	0.02	1.33
Gd (ppm)	4.67	4.62	0.08	1.70
Tb (ppm)	0.69	0.69	0.02	3.45
Dy (ppm)	3.99	4.02	0.09	2.27
Ho (ppm)	0.71	0.74	0.03	3.81
Er (ppm)	2.18	2.10	0.05	2.55
Tm (ppm)	0.33	0.32	0.01	2.51
Yb (ppm)	2.10	2.06	0.02	1.16
Lu (ppm)	0.33	0.32	0.00	1.46
Hf (ppm)	3.41	3.39	0.08	2.38
Ta (ppm)	1.93	1.61	0.04	2.36
Th (ppm)	9.03	8.77	0.16	1.84
U (ppm)	1.57	1.65	0.04	2.27

and Th. It can be seen from Fig. B.2 that, with the exception of Zn, the ICP-OES and ICP-MS results for JGb-1 are equally precise.

The precision of the MMF07-17 analyses are graphically displayed in Fig. B.3 and given in Tables B.9 and B.12. The size of the error bars displayed in Fig. B.3 indicate that the vast majority of elemental analyses for MMF07-17 are precise. Nearly all elements have RSD values <10% with the notable exception of Cr, Ni, Cu, Zn and

Table B.8. Comparison between the accepted and averaged measured element concentrations by ICP-MS and the standard deviation and relative standard deviation (RSD) of the external JGb-1 standard

	Certified JGb-1	Average JGb-1	Standard deviation	RSD (%)
TiO_2 (wt. %)	1.60	1.63	0.00	0.23
MnO (wt. %)	0.19	0.19	0.01	5.09
Fe_2O_3(T) (wt. %)	14.91	14.56	0.69	4.73
V (ppm)	635.00	640.93	16.13	2.52
Cr (ppm)	57.80	57.72	2.31	4.00
Co (ppm)	60.10	59.96	1.21	2.02
Ni (ppm)	25.40	32.44	11.02	33.96
Cu (ppm)	85.70	89.78	6.05	6.74
Zn (ppm)	109.00	112.57	6.27	5.57
Ga (ppm)	17.90	18.76	0.79	4.22
Rb (ppm)	6.87	5.80	0.48	8.25
Sr (ppm)	327.00	326.26	13.59	4.17
Y (ppm)	10.40	10.33	0.64	6.20
Zr (ppm)	32.80	33.41	1.11	3.33
Nb (ppm)	2.80	2.46	0.19	7.61
Mo (ppm)	0.59	0.37		
Cs (ppm)	0.26	0.36	0.22	62.67
Ba (ppm)	64.30	64.90	5.09	7.84
La (ppm)	3.60	3.49	0.22	6.20
Ce (ppm)	8.17	7.84	0.17	2.15
Pr (ppm)	1.13	1.13	0.03	2.55
Nd (ppm)	5.47	5.18	0.11	2.09
Sm (ppm)	1.49	1.45	0.03	1.90
Eu (ppm)	0.62	0.60	0.01	2.37
Gd (ppm)	1.61	1.51	0.10	6.42
Tb (ppm)	0.29	0.26	0.03	10.92
Dy (ppm)	1.56	1.65	0.09	5.37
Ho (ppm)	0.33	0.33	0.02	6.58
Er (ppm)	1.04	1.00	0.07	6.72
Tm (ppm)	0.16	0.15	0.01	4.61
Yb (ppm)	1.06	0.95	0.04	3.77
Lu (ppm)	0.15	0.14	0.01	5.31
Hf (ppm)	0.88	0.82	0.08	9.76
Ta (ppm)	0.18	0.14	0.02	13.40
Th (ppm)	0.48	0.52	0.18	34.51
U (ppm)	0.13	0.10	0.00	1.51

Ba which show some considerable variation for both ICP-OES and ICP-MS methods. The ICP-OES results for MMF07-17 are generally as precise as the ICP-MS results with the exception of Cu, Zn and Ba for which ICP-MS produced more precise results although both analytical methods produced fairly imprecise results for these elements.

Table B.9. ICP-OES element concentrations for sample MMF07-17 in the four sample batches analysed, the average MMF07-17 element concentrations and the standard deviation and relative standard deviation (RSD)

	Run 1	Run 2	Run 3	Run 4	Average	Standard deviation	RSD (%)
SiO_2 (wt. %)	43.62	46.76	45.97	46.54	45.72	1.44	3.15
TiO_2 (wt. %)	2.03	1.81	1.76	1.72	1.83	0.14	7.58
Al_2O_3 (wt. %)	13.70	13.10	13.59	13.80	13.55	0.31	2.31
Fe_2O_3(T) (wt. %)	17.43	15.93	16.27	16.08	16.43	0.68	4.16
MnO (wt. %)	0.24	0.22	0.22	0.22	0.22	0.01	4.18
MgO (wt. %)	5.41	4.91	4.65	4.81	4.94	0.33	6.65
CaO (wt. %)	12.45	11.38	11.67	11.78	11.82	0.45	3.85
Na_2O (wt. %)	1.48	1.65	1.89	1.70	1.68	0.17	10.10
K_2O (wt. %)	0.12	0.10	0.11	0.11	0.11	0.01	7.41
P_2O_5 (wt. %)	0.16	0.17	0.21	0.17	0.18	0.02	11.65
Sc (ppm)	43.13	40.36	39.68	39.82	40.75	1.62	3.97
V (ppm)	378.52	357.14	341.17	355.66	358.12	15.39	4.30
Cr (ppm)	84.19	42.83	48.56	45.11	55.17	19.48	35.32
Co (ppm)	61.03	50.97	48.54	59.39	54.98	6.15	11.19
Ni (ppm)	103.28	82.46	38.01	41.17	66.23	31.94	48.23
Cu (ppm)	125.88	215.55		97.32	146.25	61.69	42.18
Zn (ppm)	101.84	317.40	126.32		181.86	118.02	64.90
Sr (ppm)	435.26	408.47	432.61	425.51	425.46	12.06	2.83
Y (ppm)	38.43	33.06	34.91	33.13	34.88	2.52	7.21
Zr (ppm)	130.85	124.00	125.97	113.57	123.60	7.28	5.89
Ba (ppm)	33.18	32.00	12.40	20.20	24.45	9.94	40.66

Table B.10. ICP-OES element concentrations for sample MMLT07-28 in the four sample batches analysed, the average MMLT07-28 element concentrations and the standard deviation and relative standard deviation (RSD)

	Run 1	Run 2	Run 3	Run 4	Average	Standard deviation	RSD (%)
SiO_2 (wt. %)	46.47	47.69	47.07	47.91	47.29	0.65	1.38
TiO_2 (wt. %)	1.42	1.25	1.27	1.22	1.29	0.09	7.07
Al_2O_3 (wt. %)	15.25	14.51	14.79	14.68	14.81	0.32	2.14
Fe_2O_3(T) (wt. %)	14.77	13.58	13.76	13.26	13.84	0.65	4.73
MnO (wt. %)	0.20	0.18	0.19	0.18	0.19	0.01	5.19
MgO (wt. %)	8.14	7.72	7.35	7.02	7.56	0.48	6.41
CaO (wt. %)	11.15	10.88	10.97	10.74	10.94	0.17	1.56
Na_2O (wt. %)	1.75	1.67	1.66	1.66	1.68	0.04	2.63
K_2O (wt. %)	0.13	0.11	0.13	0.13	0.13	0.01	7.49
P_2O_5 (wt. %)	0.09	0.10	0.10	0.10	0.10	0.00	3.44
Sc (ppm)	46.33	42.83	43.70	41.99	43.71	1.88	4.30
V (ppm)	406.14	380.71	357.63	355.28	374.94	23.76	6.34
Cr (ppm)	290.62	240.46	265.29	257.53	263.47	20.86	7.92
Co (ppm)	55.94	51.72	47.51	54.35	52.38	3.68	7.03
Ni (ppm)	155.22	125.08	91.52	108.63	120.11	27.12	22.58
Cu (ppm)	131.53			137.93	134.73	4.52	3.36
Zn (ppm)	84.49	253.58	104.19		147.42	92.47	62.72
Sr (ppm)	178.91	167.20	178.25	170.58	173.73	5.77	3.32
Y (ppm)	30.25	25.46	27.06	26.25	27.25	2.10	7.70
Zr (ppm)	80.75	74.79	76.02	66.34	74.47	6.00	8.05
Ba (ppm)	33.56	33.68	20.98	24.26	28.12	6.49	23.08

Table B.11. ICP-OES element concentrations for sample MMLT07-41 in the four sample batches analysed, the average MMLT07-41 element concentrations and the standard deviation and relative standard deviation (RSD)

	Run 1	Run 2	Run 3	Run 4	Average	Standard deviation	RSD (%)
SiO_2 (wt. %)	48.81	48.61	49.07	49.23	48.93	0.27	0.56
TiO_2 (wt. %)	0.89	0.79	0.81	0.58	0.77	0.13	17.01
Al_2O_3 (wt. %)	14.00	13.79	14.24	14.20	14.06	0.21	1.49
Fe_2O_3(T) (wt. %)	12.13	11.63	11.83	11.70	11.82	0.22	1.85
MnO (wt. %)	0.17	0.16	0.18	0.17	0.17	0.01	3.39
MgO (wt. %)	8.99	9.15	8.74	8.55	8.86	0.26	2.99
CaO (wt. %)	11.11	10.62	11.00	10.74	10.87	0.23	2.10
Na_2O (wt. %)	2.37	1.99	2.06	2.04	2.12	0.18	8.28
K_2O (wt. %)	0.07	0.06	0.09	0.08	0.08	0.01	17.28
P_2O_5 (wt. %)	0.05	0.05	0.05	0.06	0.05	0.01	9.44
Sc (ppm)	45.61	44.72	45.08	44.45	44.96	0.50	1.11
V (ppm)	309.45	295.55	286.65	281.56	293.30	12.22	4.17
Cr (ppm)	405.15	370.57	414.66	399.52	397.48	18.99	4.78
Co (ppm)	48.27	48.64	41.47	47.19	46.39	3.34	7.20
Ni (ppm)	144.77	154.23	112.62	126.56	134.54	18.59	13.82
Cu (ppm)	104.70			117.11	110.91	8.78	7.91
Zn (ppm)	47.90	205.61	109.01		120.84	79.52	65.81
Sr (ppm)	129.47	123.31	138.46	130.53	130.44	6.22	4.77
Y (ppm)	18.96	18.58	19.32	18.85	18.93	0.30	1.60
Zr (ppm)	54.18	48.69	53.73	50.06	51.67	2.71	5.25
Ba (ppm)	11.99	29.89	4.63	11.80	14.58	10.77	73.86

The RSD values for MMLT07-28 are given in Tables B.10 and B.13 and displayed in Fig. B.4. The vast majority of elemental analyses for MMLT07-28 are precise and have RSD values <10%. Elements which have RSD values >10% include ICP-OES-measured Ni, Zn and Ba and ICP-MS-measured Ni, Zn, Rb, Cs, Ba, Th and U. The most significant variations in element concentrations are seen in Rb and Cs and Zn from both analytical methods. The error bars on Fig. B.4 highlight that for the same element the ICP-OES and ICP-MS analytical methods are equally precise. The only exceptions to this are Ba and Zn for which ICP-MS is more precise although both analytical methods do not produce very precise results for these elements.

Tables B.11 and B.14 and Fig. B.5 display the RSD for all elements in MMLT07-41. The majority of elemental analyses are precise and have RSD values lower than 10%. The only elements with RSD >10% are ICP-OES-measured TiO_2, K_2O, Ni, Zn and Ba and ICP-MS-measured TiO_2, Ni, Zn, Rb, Cs, Ba, La, Th and U. ICP-MS-measured Rb and Cs and Zn and Ba from both analytical methods are the elements

Table B.12. ICP-MS element concentrations for sample MMF07-17 in the four batches of samples analysed, the average MMF07-17 element concentrations and the standard deviation and relative standard deviation (RSD)

	Run 1	Run 2	Run 3	Run 4	Average	Standard deviation	RSD (%)
TiO_2 (wt. %)	2.05	1.82	1.76	1.72	1.84	0.15	8.22
MnO (wt. %)	0.24	0.22	0.23	0.22	0.23	0.01	4.71
Fe_2O_3(T) (wt. %)		15.88	14.38	15.42	15.23	0.77	5.04
V (ppm)	399.39	356.23	334.51	343.25	358.35	28.78	8.03
Cr (ppm)	85.70	44.92	49.09	36.12	53.96	21.84	40.48
Co (ppm)	56.09	52.44	49.94	50.25	52.18	2.83	5.43
Ni (ppm)	106.46	87.81	35.77	47.71	69.43	33.23	47.86
Cu (ppm)	117.32	124.54	105.45	107.00	113.58	9.01	7.93
Zn (ppm)		333.04	134.13	180.88	216.02	104.01	48.15
Ga (ppm)	23.94	21.67	22.50	22.25	22.59	0.96	4.26
Rb (ppm)	1.63	1.41	0.87	1.33	1.31	0.32	24.51
Sr (ppm)	453.60	419.73	428.76	428.59	432.67	14.58	3.37
Y (ppm)	37.78	33.25	34.61	36.79	35.61	2.05	5.77
Zr (ppm)	124.17	117.13	127.02	121.50	122.45	4.21	3.43
Nb (ppm)	14.10	12.92	12.55	13.22	13.20	0.66	5.03
Mo (ppm)		0.96			0.96		
Cs (ppm)	0.20	0.11	0.16	0.16	0.16	0.03	21.91
Ba (ppm)	30.49	29.13	25.07	18.81	25.87	5.24	20.26
La (ppm)	13.63	12.22	12.24	11.88	12.49	0.77	6.19
Ce (ppm)	29.44	26.59	28.05	26.30	27.60	1.45	5.25
Pr (ppm)	4.12	3.70	3.89	3.70	3.85	0.20	5.25
Nd (ppm)	18.04	16.10	16.80	15.55	16.62	1.07	6.45
Sm (ppm)	4.68	4.33	4.59	4.33	4.48	0.18	4.07
Eu (ppm)	1.49	1.39	1.49	1.41	1.45	0.05	3.55
Gd (ppm)	5.23	4.83	4.94	4.96	4.99	0.17	3.45
Tb (ppm)	0.99	0.82	0.88	0.91	0.90	0.07	8.17
Dy (ppm)	6.05	5.35	5.67	5.54	5.65	0.30	5.22
Ho (ppm)	1.17	1.05	1.16	1.04	1.10	0.07	6.18
Er (ppm)	3.52	3.04	3.29	3.07	3.23	0.22	6.93
Tm (ppm)	0.54	0.47	0.52	0.49	0.51	0.03	6.66
Yb (ppm)	3.53	3.10	3.16	3.18	3.24	0.19	6.00
Lu (ppm)	0.55	0.49	0.52	0.49	0.51	0.03	5.58
Hf (ppm)	3.12	3.04	3.03	3.00	3.04	0.05	1.70
Ta (ppm)	0.79	0.69	0.63	0.74	0.72	0.07	9.39
Th (ppm)	1.65	1.65	1.55	1.47	1.58	0.09	5.50
U (ppm)	0.47	0.40	0.42	0.45	0.44	0.03	7.06

which show the most variation and this is highlighted in Fig. B.5 by their large error bars. Apart from Zn and Ba, the ICP-OES and ICP-MS methods produce results with similar precision.

In summary, the repeated analyses of the external and internal standards generally have low RSD values and so the geochemical data obtained for this study can be considered precise. The standard analyses also show that there is little difference in

Table B.13. ICP-MS element concentrations for sample MMLT07-28 in the four batches of samples analysed, the average MMLT07-28 element concentrations and the standard deviation and relative standard deviation (RSD)

	Run 1	Run 2	Run 3	Run 4	Average	Standard deviation	RSD (%)
TiO_2 (wt. %)	1.48	1.27	1.26	1.21	1.31	0.12	9.34
MnO (wt. %)	0.20	0.18	0.19	0.18	0.19	0.01	5.22
Fe_2O_3(T) (wt. %)		12.92	11.72	12.90	12.51	0.69	5.48
V (ppm)	419.51	360.61	342.21	345.81	367.03	35.88	9.77
Cr (ppm)	290.94	237.14	256.96	240.43	256.37	24.63	9.61
Co (ppm)	58.47	52.21	52.53	51.58	53.70	3.21	5.97
Ni (ppm)	155.53	132.96	100.13	106.86	123.87	25.41	20.52
Cu (ppm)	135.58	165.49	148.88	150.83	150.20	12.25	8.15
Zn (ppm)		251.87	114.30	119.19	161.79	78.05	48.24
Ga (ppm)	19.03	16.95	17.41	17.60	17.75	0.90	5.05
Rb (ppm)	0.63	0.68	0.22	0.71	0.56	0.23	40.40
Sr (ppm)	178.74	154.86	165.03	160.23	164.71	10.23	6.21
Y (ppm)	29.08	25.36	26.33	28.27	27.26	1.71	6.28
Zr (ppm)	73.46	73.65	77.25	69.23	73.40	3.28	4.47
Nb (ppm)	4.00	3.85	3.64	3.80	3.82	0.15	3.88
Mo (ppm)		0.53			0.53		
Cs (ppm)	0.08	0.07	0.12	0.14	0.10	0.03	30.04
Ba (ppm)	30.52	30.74	33.94	24.05	29.81	4.15	13.91
La (ppm)	4.02	3.42	3.25	3.35	3.51	0.34	9.80
Ce (ppm)	9.98	9.30	9.53	9.29	9.53	0.32	3.40
Pr (ppm)	1.71	1.55	1.61	1.58	1.61	0.07	4.39
Nd (ppm)	8.63	7.81	8.09	7.68	8.05	0.42	5.23
Sm (ppm)	2.86	2.64	2.83	2.66	2.75	0.11	4.15
Eu (ppm)	0.99	0.92	0.96	0.95	0.96	0.03	3.12
Gd (ppm)	3.50	3.25	3.37	3.41	3.39	0.10	3.06
Tb (ppm)	0.69	0.59	0.63	0.66	0.64	0.04	6.36
Dy (ppm)	4.49	3.93	4.29	4.21	4.23	0.23	5.47
Ho (ppm)	0.88	0.80	0.89	0.81	0.85	0.05	5.52
Er (ppm)	2.66	2.32	2.56	2.42	2.49	0.15	5.90
Tm (ppm)	0.43	0.37	0.41	0.40	0.40	0.02	5.66
Yb (ppm)	2.77	2.48	2.54	2.58	2.59	0.12	4.82
Lu (ppm)	0.43	0.39	0.42	0.40	0.41	0.02	5.14
Hf (ppm)	1.81	1.91	1.94	1.93	1.90	0.06	3.17
Ta (ppm)	0.28	0.26	0.30	0.28	0.28	0.02	5.94
Th (ppm)	0.22	0.37	0.23	0.23	0.26	0.07	27.03
U (ppm)	0.08	0.08	0.05	0.08	0.08	0.02	21.00

the precision levels between the ICP-OES and ICP-MS methods. The only possible exceptions to this are Zn and Ba, for which ICP-MS produced slightly more precise results.

Table B.14. ICP-MS element concentrations for sample MMLT07-41 in the four batches of samples analysed, the average MMLT07-41 element concentrations and the standard deviation and relative standard deviation (RSD)

	Run 1	Run 2	Run 3	Run 4	Average	Standard deviation	RSD (%)
TiO_2 (wt. %)	0.88	0.77	0.82	0.60	0.77	0.12	15.58
MnO (wt. %)	0.18	0.17	0.18	0.17	0.17	0.01	3.25
Fe_2O_3(T) (wt. %)		11.41	10.27	11.58	11.09	0.72	6.45
V (ppm)	313.49	283.60	287.20	288.33	293.15	13.70	4.67
Cr (ppm)	405.15	375.14	396.96	419.70	399.24	18.62	4.66
Co (ppm)	50.23	47.76	42.91	47.95	47.21	3.08	6.53
Ni (ppm)	151.09	160.47	120.42	103.00	133.74	26.69	19.96
Cu (ppm)	103.64	114.85	120.78	126.76	116.51	9.86	8.46
Zn (ppm)		206.46	99.76	115.39	140.53	57.62	41.00
Ga (ppm)	14.62	13.33	13.49	13.81	13.81	0.57	4.14
Rb (ppm)	0.37	0.46	0.13	0.52	0.37	0.17	46.34
Sr (ppm)	132.88	119.80	125.36	116.95	123.75	7.02	5.67
Y (ppm)	20.44	18.53	18.75	20.69	19.60	1.12	5.72
Zr (ppm)	47.51	48.52	55.39	46.79	49.55	3.95	7.98
Nb (ppm)	2.53	2.46	2.40	2.50	2.47	0.06	2.25
Mo (ppm)		0.35			0.35		
Cs (ppm)	0.04	0.05	0.09	0.05	0.06	0.02	44.51
Ba (ppm)	12.53	28.04	20.23	11.29	18.02	7.76	43.07
La (ppm)	2.90	2.47	2.29	2.37	2.51	0.27	10.84
Ce (ppm)	6.60	6.38	6.34	6.36	6.42	0.12	1.84
Pr (ppm)	1.11	1.05	1.05	1.05	1.06	0.03	2.70
Nd (ppm)	5.55	5.24	5.25	5.11	5.28	0.19	3.53
Sm (ppm)	1.89	1.81	1.83	1.80	1.84	0.04	2.23
Eu (ppm)	0.68	0.65	0.65	0.67	0.66	0.02	2.73
Gd (ppm)	2.42	2.25	2.27	2.31	2.31	0.08	3.35
Tb (ppm)	0.48	0.41	0.43	0.46	0.44	0.03	6.96
Dy (ppm)	3.17	2.86	2.97	3.00	3.00	0.13	4.21
Ho (ppm)	0.63	0.59	0.63	0.59	0.61	0.03	4.19
Er (ppm)	1.93	1.72	1.82	1.75	1.80	0.09	5.11
Tm (ppm)	0.31	0.28	0.29	0.29	0.29	0.01	4.32
Yb (ppm)	2.02	1.84	1.82	1.87	1.89	0.09	4.89
Lu (ppm)	0.33	0.29	0.30	0.30	0.30	0.02	5.53
Hf (ppm)	1.16	1.25	1.27	1.30	1.24	0.06	5.02
Ta (ppm)	0.18	0.16	0.18	0.15	0.17	0.01	7.95
Th (ppm)	0.21	0.31	0.18	0.18	0.22	0.06	26.95
U (ppm)	0.07	0.07	0.04	0.07	0.06	0.02	24.18

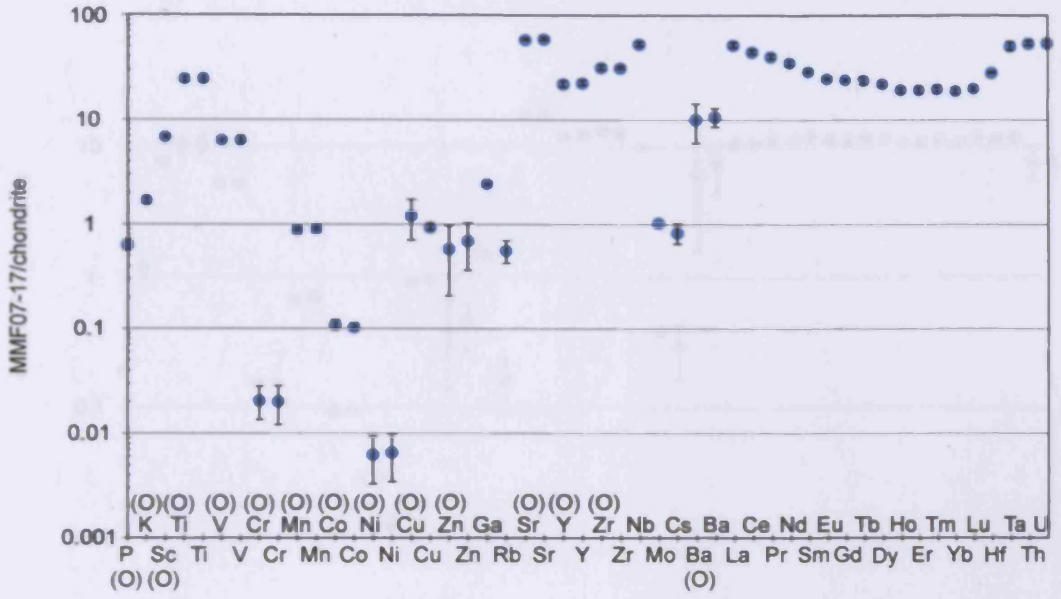

Fig. B.3. Chondrite-normalised plot displaying the averaged measured element concentrations for MMF07-17. The black error bars represent the percentage RSD and precision of the elemental analyses. (O) represents measurement by ICP-OES. All other elements measured by ICP-MS. Chondrite normalising factors from same sources as in Fig. B.1.

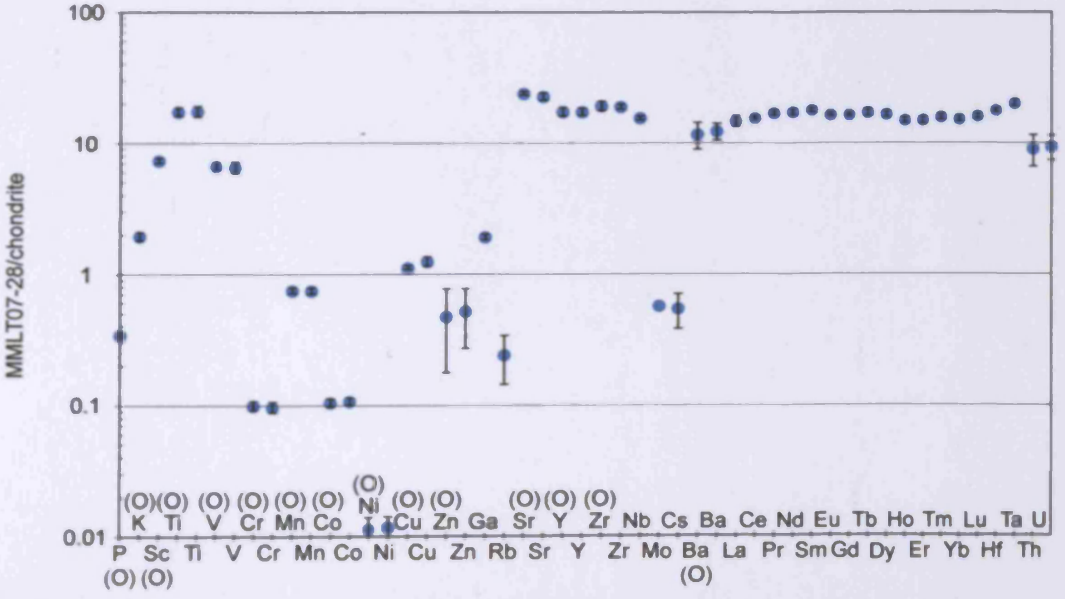

Fig. B.4. Chondrite-normalised plot displaying the averaged measured element concentrations for MMLT07-28. The black error bars represent the percentage RSD and precision of the elemental analyses. (O) represents measurement by ICP-OES. All other elements measured by ICP-MS. Chondrite normalising factors from same sources as in Fig. B.1.

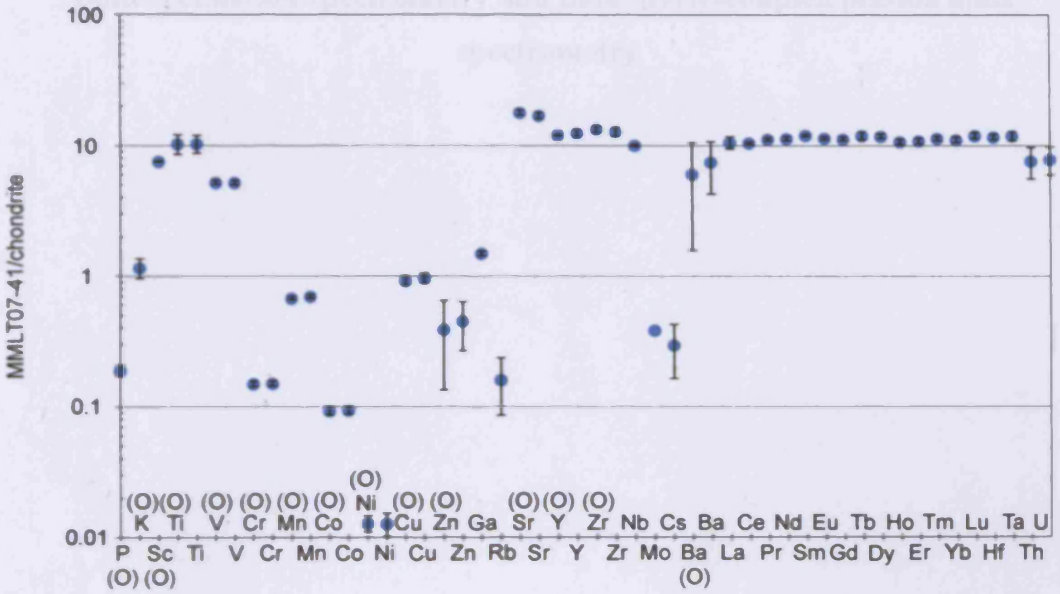

Fig. B.5. Chondrite-normalised plot displaying the averaged measured element concentrations for MMLT07-41. The black error bars represent the percentage RSD and precision of the elemental analyses. (O) represents measurement by ICP-OES. All other elements measured by ICP-MS. Chondrite normalising factors from same source as in Fig. B.1.

Appendix C: Geochemical results obtained by inductively-coupled plasma optical emission spectrometry and inductively-coupled plasma mass spectrometry

Table C.1. Elemental data obtained by inductively-coupled plasma optical emission spectrometry

Sample	MMF 07-1	MMF 07-2	MMF 07-3	MMF 07-4	MMF 07-5	MMF 07-6	MMF 07-7	MMF 07-8	MMF 07-9	MMF 07-10	MMF 07-11	MMF 07-12	MMF 07-13	MMF 07-14
Major elements (wt. %)														
SiO_2	44.64	44.60	42.73	44.65	46.63	45.11	44.51	44.26	46.35	43.25	46.79	45.57	46.69	44.51
TiO_2	2.28	2.20	2.37	2.16	2.97	2.50	2.29	2.10	1.88	1.94	1.77	2.31	1.88	2.32
Al_2O_3	13.69	13.70	13.83	12.84	11.93	13.86	13.35	14.17	13.27	15.25	12.89	13.98	12.76	13.76
$Fe_2O_3(T)$	16.52	16.43	17.19	15.61	16.50	15.20	17.49	18.41	13.95	14.95	15.42	15.48	14.65	15.36
MnO	0.23	0.23	0.21	0.23	0.22	0.21	0.24	0.23	0.19	0.21	0.22	0.22	0.19	0.26
MgO	5.03	6.16	7.89	6.20	5.29	5.96	6.32	7.19	4.91	5.86	7.17	6.88	7.44	7.49
CaO	11.27	9.66	9.40	10.93	9.24	10.24	8.30	8.27	14.68	11.15	8.10	10.30	9.15	9.14
Na_2O	2.61	3.00	2.98	2.22	2.19	3.57	3.35	2.72	0.61	4.17	3.62	2.09	3.02	3.66
K_2O	0.19	0.25	0.45	0.17	0.46	0.46	0.55	0.06	0.03	0.31	0.12	0.54	0.17	0.24
P_2O_5	0.16	0.16	0.18	0.21	0.33	0.25	0.18	0.15	0.15	0.14	0.14	0.20	0.21	0.17
LOI	4.04	4.96	4.15	4.72	4.09	3.23	4.16	3.87	3.54	3.77	2.89	2.95	3.13	3.69
Total	100.66	101.35	101.38	99.94	99.83	100.56	100.76	101.43	99.59	101.02	99.11	100.53	99.29	100.60
Trace elements (ppm)														
Sc	43.9	41.4	45.1	39.2	39.6	42.5	43.4	42.4	36.7	38.8	44.2	42.8	39.6	43.6
V	419	397	422	372	422	376	384	376	328	355	383	354	342	381
Cr	99	102	138	2740	133	141	90	86	107	109	100	161	140	112
Co	61.6	59.9	60.8	64.8	52.5	48.5	60.0	60.0	50.9	51.8	61.3	60.6	60.0	56.0
Ni	80	388	109	13200	95	57	57	58	38	701	93	95	192	136
Cu	161	146	163			99	115	118	97	102		124		144
Zn	68	85	86	256	224	79	83	96	60	74	243	108	261	59
Sr	154	191	330	128	138	142	182	254	207	229	140	208	180	247
Y	38.2	38.3	37.5	35.6	48.9	46.4	40.3	37.5	31.9	30.9	29.8	38.1	32.8	35.1
Zr	123.4	123.0	157.8	151.8	220.9	175.6	144.2	126.1	120.7	118.9	95.6	148.5	138.9	138.7
Ba	52	81	129	73	225	213	118	23	37	110	53	135	102	105

Table C.1. contd.

Sample	MMF 07-15	MMF 07-16	MMF 07-17	MMF 07-18	MMF 07-19	MMF 07-20	MMF 07-21	MMLT 07-1	MMLT 07-3	MMLT 07-6	MMLT 07-7	MMLT 07-8	MMLT 07-9	MMLT 07-11
Major elements (wt. %)														
SiO_2	47.62	46.11	43.62	44.10	46.04	44.50	44.70	49.99	47.12	47.95	49.91	47.33	50.63	49.15
TiO_2	2.05	2.22	2.03	2.26	1.78	1.69	2.06	1.17	1.25	1.42	1.14	1.17	1.43	1.30
Al_2O_3	13.54	12.28	13.70	13.61	14.32	13.06	15.38	13.22	14.67	14.00	13.17	13.53	13.41	13.60
$Fe_2O_3(T)$	15.52	16.05	17.43	18.68	15.32	17.18	17.80	13.99	14.48	15.09	13.93	14.33	14.39	14.27
MnO	0.23	0.21	0.24	0.26	0.23	0.20	0.22	0.19	0.18	0.20	0.19	0.16	0.18	0.17
MgO	7.07	6.82	5.41	5.61	6.73	7.32	6.10	6.39	6.77	6.93	6.51	7.30	6.00	7.09
CaO	5.94	8.52	12.45	9.70	10.91	8.86	6.81	10.58	11.77	10.43	11.85	9.54	9.59	10.00
Na_2O	2.48	3.66	1.48	3.04	2.35	3.10	3.57	2.14	2.07	2.39	1.99	2.92	2.22	1.56
K_2O	0.98	0.05	0.12	0.41	0.54	0.12	0.77	0.10	0.15	0.18	0.13	0.08	0.15	0.11
P_2O_5	0.16	0.22	0.16	0.17	0.14	0.14	0.14	0.08	0.08	0.11	0.08	0.08	0.11	0.10
LOI	3.07	2.93	2.99	2.99	3.08	3.76	3.15	1.22	0.42	1.42	0.75	1.66	0.44	1.81
Total	98.68	99.06	99.63	100.82	101.43	99.94	100.70	99.08	98.96	100.11	99.66	98.10	98.56	99.18
Trace elements (ppm)														
Sc	39.4	47.5	43.1	47.2	43.8	41.6	42.7	46.0	45.6	45.7	45.7	46.5	43.3	41.5
V	343	384	379	420	361	358	378	379	381	416	382	374	400	397
Cr	91	206	84	74	148	129	143	175	284	209	174	158	134	198
Co	52.2	46.6	61.0	66.5	55.0	52.0	57.5	49.5	58.3	53.7	50.7	61.2	50.5	52.0
Ni	65	82	103	68	50	85	165	113	119	113	113	123	102	114
Cu	133		126	116	107		113	185	152	123	155	294	100	166
Zn	99	204	102	98	88	172	76							
Sr	159	68	435	193	180	59	226	73	116	110	105	74	130	76
Y	32.6	37.3	38.4	41.3	33.9	29.2	32.8	27.0	28.0	32.1	27.1	26.9	30.0	29.2
Zr	126.0	138.6	130.9	142.9	113.9	106.6	118.9	65.6	73.4	75.6	64.7	60.4	88.9	70.6
Ba	501	24	33	175	152	36	210	19	28	38	29	17	22	13

Table C.1. contd.

Sample	MMLT 07-12	MMLT 07-13	MMLT 07-14	MMLT 07-15	MMLT 07-18	MMLT 07-19	MMLT 07-20	MMLT 07-22	MMLT 07-23	MMLT 07-24	MMLT 07-26	MMLT 07-28	MMLT 07-29	MMLT 07-31
Major elements (wt. %)														
SiO_2	48.87	51.37	49.13	49.39	48.14	47.56	47.62	46.59	50.14	50.05	49.56	46.47	49.34	49.78
TiO_2	1.46	0.47	1.22	1.18	1.31	1.19	1.10	1.25	0.88	0.86	1.14	1.42	0.95	1.14
Al_2O_3	13.88	14.34	14.14	13.47	13.59	13.06	13.55	13.85	13.43	13.25	14.04	15.25	14.58	13.44
$Fe_2O_3(T)$	15.12	8.49	14.73	14.35	13.84	14.13	13.09	14.12	11.54	11.46	13.50	14.77	11.08	13.22
MnO	0.19	0.14	0.19	0.20	0.16	0.20	0.19	0.21	0.16	0.18	0.19	0.20	0.16	0.20
MgO	6.30	8.66	6.71	6.73	8.14	7.24	7.63	7.60	9.27	8.67	7.58	8.14	9.02	7.98
CaO	10.23	12.54	10.43	11.03	9.96	10.58	11.16	11.60	11.54	11.86	12.26	11.15	11.43	12.00
Na_2O	2.30	1.17	2.70	1.86	2.26	1.88	4.32	3.36	2.45	1.45	1.61	1.75	3.21	2.08
K_2O	0.17	0.10	0.27	0.12	0.19	0.14	0.07	0.13	0.08	0.14	0.12	0.13	0.10	0.12
P_2O_5	0.12	0.03	0.09	0.09	0.10	0.09	0.07	0.07	0.05	0.05	0.06	0.09	0.06	0.07
LOI	0.56	1.57	0.29	0.75	1.19	0.75	1.46	1.37	1.60	1.74	1.15	2.16	0.85	0.79
Total	99.19	98.89	99.90	99.16	98.88	96.81	100.26	100.15	101.13	99.71	101.22	101.54	100.79	100.82
Trace elements (ppm)														
Sc	43.0	37.3	48.0	46.6	45.4	44.0	45.6	47.7	46.3	45.2	46.1	46.3	48.2	43.4
V	405	223	392	376	376	358	342	353	312	307	356	406	341	344
Cr	110	221	167	155	182	155	199	210	529	365	200	291	303	196
Co	49.3	31.9	44.0	47.4	57.1	54.3	53.0	55.7	48.2	43.1	50.5	55.9	43.6	50.1
Ni	80	109	101	103	90	92	99	108	141	94	182	155	115	114
Cu	107	60	43	185			155	119	88	111	137	132	64	108
Zn					160	208	59	64	67	39	47	84	61	46
Sr	117	76	82	95	101	94	112	108	86	138	109	179	100	103
Y	32.5	11.5	28.4	27.4	27.3	25.2	23.5	25.3	18.9	19.0	21.5	30.3	19.9	24.5
Zr	89.3	26.7	65.8	64.0	72.8	63.0	64.6	66.1	52.9	55.0	65.8	80.8	56.4	62.1
Ba	42	20	23	22	33	26	14	20	41	19	25	34	29	26

Table C.1. contd.

Sample	MMLT 07-33	MMLT 07-34	MMLT 07-35	MMLT 07-36	MMLT 07-37	MMLT 07-38	MMLT 07-39	MMLT 07-40	MMLT 07-41	MMLT 07-42	MMLT 07-43	MMLT 07-44	MMLT 07-45	MMM 07-1
Major elements (wt. %)														
SiO_2	50.96	48.15	46.57	51.03	51.70	50.55	46.31	48.11	48.81	48.55	48.86	46.53	45.78	47.48
TiO_2	0.98	1.04	0.89	0.68	0.73	0.69	0.95	0.92	0.89	0.96	0.82	0.98	0.98	1.54
Al_2O_3	13.21	13.88	15.73	13.72	14.41	13.40	15.13	14.36	14.00	14.09	14.14	14.91	15.49	14.87
Fe_2O_3(T)	12.45	13.62	12.51	11.70	10.26	11.31	12.00	12.19	12.13	12.39	10.30	12.55	12.54	16.18
MnO	0.18	0.19	0.14	0.16	0.14	0.17	0.17	0.17	0.17	0.17	0.13	0.17	0.17	0.27
MgO	6.85	8.09	8.52	7.70	7.90	8.16	8.60	8.70	8.99	9.37	8.12	9.65	9.36	5.99
CaO	10.61	9.39	10.35	9.88	11.44	10.83	13.46	11.66	11.11	11.26	11.46	11.79	11.71	9.86
Na_2O	2.05	2.61	1.83	2.76	1.97	1.97	2.14	2.10	2.37	2.21	1.78	2.47	3.22	2.50
K_2O	0.09	0.14	0.07	0.15	0.07	0.37	0.06	0.06	0.07	0.08	0.04	0.09	0.08	0.40
P_2O_5	0.07	0.07	0.06	0.05	0.06	0.05	0.05	0.05	0.05	0.05	0.05	0.05	0.06	0.11
LOI	1.50	1.83	2.64	1.86	1.97	1.72	1.96	2.27	2.26	2.26	2.83	2.18	2.09	0.26
Total	98.95	99.01	99.31	99.68	100.65	99.23	100.84	100.60	100.83	101.39	98.54	101.38	101.47	99.46
Trace elements (ppm)														
Sc	42.2	45.8	49.6	43.0	46.6	43.2	49.1	48.1	45.6	50.1	44.3	50.8	50.1	42.8
V	322	345	335	310	323	298	331	324	309	332	301	332	332	301
Cr	180	217	266	202	314	245	462	369	405	408	249	346	337	66
Co	43.5	48.6	44.0	39.7	44.2	39.4	51.0	49.1	48.3	53.4	40.1	53.6	51.3	63.2
Ni	123	123	128	94	168	96	118	102	145	125	129	630	87	75
Cu	153	161	118	138	129	107	119	96	105	113	84	126	117	
Zn							40	69	48	48		51	50	183
Sr	121	59	153	75	104	138	139	140	129	64	153	100	129	173
Y	22.1	24.0	21.6	19.9	20.1	19.8	20.6	20.9	19.0	21.5	20.6	21.4	21.3	28.6
Zr	53.8	62.6	52.9	48.0	50.7	48.6	55.4	50.2	54.2	55.6	48.7	57.2	58.0	91.7
Ba	9	32	13	24	18	31	18	16	12	15	13	12	15	135

Table C.1. contd.

Sample	MMM 07-2	MMM 07-6	MMM 07-7	MMM 07-11	MMM 07-12	MMM 07-14	MMM 07-15	MMM 07-17	MMM 07-20	MMM 07-21	MMM 07-22	MMM 07-25	MMM 07-26	MMM 07-28
Major elements (wt. %)														
SiO_2	47.32	49.25	45.57	48.58	46.94	49.41	49.66	48.59	47.37	47.90	49.00	48.29	46.73	47.98
TiO_2	0.50	0.86	0.70	0.91	0.90	1.01	0.88	1.52	0.67	0.35	0.81	1.57	0.60	0.36
Al_2O_3	10.08	13.37	9.80	13.02	12.96	13.63	14.29	14.33	10.62	14.55	13.86	13.39	10.62	10.35
$Fe_2O_3(T)$	11.86	12.65	12.88	12.03	11.75	13.29	12.34	13.88	12.32	12.87	12.46	15.45	12.13	10.93
MnO	0.19	0.23	0.20	0.19	0.19	0.22	0.20	0.23	0.20	0.16	0.23	0.24	0.18	0.18
MgO	20.45	8.70	18.62	9.86	9.08	8.28	8.18	6.96	16.46	9.29	8.56	6.70	17.87	19.33
CaO	8.17	12.08	9.41	11.19	10.92	11.14	11.23	10.77	10.11	11.96	11.44	11.39	9.29	10.46
Na_2O	1.18	1.65	1.43	1.78	1.93	1.85	1.87	2.60	1.37	1.59	1.70	2.51	1.26	1.07
K_2O	0.22	0.08	0.10	0.36	0.39	0.09	0.08	0.27	0.12	0.03	0.31	0.25	0.06	0.04
P_2O_5	0.04	0.05	0.06	0.06	0.06	0.07	0.06	0.14	0.04	0.01	0.06	0.13	0.04	0.01
LOI	0.26	0.01	0.60	1.09	0.95	-0.22	-0.04	0.44	0.40	-0.05	0.56	0.04	0.13	0.23
Total	100.28	98.94	99.37	99.07	96.06	98.78	98.74	99.73	99.70	98.68	99.00	99.97	98.92	100.95
Trace elements (ppm)														
Sc	30.8	43.8	31.8	37.2	34.0	43.8	41.4	40.0	33.5	40.0	44.1	40.9	30.9	35.0
V	182	300	209	295	261	355	272	329	224	202	301	379	202	166
Cr	1877	352	1588	463	297	208	167	101	1445	323	255	99	954	1494
Co	72.7	47.8	73.7	51.7	48.5	49.1	46.8	56.5	66.2	40.5	51.4	55.0	56.5	66.2
Ni	602	205	463	202	140	127	119	70	428	128	95	86	319	503
Cu														
Zn	195	145	217	152	136	205	169	166	229	104	143	187	166	182
Sr	66	81	71	105	110	84	83	167	67	63	85	157	63	59
Y	10.7	18.0	14.5	20.3	18.9	23.0	19.3	27.6	15.1	8.2	18.3	30.4	13.6	7.5
Zr	36.8	46.7	38.5	65.0	56.2	59.4	51.3	104.3	43.0	16.6	49.9	97.1	28.2	17.4
Ba	69	17	38	39	40	49	19	65	32	18	49	68	24	14

Table C.1. contd.

Sample	MMPC 07-1	MMPC 07-2	MMPC 07-3	MMW 07-2	MMW 07-3	MMW 07-4	MMW 07-7	MMW 07-8	MMW 07-9	MMW 07-10	MMW 07-11	MMW 07-12	MMW 07-15	MMW 07-16
Major elements (wt. %)														
SiO_2	52.36	48.58	49.02	44.83	43.85	44.82	43.31	44.61	44.41	43.93	43.78	45.08	43.89	44.04
TiO_2	1.24	1.84	1.41	0.57	0.54	0.54	0.47	0.51	0.51	0.49	0.53	0.60	0.54	0.62
Al_2O_3	13.61	12.51	13.03	8.21	7.81	8.09	7.70	7.77	7.68	8.06	7.40	8.91	7.79	8.39
$Fe_2O_3(T)$	8.82	14.93	13.65	13.28	13.10	12.61	11.46	12.24	12.57	11.66	12.67	12.91	12.63	12.68
MnO	0.33	0.17	0.2	0.18	0.18	0.18	0.15	0.16	0.16	0.17	0.18	0.18	0.19	0.17
MgO	7.71	6.47	7.01	21.42	21.82	20.90	25.34	22.38	20.81	24.15	20.74	19.31	22.10	20.60
CaO	8.93	10.52	9.87	8.82	8.79	8.23	5.91	7.38	8.49	7.94	10.08	9.00	9.24	8.91
Na_2O	2.69	2.15	2.32	1.02	0.83	0.96	0.37	1.12	0.94	1.08	0.85	1.02	0.76	1.09
K_2O	1.47	0.46	0.45	0.09	0.10	0.08	0.25	0.16	0.10	0.09	0.13	0.08	0.09	0.19
P_2O_5	0.22	0.14	0.16	0.03	0.03	0.03	0.03	0.13	0.09	0.03	0.03	0.04	0.03	0.16
LOI	1.98	0.91	1.54	2.58	4.20	2.91	5.53	4.31	4.86	2.81	4.32	2.88	3.98	4.53
Total	99.34	98.67	98.66	101.03	101.24	99.34	100.52	100.78	100.61	100.38	100.71	100.01	101.25	101.37
Trace elements (ppm)														
Sc	26.5	37.4	33.5	29.5	29.1	29.3	27.3	27.4	27.0	26.8	27.7	32.4	29.1	30.4
V	192	511	487	204	206	200	179	193	209	185	196	226	188	213
Cr	202	55	69	2282	2534	2113	2354	2348	2402	2210	2345	2085	2655	2176
Co	48.7	48.8	48.6	85.3	93.7	83.8	84.1	88.6	95.0	84.4	91.9	79.2	97.4	88.1
Ni	120	62	75	756	901	706	869	800	840	885	814	576	876	603
Cu	56	158	142	83	83	87		79	70		83	87	86	103
Zn	41	86	66	50	74	57	174	75	52	240	56	54	80	52
Sr	105	124	115	47	50	49	30	65	55	49	59	49	73	46
Y	23.1	24.7	24.1	11.4	12.0	11.5	9.5	11.7	11.2	10.3	10.7	13.0	11.8	12.9
Zr	58.4	58.5	58.3	26.5	26.6	23.5	30.1	25.5	24.7	27.7	23.8	40.2	24.7	26.4
Ba	46	22	32	10	11	25	160	52	36	21	28	17	26	41

Table C.1. contd.

Sample	MMW 07-17	MMW 07-19	MMW 07-24	MMW 07-25	MMW 07-26	MMW 07-27	MMB 08-1	MMB 08-2b	MMB 08-3	MMB 08-4	MMB 08-5	MMB 08-6	MMB 08-7	MMB 08-8
Major elements (wt. %)														
SiO_2	43.49	44.49	48.77	47.77	46.64	46.87	49.53	52.07	47.73	47.84	48.19	49.50	50.35	50.09
TiO_2	0.55	0.56	1.10	1.34	1.41	1.21	1.75	2.34	1.31	1.52	1.24	1.20	1.40	1.34
Al_2O_3	7.87	7.97	14.24	13.27	13.23	13.02	12.34	12.36	15.24	15.09	14.37	13.35	13.72	13.41
Fe_2O_3(T)	12.39	12.82	13.79	15.06	16.15	15.14	14.54	14.96	12.52	13.52	13.70	13.87	12.19	14.76
MnO	0.18	0.18	0.17	0.20	0.22	0.20	0.20	0.20	0.16	0.19	0.21	0.20	0.18	0.21
MgO	21.57	23.06	6.68	7.79	7.77	7.67	3.92	3.85	8.64	6.26	7.12	6.18	5.09	5.77
CaO	9.51	8.49	10.28	11.21	11.40	10.54	7.69	7.11	8.94	10.28	9.25	12.40	5.47	8.02
Na_2O	0.74	0.85	1.56	2.15	2.30	2.07	2.11	2.08	3.01	1.86	2.23	0.55	3.96	1.88
K_2O	0.10	0.07	0.06	0.26	0.20	0.36	1.18	1.58	0.32	0.21	0.15	0.02	0.12	0.97
P_2O_5	0.03	0.03	0.09	0.08	0.08	0.08	0.22	0.33	0.11	0.13	0.10	0.09	0.12	0.12
LOI	4.21	2.47	1.94	1.90	1.85	1.93	5.93	3.97	3.00	2.63	2.96	2.37	6.73	2.59
Total	100.64	100.98	98.67	101.04	101.25	99.10	99.41	100.85	100.99	99.53	99.53	99.74	99.33	99.17
Trace elements (ppm)														
Sc	29.1	30.0	42.1	45.9	48.1	44.5	34.6	34.6	38.3	42.0	45.3	44.1	43.2	44.9
V	207	220	341	360	396	341	289	335	249	284	311	312	317	332
Cr	2351	2485	121	173	134	150	21	10	356	127	85	91	60	163
Co	89.1	93.9	50.3	53.9	55.4	51.3	46.7	54.4	44.9	48.7	48.1	48.6	25.2	51.9
Ni	745	774	116	155	201	125	25	30	98	72	61	52	41	438
Cu	79	80		152	126	151								
Zn	49	56	202	62	88	62	117	177	106	115	185	104	90	118
Sr	71	48	123	117	97	70	332	301	267	301	283	395	68	228
Y	10.5	11.8	23.7	26.2	26.4	26.1	36.2	46.2	22.0	27.0	23.7	24.6	24.5	28.5
Zr	24.5	25.5	61.2	63.9	57.9	58.9	183.2	251.0	105.4	108.0	90.2	89.8	115.6	109.8
Ba	29	9	18	33	22	28	385	563	74	116	84	33	37	914

Table C.1. contd.

Sample	MMC 08-1	MMC 08-2	MMC 08-3	MMC 08-4	MMC 08-5	MMC 08-7	MMC 08-8	MMC 08-9	MMC 08-10	MMC 08-11	MMC 08-14	MMC 08-15	MMC 08-16	MMC 08-17
Major elements (wt. %)														
SiO_2	47.38	49.14	48.15	49.93	48.37	48.03	48.76	49.15	47.84	49.48	44.34	49.40	49.70	48.75
TiO_2	1.46	1.38	1.46	0.48	0.54	0.46	0.57	0.55	0.68	0.99	0.51	0.53	0.58	0.95
Al_2O_3	13.97	12.88	13.34	11.03	9.91	9.78	9.69	9.35	10.26	13.76	8.83	10.01	12.55	13.91
$Fe_2O_3(T)$	14.45	14.69	16.75	10.86	11.83	11.57	11.24	11.00	11.82	12.18	12.19	11.06	12.09	12.25
MnO	0.21	0.20	0.22	0.14	0.17	0.15	0.15	0.16	0.17	0.16	0.17	0.17	0.17	0.16
MgO	6.99	6.59	6.42	10.97	14.46	16.23	13.68	15.17	14.28	8.13	18.99	14.11	10.65	8.29
CaO	8.80	10.69	9.10	8.60	11.20	7.70	10.89	10.54	10.49	11.49	9.71	10.07	9.06	11.27
Na_2O	2.72	1.93	2.32	2.80	1.46	2.01	1.68	1.63	1.58	1.95	0.55	1.28	1.57	2.00
K_2O	0.84	0.34	0.09	0.12	0.07	0.22	0.07	0.07	0.10	0.08	0.17	0.22	1.53	0.05
P_2O_5	0.12	0.10	0.11	0.05	0.05	0.04	0.05	0.04	0.05	0.07	0.04	0.04	0.06	0.07
LOI	3.22	2.06	3.20	4.01	3.07	4.54	2.83	3.06	2.97	2.11	4.43	3.07	3.02	2.50
Total	100.16	100.00	101.16	98.99	101.12	100.74	99.60	100.72	100.25	100.42	99.93	99.96	100.99	100.19
Trace elements (ppm)														
Sc	42.7	42.6	48.8	35.0	35.3	33.0	32.8	34.7	36.6	39.9	30.4	34.4	36.6	42.6
V	380	362	410	236	257	234	241	241	254	308	234	235	269	302
Cr	178	152	137	1165	1494	1599	1284	1571	1293	184	1864	977	632	233
Co	48.0	52.6	60.4	62.2	71.5	69.6	63.4	63.3	72.0	44.4	84.5	61.2	53.5	49.6
Ni	99	89	91	367	503	566	489	593	536	110	757	481	201	97
Cu	129	155	180	94	75	90	137	74	63	81	140	149	76	122
Zn														
Sr	141	149	126	241	31	32	70	91	62	202	12	214	121	164
Y	32.2	28.3	33.4	15.9	15.7	14.2	15.7	15.9	16.8	21.6	14.4	15.1	19.9	18.7
Zr	87.7	76.6	80.8	49.1	37.8	40.7	42.0	37.5	51.7	57.9	49.1	46.6	52.7	52.5
Ba	86	45	17	54	31	67	21	17	14	18	24	15	199	13

Table C.1. contd.

Sample	MMC 08-18	MMC 08-19	MMC 08-20	MMC 08-21	MMC 08-22	MMC 08-23	MMC 08-24	MMC 08-25	MMC 08-26	MMC 08-27	MMC 08-28	MME 08-1	MME 08-2	MME 08-3
Major elements (wt. %)														
SiO_2	48.38	45.95	47.72	46.50	46.55	47.19	48.71	48.50	47.43	47.61	46.79	47.99	51.98	51.63
TiO_2	0.94	0.53	0.55	0.42	0.57	0.48	0.68	0.58	0.60	0.47	0.58	0.78	1.94	1.56
Al_2O_3	13.89	9.41	10.62	8.91	10.06	9.64	12.06	9.57	11.24	10.24	11.13	14.44	15.69	12.82
$Fe_2O_3(T)$	12.59	12.63	11.74	11.36	11.77	11.11	11.71	11.54	12.22	11.40	12.01	9.62	11.37	13.59
MnO	0.18	0.17	0.16	0.16	0.17	0.16	0.17	0.16	0.17	0.16	0.18	0.14	0.12	0.18
MgO	8.30	16.98	15.37	18.46	15.24	16.33	11.92	15.30	14.11	15.11	13.50	8.15	3.30	4.53
CaO	12.54	10.05	8.34	8.60	10.30	9.69	10.35	10.25	10.01	9.64	10.38	11.93	9.80	5.57
Na_2O	1.79	1.08	1.88	0.85	1.20	1.32	2.08	1.58	1.87	1.51	1.67	1.44	2.38	1.32
K_2O	0.04	0.29	0.10	0.04	0.23	0.03	0.31	0.11	0.14	0.12	0.22	2.57	0.63	1.48
P_2O_5	0.07	0.04	0.05	0.04	0.05	0.04	0.06	0.04	0.06	0.04	0.05	0.07	0.18	0.16
LOI	2.22	3.48	3.29	4.06	3.44	3.64	2.77	3.23	3.40	3.32	2.49	3.60	1.52	6.24
Total	100.93	100.63	99.81	99.40	99.59	99.63	100.81	100.86	101.25	99.63	99.00	100.73	98.92	99.07
Trace elements (ppm)														
Sc	43.5	31.4	35.3	28.7	35.0	33.3	39.0	33.6	40.1	34.9	40.6	32.4	18.2	41.0
V	314	239	252	220	240	229	272	248	274	242	265	248	248	347
Cr	371	1710	1407	2007	1211	1529	811	1607	1351	1577	1019	354	52	13
Co	48.8	78.9	71.6	70.6	69.4	65.1	56.3	76.9	58.1	58.5	54.0	39.3	46.0	50.4
Ni	133	682	518	665	500	554	353	643	449	511	344	132	73	52
Cu	115	79	122	62	176	106	132	76	98	77	102	150	139	129
Zn														
Sr	184	117	36	57	99	47	153	61	98	93	119	622	383	196
Y	19.6	15.0	16.6	13.8	15.7	15.7	18.8	15.3	17.5	15.7	16.8	19.7	24.7	33.8
Zr	50.8	80.2	39.1	36.2	36.5	31.8	90.5	39.2	46.2	38.8	37.3	55.5	150.7	121.2
Ba	10	23	9	10	23	7	42	27	38	30	28	1205	215	472

Table C.1. contd.

Sample	MMFR 08-11	MMFR 08-12	MMFR 08-13	MMFR 08-14	MMFR 08-15	MMFR 08-16	MMFR 08-17	MMFR 08-18	MMFR 08-21	MMFR 08-22	MMFR 08-23	MMFR 08-24	MMFR 08-25	MMFR 08-26
Major elements (wt. %)														
SiO_2	50.41	52.06	46.56	47.45	48.33	43.82	51.81	42.72	53.93	48.76	47.31	38.09	46.31	49.27
TiO_2	0.62	0.58	0.47	0.46	0.25	0.35	1.09	0.26	1.25	0.21	0.31	0.07	0.10	0.16
Al_2O_3	14.08	13.85	10.06	10.47	14.40	7.68	13.12	5.68	12.78	3.58	5.89	1.78	14.31	3.27
$Fe_2O_3(T)$	10.93	10.68	12.73	11.77	7.61	12.46	14.31	11.98	14.11	9.57	12.20	10.90	6.88	6.94
MnO	0.17	0.16	0.18	0.16	0.14	0.19	0.16	0.16	0.20	0.15	0.16	0.06	0.09	0.13
MgO	8.20	7.75	15.69	15.33	10.69	22.22	5.12	26.24	4.42	19.07	20.93	37.50	15.72	20.59
CaO	11.46	10.44	10.88	8.14	14.35	7.39	8.54	5.01	8.72	14.63	9.21	0.14	12.35	15.61
Na_2O	1.58	2.04	0.69	0.41	1.60	0.45	1.66	0.12	2.44	0.23	0.17	0.02	0.45	0.21
K_2O	0.13	0.12	0.07	0.04	0.41	0.12	1.86	0.13	0.90	0.02	0.06	0.02	0.78	0.05
P_2O_5	0.06	0.06	0.04	0.05	0.01	0.04	0.07	0.03	0.11	0.01	0.03	0.01	0.00	0.01
LOI	1.88	2.30	3.58	4.35	2.43	5.07	0.95	6.42	0.40	2.69	4.33	12.54	3.76	3.28
Total	99.53	100.03	100.95	98.63	100.22	99.77	98.69	98.76	99.26	98.92	100.60	101.14	100.77	99.52
Trace elements (ppm)														
Sc	43.8	44.8	34.0	35.3	43.3	27.4	36.7	19.5	40.0	43.7	41.1	8.7	27.8	50.0
V	282	282	228	232	185	186	341	163	335	202	182	53	89	175
Cr	323	290	1699	1747	227	2668	30	4111	10	2668	721	6520	837	3816
Co	41.6	43.4	70.0	72.6	46.0	87.2	41.5	97.5	48.9	47.8	78.4	126.2	50.8	56.7
Ni	130	148	545	631	183	936	46	1507	63	285	603	2801	298	290
Cu	102	128	55	81	17	22	30	50	111	64	582	16	62	25
Zn														
Sr	100	84	43	18	116	15	155	13	120	5	7	3	127	18
Y	19.1	18.8	15.8	14.9	8.9	12.4	24.3	9.6	27.6	7.5	9.4	2.5	4.4	7.4
Zr	45.9	40.1	37.7	35.2	14.8	27.9	73.1	26.3	99.5	9.7	19.9	6.6	8.1	7.9
Ba	15	27	10	6	71	8	189	4	139	8	11	1	27	3

Table C.1. contd.

Sample	MMFR 08-28	MMG 08-3	MMG 08-4	MMG 08-5	MMG 08-7	MMH 08-1	MMH 08-4	MMH 08-5	MMH 08-6	MMH 08-7	MMH 08-8	MMH 08-9	MMH 08-11	MMH 08-12
Major elements (wt. %)														
SiO_2	44.66	44.24	44.76	44.31	50.19	52.62	52.20	52.55	75.10	48.92	47.37	49.28	46.77	50.13
TiO_2	0.23	1.67	1.69	1.64	1.65	1.76	0.95	1.74	0.80	1.01	0.95	1.26	1.82	1.81
Al_2O_3	13.65	14.00	13.46	13.18	13.43	12.22	13.50	12.34	11.83	13.68	15.22	13.87	15.27	14.02
Fe_2O_3(T)	7.60	18.20	12.15	13.67	14.56	15.04	10.97	15.76	1.15	12.34	11.80	14.66	14.64	14.38
MnO	0.15	0.25	0.21	0.21	0.39	0.20	0.17	0.20	0.01	0.19	0.18	0.22	0.23	0.19
MgO	10.84	6.24	4.21	5.41	4.86	5.15	6.11	3.81	0.49	7.35	8.32	6.52	7.47	4.62
CaO	17.92	2.72	10.23	6.26	4.29	7.41	9.04	6.21	0.04	11.31	11.48	7.99	4.39	7.79
Na_2O	0.17	0.53	2.31	0.18	1.26	2.38	2.79	3.96	0.16	1.96	1.80	2.29	3.57	2.47
K_2O	0.14	5.17	1.28	5.63	2.53	0.48	0.54	1.67	9.67	0.13	0.20	1.09	1.28	2.40
P_2O_5	0.02	0.19	0.22	0.18	0.19	0.19	0.09	0.19	0.15	0.07	0.10	0.12	0.21	0.31
LOI	4.26	6.72	9.02	9.00	5.77	2.39	3.24	1.46	0.88	2.04	2.49	2.37	3.49	1.92
Total	99.64	99.92	99.54	99.67	99.12	99.85	99.62	99.88	100.29	99.01	99.92	99.68	99.14	100.03
Trace elements (ppm)														
Sc	38.3	44.6	42.5	41.6	42.9	38.1	39.6	37.2	9.5	44.7	43.1	48.9	36.2	36.8
V	166	371	341	330	353	329	247	336	43	288	305	350	295	270
Cr	384	21	19	19	20	11	47	28	28	231	317	291	107	26
Co	42.0	58.4	37.0	46.6	35.2	52.5	41.9	46.5	6.3	44.5	48.2	44.9	50.9	51.1
Ni	242	50	24	39	25	23	55	85	44	84	185	490	58	31
Cu	16													
Zn		102	116	125	94	112	92	136	17	92	92	116	104	111
Sr	41	104	246	146	180	250	211	175	27	116	130	452	202	242
Y	8.9	33.6	33.2	32.0	33.7	35.2	19.7	36.1	47.3	21.4	19.8	25.2	25.4	41.2
Zr	17.8	160.4	158.6	147.8	155.5	181.5	82.9	187.0	345.0	57.4	51.5	91.7	121.6	228.0
Ba	5	926	379	909	917	216	138	337	2042	15	32	205	422	920

Table C.1. contd.

Sample	MMH 08-13	MMH 08-14	MMH 08-15b	MMH 08-18	MMH 08-19	MMH 08-20	MMH 08-21	MMH 08-22	MMH 08-23b	MMHS 08-3	MMHS 08-6	MMHS 08-9	MMK 08-1	MMK 08-2
Major elements (wt. %)														
SiO_2	49.02	49.55	38.10	39.99	49.58	45.56	45.80	49.87	47.71	46.42	45.64	44.84	48.77	45.37
TiO_2	1.71	1.78	3.27	2.68	1.25	2.03	1.96	1.80	2.83	1.22	2.12	3.23	1.04	1.01
Al_2O_3	14.81	13.72	15.08	15.58	12.97	15.86	15.00	13.88	12.52	15.56	14.1	11.83	13.80	17.78
Fe_2O_3(T)	13.62	14.85	25.80	18.16	14.04	14.53	14.50	14.99	16.34	13.31	16.78	21.07	13.54	11.92
MnO	0.19	0.21	0.16	0.19	0.21	0.21	0.21	0.23	0.24	0.19	0.24	0.30	0.22	0.16
MgO	6.08	5.33	7.40	6.02	6.37	6.37	7.05	6.55	3.67	7.35	6.21	5.20	7.54	8.40
CaO	6.54	8.58	2.95	10.08	6.45	8.78	7.55	5.08	7.41	8.92	8.79	8.87	10.20	9.34
Na_2O	1.49	3.26	0.73	1.33	3.50	2.84	2.70	4.09	3.63	3.33	2.56	2.41	2.21	2.17
K_2O	1.85	0.78	1.03	0.96	1.05	0.98	1.19	0.95	1.02	0.24	0.54	0.68	0.29	0.77
P_2O_5	0.23	0.21	0.29	0.21	0.12	0.22	0.24	0.20	0.79	0.13	0.16	0.20	0.07	0.10
LOI	3.62	1.91	5.73	4.12	3.62	2.77	3.00	2.89	3.60	3.23	2.79	2.25	2.32	2.87
Total	99.15	100.17	100.53	99.32	99.16	100.15	99.20	100.53	99.76	99.91	99.93	100.89	99.99	99.89
Trace elements (ppm)														
Sc	37.9	41.2	43.1	38.9	44.6	38.5	40.1	44.2	39.5	34.2	43.2	47.3	48.2	16.3
V	284	320	748	384	298	318	348	299	389	253	433	692	328	164
Cr	144	115	17	542	89	106	101	91	28	78	20	4	102	254
Co	47.6	46.9	86.4	62.6	46.9	54.6	54.6	49.9	53.3	56.1	64.8	69.8	48.1	56.8
Ni	78	119	9	166	39	59	59	48	31	101	59	35	84	153
Cu										53	79	108		
Zn	91	94	256	98	137	105	130	154	157				98	74
Sr	363	303	49	379	365	341	288	128	256	276	213	185	147	451
Y	29.6	36.7	41.6	22.7	24.9	30.1	28.3	28.2	57.0	22.6	31.4	35.0	20.4	13.5
Zr	147.9	184.4	275.1	150.2	92.3	141.0	135.8	158.3	281.7	80.4	106.9	129.9	47.2	60.4
Ba	841	404	717	205	1140	510	422	339	274	82	166	228	27	296

Table C.1. contd.

Sample	MMK 08-3	MMK 08-4	MMK 08-5	MMK 08-6	MMK 08-7	MMK 08-10	MMK 08-11	MMT 08-1	MMT 08-2	MMT 08-3	MMT 08-4	MMT 08-5	MMT 08-6	MMT 08-7
Major elements (wt. %)														
SiO_2	48.04	48.01	45.08	45.93	46.03	46.21	45.43	41.98	39.11	41.25	39.45	46.96	40.63	41.32
TiO_2	1.01	1.16	1.30	1.73	1.19	1.61	2.99	0.10	0.08	0.12	0.03	0.21	0.22	0.22
Al_2O_3	17.38	17.92	14.86	16.09	16.79	16.36	14.33	3.44	1.86	5.14	1.06	4.61	6.55	4.94
Fe_2O_3(T)	10.14	10.55	13.39	13.67	11.27	13.39	16.09	11.30	11.18	9.82	13.74	12.05	17.10	7.15
MnO	0.13	0.13	0.18	0.19	0.14	0.18	0.22	0.11	0.10	0.13	0.12	0.23	0.20	0.16
MgO	6.65	8.27	10.47	7.14	8.76	7.10	6.89	30.13	33.14	30.34	36.86	28.78	24.27	26.73
CaO	10.93	5.36	8.44	8.22	8.94	8.85	9.25	2.14	0.17	3.39	1.54	3.45	4.55	6.54
Na_2O	2.89	4.42	1.95	2.40	1.82	2.10	3.24	0.42	0.02	0.22	0.02	0.48	0.31	0.04
K_2O	0.46	0.66	0.51	0.68	0.94	0.82	0.26	0.23	0.03	0.04	0.02	0.70	0.07	0.03
P_2O_5	0.08	0.11	0.15	0.18	0.13	0.16	0.28	0.02	0.02	0.01	0.01	0.04	0.05	0.03
LOI	2.26	4.03	3.43	3.09	3.62	2.76	2.10	10.08	13.21	8.21	6.16	1.13	6.27	11.74
Total	99.97	100.62	99.76	99.33	99.61	99.53	101.10	99.95	98.91	98.67	99.02	98.64	100.21	98.91
Trace elements (ppm)														
Sc	33.9	18.2	20.4	25.6	18.3	26.3	36.5	11.2	7.7	17.0	7.0	17.0	12.7	11.6
V	197	150	171	219	174	212	395	61	144	164	70	184	74	64
Cr	457	73	88	96	82	100	141	4195	5583	3815	3907	3023	1301	1032
Co	41.2	46.0	61.8	55.0	54.6	52.0	58.3	116.8	98.3	30.3	128.9	86.8	134.9	69.8
Ni	80	141	190	237	123	97	94	2248	2724	879	3082	1538	3613	2363
Cu								20	75	54	159	82	128	29
Zn	97	103	137	145	81	122	76							
Sr	430	200	413	440	404	431	281	23	7	12	7	20	171	86
Y	14.4	14.7	19.9	24.0	17.8	22.8	27.7	4.7	3.8	6.5	2.8	8.0	8.8	8.8
Zr	63.8	80.7	88.8	120.2	87.1	106.6	179.8	19.5	15.9	12.5	57.9	31.3	32.9	35.7
Ba	99	40	201	374	339	247	50	53	6	8	5	51	6	3

Table C.1. contd.

Sample	MMT 08-9	MMT 08-12	MMT 08-13	MMT 08-14	MMT 08-15	MMT 08-18	MMT 08-21	MMT 08-22
Major elements (wt. %)								
SiO_2	42.90	46.06	43.11	45.88	37.59	41.39	39.31	39.20
TiO_2	0.35	0.11	0.12	0.35	0.07	0.11	0.06	0.04
Al_2O_3	18.27	3.42	2.89	5.67	3.26	1.78	1.40	0.93
Fe_2O_3(T)	15.61	11.93	9.35	11.77	13.36	12.14	12.31	13.03
MnO	0.13	0.13	0.18	0.11	0.09	0.08	0.08	0.07
MgO	7.73	26.60	30.89	22.75	33.99	30.38	32.63	32.71
CaO	4.06	3.55	1.97	6.83	0.52	0.76	0.50	0.07
Na_2O	2.76	0.28	0.08	0.67	0.06	0.11	0.05	0.05
K_2O	2.42	0.05	0.09	0.12	0.03	0.04	0.12	0.21
P_2O_5	0.18	0.01	0.01	0.01	0.02	0.02	0.00	0.01
LOI	5.32	6.50	7.88	4.49	11.53	13.03	13.97	12.61
Total	99.71	98.65	96.57	98.65	100.53	99.84	100.43	98.94
Trace elements (ppm)								
Sc	15.1	12.4	18.4	31.0	10.3	9.8	6.5	6.3
V	184	72	158	197	65	100	35	30
Cr	92	2588	2264	2688	3169	2840	3928	2169
Co	30.1	66.7	75.3	96.3	133.4	125.0	112.6	280.3
Ni	563	2248	1891	1162	3839	1114	2763	23120
Cu	477	263	49	92	159	51	40	264
Zn								
Sr	728	33	10	31	6	18	8	8
Y	22.1	7.3	4.8	9.9	3.5	4.6	2.7	2.4
Zr	135.6	20.8	34.4	12.8	7.2	27.0	6.3	8.5
Ba	571	5	12	34	5	8	3	28

Appendix C: Geochemical results obtained by inductively-coupled plasma optical emission spectrometry and inductively-coupled plasma mass spectrometry

Table C.2. Elemental data collected by inductively-coupled plasma mass spectrometry

Sample	MMF 07-1	MMF 07-2	MMF 07-3	MMF 07-4	MMF 07-5	MMF 07-6	MMF 07-7	MMF 07-8
Major elements (wt. %)								
TiO_2	2.42	2.28	2.59	2.19	3.05	2.62	2.30	2.12
MnO	0.24	0.23	0.22	0.23	0.22	0.21	0.25	0.24
Fe_2O_3(T)								
Trace elements (ppm)								
V	413	384	424	351	417	381	400	399
Cr	104	104	143	2824	136	143	91	89
Co	53.8	54.8	58.5	56.5	47.2	46.1	57.5	60.9
Ni	85	373	108	13000	103	69	62	62
Cu	164	159	167	168	106	98	103	109
Zn				237	234			
Ga	22.0	20.4	23.4	20.0	22.4	19.6	19.1	23.9
Rb	3.1	4.9	8.1	2.6	7.8	4.0	6.9	0.4
Sr	158	191	340	122	133	143	183	265
Y	38.6	37.3	37.2	36.0	49.8	45.3	39.4	37.4
Zr	123.1	120.9	147.5	150.3	220.7	169.4	143.3	126.1
Nb	15.79	15.26	18.55	18.14	25.81	20.23	16.12	14.20
Mo								
Cs	0.44	0.48	0.42	0.19	0.27	0.13	0.24	0.12
Ba	52	81	126	74	223	212	118	22
La	11.58	11.57	13.31	20.12	18.64	17.26	13.86	12.22
Ce	26.26	25.87	30.64	43.87	43.66	38.86	30.83	27.54
Pr	3.84	3.78	4.47	5.81	6.26	5.53	4.35	3.92
Nd	17.11	16.70	19.56	23.86	27.45	23.68	18.89	17.22
Sm	4.69	4.54	5.14	5.08	7.37	6.02	5.02	4.60
Eu	1.55	1.48	1.83	1.64	2.12	1.79	1.46	1.56
Gd	5.23	5.06	5.48	5.75	7.74	6.44	5.49	5.18
Tb	0.97	0.94	0.98	0.92	1.28	1.17	1.03	0.97
Dy	6.08	5.93	6.00	5.85	8.19	7.11	6.30	5.98
Ho	1.20	1.16	1.13	1.13	1.58	1.37	1.23	1.15
Er	3.49	3.41	3.33	3.22	4.55	4.08	3.62	3.44
Tm	0.56	0.54	0.52	0.51	0.71	0.64	0.57	0.54
Yb	3.61	3.50	3.38	3.34	4.65	4.25	3.75	3.46
Lu	0.56	0.54	0.52	0.50	0.71	0.66	0.59	0.54
Hf	3.00	2.89	3.54	3.70	5.45	4.04	3.52	3.11
Ta	0.87	0.84	1.06	1.06	1.41	1.10	0.89	0.74
Th	1.00	0.95	1.25	1.39	2.20	1.98	1.81	1.57
U	0.28	0.27	0.37	0.35	0.54	0.55	0.53	0.45

Table C.2. contd.

Sample	MMF 07-9	MMF 07-10	MMF 07-11	MMF 07-12	MMF 07-13	MMF 07-14	MMF 07-15	MMF 07-16
Major elements (wt. %)								
TiO_2	1.93	1.95	1.80	2.31	1.90	2.34	2.07	2.31
MnO	0.20	0.22	0.22	0.22	0.20	0.26	0.23	0.20
$Fe_2O_3(T)$								
Trace elements (ppm)								
V	337	372	361	380	335	397	355	371
Cr	111	110	100	163	148	111	92	199
Co	47.1	50.0	54.8	58.1	58.4	49.1	50.3	45.8
Ni	38	675	105	100	201	139	68	91
Cu	100	99	201	147	127	152	147	110
Zn			253		269			209
Ga	23.6	21.7	17.4	19.8	16.1	19.6	17.1	19.0
Rb	0.5	4.6	1.1	8.9	2.9	3.3	15.2	0.5
Sr	205	231	132	207	174	255	157	62
Y	31.2	30.8	29.7	36.6	32.9	35.0	31.6	36.7
Zr	117.2	110.2	100.8	141.1	136.3	131.9	118.7	141.2
Nb	14.47	12.13	10.53	18.49	16.59	16.32	15.13	14.85
Mo								
Cs	0.05	0.11	0.29	0.43	0.28	0.27	0.34	0.15
Ba	33	109	52	138	100	101	496	21
La	13.57	12.65	7.95	13.31	11.91	14.25	12.36	12.88
Ce	29.29	26.91	18.88	30.62	27.72	31.26	28.09	29.39
Pr	4.04	3.76	2.78	4.41	3.97	4.47	4.02	4.10
Nd	16.91	16.08	12.89	19.44	17.50	19.59	17.66	18.12
Sm	4.28	4.17	3.70	5.01	4.71	4.90	4.42	4.72
Eu	1.27	1.34	1.34	1.72	1.46	1.51	1.35	1.47
Gd	4.51	4.45	4.28	5.47	5.00	5.28	4.78	5.28
Tb	0.82	0.82	0.73	0.98	0.84	0.95	0.86	0.89
Dy	5.01	4.99	4.83	5.98	5.37	5.78	5.19	5.83
Ho	0.96	0.96	0.95	1.13	1.04	1.08	0.98	1.16
Er	2.83	2.78	2.75	3.35	2.98	3.21	2.85	3.35
Tm	0.44	0.44	0.43	0.52	0.47	0.49	0.44	0.54
Yb	2.87	2.81	2.82	3.31	3.08	3.15	2.81	3.56
Lu	0.44	0.43	0.43	0.52	0.47	0.48	0.44	0.55
Hf	2.86	2.68	2.51	3.47	3.40	3.18	2.87	3.36
Ta	0.77	0.71	0.61	1.03	0.95	0.93	0.86	0.86
Th	1.89	1.65	0.78	1.19	1.20	1.06	1.05	1.43
U	0.55	0.50	0.20	0.34	0.30	0.30	0.29	0.35

Table C.2. contd.

Sample	MMF 07-17	MMF 07-18	MMF 07-19	MMF 07-20	MMF 07-21	MMLT 07-1	MMLT 07-3	MMLT 07-6
Major elements (wt. %)								
TiO_2	2.05	2.27	1.75	1.70	2.04	1.15	1.25	1.40
MnO	0.24	0.26	0.23	0.20	0.22	0.20	0.18	0.20
Fe_2O_3(T)						13.53	13.86	14.37
Trace elements (ppm)								
V	399	426	365	342	394	386	392	422
Cr	86	73	147	128	146	158	292	199
Co	56.1	62.0	54.8	51.6	56.8	50.2	59.1	53.1
Ni	106	72	52	81	170	111	130	110
Cu	117	114	107	87	107	201	161	142
Zn				175		102	99	144
Ga	23.9	21.5	20.0	19.8	21.4	18.1	17.6	18.8
Rb	1.6	6.1	7.4	1.6	15.4	1.7	3.0	3.7
Sr	454	196	180	56	230	75	117	112
Y	37.8	40.1	32.6	28.9	31.3	28.2	28.7	32.6
Zr	124.2	138.4	107.3	112.2	111.7	64.7	73.0	73.9
Nb	14.10	15.28	12.20	11.90	13.33	3.18	3.67	3.47
Mo								
Cs	0.20	0.21	0.23	0.32	0.89	0.15	0.11	0.20
Ba	30	178	155	34	210	17	27	38
La	13.63	14.36	11.88	10.08	12.19	3.08	3.55	4.07
Ce	29.44	31.35	25.65	22.73	26.82	8.40	9.56	11.00
Pr	4.12	4.42	3.62	3.18	3.78	1.45	1.65	1.90
Nd	18.04	19.20	15.68	14.00	16.32	7.48	8.40	9.64
Sm	4.68	4.97	4.05	3.79	4.17	2.58	2.80	3.25
Eu	1.49	1.56	1.29	1.20	1.22	0.87	0.98	1.13
Gd	5.23	5.57	4.58	4.28	4.54	3.11	3.30	3.79
Tb	0.99	1.04	0.84	0.72	0.83	0.60	0.63	0.73
Dy	6.05	6.44	5.24	4.68	5.06	4.05	4.18	4.74
Ho	1.17	1.22	1.01	0.92	0.97	0.82	0.84	0.95
Er	3.52	3.70	3.02	2.62	2.86	2.49	2.53	2.87
Tm	0.54	0.58	0.46	0.41	0.44	0.40	0.41	0.45
Yb	3.53	3.74	3.03	2.77	2.86	2.54	2.56	2.83
Lu	0.55	0.58	0.48	0.44	0.44	0.40	0.40	0.45
Hf	3.12	3.40	2.68	2.69	2.79	1.74	1.90	1.96
Ta	0.79	0.88	0.65	0.63	0.74	0.21	0.31	0.24
Th	1.65	1.74	1.47	1.44	1.69	0.20	0.24	0.28
U	0.47	0.51	0.43	0.36	0.52	0.08	0.09	0.11

Table C.2. contd.

Sample	MMLT 07-7	MMLT 07-8	MMLT 07-9	MMLT 07-11	MMLT 07-12	MMLT 07-13	MMLT 07-14	MMLT 07-15
Major elements (wt. %)								
TiO_2	1.13	1.14	1.40	1.29	1.45	0.45	1.19	1.17
MnO	0.20	0.16	0.18	0.17	0.19	0.14	0.19	0.20
$Fe_2O_3(T)$	13.28	13.32	13.76	13.38	14.46	8.13	14.12	13.74
Trace elements (ppm)								
V	404	380	407	406	410	218	407	377
Cr	158	157	139	193	101	226	163	153
Co	52.0	63.2	49.8	51.3	50.4	34.1	44.3	49.8
Ni	110	130	91	108	80	104	103	107
Cu	164	316	105	185	119	49	40	200
Zn	99	71	114	161	135	75	145	144
Ga	16.7	16.3	18.1	17.1	18.7	12.8	17.9	18.0
Rb	1.7	1.0	1.2	0.8	2.8	4.2	1.2	1.7
Sr	104	69	132	76	118	74	75	89
Y	26.9	27.2	30.0	29.3	33.7	11.2	29.0	28.2
Zr	61.2	58.4	88.4	69.4	93.0	25.6	66.5	65.8
Nb	3.07	2.77	4.00	3.45	5.13	1.40	3.73	3.27
Mo								
Cs	0.13	0.10	0.08	0.10	0.09	0.18	0.13	0.09
Ba	29	15	20	10	41	19	21	18
La	3.05	3.17	4.22	4.16	4.97	1.59	3.49	3.24
Ce	8.18	8.31	11.18	10.67	12.88	3.86	9.01	8.64
Pr	1.42	1.41	1.91	1.78	2.18	0.62	1.53	1.49
Nd	7.24	7.20	9.48	8.82	10.75	3.06	7.80	7.60
Sm	2.48	2.47	3.14	2.92	3.49	1.04	2.63	2.63
Eu	0.94	0.88	1.05	1.07	1.15	0.41	1.04	0.94
Gd	3.04	3.06	3.63	3.38	4.02	1.24	3.28	3.21
Tb	0.57	0.58	0.69	0.65	0.78	0.20	0.61	0.60
Dy	3.89	3.92	4.49	4.23	4.93	1.66	4.13	4.08
Ho	0.79	0.80	0.90	0.85	0.98	0.34	0.83	0.82
Er	2.40	2.42	2.69	2.55	2.95	1.04	2.55	2.50
Tm	0.39	0.39	0.43	0.41	0.47	0.16	0.41	0.40
Yb	2.44	2.53	2.73	2.55	3.00	1.07	2.66	2.60
Lu	0.39	0.39	0.42	0.40	0.47	0.16	0.42	0.40
Hf	1.66	1.60	2.26	1.83	2.36	0.71	1.77	1.78
Ta	0.21	0.21	0.30	0.29	0.42	0.09	0.23	0.21
Th	0.20	0.20	0.39	0.30	0.43	0.16	0.20	0.19
U	0.10	0.08	0.14	0.12	0.15	0.06	0.09	0.08

Table C.2. contd.

Sample	MMLT 07-18	MMLT 07-19	MMLT 07-20	MMLT 07-22	MMLT 07-23	MMLT 07-24	MMLT 07-26	MMLT 07-28
Major elements (wt. %)								
TiO_2	1.29	1.15	1.13	1.29	0.87	0.88	1.14	1.48
MnO	0.16	0.19	0.19	0.22	0.16	0.18	0.19	0.20
Fe_2O_3(T)								
Trace elements (ppm)								
V	365	357	351	378	308	309	353	420
Cr	176	148	192	213	524	375	196	291
Co	54.6	50.0	54.3	58.6	53.9	50.5	53.3	58.5
Ni	109	106	97	110	151	100	183	156
Cu	157	175	163	111	87	113	145	136
Zn	160	214						
Ga	17.0	16.8	17.7	18.4	14.4	15.5	16.5	19.0
Rb	0.8	1.5	0.2	0.9	0.4	1.8	0.2	0.6
Sr	98	86	116	113	85	138	107	179
Y	27.0	25.2	24.9	25.8	19.2	19.1	23.2	29.1
Zr	70.5	59.6	62.6	63.5	47.0	46.0	57.2	73.5
Nb	4.48	3.19	3.30	3.63	2.44	2.42	3.09	4.00
Mo								
Cs	0.02	0.03	0.04	0.06	0.05	0.11	0.02	0.08
Ba	29	22	13	16	17	18	24	31
La	4.29	3.19	3.41	3.56	2.77	2.84	3.20	4.02
Ce	10.87	8.60	8.27	8.63	6.21	6.29	7.70	9.98
Pr	1.74	1.40	1.41	1.48	1.05	1.04	1.32	1.71
Nd	8.57	7.19	7.26	7.56	5.33	5.37	6.67	8.63
Sm	2.80	2.45	2.46	2.53	1.78	1.79	2.26	2.86
Eu	1.01	0.91	0.88	0.92	0.68	0.65	0.84	0.99
Gd	3.39	3.10	3.02	3.11	2.26	2.23	2.77	3.50
Tb	0.63	0.57	0.61	0.62	0.46	0.45	0.55	0.69
Dy	4.25	3.91	3.96	4.08	3.05	2.92	3.61	4.49
Ho	0.85	0.80	0.79	0.81	0.61	0.59	0.72	0.88
Er	2.48	2.34	2.36	2.44	1.85	1.81	2.17	2.66
Tm	0.40	0.39	0.37	0.39	0.30	0.29	0.34	0.43
Yb	2.64	2.50	2.44	2.53	1.97	1.90	2.24	2.77
Lu	0.42	0.40	0.38	0.39	0.31	0.30	0.35	0.43
Hf	1.87	1.55	1.60	1.59	1.13	1.07	1.41	1.81
Ta	0.31	0.19	0.30	0.33	0.19	0.21	0.17	0.28
Th	0.36	0.25	0.27	0.22	0.16	0.24	0.15	0.22
U	0.11	0.07	0.07	0.07	0.06	0.07	0.06	0.08

Table C.2. contd.

Sample	MMLT 07-29	MMLT 07-31	MMLT 07-33	MMLT 07-34	MMLT 07-35	MMLT 07-36	MMLT 07-37	MMLT 07-38
Major elements (wt. %)								
TiO_2	0.93	1.13	0.94	1.05	0.88	0.64	0.69	0.66
MnO	0.16	0.20	0.18	0.20	0.15	0.16	0.14	0.17
$Fe_2O_3(T)$			11.85	13.33	11.87	11.43	9.92	10.87
Trace elements (ppm)								
V	333	344	347	351	334	309	336	282
Cr	304	194	178	206	248	204	328	242
Co	47.3	55.2	44.6	49.3	46.2	42.6	43.9	41.4
Ni	112	111	123	127	89	86	182	87
Cu	59	108	166	165	124	141	142	106
Zn			158	122	137	95	74	78
Ga	14.5	16.5	15.8	16.6	16.3	14.8	14.1	14.6
Rb	0.1	0.7	0.9	1.0	0.5	2.0	0.8	7.6
Sr	97	103	112	57	160	72	107	133
Y	20.7	23.3	22.4	24.3	22.1	20.4	20.8	19.7
Zr	49.2	53.6	49.7	59.7	49.6	44.2	45.6	44.3
Nb	2.50	3.13	2.58	3.08	2.58	2.32	2.38	2.28
Mo								
Cs	0.02	0.03	0.14	0.15	0.11	0.13	0.13	0.72
Ba	27	20	7	32	11	23	16	31
La	3.20	3.44	2.75	3.00	2.79	2.58	2.49	2.45
Ce	7.28	7.93	7.30	7.92	7.10	6.59	6.42	6.29
Pr	1.16	1.32	1.26	1.36	1.19	1.10	1.09	1.06
Nd	5.82	6.83	6.41	6.94	5.93	5.55	5.54	5.32
Sm	1.88	2.27	2.12	2.35	1.96	1.86	1.84	1.80
Eu	0.85	0.83	0.79	0.88	0.78	0.69	0.68	0.66
Gd	2.43	2.81	2.63	2.88	2.33	2.32	2.33	2.24
Tb	0.48	0.56	0.48	0.52	0.45	0.42	0.42	0.41
Dy	3.20	3.70	3.28	3.55	3.16	2.98	3.02	2.90
Ho	0.65	0.73	0.67	0.72	0.65	0.61	0.62	0.59
Er	1.95	2.20	1.98	2.17	1.99	1.85	1.88	1.79
Tm	0.31	0.35	0.32	0.35	0.33	0.30	0.30	0.29
Yb	2.03	2.28	2.02	2.21	2.11	1.91	1.96	1.85
Lu	0.32	0.36	0.31	0.34	0.33	0.29	0.31	0.29
Hf	1.18	1.40	1.37	1.63	1.37	1.25	1.28	1.24
Ta	0.16	0.32	0.18	0.19	0.17	0.15	0.16	0.15
Th	0.15	0.13	0.17	0.17	0.22	0.20	0.18	0.19
U	0.07	0.07	0.07	0.07	0.09	0.08	0.12	0.08

Table C.2. contd.

Sample	MMLT 07-39	MMLT 07-40	MMLT 07-41	MMLT 07-42	MMLT 07-43	MMLT 07-44	MMLT 07-45	MMM 07-1
Major elements (wt. %)								
TiO_2	0.95	0.94	0.88	0.98	0.80	1.00	0.98	1.55
MnO	0.18	0.18	0.18	0.19	0.13	0.18	0.18	0.28
Fe_2O_3(T)					9.80			16.04
Trace elements (ppm)								
V	340	336	313	339	304	357	350	301
Cr	465	385	405	419	242	355	338	70
Co	54.2	50.3	50.2	55.7	40.6	55.1	51.6	60.9
Ni	122	110	151	133	128	635	88	81
Cu	118	90	104	120	91	138	129	153
Zn					99			190
Ga	15.4	15.5	14.6	16.3	15.4	13.8	14.1	20.0
Rb	0.3	0.3	0.4	0.5	0.5	0.7	0.5	10.0
Sr	130	139	133	64	170	98	122	167
Y	20.3	20.3	20.4	21.8	21.3	21.2	21.0	29.4
Zr	47.9	44.0	47.5	50.2	46.1	54.2	49.3	93.4
Nb	2.39	2.41	2.53	2.64	2.34	2.88	2.60	6.32
Mo								0.7
Cs	0.03	0.03	0.04	0.04	0.12	0.14	0.04	0.09
Ba	15	14	13	16	11	15	15	135
La	3.04	2.92	2.90	2.73	2.47	2.98	2.90	8.40
Ce	6.71	6.57	6.60	6.57	6.45	6.86	6.55	19.31
Pr	1.11	1.10	1.11	1.14	1.09	1.14	1.11	2.84
Nd	5.51	5.55	5.55	5.80	5.53	5.75	5.62	12.76
Sm	1.87	1.90	1.89	2.01	1.89	1.95	1.91	3.61
Eu	0.66	0.68	0.68	0.68	0.73	0.64	0.70	1.21
Gd	2.29	2.34	2.42	2.51	2.34	2.45	2.38	4.12
Tb	0.46	0.48	0.48	0.51	0.43	0.50	0.49	0.71
Dy	3.07	3.16	3.17	3.40	3.04	3.28	3.23	4.70
Ho	0.62	0.63	0.63	0.69	0.62	0.66	0.65	0.93
Er	1.89	1.93	1.93	2.10	1.87	1.97	1.97	2.72
Tm	0.30	0.31	0.31	0.33	0.30	0.32	0.31	0.43
Yb	1.94	2.04	2.02	2.18	1.92	2.03	2.02	2.88
Lu	0.30	0.32	0.33	0.34	0.30	0.33	0.32	0.44
Hf	1.13	1.09	1.16	1.26	1.29	1.28	1.19	2.38
Ta	0.15	0.15	0.18	0.16	0.15	0.15	0.15	0.35
Th	0.13	0.14	0.21	0.17	0.20	0.16	0.13	0.73
U	0.06	0.07	0.07	0.07	0.13	0.07	0.06	0.14

Table C.2. contd.

Sample	MMM 07-2	MMM 07-6	MMM 07-7	MMM 07-11	MMM 07-12	MMM 07-14	MMM 07-15	MMM 07-17
Major elements (wt. %)								
TiO_2	0.46	0.84	0.65	0.89	0.84	0.94	0.81	1.52
MnO	0.19	0.23	0.19	0.19	0.19	0.22	0.19	0.23
Fe_2O_3(T)	11.43	12.53	12.45	11.71	11.34	12.85	11.86	13.65
Trace elements (ppm)								
V	186	296	216	288	267	336	299	326
Cr	1879	347	1579	454	286	211	168	101
Co	77.8	52.0	76.7	51.4	48.7	53.2	51.7	50.5
Ni	596	207	482	199	148	134	141	71
Cu	73	132	104	119	130	144	159	170
Zn	198	149	219	157	143	220	173	163
Ga	10.4	14.8	11.5	15.3	15.0	15.1	14.9	18.4
Rb	6.3	1.0	1.4	28.2	35.8	1.6	1.12	6.7
Sr	60	77	63	98	103	79	79	159
Y	11.3	18.4	14.5	20.8	18.9	21.9	19.2	28.3
Zr	35.8	43.6	39.8	63.7	54.0	59.3	52.9	97.8
Nb	1.69	2.32	2.98	3.03	2.89	2.61	2.37	8.99
Mo	0.3	0.5	0.3	0.4	0.3	0.5	0.4	0.3
Cs	0.23	0.01	0.03	0.78	1.42	0.06	0.03	0.04
Ba	66	14	19	36	35	47	16	63
La	3.45	2.19	2.21	4.13	3.63	2.69	2.27	8.44
Ce	7.34	5.99	5.49	9.86	8.76	7.32	6.38	19.53
Pr	0.98	0.99	0.86	1.48	1.31	1.23	1.07	2.89
Nd	4.29	5.08	4.32	6.99	6.27	6.23	5.43	13.01
Sm	1.25	1.80	1.43	2.19	2.02	2.11	1.88	3.65
Eu	0.44	0.67	0.52	0.77	0.73	0.78	0.68	1.23
Gd	1.46	2.28	1.80	2.68	2.45	2.67	2.33	4.15
Tb	0.27	0.42	0.33	0.48	0.45	0.50	0.44	0.70
Dy	1.78	2.87	2.25	3.25	3.00	3.45	3.04	4.57
Ho	0.36	0.59	0.46	0.65	0.60	0.70	0.62	0.89
Er	1.04	1.68	1.32	1.91	1.74	2.08	1.84	2.57
Tm	0.17	0.27	0.21	0.30	0.28	0.33	0.30	0.40
Yb	1.12	1.86	1.42	1.99	1.83	2.18	1.91	2.69
Lu	0.18	0.28	0.22	0.30	0.28	0.34	0.30	0.41
Hf	0.85	1.16	0.92	1.62	1.37	1.31	1.23	2.52
Ta	0.11	0.14	0.17	0.20	0.18	0.16	0.14	0.52
Th	0.90	0.15	0.23	0.72	0.58	0.27	0.32	0.82
U	0.22	0.05	0.06	0.21	0.19	0.06	0.05	0.22

Table C.2. contd.

Sample	MMM 07-20	MMM 07-21	MMM 07-22	MMM 07-25	MMM 07-26	MMM 07-28	MMPC 07-1	MMPC 07-2
Major elements (wt. %)								
TiO_2	0.65	0.33	0.80	1.57	0.58	0.34	1.21	1.78
MnO	0.20	0.17	0.22	0.23	0.17	0.18	0.32	0.17
$Fe_2O_3(T)$	12.28	8.98	12.13	14.65	10.62	10.86		
Trace elements (ppm)								
V	231	223	280	353	209	182	352	511
Cr	1511	340	247	95	949	1533	211	58
Co	71.9	46.8	49.4	51.4	58.5	74.6	51.5	48.6
Ni	430	136	102	82	311	485	118	63
Cu	105	98	128	126	95	80	58	178
Zn	248	105	144	195	167	182		
Ga	12.5	10.2	14.4	18.4	10.8	9.6	18.1	21.6
Rb	3.0	0.4	4.6	3.9	0.7	0.5	11.1	1.8
Sr	65	59	79	143	55	53	103	123
Y	15.5	8.5	18.6	28.7	13.7	8.5	24.6	24.4
Zr	44.5	17.2	46.0	94.3	27.0	14.4	57.5	58.7
Nb	2.05	0.53	2.53	7.93	1.44	0.79	3.57	3.52
Mo	0.3	0.3	0.4	0.9	0.3	0.3		
Cs	0.12	0.03	0.04	0.07	0.01	0.02	0.94	0.58
Ba	29	16	46	62	21	10	50	21
La	2.57	0.61	2.29	7.49	1.52	0.73	2.90	2.81
Ce	6.38	1.83	6.27	17.88	4.36	2.06	7.80	8.68
Pr	0.99	0.32	1.05	2.66	0.73	0.35	1.33	1.47
Nd	4.83	1.82	5.42	12.24	3.82	1.89	6.79	7.37
Sm	1.61	0.73	1.87	3.55	1.33	0.74	2.30	2.45
Eu	0.57	0.32	0.70	1.22	0.50	0.30	0.84	0.92
Gd	1.98	0.96	2.34	4.03	1.69	0.99	2.87	3.00
Tb	0.36	0.19	0.43	0.70	0.32	0.19	0.57	0.57
Dy	2.45	1.39	2.93	4.58	2.17	1.30	3.84	3.75
Ho	0.49	0.28	0.59	0.91	0.44	0.27	0.76	0.74
Er	1.42	0.84	1.73	2.62	1.25	0.78	2.31	2.24
Tm	0.23	0.13	0.28	0.42	0.20	0.13	0.36	0.34
Yb	1.48	0.86	1.84	2.73	1.30	0.82	2.38	2.29
Lu	0.23	0.13	0.29	0.42	0.20	0.13	0.37	0.36
Hf	1.10	0.30	1.23	2.37	0.67	0.35	1.50	1.51
Ta	0.13	0.04	0.15	0.45	0.09	0.05	0.19	0.19
Th	0.39	0.08	0.15	0.63	0.12	0.10	0.14	0.22
U	0.12	0.01	0.05	0.15	0.04	0.03	0.07	0.07

Table C.2. contd.

Sample	MMPC 07-3	MMW 07-2	MMW 07-3	MMW 07-4	MMW 07-7	MMW 07-8	MMW 07-9	MMW 07-10
Major elements (wt. %)								
TiO_2	1.43	0.56	0.56	0.55	0.45	0.52	0.53	0.48
MnO	0.20	0.19	0.17	0.17	0.15	0.15	0.17	0.17
$Fe_2O_3(T)$								
Trace elements (ppm)								
V	486	204	199	194	172	185	192	188
Cr	70	2335	2636	2170	2404	2406	2460	2320
Co	49.1	92.6	97.9	84.0	89.2	87.6	93.9	90.6
Ni	78	794	828	651	855	770	849	900
Cu	150	81	79	90	109	80	75	76
Zn					169			243
Ga	20.1	11.1	10.4	9.8	8.9	9.6	10.2	9.4
Rb	2.1	1.7	1.7	1.2	5.8	3.0	2.0	1.9
Sr	117	50	53	49	29	63	60	48
Y	24.5	13.1	12.3	11.8	10.5	11.4	12.0	11.1
Zr	58.5	27.4	26.6	24.7	28.8	26.4	24.7	27.8
Nb	3.54	1.11	1.05	1.04	1.10	0.94	1.01	1.42
Mo								
Cs	0.63	0.11	0.15	0.09	0.44	0.23	0.27	0.12
Ba	26	8	11	23	153	57	40	21
La	2.84	1.58	1.54	1.43	1.32	1.41	1.51	1.43
Ce	8.34	3.59	3.46	3.28	3.41	3.20	3.50	3.80
Pr	1.39	0.63	0.60	0.56	0.55	0.54	0.61	0.62
Nd	7.21	3.31	3.09	2.95	2.88	2.86	3.13	3.20
Sm	2.40	1.19	1.12	1.07	0.99	1.01	1.11	1.08
Eu	0.91	0.44	0.42	0.39	0.39	0.38	0.41	0.40
Gd	2.95	1.57	1.46	1.36	1.29	1.33	1.40	1.36
Tb	0.59	0.31	0.28	0.27	0.24	0.25	0.28	0.26
Dy	3.77	2.01	1.86	1.80	1.67	1.74	1.89	1.74
Ho	0.73	0.40	0.38	0.36	0.33	0.35	0.38	0.35
Er	2.21	1.23	1.14	1.09	0.98	1.05	1.14	1.03
Tm	0.32	0.19	0.17	0.16	0.16	0.16	0.17	0.16
Yb	2.30	1.23	1.14	1.10	1.04	1.07	1.16	1.07
Lu	0.35	0.20	0.18	0.17	0.16	0.17	0.18	0.17
Hf	1.50	0.68	0.62	0.56	0.65	0.53	0.59	0.67
Ta	0.20	0.08	0.07	0.07	0.07	0.07	0.07	0.08
Th	0.25	0.05	0.08	0.04	0.13	0.09	0.05	0.15
U	0.08	0.04	0.04	0.03	0.04	0.03	0.04	0.05

Table C.2. contd.

Sample	MMW 07-11	MMW 07-12	MMW 07-15	MMW 07-16	MMW 07-17	MMW 07-19	MMW 07-24	MMW 07-25
Major elements (wt. %)								
TiO_2	0.53	0.63	0.55	0.62	0.56	0.56	1.11	1.32
MnO	0.18	0.18	0.19	0.18	0.19	0.19	0.17	0.21
Fe_2O_3(T)								
Trace elements (ppm)								
V	189	224	198	219	201	206	326	383
Cr	2351	2122	2858	2144	2498	2587	123	179
Co	92.3	83.2	98.8	87.2	91.7	93.8	47.6	52.8
Ni	788	585	844	602	750	767	129	148
Cu	87	97	91	110	83	91	177	152
Zn							214	
Ga	10.0	12.3	10.1	11.2	10.4	10.6	16.3	17.9
Rb	2.7	2.1	2.0	5.6	1.8	1.8	0.4	3.8
Sr	61	53	74	50	75	50	115	119
Y	11.8	14.6	12.0	13.5	12.4	12.6	23.7	27.2
Zr	24.1	29.6	24.7	27.5	24.5	25.7	65.2	61.2
Nb	1.02	1.39	0.82	0.96	0.82	0.89	3.03	3.31
Mo								
Cs	0.18	0.24	0.17	0.51	0.21	0.15	0.07	0.21
Ba	29	16	26	41	31	8	14	32
La	1.50	1.65	1.36	1.45	1.36	1.41	3.05	3.10
Ce	3.46	4.40	3.12	3.47	3.20	3.26	8.32	8.76
Pr	0.60	0.75	0.55	0.63	0.57	0.58	1.40	1.51
Nd	3.15	3.94	2.95	3.26	3.03	3.07	7.20	7.78
Sm	1.13	1.39	1.09	1.21	1.10	1.16	2.39	2.65
Eu	0.41	0.49	0.42	0.47	0.42	0.42	0.86	0.94
Gd	1.38	1.76	1.36	1.51	1.41	1.46	3.06	3.25
Tb	0.28	0.34	0.28	0.31	0.29	0.29	0.55	0.65
Dy	1.88	2.29	1.82	2.09	1.93	1.96	3.79	4.24
Ho	0.38	0.46	0.37	0.43	0.38	0.39	0.75	0.84
Er	1.14	1.38	1.12	1.26	1.17	1.20	2.23	2.54
Tm	0.17	0.21	0.17	0.19	0.18	0.19	0.36	0.39
Yb	1.15	1.39	1.11	1.27	1.15	1.18	2.39	2.63
Lu	0.18	0.21	0.17	0.20	0.18	0.18	0.36	0.41
Hf	0.59	0.81	0.56	0.68	0.59	0.66	1.56	1.58
Ta	0.08	0.09	0.06	0.07	0.07	0.08	0.19	0.20
Th	0.04	0.06	0.05	0.05	0.04	0.06	0.26	0.13
U	0.04	0.05	0.04	0.04	0.03	0.03	0.06	0.06

Table C.2. contd.

Sample	MMW 07-26	MMW 07-27	MMB 08-1	MMB 08-2b	MMB 08-3	MMB 08-4	MMB 08-5	MMB 08-6
Major elements (wt. %)								
TiO_2	1.38	1.21	1.76	2.25	1.30	1.50	1.23	1.22
MnO	0.22	0.20	0.21	0.21	0.16	0.19	0.22	0.21
$Fe_2O_3(T)$			13.30	13.41	10.75	11.84	12.11	12.33
Trace elements (ppm)								
V	403	354	286	328	248	291	311	322
Cr	134	151	24	14	345	129	86	89
Co	54.8	51.9	47.3	52.2	45.5	48.5	51.1	52.4
Ni	200	121	21	23	104	81	63	54
Cu	125	147	45	52	45	113	99	109
Zn			112	169	103	118	191	108
Ga	18.7	17.7	19.7	22.0	18.2	18.0	17.2	18.2
Rb	2.5	5.0	20.4	28.1	3.3	1.6	0.8	-0.1
Sr	101	72	343	299	250	286	276	415
Y	26.8	25.9	38.1	48.4	21.4	26.8	23.9	25.1
Zr	58.6	56.2	190.5	244.1	103.6	104.3	92.9	93.1
Nb	3.21	3.16	14.06	18.18	9.91	9.42	8.56	8.89
Mo								
Cs	0.14	0.25	1.16	1.36	0.10	0.12	0.15	0.13
Ba	22	28	385	547	88	126	94	41
La	3.38	2.92	30.99	42.56	11.81	11.01	11.16	11.91
Ce	8.39	8.25	61.18	83.41	25.62	24.40	23.76	24.96
Pr	1.47	1.42	7.25	9.86	3.37	3.30	3.11	3.28
Nd	7.59	7.38	27.58	37.29	13.93	14.04	12.80	13.39
Sm	2.63	2.53	6.15	8.13	3.59	3.68	3.24	3.41
Eu	0.96	0.91	1.89	2.32	1.01	1.14	1.16	1.19
Gd	3.19	3.12	5.99	7.75	3.56	3.94	3.43	3.59
Tb	0.64	0.61	1.00	1.28	0.59	0.68	0.61	0.62
Dy	4.18	4.06	6.23	7.88	3.67	4.44	3.96	4.09
Ho	0.84	0.80	1.24	1.56	0.73	0.90	0.80	0.83
Er	2.52	2.44	3.50	4.41	1.99	2.57	2.27	2.39
Tm	0.39	0.38	0.56	0.69	0.31	0.41	0.36	0.37
Yb	2.58	2.46	3.32	4.17	1.89	2.54	2.21	2.28
Lu	0.40	0.39	0.53	0.67	0.30	0.41	0.35	0.37
Hf	1.59	1.49	4.60	5.63	2.52	2.58	2.23	2.26
Ta	0.19	0.19	0.78	1.10	0.56	0.60	0.51	0.51
Th	0.12	0.11	6.35	9.34	3.39	1.77	2.07	2.13
U	0.06	0.06	0.91	1.32	0.58	0.30	0.35	0.39

Table C.2. contd.

Sample	MMB 08-7	MMB 08-8	MMC 08-1	MMC 08-2	MMC 08-3	MMC 08-4	MMC 08-5	MMC 08-7
Major elements (wt. %)								
TiO_2	1.43	1.38	1.44	1.37	1.49	0.49	0.52	0.49
MnO	0.19	0.22	0.21	0.21	0.23	0.13	0.17	0.16
$Fe_2O_3(T)$	11.22	13.42	13.91	14.74	16.44	9.80	11.18	11.11
Trace elements (ppm)								
V	319	324	400	375	404	231	235	245
Cr	63	169	163	129	134	1113	1490	1613
Co	22.7	57.5	47.5	52.5	60.2	58.9	70.2	70.7
Ni	40	452	104	107	108	357	517	585
Cu	145	113	145	168	189	97	68	91
Zn	101	107	122	119	150	74	59	59
Ga	17.4	18.4	16.5	18.3	17.7	12.2	11.4	10.8
Rb	0.2	14.2	12.7	7.8	1.5	3.2	1.1	5.7
Sr	59	224	134	154	123	254	27	34
Y	25.3	28.3	33.1	30.7	34.7	16.0	15.2	14.3
Zr	115.1	113.9	90.2	75.8	77.0	46.8	36.4	39.1
Nb	11.03	10.67	5.41	4.45	4.22	2.83	1.64	1.95
Mo								
Cs	0.21	0.31	0.33	0.32	0.48	0.27	0.33	0.98
Ba	50	904	86	44	15	54	28	65
La	8.24	14.69	4.92	4.49	4.30	4.97	1.39	2.00
Ce	19.77	30.91	12.85	11.69	11.61	10.74	3.88	5.16
Pr	2.70	3.98	2.14	1.87	1.93	1.58	0.71	0.83
Nd	11.07	15.90	10.49	9.29	9.88	6.68	3.76	4.12
Sm	2.91	3.94	3.36	3.01	3.28	1.86	1.42	1.39
Eu	0.84	1.32	1.13	1.01	1.19	0.56	0.51	0.50
Gd	3.22	4.10	4.00	3.64	4.14	2.04	1.74	1.71
Tb	0.60	0.71	0.74	0.75	0.86	0.35	0.32	0.37
Dy	4.18	4.61	4.85	4.47	5.19	2.46	2.32	2.23
Ho	0.87	0.94	0.97	0.87	1.01	0.49	0.47	0.42
Er	2.51	2.71	2.92	2.64	3.05	1.44	1.36	1.28
Tm	0.40	0.42	0.47	0.43	0.49	0.23	0.22	0.20
Yb	2.45	2.62	3.01	2.69	3.10	1.48	1.38	1.31
Lu	0.38	0.42	0.47	0.43	0.50	0.22	0.21	0.20
Hf	2.81	2.77	2.34	1.99	2.12	1.31	1.04	1.02
Ta	0.61	0.62	0.34	0.29	0.30	0.20	0.11	0.13
Th	3.01	3.01	0.39	0.40	0.27	1.22	0.09	0.45
U	0.50	0.54	0.15	0.13	0.09	0.32	0.05	0.15

Table C.2. contd.

Sample	MMC 08-8	MMC 08-9	MMC 08-10	MMC 08-11	MMC 08-14	MMC 08-15	MMC 08-16	MMC 08-17
Major elements (wt. %)								
TiO_2	0.54	0.56	0.68	1.01	0.51	0.53	0.59	0.94
MnO	0.16	0.17	0.18	0.17	0.18	0.12	0.18	0.16
Fe_2O_3(T)	10.99	11.40	12.56	12.22	12.39	8.19	11.66	11.84
Trace elements (ppm)								
V	235	240	249	283	188	244	251	358
Cr	1311	1493	1278	154	1911	980	654	228
Co	64.8	68.7	72.6	47.3	83.2	64.2	52.9	47.7
Ni	516	609	535	110	780	482	210	110
Cu	142	102	64	92	136	143	95	131
Zn	79	106	90	128	80	326	108	74
Ga	12.3	10.9	12.7	15.9	11.6	15.9	14.6	16.2
Rb	1.8	3.0	3.3	1.3	3.4	4.6	64.9	0.7
Sr	61	82	58	204	12	208	104	177
Y	16.1	15.3	17.0	22.2	14.9	17.5	19.2	19.9
Zr	38.2	32.3	50.3	56.5	47.2	50.3	52.0	49.2
Nb	2.03	1.83	2.31	2.94	1.57	2.65	2.39	3.10
Mo								
Cs	0.19	0.56	0.42	0.28	0.34	0.49	0.75	0.24
Ba	20	15	12	16	24	72	196	11
La	3.05	1.74	2.04	3.60	1.87	4.53	4.63	2.94
Ce	7.33	4.68	5.69	8.86	4.96	9.75	9.90	7.69
Pr	1.15	0.80	0.97	1.42	0.83	1.63	1.49	1.25
Nd	5.31	4.17	4.97	6.90	4.24	7.09	6.57	6.35
Sm	1.63	1.40	1.66	2.19	1.40	2.03	1.98	2.05
Eu	0.62	0.50	0.60	0.74	0.50	0.63	0.68	0.76
Gd	1.95	1.79	2.08	2.70	1.78	2.35	2.27	2.52
Tb	0.35	0.37	0.44	0.56	0.38	0.41	0.40	0.52
Dy	2.42	2.29	2.60	3.36	2.26	2.60	2.81	3.05
Ho	0.49	0.44	0.50	0.64	0.44	0.55	0.57	0.58
Er	1.43	1.32	1.50	1.94	1.29	1.57	1.68	1.70
Tm	0.23	0.21	0.23	0.31	0.20	0.27	0.27	0.27
Yb	1.44	1.32	1.45	1.93	1.29	1.59	1.73	1.67
Lu	0.22	0.21	0.23	0.30	0.21	0.27	0.26	0.27
Hf	1.08	0.87	1.28	1.48	1.16	1.49	1.37	1.33
Ta	0.13	0.12	0.15	0.20	0.10	0.21	0.18	0.21
Th	0.15	0.12	0.14	0.42	0.09	1.22	1.01	0.17
U	0.07	0.05	0.05	0.14	0.04	0.48	0.33	0.06

Table C.2. contd.

Sample	MMC 08-18	MMC 08-19	MMC 08-20	MMC 08-21	MMC 08-22	MMC 08-23	MMC 08-24	MMC 08-25
Major elements (wt. %)								
TiO_2	0.96	0.52	0.52	0.41	0.57	0.46	0.63	0.56
MnO	0.18	0.18	0.16	0.16	0.18	0.17	0.17	0.17
Fe_2O_3(T)	12.20	12.56	11.33	10.82	12.05	10.96	11.69	11.65
Trace elements (ppm)								
V	309	235	231	211	234	212	272	246
Cr	372	1758	1422	2026	1178	1554	830	1667
Co	50.3	80.2	70.2	76.0	73.6	67.9	59.0	78.7
Ni	143	696	536	679	516	582	355	657
Cu	128	87	131	61	178	106	142	81
Zn	110	95	59	107	180	76	71	101
Ga	16.0	12.2	11.4	11.6	11.7	11.3	14.0	11.2
Rb	0.3	10.5	3.1	0.8	5.4	0.3	8.6	2.4
Sr	193	118	31	54	93	45	185	60
Y	20.2	15.2	15.7	13.2	15.8	14.7	19.4	15.7
Zr	49.4	85.7	36.3	32.9	32.4	30.9	86.1	36.4
Nb	3.09	1.88	1.77	1.75	1.65	1.56	2.62	1.70
Mo								
Cs	0.23	0.51	0.18	0.12	0.31	0.08	0.40	0.36
Ba	8	23	9	9	35	5	41	25
La	2.88	1.79	1.82	3.17	2.31	1.69	2.18	2.11
Ce	7.59	4.88	4.76	7.03	5.86	4.49	5.98	5.58
Pr	1.25	0.82	0.82	1.07	0.96	0.78	1.01	0.91
Nd	6.30	4.22	4.17	4.85	5.10	3.94	5.21	4.59
Sm	2.05	1.46	1.46	1.43	1.55	1.38	1.74	1.51
Eu	0.75	0.54	0.50	0.50	0.56	0.50	0.69	0.53
Gd	2.52	1.81	1.75	1.59	1.95	1.67	2.28	1.89
Tb	0.51	0.39	0.32	0.27	0.41	0.29	0.47	0.40
Dy	3.08	2.31	2.33	1.96	2.49	2.16	2.86	2.41
Ho	0.59	0.45	0.47	0.39	0.47	0.44	0.56	0.46
Er	1.74	1.32	1.39	1.19	1.44	1.33	1.67	1.37
Tm	0.27	0.21	0.22	0.19	0.22	0.21	0.26	0.22
Yb	1.74	1.31	1.41	1.18	1.44	1.35	1.67	1.37
Lu	0.28	0.21	0.21	0.19	0.22	0.21	0.26	0.22
Hf	1.28	1.94	1.03	0.95	0.92	0.92	2.05	0.97
Ta	0.20	0.11	0.12	0.13	0.09	0.11	0.15	0.11
Th	0.17	0.11	0.12	0.73	0.17	0.09	0.14	0.11
U	0.06	0.06	0.06	0.29	0.06	0.05	0.08	0.04

Table C.2. contd.

Sample	MMC 08-26	MMC 08-27	MMC 08-28	MME 08-1	MME 08-2	MME 08-3	MME 08-4	MME 08-5
Major elements (wt. %)								
TiO_2	0.63	0.49	0.52	0.76	1.93	1.55	1.08	0.45
MnO	0.17	0.16	0.18	0.14	0.12	0.18	0.09	0.08
Fe_2O_3(T)	11.62	11.05	11.29	9.18	11.05	12.84	7.72	4.15
Trace elements (ppm)								
V	256	227	242	236	233	381	227	109
Cr	1340	1601	1002	362	50	14	54	36
Co	64.9	68.6	61.3	43.1	42.3	52.7	62.1	12.7
Ni	498	579	359	137	77	46	94	35
Cu	102	88	100	152	149	130	130	29
Zn	110	109	100	84	117	247	142	56
Ga	12.7	11.6	12.2	17.3	23.0	19.3	13.2	11.8
Rb	2.8	4.0	4.7	29.3	14.9	76.5	44.3	98.5
Sr	88	83	113	632	401	192	61	91
Y	17.1	15.0	16.3	19.2	23.8	32.6	26.4	29.3
Zr	44.8	35.1	34.5	52.3	158.2	123.8	132.7	405.7
Nb	2.23	1.86	1.84	4.85	9.67	12.37	14.00	10.64
Mo								
Cs	0.30	0.18	0.46	0.35	0.42	11.00	0.53	1.90
Ba	36	28	26	1244	209	469	452	624
La	2.00	2.07	1.93	8.91	16.61	21.60	26.91	23.57
Ce	5.45	5.26	5.02	17.23	36.43	40.19	46.31	48.83
Pr	0.97	0.89	0.86	2.30	5.20	5.06	5.58	6.25
Nd	4.94	4.38	4.37	9.65	22.39	20.07	20.87	23.48
Sm	1.72	1.50	1.49	2.41	5.34	4.62	4.35	4.86
Eu	0.57	0.50	0.54	1.19	1.78	1.81	1.38	1.06
Gd	2.05	1.77	1.86	2.58	4.87	4.68	4.10	4.26
Tb	0.37	0.30	0.33	0.42	0.74	0.80	0.64	0.69
Dy	2.63	2.24	2.41	2.82	4.10	4.83	3.86	4.19
Ho	0.53	0.45	0.49	0.55	0.71	0.94	0.75	0.82
Er	1.55	1.37	1.47	1.65	1.94	2.80	2.21	2.57
Tm	0.24	0.22	0.24	0.26	0.28	0.44	0.35	0.43
Yb	1.54	1.39	1.52	1.60	1.69	2.83	2.22	2.87
Lu	0.24	0.22	0.24	0.24	0.24	0.43	0.34	0.44
Hf	1.21	1.00	1.02	1.37	3.66	2.89	3.07	8.03
Ta	0.15	0.12	0.12	0.36	0.73	1.06	0.93	0.87
Th	0.15	0.31	0.14	1.06	1.73	4.44	5.60	6.75
U	0.07	0.12	0.07	0.22	0.41	1.03	0.61	4.40

Table C.2. contd.

Sample	MME 08-6	MME 08-7	MMFR 08-1	MMFR 08-2	MMFR 08-3	MMFR 08-4	MMFR 08-5	MMFR 08-6
Major elements (wt. %)								
TiO_2	0.45	0.96	1.87	0.61	0.56	0.69	0.59	1.69
MnO	0.08	0.07	0.17	0.18	0.18	0.16	0.17	0.22
Fe_2O_3(T)	3.47	5.65	14.21	12.16	11.82	10.94	11.39	15.05
Trace elements (ppm)								
V	74	153	468	262	245	279	271	421
Cr	25	50	129	1095	1351	338	726	163
Co	10.1	45.8	46.7	65.6	70.3	47.7	55.1	48.2
Ni	10	65	69	437	550	87	237	82
Cu	26	67	166	117	126	121	119	182
Zn	51	87	95	207	100	108	112	140
Ga	10.7	12.4	19.2	14.8	12.8	12.4	13.6	19.5
Rb	88.5	53.5	2.9	1.0	0.7	0.4	2.7	8.4
Sr	99	108	86	107	32	41	87	87
Y	29.4	29.3	39.3	17.7	16.1	20.3	19.3	38.9
Zr	401.3	122.2	124.3	39.8	37.7	51.0	45.4	106.7
Nb	10.58	13.30	7.04	2.08	2.04	2.56	2.33	6.14
Mo								
Cs	1.56	0.62	0.30	0.26	0.28	0.17	0.18	0.31
Ba	549	554	55	15	13	13	29	102
La	26.35	26.05	6.51	2.74	2.15	2.67	2.43	6.70
Ce	51.02	46.26	17.13	6.78	5.78	7.15	6.44	16.68
Pr	6.71	5.51	2.68	1.07	0.96	1.18	1.07	2.65
Nd	24.86	20.78	12.99	5.34	4.89	5.69	5.09	12.76
Sm	4.92	4.32	3.96	1.70	1.60	1.99	1.78	3.91
Eu	1.05	1.42	1.27	0.78	0.46	0.69	0.56	1.34
Gd	4.41	4.22	4.81	2.17	1.94	2.47	2.25	4.62
Tb	0.70	0.67	1.00	0.45	0.42	0.49	0.44	0.97
Dy	4.21	4.06	5.99	2.76	2.49	3.18	2.85	5.71
Ho	0.82	0.80	1.15	0.53	0.48	0.60	0.54	1.12
Er	2.53	2.42	3.50	1.58	1.44	1.82	1.62	3.42
Tm	0.41	0.38	0.57	0.25	0.23	0.29	0.26	0.55
Yb	2.72	2.38	3.60	1.60	1.43	1.87	1.68	3.52
Lu	0.43	0.37	0.57	0.26	0.23	0.30	0.26	0.57
Hf	8.09	2.88	3.16	1.09	1.04	1.45	1.26	2.78
Ta	0.73	1.05	0.48	0.15	0.14	0.16	0.14	0.41
Th	6.37	5.00	0.74	0.15	0.13	0.16	0.17	0.55
U	3.61	0.54	0.24	0.05	0.05	0.06	0.06	0.19

Table C.2. contd.

Sample	MMFR 08-7	MMFR 08-8	MMFR 08-9	MMFR 08-10	MMFR 08-11	MMFR 08-12	MMFR 08-13	MMFR 08-14
Major elements (wt. %)								
TiO_2	1.77	0.46	0.56	0.47	0.64	0.60	0.47	0.48
MnO	0.23	0.19	0.18	0.19	0.17	0.16	0.18	0.16
Fe_2O_3(T)	15.84	12.83	12.11	12.73	10.80	10.47	12.21	11.44
Trace elements (ppm)								
V	411	209	250	204	289	286	208	222
Cr	123	1670	1013	2194	315	231	1657	1734
Co	50.8	88.1	68.0	86.1	45.3	44.5	75.4	77.0
Ni	69	762	392	823	129	137	529	656
Cu	114	62	106	53	122	139	63	85
Zn	135	90	185	84	98	100	110	88
Ga	19.5	10.9	12.8	10.8	14.7	13.9	12.0	12.6
Rb	5.0	0.3	3.0	1.3	2.9	2.2	2.7	1.5
Sr	232	7	61	21	96	86	35	14
Y	38.7	13.9	17.3	13.9	20.1	19.7	15.4	15.6
Zr	111.0	29.0	39.7	30.4	46.3	39.9	36.3	36.1
Nb	7.50	1.48	2.02	1.64	2.20	2.10	1.82	1.69
Mo								
Cs	0.33	0.29	0.43	0.46	0.41	0.46	0.84	0.45
Ba	55	2	26	6	15	26	9	5
La	7.71	1.55	2.11	1.97	2.03	2.15	1.76	1.29
Ce	18.75	4.32	5.71	4.99	5.59	5.85	4.91	3.96
Pr	2.88	0.73	0.95	0.82	0.96	0.99	0.83	0.72
Nd	13.68	3.86	4.86	4.10	4.69	5.16	4.06	3.72
Sm	4.05	1.35	1.63	1.31	1.70	1.73	1.42	1.41
Eu	1.33	0.44	0.54	0.45	0.66	0.64	0.51	0.46
Gd	4.75	1.69	2.02	1.67	2.22	2.18	1.82	1.82
Tb	0.98	0.36	0.43	0.35	0.45	0.49	0.36	0.37
Dy	5.69	2.16	2.62	2.13	2.91	2.94	2.33	2.38
Ho	1.11	0.41	0.51	0.41	0.57	0.58	0.45	0.46
Er	3.32	1.22	1.53	1.24	1.74	1.77	1.34	1.36
Tm	0.53	0.20	0.25	0.19	0.28	0.29	0.22	0.21
Yb	3.38	1.24	1.53	1.23	1.86	1.85	1.38	1.39
Lu	0.54	0.20	0.24	0.19	0.30	0.30	0.21	0.22
Hf	2.84	0.82	1.06	0.85	1.31	1.15	1.04	1.07
Ta	0.49	0.10	0.13	0.11	0.14	0.14	0.12	0.11
Th	0.82	0.08	0.14	0.10	0.12	0.14	0.11	0.10
U	0.23	0.04	0.05	0.04	0.05	0.07	0.05	0.04

Table C.2. contd.

Sample	MMFR 08-15	MMFR 08-16	MMFR 08-17	MMFR 08-18	MMFR 08-21	MMFR 08-22	MMFR 08-23	MMFR 08-24
Major elements (wt. %)								
TiO_2	0.23	0.35	1.07	0.27	1.27	0.19	0.27	0.06
MnO	0.14	0.19	0.16	0.17	0.20	0.16	0.16	0.06
Fe_2O_3(T)	7.51	12.01	14.22	11.71	14.20	9.70	11.72	10.75
Trace elements (ppm)								
V	180	182	358	156	348	200	184	53
Cr	222	2642	27	4058	7	2691	717	6510
Co	45.1	94.1	38.9	95.3	46.0	45.1	84.2	137.3
Ni	173	964	36	1488	57	343	611	2854
Cu	19	25	30	57	120	58	609	10
Zn	53	136	104	126	121	27	71	53
Ga	11.6	9.3	18.7	7.7	18.6	5.1	7.0	3.3
Rb	9.9	3.4	73.2	7.2	28.8	0.7	0.7	0.3
Sr	106	15	158	11	118	6	4	3
Y	8.2	11.8	25.9	8.8	29.5	7.2	8.8	1.1
Zr	11.0	26.5	78.9	24.1	105.0	8.6	18.3	2.3
Nb	0.57	1.31	5.53	1.32	4.87	0.32	1.10	0.16
Mo								
Cs	0.55	1.01	5.79	0.74	0.88	0.34	0.31	0.26
Ba	72	6	197	3	142	7	9	0
La	1.02	1.68	11.10	2.87	12.49	0.51	0.96	0.40
Ce	2.49	4.29	22.75	5.75	26.01	1.42	2.57	0.83
Pr	0.40	0.68	3.01	0.79	3.39	0.26	0.43	0.12
Nd	2.09	3.35	12.44	3.45	14.36	1.42	2.05	0.56
Sm	0.75	1.09	3.15	0.95	3.56	0.56	0.73	0.17
Eu	0.33	0.37	0.93	0.38	1.14	0.17	0.15	0.05
Gd	0.96	1.35	3.46	1.09	4.02	0.78	0.94	0.15
Tb	0.21	0.30	0.67	0.23	0.78	0.18	0.19	0.04
Dy	1.31	1.79	3.85	1.37	4.51	1.13	1.30	0.24
Ho	0.25	0.35	0.73	0.26	0.86	0.23	0.26	0.05
Er	0.75	1.05	2.17	0.80	2.62	0.68	0.80	0.15
Tm	0.12	0.17	0.34	0.13	0.42	0.11	0.13	0.02
Yb	0.75	1.03	2.16	0.81	2.68	0.69	0.92	0.16
Lu	0.12	0.16	0.35	0.13	0.43	0.11	0.15	0.03
Hf	0.38	0.71	1.99	0.67	2.70	0.27	0.58	0.07
Ta	0.04	0.09	0.36	0.10	0.36	0.02	0.07	0.01
Th	0.13	0.11	2.52	0.57	2.60	0.05	0.12	0.06
U	0.04	0.06	0.68	0.19	0.59	0.02	0.06	0.02

Table C.2. contd.

Sample	MMFR 08-25	MMFR 08-26	MMFR 08-28	MMG 08-3	MMG 08-4	MMG 08-5	MMG 08-7	MMH 08-1
Major elements (wt. %)								
TiO_2	0.08	0.15	0.24	1.67	1.68	1.63	1.66	1.76
MnO	0.09	0.14	0.15	0.26	0.23	0.21	0.41	0.21
Fe_2O_3(T)	6.67	6.96	7.67	16.01	11.29	11.85	12.89	13.31
Trace elements (ppm)								
V	89	169	154	367	339	326	352	326
Cr	840	3978	394	24	22	22	23	12
Co	60.2	69.9	39.9	60.6	32.0	44.2	32.9	52.1
Ni	321	298	254	51	19	42	21	18
Cu	63	29	14	114	122	115	125	70
Zn	48	57	13	112	118	120	93	112
Ga	9.7	4.6	12.0	20.8	19.9	19.0	20.3	20.3
Rb	39.4	1.6	0.9	219.9	57.1	310.8	97.8	8.1
Sr	128	17	41	93	233	135	175	241
Y	2.8	6.4	8.6	33.9	32.5	32.1	33.7	35.4
Zr	4.3	11.2	13.8	161.4	160.7	150.4	155.7	182.6
Nb	0.14	0.21	0.79	19.09	18.69	17.50	18.18	21.14
Mo								
Cs	3.08	0.25	0.29	8.67	9.52	8.25	5.32	0.18
Ba	27	5	5	909	385	902	911	218
La	0.35	0.66	1.35	23.55	21.96	25.65	22.61	24.28
Ce	0.84	1.54	3.19	44.11	43.69	48.05	45.84	52.61
Pr	0.14	0.25	0.51	5.26	5.37	5.82	5.67	6.47
Nd	0.75	1.27	2.44	20.77	21.15	22.65	22.28	24.41
Sm	0.27	0.52	0.77	4.92	4.94	5.33	5.17	5.67
Eu	0.14	0.21	0.21	1.23	1.74	1.31	1.43	1.64
Gd	0.32	0.71	1.02	4.88	4.89	5.26	5.21	5.27
Tb	0.08	0.15	0.22	0.84	0.82	0.86	0.88	0.91
Dy	0.51	1.03	1.34	5.49	5.32	5.32	5.58	5.83
Ho	0.10	0.19	0.26	1.13	1.08	1.06	1.13	1.18
Er	0.30	0.59	0.79	3.21	3.13	3.00	3.20	3.47
Tm	0.05	0.09	0.12	0.51	0.50	0.47	0.50	0.55
Yb	0.30	0.59	0.76	3.16	3.14	2.98	3.10	3.52
Lu	0.05	0.09	0.12	0.51	0.50	0.48	0.50	0.56
Hf	0.13	0.31	0.43	3.89	3.85	3.62	3.77	4.39
Ta	0.01	0.01	0.06	1.07	0.99	0.96	1.06	1.13
Th	0.03	0.04	0.25	5.14	5.06	4.86	5.11	7.28
U	0.02	0.03	0.08	1.14	1.12	1.08	1.13	1.35

Table C.2. contd.

Sample	MMH 08-4	MMH 08-5	MMH 08-6	MMH 08-7	MMH 08-8	MMH 08-9	MMH 08-11	MMH 08-12
Major elements (wt. %)								
TiO_2	0.96	1.72	0.82	1.02	0.93	1.24	1.80	1.83
MnO	0.18	0.21	0.01	0.19	0.18	0.22	0.23	0.19
Fe_2O_3(T)	10.24	14.04	1.28	10.91	10.17	13.18	12.74	12.80
Trace elements (ppm)								
V	237	323	39	278	298	342	293	268
Cr	52	31	30	232	310	296	106	29
Co	41.0	48.8	5.7	48.6	49.9	48.2	53.0	54.1
Ni	57	94	35	90	195	538	55	31
Cu	83	44	1	96	110	68	45	49
Zn	89	122	17	94	94	117	108	112
Ga	16.2	19.7	11.4	15.3	14.7	18.4	19.6	21.8
Rb	7.6	52.1	192.8	1.0	2.9	14.5	13.4	28.2
Sr	211	170	16	112	117	448	197	234
Y	19.7	37.8	48.3	20.8	19.3	25.2	24.9	41.5
Zr	84.5	191.8	348.8	59.2	51.9	93.3	121.5	235.9
Nb	8.36	22.16	22.84	2.39	2.15	9.16	13.87	17.09
Mo								
Cs	0.17	2.05	0.47	0.22	0.24	0.24	0.12	0.12
Ba	154	347	2066	29	40	206	412	966
La	11.16	29.24	41.83	2.55	3.08	12.66	12.74	40.43
Ce	23.03	58.96	82.66	7.24	7.53	27.18	29.17	80.35
Pr	2.87	7.05	9.12	1.21	1.23	3.43	3.94	9.64
Nd	11.33	26.80	32.13	6.21	5.88	13.54	16.41	36.30
Sm	2.65	5.99	6.49	2.15	1.90	3.36	4.04	7.78
Eu	0.99	1.67	1.37	0.80	0.72	1.18	1.37	2.20
Gd	2.75	5.69	6.48	2.61	2.29	3.48	4.02	7.27
Tb	0.47	0.97	1.20	0.49	0.43	0.62	0.67	1.16
Dy	3.16	6.11	7.81	3.33	2.91	4.08	4.30	6.99
Ho	0.65	1.23	1.56	0.69	0.61	0.85	0.85	1.37
Er	1.90	3.53	4.44	2.01	1.74	2.44	2.40	3.82
Tm	0.31	0.57	0.71	0.33	0.29	0.40	0.37	0.59
Yb	1.92	3.45	4.25	2.01	1.78	2.46	2.27	3.59
Lu	0.32	0.56	0.67	0.33	0.29	0.40	0.36	0.57
Hf	1.94	4.56	8.40	1.39	1.25	2.32	2.81	5.50
Ta	0.52	1.18	1.48	0.18	0.16	0.54	0.83	0.89
Th	2.75	7.24	21.61	0.16	0.17	1.92	1.42	6.27
U	0.49	1.34	3.20	0.03	0.04	0.39	0.26	0.74

Table C.2. contd.

Sample	MMH 08-13	MMH 08-14	MMH 08-15b	MMH 08-18	MMH 08-19	MMH 08-20	MMH 08-21	MMH 08-22
Major elements (wt. %)								
TiO_2	1.72	1.77	3.25	2.65	1.27	1.97	1.92	1.79
MnO	0.20	0.22	0.17	0.20	0.21	0.23	0.22	0.23
Fe_2O_3(T)	12.68	13.23	22.31	16.40	12.72	13.06	13.22	13.11
Trace elements (ppm)								
V	286	325	745	377	302	318	342	290
Cr	151	121	19	546	90	111	107	91
Co	49.4	48.1	80.7	61.2	50.6	56.8	53.9	50.4
Ni	81	119	11	185	41	60	58	42
Cu	111	117	5	62	132	53	34	158
Zn	100	100	258	95	133	108	134	158
Ga	18.6	19.2	33.9	21.3	16.7	21.4	17.8	17.0
Rb	22.4	9.9	7.9	13.7	17.0	11.0	14.8	10.5
Sr	367	298	49	381	369	344	281	118
Y	29.5	37.6	42.6	22.9	25.6	30.8	28.2	29.0
Zr	147.5	181.3	282.4	153.8	93.7	144.1	137.5	158.9
Nb	21.21	17.39	15.77	20.64	8.99	16.83	16.04	18.12
Mo								
Cs	0.20	0.10	0.22	0.29	0.51	0.18	0.16	0.13
Ba	865	414	716	209	1160	527	406	330
La	18.07	23.25	38.69	12.74	13.30	17.88	16.63	19.23
Ce	39.50	49.27	75.51	31.52	27.77	39.23	36.81	39.68
Pr	5.08	6.19	8.87	4.53	3.49	5.21	4.88	5.00
Nd	20.50	24.67	33.02	19.98	13.85	21.48	20.41	19.47
Sm	4.90	5.78	7.11	5.19	3.39	5.25	5.04	4.43
Eu	1.56	1.76	2.17	1.09	1.24	1.99	1.53	1.28
Gd	4.74	5.78	6.69	4.78	3.55	5.08	4.86	4.18
Tb	0.78	0.96	1.13	0.76	0.62	0.85	0.79	0.72
Dy	4.96	6.17	7.08	4.37	4.08	5.24	4.92	4.77
Ho	0.98	1.24	1.44	0.80	0.83	1.01	0.97	0.99
Er	2.76	3.51	4.11	2.02	2.40	2.80	2.63	2.98
Tm	0.43	0.54	0.65	0.29	0.38	0.44	0.41	0.50
Yb	2.66	3.38	4.07	1.66	2.41	2.59	2.52	3.16
Lu	0.42	0.53	0.65	0.25	0.39	0.41	0.39	0.51
Hf	3.48	4.34	6.75	3.91	2.17	3.37	3.30	3.75
Ta	1.20	0.90	0.85	1.25	0.48	0.95	0.96	0.97
Th	3.02	3.83	9.71	1.43	1.85	1.68	1.66	3.15
U	0.61	0.52	0.96	0.37	0.38	0.31	0.32	0.45

Table C.2. contd.

Sample	MMH 08-23b	MMHS 08-3	MMHS 08-6	MMHS 08-9	MMK 08-1	MMK 08-2	MMK 08-3	MMK 08-4
Major elements (wt. %)								
TiO_2	2.85	1.24	2.08	3.23	1.05	1.01	1.06	1.12
MnO	0.24	0.20	0.23	0.31	0.22	0.17	0.14	0.13
Fe_2O_3(T)	15.02	13.14	17.05	20.43	11.97	10.72	9.24	9.28
Trace elements (ppm)								
V	386	266	448	714	327	155	196	151
Cr	34	60	22	2	101	256	469	74
Co	54.2	54.6	62.9	65.4	51.0	54.1	45.8	48.2
Ni	27	107	60	36	87	162	84	152
Cu	209	50	90	165	161	57	30	10
Zn	138	87	124	181	101	79	111	95
Ga	23.3	19.0	20.7	22.5	16.6	18.3	19.3	14.4
Rb	21.3	5.6	12.4	16.7	5.4	15.1	4.8	5.3
Sr	252	275	212	184	135	455	427	181
Y	56.7	24.0	30.8	38.3	19.0	12.7	14.8	13.9
Zr	286.6	85.1	110.5	145.1	47.1	62.8	63.6	80.6
Nb	30.53	16.85	24.67	29.25	3.00	6.16	5.30	7.12
Mo								
Cs	1.17	0.47	1.23	1.45	0.21	0.27	0.20	0.39
Ba	274	84	161	230	39	301	115	47
La	45.73	13.34	17.89	21.12	3.08	8.25	7.51	8.72
Ce	96.57	27.33	34.54	43.82	8.14	17.63	16.37	19.05
Pr	11.71	3.55	4.65	5.57	1.31	2.35	2.24	2.56
Nd	45.41	14.59	16.87	23.04	6.32	9.70	9.50	10.65
Sm	10.09	3.34	4.43	5.32	2.09	2.30	2.35	2.57
Eu	2.68	1.12	1.54	1.78	0.78	1.02	1.00	0.82
Gd	9.52	3.42	4.98	5.67	2.46	2.21	2.34	2.38
Tb	1.54	0.65	0.98	1.04	0.45	0.35	0.38	0.39
Dy	9.47	3.73	4.78	5.94	3.08	2.21	2.37	2.42
Ho	1.88	0.71	0.95	1.12	0.65	0.43	0.47	0.47
Er	5.19	2.10	3.01	3.35	1.83	1.18	1.30	1.33
Tm	0.81	0.34	0.43	0.53	0.29	0.18	0.20	0.21
Yb	4.94	2.11	2.96	3.36	1.78	1.10	1.23	1.24
Lu	0.78	0.33	0.45	0.53	0.29	0.18	0.19	0.19
Hf	6.95	2.10	3.00	3.45	1.08	1.39	1.37	1.82
Ta	1.73	1.05	1.65	1.84	0.18	0.39	0.30	0.43
Th	8.89	1.77	2.24	2.84	0.28	0.63	0.64	0.94
U	1.18	0.43	0.56	0.77	0.08	0.12	0.11	0.20

Table C.2. contd.

Sample	MMK 08-5	MMK 08-6	MMK 08-7	MMK 08-10	MMK 08-11	MMT 08-1	MMT 08-2	MMT 08-3
Major elements (wt. %)								
TiO_2	1.32	1.75	1.20	1.61	2.98	0.09	0.06	0.11
MnO	0.19	0.20	0.14	0.18	0.23	0.11	0.10	0.13
Fe_2O_3(T)	12.12	12.28	10.05	11.41	14.61	11.01	10.85	9.37
Trace elements (ppm)								
V	176	220	167	209	375	59	130	166
Cr	91	102	82	100	145	4230	5535	3803
Co	60.4	57.3	58.1	53.1	52.2	119.3	100.6	36.4
Ni	202	248	136	103	105	2295	2856	920
Cu	27	48	64	57	13	12	79	50
Zn	127	151	88	123	82	69	122	329
Ga	17.3	19.5	18.0	18.4	22.3	4.7	3.3	5.7
Rb	9.9	11.7	21.0	18.7	1.6	8.3	0.9	0.6
Sr	424	441	418	429	267	18	4	8
Y	20.2	24.6	17.8	21.8	28.4	4.1	2.4	5.2
Zr	91.3	121.4	87.1	108.6	187.2	16.7	12.3	11.6
Nb	8.51	11.32	8.01	9.47	32.34	0.91	0.57	0.46
Mo								
Cs	0.26	0.29	0.56	0.43	0.16	0.63	0.33	0.45
Ba	205	380	335	242	62	54	5	6
La	12.38	13.07	11.57	13.32	18.68	3.34	2.53	2.04
Ce	27.22	29.81	25.15	29.12	45.81	6.03	5.03	3.37
Pr	3.59	4.09	3.37	3.90	6.45	0.68	0.64	0.49
Nd	14.62	17.26	13.72	16.20	27.35	2.40	2.38	1.93
Sm	3.47	4.26	3.20	3.90	6.77	0.55	0.40	0.51
Eu	1.37	1.59	1.24	1.42	2.28	0.17	0.10	0.22
Gd	3.32	4.14	3.08	3.72	6.10	0.57	0.37	0.58
Tb	0.54	0.68	0.49	0.60	0.95	0.10	0.05	0.10
Dy	3.34	4.18	3.03	3.73	5.37	0.63	0.35	0.72
Ho	0.65	0.82	0.60	0.73	0.96	0.12	0.07	0.14
Er	1.84	2.25	1.65	2.05	2.52	0.37	0.21	0.45
Tm	0.28	0.34	0.25	0.31	0.37	0.06	0.04	0.07
Yb	1.67	2.12	1.52	1.90	2.09	0.40	0.25	0.52
Lu	0.26	0.33	0.24	0.30	0.31	0.06	0.04	0.09
Hf	2.08	2.90	2.02	2.56	4.51	0.52	0.36	0.35
Ta	0.51	0.67	0.46	0.61	1.84	0.06	0.04	0.04
Th	1.19	1.39	1.13	1.26	2.21	0.90	0.47	0.44
U	0.24	0.31	0.22	0.24	0.54	0.31	0.53	2.57

Table C.2. contd.

Sample	MMT 08-4	MMT 08-5	MMT 08-6	MMT 08-7	MMT 08-9	MMT 08-12	MMT 08-13	MMT 08-14
Major elements (wt. %)								
TiO_2	0.03	0.18	0.22	0.21	0.37	0.11	0.11	0.32
MnO	0.12	0.23	0.20	0.16	0.13	0.13	0.18	0.11
Fe_2O_3(T)	13.23	11.57	16.11	6.80	14.81	11.74	8.98	11.54
Trace elements (ppm)								
V	66	188	70	58	176	70	153	193
Cr	3966	3120	1334	1041	91	2604	2327	2831
Co	131	89	137	73	31	69	80	101
Ni	3153	1608	3431	2337	574	2297	1855	1144
Cu	155	86	148	26	451	283	42	98
Zn	114	114	314	81	194	82	95	80
Ga	2.6	6.7	8.3	6.5	14.1	5.1	4.5	8.4
Rb	0.0	22.7	0.8	0.8	114.7	1.0	5.0	0.8
Sr	4	19	169	83	735	28	7	29
Y	1.4	7.2	8.2	7.8	23.9	6.4	3.7	9.6
Zr	59.1	28.1	31.2	33.5	141.2	21.1	12.2	15.1
Nb	0.67	1.02	2.21	2.21	6.63	0.74	0.40	0.23
Mo								
Cs	0.02	2.52	0.22	0.05	6.95	0.36	3.99	0.02
Ba	4	53	5	3	599	4	12	36
La	0.72	3.39	4.93	5.36	29.94	4.66	1.02	0.95
Ce	1.40	6.85	8.90	10.61	49.04	9.21	2.14	2.24
Pr	0.20	0.95	1.24	1.49	6.67	1.19	0.31	0.36
Nd	0.71	3.59	4.62	5.47	22.95	4.18	1.25	1.85
Sm	0.17	0.85	1.08	1.21	4.45	0.85	0.35	0.76
Eu	0.08	0.28	0.37	0.28	1.91	0.24	0.12	0.18
Gd	0.16	0.93	1.13	1.19	4.02	0.87	0.38	1.09
Tb	0.03	0.16	0.20	0.20	0.62	0.15	0.07	0.21
Dy	0.23	1.06	1.24	1.22	3.48	0.93	0.55	1.49
Ho	0.05	0.20	0.23	0.22	0.63	0.18	0.11	0.29
Er	0.14	0.63	0.71	0.70	1.86	0.53	0.37	0.87
Tm	0.02	0.10	0.11	0.11	0.30	0.09	0.06	0.14
Yb	0.17	0.65	0.73	0.75	1.99	0.57	0.46	0.92
Lu	0.03	0.10	0.11	0.12	0.34	0.09	0.07	0.14
Hf	1.27	0.82	0.93	1.04	3.44	0.65	0.55	0.49
Ta	0.04	0.06	0.16	0.17	0.55	0.06	0.03	0.02
Th	0.19	1.20	1.45	1.07	11.06	0.87	0.32	0.09
U	0.14	0.61	0.48	0.33	8.70	0.32	0.14	0.02

Table C.2. contd.

Sample	MMT 08-15	MMT 08-18	MMT 08-21	MMT 08-22
Major elements (wt. %)				
TiO_2	0.06	0.11	0.05	0.04
MnO	0.09	0.08	0.08	0.07
$Fe_2O_3(T)$	12.96	11.57	11.71	12.53
Trace elements (ppm)				
V	66	99	29	23
Cr	3242	2846	4066	2185
Co	139	130	117	302
Ni	4000	1171	2890	25350
Cu	178	56	37	299
Zn	78	64	86	129
Ga	4.9	3.4	2.9	1.7
Rb	0.4	1.0	5.4	5.8
Sr	4	14	5	6
Y	2.3	3.2	1.3	1.2
Zr	8.0	25.0	6.6	7.3
Nb	0.12	0.64	0.27	0.16
Mo				
Cs	0.10	0.37	1.00	1.24
Ba	4	9	5	30
La	0.51	2.31	1.19	3.76
Ce	1.22	3.59	1.99	4.52
Pr	0.17	0.46	0.24	0.41
Nd	0.70	1.80	0.83	1.22
Sm	0.22	0.43	0.17	0.17
Eu	0.06	0.07	0.04	0.05
Gd	0.26	0.44	0.18	0.17
Tb	0.05	0.08	0.03	0.03
Dy	0.39	0.48	0.22	0.21
Ho	0.08	0.10	0.04	0.04
Er	0.25	0.30	0.14	0.13
Tm	0.04	0.05	0.02	0.02
Yb	0.30	0.35	0.16	0.15
Lu	0.05	0.06	0.03	0.02
Hf	0.22	0.69	0.18	0.21
Ta	0.01	0.05	0.02	0.01
Th	0.11	0.52	0.08	0.13
U	0.03	0.36	0.07	0.09

Appendix D: Preparation of rock samples for Sr-Nd-Pb-Hf-Os isotopic analysis and results

D.1. Sample selection and initial preparation

Care was taken in sample selection to choose the least altered samples that were representative of each segment of the Circum-Superior LIP. This was achieved by examining polished thin sections the major and trace element chemistry of all the rocks samples. Samples were initially cut using a diamond-bladed mechanical rock saw to remove any weathered surfaces. The samples were then crushed to a coarse grit using a steel jaw crusher and ground into a fine powder using an agate planetary ball mill. The initial preparation steps were conducted at Cardiff University. Unfortunately it was not possible to obtain isotopic analyses from all segments of the Circum-Superior LIP as permission for a second visit to the isotopic laboratories was not granted.

D.2. Preparation for Sr-Nd-Pb isotopic analyses

D.2.1. Leaching

Samples were prepared for Sr-Nd-Pb isotopic analysis at the NERC Isotope Geosciences Laboratory (NIGL) in Keyworth under the supervision of Dr. Ian Millar. The methods for preparing samples for Sr-Nd-Pb isotopic analysis are outlined in detail in Royse et al. (1998) and Kempton & McGill (2002) and are summarised here. Approximately 0.2 g of each sample was weighed out and then leached. Leaching serves to remove secondary phases from slightly altered rocks. Leaching was achieved by adding ~5 ml of 6M HCl to each sample and heating at ~100°C for three hours. Each sample was then centrifuged for five minutes at 4000 rpm, after which the acid leachate was removed and discarded and ~5 ml of deionised water added to the remaining sample material. After half an hour the water was removed and the samples were transferred to clean Savillex beakers ready for the next stage.

D.2.2. Sample dissolution

To dissolve silicate material strong acids need to be used. To each sample beaker, ~1 ml of Teflon-distilled (TD) 16M HNO_3 was added prior to the addition of ~4 ml of TD 29M HF. The beakers were sealed and placed on the hotplate at ~60°C overnight. After being taken off the hotplate and allowed to cool, the lids were removed and the beakers returned to the hotplate until the solutions had evaporated to dryness. Once dry, ~2 ml of TD 16M HNO_3 was added to each beaker on the hotplate and allowed to evaporate to dryness. When dry, ~2 ml of TD 6M HCl was added to the beakers which were then sealed and kept on the hotplate for about half an hour. The lids were then removed and the solutions allowed to evaporate to dryness. 1 ml of 1M HBr was added to each beaker, the beakers then sealed and ready for the next stage.

D.2.3. Chemical separation of Pb

To separate the Pb fraction from the rest of the sample anion exchange columns are used. The columns are pre-cleaned polypropylene tubes fitted with a porous polyethylene frit in the tip. After setting up the columns with waste beakers beneath, one column volume of quartz-distilled (QD) 6M HCl was added to each column and allowed to drain through. Then about five drops of pre-cleaned Dowex AG1-X8 resin were added to each column. The resin was then washed by adding one column volume of TD 6M HCl to each column and allowed to drain through. This was followed by adding one column volume of deionised water to each column and allowed to drain through. The acid wash and water wash were then repeated. Afterwards, half a column volume of 1M HBr was added to each column. Clean Savillex beakers were then placed under the columns.

Each sample (currently in 1 ml of 1M HBr) was transferred to the columns using a clean pipette. Once the sample solution had eluted, half a column volume of 1M HBr was added to each column. When this had drained through, three-quarters of a column volume of 1M HBr was added to each column and allowed to drain through. The clean collector beakers were then removed and sealed and used for Sr and Nd chemical separation (see section D.2.4). Clean Savillex beakers were placed under the columns to collect the Pb fraction. This was done by adding one column volume

of TD 6M HCl and allowing to drain. 1 ml of TD 16M HNO_3 was pipetted into the Pb fraction beakers which were then transferred to the hotplate and the solutions allowed to evaporate to dryness.

D.2.4. Chemical separation of Sr and Nd

To separate Sr and Nd fractions from the rest of the sample quartz columns are used. The separation of Sr uses Dowex AG 50W-X8 resin and the separation of Nd uses S-X8 biobeads coated in bis diethylhexyl hydrogen phosphate (HDEHP).

Firstly the excess Br needs to be removed from the Sr-Nd fractions collected during the Pb chemical separation procedure. This was achieved by adding 2 ml of TD 16M HNO_3 to each sample beaker and then evaporated to dryness before adding 2 ml of 2.5M HCl to leave cold overnight.

The sample solutions were then transferred to a centrifuge tube and centrifuged for five minutes at 3000 rpm. Then 1.5 ml of the solution from the centrifuge tubes were added to the quartz columns with Dowex AG 50W-X8 resin. Afterwards, 1 ml of 2.5M HCl was added to each column to wash in the sample. This step was then repeated. An additional 45 ml of 2.5M HCl was added to each column and allowed to drain through. Clean Savillex beakers were then placed under each column and 9 ml of 2.5M HCl added to collect the Sr fraction. This solution was then evaporated to dryness on a hotplate. To collect the REE fraction, 10 ml of 6M HCl was eluted through the columns and collected in clean Savillex beakers before evaporation to dryness on a hotplate. 1 ml of 0.25M HCl was then added to each of these beakers. 0.5 ml of each solution was taken up by a clean pipette and loaded onto each quartz column with HDEHP-coated S-X8 biobeads and allowed to drain through the resin. Two steps of adding 0.5 ml of 0.25M HCl and allowing to drain through were then performed. After this, an additional 6.4 ml of 0.25M HCl was added and drained through. To collect the Nd fraction, 3.5 ml of 0.3M HCl was added to each column and collected in clean Savillex beakers. 2 µl of chlorophosphonazo III was then added to each solution before evaporation to dryness on a hotplate.

D.2.5. Loading

The Pb separates were dissolved in ~1 ml of 2% HNO_3 and doped with Tl solution in polystyrene cups that fit into the mass spectrometers. The Sr and Nd fractions were loaded onto outgassed Ta single and double filaments respectively. The filaments were outgassed at 3.5 A for ten minutes. When loading the Sr fraction, initially 1 µl of 1M H_3PO_4 was loaded onto the Ta filament at a current just below 1 A and dried to a small spot. 3 µl of deionised water was added to the Sr fraction and then 1 µl of this solution loaded onto the spot of H_3PO_4. When dried, the filament was turned to a current of ~2 A and held there for a few seconds until phosphoric fumes were liberated. For Nd, 2 µl of 0.6M HCl was added to the Nd fraction and then pipetted onto the filament which was turned up to a current just below 1 A. After the solution had dried, the current was turned down.

D.2.6. Mass spectrometric analysis

Analyses of Sr and Nd isotopes were carried out using the Thermo-Electron Triton 1 thermal ionisation mass spectrometer at NIGL. Analysis of Pb isotopes was carried out using the Nu Plasma multi-collector ICP-MS at NIGL. All samples were run on the mass spectrometers by Dr. Ian Millar.

D.3. Preparation for Hf isotopic analyses

D.3.1. Leaching

Samples were prepared for Hf isotopic analysis at NIGL under the supervision of Dr. Ian Millar. The method for preparing samples for Hf isotopic analysis is outlined in detail in Kempton et al. (2001) and is summarised here. Samples were weighed and leached using the same method described in section D.2.1.

D.3.2. Sample dissolution

2 ml of 16M HNO_3 was added to each sample beaker prior to the addition of 10 ml of 29M HF. The beakers were left on the hotplate overnight at ~120°C. After being

allowed to cool the solutions were evaporated to dryness. 4 ml of 4N HF was added to each beaker and these were then sealed and agitated. The slurry was then transferred to centrifuge tubes and centrifuged at 4000 rpm for ninety minutes. The sample was then decanted into the centrifuge tubes and centrifuged again. A final 2 ml of 4N HF was added directly to the residues in the centrifuge tubes before a final centrifuging stage.

D.3.3. Chemical separation of Hf

The extraction of Hf from the rest of the sample was achieved using large anion exchange columns with BioRad anion exchange resin AG1-X8. Sample solutions were loaded on to the columns and the undesired elements were eluted by first adding 6 ml of 4N HF, then 200 ml of 4N HF, and then 30 ml of 4N HF. Solutions were then collected in clean Savillex beakers by adding 60 ml of 1N HF-1N HCl to each column. 30 µl of 36.6N H_2SO_4 was then added to each beaker and the solutions were dried down on the hotplate. Afterwards 1 ml of 0.52N H_2SO_4-5% H_2O_2 was added to each sample and the solutions pipetted into a second set of columns. The sample beakers were washed with 1 ml of 0.52N H_2SO_4-5% H_2O_2 and added to the appropriate columns. An additional 1 ml of 0.52N H_2SO_4-5%H_2O_2 was eluted through the columns, followed by 12 ml of the same solution. The Hf fraction was collected in the clean Savillex beakers by adding 13 ml of 1N HF-2N HCl to each column. The Hf solutions were then dried down on a hotplate.

D.3.4. Loading

The dry Hf fractions were transferred into 1 ml microcentrifuge tubes in a dilute solution of 2% HNO_3 and 0.1M HF and placed into the mass spectrometer.

D.3.5. Mass spectrometric analysis

Analysis of Hf isotopes was carried out using the VG Plasma P54 multi-collector ICP-MS at NIGL. The samples were run on the mass spectrometer by Dr. Ian Millar.

D.4. Preparation for Os isotopic analysis

Samples were prepared for Os isotopic analysis at the Open University under the supervision of Dr. Ian Parkinson.

D.4.1. Dissolution and oxidation

2 g of each powdered sample was weighed out and transferred to carius tubes which were then temporarily sealed with parafilm and placed in a freezer for a couple of hours. Whilst the carius tubes were chilling, Os and Re spikes for each sample were weighed out and transferred to separate clean Teflon beakers. The addition of a known volume and concentration of spike enables the determination of the detection efficiency of the measuring instrument and the concentration of the isotope of interest in the sample.

Since the actual Os concentrations of the samples were not known prior to the isotopic work, they were estimated based on their Ni concentrations. The Os concentrations were estimated by a regression equation ($y = -0.0003x^2 + 1.7116x - 198.84$) generated from a polynomial curve fitted through a compiled Os(ppt)-Ni(ppm) dataset for a range of mafic and ultramafic rocks including MORB, OIB, continental flood basalts and komatiites. The predicted Os concentrations were then used in further regression equations created by Open University scientists to calculate the volume of spike solution to be added in each case. For samples with >300 ppm Ni the Os(DTM2) spike was used and for samples with <300 ppm Ni the Os(vdil2) spike was used. For the high Ni samples, the volume of Os(DTM2) spike was calculated using the regression equation $y = 0.0549x - 0.00001$, where x is the predicted mass of Os in ng in the sample and y is the spike volume in ml. For lower Ni samples, the volume of spike Os(vdil2) was calculated using the regression equation $y = 0.5111x - 0.0000004$, where x is the predicted mass of Os in ng in the sample and y is the spike volume in ml. For Re, the volume of spike added was kept constant with 0.035 g of Re(DTM) spike solution added to each sample.

The carius tubes were removed from the freezer after a couple of hours and placed in dry ice in a Dewar flask. To each tube was added 1 ml of 12M HCl followed by the

Os and Re spike solutions, a further 2 ml of 12M HCl and then 9 ml of 15M HNO_3. The tubes were left until the solutions had frozen, at which point the tubes were sealed with a propane torch and allowed to equilibrate at room temperature. After this, the tubes were wrapped in aluminium foil and placed in steel scaffold-pipes. The pipes were then placed in an oven at 180°C for five days. After five days, the pipes were removed and rinsed with deionised water and placed in a freezer for several hours. When the pipes had sufficiently chilled the necks of the carius tubes were punctured with a hot flame and scoured right the way round. The scours were then flamed until cracks propagated and the upper portions of the tubes were then snapped off to access the aqua regia sample solutions.

D.4.2. Os purification

Before the carius tubes were opened, 8 ml of CCl_4 was added to eighteen clean Teflon beakers which were then sealed and placed in the freezer for several hours. After the carius tubes had been opened and the CCl_4 solutions removed from the freezer, the aqua regia solutions were pipetted from the carius tubes into the beakers containing CCl_4. The beakers were then sealed, shaken and left to stand for around three hours before being placed in the freezer. A new set of clean beakers with 10 ml of HBr in them was also placed in the freezer for several hours.

Once chilled, all the beakers were removed from the freezer. In the beakers containing aqua regia and CCl_4, the two solutions form two distinctive layers with the aqua regia above the CCl_4. The upper layer of aqua regia in each beaker was pipetted into a new clean beaker which was then sealed and set aside for later Re purification. The lower layer of CCl_4 (containing the Os) was pipetted into the beakers with 10 ml of HBr. These beakers were then sealed, shaken, left to stand overnight and then placed in the freezer for a couple of hours. After the beakers were removed from the freezer, two distinct layers were visible. The upper layer of HBr (containing the Os) in each beaker was pipetted into a new clean beaker and evaporated to dryness on a hotplate. The lower layer of CCl_4 in each beaker was discarded.

The residues from evaporation were dissolved in very small volumes of acetone. ~2 µl of HBr was then added and the whole mixture transferred to the centre of an upturned lid of a conical beaker and evaporated to dryness. Whilst the solutions on the lids were evaporating, eighteen tiny drops of HBr were pipetted into the apexes of eighteen conical beakers which were then turned upside down. Two drops of CrO_3 were pipetted onto the dried residues on the lids and the lids then put on to the conical beakers upside down. The beakers were wrapped in aluminium foil, with a little gap left near the apex of each beaker, and placed on a hotplate at 120°C for three hours. After this time had elapsed, the beakers were carefully removed from the hotplate, unwrapped and opened. The lids were rinsed thoroughly with deionised water and dried. The conical beakers were heated until the tiny drops of HBr in the apexes (containing the Os) had reduced in size to a volume of ~0.5 µl. The lids were then replaced on the beakers the right way up.

D.4.3. Re purification

The aqua regia solutions previously set aside were dried down to as small a residue as practicable. To each residue was added 2 ml of 2N HNO_3 and then these mixtures placed on a hotplate at 120°C for about half an hour to dissolve the residue. For each sample two centrifuge tubes were set aside. Into the first set of tubes the nitric solutions were decanted. 2 ml of iso-amylol was added to each of these tubes which were then shaken for two minutes and centrifuged at 4000 rpm for four minutes. The iso-amylol and HNO_3 formed two distinct layers in these tubes. The upper layers of iso-amylol (containing the Re) were transferred into the second set of centrifuge tubes followed by 2 ml of new 2N HNO_3. The tubes were shaken for two minutes and then centrifuged at 4000 rpm for four minutes. The bottom layer of HNO_3 was then extracted and discarded and another 2 ml of 2N HNO_3 added to the tubes which were then shaken and centrifuged. Again the bottom layer of HNO_3 was extracted and another 2 ml of 2N HNO_3 added to the tubes which were then shaken and centrifuged. This washing procedure removed other elements but left Re in the iso-amylol. The bottom layer of HNO_3 was extracted from each tube and discarded. 2 ml of deionised water was then added to each tube and each tube shaken for two minutes and centrifuged at 4000 rpm for four minutes. This centrifuge process again produced two layers in the tubes, an upper layer of iso-amylol and a bottom layer of

water (now containing the Re). The bottom layers of water were extracted with pipettes which were then thoroughly rinsed with deionised water before transferring the Re-containing water into new clean beakers. These aqueous solutions were then evaporated to dryness.

D.4.4. Loading

The Os- and Re-containing solutions were loaded onto single filaments made from high purity Pt ribbon. The filaments were thoroughly cleaned and degassed beforehand. The filaments were degassed by exposing them to a current of 2.5 A for one minute. Whilst loading, the current passing through the filament was held constant at 0.55 A. For Os, the tiny drops of HBr in the conical beakers were loaded using clean micro-syringes and polyethylene catheters. After adding the HBr, ~1 µl of $Ba(OH)_2$ was loaded onto the filaments leaving a milky white salt. For Re, the residues were dissolved in tiny drops of deionised water which were then loaded in the same way as for Os including the addition of $Ba(OH)_2$.

D.4.5. Mass spectrometric analysis

Analysis of Os isotopes was carried out using the Thermo-Finnigan Triton high resolution multi-collector mass spectrometer by negative thermal ionisation mass spectrometry in secondary electron multiplier mode at the Open University. Re and Os concentrations were also measured via isotope dilution.

D.5. Age-correcting

Given the age of the Circum-Superior LIP it is necessary to age-correct the measured isotopic ratios.

D.5.1. Sr isotopes

To age-correct the Sr isotopic data the sum of all the Sr isotope ratios (with ^{86}Sr as the denominator) and the percentage of each isotope (^{84}Sr, ^{86}Sr, ^{87}Sr and ^{88}Sr) have to be calculated (Equations D.1 to D.5).

Table D.1. Values used in age-correcting the isotope data

	Value	Reference
Sr isotopes		
$(^{88}Sr/^{86}Sr)^{P}_{UR}$	8.375209	Steiger & Jager (1977)
$(^{84}Sr/^{86}Sr)^{P}_{UR}$	0.056492	Thirlwall (1991)
^{88}Sr (amu)	87.9056167	de Laeter et al. (2003)
^{87}Sr (amu)	86.9088816	de Laeter et al. (2003)
^{86}Sr (amu)	85.9092647	de Laeter et al. (2003)
^{84}Sr (amu)	83.913426	de Laeter et al. (2003)
Rb (amu)	85.4678	Wieser (2006)
^{87}Rb (% abundance)	27.83	Rosman & Taylor (1998)
$\lambda\ ^{87}Rb\ (y^{-1})$	1.42×10^{-11}	Steiger & Jager (1977)
Nd isotopes		
$(^{142}Nd/^{144}Nd)^{P}_{CHUR}$	1.141827	Wasserburg et al. (1981)
$(^{143}Nd/^{144}Nd)^{P}_{CHUR}$	0.512638	DePaolo & Wasserburg (1976)
$(^{145}Nd/^{144}Nd)^{P}_{CHUR}$	0.348417	Wasserburg et al. (1981)
$(^{146}Nd/^{144}Nd)^{P}_{CHUR}$	0.7219	Wasserburg et al. (1981)
$(^{148}Nd/^{144}Nd)^{P}_{CHUR}$	0.241578	Wasserburg et al. (1981)
$(^{150}Nd/^{144}Nd)^{P}_{CHUR}$	0.236418	Wasserburg et al. (1981)
$(^{147}Sm/^{144}Nd)^{P}_{CHUR}$	0.1967	DePaolo & Wasserburg (1976)
^{142}Nd (amu)	141.907719	de Laeter et al. (2003)
^{143}Nd (amu)	142.909810	de Laeter et al. (2003)
^{144}Nd (amu)	143.910083	de Laeter et al. (2003)
^{145}Nd (amu)	144.912569	de Laeter et al. (2003)
^{146}Nd (amu)	145.913113	de Laeter et al. (2003)
^{148}Nd (amu)	147.916889	de Laeter et al. (2003)
^{150}Nd (amu)	149.920887	de Laeter et al. (2003)
Sm (amu)	150.36	Wieser (2006)
^{147}Sm (% abundance)	14.99	Rosman & Taylor (1998)
$\lambda\ ^{147}Sm\ (y^{-1})$	6.54×10^{-12}	Lugmair & Marti (1978)
Pb isotopes		
^{204}Pb (amu)	203.973028	de Laeter et al. (2003)
^{206}Pb (amu)	205.974449	de Laeter et al. (2003)
^{207}Pb (amu)	206.975880	de Laeter et al. (2003)
^{208}Pb (amu)	207.976636	de Laeter et al. (2003)
U (amu)	238.02891	Wieser (2006)
Th (amu)	232.03806	Wieser (2006)
^{238}U (% abundance)	99.2745	Rosman & Taylor (1998)
^{235}U (% abundance)	0.72	Rosman & Taylor (1998)
^{232}Th (% abundance)	100	Rosman & Taylor (1998)
$\lambda\ ^{238}U\ (y^{-1})$	1.55125×10^{-10}	Steiger & Jager (1977)
$\lambda\ ^{235}U\ (y^{-1})$	9.8485×10^{-10}	Steiger & Jager (1977)
$\lambda\ ^{232}Th\ (y^{-1})$	4.9475×10^{-11}	Steiger & Jager (1977)

Table D.1. contd.

	Value	Reference
Hf isotopes		
$(^{174}Hf/^{177}Hf)^{P}_{CHUR}$	0.008659	Thirlwall & Anczkiewicz (2004)
$(^{176}Hf/^{177}Hf)^{P}_{CHUR}$	0.282772	Blichert-Toft & Albarede (1997)
$(^{178}Hf/^{177}Hf)^{P}_{CHUR}$	1.46734	Thirlwall & Anczkiewicz (2004)
$(^{179}Hf/^{177}Hf)^{P}_{CHUR}$	0.7325	Thirlwall & Anczkiewicz (2004)
$(^{180}Hf/^{177}Hf)^{P}_{CHUR}$	1.88676	Thirlwall & Anczkiewicz (2004)
$(^{176}Lu/^{177}Hf)^{P}_{CHUR}$	0.0332	Blichert-Toft & Albarede (1997)
^{174}Hf (amu)	173.940042	de Laeter et al. (2003)
^{176}Hf (amu)	175.941403	de Laeter et al. (2003)
^{177}Hf (amu)	176.9432204	de Laeter et al. (2003)
^{178}Hf (amu)	177.9436981	de Laeter et al. (2003)
^{179}Hf (amu)	178.9458154	de Laeter et al. (2003)
^{180}Hf (amu)	179.9465488	de Laeter et al. (2003)
Lu (amu)	174.9668	Wieser (2006)
^{176}Lu (% abundance)	2.59	Rosman & Taylor (1998)
$\lambda\ ^{176}Lu\ (y^{-1})$	1.865×10^{-11}	Scherer et al. (2001)
Os isotopes		
$(^{184}Os/^{188}Os)^{P}_{CHUR}$	0.0013313	Shirey & Walker (1998)
$(^{186}Os/^{188}Os)^{P}_{CHUR}$	0.119848	Shirey & Walker (1998)
$(^{187}Os/^{188}Os)^{P}_{CHUR}$	0.12757	Walker et al. (1989)
$(^{189}Os/^{188}Os)^{P}_{CHUR}$	1.21967	Shirey & Walker (1998)
$(^{190}Os/^{188}Os)^{P}_{CHUR}$	1.98451	Shirey & Walker (1998)
$(^{192}Os/^{188}Os)^{P}_{CHUR}$	3.08271	Luck & Allegre (1983)
$(^{187}Re/^{188}Os)^{P}_{CHUR}$	0.3972	Walker et al. (1989)
^{184}Os (amu)	183.952491	de Laeter et al. (2003)
^{186}Os (amu)	185.953838	de Laeter et al. (2003)
^{187}Os (amu)	186.9557476	de Laeter et al. (2003)
^{188}Os (amu)	187.9558357	de Laeter et al. (2003)
^{189}Os (amu)	188.958145	de Laeter et al. (2003)
^{190}Os (amu)	189.958445	de Laeter et al. (2003)
^{192}Os (amu)	191.961479	de Laeter et al. (2003)
Re (amu)	186.207	Wieser (2006)
^{187}Re (% abundance)	62.60	Rosman & Taylor (1998)
$\lambda\ ^{187}Re\ (y^{-1})$	1.666×10^{-11}	Smoliar et al. (1996)

$$\Sigma Sr = \left(\frac{^{84}Sr}{^{86}Sr}\right)^{P}_{UR} + \frac{^{86}Sr}{^{86}Sr} + \left(\frac{^{87}Sr}{^{86}Sr}\right)_{m} + \left(\frac{^{88}Sr}{^{86}Sr}\right)^{P}_{UR}$$

Equation D.1

where Σ Sr is the sum of Sr isotope ratios, the subscript m denotes the measured isotopic ratio and the subscript UR denotes the isotopic ratio of a uniform reservoir of chondritic composition at the present day (superscript P). The chondritic Sr isotopic ratios are given in Table D.1. The $^{86}Sr/^{86}Sr$ isotopic ratio is equal to 1.

$$\%^{84}Sr = \frac{100}{\Sigma Sr} \times \left(\frac{^{84}Sr}{^{86}Sr}\right)^{P}_{UR}$$

Equation D.2

$$\%^{86}Sr = \frac{100}{\Sigma Sr} \times \frac{^{86}Sr}{^{86}Sr}$$

Equation D.3

$$\%^{87}Sr = \frac{100}{\Sigma Sr} \times \left(\frac{^{87}Sr}{^{86}Sr}\right)_{m}$$

Equation D.4

$$\%^{88}Sr = \frac{100}{\Sigma Sr} \times \left(\frac{^{88}Sr}{^{86}Sr}\right)^{P}_{UR}$$

Equation D.5

The previous five equations are then used to calculate the atomic mass of Sr in each sample (Equation D.6).

$$Sr\ (amu) = \left(\frac{\%^{84}Sr}{100} \times {}^{84}Sr\ (amu)\right) + \left(\frac{\%^{86}Sr}{100} \times {}^{86}Sr\ (amu)\right) + \left(\frac{\%^{87}Sr}{100} \times {}^{87}Sr\ (amu)\right) + \left(\frac{\%^{88}Sr}{100} \times {}^{88}Sr\ (amu)\right)$$

Equation D.6

where the atomic mass of Sr is measured in atomic mass units (amu). The mass of each Sr isotope is given in Table D.1.

The next step is to calculate the $^{87}Rb/^{86}Sr$ ratio as follows.

$$\frac{{}^{87}Rb}{{}^{86}Sr} = \frac{Rb}{Sr} \times \frac{Sr\ (amu)}{85.4678} \times \frac{27.83}{\%^{86}Sr}$$

Equation D.7

where Rb and Sr are the measured concentrations (ppm) of these elements in the leached sample and the numbers 85.4678 and 27.83 are the atomic mass of Rb (in amu) and the percentage abundance of ^{87}Rb respectively.

The final equation to calculate the initial Sr isotopic ratio is given below.

$$\left(\frac{{}^{87}Sr}{{}^{86}Sr}\right)_i = \left(\frac{{}^{87}Sr}{{}^{86}Sr}\right)_m - \frac{{}^{87}Rb}{{}^{86}Sr}\left(e^{\lambda t} - 1\right)$$

Equation D.8

where the subscripts i denotes the initial isotopic ratio, t is the age of the rock in years, and λ is the decay constant of ^{87}Rb ($1.42 \times 10^{-11}\ y^{-1}$).

D.5.2. Nd isotopes

The equations below are used to age-correct the Nd isotopic data. Initially the sum of all the Nd isotope ratios (with ^{144}Nd as the denominator) and the percentage of each

Nd isotope (^{142}Nd, ^{143}Nd, ^{144}Nd, ^{145}Nd, ^{146}Nd, ^{148}Nd and ^{150}Nd) needs to be known and are calculated using Equations D.9-D.16.

$$\Sigma Nd = \left(\frac{^{142}Nd}{^{144}Nd}\right)^{P}_{CHUR} + \left(\frac{^{143}Nd}{^{144}Nd}\right)_{m} + \frac{^{144}Nd}{^{144}Nd} + \left(\frac{^{145}Nd}{^{144}Nd}\right)^{P}_{CHUR} + \left(\frac{^{146}Nd}{^{144}Nd}\right)^{P}_{CHUR} + \left(\frac{^{148}Nd}{^{144}Nd}\right)^{P}_{CHUR} + \left(\frac{^{150}Nd}{^{144}Nd}\right)^{P}_{CHUR}$$

Equation D.9

where Σ Nd is the sum of Nd isotope ratios, the subscript m denotes the measured isotopic ratio and the subscript CHUR denotes the isotopic ratio of the chondritic uniform reservoir (CHUR) at the present day (superscript P). The Nd isotopic ratios of CHUR are given in Table D.1. The ^{144}Nd/^{144}Nd isotopic ratio is equal to 1.

$$\%^{142}Nd = \frac{100}{\Sigma Nd} \times \left(\frac{^{142}Nd}{^{144}Nd}\right)^{P}_{CHUR}$$

Equation D.10

$$\%^{143}Nd = \frac{100}{\Sigma Nd} \times \left(\frac{^{143}Nd}{^{144}Nd}\right)_{m}$$

Equation D.11

$$\%^{144}Nd = \frac{100}{\Sigma Nd} \times \frac{^{144}Nd}{^{144}Nd}$$

Equation D.12

$$\%^{145}Nd = \frac{100}{\Sigma Nd} \times \left(\frac{^{145}Nd}{^{144}Nd}\right)^{P}_{CHUR}$$

Equation D.13

$$\%^{146}Nd = \frac{100}{\sum Nd} \times \left(\frac{^{146}Nd}{^{144}Nd} \right)^{P}_{CHUR}$$

Equation D.14

$$\%^{148}Nd = \frac{100}{\sum Nd} \times \left(\frac{^{148}Nd}{^{144}Nd} \right)^{P}_{CHUR}$$

Equation D.15

$$\%^{150}Nd = \frac{100}{\sum Nd} \times \left(\frac{^{150}Nd}{^{144}Nd} \right)^{P}_{CHUR}$$

Equation D.16

The next step in the age-correction of Nd isotopes is to calculate the atomic mass of Nd in each sample.

$$Nd\ (amu) = \left(\frac{\%^{142}Nd}{100} \times {}^{142}Nd\,(amu) \right) + \left(\frac{\%^{143}Nd}{100} \times {}^{143}Nd(amu) \right) + \left(\frac{\%^{144}Nd}{100} \times {}^{144}Nd\,(amu) \right) + \left(\frac{\%^{145}Nd}{100} \times {}^{145}Nd(amu) \right) + \left(\frac{\%^{146}Nd}{100} \times {}^{146}Nd\,(amu) \right) + \left(\frac{\%^{148}Nd}{100} \times {}^{148}Nd\,(amu) \right) + \left(\frac{\%^{150}Nd}{100} \times {}^{150}Nd(amu) \right)$$

Equation D.17

where the atomic mass of Nd is measured in atomic mass units (amu). The mass of each Nd isotope is given in Table D.1.

The next equation calculates the $^{147}Sm/^{144}Nd$ ratio.

$$\frac{^{147}Sm}{^{144}Nd} = \frac{Sm}{Nd} \times \frac{Nd(amu)}{150.36} \times \frac{14.99}{\%^{144}Nd}$$

Equation D.18

where Sm and Nd are the measured concentrations (ppm) of these elements in the leached sample and the numbers 150.36 and 14.99 are the atomic mass of Sm (in amu) and the percentage abundance of ^{147}Sm respectively.

The final equation to calculate the initial Nd isotopic ratio is as follows.

$$\left(\frac{^{143}Nd}{^{144}Nd}\right)_i = \left(\frac{^{143}Nd}{^{144}Nd}\right)_m - \frac{^{147}Sm}{^{144}Nd}\left(e^{\lambda t} - 1\right)$$

Equation D.19

where the subscript i denotes the initial Nd isotopic ratio, t is the age of the rock in years, and λ is the decay constant for ^{147}Sm (6.54×10^{-12} y^{-1}).

The initial epsilon Nd value is calculated using the equation below.

$$\varepsilon Nd_i = \left(\frac{\left(\frac{^{143}Nd}{^{144}Nd}\right)_i}{\left(\frac{^{143}Nd}{^{144}Nd}\right)^t_{CHUR}} - 1\right) \times 10000$$

Equation D.20

where the subscript i denotes the initial isotopic ratio of the sample and $(^{143}Nd/^{144}Nd)^t_{CHUR}$ is the $^{143}Nd/^{144}Nd$ isotopic ratio of the chondritic uniform reservoir (CHUR) at the time (t) in years to which the rock sample has been age-corrected. The $^{143}Nd/^{144}Nd$ isotopic ratio of CHUR at time t can be calculated using Equation D.19 by using the using the present day $^{143}Nd/^{144}Nd$ ratio of CHUR of 0.512638 and the $^{147}Sm/^{144}Nd$ ratio of CHUR of 0.1967 (DePaolo & Wasserburg, 1976).

D.5.3. Pb isotopes

To age-correct Pb isotope ratios the sum of the Pb isotope ratios (with ^{204}Pb as the denominator) needs to be known, as does the percentage of each Pb isotope (^{204}Pb,

^{206}Pb, ^{207}Pb and ^{208}Pb). These values are worked out using the following equations (Equations D.21 to D.25).

$$\Sigma Pb = \frac{^{204}Pb}{^{204}Pb} + \left(\frac{^{206}Pb}{^{204}Pb}\right)_m + \left(\frac{^{207}Pb}{^{204}Pb}\right)_m + \left(\frac{^{208}Pb}{^{204}Pb}\right)_m$$

Equation D.21

where Σ Pb is the sum of Pb isotope ratios, the subscript m denotes the measured isotopic ratio and the $^{204}Pb/^{204}Pb$ ratio is 1.

$$\%^{204}Pb = \frac{100}{\Sigma Pb} \times \frac{^{204}Pb}{^{204}Pb}$$

Equation D.22

$$\%^{206}Pb = \frac{100}{\Sigma Pb} \times \left(\frac{^{206}Pb}{^{204}Pb}\right)_m$$

Equation D.23

$$\%^{207}Pb = \frac{100}{\Sigma Pb} \times \left(\frac{^{207}Pb}{^{204}Pb}\right)_m$$

Equation D.24

$$\%^{208}Pb = \frac{100}{\Sigma Pb} \times \left(\frac{^{208}Pb}{^{204}Pb}\right)_m$$

Equation D.25

The next stage in the age-correction process for Pb isotope ratios is to calculate the atomic mass of Pb in each sample and this is achieved using the following equation.

$$Pb\,(amu) = \left(\frac{\%^{204}Pb}{100} \times {}^{204}Pb(amu)\right) + \left(\frac{\%^{206}Pb}{100} \times {}^{206}Pb(amu)\right) + \left(\frac{\%^{207}Pb}{100} \times {}^{207}Pb(amu)\right) + \left(\frac{\%^{208}Pb}{100} \times {}^{208}Pb(amu)\right)$$

Equation D.26

where the atomic mass of Pb is measured in atomic mass units (amu). The mass of each Pb isotope is given in Table D.1.

The following three equations calculate the $^{238}U/^{204}Pb$, $^{235}U/^{204}Pb$ and $^{232}Th/^{204}Pb$ ratios.

$$\frac{^{238}U}{^{204}Pb} = \frac{U}{Pb} \times \frac{Pb\,(amu)}{238.02891} \times \frac{99.2745}{\%^{204}Pb}$$

Equation D.27

where U and Pb are the measured concentrations of these elements (ppm) in the leached sample and the numbers 238.02891 and 99.2745 are the atomic mass of U (in amu) and the percentage abundance of ^{238}U respectively.

$$\frac{^{235}U}{^{204}Pb} = \frac{U}{Pb} \times \frac{Pb\,(amu)}{238.02891} \times \frac{0.72}{\%^{204}Pb}$$

Equation D.28

where the numbers 238.02891 and 0.72 are the atomic mass of U (in amu) and the percentage abundance of ^{235}U respectively.

$$\frac{^{232}Th}{^{204}Pb} = \frac{Th}{Pb} \times \frac{Pb\,(amu)}{232.03806} \times \frac{100}{\%^{204}Pb}$$

Equation D.29

where the numbers 232.03806 and 100 are the atomic mass of Th (in amu) and the percentage abundance of ^{232}Th respectively.

The final set of equations to calculate the initial Pb isotope ratios are as follows.

$$\left(\frac{^{206}Pb}{^{204}Pb}\right)_i = \left(\frac{^{206}Pb}{^{204}Pb}\right)_m - \frac{^{238}U}{^{204}Pb}\left(e^{\lambda t} - 1\right)$$

Equation D.30

where the subscript i denotes the initial Pb isotopic ratio and λ is the decay constant for ^{238}U and is 1.55125×10^{-10} y^{-1}.

$$\left(\frac{^{207}Pb}{^{204}Pb}\right)_i = \left(\frac{^{207}Pb}{^{204}Pb}\right)_m - \frac{^{235}U}{^{204}Pb}\left(e^{\lambda t} - 1\right)$$

Equation D.31

where λ is the decay constant for ^{235}U and is 9.8485×10^{-10} y^{-1}.

$$\left(\frac{^{208}Pb}{^{204}Pb}\right)_i = \left(\frac{^{208}Pb}{^{204}Pb}\right)_m - \frac{^{232}Th}{^{204}Pb}\left(e^{\lambda t} - 1\right)$$

Equation D.32

where λ is the decay constant for ^{232}Th and is 4.9475×10^{-11} y^{-1}.

D.5.4. Hf isotopes

Initially the sum of the Hf isotope ratios (with ^{177}Hf as the denominator) and the percentage of each isotope are calculated using the equations below.

$$\Sigma Hf = \left(\frac{^{174}Hf}{^{177}Hf}\right)^P_{CHUR} + \left(\frac{^{176}Hf}{^{177}Hf}\right)_m + \frac{^{177}Hf}{^{177}Hf} + \left(\frac{^{178}Hf}{^{177}Hf}\right)^P_{CHUR} + \left(\frac{^{179}Hf}{^{177}Hf}\right)^P_{CHUR} + \left(\frac{^{180}Hf}{^{177}Hf}\right)^P_{CHUR}$$

Equation D.33

where Σ Hf is the sum of Hf isotope ratios, the subscript m denotes the measured isotopic ratio and the subscript CHUR denotes the isotopic ratio of the chondritic uniform reservoir (CHUR) at the present day (superscript P). The Hf isotopic ratios of CHUR are given in Table D.1. The $^{177}Hf/^{177}Hf$ isotopic ratio is equal to 1.

$$\%^{174}Hf = \frac{100}{\Sigma Hf} \times \left(\frac{^{174}Hf}{^{177}Hf} \right)^{P}_{CHUR}$$

Equation D.34

$$\%^{176}Hf = \frac{100}{\Sigma Hf} \times \left(\frac{^{176}Hf}{^{177}Hf} \right)_{m}$$

Equation D.35

$$\%^{177}Hf = \frac{100}{\Sigma Hf} \times \frac{^{177}Hf}{^{177}Hf}$$

Equation D.36

$$\%^{178}Hf = \frac{100}{\Sigma Hf} \times \left(\frac{^{178}Hf}{^{177}Hf} \right)^{P}_{CHUR}$$

Equation D.37

$$\%^{179}Hf = \frac{100}{\Sigma Hf} \times \left(\frac{^{179}Hf}{^{177}Hf} \right)^{P}_{CHUR}$$

Equation D.38

$$\%^{180}Hf = \frac{100}{\Sigma Hf} \times \left(\frac{^{180}Hf}{^{177}Hf} \right)^{P}_{CHUR}$$

Equation D.39

The next stage is to determine the atomic mass of Hf in each sample and this is achieved using the following equation.

$$Hf\ (amu) = \left(\frac{\%^{174}Hf}{100} \times {}^{174}Hf(amu)\right) + \left(\frac{\%^{176}Hf}{100} \times {}^{176}Hf(amu)\right) + \left(\frac{\%^{177}Hf}{100} \times {}^{177}Hf(amu)\right) + \left(\frac{\%^{178}Hf}{100} \times {}^{178}Hf(amu)\right) + \left(\frac{\%^{179}Hf}{100} \times {}^{179}Hf(amu)\right) + \left(\frac{\%^{180}Hf}{100} \times {}^{180}Hf(amu)\right)$$

Equation D.40

where the atomic mass of Hf is measured in atomic mass units (amu). The mass of each Hf isotope is given in Table D.1.

The next equation is used to calculate the $^{176}Lu/^{177}Hf$ ratio.

$$\frac{^{176}Lu}{^{177}Hf} = \frac{Lu}{Hf} \times \frac{Hf(amu)}{174.9668} \times \frac{2.59}{\%^{176}Hf}$$

Equation D.41

where Lu and Hf are the measured concentrations of these elements (ppm) in the leached sample and the numbers 174.9668 and 2.59 are the atomic mass of Lu (in amu) and the percentage abundance of ^{176}Lu respectively.

The final equation to calculate the initial Hf isotopic ratio is given below.

$$\left(\frac{^{176}Hf}{^{177}Hf}\right)_i = \left(\frac{^{176}Hf}{^{177}Hf}\right)_m - \frac{^{176}Lu}{^{177}Hf}\left(e^{\lambda t} - 1\right)$$

Equation D.42

where the subscript i denotes the initial Hf isotopic ratio and λ is the decay constant for ^{176}Lu ($1.865 \times 10^{-11}\ y^{-1}$).

The epsilon Hf value is calculated using the following equation.

$$\varepsilon Hf_t = \left(\frac{\left(\frac{^{176}Hf}{^{177}Hf} \right)_t}{\left(\frac{^{176}Hf}{^{177}Hf} \right)^t_{CHUR}} - 1 \right) \times 10000$$

Equation D.43

where the subscript i denotes the initial isotopic ratio of the sample and $(^{176}Hf/^{177}Hf)^t_{CHUR}$ is the $^{176}Hf/^{177}Hf$ isotopic ratio of the chondritic uniform reservoir (CHUR) at the time (t) in years to which the rock sample has been age-corrected. The $^{176}Hf/^{177}Hf$ isotopic ratio of CHUR at time t can be calculated using Equation D.42 by using the using the present day $^{176}Hf/^{177}Hf$ ratio of CHUR of 0.282772 and the $^{176}Lu/^{177}Hf$ ratio of CHUR of 0.0332 (Blichert-Toft & Albarede, 1997).

D.5.5. Os isotopes

The equations below are used to age-correct the Os isotopic data. Initially the sum of all the Os isotope ratios (with ^{188}Os as the denominator) and the percentage of each Os isotope (^{184}Os, ^{186}Os, ^{187}Os, ^{188}Os, ^{190}Os and ^{192}Os) need to be calculated.

$$\Sigma Os = \left(\frac{^{184}Os}{^{188}Os} \right)^P_{CHUR} + \left(\frac{^{186}Os}{^{188}Os} \right)^P_{CHUR} + \left(\frac{^{187}Os}{^{188}Os} \right)_m + \frac{^{188}Os}{^{188}Os} + \left(\frac{^{190}Os}{^{188}Os} \right)^P_{CHUR} + \left(\frac{^{192}Os}{^{188}Os} \right)^P_{CHUR}$$

Equation D.44

where Σ Os is the sum of Os isotope ratios, the subscript m denotes the measured isotopic ratio and the subscript CHUR denotes the isotopic ratio of the chondritic uniform reservoir (CHUR) at the present day (superscript P). The Os isotopic ratios of CHUR are given in Table D.1. The $^{188}Os/^{188}Os$ isotopic ratio is equal to 1.

$$\%^{184}Os = \frac{100}{\Sigma Os} \times \left(\frac{^{184}Os}{^{188}Os} \right)^P_{CHUR}$$

Equation D.45

$$\%^{186}Os = \frac{100}{\sum Os} \times \left(\frac{^{186}Os}{^{188}Os} \right)^{P}_{CHUR}$$

Equation D.46

$$\%^{187}Os = \frac{100}{\sum Os} \times \left(\frac{^{187}Os}{^{188}Os} \right)^{P}_{CHUR}$$

Equation D.47

$$\%^{188}Os = \frac{100}{\sum Os} \times \frac{^{188}Os}{^{188}Os}$$

Equation D.48

$$\%^{189}Os = \frac{100}{\sum Os} \times \left(\frac{^{189}Os}{^{188}Os} \right)^{P}_{CHUR}$$

Equation D.49

$$\%^{190}Os = \frac{100}{\sum Os} \times \left(\frac{^{190}Os}{^{188}Os} \right)^{P}_{CHUR}$$

Equation D.50

$$\%^{192}Os = \frac{100}{\sum Os} \times \left(\frac{^{192}Os}{^{188}Os} \right)^{P}_{CHUR}$$

Equation D.51

The next stage is to determine the atomic mass of Os in each sample and this is achieved using the following equation.

$$Os\ (amu) = \left(\frac{\%^{184}Os}{100} \times {}^{184}Os(amu)\right) + \left(\frac{\%^{186}Os}{100} \times {}^{186}Os(amu)\right) + \left(\frac{\%^{187}Os}{100} \times {}^{187}Os(amu)\right) + \left(\frac{\%^{188}Os}{100} \times {}^{188}Os(amu)\right) + \left(\frac{\%^{189}Os}{100} \times {}^{189}Os(amu)\right) + \left(\frac{\%^{190}Os}{100} \times {}^{190}Os(amu)\right) + \left(\frac{\%^{192}Os}{100} \times {}^{192}Os(amu)\right)$$

Equation D.52

where the atomic mass of Os is measured in atomic mass units (amu). The mass of each Os isotope is given in Table D.1

The next equation is used to calculate the $^{187}Re/^{188}Os$ isotopic ratio.

$$\frac{^{187}Re}{^{188}Os} = \frac{Re}{Os} \times \frac{Os(amu)}{186.207} \times \frac{62.60}{\%^{188}Os}$$

Equation D.53

where Re and Os are the measured concentrations of these elements (ppm) in the sample and the numbers 186.207 and 62.60 are the atomic mass of Re (in amu) and the percentage abundance of ^{187}Re respectively.

The final equation to calculate the initial Os isotopic ratio is given below.

$$\left(\frac{^{187}Os}{^{188}Os}\right)_i = \left(\frac{^{187}Os}{^{188}Os}\right)_m - \frac{^{187}Re}{^{188}Os}\left(e^{\lambda t} - 1\right)$$

Equation D.54

where the subscript i denotes the initial Os isotopic ratio and λ is the decay constant for ^{187}Re ($1.666 \times 10^{-11}\ y^{-1}$).

The gamma Os value is calculated using the following equation.

$$\gamma Os_i = \left(\frac{\left(\frac{^{187}Os}{^{188}Os} \right)_i}{\left(\frac{^{187}Os}{^{188}Os} \right)^t_{CHUR}} - 1 \right) \times 100$$

Equation D.55

where the subscript i denotes the initial isotopic ratio of the sample and $(^{187}Os/^{188}Os)^t_{CHUR}$ is the $^{187}Os/^{188}Os$ isotopic ratio of the chondritic uniform reservoir (CHUR) at the time (t) in years to which the rock sample has been age-corrected. The $^{187}Os/^{188}Os$ isotopic ratio of CHUR at time t can be calculated using Equation D.54 by using the using the present day $^{187}Os/^{188}Os$ ratio of CHUR of 0.12757 and the $^{187}Re/^{188}Os$ ratio of CHUR of 0.3972 (Walker et al., 1989).

D.5.6. Preparation for the determination of Rb, Sr, Sm, Nd, U, Th, Pb, Lu and Hf concentrations by ICP-MS

As noted in section D.4, the concentrations of Re and Os in samples necessary to age-correct the Os isotopic data were measured by isotope dilution at the Open University. Unfortunately for financial reasons, the concentrations of Rb, Sr, Sm, Nd, U, Th, Pb, Lu and Hf required for age-correcting the Sr-Nd-Pb-Hf isotopic data were unable to be measured by isotope dilution at NIGL. These elemental concentrations were instead obtained by ICP-MS at Cardiff University. The concentrations of these elements given in Tables C.1 and C.2 could not be used to age-correct the isotope data as these were concentrations obtained from unleached samples whereas the isotopic measurements were made on samples which had been leached in 6M HCl. Therefore the eighteen samples selected for isotopic analyses were leached in 6M HCl at Cardiff University using the same procedure used at NIGL and described in section D.2.1. As the lithium metaborate flux used in the fusion method detailed in Appendix B contaminates the sample with Pb, the eighteen samples were prepared for ICP-MS by an acid digestion method outlined below.

To prepare the samples, 0.1 ± 0.001 g of each leached sample was weighed into a clean Teflon vial. To each vial was added 0.5 ml of concentrated HNO_3 followed by

4 ml of concentrated HF. Each vial was then sealed and placed on a hotplate at 120°C for three days for each sample to digest. After each sample solution was taken off the hotplate and allowed to cool, the vials were placed lidless on a hotplate at 140°C in order for the solutions to evaporate until a clear gel could be identified in the bottom of each vial. 2 ml of concentrated HNO_3 was added to each vial and the vials placed lidless on a hotplate at 130°C until the solutions had evaporated to incipient dryness. This addition and evaporation of acid was then repeated. After the second evaporation, 5 ml of 5M HNO_3 was added to each vial which was then sealed and placed on a hotplate at 120°C overnight to dissolve any residue. The vials were then allowed to cool and each solution spiked with 1 ml of 2500 ppb Rh-Re solution and made up to 50 ml in a volumetric flask with 18.2 Ω deionised water. 2 ml of each solution was added to 8 ml of 2% HNO_3 and run on the ICP-MS to obtain the trace element concentrations.

For samples MMH08-7, MMM07-20, MMW07-4 and MMW07-24 a further step was needed when making up the solutions to 50 ml. These four samples were not completely dissolved in the HF-HNO_3 acid solution. Their solutions contained black solid residue, mostly likely to be Cr-spinel which is not strongly attacked by HF. When these four sample solutions were poured into the volumetric flask, they were poured through grade 1 Whatman filter paper in order to remove the black solid residue from the solution to be analysed. The removal of Cr-spinel was not considered likely to affect the concentration of the elements required for age-correcting the isotopic data.

D.5.7. Accuracy of elemental data

To assess the accuracy of the elemental data used for age-correcting the isotopic data, nine external standards were prepared for analysis using the HF-HNO_3 acid digestion method along with the eighteen samples chosen for isotopic analysis. The nine standards chosen were JB-1a, JGb-1, BIR-1, W2, JA-2, MRG-1, JG-3, JB-3 and JP-1. JB-1a, BIR-1 and JB-3 are all basalts while JGb-1 and MRG-1 are gabbros. W2, JA-2, JG-3 and JP-1 are a dolerite, andesite, granodiorite and peridotite respectively. JB-1a, JGb-1, JA-2, JG-3, JB-3 and JP-1 are issued by the Geological Survey of Japan. BIR-1 and W2 are issued by the United States Geological Survey

Table D.2. Measured element concentrations for the geochemical reference standards prepared by the HF-HNO_3 acid digestion method and their percentage differences from the accepted values

	JB-1a	% error	JGb-1	% error	BIR-1	% error	W2	% error	JA-2	% error
Sc	27.06	3.03	34.32	4.15	42.63	3.12	33.60	6.68	18.21	7.11
TiO_2	1.27	0.63	1.62	1.06	0.96	0.10	1.07	0.85	0.69	4.09
V	207.79	1.36	653.76	2.95	335.37	8.18	270.48	4.03	126.31	0.25
Cr	436.27	11.29	62.89	8.81	430.96	16.48	97.10	5.54	443.93	1.82
MnO	0.15	2.67	0.19	1.58	0.17	1.14	0.17	0.60	0.11	2.78
Co	36.20	6.21	59.75	0.58	50.99	1.94	42.06	2.18	27.91	5.38
Ni	105.53	24.08	29.47	16.02	128.23	24.57	54.82	21.69	99.22	23.68
Cu	53.09	6.36	80.47	6.10	111.31	10.95	96.66	12.12	26.68	10.15
Zn	83.23	1.37	98.30	9.82	61.02	12.83	65.71		55.63	14.02
Ga	17.30	3.37	17.94	0.20	14.37	10.21	16.34	3.91	16.55	2.09
Rb	43.16	10.10	6.65	3.19	0.25	1.60	21.61	8.05	88.28	21.10
Sr	448.39	1.45	332.09	1.56	108.59	0.55	190.69	1.71	257.09	3.66
Y	23.48	2.17	9.76	6.13	15.64	2.25	21.71	9.54	18.25	0.27
Zr	147.86	2.68	27.68	15.63	14.41	7.06	85.84	8.69	126.46	9.01
Nb	29.43	9.41	2.38	15.18	0.57	5.33	7.50	5.08	9.87	4.20
Cs	1.27	2.75	0.24	8.85	0.007	40.00	0.91	8.08	5.54	19.55
Ba	580.20	15.12	67.03	4.24	7.03	0.41	182.00	0.00	366.50	14.17
La	39.72	5.65	3.45	4.31	0.57	7.42	10.55	7.42	17.16	8.63
Ce	66.08	0.27	7.63	6.63	1.84	5.85	22.21	7.48	34.25	4.73
Pr	6.41	12.18	1.00	11.15	0.32	14.74	2.64		3.52	8.36
Nd	25.93	0.27	5.10	6.82	2.28	8.80	12.56	10.29	14.88	7.05
Sm	4.99	1.60	1.41	5.37	1.05	4.36	3.20	1.63	3.20	2.89
Eu	1.50	2.47	0.60	4.03	0.49	9.44	1.08	2.00	0.96	2.69
Gd	4.92	5.29	1.53	5.16	1.57	15.03	3.47	3.75	3.18	3.79
Tb	0.71	2.46	0.26	8.97	0.34	6.67	0.59	6.67	0.50	12.73
Dy	4.01	0.45	1.68	7.63	2.41	3.76	3.68	3.26	2.96	5.82
Ho	0.76	7.04	0.34	2.42	0.53	7.19	0.73	3.55	0.59	17.80
Er	2.21	1.33	0.98	5.77	1.61	5.53	2.13	14.88	1.75	18.11
Tm	0.33	0.30	0.15	6.88	0.26	1.54	0.33	14.47	0.27	2.50
Yb	2.07	1.33	0.94	11.42	1.61	2.18	2.04	0.63	1.76	8.70
Lu	0.32	3.33	0.15	2.67	0.26	1.54	0.31	3.44	0.27	1.48
Hf	3.58	4.99	0.83	6.25	0.58	3.33	2.33	8.87	3.15	10.07
Ta	1.75	9.43	0.15	16.67	0.05		0.48	4.00	0.70	12.13
Pb	6.85	1.38	1.63	15.05	3.36	11.93	9.13	1.80	22.73	18.39
Th	9.08	0.54	0.53	10.00	0.03	0.00	2.13	3.36	5.23	3.96
U	1.71	8.79	0.11	17.69	0.01	10.00	0.50	6.04	2.49	12.58

Table D.2. contd.

	MRG-1	% error	JG-3	% error	JB-3	% error	JP-1	% error
Sc	56.37	4.38	8.50	2.93	32.53	3.77	5.73	20.84
TiO_2	3.97	6.07	0.45	5.42	1.40	2.78	0.00	33.33
V	567.42	9.12	66.40	5.28	388.50	4.43	19.33	29.98
Cr	402.95	15.17	22.11	1.29	69.84	20.21	1222	56.50
MnO	0.17	1.76	0.07	4.23	0.18	2.26	0.11	10.74
Co	81.35	9.61	9.95	14.97	33.24	3.08	108.23	6.70
Ni	167.78	13.96	8.28	42.10	41.93	15.83	1705	30.68
Cu	134.61	0.29	6.63	2.72	178.11	8.19	5.15	23.36
Zn	193.09	1.62	34.18	26.50	103.39	3.39	29.27	29.99
Ga	17.38		15.28	10.67	18.57	6.23	0.39	44.29
Rb	8.23	3.24	77.64	15.36	15.67	3.77	0.39	51.63
Sr	280.79	5.56	364.5	3.80	397.49	1.37	1.87	43.61
Y	13.43	4.07	15.78	8.79	25.94	3.57	0.12	92.53
Zr	101.56	5.97	19.69	86.33	94.76	3.11	5.01	15.32
Nb	21.20	6.00	5.92	0.70	2.06	16.80	0.06	96.28
Cs	0.67	16.67	2.04	14.66	0.99	4.79	0.04	72.67
Ba	52.77	13.49	393.10	15.64	253.10	3.31	8.43	56.77
La	9.03	7.90	21.02	2.06	8.25	6.33	0.04	55.95
Ce	24.73	4.90	41.24	2.32	19.70	8.39	0.06	70.00
Pr	3.40	0.03	4.20	10.74	2.81	9.65	0.01	55.00
Nd	17.97	6.41	16.86	1.98	14.93	4.29	0.04	41.67
Sm	4.49	0.18	3.23	4.78	4.03	5.57	0.01	42.11
Eu	1.40	1.01	0.88	2.78	1.26	4.70	0.01	25.00
Gd	3.98	0.55	3.05	4.52	4.15	11.09	0.01	26.67
Tb	0.57	12.16	0.45	3.26	0.69	5.07	0.00	33.33
Dy	2.92	0.52	2.55	1.62	4.28	5.75	0.02	31.82
Ho	0.48	1.63	0.50	31.58	0.85	6.75	0.00	77.78
Er	1.20	7.50	1.50	1.38	2.48	0.24	0.01	31.25
Tm	0.15	39.09	0.24	2.08	0.39	8.33	0.00	95.12
Yb	0.85		1.51	14.63	2.41	5.65	0.02	13.64
Lu	0.12	0.00	0.24	9.23	0.38	3.08	0.00	9.09
Hf	3.80	1.12	0.69	83.92	2.67	0.04	0.12	42.00
Ta	0.84	5.12	0.58	16.71	0.13	11.33	0.01	50.00
Pb	5.51	44.87	12.21	4.37	15.59	179.41	0.50	313.33
Th	0.76	18.82	7.60	8.22	1.26	1.02	0.01	95.79
U	0.24	1.67	1.94	12.08	0.49	2.92	0.02	47.22

Element concentrations given in ppm except for TiO_2 and MnO which are given in wt. %.
The accepted values for the standards are given in Table D.3.

Table D.3. Accepted concentration values for the geochemical reference standards used to assess the accuracy of the data obtained from the batch of samples prepared by the HF-HNO_3 acid digestion method

	JB-1a	JGb-1	BIR-1	W2	JA-2	MRG-1	JG-3	JB-3	JP-1
Sc	27.90	35.80	44.00	36.00	19.60	54.00	8.76	33.80	7.24
TiO_2	1.28	1.60	0.96	1.06	0.66	3.74	0.48	1.44	0.006
V	205.00	635.00	310.00	260.00	126.00	520.00	70.10	372.00	27.60
Cr	392.00	57.80	370.00	92.00	436.00	475.00	22.40	58.10	2807
MnO	0.15	0.19	0.175	0.167	0.108	0.17	0.071	0.177	0.121
Co	38.60	60.10	52.00	43.00	29.50	90.00	11.70	34.30	116.00
Ni	139.00	25.40	170.00	70.00	130.00	195.00	14.30	36.20	2460
Cu	56.70	85.70	125.00	110.00	29.70	135.00	6.81	194.00	6.72
Zn	82.10	109.00	70.00		64.70	190.00	46.50	100.00	41.80
Ga	17.90	17.90	16.00	17.00	16.90		17.10	19.80	0.70
Rb	39.20	6.87	0.25	20.00	72.90	8.50	67.30	15.10	0.80
Sr	442.00	327.00	108.00	194.00	248.00	266.00	379.00	403.00	3.32
Y	24.00	10.40	16.00	24.00	18.30	14.00	17.30	26.90	1.54
Zr	144.00	32.80	15.50	94.00	116.00	108.00	144.00	97.80	5.92
Nb	26.90	2.80	0.60	7.90	9.47	20.00	5.88	2.47	1.48
Cs	1.31	0.26	0.005	0.99	4.63	0.57	1.78	0.94	0.15
Ba	504.00	64.30	7.00	182.00	321.00	61.00	466.00	245.00	19.50
La	37.60	3.60	0.62	11.40	15.80	9.80	20.60	8.81	0.084
Ce	65.90	8.17	1.95	24.00	32.70	26.00	40.30	21.50	0.19
Pr	7.30	1.13	0.38		3.84	3.40	4.70	3.11	0.02
Nd	26.00	5.47	2.50	14.00	13.90	19.20	17.20	15.60	0.072
Sm	5.07	1.49	1.10	3.25	3.11	4.50	3.39	4.27	0.019
Eu	1.46	0.62	0.54	1.10	0.93	1.39	0.90	1.32	0.004
Gd	4.67	1.61	1.85	3.60	3.06	4.00	2.92	4.67	0.015
Tb	0.69	0.29	0.36	0.63	0.44	0.51	0.46	0.73	0.003
Dy	3.99	1.56	2.50	3.80	2.80	2.90	2.59	4.54	0.022
Ho	0.71	0.33	0.57	0.76	0.50	0.49	0.38	0.80	0.018
Er	2.18	1.04	1.70	2.50	1.48	1.12	1.52	2.49	0.016
Tm	0.33	0.16	0.26	0.38	0.28	0.11	0.24	0.42	0.041
Yb	2.10	1.06	1.65	2.05	1.62		1.77	2.55	0.022
Lu	0.33	0.15	0.26	0.32	0.27	0.12	0.26	0.39	0.0044
Hf	3.41	0.88	0.60	2.56	2.86	3.76	4.29	2.67	0.20
Ta	1.93	0.18		0.50	0.80	0.80	0.70	0.15	0.02
Pb	6.76	1.92	3.00	9.30	19.20	10.00	11.70	5.58	0.12
Th	9.03	0.48	0.03	2.20	5.03	0.93	8.28	1.27	0.19
U	1.57	0.13	0.01	0.53	2.21	0.24	2.21	0.48	0.036

Element concentrations given in ppm except for TiO_2 and MnO which are given in wt. %. The element concentrations for JB-1a, JGb-1, JA-2, JG-3, JB-3 and JP-1 are from Imai et al. (1995). The element concentrations for BIR-1, W2 and MRG-1 are from Govindaraju (1994).

while MRG-1 is issued by the Canadian Certified Reference Materials Project. The measured element concentrations of these standards are given in Table D.2 along with their percentage differences from the accepted values. Table D.3 provides the accepted values of the nine standards. The percentage errors for the elements of interest are low for all the standards except for the peridotite JP-1. As all the other standards contain elemental concentrations of a similar magnitude to those in the samples, the failure of the mass spectrometer to accurately measure the low elemental concentrations of JP-1 was not considered a problem. Aside from JP-1, the percentage errors for the elements of interest are generally less than 10%. For a few of the standards the percentage errors for U and Pb exceed 10%. This may in part be due to the larger uncertainties in the accepted concentrations of these two elements in the reference standards (Govindaraju, 1994; Imai et al, 1995). In summary, the similarity of the measured standard materials to the published values suggest that the results obtained via the HF-HNO_3 acid digestion preparatory method are accurate and can be relied upon during interpretation.

D.6. Isotopic results

D.6.1. Sr isotopes

The measured Sr isotope ratios, age-corrected Sr isotope ratios and Rb and Sr concentrations of the leached samples are given in Table D.4. $^{87}Sr/^{86}Sr$ was normalised during run time to a $^{86}Sr/^{88}Sr$ value of 0.1194. The measured $^{87}Sr/^{86}Sr$ ratios are reported relative to the accepted value of $^{87}Sr/^{86}Sr$ for NBS 987 of 0.71025. The measured $^{87}Sr/^{86}Sr$ for NBS 987 was 0.710256 ± 0.000006 (1σ) (n=10). The minimum uncertainty for $^{87}Sr/^{86}Sr$ is derived from the external precision of standard measurements and is 17 ppm (2σ). For all cases, within-run errors are <14 ppm (2σ) and are less than the external reproducibility. Blanks for Sr were less than 1 ng.

D.6.2. Nd isotopes

The measured Nd isotope ratios, age-corrected Nd isotope ratios, age-corrected εNd values and Sm and Nd concentrations of the leached samples are given in Table D.5. $^{143}Nd/^{144}Nd$ was normalised during run time to a $^{146}Nd/^{144}Nd$ value of 0.7219. The

Table D.4. Sr isotope data

Sample	$^{87}Sr/^{86}Sr$ measured	±	Rb (ppm)	Sr (ppm)	$^{87}Rb/^{86}Sr$	$^{87}Sr/^{86}Sr$ initial
MMF07-2	0.704166	0.000004	5.34	192.03	0.080376	0.701992
MMF07-7	0.705257	0.000005	8.97	213.13	0.121694	0.701965
MMF07-14	0.703776	0.000005	3.96	282.40	0.040593	0.702678
MMF07-17	0.703125	0.000010	1.67	488.48	0.009881	0.702858
MMLT07-28	0.702340	0.000006	0.62	186.18	0.009565	0.702081
MMLT07-41	0.702593	0.000005	0.29	133.57	0.006170	0.702426
MMM07-14	0.702351	0.000005	0.32	67.32	0.013812	0.701978
MMM07-17	0.703886	0.000005	3.44	144.95	0.068570	0.702031
MMM07-20	0.704506	0.000005	0.79	55.35	0.041152	0.703392
MMM07-26	0.702784	0.000007	0.68	42.38	0.046348	0.701530
MMPC07-2	0.702630	0.000010	1.30	120.75	0.031070	0.701790
MMW07-4	0.703090	0.000004	0.61	57.59	0.030825	0.702256
MMW07-24	0.702116	0.000005	0.36	144.20	0.007185	0.701921
MMB08-6	0.703980	0.000006	0.36	415.39	0.002527	0.703911
MMH08-5	0.712234	0.000005	2.86	174.07	0.047470	0.710950
MMH08-7	0.703429	0.000005	1.29	109.09	0.034193	0.702504
MMH08-12	0.712609	0.000005	35.07	243.22	0.417287	0.701319
MMH08-20	0.706805	0.000006	13.88	376.00	0.106811	0.703915

Errors in table reported as two standard errors (2se). Initial $^{87}Sr/^{86}Sr$ calculated to an age of 1880 Ma.

Table D.5. Nd isotope data

Sample	$^{143}Nd/^{144}Nd$ measured	±	Sm (ppm)	Nd (ppm)	$^{147}Sm/^{144}Nd$	$^{143}Nd/^{144}Nd$ initial	εNd_i
MMF07-2	0.512811	0.000011	2.10	6.57	0.193377	0.510419	+4.19
MMF07-7	0.512741	0.000008	2.21	6.85	0.195176	0.510326	+2.38
MMF07-14	0.512701	0.000030	2.40	7.61	0.190544	0.510344	+2.73
MMF07-17	0.512512	0.000011	3.30	11.36	0.175825	0.510337	+2.60
MMLT07-28	0.512914	0.000010	2.82	8.38	0.203718	0.510394	+3.72
MMLT07-41	0.512931	0.000018	1.72	5.11	0.203373	0.510415	+4.12
MMM07-14			1.82	4.88			
MMM07-17			3.24	11.41			
MMM07-20	0.512853	0.000007	1.60	4.78	0.202113	0.510352	+2.89
MMM07-26			1.53	4.39			
MMPC07-2	0.513173	0.000015	1.68	4.65	0.218102	0.510475	+5.29
MMW07-4			1.12	3.10			
MMW07-24	0.512985	0.000094	2.03	5.72	0.215096	0.510324	+2.35
MMB08-6	0.511979	0.000007	3.05	12.19	0.151238	0.510108	-1.89
MMH08-5	0.511698	0.000006	3.50	14.85	0.142535	0.509935	-5.29
MMH08-7	0.513013	0.000009	1.53	4.32	0.213312	0.510374	+3.33
MMH08-12	0.511357	0.000110	6.53	31.53	0.125202	0.509808	-7.77
MMH08-20	0.512015	0.000009	4.82	20.40	0.142922	0.510247	+0.84

Errors in table reported as two standard errors (2se). Initial $^{143}Nd/^{144}Nd$ and εNd are calculated to an age of 1880 Ma.

measured $^{143}Nd/^{144}Nd$ ratios are reported relative to the accepted value of $^{143}Nd/^{144}Nd$ for La Jolla of 0.51186. The measured $^{143}Nd/^{144}Nd$ for La Jolla was 0.511844 ± 0.000005 (1σ) (n=3). The minimum uncertainty for $^{143}Nd/^{144}Nd$ is derived from the external precision of standard measurements and is 20 ppm (2σ). For most cases the within-run errors are less than the external reproducibility. However, for samples MMF07-14, MMW07-24 and MMH08-12 within-run standard errors were much higher than the external reproducibility and are 59 ppm (2σ), 183 ppm (2σ) and 216 ppm (2σ) respectively. Blanks for Nd were less than 200 pg.

D.6.3. Pb isotopes

The measured Pb isotope ratios, age-corrected Pb isotope ratios and U, Th and Pb concentrations of the leached samples are given in Table D.6. Mass fractionation was corrected for during the run using the Tl-doping method. A $^{203}Tl/^{205}Tl$ value of 0.41876 was used, which was determined empirically by cross-calibration with NBS 981. The measured $^{206}Pb/^{204}Pb$, $^{207}Pb/^{204}Pb$ and $^{208}Pb/^{204}Pb$ ratios are reported relative to the accepted values of $^{206}Pb/^{204}Pb$, $^{207}Pb/^{204}Pb$ and $^{208}Pb/^{204}Pb$ for NBS 981 of 16.9417, 15.4996 and 36.7240 respectively. The samples were run in two different batches. The measured $^{206}Pb/^{204}Pb$, $^{207}Pb/^{204}Pb$ and $^{208}Pb/^{204}Pb$ for NBS 981 in the first batch were 16.9443 ± 0.0007 (1σ) (n=13), 15.5006 ± 0.0009 (1σ) (n=13) and 36.7281 ± 0.0028 (1σ) (n=13) respectively. The measured $^{206}Pb/^{204}Pb$, $^{207}Pb/^{204}Pb$ and $^{208}Pb/^{204}Pb$ for NBS 981 in the second batch were 16.9449 ± 0.0010 (1σ) (n=28), 15.5009 ± 0.0008 (1σ) (n=28) and 36.7301 ± 0.0027 (1σ) (n=28) respectively. Minimum uncertainties for the Pb isotope ratios are derived from the external precision of standard measurements and the reproducibility is better than ±0.015% (2σ). Blanks for Pb were less than 500 pg.

D.6.4. Hf isotopes

The measured Hf isotope ratios, age-corrected Hf isotope ratios, age-corrected εHf values and Lu and Hf concentrations of the leached samples are given in Table D.7. $^{176}Hf/^{177}Hf$ was normalised during run time to a $^{179}Hf/^{177}Hf$ value of 0.7325. The measured $^{176}Hf/^{177}Hf$ ratios are reported relative to the accepted value of $^{176}Hf/^{177}Hf$ for JMC 475 of 0.282160. The samples were run in three batches. The measured

Table D.6. Pb isotope data

Sample	$^{206}Pb/^{204}Pb$ measured	±	$^{207}Pb/^{204}Pb$ measured	±	$^{208}Pb/^{204}Pb$ measured	±	U (ppm)	Th (ppm)	Pb (ppm)	$^{206}Pb/^{204}Pb$ initial	$^{207}Pb/^{204}Pb$ initial	$^{208}Pb/^{204}Pb$ initial
MMF07-2(1)	19.8677	0.0049	15.5885	0.0051	38.4701	0.0162	0.26	0.62	0.67	11.4448	14.6198	32.4919
MMF07-7(2)	20.4442	0.0056	15.7679	0.0041	37.9435	0.0134	0.39	0.79	1.25	13.5719	14.9775	33.8372
MMF07-14							0.26	0.34	0.13			
MMF07-17							0.45	1.14	3.01			
MMLT07-28(2)	19.6857	0.0056	15.7366	0.0043	39.1866	0.0140	0.09	0.29	0.40	14.6348	15.1557	34.4294
MMLT07-41(1)	19.8244	0.0097	15.6648	0.0086	39.1901	0.0241	0.07	0.19	0.18	11.3369	14.6887	32.1131
MMM07-14(2)	18.6277	0.0059	15.4432	0.0048	38.4995	0.0146	0.05	0.13	1.01	17.5126	15.3149	37.6620
MMM07-17(2)	18.3716	0.0065	15.3280	0.0059	38.0252	0.0171	0.26	0.55	5.05	17.2766	15.2021	37.3331
MMM07-20(1)	19.9078	0.0043	15.8407	0.0043	39.4305	0.0137	0.11	0.34	1.75	18.4732	15.6757	38.1281
MMM07-26(2)	18.1022	0.0062	15.4387	0.0050	38.2879	0.0157	0.02	0.07	0.31	16.5342	15.2583	36.9130
MMPC07-2							0.09	0.22	0.28			
MMW07-4							0.03	0.10	0.53			
MMW07-24							0.07	0.18	0.86			
MMB08-6(1)	17.6195	0.0046	15.8473	0.0054	39.2799	0.0162	0.34	1.87	4.46	15.9534	15.6557	36.5829
MMH08-5(2)	23.2826	0.0068	16.5643	0.0046	44.1926	0.0163	1.10	2.92	3.63	15.7176	15.6943	38.2246
MMH08-7(2)	17.7269	0.0050	15.6996	0.0044	37.4243	0.0135	0.13	0.13	3.77	16.9804	15.6138	37.2105
MMH08-12(2)	18.2309	0.0049	15.7051	0.0040	42.5904	0.0143	0.69	4.30	4.78	14.9750	15.3306	36.5181
MMH08-20(2)	17.0667	0.0050	15.5921	0.0045	38.2023	0.0143	0.32	1.52	3.83	15.2912	15.3879	35.7237

Errors in table reported as two standard errors (2se). The numbers in parentheses refer to which batch the samples were run in. In (1) the measured $^{206}Pb/^{204}Pb$, $^{207}Pb/^{204}Pb$ and $^{208}Pb/^{204}Pb$ for NBS 981 were 16.9443 ± 0.0007 (1σ) (n=13), 15.5006 ± 0.0009 (1σ) (n=13) and 36.7281 ± 0.0028 (1σ) (n=13) respectively. In (2) the measured $^{206}Pb/^{204}Pb$, $^{207}Pb/^{204}Pb$ and $^{208}Pb/^{204}Pb$ for NBS 981 were 16.9449 ± 0.0010 (1σ) (n=28), 15.5009 ± 0.0008 (1σ) (n=28) and 36.7301 ± 0.0027 (1σ) (n=28) respectively. Initial Pb isotope ratios are calculated to an age of 1880 Ma.

$^{176}Hf/^{177}Hf$ for JMC 475 in the first, second and third batches were 0.282153 ± 0.000004 (1σ) (n=10), 0.282155 ± 0.000004 (1σ) (n=11), and 0.282142 ± 0.000005 (1σ) (n=14) respectively. The minimum uncertainty for $^{176}Hf/^{177}Hf$ is derived from the external precision of standard measurements and averages 31 ppm (2σ). For most cases the within-run errors are <27 ppm (2σ) and less than the external reproducibility. However, for samples MMLT07-28, MMM07-20 and MMW07-24 the within-run errors were slightly higher than the external reproducibility for the particular sample batch and are 30 ppm (2σ), 34 ppm (2σ) and 36 ppm (2σ) respectively. Blanks for Hf were less than 40 pg.

Table D.7. Hf isotope data

Sample	$^{176}Hf/^{177}Hf$ measured	±	Lu (ppm)	Hf (ppm)	$^{176}Lu/^{177}Hf$	$^{176}Hf/^{177}Hf$ initial	εHf_i
MMF07-2[1]	0.282421	0.000002	0.45	3.43	0.018454	0.281762	+6.21
MMF07-7[1]	0.282297	0.000002	0.46	3.63	0.018104	0.281651	+2.27
MMF07-14[2]	0.282262	0.000003	0.38	3.71	0.014363	0.281749	+5.76
MMF07-17[1]	0.282406	0.000003	0.51	3.69	0.019503	0.281710	+4.37
MMLT07-28[1]	0.284826	0.000004	0.35	0.74	0.067528	0.282416	+29.44
MMLT07-41[1]	0.284640	0.000003	0.25	0.55	0.063320	0.282381	+28.17
MMM07-14[3]	0.282824	0.000003	0.37	1.84	0.028750	0.281798	+7.48
MMM07-17[3]	0.282542	0.000004	0.40	2.71	0.021133	0.281788	+7.11
MMM07-20[1]	0.282719	0.000005	0.24	1.28	0.026529	0.281772	+6.56
MMM07-26[3]	0.282824	0.000005	0.25	1.19	0.029898	0.281757	+6.03
MMPC07-2[1]	0.282735	0.000002	0.36	2.14	0.023868	0.281883	+10.49
MMW07-4[1]	0.282851	0.000003	0.18	0.93	0.027621	0.281865	+9.86
MMW07-24[1]	0.283198	0.000005	0.31	1.27	0.035214	0.281942	+12.59
MMB08-6[1]	0.282465	0.000002	0.30	1.70	0.024936	0.281575	-0.43
MMH08-5[3]	0.282087	0.000004	0.49	4.32	0.016123	0.281512	-2.69
MMH08-7[2]	0.283495	0.000003	0.24	1.70	0.042400	0.281982	+14.03
MMH08-12[3]	0.281931	0.000003	0.47	4.61	0.014437	0.281416	-6.09
MMH08-20[2]	0.282294	0.000003	0.32	2.39	0.019180	0.281610	+0.81

Errors in table reported as two standard errors (2se). The numbers in parentheses refer to which batch the samples were run in. In (1) the measured $^{176}Hf/^{177}Hf$ for JMC 475 was 0.282153 ± 0.000004 (1σ) (n=10). In (2) the measured $^{176}Hf/^{177}Hf$ for JMC 475 was 0.282155 ± 0.000004 (1σ) (n=10). In (3) the measured $^{176}Hf/^{177}Hf$ for JMC 475 was 0.282142 ± 0.000005 (1σ) (n=14). Initial $^{176}Hf/^{177}Hf$ and εHf are calculated to an age of 1880 Ma.

D.6.5. Os isotopes

The measured Os isotope ratios, age-corrected Os isotope ratios, age-corrected γOs values and Re and Os concentrations of the samples are given in Table D.8.

Table D.8. Os isotope data

Sample	$^{187}Os/^{188}Os$ measured	±	Re (ppt)	±	Os (ppt)	±	$^{187}Re/^{188}Os$	$^{187}Os/^{188}Os$ initial	γOs_i
MMF07-14	8.827303	0.000099	2246	4	48	0.29	477.885549	-6.377323	-5648.8
MMF07-17	2.413718	0.000979	1366	1	89	7.80	96.090163	-0.643531	-659.9
MMLT07-28	3.031068	0.000061	1769	6	124	1.41	94.989505	0.008838	-92.3
MMLT07-35			965	2					
MMLT07-41	0.501781	0.000047	472	2	97	0.88	24.545963	-0.279184	-342.9
MMM07-17	17.307328	0.013210	977	2	20	0.06	778.294076	-7.455233	-6586.6
MMM07-20	0.252386	0.000015	1038	7	876	1.02	5.801237	0.067811	-41.0
MMM07-26	0.315054	0.000024	1172	1	658	0.97	8.790252	0.035379	-69.2
MMW07-4	0.170420	0.000013	580	1	1562	2.63	1.800458	0.113136	-1.6
MMW07-24	10.512965	0.001149	1800	2	53	0.09	387.784453	-1.824963	-1687.9
MMC08-21	0.231915	0.000106	939	6	926	1.68	4.955189	0.074259	-35.4
MMH08-7	10.721301	0.001765	1498	2	45	0.09	380.597932	-1.387977	-1307.7
MMH08-12	7.206796	0.043285	321	1	8	0.31	370.418604	-4.578612	-4083.7
MMH08-20	14.533058	0.008249	770	2	13	0.03	838.591862	-12.147964	-10669.7
MMT08-12	0.209471	0.000011	1962	3	3066	3.12	3.116926	0.110301	-4.1

Errors in table reported as two standard errors (2se). Initial $^{187}Os/^{188}Os$ and γOs are calculated to an age of 1880 Ma.

$^{187}Os/^{188}Os$ was normalised during run time to a $^{192}Os/^{188}Os$ value of 3.08271 and corrected using $^{18}O/^{16}O$ and $^{17}O/^{16}O$ ratios of 0.002047 and 0.00037 respectively. The measured $^{187}Os/^{188}Os$ ratios are reported relative to the accepted value of $^{187}Os/^{188}Os$ for the Johnson-Matthey Os standard of 0.17398. The measured $^{187}Os/^{188}Os$ for the Johnson-Matthey Os standard was 0.17402 ± 0.00020 (1σ) (n=3). The minimum uncertainty for $^{187}Os/^{188}Os$ is derived from the external precision of standard measurements and is 2299 ppm (2σ). For the majority of samples the within-run errors are less than the external reproducibility and are <1646 ppm (2σ). However, for samples MMF07-17, MMM07-17, MMC08-21, MMH08-12 and MMH08-20 the within-run errors were larger than the external reproducibility and are 4056 ppm (2σ), 7633 ppm (2σ), 4553 ppm (2σ), 6.01% (2σ) and 5676 ppm (2σ) respectively. Blanks for Re and Os were less than 6 pg and 0.2 pg respectively.

Appendix E: Scanning electron microscopy results of olivine analyses

E.1. Preparation of samples

Thin rectangular slices of all rock samples were obtained using a diamond-bladed mechanical rock saw at Cardiff University. These were made into polished thin sections either at Cardiff University by Mr. Lawrence Badham or at Keele University by Mr. Peter Greatbatch. The polished thin sections chosen to be analysed were coated in carbon prior to being placed in the sample chamber of the scanning electron microscope.

E.2. Scanning electron microscope

The chemistry of olivine crystals was measured using the analytical scanning electron microscope at Cardiff University under the supervision of Mr. Peter Fisher. The microscope is a Cambridge Instruments LEO S360 Scanning Electron Microscope and is coupled to an Oxford Instruments INCA energy dispersive X-ray analysis system. A variety of standards supplied by Microanalysis Consultants were used for calibration and the instrument drift was monitored with a Co reference material. Only results where the total weight percentages were within ±1.5% of 100 wt. % were collected.

E.3. Results

Only olivines from four samples of the Winnipegosis Belt were analysed by the scanning electron microscope. Where possible, measurements were made in several sections of the olivine crystals. The results are displayed in Table E.1. The concentration of the elements in olivine crystals were measured in weight percent and then converted to atomic percent using the atomic masses of the relevant elements given in de Laeter et al. (2003). Forsterite number (Fo = 100Mg/(Mg+Fe)) was calculated using the atomic percentages of Mg and Fe.

Table E.1. Scanning electron microscope analyses of olivine crystals

Mg	Fe	Si	O	Ni	Cr	Al	Total	Fo
Sample MMW07-9								
Olivine crystal #1								
29.48	7.56	19.01	43.49	0.35	0.13	0.13	100.14	90.0
29.53	7.51	19.11	43.46	0.37			99.98	90.0
Olivine crystal #2								
29.58	8.16	19.11	43.66	0.33			100.83	89.3
29.44	8.10	19.15	43.61	0.37			100.68	89.3
Olivine crystal #3								
29.05	7.87	18.75	42.83	0.35			98.86	89.4
29.94	8.03	18.77	42.90	0.35	0.16		99.15	89.2
29.41	7.89	19.11	43.47	0.30			100.18	89.5
Olivine crystal #4								
29.29	8.25	19.12	43.42				100.08	89.1
29.16	8.20	18.97	43.15				99.48	89.1
Olivine crystal #5								
29.57	7.83	19.11	43.57	0.32			100.40	89.7
29.26	7.32	18.85	42.90	0.26			98.58	90.2
29.37	7.63	19.05	43.32	0.35			99.72	89.8
29.46	7.50	19.09	43.29				99.34	90.0
Olivine crystal #6								
29.81	7.76	19.19	43.77	0.26			100.79	89.8
29.77	7.29	18.99	43.40	0.30			99.74	90.4
29.70	7.12	19.06	43.31				99.20	90.6
Sample MMW07-12								
Olivine crystal #1								
30.03	7.13	18.97	43.52	0.37			100.03	90.6
29.47	6.96	19.02	43.12	0.26			98.82	90.7
Olivine crystal #2								
29.55	7.56	19.10	43.44	0.26			99.92	90.0
Olivine crystal #3								
29.44	7.93	18.95	43.32	0.31			99.96	89.5
29.63	7.64	19.09	43.43				99.79	89.9
Olivine crystal #4								
29.12	7.72	18.84	42.84				98.52	89.7
28.78	8.17	18.71	42.70	0.40			98.76	89.0
Olivine crystal #5								
29.33	7.71	18.96	43.11				99.11	89.7
29.48	7.56	18.82	43.10	0.33			99.30	90.0
29.80	7.48	19.10	43.60	0.35			100.33	90.1
29.61	7.56	19.04	43.44		0.19		99.85	90.0
Olivine crystal #6								
29.37	7.68	18.90	43.13	0.27			99.36	89.8
29.54	7.97	19.10	43.56	0.30			100.47	89.5
29.27	7.73	18.68	42.85	0.34			98.86	89.7

Table E.1. contd.

Mg	Fe	Si	O	Ni	Cr	Al	Total	Fo
Sample MMW07-17								
Olivine crystal #1								
27.38	11.83	18.80	42.90	0.29			101.19	84.2
Olivine crystal #2								
29.73	8.15	19.33	43.92				101.13	89.3
26.40	12.29	18.53	42.00				99.22	83.2
Olivine crystal #3								
29.13	7.54	18.92	42.95				98.81	89.9
29.41	7.39	19.02	43.21	0.28			99.31	90.1
29.33	7.72	19.07	43.24				99.36	89.7
Olivine crystal #4								
29.57	8.03	19.01	43.51	0.31			100.43	89.4
29.79	7.57	19.18	43.72	0.35			100.61	90.0
Olivine crystal #5								
29.64	7.68	18.82	43.22	0.31			99.66	89.8
29.63	7.44	18.99	43.45	0.36	0.17		100.05	90.2
Olivine crystal #6								
29.85	7.67	18.95	43.53	0.38			100.37	89.9
29.44	7.67	18.95	43.25	0.36			99.67	89.8
29.30	7.51	18.98	43.06				98.85	90.0
Olivine crystal #7								
29.54	8.08	19.41	43.95	0.29			101.29	89.4
29.53	7.95	19.06	43.51	0.31			100.36	89.5
Olivine crystal #8								
29.83	8.01	19.04	43.70	0.28			100.86	89.5
29.03	8.13	18.93	43.10	0.38			99.58	89.1
Olivine crystal #9								
29.66	7.48	18.93	43.32	0.33			99.72	90.1
29.12	8.14	18.99	43.23	0.37			99.85	89.2
29.93	8.02	19.10	43.83	0.28			101.17	89.6
Olivine crystal #10								
29.72	7.53	19.11	43.58	0.36			100.29	90.1
29.63	7.67	18.99	43.42	0.33			100.03	89.9
Sample MMW07-19								
Olivine crystal #1								
30.03	7.38	19.33	43.95	0.18			100.86	90.3
Olivine crystal #2								
27.22	12.09	18.72	42.71				100.74	83.8
Olivine crystal #3								
29.00	8.03	18.87	42.89				98.79	89.2
29.39	7.45	18.82	43.01	0.34			99.02	90.0
28.95	8.11	18.69	42.74	0.26			98.75	89.1
29.00	7.78	18.76	42.76	0.26			98.56	89.5

Table E.1. contd.

Mg	Fe	Si	O	Ni	Cr	Al	Total	Fo
Olivine crystal #4								
29.44	7.64	19.10	43.32				99.50	89.8
29.55	7.80	19.00	43.42	0.32			100.09	89.7
Olivine crystal #5								
29.98	7.91	19.17	43.93	0.37			101.36	89.7
29.18	8.06	18.96	43.18	0.24			99.61	89.3
Olivine crystal #6								
23.96	15.63	18.13	40.97	0.28			98.96	77.9
29.67	7.87	19.08	43.62	0.36			100.60	89.7
29.77	7.63	19.08	43.51				99.99	90.0
Olivine crystal #7								
28.56	8.27	18.78	42.56				98.17	88.8
29.19	8.02	18.93	43.15	0.28			99.57	89.3
29.64	7.67	18.90	43.32	0.31			99.84	89.9
Olivine crystals #8								
29.08	7.92	18.76	42.78				98.53	89.4
29.09	7.61	18.80	42.82	0.31			98.62	89.8

Element concentrations and totals given in wt. %.

Appendix F: Petrogenetic modelling constraints

F.1. Equations

The equation for non-modal batch melting is given below.

$$C_L = \frac{C_O}{D + F - FP}$$

Equation F.1

where C_L is the trace element concentration in the melt, C_O is the trace element concentration in the source, D is the bulk distribution co-efficient at the onset of melting, F is the fraction of melting and P is the bulk distribution co-efficient of the minerals which make up the melt.

The equation for the residue of non-modal batch melting is given below.

$$C_s = C_O\left(\frac{D - FP}{1 - F}\right)\left(\frac{1}{D + F - FP}\right)$$

Equation F.2

where C_S is the trace element concentration in the solid residue.

The equation for Rayleigh or fractional crystallisation is given below.

$$C_L = C_O F^{(D-1)}$$

Equation F.3

where C_O is redefined as the trace element concentration of the primary magma, D as the bulk distribution co-efficient of the fractionating assemblage and F as the fraction of melt remaining.

The equation for the residue of fractional crystallisation is given below.

$$C_R = C_O\left(\frac{1-F^D}{1-F}\right)$$

Equation F.4

where C_R is the trace element concentration in the total solid residue.

The equation for assimilation with concomitant fractional crystallisation (AFC) is given below.

$$C_L = C_O\left(f' + \frac{r}{r-1+D}\cdot\frac{C_A}{C_O}(1-f')\right)$$

Equation F.5

where r is the ratio of the assimilation rate to the fractional crystallisation rate, C_A is the trace element concentration in the assimilant, and f' is given by the equation below.

$$f' = F^{\frac{-(r-1+D)}{r-1}}$$

Equation F.6

The equation for simple binary mixing, for example between magma and a crustal assimilant, is given below.

$$C_{Mix} = \frac{C_{Magma} + xC_A}{1-x}$$

Equation F.7

where C_{Mix} is the trace element concentration in the resultant mixture, C_{Magma} is the trace element concentration in the uncontaminated magma, and x is the fraction of assimilant added to the magma.

F.2. Mineral modes

The modal mineralogy used in equations for melting of spinel lherzolite is that of Johnson et al. (1990) and is given in Table F.1.

Table F.1. Mineral modes for spinel lherzolite

	Olivine	Orthopyroxene	Clinopyroxene	Spinel
Spinel lherzolite	0.55	0.25	0.18	0.02

F.3. Melting modes

The melting modes used for determining P values in equations for melting of spinel lherzolite are those of Johnson et al. (1990) and are given in Table F.2.

Table F.2. Melting modes for spinel lherzolite

	Olivine	Orthopyroxene	Clinopyroxene	Spinel
Spinel lherzolite	0.10	0.20	0.67	0.02

F.4. Partition co-efficients

The partition co-efficients used to calculate D values in partial melting, fractional crystallisation and AFC equations in the current study are given in Table F.3.

Table F.3. Partition co-efficients used in the petrogenetic modelling in the current study for trace elements between ultramafic-mafic melts and olivine, orthopyroxene, clinopyroxene, spinel, plagioclase and magnetite crystals

	Olivine	Orthopyroxene	Clinopyroxene	Spinel	Plagioclase	Magnetite
Th	0.0000001	0.0004	0.014	0.013	0.3435	0.1
Nb	0.0001	0.002825	0.00605	0.01	0.09725	0.7
Ta	0.0001	0.002825	0.00605	0.01	0.0795	0.23
La	0.000007	0.0000535	0.05025	0.0006	0.0631	0.015
Ce	0.00001	0.0026	0.089	0.0006	0.0457	0.016
Pr	0.00004	0.0065	0.1335	0.0006	0.1375	0.02
Nd	0.00007	0.010267	0.178	0.0006	0.0478	0.026
Zr	0.0005	0.01775	0.1975	0.07	0.0094	0.71
Hf	0.0038	0.027225	0.2115	0.003	0.082	0.16
Sm	0.0007	0.018	0.3775	0.0006	0.06575	0.024
Eu	0.00095	0.0215	0.458	0.0006	0.3254	0.025
Ti	0.015	0.082	0.3955	0.15	0.0473	16.5
Gd	0.002	0.028	0.487	0.0009	0.07175	0.018

Table F.3. contd.

	Olivine	Orthopyroxene	Clinopyroxene	Spinel	Plagioclase	Magnetite
Tb	0.003	0.035	0.516	0.0012	0.084	0.019
Dy	0.004	0.041	0.5455	0.0015	0.057167	0.018
Y	0.007365	0.0935	0.412	0.002	0.00989	0.0039
Ho	0.0065	0.05	0.603	0.00225	0.0592	0.017
Er	0.009	0.063917	0.66	0.003	0.07633	0.017
Tm	0.015	0.078	0.66	0.00375	0.072	0.017
Yb	0.023	0.093917	0.5165	0.0045	0.0903	0.018
Lu	0.03	0.1	0.536	0.00525	0.1175	0.023

Partition co-efficient data from the following sources: Olivine – Kelemen et al. (1993), Beattie (1994) and Bedini & Bodinier (1999); Orthopyroxene – McKenzie & O'Nions (1991), Kelemen et al. (1993) and Salters & Longhi (1999); Clinopyroxene – Hauri et al. (1994) and Johnson (1998); Spinel – Keleman et al. (1993) and Elkins et al. (2008); Plagioclase – Aigner-Torres et al. (2007); Magnetite – Haskin et al. (1966), Okamoto (1979), Lemarchand et al. (1987) and Nielsen et al. (1992). The partition co-efficients for Ta in olivine, orthopyroxene, clinopyroxene and spinel have been assigned the same as for Nb due to the lack of published data on Ta. The partition co-efficients for Pr, Gd, Tb, Ho, Tm and Lu in olivine, orthopyroxene, clinopyroxene and spinel have been inferred due to the lack of published data on these elements. The partition co-efficients for Pr, Dy, Er and Tm in magnetite have been inferred due to a lack of published data on these elements.

F.5. End-member compositions

The trace element compositions of source regions, primary magmas and contaminants used in petrogenetic modelling are given in Table F.4.

Table F.4. Trace element compositions of source regions, primary magmas and contaminants

	Primitive mantle (PM)	Depleted MORB mantle (DMM)	Average continental crust (CC)	PM-1%CC	MMC08-23 + 2.64% olivine	MMFR08-8 + 9.45% olivine
Th	0.085	0.0079	5.6	0.03	0.09	0.07
Nb	0.713	0.1485	12	0.60	1.52	1.35
Ta	0.041	0.0096	1.1	0.03	0.10	0.09
La	0.687	0.192	18	0.51	1.65	1.42
Ce	1.775	0.55	42	1.37	4.37	3.94
Pr	0.276	0.107	5	0.23	0.76	0.66
Nd	1.354	0.581	20	1.17	3.84	3.52
Zr	11.2	5.082	123	10.07	30.55	27.59
Hf	0.309	0.157	3.7	0.27	0.89	0.75
Sm	0.444	0.239	3.9	0.41	1.35	1.23
Eu	0.168	0.096	1.2	0.16	0.48	0.40
Ti	1300	716.3	4200	1270.71	2746.94	2527.57
Gd	0.596	0.358	3.6	0.57	1.62	1.54
Tb	0.108	0.07	0.56	0.10	0.28	0.33
Dy	0.737	0.505	3.5	0.71	2.10	1.97
Y	4.55	3.328	20	4.39	14.80	12.45
Ho	0.164	0.115	0.76	0.16	0.43	0.38
Er	0.48	0.348	2.2	0.46	1.30	1.12
Tm	0.074				0.21	0.18
Yb	0.493	0.365	2	0.48	1.32	1.13
Lu	0.074	0.058	0.33	0.07	0.21	0.18

Table F.4. contd.

	MMW07-9 + 0.09% olivine	MMM07-7 + 9.63% olivine	MMM07-20 + 8.48% olivine	Beauparlant Formation semi-pelite	Archaean biotite schist
Th	0.05	0.21	0.36	10.18	0.80
Nb	1.01	2.72	1.89	12.40	3.00
Ta	0.07	0.16	0.12		0.20
La	1.50	2.01	2.37	34.98	4.80
Ce	3.49	5.01	5.88	73.60	12.60
Pr	0.61	0.78	0.91	9.28	1.70
Nd	3.13	3.94	4.45	34.66	8.77
Zr	24.64	35.73	40.33	139.90	65
Hf	0.59	0.84	1.01	3.50	1.90
Sm	1.10	1.31	1.48	6.07	2.45
Eu	0.41	0.47	0.53	1.39	0.90
Ti	3111.78	3702.81	3668.06	5100	6420
Gd	1.40	1.64	1.83	4.88	3.00
Tb	0.28	0.30	0.33	0.67	0.57
Dy	1.89	2.05	2.25	3.64	3.80
Y	11.60	13.24	14.08	19.33	20.70
Ho	0.38	0.42	0.45	0.73	0.77
Er	1.14	1.20	1.31	2.00	2.40
Tm	0.17	0.19	0.21	0.27	0.36
Yb	1.16	1.30	1.37	1.70	2.30
Lu	0.18	0.20	0.22	0.24	0.372

	Lower Sedimentary Formation argillite	Average Thompson Nickel Belt Archaean gneiss
Th	9.80	7.20
Nb	13.50	4.21
Ta	0.90	0.21
La	32.00	23.32
Ce	53.50	39.72
Pr	7.40	4.41
Nd	27.81	15.38
Zr	92.80	84.47
Hf	2.49	2.70
Sm	5.25	2.57
Eu	1.20	0.71
Ti	1560	1179.20
Gd	5.00	1.84
Tb	0.75	0.25
Dy	4.30	1.34
Y	28.50	7.77
Ho	0.92	0.26
Er	2.60	0.72
Tm	0.39	0.10
Yb	2.30	0.65
Lu	0.363	0.10

All concentration values are given in ppm. Data sources: PM - Sun & McDonough (1989); DMM - Workman & Hart (2005); CC – Rudnick & Fountain (1995); Beauparlant Formation semi-pelite – Mungall (2007); Archaean biotite schist and Lower Sedimentary Formation argillite – Desharnais (2005); Average Thompson Nickel Belt Archaean gneiss – Burnham et al. (2004).

Appendix G: Unpublished geochemical data for ~1880 Ma igneous rocks from the Bastar craton, India and the Slave craton, Canada

Table G.1. Unpublished geochemical data courtesy of R.K. Srivastava from ~1880 Ma BD2 dykes in the Bastar craton, India

Original sample number	B1	B2	B3	B4	B5	B6	B7	B8	B9
SiO_2	49.27	49.35	47.79	53.65	49.42	48.94	48.39	49.05	48.23
TiO_2	2.42	2.51	2.81	2.13	2.44	2.64	2.05	2.72	1.79
Al_2O_3	13.17	12.97	13.38	13.00	12.52	12.12	13.11	11.40	14.49
$Fe_2O_3(T)$	16.76	17.47	17.91	16.51	17.77	18.05	18.43	19.05	12.49
MnO	0.25	0.26	0.26	0.24	0.27	0.26	0.26	0.28	0.20
MgO	4.84	5.47	5.06	1.77	5.55	4.35	4.61	5.23	6.58
CaO	9.23	9.42	9.14	6.78	9.70	9.06	9.12	7.39	11.26
Na_2O	2.29	1.95	2.12	2.64	2.11	2.05	2.32	2.25	2.45
K_2O	1.27	0.78	0.76	1.47	0.66	0.78	0.60	0.63	0.69
P_2O_5	0.32	0.30	0.34	0.71	0.27	0.29	0.21	0.38	0.29
LOI	0.31	0.04	0.44	1.04	-0.11	0.43	0.62	1.65	1.02
Total	100.12	100.53	100.00	99.94	100.60	98.97	99.74	100.04	99.49
Sc	39.2	42.6	38.2	25.7	43.6	39.9	41.9	40.7	34.3
V	290	294	442	100	390	381	466	388	272
Cr	141	178	113	29	136	56	67	112	161
Co	58.0	58.0	56.5	39.8	65.2	57.8	48.9	59.7	49.1
Ni	103	197	89	25	105	48	70	69	81
Cu	201	202	109	74	193	104	269	137	61
Zn	285	255	196	209	178	189	194	184	125
Ga	20.2	19.5	20.6	26.1	19.4	20.1	18.8	18.1	18.4
Rb	79.2	47.1	32.6	49.1	23.4	43.0	21.0	23.6	29.9
Sr	158	135	130	157	124	126	165	117	314
Y	50.1	51.3	53.8	111.8	48.1	53.8	42.2	60.0	22.8
Zr	212.3	199.4	211.7	178.0	191.7	240.1	123.6	222.1	129.2
Nb	13.36	11.71	14.02	20.99	11.27	13.33	5.97	12.76	15.20
Cs	1.18	1.38	0.79	0.73	0.76	1.92	0.24	0.70	5.18
Ba	207	159	141	360	135	155	224	153	203
La	20.15	19.81	17.96	48.63	14.92	18.77	10.29	19.18	15.77
Ce	45.09	44.49	41.69	107.73	34.08	42.63	23.59	44.23	35.05
Pr	6.25	6.15	5.79	14.72	4.86	5.90	3.55	6.22	4.71
Nd	27.36	27.04	25.82	63.16	22.01	26.40	16.29	28.13	19.95
Sm	6.92	6.90	6.72	15.67	5.82	6.74	4.56	7.46	4.57
Eu	1.97	1.92	1.97	4.11	1.76	1.99	1.54	2.03	1.54
Gd	7.64	7.59	7.82	17.14	6.83	8.03	5.59	8.77	4.63
Tb	1.40	1.39	1.46	3.04	1.27	1.47	1.09	1.65	0.78
Dy	7.85	7.90	8.35	16.95	7.37	8.36	6.38	9.37	4.03
Ho	1.61	1.60	1.73	3.44	1.52	1.73	1.36	1.93	0.77
Er	4.96	4.94	5.33	10.66	4.79	5.34	4.25	5.92	2.21
Tm	0.71	0.71	0.78	1.53	0.70	0.79	0.64	0.85	0.31
Yb	4.53	4.56	5.14	9.79	4.52	5.08	4.20	5.63	1.93
Lu	0.72	0.72	0.79	1.52	0.71	0.79	0.66	0.86	0.28
Hf	4.93	4.59	4.84	4.16	4.41	5.44	3.08	5.19	3.12
Ta	0.95	0.93	0.97	1.67	0.72	0.88	0.38	0.89	0.98
Th	4.66	4.62	3.67	11.37	3.12	4.31	1.10	4.43	2.25
U	1.37	1.39	1.02	3.24	0.89	1.15	0.37	0.99	0.57

Table G.1. contd.

Original sample number	B10	P1	P2	P3	P4	P5	P6	P7	P8
SiO_2	51.29	45.62	49.94	44.02	44.62	45.02	45.05	44.88	44.19
TiO_2	2.44	1.52	1.82	0.24	0.24	0.29	0.34	0.27	0.20
Al_2O_3	13.00	10.84	12.24	5.86	6.24	6.95	8.16	7.43	7.13
$Fe_2O_3(T)$	17.07	14.89	17.16	12.66	12.96	12.90	12.25	12.48	12.18
MnO	0.25	0.26	0.23	0.18	0.19	0.19	0.18	0.19	0.19
MgO	4.11	7.47	3.58	28.12	27.83	25.29	24.04	25.54	26.33
CaO	9.50	11.25	4.39	4.40	4.50	4.98	6.00	5.22	5.06
Na_2O	0.95	1.45	2.32	0.15	0.29	0.42	0.78	0.49	0.28
K_2O	1.04	2.86	1.91	0.25	0.27	0.28	0.35	0.28	0.17
P_2O_5	0.41	0.46	0.25	0.05	0.05	0.05	0.10	0.06	0.04
LOI	0.74	2.46	5.48	3.84	3.04	2.83	2.40	2.30	3.22
Total	100.80	99.06	99.33	99.77	100.23	99.21	99.66	99.14	99.00
Sc	35.2	40.9	40.1	19.0	18.9	21.4	23.8	22.1	20.0
V	440	266	337	101	108	115	126	110	95
Cr	26	68	20	2920	3444	2768	2782	2997	2930
Co	49.1	52.3	56.9	118.0	121.7	110.7	107.3	114.0	111.8
Ni	49	65	44	933	1111	867	857	918	939
Cu	222	91	151	44	46	68	61	47	52
Zn	223	207	137	89	76	137	96	94	138
Ga	21.5	15.2	19.9	6.6	7.1	8.0	8.8	7.8	7.2
Rb	49.2	51.7	40.4	10.7	11.7	12.3	13.5	12.0	7.0
Sr	149	237	109	41	49	52	62	50	65
Y	51.4	36.3	38.8	6.5	7.0	8.2	9.8	8.2	5.8
Zr	208.7	128.7	171.5	17.0	22.2	21.3	30.9	26.3	13.8
Nb	10.36	8.75	12.05	1.27	1.50	1.61	1.86	1.65	1.16
Cs	0.54	0.21	0.17	1.03	1.13	1.10	1.61	2.02	1.60
Ba	95	1295	365	61	70	74	81	74	46
La	22.21	15.63	21.14	3.93	4.05	5.08	5.83	4.62	2.92
Ce	46.75	33.22	43.05	7.62	7.82	9.70	11.22	8.95	5.66
Pr	6.53	4.39	5.57	0.93	0.97	1.17	1.35	1.09	0.71
Nd	27.77	18.66	22.90	3.65	3.75	4.58	5.40	4.30	2.85
Sm	6.53	4.48	5.43	0.81	0.87	1.01	1.19	0.98	0.67
Eu	1.99	1.51	1.70	0.27	0.28	0.33	0.39	0.32	0.25
Gd	7.54	5.25	5.79	0.87	0.89	1.12	1.33	1.06	0.72
Tb	1.36	0.97	1.05	0.18	0.18	0.23	0.25	0.22	0.15
Dy	7.85	5.59	6.00	1.04	1.05	1.26	1.49	1.21	0.87
Ho	1.64	1.14	1.22	0.22	0.22	0.27	0.31	0.26	0.19
Er	5.11	3.55	3.84	0.69	0.70	0.86	0.99	0.81	0.59
Tm	0.75	0.53	0.56	0.10	0.11	0.13	0.15	0.12	0.09
Yb	5.00	3.37	3.60	0.69	0.72	0.87	0.98	0.83	0.61
Lu	0.78	0.53	0.57	0.11	0.11	0.13	0.16	0.13	0.10
Hf	4.82	3.24	3.93	0.43	0.54	0.53	0.76	0.64	0.38
Ta	0.69	0.55	0.79	0.08	0.09	0.11	0.13	0.11	0.07
Th	3.74	4.20	8.76	1.41	1.53	1.67	2.08	1.53	0.94
U	1.13	1.25	3.01	0.31	0.32	0.36	0.45	0.34	0.21

Table G.1. contd.

Original sample number	P9	P10	P11
SiO_2	43.98	47.88	45.91
TiO_2	0.30	0.47	0.39
Al_2O_3	7.11	10.19	9.21
Fe_2O_3(T)	12.81	11.30	12.47
MnO	0.19	0.18	0.19
MgO	25.86	16.84	21.06
CaO	5.17	7.66	6.69
Na_2O	0.27	0.83	0.69
K_2O	0.31	0.33	0.51
P_2O_5	0.05	0.08	0.06
LOI	3.80	2.53	2.09
Total	99.84	98.29	99.28
Sc	21.8	30.6	26.8
V	113	155	144
Cr	2933	2207	2382
Co	111.0	78.1	98.6
Ni	871	2858	720
Cu	49	81	70
Zn	95	100	105
Ga	7.7	10.6	9.9
Rb	12.2	14.4	18.4
Sr	53	89	101
Y	8.3	14.1	11.3
Zr	22.8	42.0	40.1
Nb	1.71	2.55	2.39
Cs	2.48	2.09	4.03
Ba	72	129	130
La	4.85	7.95	6.66
Ce	9.40	15.35	12.84
Pr	1.14	1.86	1.59
Nd	4.53	7.37	6.22
Sm	1.03	1.65	1.44
Eu	0.33	0.51	0.47
Gd	1.10	1.82	1.51
Tb	0.21	0.36	0.30
Dy	1.26	2.08	1.72
Ho	0.26	0.42	0.36
Er	0.83	1.37	1.17
Tm	0.12	0.20	0.18
Yb	0.84	1.34	1.12
Lu	0.14	0.21	0.18
Hf	0.59	1.07	0.96
Ta	0.11	0.19	0.15
Th	1.62	2.96	2.37
U	0.37	0.66	0.52

Major element oxide, LOI and total concentration values in wt. %. Trace element concentration values in ppm. Major elements determined by ICP-OES and trace elements determined by ICP-MS.

Table G.2. Unpublished geochemical data courtesy of A.N. LeCheminant, A.E. Lalonde and R.E. Ernst from ~1880 Ma Ghost dykes, Morel sills and Mara River sheets in the Slave craton, Canada

Original sample number	LAA95 T118-3A	LAA95 T118-3B	LAA95 T150-1	LAA95 T151-1A	LAA97 T17-1	LAA97 T33-1A	LAA97 T46-1	LAA97 T51-1
Unit	Ghost dykes	Ghost dykes	Ghost dykes	Ghost dykes	Ghost dykes	Ghost dykes	Ghost dykes	Ghost dykes
SiO_2	51.05	47.19	45.98	47.30	46.65	47.94	48.30	50.58
TiO_2	1.83	1.62	1.80	1.13	2.88	2.35	1.34	1.16
Al_2O_3	14.24	12.59	13.56	15.45	12.90	17.69	14.55	14.39
$Fe_2O_3(T)$	9.25	18.41	16.79	14.22	17.88	13.92	13.12	9.46
MnO	0.23	0.22	0.22	0.18	0.25	0.24	0.17	0.18
MgO	8.12	5.37	7.01	7.90	5.90	4.30	7.71	8.32
CaO	9.44	8.58	8.68	8.92	10.47	11.38	11.12	9.75
Na_2O	2.78	2.30	2.85	2.03	2.53	2.24	1.68	2.78
K_2O	1.53	0.96	0.95	0.97	0.86	0.09	0.32	1.55
P_2O_5	0.22	0.17	0.26	0.10	0.15	0.08	0.07	0.22
LOI	1.71	1.82	1.74	2.72	0.92	1.19	2.09	1.50
Total	100.40	99.23	99.85	100.91	101.39	101.42	100.48	99.90
Sc	27.9	45.4	36.3	31.1	48.0	33.8	43.0	28.8
V	302	288	291	256	396	328	221	211
Cr	414	91	216	207	97	79	137	134
Co	67.4	60.2	63.7	59.7	59.0	62.9	68.4	70.7
Ni	6170	86	144	127	40	83	115	129
Cu	55	152	120	149	227	186	114	59
Zn	41	76	71	91	77	92	81	43
Ga	23.2	22.3	23.6	18.8	24.9	22.9	21.9	20.1
Rb	51.7	49.4	16.0	39.3	49.3	32.7	67.7	14.5
Sr	221	203	200	195	167	175	188	223
Y	29.9	28.1	30.3	20.1	45.4	38.7	23.5	16.2
Zr	116.6	111.8	103.9	56.2	159.3	133.8	85.4	55.1
Nb	6.11	5.99	5.06	2.36	8.89	6.95	4.04	2.55
Cs	0.96	0.84	0.61	0.89	1.15	1.43	1.36	0.95
Ba	231	185	60	69	103	120	91	45
La	17.07	18.16	12.57	4.02	18.48	11.95	9.37	4.12
Ce	27.77	26.60	20.28	9.14	32.03	24.29	16.69	9.27
Pr	3.76	3.62	3.12	1.43	4.77	3.69	2.53	1.52
Nd	15.91	15.40	14.54	6.89	21.52	16.87	11.67	7.32
Sm	4.00	3.86	4.07	2.12	5.93	4.73	3.25	2.23
Eu	1.37	1.31	1.36	0.96	1.89	1.55	1.10	0.93
Gd	4.38	4.22	4.50	2.59	6.60	5.40	3.48	2.48
Tb	0.78	0.77	0.81	0.49	1.22	0.99	0.63	0.46
Dy	4.90	4.69	4.93	3.21	7.54	6.23	3.88	2.81
Ho	0.94	0.90	0.93	0.63	1.46	1.20	0.72	0.52
Er	2.81	2.66	2.68	1.88	4.28	3.56	2.12	1.47
Tm	0.43	0.41	0.40	0.30	0.65	0.55	0.32	0.23
Yb	2.77	2.66	2.58	1.93	4.18	3.49	2.02	1.41
Lu	0.43	0.41	0.38	0.30	0.64	0.54	0.31	0.22
Hf	2.84	2.76	2.60	1.36	4.27	3.38	2.14	1.41
Ta	0.32	0.33	0.29	0.14	0.52	0.40	0.23	0.15
Th	2.58	2.40	1.11	0.32	2.39	1.73	0.84	0.29
U	0.45	0.41	0.27	0.09	0.57	0.42	0.18	0.08

Table G.2. contd.

Original sample number	LAA97 T51-3	L658.1	L659.8 A	L665A	L666	L671	L679.8	FA66-030-05
Unit	Ghost dykes	Morel sills	Morel sills	Morel sills	Morel sills	Morel sills	Morel sills	Mara River sheet
SiO_2	52.92	52.65	52.49	49.68	48.71	44.28	46.18	51.26
TiO_2	2.43	0.90	0.90	2.17	0.96	3.68	0.94	0.96
Al_2O_3	14.70	14.54	14.28	11.95	14.76	14.79	15.54	15.34
$Fe_2O_3(T)$	10.78	11.63	11.46	17.23	15.32	15.52	12.40	11.56
MnO	0.26	0.20	0.16	0.26	0.17	0.25	0.18	0.17
MgO	5.88	6.24	5.75	5.93	6.59	7.49	8.81	5.76
CaO	7.87	7.08	8.15	9.71	8.87	11.37	11.32	9.41
Na_2O	2.58	2.44	2.49	2.05	2.48	2.11	1.96	2.24
K_2O	1.82	1.93	1.76	0.41	1.44	0.78	1.08	1.80
P_2O_5	0.11	0.11	0.11	0.27	0.12	0.11	0.06	0.11
LOI	1.32	2.38	2.12	0.14	1.32	1.09	1.01	1.06
Total	100.68	100.12	99.66	99.75	100.74	101.50	99.45	99.66
Sc	29.0	30.9	29.7	40.8	38.7	49.5	39.3	34.6
V	386	223	220	414	234	504	233	258
Cr	147	29	84	98	220	77	28	34
Co	61.6	46.6	48.1	52.3	50.3	59.8	51.8	49.2
Ni	30	115	293	83	368	98	120	110
Cu	93	70	85	212	122	125	133	77
Zn	73	78	53	70	63	61	62	94
Ga	24.4	19.1	20.0	20.9	19.9	21.1	19.9	20.3
Rb	60.9	102.7	59.4	21.6	62.1	11.1	61.9	79.5
Sr	181	203	199	242	203	243	206	213
Y	40.4	24.2	23.7	30.1	25.9	37.6	24.2	25.5
Zr	133.8	126.6	134.4	117.9	134.1	201.8	134.8	128.3
Nb	7.58	7.31	7.58	9.33	7.59	26.16	7.99	7.92
Cs	6.43	1.26	0.95	0.87	2.13	0.54	1.50	2.23
Ba	67	567	499	119	493	159	525	507
La	12.12	31.84	26.90	18.69	47.88	38.08	32.62	34.25
Ce	27.54	52.01	54.38	26.42	54.74	55.52	53.71	53.17
Pr	4.09	6.41	6.62	3.94	6.60	7.72	6.55	6.47
Nd	18.46	23.64	24.37	17.81	24.38	32.45	24.09	23.83
Sm	5.19	4.55	4.67	4.75	4.63	7.33	4.62	4.61
Eu	1.58	1.17	1.26	1.54	1.25	2.29	1.28	1.27
Gd	5.70	4.28	4.28	4.94	4.29	6.97	4.25	4.29
Tb	1.06	0.67	0.70	0.87	0.69	1.15	0.68	0.69
Dy	6.58	3.89	3.97	5.02	4.03	6.47	3.97	4.02
Ho	1.26	0.73	0.75	0.93	0.76	1.17	0.75	0.76
Er	3.65	2.17	2.24	2.65	2.26	3.35	2.21	2.23
Tm	0.55	0.34	0.35	0.40	0.35	0.48	0.34	0.35
Yb	3.60	2.18	2.25	2.55	2.24	3.09	2.21	2.25
Lu	0.55	0.34	0.35	0.40	0.35	0.48	0.35	0.35
Hf	3.62	2.97	3.20	2.98	3.23	4.83	3.30	3.07
Ta	0.45	0.45	0.46	0.52	0.48	1.38	0.48	0.46
Th	2.23	6.04	6.44	1.28	6.64	2.12	6.45	5.82
U	0.53	1.61	1.69	0.38	1.75	0.51	1.73	1.58

Major element oxide, LOI and total concentration values in wt. %. Trace element concentration values in ppm. Major elements determined by ICP-OES and trace elements determined by ICP-MS.